

---

# Design, Synthesis and Applications of Small Molecular Probes in Studying Canonical and Non-Canonical DNA Structures

*A Thesis Submitted for the Degree of*

**Doctor of Philosophy**

*By*

**Nagarjun Narayanaswamy**



**Bioorganic Chemistry Laboratory, New Chemistry Unit  
Jawaharlal Nehru Centre for Advanced Scientific Research  
(A Deemed University)**

**Bengaluru-560064, India**

**July 2015**

---

---

# Design, Synthesis and Applications of Small Molecular Probes in Studying Canonical and Non-Canonical DNA Structures

*A Thesis Submitted for the Degree of*

**Doctor of Philosophy**

*By*

**Nagarjun Narayanaswamy**



**Bioorganic Chemistry Laboratory, New Chemistry Unit  
Jawaharlal Nehru Centre for Advanced Scientific Research  
(A Deemed University)**

**Bengaluru-560064, India**

**July 2015**

---

---

*Dedicated to my parents and APRDC*

---

---

---

## **TABLE OF CONTENTS**

Certificate	I
Declaration	III
Acknowledgements	V
Preface	VII
<b>Chapter 1: Introduction</b>	<b>1</b>
1.1 Primary structure analysis of nucleic acids	4
1.2 Canonical base pairing	6
1.3 Non-canonical base pairing	7
1.4 Secondary structure of nucleic acids	8
1.5 Biological significance of nucleic acids structures	16
1.6 Factors that influence the stability of nucleic acids structures	18
1.7 Nucleic acids-small molecule interactions	20
1.8 Fluorescence probes for canonical and non-canonical DNA structures	27
1.9 Small molecule guided hybrid DNA structures	31
1.10 Our objective	34
1.11 References	36
<b>Chapter 2: A Thiazole coumarin (TC) turn-on fluorescence probe for AT-base pair detection and multipurpose applications in different biological systems</b>	<b>49</b>
2.1 Synthesis of probes <b>TC</b> , <b>CL</b> and <b>TP</b>	53
2.2 Photophysical properties of probes <b>TC</b> , <b>CL</b> and <b>TP</b>	54
2.3 Selective fluorescence enhancement in presence of dsDNA containing AT-base pairs	57
2.4 Concentration dependent study of probe <b>TC</b> in presence of dsDNAs	59
2.5 Gel-electrophoresis study of probe <b>TC</b> in presence of dsDNAs	61
2.6 FRET study between probe <b>TC</b> against Hoechst 33258 in presence of (AT) <sub>20</sub>	62
2.7 Thermal studies of probe <b>TC</b> in presence of dsDNAs	65

---

---

---

2.8	Simulation studies of probe <b>TC</b> binding to dsDNA	66
2.9	Cellular uptake and selective DNA-imaging properties of probe <b>TC</b>	68
2.10	Fidelity of probe <b>TC</b> to dsDNA	70
2.11	Application of probe <b>TC</b> in cell cycle analysis	72
2.12	Cytotoxicity studies of probe <b>TC</b>	73
2.13	Preferential fluorescence staining of malaria parasites	74
2.14	Conclusion	75
2.15	Experimental section	
	General information	77
	Synthetic procedures for probes <b>TC</b> , <b>CL</b> and <b>TP</b>	77
	Sample preparation for UV-vis and fluorescence measurements	79
	Experimental procedures for photophysical and cell imaging studies	80
2.16	References	83

<b>Chapter 3: Sequence-specific recognition of DNA minor groove by an NIR fluorescence switch-on probe and its potential applications</b>	89	
3.1	Synthesis and NIR-activation of probe <b>QCy-DT</b>	94
3.2	Photophysical properties of probe <b>QCy-DT</b>	96
3.3	Switch-on NIR fluorescence of probe <b>QCy-DT</b> in the presence of DNA	99
3.4	Base pair-specific recognition and switch-on fluorescence in the presence of DNA	103
3.5	Binding stoichiometry, affinity and quantum yield of probe <b>QCy-DT</b> for DNA	105
3.6	Mode of AT-rich DNA recognition by probe <b>QCy-DT</b>	108
3.7	Sequence-specific recognition of DNA by probe <b>QCy-DT</b>	112
3.8	Fluorescence imaging, cytotoxicity studies and photostability of probe <b>QCy-DT</b>	115
3.9	Selective staining of <i>Plasmodium falciparum</i> nucleus and toxicity to malaria parasites by minor groove binding probe <b>QCy-DT</b>	118
3.10	Conclusion	119
3.11	Experimental section	
	General information	121
	Synthetic procedure for probe <b>QCy-DT</b>	121
	Sample preparation for UV-vis, fluorescence and CD measurements	122

---

---

Experimental procedures for photophysical and cell imaging studies	122
3.12 References	127

#### **Chapter 4: Spatiotemporal cellular ROS targeting by stimuli responsive NIR**

<b>fluorescence combination probe</b>	135
4.1 H <sub>2</sub> O <sub>2</sub> triggered activation of DNA minor groove binder	140
4.2 Synthesis of <b>QCy-BOH</b>	141
4.3 NMR analysis of H <sub>2</sub> O <sub>2</sub> triggered release of DNA minor groove binder	142
4.4 Photophysical properties of <b>QCy-BOH</b> in presence of H <sub>2</sub> O <sub>2</sub>	143
4.5 Photophysical properties of <b>QCy-BOH</b> in presence of Drew-AT and H <sub>2</sub> O <sub>2</sub>	146
4.6 Probing of <i>in situ</i> generated H <sub>2</sub> O <sub>2</sub> using combination probe <b>QCy-BOH</b> ∩Drew-AT	149
4.7 Fluorescence imaging and cytotoxicity studies of <b>QCy-BOH</b> in presence of H <sub>2</sub> O <sub>2</sub>	154
4.8 Probing of <i>in situ</i> generated H <sub>2</sub> O <sub>2</sub> in live cells using <b>QCy-BOH</b>	156
4.9 Conclusion	157
4.10 Experimental section	
General information	159
Synthetic procedure for <b>QCy-BOH</b>	159
Sample preparation for UV-vis, fluorescence and CD measurements	161
Experimental procedures for photophysical and cell imaging studies	161
4.11 References	163

#### **Chapter 5: Small molecule and proton induced non-canonical DNA-structures and their significance**

Chapter 5a: Molecular beacon based DNA-switch for accurate and reversible pH sensing	171
5.1 Design principle	173
5.2 Photophysical properties of Cy3 and Cy5 labeled DNA-switch	175
5.3 Circular dichroism (CD) studies of DNA-switch	178
5.4 Structural transformation of DNA-switch in vesicles	180
5.5 Conclusion	182
5.6 Experimental section	
General information	183

---

---

Sample preparation for UV-vis, fluorescence and CD measurements	183
FRET efficiency between Cy3 and Cy5 dyes	184
Preparation of vesicles	184
Chapter 5b: Small molecule induced non-canonical secondary DNA structure of alternative guanine-adenine rich sequences	
	186
5.7 Photophysical properties small molecules in presence of deoxyoligonucleotides	188
5.8 Binding stoichiometry of coralyne with d(GA) <sub>6</sub>	192
5.9 Temperature dependent stability and binding kinetics of coralyne with d(GA) <sub>6</sub>	192
5.10 CD studies of coralyne in presence of d(GA) <sub>6</sub>	194
5.11 Effect of sequence length and salt concentration on the stability of coralyne/d(GA) <sub>6</sub>	197
5.12 Discussion	199
5.13 Conclusion	200
5.14 Experimental section	
General information	200
Sample preparation for UV-vis and CD measurements	201
Chapter 5c: Fluorescence reporting of G-quadruplex structures and modulating their DNAzyme activity using polyethylenimine-pyrene conjugate	
	202
5.15 Synthesis of polyethylenimine (PEI)-chromophore conjugates	204
5.16 Photophysical properties of PEI-chromophore conjugates	204
5.17 Preferential fluorescence in presence of G-quadruplex forming sequences	207
5.18 Isothermal titration calorimetry (ITC) measurements of <b>PEI-Py</b> in presence of deoxyoligonucleotides	210
5.19 CD studies of <b>PEI-Py</b> in presence of G-quadruplex structures	211
5.20 DNAzyme activity of <b>PEI-Py</b> in presence G-quadruplex/hemin complex	213
5.21 Conclusion	217
5.22 Experimental section	
General information	217
Synthetic procedure of PEI-conjugates	218
Sample preparation for UV-vis, fluorescence and CD measurements	219

---

---

5.23	References	219
------	------------	-----

**Chapter 6: Exploring canonical and non-canonical hydrogen bonding potential of adenine for construction of hybrid DNA structures** 233

Chapter 6a: Exploring hydrogen bonding and weak aromatic interactions induced assembly of adenine and thymine functionalised naphthalenediimides 235

6.1 Synthesis of naphthalenediimide-nucleobase conjugates 236

6.2 Photophysical properties of **NDI-AA** and **NDI-TT** 237

6.3 Photophysical properties of naphthalenediimide-nucleobase conjugates in presence of molecular clamps 238

6.4 Morphological studies of naphthalenediimide-nucleobase conjugates 240

6.5 NMR analysis of naphthalenediimide -nucleobase conjugates in presence of molecular clamps 242

6.6 Conclusion 244

6.7 Experimental section

General information 244

Synthetic procedures for naphthalenediimide-nucleobase conjugates 245

Sample preparation for morphological studies 247

Chapter 6b: Double zipper helical assembly of deoxyoligonucleotides: mutual templating and chiral imprinting to form hybrid DNA ensembles 249

6.8 Synthesis of adenine appended perylenediimide (**APA**) 249

6.9 Photophysical properties of hybrid DNA ensembles 250

6.10 Circular dichroism studies of hybrid DNA ensembles 252

6.11 Stoichiometry binding of hybrid DNA ensembles 255

6.12 pH effect on the formation of hybrid DNA ensembles 256

6.13 Thermal melting studies of hybrid DNA ensembles 259

6.14 Morphological studies of hybrid DNA ensembles 259

6.15 Theoretical studies of hybrid DNA ensembles 261

6.16 Conclusion 265

6.17 Experimental section

---



---

General information	266
Synthetic procedures for <b>APA</b>	267
Sample preparation for UV-vis, fluorescence and CD measurements	267
6.18 References	269
<b>Appendix</b>	275
<b>List of publications</b>	291

---

## **CERTIFICATE**

*I hereby certify that the work described in this thesis entitled “**Design, Synthesis and Applications of Small Molecular Probes in Studying Canonical and Non-Canonical DNA Structures**” has been carried out by **Mr. Nagarjun N** under my supervision at the Bioorganic Chemistry Laboratory, New Chemistry Unit, Jawaharlal Nehru Centre for Advanced Scientific Research, Bengaluru, India and that it has not been submitted elsewhere for the award of any degree or diploma.*

**Prof. T. Govindaraju**

(Research Supervisor)

## **DECLARATION**

*I hereby declare that the matter embodied in the thesis entitled “**Design, Synthesis and Applications of Small Molecular Probes in Studying Canonical and Non-Canonical DNA Structures**” is the resultant of the investigations carried out by me at the Bioorganic Chemistry Laboratory, New Chemistry Unit, Jawaharlal Nehru Centre for Advanced Scientific Research, Bengaluru, India under the supervision of **Prof. T. Govindaraju** and that it has not been submitted elsewhere for the award of any degree or diploma.*

*In keeping with the general practice in reporting the scientific observations, due acknowledgement has been made whenever the work described is based on the findings of other investigators. Any omission that might have occurred due to oversight or error in judgement is regretted.*

**Nagarjun N**

(Ph D student)

## **ACKNOWLEDGEMENTS**

*First and foremost, I would like to express my sincere gratitude to my research supervisor Prof. T. Govindaraju, Bioorganic Chemistry Laboratory, New Chemistry Unit, JNCASR, for his continued support, motivation, infinite patience and guidance throughout my PhD career. It has been a great privilege and honor to be associated with him.*

*I would like to thank Prof. C. N. R. Rao, FRS, the Chairman, New Chemistry Unit for being the source of inspiration, generous support and encouragement throughout my stay in JNCASR. I also thank him for providing the infrastructure and facilities to carry out my research work.*

*I am thankful to Prof. P. Balaram and Prof. Siddhartha P. Sarma of IISc and Prof. Subi J. George, Dr. Jayanta Haldar and Dr. Sridhar Rajaram of JNCASR for their excellent courses.*

*I would like to thank Prof. Swapan K. Pati, Dr. Pralok K. Samanta, Subhajith, Prof. Tapas K. Kundu, Dr. Manoj Kumar, Dr. Sadhan Das, Prof. U. Deva Priyakumar and Dr. Gorle Suresh, Prof. Suman K Dhar, Dr. Rahul Sharma, Khadija bhanu, Prof. Paturu Kondaiah and Sivakrishna for fruitful collaborations.*

*I would like to thank Academics, Administration and NCU Office staff for their constant help.*

*I am thankful to my wonderful lab mates Dr. Maity, Dr. Avinash, Mr. Pandu, Mr. Shivaprasad, Mr. Rajasekhar, Ms. Suseela, Ms. Malabika, Dr. Madhu, Dr. Chandrasekhar, Dr. Sangita, Ms. Manju, Ms. Shilpa, Mr. Anand, Mr. Sandeepa, Mr. Manjunath, Mr. Sarkar, Dr. Atul and Dr. Sasi Kumar for their help and friendly environment in lab. I would like to thank POCE and SRF students, Vikas, Puja, Vinotha, Tandriila, Mona, Ananya and Chandrasekhar.*

*I am very much grateful to Sri. Vishwanatham Shetty garu for his inspirational chemistry teaching which motivated me to take up chemistry as the subject of my higher study and research career.*

*It is indeed a great pleasure to express my sincere thank to my APRDC, Nagarjuna Sagar for the most memorable moments of life.*

*It is great privilege to express my heartfelt regards to all my teachers during the entire tenure of my educational career especially all the faculty members of School of Chemistry, University of Hyderabad and all the lecturers of Andhra Pradesh Residential Degree College (APRDC).*

*My cordial thanks to my APRDC seniors Eshwar, Bharani Shashank, Sandeep and friends Satya, Omkar and Moses for their support from my college days onwards. I specially thank to all my friends from school, intermediate, degree, M.Sc and JNC friends (especially my jaffa-friends) for their unforgettable company throughout my academic life. I cannot imagine my life without their support and encouragements. Thank you all.*

*I thank JNCASR Library, Comp Lab, Hostel, and Health Center for providing and maintaining the various facilities that have helped me immensely.*

*Finally and most importantly, I am grateful to my family, especially my parents and brothers for their love, moral support and constant encouragement throughout my life. Their love, blessings and affection made me what I am today. This thesis is a minor recognition to my parents for their love and support.*

## PREFACE

This thesis has been divided into six chapters which cover summary on the role of DNA in chemistry, biology and materials science, small fluorescence probes to study canonical DNA structures and their biological utility, and exploiting non-canonical hydrogen bonded interactions among nucleobases to create small molecule templated novel hybrid DNA systems with functional properties.

*First chapter* gives an overview of basic structural information on canonical (Watson-Crick) (A, B and Z-DNA) and non-canonical hydrogen bonded [H-DNA, G-Quadruplex, I-motif, A-motif and poly d(GA)<sub>n</sub> duplex] nucleic acids structures and their biological significance. The unique molecular recognition, persistence length and size of DNA inspire researchers to create novel molecular architectures for numerous applications in biology and material science. Hence, it is crucial to understand the significance of canonical and non-canonical hydrogen bonding interactions among nucleobases in creating such molecular architectures. In this context, we use fluorescence probes and nucleobase conjugates as tool box to exploit canonical and non-canonical hydrogen bonding interactions for understanding and creating novel DNA systems for numerous applications in biology and material science.

*Second chapter* deals with the development of AT-base pair selective red fluorescence DNA probe for multiple biological applications. We have designed three hemicyanine based probes such as **TC**, **CL** and **TP** and studied their interactions with DNA. **TC** showed strong fluorescence enhancement in the presence of DNA containing AT-base pairs over GC-rich DNA, single stranded DNA, RNA and proteins. The fluorescence staining of HeLa S3 and HEK 293 cells with **TC** revealed selective staining of DNA in the nucleus over the cytoplasmic region without RNase treatment. Further, cell cycle analysis, metaphase chromosome and malaria parasite DNA imaging studies confirm the *in vivo* diagnostic and possible therapeutic applications of probe **TC**.

In *third chapter*, we present sequence-specific recognition of AT-rich DNA minor groove by switch-on NIR fluorescence probe **QCy-DT**. The minor groove recognition is preferred as it circumvent probe induced structural changes and artifacts in the DNA by intercalators. This works give the glimpse of sequence-specific recognition of DNA containing 5'-A(AATT)T-3'

sequences with strong fluorescence enhancement. Subsequently in *fourth chapter*, we introduce stimuli responsive NIR fluorescence-based minor groove binder **QCy-BOH**.

*Fifth chapter* outline the small molecule and pH promoted secondary structures of oligonucleotides supported by non-canonical hydrogen bonding interactions. Herein, the *first subchapter* deals with reversible structural transition of adenine-rich molecular beacon (**LMB**) induced by non-conical hydrogen bonding interactions for accurate and sensitive reporting of pH in the range of 3-4. In the *second subchapter*, we show the structural transitions of poly d(GA)<sub>n</sub> sequence from random coil to ordered secondary structure in presence of small molecules. In the *third subchapter*, we discuss preferential fluorescence reporting of non-canonical G-quadruplex structure using polyethylenimine-pyrene conjugate (**PEI-Py**). We also demonstrate the modulation of DNAzyme activity of G-quadruplex/hemin complex. Overall, this chapter highlights the use external agents induced structural transitions of A-rich and GA-rich sequences through the non-canonical A-A and A-G base pairing interactions and selective reporting of G-quadruplex structure with modulation of DNAzyme activity.

*Sixth chapter* demonstrate the potential of arylenediimide-nucleobase conjugates to template oligonucleotides to form hybrid DNA systems. In the *first subchapter*, we present adenine and thymine conjugated naphthalene diimides (**NDI-AA** and **NDI-TT**) and their interactions with molecular clamps. In *second subchapter*, we discuss versatility of adenine in forming complementary and non-complementary hydrogen bonding with other nucleobases. Subsequently, adenine conjugated perylenediimide (**APA**) was employed as molecular template to produce novel hybrid DNA ensembles. These studies reveal the use of canonical (A-T) and non-canonical (A-A and A-G) hydrogen bonding interactions to produce stimuli responsive and well-ordered molecular architectures (hybrid DNA ensembles) for biotechnological applications.

In summary, the fundamental and structural aspects of canonical and non-canonical DNA structures and objective of the work is presented in the introduction chapter. The second, third and fourth chapters describe the development of fluorescence probes for various *in vitro* and *in vivo* applications in living cells. The fifth and sixth chapters demonstrate the importance of small molecular templates to bring about structural transitions of single stranded DNA and creating novel DNA systems with functional properties.

---

# Chapter 1: Introduction



Deoxyribonucleic acid (DNA) is one of the essential biomacromolecules, store and transmit genetic information and thereby play a vital role in most of the biological processes in living organisms. In 1869, Friedrich Miescher isolated the phosphorous-containing substance from the human pus cells which he termed as “*nuclien*” subsequently the term evolved into current form *i.e.*, *nucleic acids*.<sup>1</sup> Oswald Avery, Colin MacLeod and Maclyn McCarty proposed DNA to be the carrier of genetic information and not the proteins.<sup>2</sup> Later, Alfred Hershey and Martha Chase showed that DNA is the genetic material and then DNA draw attention of the scientific community to find its structure. Initially, Levene and Jacobs proposed a cyclic structure for DNA where four nucleotides connected in large ring with phosphodiester linkage.<sup>3,4</sup> In 1950, Erwin Chargaff discovered the *complementary base-rule* which states that equimolar base ratios (*i.e.* the number of guanines are equal to the number of cytosines, and the number of adenines are equal to the number of thymines).<sup>5</sup> First X-ray diffraction pattern seen by William Astbury identified DNA as having a regular structure.<sup>6</sup> Based on the X-ray fiber diffraction data from Rosalind Franklin and Maurice Wilkins, in 1953 Francis Crick and James Watson proposed antiparallel right handed double helical structure for DNA.<sup>7-9</sup> Finally, in 1962 Francis Crick and James Watson received the Nobel prize in physiology or medicine for their phenomenal discovery of double helical DNA-structure along with Maurice Wilkins.

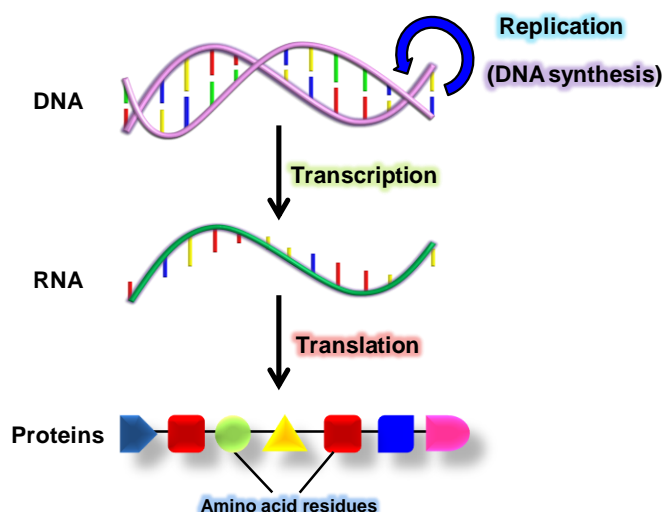


**Figure 1.** Schematic view of information flow from DNA (deoxyribonucleic acid) to RNA (ribonucleic acid) to proteins. Replication process represents the synthesis of DNA, RNA synthesized from DNA through the transcription process and followed by translation process for the synthesis of proteins from RNA.

Soon after the discovery of DNA structure, enormous effort was devoted by the scientific community to understand the role of DNA in molecular biology. Now, we know that DNA is responsible development, function, reproduction and heredity of most of the life forms through genetic information flow from one generation to the next generation. All the genetic information that encoded in DNA is transformed through the replication process in which parental DNA synthesizes its own copies of new daughter DNA strands. Further, DNA is transcribed to mRNA in the cell nucleus, mRNA further translated to proteins in the cytoplasm (Figure 1).<sup>10</sup> The translated proteins are the work horse of the cell and responsible for all the biological processes including growth, metabolizing food, fight against infections among many other physiological functions, to sustain the life.

### 1.1 Primary structure analysis of nucleic acids

Nucleic acids (DNA: deoxyribonucleic acid and RNA: ribonucleic acid) are long polymers consists of repeating units of nucleotides with variable nucleobases. The combination of sugar and nitrogenous base (nucleobase) together called as *nucleoside* and adding a phosphate group to the nucleoside is called as *nucleotides* (Figure 2). In general, nucleotide composed of three primary units 1) nucleobase, 2) pentose sugar (ribose in RNA and 2-deoxyribose in DNA) and 3) phosphate group.

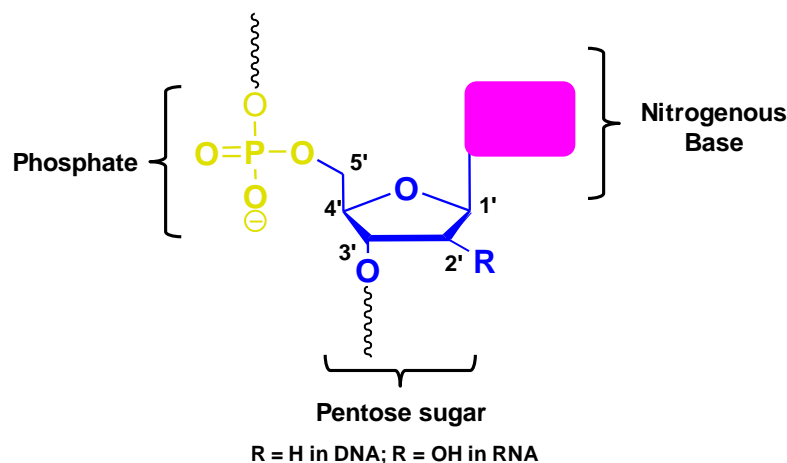


**Figure 2.** Molecular structure of nucleotide in DNA and RNA.

Nucleobases are of two types namely purine and pyrimidine bases. Adenine (A) and guanine (G) are bicyclic purine bases whereas thymine (T) and cytosine (C) are monocyclic

pyrimidine bases (Figure 3). Adenine, guanine and cytosine are found in both DNA and RNA. However, thymine (T) mainly found in DNA while uracil (U) specific to RNA. These nucleobases are connected through the  $N^1$ -position (pyrimidines) and  $N^9$ -position (purines) to the sugar via  $\beta$ -glycosidic bond at C1' position. The rotation around  $N$ -glycosidic bond between the base and sugar moiety results in *syn*- and *anti*-conformation. In *syn-form* nucleobase is placed above the sugar moiety where as in *anti-form* base is turned away from the sugar moiety (Figure 4).

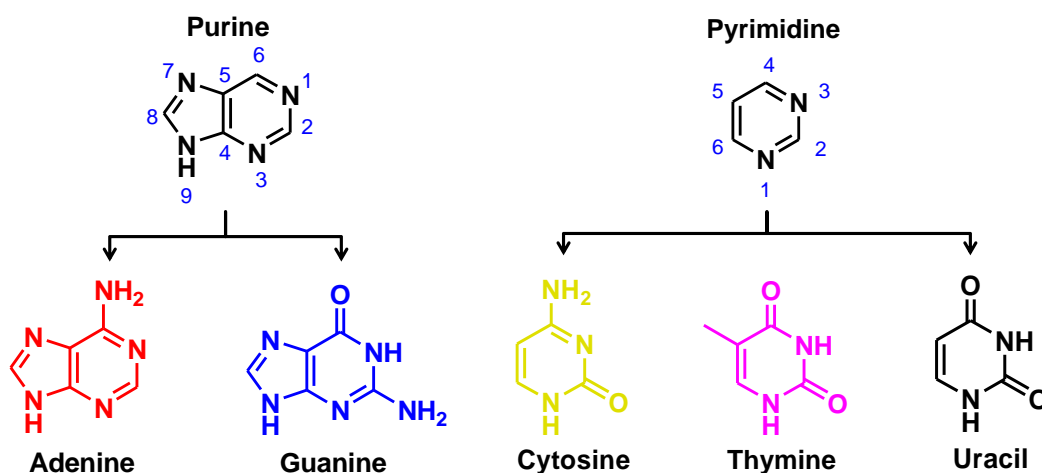


**Figure 3.** Molecular structure of nucleobases adenine (A), guanine (G), cytosine (C), and thymine (T) in DNA. Uracil (U) exists in RNA in place of thymine (T).

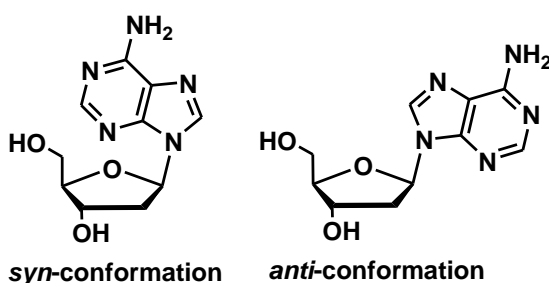


**Figure 4.** Schematic view of *syn*- (left) and *anti*-conformations (right) for the 2-deoxyadenosine.

2-Deoxyribose is the common D-sugar form that exists in DNA in puckered conformation. The *puckered* conformation of sugar helps in minimizing the non-bonded interactions (van der Waals) and maximizing the hydrogen bonding interactions of nucleobases.<sup>11</sup> The puckered conformations are identified based on the displacement of C2'

and C3' carbon atoms from the C1'-O4'-C4' plane (Figure 5). In solution, C2'-*endo* and C3'-*endo* conformations are in equilibrium with separation energy of less than 2 to 5 kJ/mol. Normally, C2'-*endo* conformation seen in B-DNA and C3'-*endo* seen in A-DNA/RNA and both are seen in Z-DNA.<sup>12</sup> Phosphate-group bridges the nucleosides through the phosphodiester bonds between the 5'-OH of the one nucleoside and 3'-OH of the other nucleoside.

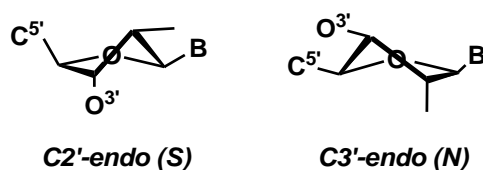


**Figure 5.** Structures of C2'-*endo* (S) and C3'-*endo* (N) preferred sugar puckered conformation in nucleotides.

## 1.2 Canonical (Watson-Crick) base pairing

Masson Gulland was the first person to propose the existence of hydrogen bonds between the nucleotides in single chain or in adjacent chain by linking the purine–pyrimidine hydroxyl groups and some of the imino groups.<sup>12</sup> Based on this concept while proposing DNA structure Watson had tried various possible hydrogen bonding patterns from enolic-tautomeric forms of nucleobases for pairing including homo and hetero base pairs (Figure 6).

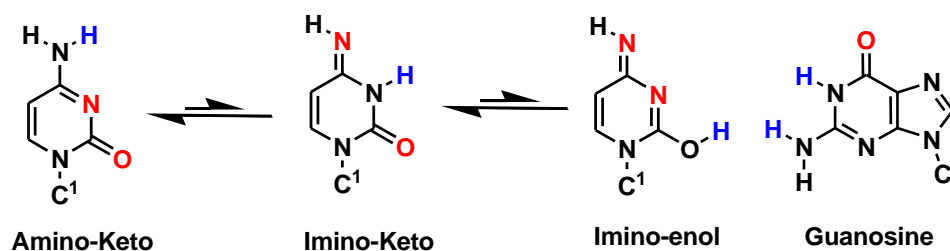


**Figure 6.** “Keto-enol” tautomeric equilibria of 2-deoxycytidine (left) and structure of guanosine.

However, Crick rejected such hydrogen bonding models due to the symmetry of B-DNA and violation of Chargaff’s rule of 1:1 base ratios between purine and pyrimidines. Based on the advice of Jerry Donohue, Watson changed the tautomeric forms to keto forms

of guanine and thymine bases.<sup>13,14</sup> Then, simple correlation was found involving two hydrogen bonds between adenine and thymine or three hydrogen bonds between guanine and cytosine base pairs (Figure 7). According to Watson-Crick (WC) base pairing, adenine and thymine forms the two hydrogen bonded base pair through the hydrogen donors ( $N^6$  of A and  $N^3$  of T) of each base to electronegative atoms  $N^1$  of adenine and  $O^4$  of thymine. Similarly, guanine and cytosine forms three hydrogen bonded base pair through the hydrogen donors ( $N^1$  and  $N^2$  of guanine and  $N^4$  of cytosine) of each base to electronegative atoms  $O^2$  and  $N^3$  of cytosine and  $O^6$  of guanine to complete base pair pattern. These hydrogen bonding patterns in nucleic acids are well supported by X-ray crystallography and NMR spectroscopy analysis. Similar hydrogen bonding patterns also observed in RNA where uracil (U) has present in place of thymine (T). In a typical WC base pairing, the distance between heteroatoms involved in hydrogen bonding (N-N and N-O atoms) ranges from 2.8-2.95 Å with average strengths of 6-10 kJ/mol.<sup>12</sup>

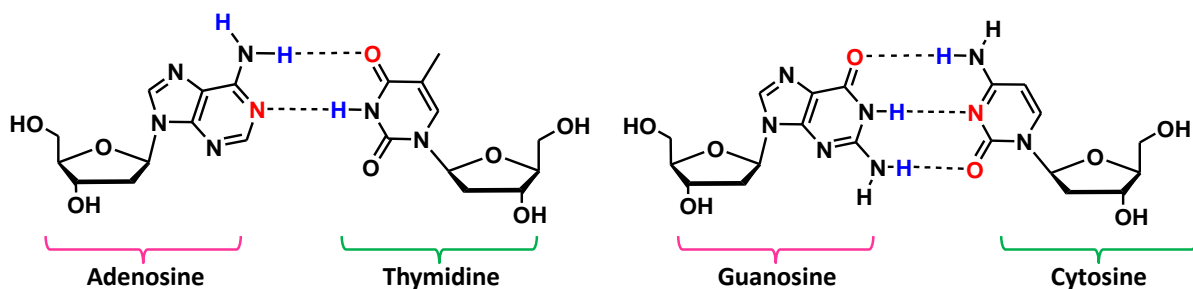


**Figure 7.** WC base pairing interactions of complementary nucleobases. **A=T** base pair with two hydrogen bonds (left) and **G≡C** base pair with three hydrogen bonds (right) between nucleosides.

### 1.3 Non-canonical (Non WC) base pairing

Apart from WC base pairing, non-canonical base pairing interactions play an important role in the stabilization of higher order secondary structures of DNA and RNA.<sup>15</sup> In WC base pairing, adenine always forms complementary hydrogen bonding with thymine and guanine forms hydrogen bonding with cytosine. Normally, pairing geometry of nucleobases depends on the hydrogen bonding interactive site and orientation of glycosidic bond. Generally, purine bases have two types of hydrogen bonding interactive sites of which one is WC site which involves hydrogen bonding interactions involving  $N^1$  and  $N^6-H$  positions of adenine and  $N^1-H$ ,  $N^2-H$  and  $O^6$  positions of guanine nucleobase. The other type is Hoogsteen (HG)

site which involves  $N^6$ -H and  $N^7$  positions of adenine,  $O^6$  and  $N^7$  positions of guanine nucleobases in hydrogen bonding with both complementary (T and C) and non-complementary (A, G and homo-base pairing) nucleobases (Figure 8a). In non-canonical base pairing motifs, nucleobases might involve at least two hydrogen bonds including reverse WC, HG and Wobble (mismatch pair U-G or A-I in RNA; I = Inosine) base pairs (Figure 8b and 8c). Self-assembly of nucleobases is governed by hydrogen bonding interactions, where one nucleobase can form hydrogen bonding with any nucleobase (complementary and non-complementary like A-G, U-G, T-G) and also have ability to form homo-base pairs (A-A, G-G, C-C).<sup>15</sup> Especially, under specific physiological conditions adenine, guanine and cytosine are able to form homo-base pairing interactions results in the formation of A-motif, G-quadruplex and *i*-motif secondary structures respectively (The detailed hydrogen bonding modes are described in following sections).

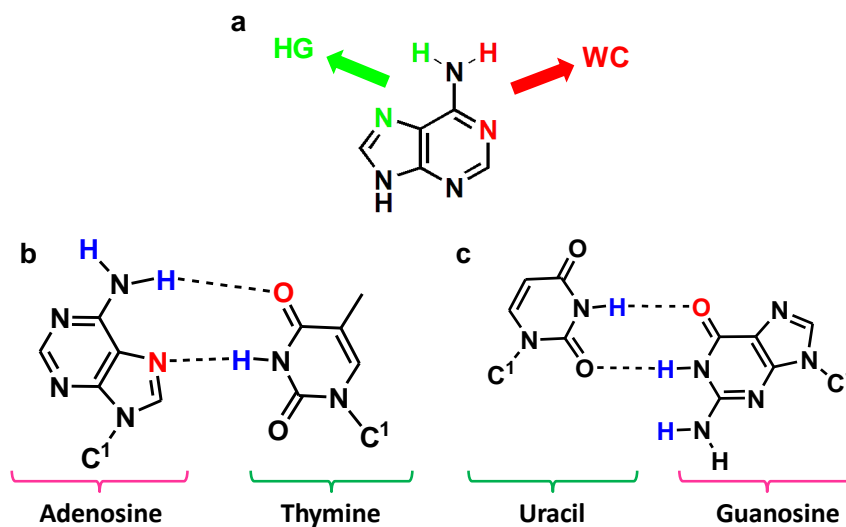


**Figure 8.** (a) Schematic view of WC and Hoogsteen (HG) hydrogen bonding interactive sites of adenine (purine bases). (b) HG base pairing interaction of A:T base pairs. (c) Wobble base pairing interaction of U:G base pairs.

#### 1.4 Secondary structure of nucleic acids

Typical complementary and non-complementary hydrogen bonding ability of nucleobases allows nucleic acids to fold into various canonical and non-canonical secondary structures. These secondary structures include canonical hydrogen bonded duplex, hairpin and non-

canonical hydrogen bonded homoduplex A-motif, poly d(GA)<sub>n</sub> homoduplex, H-DNA, G-quadruplex and *i*-motifs. All these secondary structures of nucleic acids have their own structural and biological significance.

**1.4.1 Duplex DNA.** DNA is made of two long polymeric chains held together by hydrogen bonding interactions in an antiparallel direction.<sup>7</sup> The backbone of each long polymer of the helix is constructed from alternating sugar and phosphate backbone residues. In antiparallel helical structure of DNA, nucleobases are in *anti*-conformation which makes the hydrogen bonding face of nucleobases projected away from the sugar moiety. This conformation allows the negatively charged phosphate groups pointing outside and makes them easily accessible to polar media whereas the hydrogen bonded faces of nucleobases points inside and creates hydrophobic cavity.

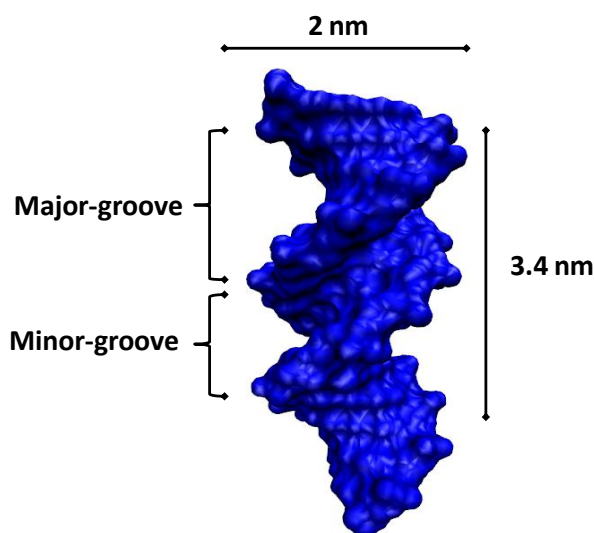


**Figure 9.** View of major and minor grooves of B-DNA duplex. (Model structure of duplex formed by the self-complementary sequence 5'-GCGCAAATTTGCGC-3', known as Drew-AT). Typical dimensions of helical pitch and width are indicated. (Adapted from: <http://structure.usc.edu/make-na/server.html>)

In antiparallel mode, two long polymers twist each other to form right handed helix and create gaps between each set of phosphate backbones. The gap between the phosphate backbone result in formation of grooves with different depth and width namely major or minor grooves (Figure 9). The major groove is wider than minor groove in typical B-DNA

double helix. The relative dimensions of major and minor grooves depend on base pair orientation, displacement and sequence.<sup>16</sup> Minor groove of G-C rich sequences is always wider than A-T rich sequence and in A-T rich sequences groove width varies in the range of 3-4 Å. Moreover, edges of base pairs and sugar-phosphate back bones of the walls of the both major and minor grooves are crucial for the recognition of proteins and small molecules.

DNA mainly exists in three different conformations, namely A-, B- and Z-DNA (Figure 10). Depending on water content, they can exist in hydrated and non-hydrated forms. The hydrated form is called as B-DNA, non-hydrated is called as A-DNA. Conversion of hydrated form (B-DNA) to non-hydrated form (A-DNA) was first observed by Rosalind Franklin from the X-ray analysis pattern.<sup>9</sup> The unusual Z-DNA conformer occurs at high salt concentration preferably in alternating poly (dG-dC)<sub>n</sub> sequences.<sup>17</sup> One of the common feature in all these conformations is their helical structure. A- and B-DNA conformers adapt right-handed helices and Z-DNA conformer adapts left-handed helical structure.

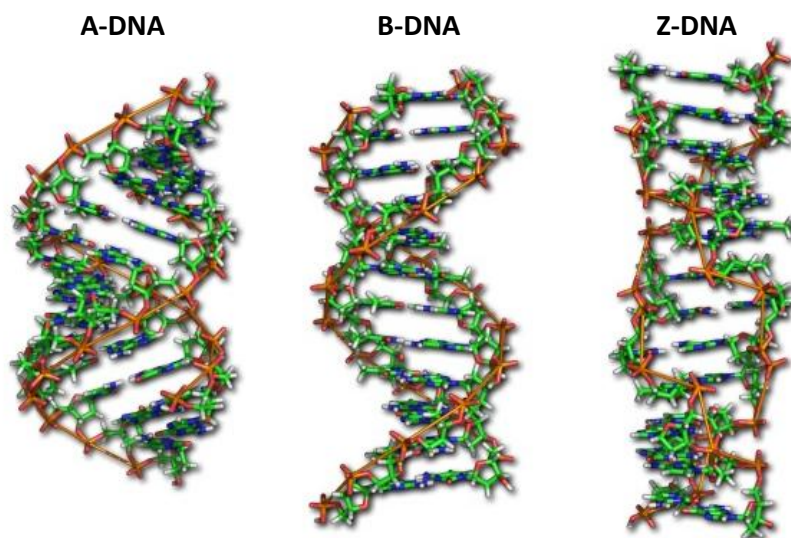


**Figure 10.** A-, B- and Z- forms of DNA duplex.<sup>18</sup>

Typically, B-DNA contains wider major and narrow minor groove with 10 bases per helical turn and 3.3-3.4 Å distance between the base pairs (Figure 9). Interestingly, A-DNA contains 11 bases per helical turn and the major groove is narrow and deep and the minor groove is broad and shallow which is opposite to B-DNA form. The distance between the base pairs in A-DNA is 2.6 Å. However, Z-DNA contains completely different features like



the major groove has a convex surface and the minor groove adapts a narrow and deep and distance between the base pairs is 3.7 Å. One more common difference between B-DNA and A-DNA is sugar pucker mode. Sugar exists in C2'-*endo* and C3'-*endo* pucker mode in B-DNA and A-DNA respectively and both pucker modes exist in Z-DNA. The structural features of all three conformations are summarized in Table. 1

**Table 1.** The characteristic parameters of A-, B- and Z-forms of DNA duplex.

Characteristic	A-DNA	B-DNA	Z-DNA
Conditions require to produce structure	75% water	92% water	Alternating purine and pyrimidine bases
Helix direction	Right-handed	Right-handed	Left-handed
Average base pairs per turn	11	10	12
Rotation per base pair	32.7°	36°	-30°
Distance between adjacent bases	2.6 Å	3.4 Å	3.7 Å
Diameter	2.3 nm	1.9 nm	1.8 nm
Overall shape	Short and wide	Long and narrow	Elongated and narrow

**1.4.2 Hairpin conformation.** Hairpin is a distinctive and important DNA-conformation, in which the ends of single stranded DNA are complementary to each other to form duplex structure while the central portion remains as single stranded but in the form of bent loop (Figure 11). Hairpin can switch between open and closed conformations.

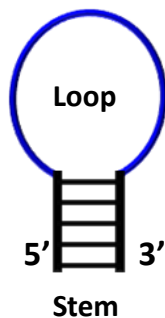


**Figure 11.** DNA-hairpin (molecular beacon) structure with single stranded loop and stem in the duplex form.

Recently, these hairpin structures are conjugated with chromophores (e.g., donor and acceptor fluorophores for FRET-based measurements) at the 5'- and 3'-ends and studied their structural transitions. Chromophore conjugated hairpins are called as molecular beacons (MB).<sup>19</sup> Depending on the target sequence or external stimuli, it switches between closed- and open-states and such structural transition leads to alterations in the proximity of donor and acceptor fluorophores.

**1.4.3 Poly (dA)<sub>n</sub> homoduplex (A-motif).** Most of the structural studies on nucleic acids revealed that nucleobases exists in WC base pairing interactions in all the three conformations (A, B and Z) of DNA. Later, it has been found that synthetic homopolymers of DNA and RNA generate unusual conformations with non-WC (non-canonical) base pairing interactions. Interestingly, Fresco and Rich have found that poly (rA)<sub>n</sub> exists in parallel right handed homoduplex conformation under acidic conditions, known as pi-helix.<sup>20,21</sup>

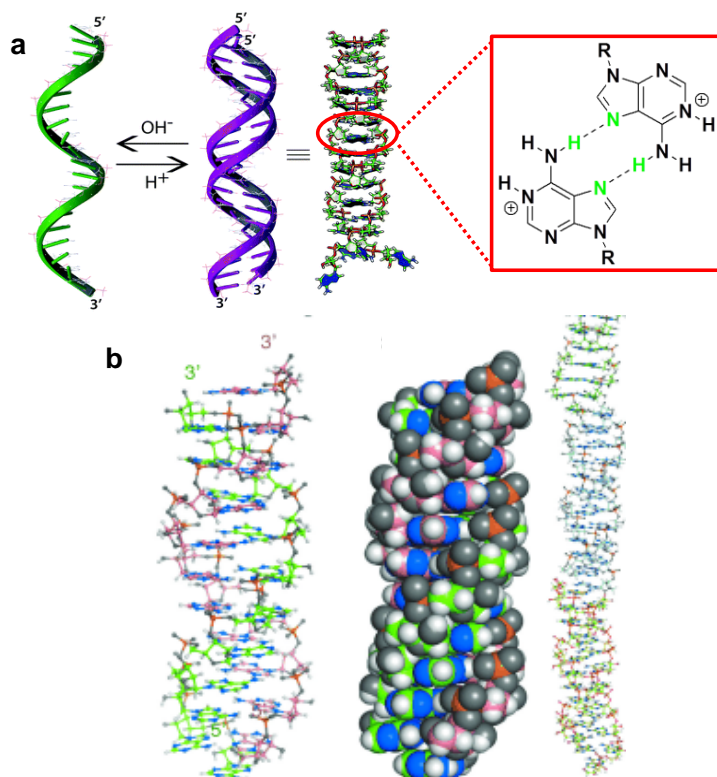


**Figure 12.** (a) pH induced structural transition of random coiled poly (dA)<sub>n</sub> to non-canonical right handed parallel homoduplex structure (A-motif). *Inset:* show the reverse HG [AH<sup>+</sup>-H<sup>+</sup>A] base pairing interactions between protonated adenines.<sup>26</sup> (b) X-ray crystal structure of poly (rA)<sub>11</sub> duplex show the formation of right handed parallel A-motif structure.<sup>25</sup> Adapted from Ref. 25 and 26.

Subsequently, it was also found at neutral pH that poly (rA)<sub>n</sub> exists in ordered single stranded helix with nine nucleotides per turn.<sup>22,23</sup> This characteristic helix of poly (rA)<sub>n</sub> have specific interactions with proteins called poly (rA) binding proteins (PABPs), which can distinguish the adenine-rich RNA over random coil ssRNA. Recently, Yamuna Krishnan and coworkers have showed the formation of right-handed parallel homoduplex of poly (dA)<sub>n</sub> under acidic conditions using NMR spectroscopy and thermal denaturation studies (Figure 12a).<sup>24</sup> Under acidic conditions, the protonation of *N*<sup>1</sup> position of adenine triggers the formation of right handed parallel homoduplexes of poly (dA)<sub>n</sub> held together by AH<sup>+</sup>-H<sup>+</sup>A reverse HG hydrogen bonding and electrostatic interactions with phosphate backbone.<sup>24</sup> Safaee *et al.* have got the ordered single crystal of poly (rA)<sub>11</sub> duplex with 1 Å resolution in presence of ammonium ions which showed the existence of reverse HG hydrogen bonding between the adenine-adenine base pairs along with electrostatic interactions with phosphate backbone (Figure 12b).<sup>25</sup>

**1.4.4 d(GA)<sub>n</sub> homoduplex.** The polymorphic nature of DNA mainly depends on the sequence and external or specific physiological environmental conditions. For example depending on water content, DNA can exist in hydrated B-DNA and dehydrated A-DNA conformations.<sup>9</sup> Alternating poly (dG-dC)<sub>n</sub> sequence is able to transform from right handed B-DNA conformation to left handed Z-DNA conformation depending on salt concentration.<sup>17</sup> Similarly, poly d(GA)<sub>n</sub> is a peculiar sequence and highly polymorphic in nature. Depending on the salt, pH and temperature conditions it can exist in various structural conformations like parallel, antiparallel and single stranded conformations.<sup>27-33</sup> At neutral pH and in presence of MgCl<sub>2</sub> (10 mM), d(GA)<sub>7</sub> exists in parallel homoduplex conformation and the obtained duplex was stable over pH range 4-9.<sup>30</sup> In parallel conformation, d(GA)<sub>n</sub> is right handed helix and constituted of alternating symmetrical G<sub>syn</sub>-G<sub>syn</sub> and A<sub>anti</sub>-A<sub>anti</sub> base pairs with *N*<sup>1</sup>-H...*O*<sup>6</sup> and *N*<sup>6</sup>-H...*N*<sup>7</sup> hydrogen bonds, respectively. However, at neutral pH and in presence of Zn<sup>2+</sup> ions d(GA)<sub>20</sub> exist in antiparallel conformation.<sup>33</sup> Interestingly, same sequence exists in ordered single stranded (intramolecular helix) form under pH < 6 conditions in presence of Na<sup>+</sup> (10 mM).<sup>31</sup> Under acidic conditions, the protonation of adenine *N*<sup>1</sup>-position leads to the formation of electrostatic interactions with phosphate backbone.

**1.4.5 Triplex (H-DNA).** Among nucleobases, purines are distinct from the pyrimidines due to their inherent ability to form hydrogen bonding interactions through WC and HG sites.

This special ability of purines drives the recognition of duplex B-DNA by another additional single stranded DNA through the HG base pairing interactions.<sup>34-37</sup> HG base pairing is possible in two ways *i.e.*, parallel and antiparallel directions. In parallel or *pyrimidine binding* motif, the third strand (homopyrimidine strand) forms the parallel HG base pairing with polypurine strand of duplex DNA through  $\underline{C}^+-GC$  or  $\underline{T}-AT$  base triplets (Figure 13).<sup>38,39</sup> In antiparallel or *purine binding* motif, the third strand (homopurine strand) forms reverse HG base pairing with duplex DNA and the third strand is antiparallel to polypurine strand through  $\underline{G}-GC$  or  $\underline{A}-AT$  base triplets (Figure 13).<sup>35</sup>

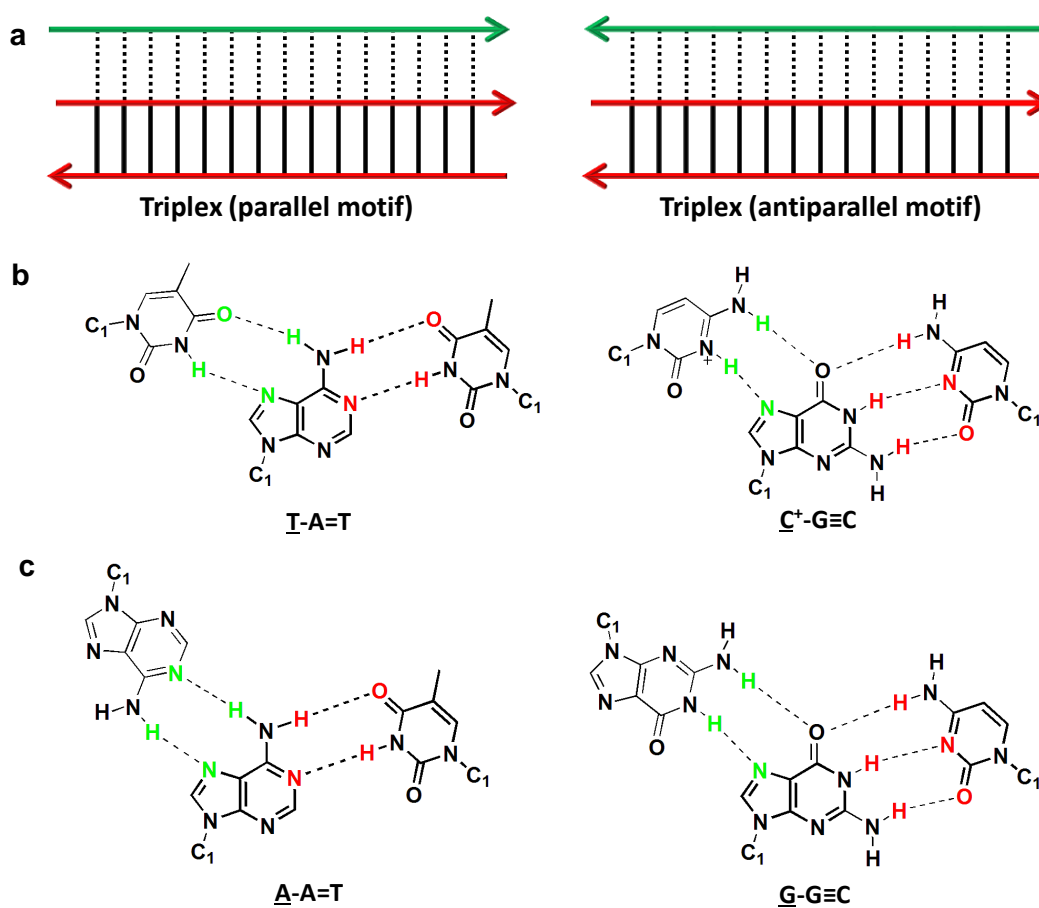


**Figure 13.** Triplex DNA structures. (a) View of parallel and antiparallel triplex structures. Dotted line represents the HG base pairing and thick line represents the WC base pairing interactions of nucleobases. (b) Hydrogen bonding patterns of nucleobases in parallel triplex structure. (c) Hydrogen bonding patterns of nucleobases in antiparallel triplex structure.

**1.4.6 G-quadruplex DNA.** Four-stranded G-quadruplex is a classic example of non-canonical secondary DNA structure that formed by the G-rich sequences.<sup>40-42</sup> Normally, G-

quadruplex structures are formed by the stacking of square tetrads of guanine bases through HG hydrogen bonding at  $N^1-O^6$  and  $N^2-N^7$  positions (Figure 14). Further, these square tetrads of G-quadruplexes are stabilized by the  $\pi$ - $\pi$  stacking and electrostatic interactions of mono- and divalent cations with  $O^6$  lone pairs of guanines. G-quadruplex DNA structures are highly polymorphic in nature and depending on the number of strands, relative orientation of strands and cations these structures exist in various conformations. G-quadruplex structures may be classified into uni, bi and tetra molecular structures depending on number of strands required for forming the G-quadruplex structure.

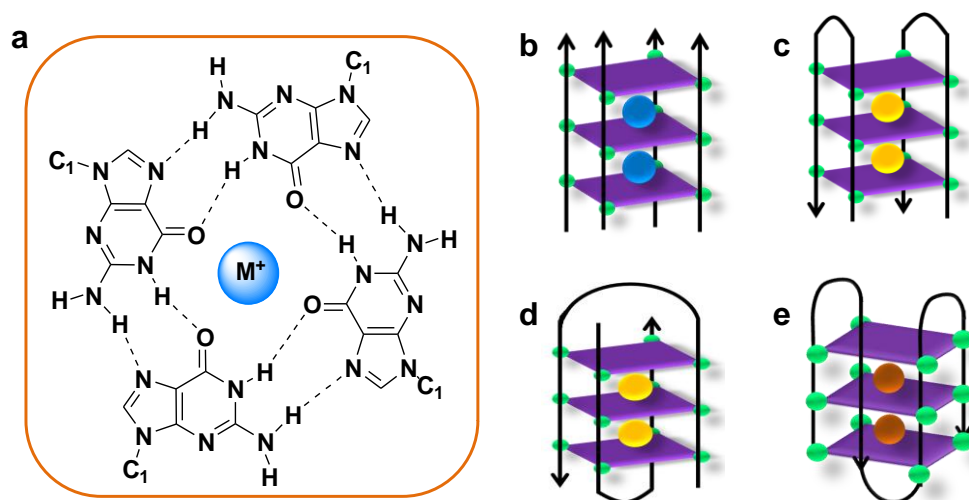


**Figure 14.** G-quadruplex structure. (a) HG hydrogen bonding interactions of guanine to form the square tetrad complex. (b-e) Various forms of G-quadruplex structures, b: tetra molecular parallel stranded G-quadruplex; c: bimolecular parallel stranded G-quadruplex formed from hairpin dimerization with edgewise loops; d: bimolecular antiparallel G-quadruplex with diagonal loops; and e: a unimolecular antiparallel G-quadruplex structure.

The relative orientation (5' to 3' directionality) of DNA strands with one another leads to various possible conformations. Typically, in parallel G-quadruplex structures all four strands are in the same direction, in mixed hybrid G-quadruplex structure three strands are in one direction and the fourth in the opposite direction and in anti-parallel G-quadruplex structures two strands are in one direction and the other two are in the opposite direction (Figure 14b-e).<sup>41,42</sup>

**1.4.7 *i*-Motif DNA.** *i*-Motif is a four stranded DNA structure formed by the cytosine (C) rich containing sequences which are complementary to G-quadruplex forming sequences.<sup>43,44</sup> Under acidic conditions ( $\text{pH} \leq 6$ ) cytosine residues undergo protonation at  $N^3$ -position ( $\text{pK}_a \sim 4.2$ ) and drives the formation of  $\text{C}-\text{C}^+$  base pair. The resulted  $\text{C}-\text{C}^+$  base pairing leads to the conformational change from a random coil structure to non-canonical tetraplex structure with promising stability. In contrast to G-quadruplex structure, *i*-motif consists of tetraplex structure with two interweaving ladders held together with  $\text{C}-\text{C}^+$  bonds (Figure 15). The intriguing property of folding and unfolding nature of *i*-motif structure inspired the design of various pH-based DNA sensors.<sup>45,46</sup>

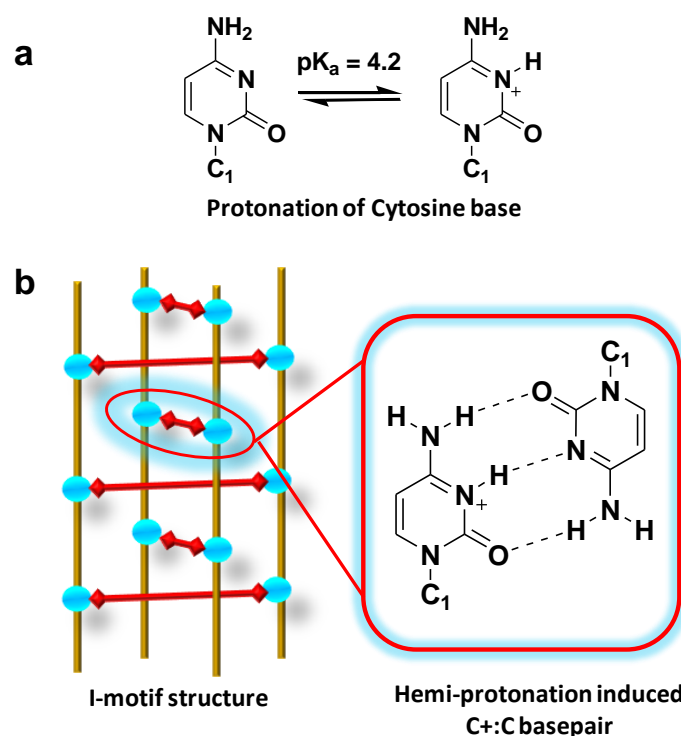


**Figure 15.** *i*-Motif structure. (a) The equilibrium between cytosine and protonated cytosine under acidic conditions. (b) View of tetramolecular *i*-motif structure. *Inset:* the cytosine-cytosine base pair involved in *i*-motif formation.

## 1.5 Biological significance of canonical and non-canonical hydrogen bonded nucleic acids structures

DNA stores the genetic information responsible for development, function and reproduction in most of the living organisms and therefore all the cellular processes are directly or

indirectly associated with DNA. Among three DNA polymorphic conformations, B-DNA is the most stable and abundant DNA polymorph found in physiological conditions and accountable for most of the biological functions associated with DNA. Z-DNA (left handed) is another polymorph of duplex DNA, known to prevent the reformation of nucleosomes and thereby stimulates the transcription.<sup>47,48</sup> Recently, it has been found that the sequence which has propensity to switch between B-DNA to Z-DNA exists near the transcription start sequences.<sup>49</sup> In contrast to B- and Z-DNA, A-DNA is high energetic polymorph it does not exist under physiological conditions but has been observed in ternary complex of DNA and polymerase beta.<sup>50,51</sup> Interestingly, under certain physiological conditions repetitive DNA sequences are known to fold into various non B-DNA conformations including hairpin, poly (dA)<sub>n</sub> homoduplex (A-motif), poly d(GA)<sub>n</sub> homoduplex, triplex (H-DNA) and tetraplexes.<sup>15,26,52</sup> These non B-DNA (non-canonical) structures may affect gene metabolism and plays crucial role in certain biological processes. For example, single stranded poly (rA)<sub>n</sub> is a tail component of mRNA in all eukaryotic cells which plays a vital role in stability of mRNA and initiation of translation.<sup>53</sup> In eukaryotic cells, mRNA consists 200 adenines and its length gradually decreased by the exonuclease (enzyme which digest mRNA). When the length of poly (rA) tail reaches 30As, the mRNA is rapidly destroyed.<sup>54</sup>

Polypurine.polypyrimidine sequences are abundant in eukaryotic genome. Typically, 0.4% of total mammalian genome consists of polypurine.polypyrimidine [d(GA.CT)<sub>n</sub>] and plays an important role in various biological process of eukaryotic organisms.<sup>55-57</sup> These stretches present in both chromatin and supercoiled plasmids exhibit hypersensitivity to single strand specific nucleases.<sup>58</sup> One of the common feature in all A, B, Z-DNA, A-motif and poly d(GA)<sub>n</sub> homoduplex is that all are in duplex conformation and requires two strands to form stable secondary structure. There are certain secondary structures of DNA which required more than two strands *viz.*, triplex (H-DNA) and tetraplex DNA structures (G-quadruplex and *i*-motif). Homopurine-homopyrimidine tracts are highly specific sequences present in the regulatory regions of eukaryotic genome and plays vital role in gene expression.<sup>59</sup> It has been shown that these homopurine-homopyrimidine sequences form intramolecular triple-helical DNA (triplex or H-DNA) in chromatin regions and *in vivo* existence of these non B-DNA structures have been tracked in various cells with antibody specific for triplex DNA.<sup>60,61</sup>

Telomere is a repeating guanine-rich single stranded sequences present at 3'-end of most of eukaryotic chromosomes, protects degradation from exonucleases and fusion with other chromosomes.<sup>62</sup> (TTAGGG)<sub>n</sub> is the common repeating block found in the telomere sequence of all vertebrates and serve as buffers to chromosomes, which shorten during cell division.<sup>63-66</sup> Each replication results in shortening of the telomere ends which is known as end-replication problem. After series of replications, telomeres are identified as double-break strands results in over expression of p53 (tumor suppressor protein) protein that initiates the cell death through apoptosis or senescence.<sup>67</sup> Telomerase is a reverse transcriptase enzyme which contains 3 subunits, human telomerase reverse transcriptase (TERT), an RNA subunit (TERC) and the protein dyskerin (DKSKI).<sup>68</sup> Telomerase binds the 3'-end of telomere and adds the TTAGGG sequence through the reverse transcriptase activity.<sup>69,70</sup> The telomerase enzymes are over expressed in 80 to 90% of cancer cells which avoids the limit on cell division and leads to uncontrolled growth.<sup>71,72</sup> Human telomeric repeat sequence d(TTAGGG)<sub>n</sub> is known to fold into quadruplex structures in presence of monovalent ions (Na<sup>+</sup> and K<sup>+</sup>) with HG hydrogen bonding interactions and affects the DNA replication, transcription and telomere maintenance.<sup>40,42,73-75</sup> Recent studies have shown that the stabilization of these non-canonical G-quadruplex structures with small molecules has the ability to activate DNA damage response machinery in cancer cells.<sup>76</sup>

### **1.6 Factors that influence the stability of nucleic acids structures**

In chemist's point of view duplex formation appears to violate many rules which are used to design molecular recognition systems.<sup>77</sup> First, columbic law, cations binds anions and anions binds cations. In case of DNA, polyanionic chain binds polyanionic chain. According to columbic law, under physiological conditions DNA should not exist in duplex conformation. Second, hydrogen bonding in water, water is strong competitor for hydrogen bonds, but hydrogen bonds still exist between the nucleobases and stabilize the duplex. Apart from these two, entropy is another important factor which strongly opposes the formation of duplex conformation. Formation of ordered right handed DNA duplex structure from random coiled single stranded DNAs results in loss of translational as well as rotational freedom of the internal strands. However, enthalpy factor strongly favor the spontaneous formation of duplex. The enthalpy of duplex formation is mainly depends on two forces, the planar



*hydrogen bonding* (base-pairing) of nucleobases and the vertical stacking of nucleobases bases through the  $\pi$ - $\pi$  *interactions* (base stacking).

**1.6.1 Hydrogen bonding interactions.** Self-assembly is the most indispensable process in biological systems in which molecules organize themselves into ordered structure or pattern from a disordered system supported by non-covalent forces or interactions.<sup>78</sup> In order to form specific structures of biomacromolecules (proteins, DNA and RNA), non-covalent interactions such as hydrogen bonding,  $\pi$ - $\pi$  stacking, van der Waals, hydrophobic and electrostatic interactions are to be controlled and employed effectively.<sup>79,80</sup> Hydrogen bonding is bridging of hydrogen atom between two high electronegative atoms. Normally, hydrogen bonds are two types one *intermolecular hydrogen bonding* in which hydrogen bonds form between two different molecules like DNA and other one is *intramolecular hydrogen bonding* in that hydrogen bonds formed with in the molecule like salicylaldehyde or  $\alpha$ -helix of proteins. In comparison, strength of hydrogen bonds is weaker than covalent and ionic bonds and stronger than van der Waals forces. In case of DNA, WC hydrogen bonding between adenine-thymine and guanine-cytosine base pairs is responsible for the duplex formation of DNA with promising stability. Further, hydrogen bonding interactions of nucleobases are crucial for the formation of non-canonical ordered secondary structures such as A-motifs, G-quadruplex and *i*-motifs.<sup>15,26</sup> These non-canonical structures open up new directions in the development of DNA-based molecular scaffolds for various diagnostic and imaging applications.

**1.6.2 Aromatic  $\pi$ - $\pi$  interactions.** The  $\pi$ - $\pi$  interactions between aromatic systems are considered as one of the major non-covalent forces, play crucial role in biological processes especially in stacking of DNA base pairs, protein-ligand interaction and recognition of biological receptors with small molecules. In DNA, hydrogen bonding interactions are mainly governed by electrostatic point-to-point interactions and  $\pi$ - $\pi$  aromatic interactions governed by combinations of various types of interactions, including van der Waals, electrostatic and hydrophobic interactions. van der Waals interactions are important weak interactions attributed to dispersive forces originating from the transient dipoles of electronic structures of atoms or molecules, varies with sixth power of the distance between the dipoles. Electrostatic interactions are mainly governed by the interactions between partial atomic charges of electronegative atoms like nitrogen and oxygen of nucleobases by polarizing

electron density from the neighboring atoms. Hydrophobic interactions are attributed to interactions of aromatic nonpolar residues with solvent molecules and resulting desolvation effect.

### **1.7 Nucleic acids-small molecule interactions**

Nucleic acids (DNA/RNA) are the basic carriers of genetic and hereditary information. DNA and RNA are crucial for many biological process including the storage, transport, processing, expression of the genetic information, maintaining genome integrity and stability. In living cells, DNA mostly exists in double stranded conformation and RNA exists in both single and double stranded conformations. However, during DNA metabolism process such as replication and transcription DNA duplex partially unwound into single stranded forms in repetitive DNA sequences. Typically, human genome contains more than 50 % of repetitive DNA sequence in total genomic DNA.<sup>26</sup> These repetitive DNA sequences, depending on the external environmental conditions can fold into various non-canonical forms such as hairpin, triplex, tetraplexes (G-quadruplex and *i*-motif), A-motif , poly(GA)<sub>n</sub> homoduplex, three-way and four-way branches. These non-canonical structures plays significant role in many biological processes. Biological significance and functions of nucleic acids make them traditionally attractive targets for many gene-related diseases such human cancer, parasitic and viral infections.

Particularly, targeting DNA with small molecules is a unique and versatile approach in designing diagnostics and therapeutics for many diseases. Indeed, various small molecule-based drugs have been designed as anticancer agents targeting nucleic acids. Normally, small molecules interact with DNA in two different ways, covalent (DNA-alkylation) and non-covalent (intercalation and groove binding modes) interactions. DNA-small molecule interactions through covalent approach are irreversible in nature whereas non-covalent approach is reversible process. Nitrogen mustards are the first class of small molecules used to target the DNA for cancer chemotherapy.<sup>81,82</sup> In 1946, Alfred Gilman and Frederick Phillips have determined that these nitrogen mustards form intra- and inter-strand covalent cross links through the alkylation of nucleobases and decreases the proliferative rates of cancer cells. Especially, these nitrogen mustards (alkylating agents) target the DNA by alkylating the nucleophilic centers of nitrogenous atoms include  $N^7$  of guanine and  $N^3$  of adenine. Later, a wide range of DNA-alkylating agents such as temozolomide, chlorambucil

and melphalan have been developed and used for cancer chemotherapy. Although, DNA-alkylating agents are good anticancer agents but non-specific DNA binding and high toxicity limit their potential application in anticancer therapy (Figure 16).<sup>83</sup>

Barnett Rosenberg serendipitously discovered a platinum-based compound, *cis*-diamminedichloroplatinum(II) or *cis*-platin remarkably inhibits the proliferation of bacteria cells and induced filamentous cell growth (Figure 16).<sup>83,84</sup> This platinum based compound primarily binds to adjacent guanine residues through the covalent cross linking in major groove which results in bending of DNA major groove direction. This distortion allows various proteins to bind in minor groove and such protein-DNA binding interactions leads to abnormal changes in functioning of DNA. The major drawback with platinum based compounds is decrease in activity due to cross reactivity with sulfur containing compounds like glutathione and cysteine.

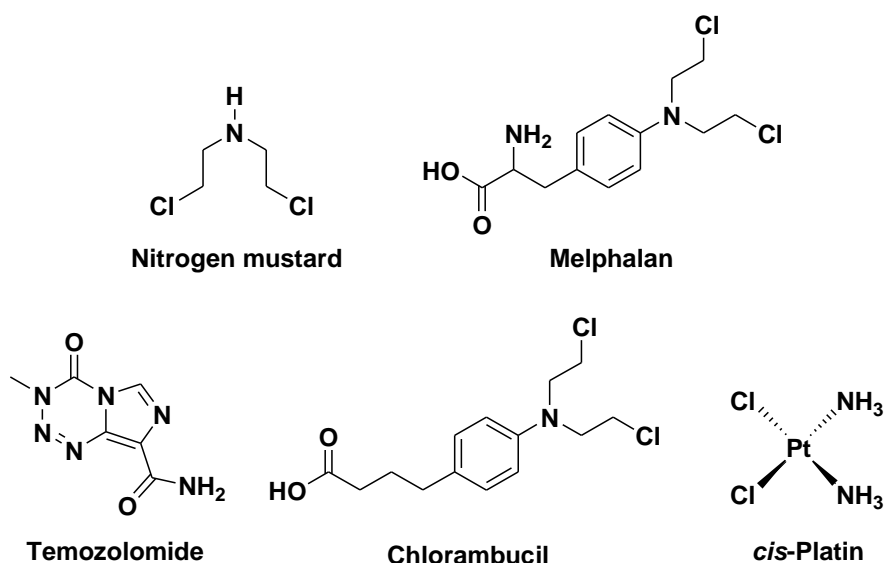


**Figure 16.** Molecular structures of DNA-alkylating agents.

**1.7.1 DNA intercalators.** Noncovalent small molecule-DNA interactions are further classified into two major categories such as intercalators and groove binders (Figure 17). Among all the small molecule-DNA binding modes, intercalation is an important binding mode especially in terms of functioning as anticancer agents. Leonard Lerman was the first person to propose the mode of intercalation in his studies on acridines with DNA complex.<sup>85</sup>

Soon after, thousands of compounds have been developed as potential anticancer and antimalarial agents include organic- anthracine, daunomycin, quinacrine, ethidium bromide (EtBr), anthracyclines, actinomycins and inorganic- octahedral (particularly ruthenium(II) and rhodium(III)) and square-planar (particularly platinum(II)) complexes (Figure 18).<sup>86-89</sup> Intercalation is entropy driven process in which a flat aromatic compound is inserted between the base pairs through the dipole-dipole and  $\pi$ -stacking interactions. Most importantly, intercalation mode causes the structural distortion of regular duplex form of DNA and results in partial unwinding and lengthening of DNA. According to *neighbor exclusion principle*, an intercalator molecule after binding to one of the DNA packet does not allow the next intercalator molecule to bind neighboring or adjacent binding packets. The binding of first intercalators molecule induces slight distortion in adjacent binding sites which eventually leads to significant changes in local structure of DNA.<sup>90</sup> Most of the organic intercalators often used for anticancer agents,<sup>86</sup> fluorescence probe for DNA,<sup>90</sup> among other applications.<sup>91</sup>

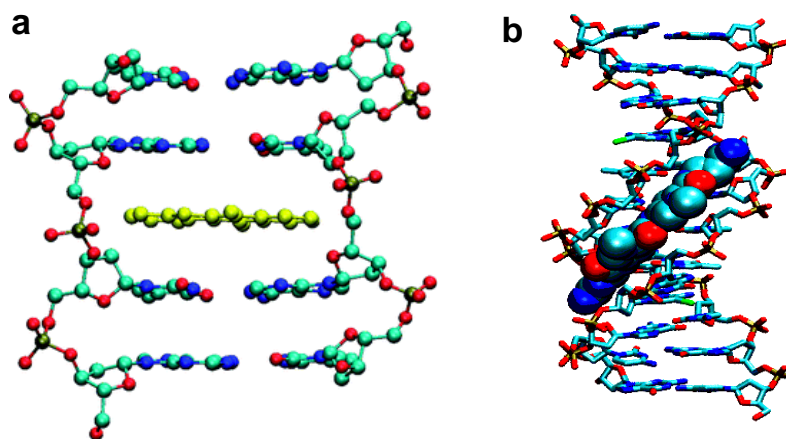


**Figure 17.** Classical DNA-small molecule binding modes. (a) DNA-intercalation mode and (b) Groove binding mode. Adapted from Ref. 80.

Daunomycin is a well-known example of a intercalator used as anticancer drug which preferentially binds GC-rich DNAs over AT-rich sequences.<sup>92</sup> X-ray crystallographic studies on the interaction of daunomycin with d(CGTACG) showed flat aromatic ring intercalates between C (cytosine) and N (nucleotide) site of 5'-GCN-3' sequences and side amino sugar group interacts with AT-base pair from outside the intercalation site.<sup>93</sup> Recently,

naphthalenediimide (NDI) based new class of threading intercalators have been designed in which the flat aromatic group intercalate with base pairs while positively charged sides chains projected towards the minor and major grooves.

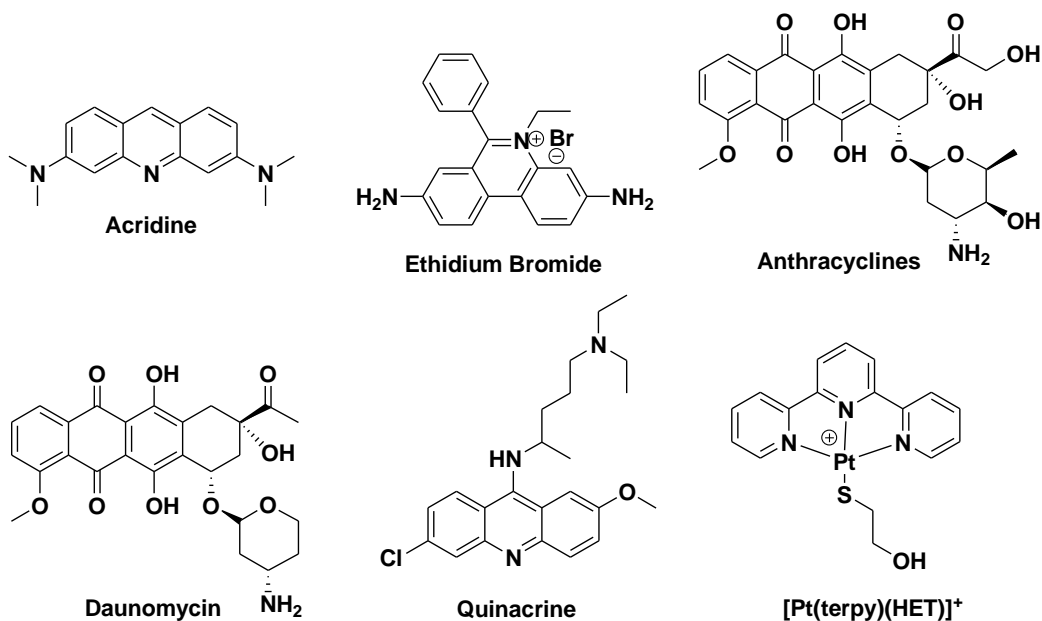


**Figure 18.** Chemical structures of DNA intercalating molecules.

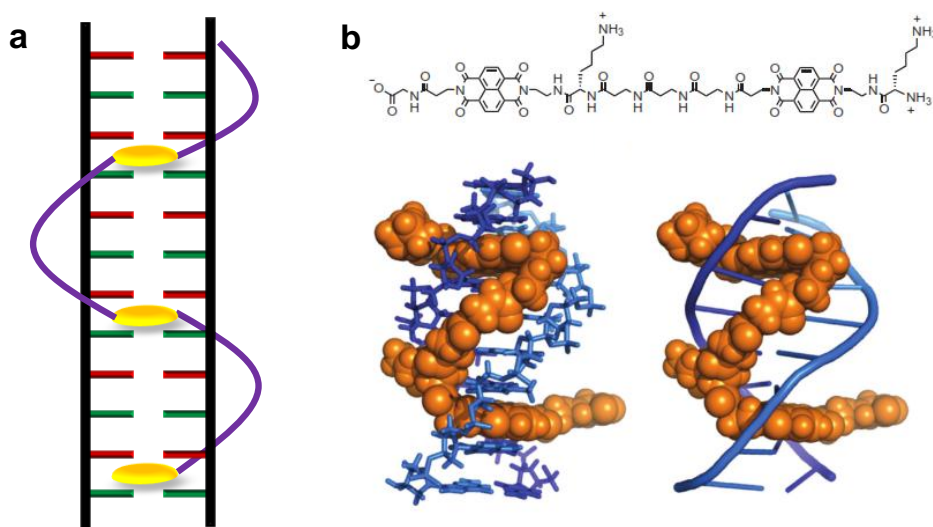


**Figure 19.** DNA-threading intercalators. (a) Schematic view of binding of threading intercalators to DNA duplex. (b) Molecular modeling view of binding of bis-intercalator (gly-gly-NDI-gly-Lys-βAla<sub>4</sub>-NDI-gly-Lys) to d(CGATAAGC).d(GCTTATCG) duplex. Adapted from Ref. 96.

Brent Iverson and coworkers have extensively studied a series of peptide-NDI conjugates as bis- and poly-intercalator to target the DNA with high affinity and extremely slow dissociation rate constant.<sup>94-96</sup> They have conjugated the imide positions of NDI with two different peptides such as  $\beta$ -alanyl- $\beta$ -alanyl- $\beta$ -alanyl-L-lysine (- $\beta$ Ala<sub>3</sub>-Lys-) and glycyl-glycyl-glycyl-L-lysine (-gly<sub>3</sub>-Lys) as a selective minor and major groove binding linkers, respectively (Figure 19).<sup>94,95</sup>

**1.7.2 DNA groove binders.** Groove binders are another important class of DNA binders with promising sequence selectivity which is lacking in case of intercalators. Generally, inherent asymmetry of sugar-phosphate backbones in canonical B-DNA results in the formation major and minor grooves with characteristic features. As the name implies major groove is wider than minor groove and width for averaged-sequence canonical B-DNA are 11.6 and 6.0 Å respectively (Figure 20a). The inherent hydrogen bond donating and accepting ability of base pair edges makes them versatile sites to recognize the minor and major grooves through hydrogen bonding interactions (Figure 20b). In cells, proteins can easily recognize wider DNA major groove through hydrogen bonding interactions in sequence selective manner.<sup>97</sup> However, the narrow size of minor groove restricts the binding of proteins but the inherent size constraints favors the binding of small molecules though hydrogen bonding and van der Waals interactions. Especially, duplex of polypurine-polypyrimidine sequence can be recognized by the third strand through the HG hydrogen bonding interactions with the bases of polypurine strands and these strands are called triplex-forming oligonucleotides (TFOs).<sup>98,99</sup> Peptide nucleic acids (PNAs) are the best examples of TFOs with modified peptide backbone, PNAs can block the transcription process by competition with transcription factor binding or RNA polymerase.<sup>100-102</sup>

Targeting DNA minor groove with small molecule is considered as a promising molecular recognition strategy in molecular biology. Minor groove binding mode was first proposed by Roger Wartell *et al.* in 1974, from their phenomenal work on the interaction of netropsin with DNA.<sup>16,103</sup> Netropsin and distamycin-A are the first natural products composed of N-methyl pyrrole and amide groups that selectively recognize the AT-rich regions of minor groove through the hydrogen bonding and van der Waals interactions in a selective manner to specific DNA sequence (5'-AATT-3') (Figure 21).<sup>104</sup> After this, various netropsin and distamycin analogues including dimers have been synthesized and studied their

---

binding to AT-rich DNA by DNA foot printing, NMR spectroscopy and single crystal X-ray diffraction (XRD) data.<sup>105</sup>

One of the common structural features of most of the reported minor groove binders is their molecular curvature which complement the DNA minor groove concavity which is known as *isohelicity*, enhance the binding affinity of molecule with DNA minor groove.<sup>16</sup> Apart from molecular curvature, the hydrophobic surface and positively charged tails also gives additional stability to minor groove binder through van der Waals interactions with interior hydrophobic walls of minor groove and electrostatic interaction with negatively charged phosphate backbone. From the single crystal X-ray diffraction (XRD) data of netropsin and 5'-AATT-3' in 1:1 ratio showed the orientation of amide bond towards the groove and participate in bifurcated hydrogen bonding with two consecutive A:T base pairs and amidine group also participate in hydrogen bonding with base pairs.<sup>106</sup> This provided clear understanding that, depending on number of hydrogen bond donors and acceptors at the base edges minor groove provides the discrimination between A:T and G:C base pairs (Figure 20b represents the hydrogen bonding sites in minor and major grooves).

Mary Kopka *et al.* and William Lown *et al.* proposed that replacement of N-methyl pyrrole with imidazole might change the binding specificity from A:T to G:C base pairs.<sup>106,107</sup> Various imidazole based netropsin analogues have been synthesized and studied their binding ability but in this process their preference for either A:T base pairs or G:C base pairs was lost. Further studies showed that just changing imidazole to pyrrole may not help in achieving the preferential binding to G:C base pairs, but may useful in differentiating G:C and C:G from A:T base pairs.<sup>108</sup> Instead of binary code of two heterocyclic code (Im/Py), three heterocyclic code such Im/Py/Py has been synthesized by Peter Dervan group and achieved the preferential binding for five base pair sequence of WGWCW (W: either A:T or T:A) with two G:C pairs, one at second and other at the fourth position.<sup>109</sup> Later, Dervan and coworkers have designed sequence-selective N-methylpyrrole and N-methylimidazole containing crescent-shaped hairpin oligopeptide molecules that selectively recognize the minor groove DNA through the hydrogen bonding interactions with high binding affinity.<sup>110-112</sup> They introduced one more additional heterocyclic 3-hydroxypyrrole (Hp) group and successfully achieved the selective discrimination of all four WC base pairs.<sup>110</sup> However, synthesis is one of the major drawbacks with polyamides.

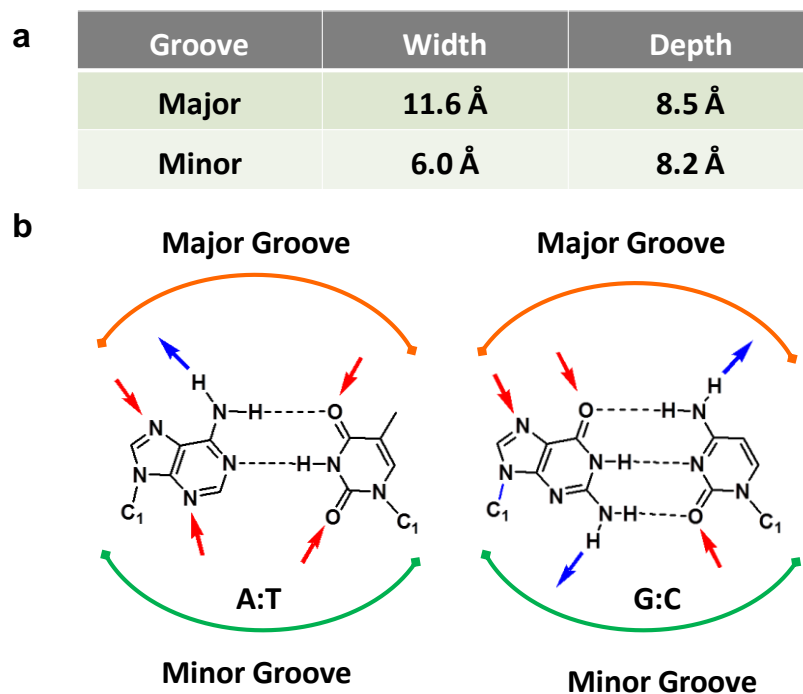


**Figure 20.** DNA minor and major grooves. (a) Typical dimensions of DNA minor and major groove width and depth. (b) Schematic representation of hydrogen bonding donors (blue color arrows) and acceptors (red color arrows) available at the edges of A:T and G:C WC base pairs in minor and major grooves. The directionality of hydrogen bonds is indicated by the arrows.

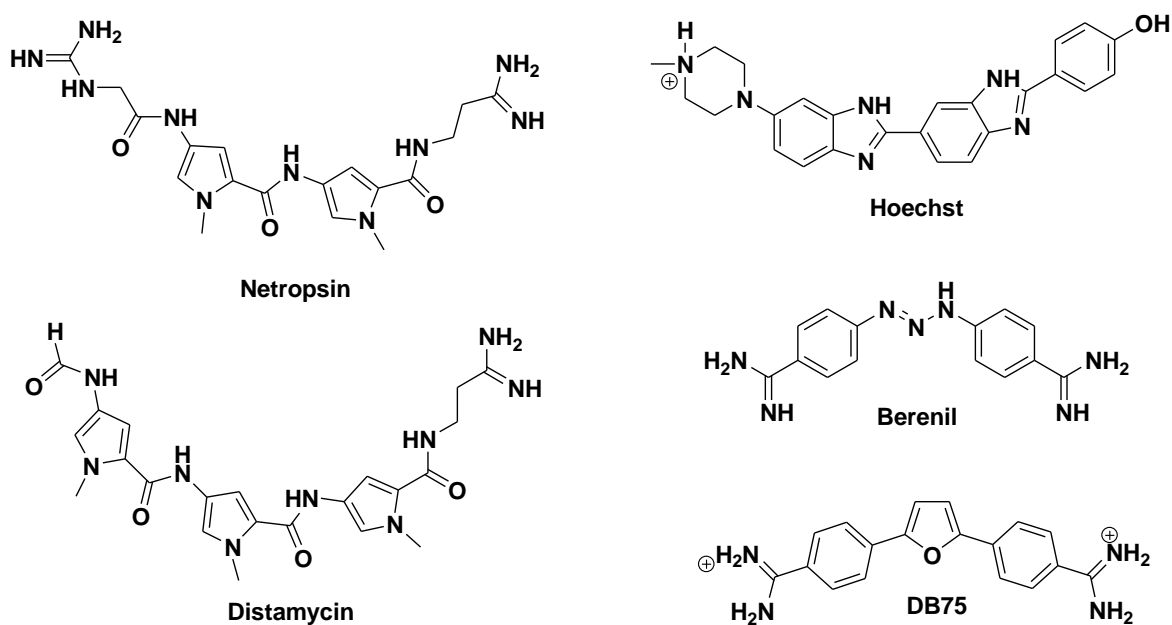


**Figure 21.** Molecular structures of DNA minor groove binders.



Later, David Wilson and coworkers have developed phenyl-furan-benzimidazole diamidine based cell permeable and sequence selective small molecules with strong binding affinity to DNA minor groove (Figure 21).<sup>113,114</sup> Hoechst 33258 and DAPI are often used as fluorescence stains that binds to minor groove of A:T rich sequences. Recent studies have shown that most of the minor groove binders actually targets the AT-sequences of AT-rich mitochondrial kinetoplast DNA of eukaryotic parasites.<sup>113,115</sup> These binding interactions induces the topological changes in AT-rich sequences which generates the biological responses against the diseases and also serves as model systems to get insights into the structural organization of DNA molecular recognition.<sup>115</sup>

### **1.8 Fluorescence probes for canonical and non-canonical DNA structures**

From the above description, it is clear that small molecules interact with DNA either through the intercalation or groove binding mode while they are also known to induce the structural reorganization of genomic DNA. Thus, facilitate novel approaches for understanding genome sequence, variations in the sequence and its structural organization in cell nucleus. These structural changes and reorganization of nucleic acids can be probed by using various analytical tools such as UV-vis absorption spectroscopy, circular dichroism (CD) spectroscopy, DNA-foot printing assay, viscosity measurements, isothermal calorimetry (ITC), mass analysis, X-ray crystallography and nuclear magnetic resonance (NMR) spectroscopy. Many of these techniques are applicable only to study the *in vitro* interactions of small molecules and DNA. To understand structural and functional aspects of nucleic acids, and *in vivo* imaging of cell nucleus it is necessary to develop DNA binding fluorescence probes.<sup>116</sup>

Fluorescence spectroscopy has become powerful tool in molecular and cell biology and plays vital role in the modern era of chemistry and biology.<sup>117,118</sup> Fluorescence based techniques provide additional advantage of real time monitoring of folding and structural reorganization of biological macromolecules in living cells.<sup>119,120</sup> Various small molecule-based fluorescence probes have been designed to target wide range of biological macromolecules including constituents of cell surface, cell membrane, proteins and enzyme substrates.<sup>121-123</sup> Compared to other biological macromolecules, relatively very few fluorescence probes are available for nucleic acids and these probes are limited by their low sensitivity towards the conformational changes of nucleic acids. Further, fluorescence

imaging of DNA is widely used to stain the nuclei of live or fixed cells and probe the structural reorganization of chromosome in cell nucleus.<sup>123</sup> Recently, two photon and near infrared (NIR) based fluorescence techniques are gaining considerable attention which avoids the autofluorescence of cellular components and cellular damage from the UV-light.<sup>125-127</sup> Hoechst (bis-benzimidazole probes), DAPI, ethidium bromide (EtBr), propidium iodide (PI), SYBR green I (SG), PicoGreen (PG), thiazole orange (TO) and thioflavin T (ThT) are well-known examples of DNA binding fluorescence probes. Fluorescence and DNA binding properties of some of the known fluorescence probes are described below.

**1.8.1 Hoechst (bis-benzimidazole) probes.** Hoechst dyes are class of bis-benzimidazoles derivative with N-methylpiperazine and phenyl groups at the terminal (Figure 21). These dyes are almost non-fluorescent in unbound form and fluoresces brightly upon binding with DNA duplex and has been widely used for the quantification of DNA and as a fluorescence chromosomal stain in optical microscopy imaging.<sup>128</sup> Hoechst dyes strongly bind in the minor groove of AT-rich sequences of DNA duplex.<sup>129</sup> Similar to other minor groove binders, crescent shape and flat aromatic rings of Hoechst helps smooth fit into the hydrophobic and convex walls of AT-rich minor grooves of DNA and positively charged N-methylpiperazine group helps in binding to strongly electronegative potential AT-rich minor groove than the GC-rich minor groove.<sup>16</sup> Further, the hydrogen bond donors-acceptors of Hoechst offers to recognize AT-rich minor grooves in sequence selective manner.<sup>130</sup> Interestingly, fluorescence and DNase foot printing studies showed the preferential binding (> 170 folds) towards 5'-AATT-3' than 5'-TTAA-3' in nanomolar affinity.<sup>131</sup> The crystal structure of Hoechst upon complex with DNA duplex containing 5'-GAATTC-3' showed that dye covers the AATT, ATTC or GAAT in which the phenyl ring projects towards the narrow AT-tract.<sup>130</sup> High resolution NMR studies of Hoechst showed similar binding behavior in solution state upon binding to the dodecamer DNA duplex with central 5'-AATT-3'.<sup>132</sup>

**1.8.2 4',6-Diamidino-2-phenylindole (DAPI).** Aromatic diamidines, such as 4',6-diamidino-2-phenylindole (DAPI) is routinely used to quantify DNA fluoremetrically in solution as well as in fixed cells (shown in Figure 22).<sup>133</sup> Similar to Hoechst dye, DAPI prefer to bind the minor groove of B-DNA duplex at the edges of continuous three AT-base pairs in sequence selective manner with nanomolar affinity.<sup>134-136</sup> Fluorescence studies and DNase foot printing assay showed the binding affinity is similar to minor groove binder distamycin in AT-base

---

pair regions. However, in mixed AT- and GC-base pairs its binding mode is similar to classical intercalators. Unlike Hoechst, depending on DNA sequence DAPI can bind in minor groove as well as intercalator mode.<sup>137</sup>

**1.8.3 Ethidium bromide.** Ethidium bromide (EtBr) is phenanthridinium heterocyclic dye widely used in nucleic acids binding studies (shown in Figure 18) and fluorescence DNA marker in gel-electrophoresis studies. Unlike Hoechst and DAPI, EtBr binds DNA and RNA in an intercalation mode.<sup>138</sup> Viscometric and hydrodynamic measurements showed lengthening and stiffening of the DNA helix with increasing concentration of EtBr and these spectral changes suggested its DNA binding in intercalation mode.<sup>139</sup> X-ray crystallographic analysis of EtBr and dinucleoside monophosphate 5-iodouridylyl(3'-5')adenosine complex showed the intercalation mode in which phenyl and ethyl groups are projected towards the grooves. The amine groups of EtBr buried inside the base pairs and forms hydrogen bonding to neighboring water molecules.<sup>140</sup>

**1.8.4 Propidium iodide.** Propidium iodide (PI) belongs to phenanthroline heterocyclic family (shown in Figure 22). Similar to EtBr, PI binds to DNA through intercalation between the nucleobases with no sequence specificity and shows ~20-30 fold enhancement in fluorescence.<sup>141</sup> PI binds with a stoichiometry of one dye per 4–5 base pairs of DNA. The large stoke shift and red fluorescence nature makes it suitable probe for various applications including fluorescence microscopy, flow cytometry and counterstain in multicolor fluorescent techniques.<sup>142</sup> However, the non-specific binding with RNA requires RNase treatment to distinguish the binding between DNA and RNA. PI is cell impermeable and high toxicity which limit its potential use in live imaging. It is commonly used as a fluorescence marker to identify the dead cells (necrotic cells) population in culture and in flow cytometry.<sup>143</sup>

**1.8.5 SYBR Green I.** SYBR green I (SG) is a class of monomeric unsymmetrical cyanine dye comprising of N-alkylated benzothiazole and quinoline ring with N-alkylated substituents (shown in Figure 22). Upon binding DNA duplex, SG shows more than 1000-fold enhancement in fluorescence with intercalation binding mode at ~0.15 dye/base pair ratio and at higher dye/base pair ratio it shows the minor groove binding mode.<sup>144</sup> In contrast to classical intercalator EtBr and PI, SG shows significant AT-preference. At higher dye/base pair ratios, fluorescence intensity of SG/dA.dT complex is higher compared to SG/dG.dC

complex. High fluorescence enhancement upon binding with DNA makes SYBR green I a useful DNA fluorescence marker in gel-electrophoresis and real time PCR applications.<sup>145,146</sup>

**1.8.6 PicoGreen.** PicoGreen (PG) also belongs to unsymmetrical cyanine dye family. The chemical structure of PG is (2-(n-bis-(3-dimethylaminopropyl)-amino)-4-(2,3-dihydro-3-methyl-(benzo-1,3-thiazol-2yl)-methylidene)-1-phenyl-quinolinium) is shown in Figure 22.<sup>147</sup> Upon binding with DNA, PG shows ~1000-fold enhancement fluorescence with polymeric DNA duplex and it also binds to small DNA duplexes (<20 bp) with picogram sensitivity.<sup>148</sup> Similar to SG, PG binds DNA in intercalation mode and electrostatic interactions with phosphate backbone also significantly contribute to stabilization. Further, the competitive binding studies between PG and Hoechst confirm that PG also binds to the DNA minor groove.<sup>147</sup> The drastic increase in fluorescence emission of PG upon interaction with DNA makes it a fluorescence probe for gel-electrophoresis, real time PCR, chromosomal staining and other applications.<sup>149,150</sup>

**1.8.7 Thiazole orange.** Thiazole orange (TO) is asymmetric cyanine dye consists of positively charged benzothiazole and N-methyl quinoline groups (shown in Figure 22). Thiazole orange binds the DNA in an intercalation mode with ~18,900-folds fluorescence enhancement.<sup>151</sup> Unlike other cyanine dyes such as SG and PG, TO binds DNA both in monomeric and dimeric form with the change in absorption maxima. However, TO shows non-specific binding with single strand DNAs and RNA. Later, Alexander Glazer and coworkers have reported the homodimers of thioazole orange (TOTO).<sup>152</sup> Homodimeric thiazole orange form (TOTO) is almost non-fluorescent in unbound form and upon binding with DNA shows ~1000-fold enhancement in fluorescence. DNA:TOTO complexes are highly stable, even after gel-electrophoresis these complexes are still intact. NMR studies of DNA:TOTO complexes showed the preferential binding affinity towards the oligonucleotides containing (5'-CTAG-3')<sub>2</sub> or (5'-CCGG-3')<sub>2</sub> sequences.<sup>153</sup> Later, it has been found that TO shows promising fluorescence enhancement in intramolecular human telomere (Te-22) G-quadruplex structure specifically in presence of K<sup>+</sup> and Na<sup>+</sup>.<sup>154</sup> Fluorescence intercalator displacements (FID) studies confirms that TO binds more tightly to the loops of the G-quadruplex structures. TO shows more fluorescence enhancement in presence of triplex and G-quadruplex structure compare to DNA duplex structure. Gel-electrophoresis studies showed the staining of both triplex and G-quadruplex structures.<sup>155</sup>

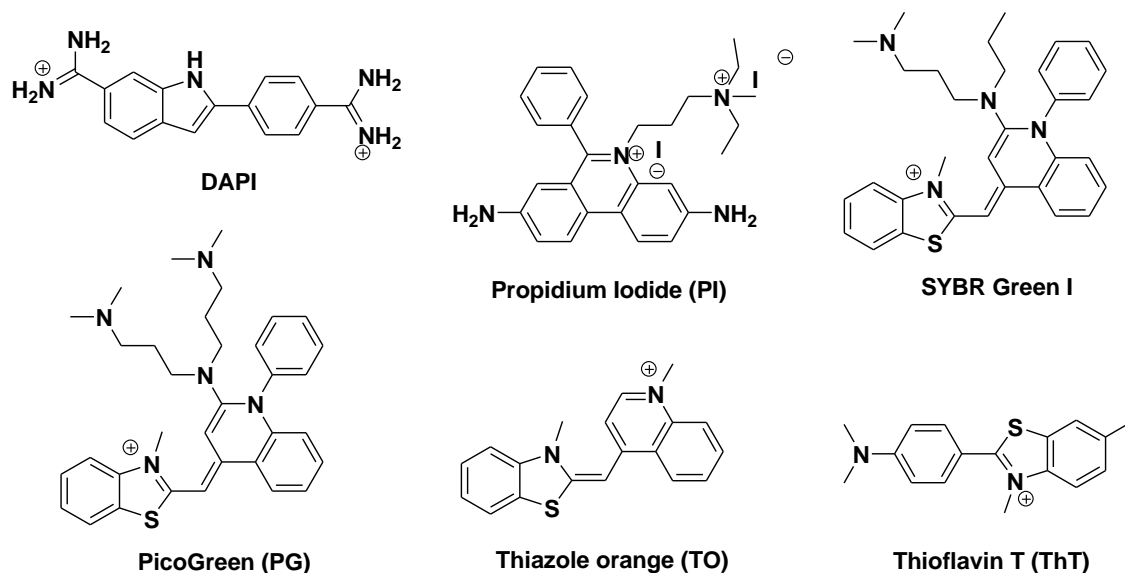


**Figure 22.** Molecular structures of DNA binding fluorescence probes.

**1.8.8 Thioflavin T.** Thioflavin T (ThT) (3,6-dimethyl-2-(4-dimethylaminophenyl) benzo-thiazolium cation) is a green fluorescence probe extensively used to stain the  $\beta$ -Amyloid fibrils (shown in Figure 22).<sup>156</sup> Recently, Mohanty *et al.* showed that ThT binds the G-quadruplex structures both in absence and presence of Tris-buffer/salt with 2100-folds fluorescence enhancement compare to duplex structures.<sup>157</sup> In water, ThT induces the antiparallel G-quadruplex structures of Te-22 whereas in Tris-buffer it induces the parallel G-quadruplex structure with similar fluorescence enhancement. Further, high-throughput assay showed the fluorescence sensing of most of the G-quadruplex forming sequences.<sup>158</sup>

### 1.9 Small molecule guided hybrid DNA-structures

B-DNA is a regular, well-defined right handed helical structure with canonical WC base pairing and  $\pi$ - $\pi$  stacking interactions of nucleobases. The unique molecular recognition of nucleobases, persistence length  $\sim 50$  nm (length of duplex DNA which required for maintaining stiffness), thickness  $\sim 2$  nm and convenient chemical synthesis of DNA makes it as a versatile building block for the construction of various nanostructures. The inherent molecular features of DNA lead to its use as a robust build block in the celebrated area of DNA nanotechnology to construct numerous molecular architectures for multiple applications including material and biology.<sup>159-162</sup> Nadrian Seeman and coworkers pioneered the field of DNA nanotechnology, they have constructed various 1D and 2D nanostructures

with precise size and shape by simply relied on the complementary base pairing and B-DNA duplex formation.<sup>162-164</sup> Recently, 3D nanostructures have been created using DNA motifs with sticky ends.<sup>165,166</sup> Moreover, high predictability and directionality of DNA makes it a novel material for the precise templating of nanoparticles,<sup>167</sup> multivalent quantum dots,<sup>168</sup> proteins such as streptavidin,<sup>169</sup> fluorescent proteins<sup>170</sup> and multi-enzyme complexes.<sup>171</sup> Furthermore, duplex DNA has been also employed in templated directed assembly of conjugated polyelectrolytes, polymers like polyanilines and polypyrroles through the electrostatic interactions.<sup>172-174</sup>

Apart from these applications, DNA has been employed in template mediated self-assembly of  $\pi$ -conjugated systems with precise size and shape of self-assembled molecules *via* bottom-up approach by interfacing the biology and materials science.<sup>175,176</sup> Recently, Bruce Armitage and coworkers have shown DNA mediated templated assembly of cyanine dyes in well-defined helical aggregates.<sup>177-179</sup> They were intend to investigate the photocleavage properties of DNA and RNA in presence of cyanine dyes. In preliminary study, they have studied the ground state interactions between benzothiazole based dye DiSC<sub>2</sub> (5) and [Poly(dA-dT)]<sub>2</sub> (an alternative adenine and thymine containing self-complementary double stranded DNA) in aqueous solution.<sup>177</sup> From UV-vis spectra, they observed blue shift (~60 nm) in the absorption maxima with increasing concentration of DNA and these spectral changes attributed to the formation of H-type (cofacial dimers) aggregates of cyanine dyes along the DNA. They have recorded the CD spectra of DiSC<sub>2</sub> (5) in presence of [Poly(dA-dT)]<sub>2</sub> and shorter alternative A-T sequence containing AT-5 and AT-10 self-complementary DNA sequences. CD spectra showed strong positive and negative CD signals at zero cross over point at the blue shifted absorption band. CD intensity is very week in presence of AT-5 and strong in presence of AT-10 and [Poly(dA-dT)]<sub>2</sub>. The observed strong positive and negative CD signals attributed to the formation of helical aggregates of cyanine dyes by an end-end interaction between adjacent dimers in the minor groove (Figure 23a). However, end-end adjacent dimer stacking is not possible in presence of smaller AT-5 because there is only one dimer possible in AT-5 sequence.<sup>177</sup> Formation of template mediated helical aggregates of cyanine dyes mainly depends on the structure of dye, and concentration, and DNA sequence and length.<sup>179</sup> Overall, from the above studies they have confirmed that DNA minor groove can serve as a template to form the helical supramolecular

polymers of symmetrical cationic cyanine dyes in cooperative fashion through the van der Waals and hydrophobic interactions (Figure 23b).

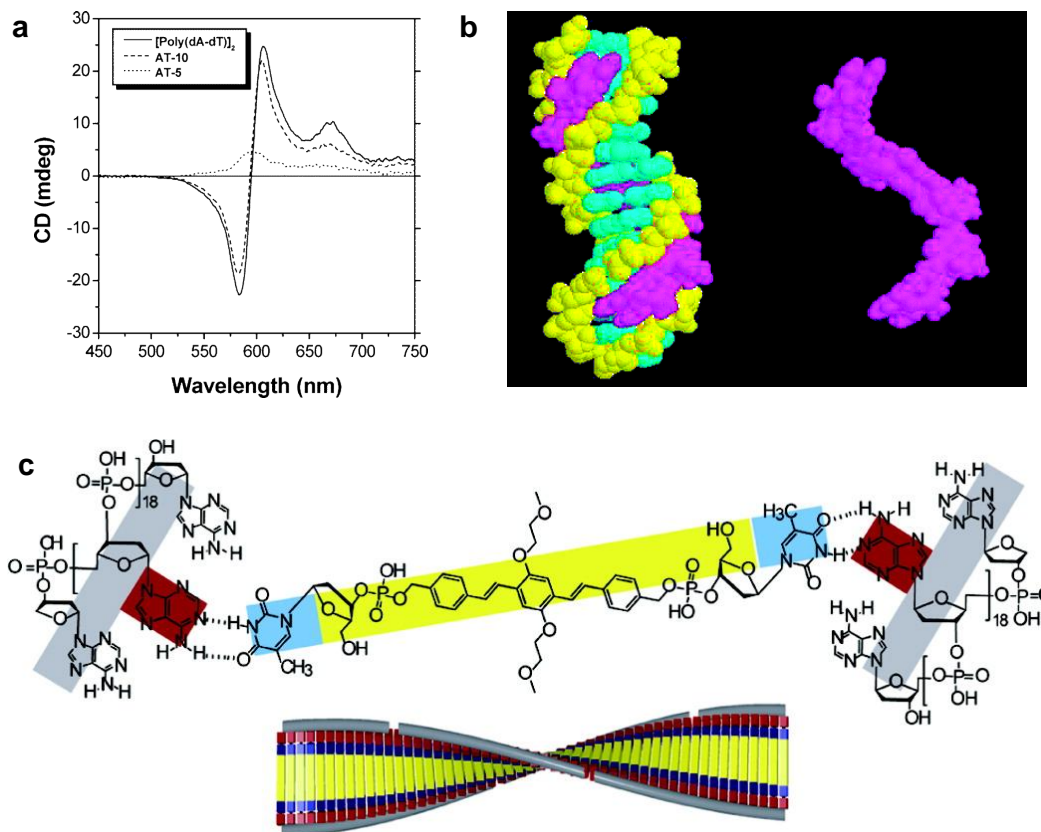


**Figure 23.** DNA mediated templated self assembly of chromophores. (a) CD spectra of DiSC<sub>2</sub>(5) in presence of [Poly(dA-dT)]<sub>2</sub> and shorter alternative A-T sequence containing AT-5 and AT-10 DNA duplexes. (b) Molecular model of self assembly of three DiSC<sub>2</sub>(5) dimers in the minor groove of DNA template. (c) Formation of right handed helical assemblies of bis-thymidine-appended oligophenylenevinylene (OPV) systems in presence of dA<sub>n</sub>. Adapted from Ref 179 and 180.

We have summarized the role of hydrophobic and van der Waals interactions in DNA duplex with chromophores to form helical assemblies. Although, single stranded DNAs are in random coil conformation, they have been used as an effective template to form ordered helical assemblies with chromophores through the hydrogen bonding interactions. Shimizu and his coworkers have done significance amount of work on single stranded DNAs templated ordered helical assemblies of chromophores.<sup>180-185</sup> They have designed diamino triazine functionalized naphthalene and  $\pi$ -conjugated oligo(p-phenylene)vinylene (OPV)

derivative, and employed complementary dT<sub>n</sub> as a template to drive the helical assemblies of these designed molecules.

CD spectra showed the formation of right handed helical assemblies of chromophores through the  $\pi$ - $\pi$  stacking interaction of chromophores and hydrogen bonding interactions between diamino triazine and complementary thymine of dT<sub>n</sub>. Using the complementary A-T base pairing interactions, right handed helical stacks of bisthymidine-appended oligophenylenevinylene system are formed from dA<sub>n</sub> in ladder like form (Figure 23b).<sup>180</sup> Similarly, A bis-thymidylic acid appended anthracene chromophores have been employed for the binary self-assembly with dA<sub>n</sub> through the formation of helical J-aggregates.<sup>181</sup> Recently, Milan Balaz and coworkers have employed similar strategy to form the helical assemblies of porphyrin–diaminopurine conjugate.<sup>186,187</sup>

### 1.10 Our objective

The main objective of this thesis is to develop small molecular probes for both canonical and non-canonical DNA structures for understanding their structural transitions, and their significant role in biological systems and constructing novel hybrid DNA systems. Nucleic acids are the fundamental carriers of genetic information in all living organisms. Understanding their biological significance and structural reorganization in cell nucleus is crucial to design new DNA targeted diagnostics and therapeutic agents. Therefore, recognition of nucleic acids using small molecule-based fluorescence probes plays a crucial role in genetic engineering, diagnosis, forensic and bioinformatics. Towards this, various small molecular fluorescence probes have been designed and employed for imaging DNA in live and fixed cells. However, most of the reported fluorescence probes suffer from common problems such as UV-excitation, non-specificity, low fluorescence quantum yield, poor aqueous solubility, insufficient photostability, non-specificity, selectivity and cell impermeability. These drawbacks of existing probes led us to design new DNA binding fluorescence probes for various biological applications including cell imaging and diagnosis.

**For biological applications, we set out to design better fluorescence probe with the following properties**

1. High aqueous solubility



2. Long excitation/emission wavelength
3. Switch-on fluorescence
4. High fluorescence quantum yield
5. Good photostability
6. Fidelity towards DNA duplex and sequence selectivity
7. Sensitive at lower concentration
8. Good cell permeability
9. Non-toxicity to cells.

To achieve these versatile properties, we presumed that probes with cyanine back bone are the ideal candidates due to their inherent photophysical properties. In this thesis, we present hemicyanine and quinone cyanine (QCy) based DNA binding fluorescence probes with superior properties like, ease of synthesis through straightforward synthetic routes, good aqueous solubility, longer excitation/emission wavelength, large Stokes shift, non-fluorescent in unbound state and strongly (switch-on) fluoresce upon binding, and non-toxicity. In the second, third and fourth chapters, we present the fluorescence properties of these probes in presence of canonical B-DNA. In the fifth chapter, we have studied the structural transitions of non-canonical DNA structures such as parallel homoduplex of polyadenine (*i.e.*, A-motif), homoduplex of poly d(GA)<sub>n</sub> sequence and G-quadruplexes in presence of pH, small molecule and polyethylenimine–pyrene conjugates respectively. The unique size and shape of DNA is suitable for the templated mediated self-assembly of  $\pi$ -conjugated system like cyanine dyes, oligophenylenevinylene and porphyrins based on van der Waals and hydrogen bonding interactions. To the best of our knowledge, nucleobase conjugated n-type semiconducting arylenediimides are not been employed for templated mediated self-assembly approaches. In the sixth chapter, we report arylenediimide-nucleobase conjugate to create new hybrid DNA ensembles through mutual templating effect supported by both canonical and non-canonical hydrogen bonding interactions. We hope this strategy opens up new avenues in the templated DNA nanotechnology for functional applications.

### 1.11 References

1. Miescher, F. Ueber die chemische Zusammensetzung der Eiterzellen. *Med.-Chem. Unters.* **1871**, *4*, 441 – 460.
2. Avery, O. T.; MacLeod, C. M.; McCarty, M. Studies on the chemical nature of the substance inducing transformation of Pneumococcal types. *J. Exp. Med.* **1944**, *79*, 137-158.
3. Levene, P. A.; Jacobs, W. A. Structure of Thymus Nucleic Acid. *J. Biol. Chem.* **1912**, *12*, 411-420.
4. Levene, P. A. The structure of yeast nucleic acid. IV. Ammonia hydrolysis. *J. Biol. Chem.* **1919**, *40*, 415-424.
5. Chargaff, E.; Magasanik, B.; Doniger, R.; Vischer, E. The nucleotide composition of ribonucleic acids. *J. Am. Chem. Soc.* **1949**, *71*, 1513-1514.
6. Astbury, W. T. X-ray studies of nucleic acids. *Symp. Soc. Exp. Biol.* **1947**, 66-76.
7. Watson, J. D.; Crick, F. H. Molecular structure of nucleic acids; a structure for deoxyribose nucleic acid. *Nature* **1953**, *171*, 737-738.
8. Wilkins, M. H.; Stokes, A. R.; Wilson, H. R. Molecular structure of deoxypentose nucleic acids. *Nature* **1953**, *171*, 738-740.
9. Franklin, R. E.; Gosling, R. G. Molecular configuration in sodium thymonucleate. *Nature* **1953**, *171*, 740-741.
10. Crick, F. H. C. Central dogma of molecular biology. *Nature* **1970**, *227*, 561-563.
11. Saenger, W. Principles of nucleic acid structure, Springer-Verlag: New York, **1984**.
12. Blackburn, G. M.; Gait, M. J.; Loakes, D.; Williams, D. M. Nucleic Acids in Chemistry and Biology, RSC Publishing, Cambridge, UK, **2006**.
13. Judson, H. F. The eighth day of creation: makers of the revolution in biology, Simon and Schuster: New York, **1979**.
14. Watson, J. D. The double helix; a personal account of the discovery of the structure of DNA, 1st ed., Atheneum, New York, **1968**.
15. Jissy, A. K.; Datta, A. Design and applications of non-canonical DNA base pairs. *J. Phys. Chem. Lett.* **2014**, *5*, 154-166.
16. Neidle, S. DNA minor-groove recognition by small molecules. *Nat. Prod. Rep.* **2001**, *18*, 291–309.
17. Pohl, F. M.; Jovin, T. M. Salt-Induced Cooperative Conformational Change of a Synthetic DNA - Equilibrium and Kinetic Studies with Poly(dG-dC). *J. Mol. Biol.* **1972**, *67*, 375-396.
18. A, B, Z-DNA structures. Source: <http://www.richardwheeler.net>

19. Tyagi, S.; Kramer, F. R. Molecular beacons: probes that fluoresce upon hybridization. *Nat. Biotechnol.* **1996**, *14*, 303-308.
20. Fresco, J. R. Polynucleotides. II. The x-ray diffraction patterns of solutions of the randomly coiled and helical forms of polyriboadenylic acid. *J. Mol. Biol.* **1959**, *1*, 106-110.
21. Rich, A.; Davies, D. R.; Crick, F. H. C.; Watson, J. D. The molecular structure of polyadenylic acid. *J. Mol. Biol.* **1961**, *3*, 71-86.
22. Saenger, W.; Riecke, J.; Suck, D. A structural model for the polyadenylic acid single helix. *J. Mol. Biol.* **1975**, *93*, 529-534.
23. Zimmerman, S. B.; Davies, D. R.; Navia, M. A. An ordered single-stranded structure for polyadenylic acid in denaturing solvents. An X-ray fibre diffraction and model building study. *J. Mol. Biol.* **1977**, *116*, 317-330.
24. Chakraborty, S.; Sharma, S.; Maiti, P. K.; Krishnan, Y. The poly dA helix: a new structural motif for high performance DNA-based molecular switches. *Nucleic Acids Res.* **2009**, *37*, 2810-2817.
25. Safaee, N.; Noronha, A. M.; Rodionov, D.; Kozlov, G.; Wilds, C. J.; Sheldrick, G. M.; Gehring, K. Structure of the parallel duplex of poly(A) RNA: evaluation of a 50 year-old prediction. *Angew. Chem., Int. Ed.* **2013**, *52*, 10370-10373.
26. Choi, J.; Majima, T. Conformational changes of non-B DNA. *Chem. Soc. Rev.* **2011**, *40*, 5893-5909.
27. Casasnovas, J. M.; Huertas, D.; Ortiz-Lombardia, M.; Kypr, J.; Azorin, F. Structural polymorphism of d(GA.TC)<sub>n</sub> DNA sequences. Intramolecular and intermolecular associations of the individual strands. *J. Mol. Biol.* **1993**, *233*, 671-681.
28. Huertas, D.; Bellolell, L.; Casasnovas, J. M.; Coll, M.; Azorin, F. Alternating d(GA)<sub>n</sub> DNA sequences form antiparallel stranded homoduplexes stabilized by the formation of G.A base pairs. *EMBO J.* **1993**, *12*, 4029-4038.
29. Evertsz, E. M.; Rippe, K.; Jovin, T. M. Parallel-stranded duplex DNA containing blocks of trans purine-purine and purine-pyrimidine base pairs. *Nucleic Acids Res.* **1994**, *22*, 3293-3303.
30. Rippe, K.; Fritsch, V.; Westhof, E.; Jovin, T. M. Alternating d(G-A) sequences form a parallel-stranded DNA homoduplex. *EMBO J.* **1992**, *11*, 3777-3786.
31. Dolinnaya, N. G.; Fresco, J. R. Single-stranded nucleic acid helical secondary structure stabilized by ionic bonds: d(A<sup>+</sup>-G)<sub>10</sub>. *Proc. Natl. Acad. Sci. U.S.A.* **1992**, *89*, 9242-9246.
32. Dolinnaya, N. G.; Braswell, E. H.; Fossella, J. A.; Klump, H.; Fresco, J. R. Molecular and thermodynamic properties of d(A<sup>+</sup>-G)<sub>10</sub>, a single-stranded nucleic acid helix without paired or stacked bases. *Biochemistry* **1993**, *32*, 10263-10270.

33. Ortiz-Lombardia M.; Eritja, R.; Azorin, F.; Kypr, J.; Tejralova, I.; Vorlickova, M. Divalent zinc cations induce the formation of two distinct homoduplexes of a d(GA)<sub>20</sub> DNA sequence. *Biochemistry* **1995**, *34*, 14408-14415.
34. Felsenfeld, G.; Davies, D. R.; Rich, A. Formation of a three-stranded polynucleotide molecule. *J. Am. Chem. Soc.* **1957**, *79*, 2023-2024.
35. Hoogsteen, K. The structure of crystals containing a hydrogen-bonded complex of 1-methylthymine and 9-methyladenine. *Acta Crystallogr.* **1959**, *12*, 822-823.
36. Le Doan, T.; Perrouault, L.; Praseuth, D.; Habhoub, N.; Decout, J. L.; Thuong, N. T.; Lhomme, J.; Hélène, C. Sequence-specific recognition, photocrosslinking and cleavage of the DNA double helix by an oligo-[alpha]-thymidylate covalently linked to an azidoproflavine derivative. *Nucleic Acids Res.* **1987**, *15*, 7749-7760.
37. Frank-Kamenetskii, M. D.; Mirkin, S. M. Triplex DNA structures. *Annu. Rev. Biochem.* **1995**, *64*, 65-95.
38. Vlieghe, D.; Van-Meervelt, L.; Dautant, A.; Gallois, B.; Précigoux, G.; Kennard, O. Parallel and antiparallel (G.GC)<sub>2</sub> triple helix fragments in a crystal structure. *Science* **1996**, *273*, 1702-1705.
39. Rhee, S.; Han, Z.; Liu, K.; Miles, H. T.; Davies, D. R. Structure of a triple helical DNA with a triplex-duplex junction. *Biochemistry* **1999**, *38*, 16810-16815.
40. Sen, D.; Gilbert, W. Formation of parallel four-stranded complexes by guanine-rich motifs in DNA and its implications for meiosis. *Nature* **1988**, *334*, 364-366.
41. Huppert, J. L. Four-stranded nucleic acids: structure, function and targeting of G-quadruplexes. *Chem. Soc. Rev* **2008**, *37*, 1375-1384.
42. Balasubramanian, S.; Hurley, L. H.; Neidle, S. Targeting G-quadruplexes in gene promoters: a novel anticancer strategy?. *Nat. Rev. Drug Discov.* **2011**, *10*, 261-275.
43. Gehring, K.; Leroy, J. L.; Gueron, M. A tetrameric DNA structure with protonated cytosine-cytosine base pairs. *Nature* **1993**, *363*, 56-565.
44. Leroy, J. L.; Gueron, M.; Mergny, J. L.; Helene, C. Intramolecular folding of a fragment of the cytosine-rich strand of telomeric DNA into an *i*-motif. *Nucleic Acids Res.* **1994**, *22*, 1600-1606.
45. Liu, D.; Balasubramanian, S. A proton-fuelled DNA nanomachine. *Angew. Chem., Int. Ed.* **2003**, *42*, 5734-5736.
46. Modi, S.; Swetha, M. G.; Goswami, D.; Gupta, G. D.; Mayor, S.; Krishnan, Y. A DNA nanomachine that maps spatial and temporal pH changes inside living cells. *Nat. Nanotechnol.* **2009**, *4*, 325-330.
47. Garner, M. M.; Felsenfeld, G. Effect of Z-DNA on nucleosome placement. *J. Mol. Biol.* **1987**, *196*, 581-590.

48. Rich, A.; Zhang, S. G. Z-DNA: the long road to biological function. *Nat. Rev. Genet.* **2003**, *4*, 566-572.
49. Champ, P. C.; Maurice, S.; Vargason, J. M.; Camp, T.; Ho, P. S. Distributions of Z-DNA and nuclear factor I in human chromosome 22: a model for coupled transcriptional regulation. *Nucleic Acids Res.* **2004**, *32*, 6501-6510.
50. Pelletier, H.; Sawaya, M. R.; Kumar, A.; Wilson, S. H.; Kraut, J. Structures of ternary complexes of rat DNA-polymerase-beta, a DNA template-primer, and Ddctp. *Science* **1994**, *264*, 1891-1903.
51. Sawaya, M. R.; Pelletier, H.; Kumar, A.; Wilson, S. H.; Kraut, J. Crystal-structure of rat DNA-polymerase-beta - evidence for a common polymerase mechanism. *Science* **1994**, *264*, 1930-1935.
52. Krishnan, Y.; Simmel, F. C. Nucleic Acid Based Molecular Devices. *Angew. Chem. Int. Ed.* **2011**, *50*, 3124-3156.
53. Gallie, D. R. A tale of two termini: a functional interaction between the termini of an mRNA is a prerequisite for efficient translation initiation. *Gene* **1998**, *216*, 1-11.
54. Alberts, B. Molecular biology of the cell, Garland Science, New York, 4th edn, **2002**.
55. Manor, H.; Rao, B. S.; Martin, R. G. Abundance and degree of dispersion of genomic d(GA)<sub>n</sub>.d(TC)<sub>n</sub> sequences. *J. Mol. Evol.* **1988**, *27*, 96-101.
56. Wells, R. D.; Collier, D. A.; Hanvey, J. C.; Shimizu, M.; Wohlrab, F. The chemistry and biology of unusual DNA structures adopted by oligopurine.oligopyrimidine sequences. *FASEB J.* **1988**, *2*, 2939-2949.
57. Tripathi, J.; Brahmachari, S. K. Distribution of simple repetitive (TG/CA)<sub>n</sub> and (CT/AG)<sub>n</sub> sequences in human and rodent genomes. *J. Biomol. Struct. Dynam.* **1991**, *9*, 387-397.
58. Yagil, G. Paranemic structures of DNA and their role in DNA unwinding. *CRC Crit. Rev. Biochem. Mol. Biol.* **1991**, *26*, 475-559.
59. Birnboim, H. C.; Sederoff, R. R.; Patterson, M. C. Distribution of polypyrimidine.purine segments in DNA from diverse organisms. *Eur. J. Biochem.* **1979**, *98*, 301-307.
60. Mirkin, S. M.; Frank-Kamenetskii, M. D. H-DNA and related structures. *Annu. Rev. Biophys. Biomol. Struct.* **1994**, *23*, 541-576.
61. Agazie, Y. M.; Lee, J. S.; Burkholder, G. D. Characterization of a new monoclonal antibody to triplex DNA and immunofluorescent staining of mammalian chromosome. *J. Biol. Chem.* **1994**, *269*, 7019-7023.
62. Blackburn, E. Switching and signaling at the telomere. *Cell* **2001**, *106*, 661-673.
63. Muller, H. J. The remaking of chromosomes. *Collecting Net.* **1938**, *13*, 181-198.

64. Muller, H. J. Induced mutations in *Drosophila*. *Cold Spring Harbor Symposia on Quantitative Biology* **1941**, *9*, 151-167.
65. McClintock, B. The behavior in successive nuclear divisions of a chromosome broken at meiosis. *Proc. Natl. Acad. Sci. U.S.A* **1939**, *25*, 405-416.
66. McClintock, B. The stability of broken ends of chromosomes in *Zea mays*. *Genetics* **1941**, *26*, 234-282.
67. Aubert, G.; Lansdorp, P. M. Telomeres and aging. *Physiol Rev.* **2008**, *88*, 557-579.
68. Cohen, S. B.; Graham, M. E.; Lovrecz, G. O.; Bache, N.; Robinson, P. J.; Reddel, R. R. Protein composition of catalytically active human telomerase from immortal cells. *Science* **2007**, *315*, 1850-1853.
69. Wyatt, H. D.; West, S. C.; Beattie, T. L. InTERTpreting telomerase structure and function. *Nucleic Acids Res.* **2010**, *38*, 5609-5622.
70. Hiyama, E.; Hiyama, K. Telomere and telomerase in stem cells. *Br. J. Cancer.* **2007**, *96*, 1020-1024.
71. Kim, N. W.; Piatyszek, M. A.; Prowse, K. R.; Harley, C. B.; West, M. D.; Ho, P. L.; Coviello, G. M.; Wright, W. E.; Weinrich, S. L.; Shay, J. W. Specific association of human telomerase activity with immortal cells and cancer. *Science* **1994**, *266*, 2011-2015.
72. Shay, J. W.; Bacchetti, S. A survey of telomerase activity in human cancer. *Eur. J. Cancer.* **1997**, *33*, 787-791.
73. Cheung, I.; Schertzer, M.; Rose, A.; Lansdorp, P. M. Disruption of dog-1 in *Caenorhabditis elegans* triggers deletions upstream of guanine-rich DNA. *Nat. Genet.* **2002**, *31*, 405-409.
74. Wang, X. D.; Ou, T. M.; Lu, Y. J.; Li, Z.; Xu, Z.; Xi, C.; Tan, J. H.; Huang, S. L.; An, L. K.; Li, D.; Gu, L. Q.; Huang, Z. S. Turning off transcription of the bcl-2 gene by stabilizing the bcl-2 promoter quadruplex with quindoline derivatives. *J. Med. Chem.* **2010**, *53*, 4390-4398.
75. Siddiqui-Jain, A.; Grand, C. L.; Bearss, D. J.; Hurley, L. H. Direct evidence for a G-quadruplex in a promoter region and its targeting with a small molecule to repress c-MYC transcription. *Proc. Natl. Acad. Sci. USA* **2002**, *99*, 11593-11598.
76. Rodriguez, R.; Miller, K. M.; Forment, J. V.; Bradshaw, C. R.; Nikan, M.; Britton, S.; Oelschlaegel, T.; Xhemalce, B.; Balasubramanian, S.; Jackson, S. P. Small-molecule-induced DNA damage identifies alternative DNA structures in human genes. *Nat. Chem. Biol.* **2012**, *8*, 301-310.
77. Benner, S. A. Understanding nucleic acids using synthetic chemistry. *Acc. Chem. Res.* **2004**, *37*, 784-797.
78. Whitesides, G. M.; Grzybowski, B. Self-assembly at all scales. *Science* **2002**, *295*, 2418-2421.

- 
79. Müller-Dethlefs, K.; Hobza, P. Noncovalent interactions: a challenge for experiment and theory. *Chem. Rev.* **2000**, *100*, 143-168.
  80. Černý, J.; Hobza, P. Non-covalent interactions in biomacromolecules. *Phys. Chem. Chem. Phys.* **2007**, *9*, 5291-5303.
  81. Ward, K. Jr. The chlorinated ethylamines: a new type of vesicant. *J. Am. Chem. Soc.* **1935**, *57*, 914–916.
  82. Gilman, A.; Philips, F. S. The biological actions and therapeutic applications of  $\beta$ -chloroethyl amines and sulfides. *Science* **1946**, *103*, 409–415.
  83. Hurley, L. H. DNA and its associated processes as targets for cancer therapy. *Nat. Rev. Cancer.* **2002**, *2*, 188-200.
  84. Rosenberg, B.; Camp, L. V. Inhibition of cell division in *Escherichia coli* by electrolysis products from a platinum electrode. *Nature* **1965**, *205*, 698–699.
  85. Lerman, L. S. Structural considerations in the interaction of DNA and acridines. *J. Mol. Biol.* **1961**, *3*, 18–30.
  86. Wheate, N. J.; Brodie, C. R.; Collins, J. G.; Kemp, S.; Aldrich-Wright, J. R. DNA intercalators in cancer therapy: Organic and inorganic drugs and their spectroscopic tools of analysis. *Med. Chem.* **2007**, *7*, 627-648.
  87. Ihmels, H.; Otto, D. Intercalation of organic dye molecules into double-stranded DNA general principles and recent developments. *Top. Curr. Chem.* **2005**, *258*, 161-204.
  88. Jonathan, B. C. Energetics of drug–DNA interactions. *Biopolymers* **1997**, *44*, 201-215.
  89. Zeglis, B. M.; Pierre, V. C.; Barton, J. K. Metallo-intercalators and metallo-insertors. *Chem. Commun.* **2007**, 4565–4579.
  90. Armitage, B. A. DNA Binders and Related Subjects. *Top. Curr. Chem.* **2005**, *253*, 55-76.
  91. Cholody, W. M.; Kosakowska-Cholody, T.; Hollingshead, M. G.; Hariprakash, H. K.; Michejda, C. J. A new synthetic agent with potent but selective cytotoxic activity against cancer. *J. Med. Chem.* **2005**, *48*, 4474-4481.
  92. Chaires, J. B.; Dattagupta, N.; Crothers, D. M. Studies on interaction of anthracycline antibiotics and deoxyribonucleic acid: equilibrium binding studies on the interaction of daunomycin with deoxyribonucleic acid. *Biochemistry* **1982**, *21*, 3933-3940.
  93. Moore, M. H.; Hunter, W. N.; Destaintot, B. L.; Kennard, O. DNA-drug interactions. The crystal structure of d(CGATCG) complexed with daunomycin. *J. Mol. Biol.* **1989**, *206*, 693-705.
  94. Guelev, V.; Sorey, S.; Hoffman, D.W.; Iverson, B. L. Changing DNA grooves – a 1,4,5,8-naphthalene tetracarboxylic diimide bis-intercalator with the linker ( $\beta$ -Ala)<sub>3</sub>-Lys in the minor groove. *J. Am. Chem. Soc.* **2002**, *124*, 2864–2865.
-

95. Lee, J.; Guelev, V.; Sorey, S.; Hoffman, D. W.; Iverson, B. L. NMR structural analysis of a modular threading tetraintercalator bound to DNA. *J. Am. Chem. Soc.* **2004**, *126*, 14036-14042.
96. Holman, G. G.; Zewail-Foote, M.; Smith, A. R.; Kenneth A. Johnson, K. A.; Iverson, B. L. A sequence-specific threading tetra-intercalator with an extremely slow dissociation rate constant. *Nat. Chem.* **2011**, *3*, 875-881.
97. Schleif, R. DNA binding by proteins. *Science* **1988**, *241*, 1182-1187.
98. Thuong, N. T.; Hélène, C. Sequence-Specific recognition and modification of double-helical DNA by oligonucleotides. *Angew. Chem., Int. Ed.* **1993**, *32*, 666-690.
99. Jain, A. K.; Bhattacharya, S. Groove binding ligands for the interaction with parallel-stranded ps-duplex DNA and triplex DNA. *Bioconjugate Chem.* **2010**, *21*, 1389-1403.
100. Nielsen, P. E. Peptide nucleic acids as therapeutic agents. *Curr. Opin. Struct. Biol.* **1999**, *9*, 353-357.
101. Ganesh, K. N.; Nielsen, P. E. Peptide nucleic acids: Analogs and derivatives. *Curr. Org. Chem.* **2000**, *4*, 931-943.
102. Ganesh, K. N.; Kumar, V. A. Conformationally constrained PNA analogs: Structural evolution towards DNA/RNA binding selectivity. *Acc. Chem. Res.* **2005**, *38*, 404-412.
103. Wartell, R. M.; Larson, J. E.; Wells, R. D. Netropsin. A specific probe for A-T regions of duplex deoxyribonucleic acid. *J. Biol. Chem.* **1974**, *249*, 6719-6731.
104. Kopka, M. L.; Yoon, C.; Goodsell, D.; Pjura, P.; Dickerson, R. E. The molecular origin of DNA-drug specificity in netropsin and distamycin. *Proc. Nat. Acad. Sci. USA* **1985**, *82*, 1376-1380.
105. Bailly, C.; Chaires, J. B. Sequence-specific DNA minor groove binders. Design and synthesis of netropsin and distamycin analogues. *Bioconjugate Chem.* **1998**, *9*, 513-537.
106. Kopka, M. L.; Yoon, C.; Goodsell, D.; Pjura, P.; Dickerson, R. E. Binding of an antitumor drug to DNA, Netropsin and C-G-C-G-A-A-T-T-BrC-G-C-G. *J. Mol. Biol.* **1985**, *183*, 553-563.
107. Lown, J. W.; Krowicki, K.; Bhat, U. G.; Skorobogaty, A.; Ward, B.; Dabrowiak, J. C. Molecular recognition between oligopeptides and nucleic acids: novel imidazole-containing oligopeptides related to netropsin that exhibit altered DNA sequence specificity. *Biochemistry* **1986**, *25*, 7408-7416.
108. Mrksich, M.; Wade, W. S.; Dwyer, T. J.; Geierstanger, B. H.; Wemmer, D. E.; Dervan, P. B. Antiparallel side-by-side dimeric motif for sequence-specific recognition in the minor groove of DNA by the designed peptide 1-methylimidazole-2-carboxamide netropsin. *Proc. Nat. Acad. Sci. USA* **1992**, *89*, 7586-7590.



- 
109. Wade, W. E.; Mrksich, M.; Dervan, P. B. Design of peptides that bind in the minor groove of DNA at 5'-(A,T)G(A,T)C(A,T)-3' sequences by a dimeric side-by-side motif. *J. Am. Chem. Soc.* **1992**, *114*, 8783-8794.
  110. Dervan, P. B. Design of sequence-specific DNA-binding molecules. *Science* **1986**, *232*, 464-471.
  111. White, S.; Szewczyk, J. W.; Turner, J. M.; Baird, E. E.; Dervan, P. B. Recognition of the four Watson-Crick base pairs in the DNA minor groove by synthetic ligands. *Nature* **1998**, *391*, 468-471.
  112. Dervan, P. B. Molecular recognition of DNA by small molecules. *Bioorg. Med. Chem.* **2001**, *9*, 2215-2235.
  113. Wilson, W. D.; Tanious, F. A.; Mathis, A.; Tevis, D.; Hall, J. E.; Boykin, D. W. Anti-parasitic compounds that target DNA. *Biochimie* **2008**, *90*, 999-1014.
  114. Nguyen, B.; Neidle, S.; Wilson, W. D. A role for water molecules in DNA-ligand minor groove recognition. *Acc. Chem. Res.* **2009**, *42*, 11-21.
  115. Ginsburg, H.; Nissani, E.; Krugliak, M.; Williamson, D. H. Selective toxicity to malaria parasites by non-intercalating ligands. *Molecular and Biochemical Parasitology* **1993**, *58*, 7-16.
  116. Crissman, H. A.; Hirons, G. T. Staining of DNA in live and fixed cells. *Methods Cell Biol.* **1994**, *41*, 195-209.
  117. Lakowicz, J. R. Principles of Fluorescence Spectroscopy. 3rd ed., Springer, New York, **2006**.
  118. Haugland, R. P., Spence, M. T. Z., Johnson, I. D., and Basey, A. The handbook: a guide to fluorescent probes and labeling technologies. 10th ed., Molecular Probes, Eugene, OR, **2005**.
  119. Johnson, I. Fluorescent probes for living cells. *Histochem. J.* **1998**, *30*, 123-140.
  120. Zhang, J.; Campbell, R. E.; Ting, A. Y.; Tsien, R. Y. Creating new fluorescent probes for cell biology. *Nat. Rev. Mol. Cell Biol.* **2002**, *3*, 906-918.
  121. Sinkeldam, R. W.; Greco, N. J.; Tor, Y. Fluorescent analogs of biomolecular building blocks: design, properties, and applications. *Chem. Rev.* **2010**, *110*, 2579-619.
  122. Wysocki, L. M.; Lavis, L. D. Advances in the chemistry of small molecule fluorescent probes. *Curr. Opin. Chem. Biol.* **2011**, *15*, 752-759.
  123. Lavis, L. D.; Raines, R. T. Bright ideas for chemical biology. *ACS Chem Biol.* **2008**, *3*, 142-155.
  124. Zink, D.; Cremer, T. Cell nucleus: chromosome dynamics in nuclei of living cells. *Curr. Biol.* **1998**, *8*, R321-R324.
  125. Zipfel, W. R.; Williams, R. M.; Webb, W. W. Nonlinear magic: multiphoton microscopy in the biosciences. *Nat. Biotechnol.* **2003**, *21*, 1369-1377.
-

126. Oheim, M.; Michael, D. J.; Geisbauer, M.; Madsen, D.; Chow, R. Principles of two-photon excitation fluorescence microscopy and other nonlinear imaging approaches. *Adv. Drug Delivery Rev.* **2006**, *58*, 788-808.
127. Lee, H.; Akers, W.; Bhushan, K.; Bloch, S.; Sudlow, G.; Tang, R.; Achilefu, S. Near-infrared pH-activatable fluorescent probes for imaging primary and metastatic breast tumors. *Bioconjugate Chem.* **2011**, *22*, 777-784
128. Latt, S. A.; Wohlleb, J. J. Optical Studies of the interaction of Hoechst 33258 with DNA, chromatin, and metaphase chromosomes. *Chromosoma* **1975**, *52*, 297-316.
129. Moon, J. H.; Kim, S. K.; Sehlstedt, U.; Rodger, A.; Nordén, B. DNA Structural Features Responsible for Sequence-Dependent Binding Geometries of Hoechst 33258. *Biopolymers* **1996**, *38*, 593-606.
130. Pjura, P. E.; Grzeskowiak, K.; Dickerson, R. E. Binding of Hoechst 33258 to the Minor Groove of B-DNA. *J. Mol. Biol.* **1987**, *197*, 257-271.
131. Breusegem, S. Y.; Clegg, R. M.; Loontjens, F. G. Base-sequence Specificity of Hoechst 33258 and DAPI Binding to Five (A/T)<sub>4</sub> DNA Sites with Kinetic Evidence for More Than One High-Affinity Hoechst 33258-AATT Complex. *J. Mol. Biol.* **2002**, *315*, 1049-1061.
132. Fede, A.; Billeter, M.; Leupin, W.; Wuethrich, K. Determination of the NMR Solution Structure of the Hoechst 33258-d-(GTGGAATTCCAC)<sub>2</sub> Complex and Comparison with the X-ray Crystal Structure. *Structure* **1993**, *1*, 177-186.
133. Kapuscinski, J.; Skoczylas, B. Fluorescent complexes with DAPI 4',6-diamidine-2-phenylindole. 2HCl or DCI 4',6-dicarboxyamido-2-phenylindole. *Nucleic Acids Res.* **1978**, *5*, 3775-3799.
134. Kapuscinsky, J.; Szer, W. Interactions of 4',6-diamidine-2-phenylindole with synthetic polynucleotides. *Nucleic Acids Res.* **1979**, *6*, 3519-3535.
135. Larsen, T. A.; Goodsell, D. A.; Cascio, D.; Grzeskowiak, K.; Dickerson, R. E. The structure of DAPI bound to DNA. *J. Biomol. Struct. Dynam.* **1989**, *7*, 477-491.
136. Loontjens, F. G.; McLaughlin, L. W.; Diekmann, S.; Clegg, R. M. Binding of Hoechst 33258 and 4',6-diamidino-2-phenylindole to self-complementary decadeoxynucleotides with modified exocyclic base substituents. *Biochemistry* **1991**, *30*, 182-189.
137. Wilson, W. D.; Tanius, F. A.; Barton, H. J.; Jones, R. L.; Fox, K.; Wydra, R. L.; Strekowski, L. DNA sequence dependent binding modes of 4',6-diamidino-2-phenylindole (DAPI). *Biochemistry* **1990**, *29*, 8452-8461.
138. Waring, M. J. Complex formation between Ethidium Bromide and nucleic Acids. *J. Mol. Biol.* **1965**, *13*, 269-282.

139. Waring, M. J. Complex formation with DNA and inhibition of Escherichia coli RNA polymerase by ethidium bromide. *Biochim. Biophys. Acta.* **1964**, *87*, 358-361.
140. Tsai, C.-C.; Jain, S. C.; Sobell, H. M. X-Ray crystallographic visualization of drug-nucleic acid intercalative binding: structure of an Ethidium-dinucleoside monophosphate crystalline Complex, Ethidium: 5-Iodouridylyl(3'-5')Adenosine. *Proc. Natl. Acad. Sci. U.S.A* **1975**, *72*, 628-632.
141. Arndt-Jovin, D. J.; Jovin, T. M. Fluorescence labeling and microscopy of DNA. *Methods Cell. Biol.* **1989**, *30*, 417-448.
142. Fraker, P. J.; King, L. E.; Lill-Elghanian, D.; Telford, W. G. Quantification of apoptotic events in pure and heterogeneous populations of cells using the flow cytometer. *Methods Cell. Biol.* **1995**, *46*, 57-76.
143. Riccardi, C.; Nicoletti, I. Analysis of apoptosis by propidium iodide staining and flow cytometry. *Nat. Protoc.* **2006**, *1*, 1458-1461.
144. Zipper, H.; Brunner, H.; Bernhagen, J.; Vitzthum, F. Investigations on DNA intercalation and surface binding by SYBR Green I, its structure determination and methodological implications. *Nucleic Acids Res.* **2004**, *32*, e103.
145. Vitzthum, F.; Geiger, G.; Bisswanger, H.; Brunner, H.; Bernhagen, J. A quantitative fluorescence-based microplate assay for the determination of double-stranded DNA using SYBR Green I and a standard ultraviolet transilluminator gel imaging system. *Anal. Biochem.* **1999**, *276*, 59-64.
146. Giglio, S.; Monis, P. T.; Saint, C. P. Demonstration of preferential binding of SYBR Green I to specific DNA fragments in real-time multiplex PCR. *Nucleic Acids Res.* **2003**, *31*, e136.
147. Dragan, A. I.; Casas-Finet, J. R.; Bishop, E. S.; Strouse, R. J.; Schenerman, M. A.; Geddes, C. D. Characterization of PicoGreen interaction with dsDNA and the origin of its fluorescence enhancement upon binding. *Biophys. J.* **2010**, *99*, 3010-3019.
148. Singer, V. L.; Jones, L. J.; Yue, S. T.; Haugland, R. P. Characterization of PicoGreen reagent and development of a fluorescence-based solution assay for double-stranded DNA quantitation. *Anal. Biochem.* **1997**, *249*, 228-238.
149. Noothi, S. K.; Kombrabail, M.; Rao, B. J.; Krishnamoorthy, G. Fluorescence characterization of the structural heterogeneity of polytene chromosomes. *J. Fluoresc.* **2010**, *20*, 37-41.
150. Noothi, S. K.; Kombrabail, M.; Kundu, T. K.; Krishnamoorthy, G.; Rao, B. J. Enhanced DNA dynamics due to cationic reagents, topological states of dsDNA and high mobility group box 1 as probed by PicoGreen. *FEBS J.* **2009**, *276*, 541-551.

151. Nygren, J.; Svanvik, N.; Kubista, M. The Interactions between the fluorescent dye Thiazole Orange and DNA. *Biopolymers* **1998**, *46*, 39-51.
152. Rye, H. S.; Yue, S.; Wemmer, D. E.; Quesada, M. A.; Haugland, R. P.; Mathies, R. A.; Glazer, A. N. Stable fluorescent complexes of double-stranded DNA with bis-intercalating asymmetric cyanine dyes: properties and applications. *Nucleic Acids Res.* **1992**, *11*, 2803–2812.
153. Hansen, L. F.; Jensen, L. K.; Jacobsen, J. P. Bis-intercalation of a homodimeric thiazole orange dye in DNA in symmetrical pyrimidine–pyrimidine–purine–purine oligonucleotides. *Nucleic Acids Res.* **1996**, *24*, 859–867.
154. Monchaud, D.; Allain, C.; Teulade-Fichou, M. P. Thiazole Orange; A useful probe for fluorescence sensing of G-Quadruplex-ligand interactions. *Nucleosides Nucleotides Nucleic Acids* **2007**, *26*, 1585– 588.
155. Lubitz, I.; Zikich, D.; Kotlyar, A. Specific high-affinity binding of Thiazole Orange to Triplex and G-quadruplex DNA. *Biochemistry* **2010**, *49*, 3567– 3574.
156. Rogers, D. R. Screening for amyloid with the thioflavin-T fluorescent method. *Am. J. Clin. Pathol.* **1965**, *44*, 59–61.
157. Mohanty, J.; Barooah, N.; Dhamodharan, V.; Harikrishna, S.; Pradeepkumar, P. I.; Bhasikuttan, A. C. Thioflavin T as an efficient inducer and selective fluorescent sensor for the human telomeric G-quadruplex DNA. *J. Am. Chem. Soc.* **2013**, *135*, 367–376.
158. Renaud de la Faverie, A.; Guédin, A.; Bedrat, A.; Yatsunyk, L. A.; Mergny, J.-L. Thioflavin T as a fluorescence light-up probe for G4 formation. *Nucleic Acids Res.* **2014**, *42*, e65.
159. Endo, M.; Sugiyama, H. Chemical approaches to DNA nanotechnology. *ChemBioChem* **2009**, *10*, 2420-2443.
160. Feldkamp, U.; Niemeyer, C. M. Rational design of DNA nanoarchitectures. *Angew. Chem., Int. Ed.* **2006**, *45*, 1856-1876.
161. Seeman, N. C. DNA in a material world. *Nature* **2003**, *421*, 427-431.
162. Lu, Y.; Liu, J. Smart nanomaterials inspired by biology: dynamic assembly of error-free nanomaterials in response to multiple chemical and biological stimuli. *Acc. Chem. Res.* **2007**, *40*, 315-323.
163. Seeman, N. C. An overview of structural DNA nanotechnology. *Mol. Biotechnol.* **2007**, *37*, 246-257.
164. Dietz, H.; Douglas, S. M.; Shih, W. M. Folding DNA into twisted and curved nanoscale shapes. *Science* **2009**, *325*, 725-730.
165. Douglas, S. M.; Dietz, H.; Liedl, T.; Högberg, B.; Graf, F.; Shih, W. M. Self-assembly of DNA into nanoscale three-dimensional shapes. *Nature* **2009**, *459*, 414-418.

166. Zheng, J.; Birktoft, J. J.; Chen, Y.; Wang, T.; Sha, R.; Constantinou, P. E.; Ginell, S. L.; Mao, C.; Seeman, N. C. From molecular to macroscopic via the rational design of a self-assembled 3D DNA crystal. *Nature* **2009**, *461*, 74-77.
167. Rosi, N. L.; Mirkin, C. A. Nanostructures in biodiagnostics. *Chem. Rev.* **2005**, *105*, 1547-1562.
168. Tikhomirov, G.; Hoogland, S.; Lee, P. E.; Fischer, A.; Sargent, E. H.; Kelley, S. O. DNA-based programming of quantum dot valency, self-assembly and luminescence. *Nat. Nanotechnol.* **2011**, *6*, 485-490.
169. Yan, H.; Park, S. H.; Finkelstein, G.; Reif, J. H.; LaBean, T. H. DNA-templated self-assembly of protein arrays and highly conductive nanowires. *Science* **2003**, *301*, 1882-1884.
170. Kukolka, F.; Schoeps, O.; Woggon, U.; Niemeyer, C. M. DNA-directed assembly of supramolecular fluorescent protein energy transfer systems. *Bioconjug. Chem.* **2007**, *18*, 621-627.
171. Niemeyer, C. M.; Koehler, J.; Wuerdemann, C. DNA-directed assembly of bienzymic complexes from *in vivo* biotinylated NAD(P)H:FMN oxidoreductase and luciferase. *ChemBioChem* **2002**, *3*, 242-245.
172. Datta, B.; Schuster, G. B.; McCook, A.; Harvey, S. C.; Zakrzewska, K. DNA-directed assembly of polyanilines: modified cytosine nucleotides transfer sequence programmability to a conjoined polymer. *J. Am. Chem. Soc.* **2006**, *128*, 14428-14429.
173. Datta, B.; Schuster, G. B. DNA-directed synthesis of aniline and 4-aminobiphenyl oligomers: programmed transfer of sequence information to a conjoined polymer nanowire. *J. Am. Chem. Soc.* **2008**, *130*, 2965-2973.
174. Chen, W.; Güler, G.; Kuruvilla, E.; Schuster, G. B.; Chiu, H.-C.; Riedo, E. Development of self-organizing, self-directing molecular nanowires: synthesis and characterization of conjoined DNA-2,5-bis(2-thienyl)pyrrole oligomers. *Macromolecules* **2010**, *43*, 4032-4040.
175. Teo, Y. N.; Kool, E. T. DNA-multichromophore systems. *Chem. Rev.* **2012**, *112*, 4221-4245.
176. Malinovskii, V. L.; Wenger, D.; Häner, R. Nucleic acid-guided assembly of aromatic chromophores. *Chem. Soc. Rev.* **2010**, *39*, 410-422.
177. Seifert, J. L.; Connor, R. E.; Kushon, S. A.; Wang, M.; Armitage, B. A. Spontaneous assembly of helical cyanine dye aggregates on DNA nanotemplates. *J. Am. Chem. Soc.* **1999**, *121*, 2987-2995.
178. Wang, M.; Silva, G. L.; Armitage, B. A. DNA-templated formation of a helical cyanine dye J-aggregate. *J. Am. Chem. Soc.* **2000**, *122*, 9977-9986.
179. Hannah, K. C.; Armitage, B. A. DNA-templated assembly of helical cyanine dye aggregates: a supramolecular chain polymerization. *Acc. Chem. Res.* **2004**, *37*, 845-853.
-

180. Iwaura, R.; Hoeben, F. J. M.; Masuda, M.; Schenning, A. P. H. J.; Meijer, E. W.; Shimizu, T. Molecular-level helical stack of a nucleotide-appended oligo(p-phenylenevinylene) directed by supramolecular self-assembly with a complementary oligonucleotide as a template. *J. Am. Chem. Soc.* **2006**, *128*, 13298-13304.
181. Iwaura, R.; Kameyama, M. O.; Iizawa, T. Construction of helical J-aggregates self-assembled from a thymidylic acid appended anthracene dye and DNA as a template. *Chem. Eur. J.* **2009**, *15*, 3729–3735.
182. Janssen, P. G. A.; Vandenberg, J.; van Dongen, J. L. J.; Meijer, E. W.; Schenning, A. P. H. J. ssDNA templated self-assembly of chromophores. *J. Am. Chem. Soc.* **2007**, *129*, 6078-6079.
183. Janssen, P. G. A.; Jabbari-Farouji, S.; Surin, M.; Vila, X.; Gielen, J. C.; de Greef, J. T. F. A.; Vos, M. R. J.; Bomans, P. H. H.; Sommerdijk, N. A. J. M.; Christianen, P. C. M.; Leclère, P. H.; Lazzaroni, R.; van der Schoot, P.; Meijer, E. W.; Schenning, A. P. H. J. Insights into templated supramolecular polymerization: binding of naphthalene derivatives to ssDNA templates of different lengths. *J. Am. Chem. Soc.* **2009**, *131*, 1222–1231.
184. Janssen, P. G. A.; Ruiz-Carretero, A.; González-Rodríguez, D.; Meijer, E. W.; Schenning, A. P. H. J. pH-switchable helicity of DNA-templated assemblies. *Angew. Chem., Int. Ed.* **2009**, *48*, 8103-8106.
185. Surin, M.; Janssen, P. G. A.; Lazzaroni, R.; Leclère, Ph.; Meijer, E. W.; Schenning, A. P. H. J. Supramolecular organization of ssDNA-templated  $\pi$ -conjugated oligomers via hydrogen bonding. *Adv. Mater.* **2009**, *21*, 1126–1130.
186. Sargsyan, G.; Schatz, A. A.; Kubelka, J.; Balaz, M. Formation and helicity control of ssDNA templated porphyrin nanoassemblies. *Chem. Commun.* **2013**, *49*, 1020–1022.
187. Sargsyan, G.; Leonard, B. M.; Kubelka, J.; Balaz, M. Supramolecular ssDNA templated porphyrin and metalloporphyrin nanoassemblies with tunable helicity. *Chem. – Eur. J.* **2014**, *20*, 1878–1892.

---

# Chapter 2

**A Thiazole Coumarin (TC) Turn-On Fluorescence Probe for  
AT-Base Pair Detection and Multipurpose Applications in  
Different Biological Systems**

Small organic dyes capable of exhibiting turn-on fluorescence through sequence-specific interaction with nucleic acids play an integral role in fluorescence spectroscopy, diagnostics, imaging and biomedical applications.<sup>1,2</sup> Selective targeting of double-stranded (ds) DNA using organic dyes offers powerful strategies to develop i) probes for molecular biology and immunohistochemistry, flow cytometry and DNA quantitation, ii) genome-specific binders of potential theranostic interest in conjugation with predesigned oligonucleotides, and iii) diagnostic therapy of gene-related human diseases especially cancer, and parasitic and viral infections.<sup>3-5</sup> In this regard, various small sequence-specific fluorophores have been developed for biological assays, including cell imaging and DNA-quantitation in cells.<sup>6</sup>

The discovery of DNA as a genetic material and its double helical structure led to numerous studies directed at understanding DNA-small molecule interactions.<sup>7-10</sup> Typically, DNA-small molecule interaction has two prominent modes *viz.*, intercalation and minor groove binding. The research efforts of Dervan<sup>11,12</sup> and Lown<sup>13</sup> have set forth the foundation for developing a series of small molecules with affinity for the AT-rich minor groove of B-DNA. 4',6-Diamidino-2-phenylindole (DAPI)<sup>14</sup> and bisbenzimidides (Hoechst dyes)<sup>15</sup> are some of the well-studied nuclear staining agents that bind with the minor groove. Unfortunately, these blue-emitting DNA binders require ultraviolet (UV) light for excitation which is known to cause cellular DNA damage through free radical generation, eventually causing cell death.<sup>16</sup> Moreover, Hoechst dyes despite being faithful to the AT-rich minor groove of DNA, are nonetheless prone to fasten onto GC-rich and also show binding affinity towards single-stranded (ss) DNA and RNA.<sup>17,18</sup> Similarly, DAPI suffers from the disadvantages of non-specific binding to RNA<sup>19</sup> and requirement of high concentration for effective imaging thereby limiting its use only to fixed cells.<sup>20</sup> Apart from minor groove binders, ethidium bromide (EtBr) and propidium iodide (PI) have been used for cell staining and gel-imaging studies. However, impermeable nature of these dyes limited their application to fixed and dead cells only.<sup>15</sup> Recently, cyan and green fluorescence DNA-selective probes such as BENA435<sup>21</sup> and C61<sup>22</sup> have been reported. However, these probes, upon binding to DNA exhibit fluorescence enhancement with low quantum yields. Thomas *et al.* recently reported a dinuclear Ruthenium(II) polypyridyl complex as a DNA-staining probe which nonetheless required high concentration for cellular imaging.<sup>23</sup>



Apart from these molecules, a large number of cyanine dyes have been extensively used in DNA gel staining, microchip-based DNA sensing and fluorescence staining of DNA in cells.<sup>24-27</sup> Among the cyanine family dyes, thiazole orange (TO) and yellow orange (YO) are two important classes of fluorescence probes that display significant fluorescence enhancement upon binding to DNA. Further, the homodimeric forms of TOTO-1 and YOYO-1 are found to be highly sensitive for DNA detection.<sup>28-31</sup> However, these cyanine-based probes also exhibit significant fluorescence enhancement in the presence of RNA and ssDNA.<sup>32-34</sup> Recently, two other classes of cyanine dyes SYBR green I and PicoGreen I have been developed and successfully used for DNA staining in the picogram scale, although they also show fluorescence enhancement in the presence of ssDNA.<sup>18,35</sup>

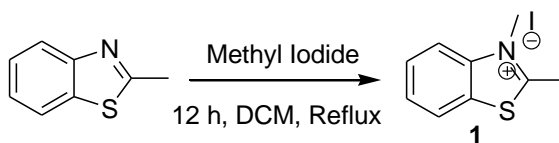
The limitations of existing probes discussed above necessitates the need for development of highly specific DNA-selective probes with i) long-wavelength excitation/emission, ii) strong turn-on fluorescence, iii) increased cell permeability, iv) non-toxicity to live cells, v) fidelity to dsDNA, and vi) sensitivity at low concentrations. In the present study, we demonstrate a turn-on red fluorescence hemicyanine probe **TC** as an effective cell-permeable, base-pair specific dsDNA recognition and nuclear DNA staining probe.<sup>36</sup> Inspired by the basic core structure of cyanine probes, we have designed three hemicyanine-based molecular probes namely thiazole-coumarin (**TC**), coumarin-lepidine (**CL**) and thiazole-pyrene (**TP**) with the objective of finding a superior DNA probe. To elucidate the role of positively charged quaternary amine group in benzothiazole-based probes, we have replaced the benzothiazole group with a quinoline moiety in **CL**. Similarly, coumarin group has been substituted with the hydrophobic pyrene in **TP** to understand the role of heterocyclic fluorophore moieties (coumarin/quinoline) in the benzothiazole-based probes.

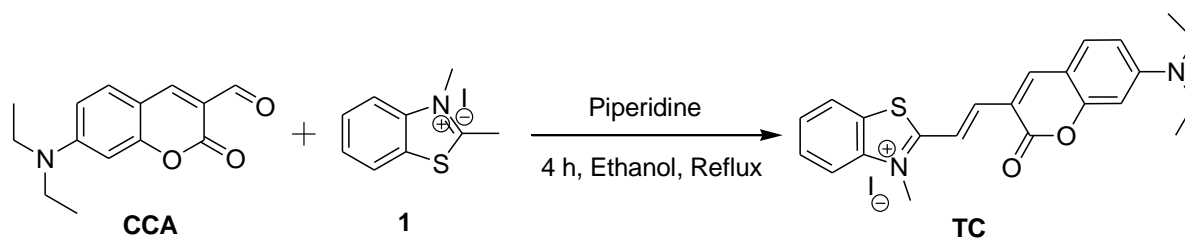
The choice of coumarin chromophore in the probes is owing to its excellent fluorescence properties in the visible region.<sup>37</sup> Further, these probes are likely to display excitation and emission in the longer wavelength of the visible region owing to extended conjugation, an essential prerequisite to avoid autofluorescence and DNA photo-damage during cellular imaging. One of the main characteristic optical properties of a dye to qualify as a potential DNA binding and staining reagent is that it must be non-fluorescent or weakly

fluorescent in the unbound state and display highly enhanced fluorescence in the longer wavelength of the visible region (red) upon interaction with DNA. Interestingly, all three hemicyanine probes are almost non-fluorescent in Tris-HCl buffer solution (100 mM, pH = 7.4) with very low quantum yields, a property that partially satisfies one of the primary requirements of a suitable turn-on fluorescence DNA binding probe. Intramolecular twisting of unsymmetrical cyanine dyes has been shown to be responsible for efficient quenching of fluorescence in unconstrained environments while their binding to compact packets of DNA results in enhanced fluorescence due to restriction of intramolecular twisting.<sup>38,39</sup> Similar molecular transformations are anticipated from our hemicyanine probes upon interaction with DNA.

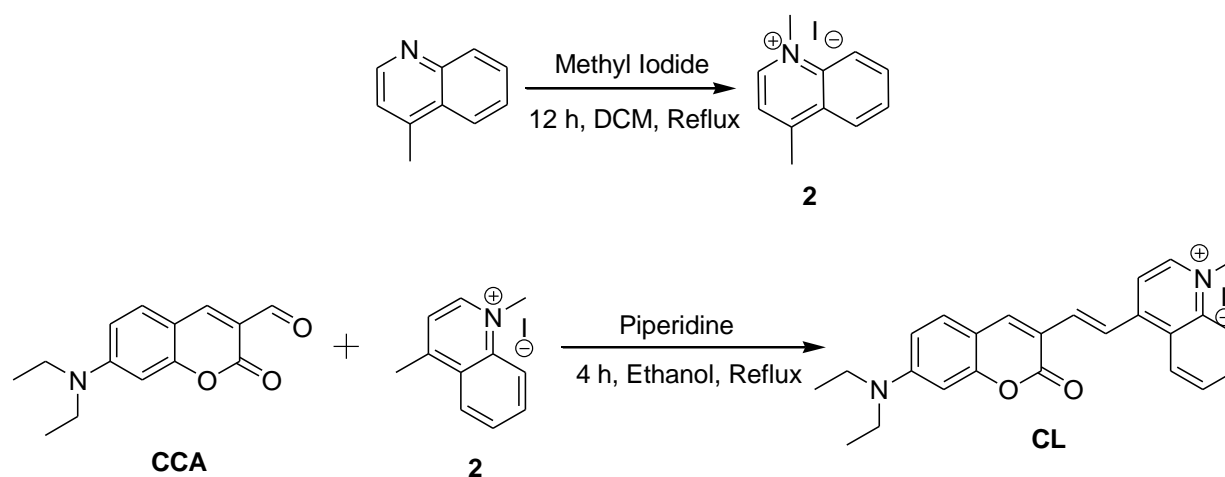
## 2.1 Synthesis of probes TC, CL and TP

Probes **TC**, **CL** and **TP** were synthesized by simple Knoevenagel condensation of *N*, *N*-ditheyl 7-(diethylamino)-2-oxo-2H-chromene-3-carbaldehyde (**CCA**) or pyrene-1-carbaldehyde with *N*-methylated benzothiazole (**1**) or lepidine (**2**) in presence of piperidine base. First, we treated 2-methyl benzothiazole and lepidine in presence of methyl iodide in dichloromethane under reflux conditions to get *N*-methylated benzothiazole (**1**) and lepidine (**2**) in good yields. The obtained *N*-methylated benzothiazole (**1**) was reacted with 7-(diethylamino)-2-oxo-2H-chromene-3-carbaldehyde (**CCA**) in presence of piperidine base in ethanol solvent under reflux conditions to offer probe **TC** and **CL** respectively in good yields (Scheme 1 and 2). *N*-methylated benzothiazole was treated to pyrene-1-carbaldehyde in presence of piperidine base to get probe **TP** in good yield (Scheme 3). The obtained compounds were well characterized by nuclear magnetic resonance (NMR) and High-resolution mass spectroscopy (HRMS).

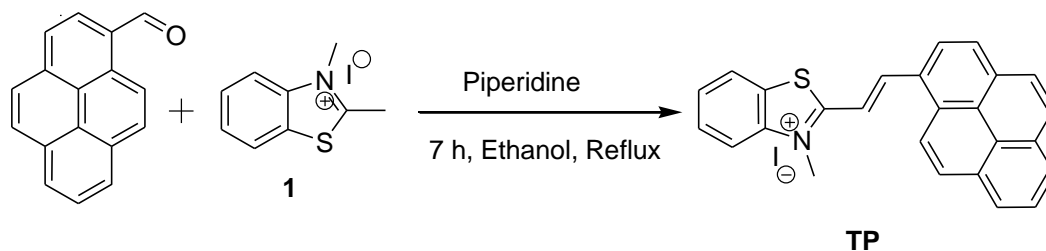




Scheme 1. Synthesis of probe TC.



Scheme 2. Synthesis of probe CL.



Scheme 3. Synthesis of probe TP.

## 2.2 Photophysical properties of probe TC, CL and TP

We first studied molecular interactions of **TC**, **CL** and **TP** in the absence and presence of DNA through photophysical (absorption and emission) measurements in Tris-HCl buffer (100 mM, pH = 7.4) solution. **TC**, **CL** and **TP** showed absorption in the visible region with absorption maxima at 528, 519 and 460 nm, respectively (Figure 1a). Interestingly, the

absorption spectrum of **TC** in the presence of dsDNA (AT)<sub>10</sub> showed a significant bathochromic shift ( $\Delta\lambda_{\text{max}} = 14$  nm) along with hypochromicity (Figure 1b). Emission spectra of **TC**, **CL** and **TP** exhibited very weak fluorescence with maxima at 641, 689 and 623 nm, respectively, and large Stokes shifts (Figure 2a). Next, we recorded the emission spectra of probes in the presence of DNA duplexes [(AT)<sub>10</sub> and (GC)<sub>10</sub>].

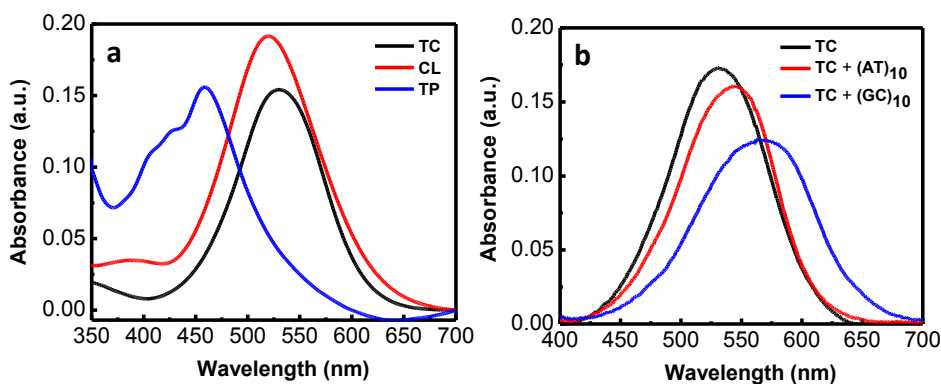


**Figure 1.** Photophysical properties of the probes. (a) UV-vis spectra of probes **TC**, **CL** and **TP** (10  $\mu\text{M}$ ) in Tris-HCl (100 mM, pH = 7.4) buffer solution. (b) UV-vis spectra of probe **TC** (10  $\mu\text{M}$ ) in the presence of (AT)<sub>10</sub> and (GC)<sub>10</sub>.

**TC** (10  $\mu\text{M}$ ) showed strong fluorescence enhancement in the presence of (AT)<sub>10</sub> which further increased with DNA concentration (0 to 12  $\mu\text{M}$ ) with overall  $\sim 8$ -fold enhancement accompanied by hypsochromic shift ( $\Delta\lambda_{\text{max}} = 26$  nm) in the emission maxima at 615 nm. Interestingly, **TC** did not display such fluorescence enhancement in the presence of (GC)<sub>10</sub>. Emission spectra of **CL** (10  $\mu\text{M}$ ) showed  $\sim 30$  and  $\sim 6$ -fold fluorescence enhancement in the presence of (AT)<sub>10</sub> and (GC)<sub>10</sub>, respectively, although with lower fluorescence intensity (QY: 0.040 and 0.007, respectively). We did not observe a detectable change in the emission spectra of **TP** (10  $\mu\text{M}$ ) in the presence of (AT)<sub>10</sub> and (GC)<sub>10</sub> (Figure 2a). These fluorescence emission studies of **TC**, **CL** and **TP** in the presence of (AT)<sub>10</sub> and (GC)<sub>10</sub> clearly indicate **TC** as an effective and selective turn-on fluorescence probe for DNA containing AT-base pairs (Figure 2b and 2c). The proficiency of probe **TC** as compared to **CL** and **TP** may be explained by the positively charged benzothiazole conjugated *N,N*-diethylamino-coumarin fluorophore that balanced amphiphilicity, and the possibility to achieving maximum  $\pi$ -electron overlap through molecular planarity (benzothiazole and coumarin) in a constrained environment.

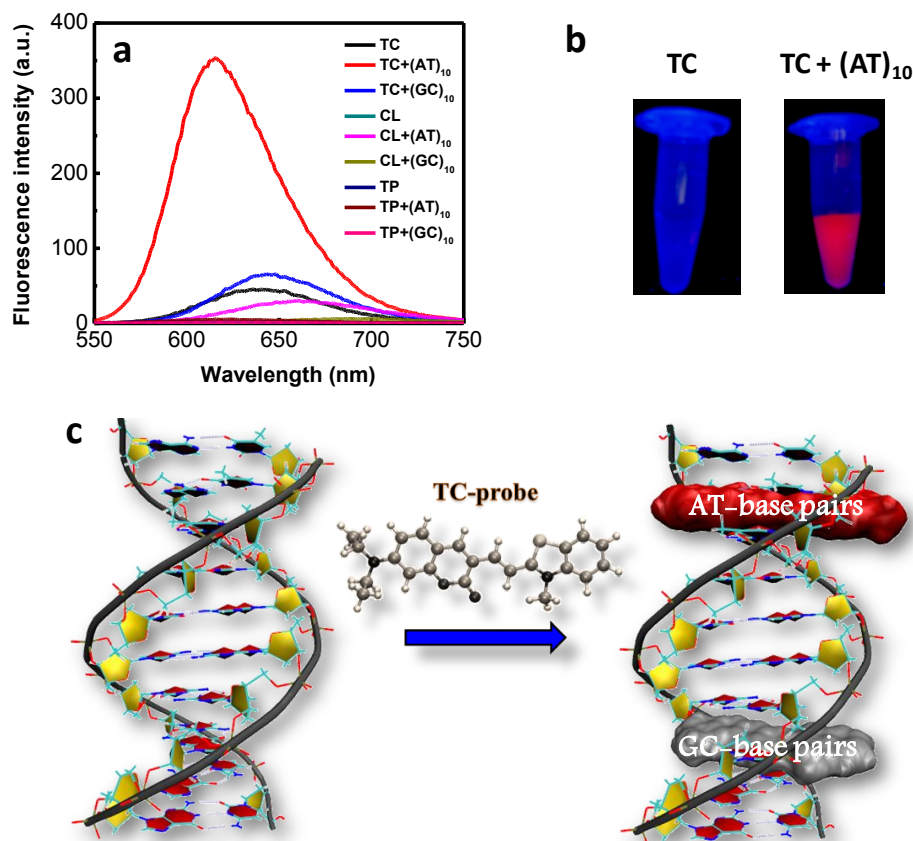


**Figure 2.** Selective AT-base pair fluorescence probe. (a) Fluorescence spectra of all the probes **TC**, **CL** and **TP** (10  $\mu\text{M}$ ) in presence of  $(\text{AT})_{10}$  and  $(\text{GC})_{10}$  in Tris-HCl (100 mM, pH = 7.4) buffer solution. (b) Photographs of **TC** and **TC**+  $(\text{AT})_{10}$  samples illuminated under UV light (365 nm). (c) Preferential fluorescence of probe **TC** in presence of DNA which consist of AT-rich and GC-rich base pairs.

In addition to this, the remarkable turn-on fluorescence enhancement of **TC** only in the presence of dsDNA containing AT-base pairs indicates that the AT-region provides favorable constrained environment to **TC** by restricting its intramolecular twisting. This was further verified by recording the emission spectra of **TC** with increasing glycerol percentage in Tris-HCl buffer solution. The emission spectra showed an increase in fluorescence intensity with the percentage of glycerol content (Figure 3a). Addition of glycerol increases the viscosity of the buffer solution. This viscous nature of glycerol aids in freezing the intramolecular rotation of probe **TC** to attain the planer molecular structure. The planar structure of **TC** leads to maximum electron delocalization which is further reflected in the enhanced fluorescence of probe **TC**. A similar effect *i.e.*, ‘freezing of intramolecular twisting’ is

assumed to occur when **TC** binds to dsDNA. These results confirm that the origin of the fluorescence enhancement of probe **TC** in the presence of dsDNA containing AT-base pairs is due to the restriction of intramolecular twisting. Further, we recorded the fluorescence spectra of **TC** in the presence of oligonucleotides (dA<sub>10</sub>, dT<sub>10</sub>, dG<sub>10</sub> and dC<sub>10</sub>). **TC** did not show significant changes in its emission behavior in the presence of ssDNA (Figure 3b). Therefore, the selectivity of **TC** for AT-region of dsDNA over ssDNA is a highly useful property because most of the commonly employed staining dyes such as ethidium bromide (EtBr), SYTO, Picogreen I and SYBR green I show weak fluorescence enhancement in the presence of ssDNA sequences.

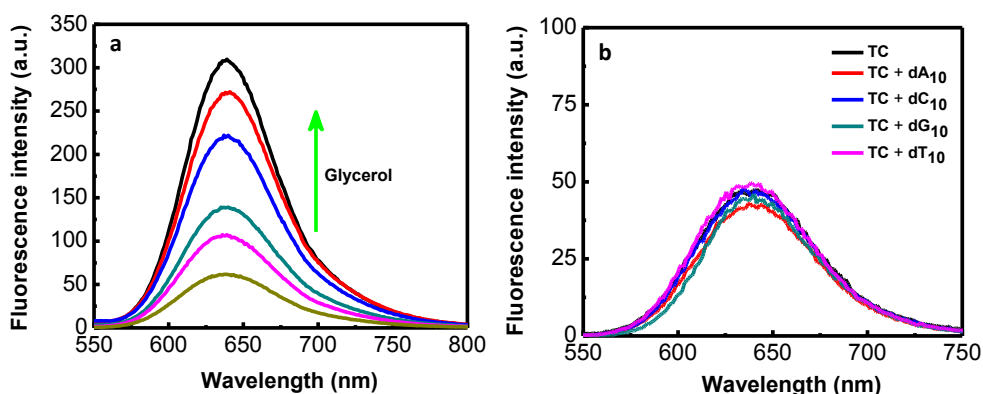


**Figure 3.** Emission spectra of probe **TC** in presence of glycerol and ssDNAs. (a) Fluorescence spectra of **TC** (10  $\mu$ M) in Tris-HCl (100 mM, pH = 7.4) buffer solution with increasing glycerol percentage from 0 to 100%. (b) Fluorescence spectra of **TC** (10  $\mu$ M) in all ssDNAs dA<sub>10</sub>, dT<sub>10</sub>, dG<sub>10</sub> and dC<sub>10</sub> in Tris-HCl buffer solution.

### 2.3 Selective fluorescence enhancement in the presence of dsDNA containing AT-base pairs

Highly selective turn-on fluorescence enhancement of **TC** towards (AT)<sub>10</sub> prompted us to explore its sequence-selective binding affinity towards various other dsDNA strands. We selected three different dsDNA (AT)<sub>20</sub>, self-complementary mixed sequences (D1)<sub>mix</sub> and (D2)<sub>mix</sub> composed of a variable number of consecutive AT-base pairs, *i.e.*, 20, 4 (two sets) and 2 (two sets), respectively (Table 1). **TC** (10  $\mu$ M) displayed  $\sim$ 16-fold fluorescence enhancement with 20 consecutive AT-base pairs in (AT)<sub>20</sub> which is two-fold higher than (AT)<sub>10</sub>. Next, we recorded the emission spectra of self-complementary AT-rich d(AATT)<sub>5</sub>

sequence.<sup>40</sup> The fluorescence measurements of probe **TC** showed ~16-fold enhancement in the presence of d(AATT)<sub>5</sub> (Figure 4). The mixed dsDNA (D1)<sub>mix</sub> and (D2)<sub>mix</sub> with 4 (two sets) and 2 (two sets) consecutive AT-base pairs exhibited fluorescence enhancement of ~ 6 and 1.5-folds, respectively (Figure 5a). These data were further validated by recording the emission spectra of **TC** (10 μM) with increasing concentration (0 μM to 12 μM) of dsDNA (AT)<sub>20</sub>, (AT)<sub>10</sub>, (D1)<sub>mix</sub> and (D2)<sub>mix</sub> that displayed overall ~16, ~8, ~6 and ~1.5-fold fluorescence enhancement respectively with hypsochromic shift in the fluorescence maxima (Figure 5b).

**Table 1.** Sequence information of DNA used in this study.

Code	DNA duplex	Sequence
(AT) <sub>10</sub>	dA <sub>10</sub> -dT <sub>10</sub>	5'-AAAAAAAAAA-3' 3'-TTTTTTTTTT-5'
(GC) <sub>10</sub>	dG <sub>10</sub> -dC <sub>10</sub>	5'-GGGGGGGGGG-3' 3'-CCCCCCCCCC-5'
(AT) <sub>20</sub>	dA <sub>20</sub> -dT <sub>20</sub>	5'-AAAAAAAAAAAAAAAAAAAA-3' 3'-TTTTTTTTTTTTTTTTTTTT-5'
d(AATT) <sub>5</sub>	d(AATT) <sub>5</sub>	5'-AATTAATTAATTAATTAATT-3' 3'-TTAATTAATTAATTAATTA-5'
(D1) <sub>mix</sub>	mixed DNA	5'- CGATAAGCGCTTATCG-3' 3'-GCTATTGCGGAATAGC-5'
(D2) <sub>mix</sub>	mixed DNA	5'- CGGTACCGCGGTACCG -3' 3'-GCCATGGCGCCATGGC-5'

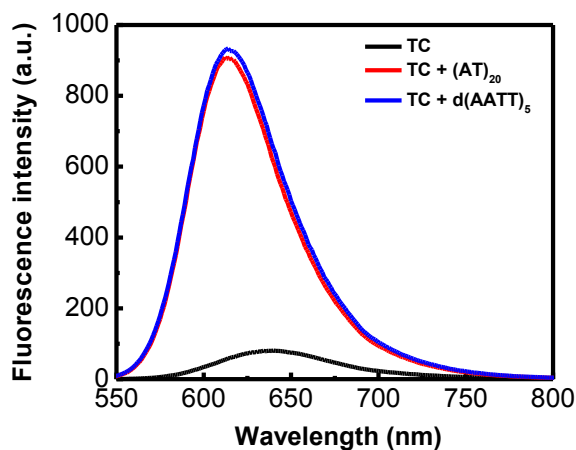


**Figure 4.** Emission spectra of probe **TC** (10 μM) in presence of (AT)<sub>20</sub> and self complementary d(AATT)<sub>5</sub> DNA duplexes.

Further, we determined the quantum yield of probe **TC** in buffer solution. In the absence of dsDNA, **TC** showed very low quantum yield ( $\Phi_F = 0.03$ ). However, the quantum yield increased significantly ( $\Phi_F = \sim 0.36$ ) upon binding with  $(AT)_{20}$ . In general, above discussed studies revealed significant red fluorescence enhancement with increasing number of AT-base pairs in dsDNA and increased quantum yield specifically in the presence of AT-rich regions, thereby suggesting the preferential binding affinity of **TC** towards AT-sites rather than GC-sites.

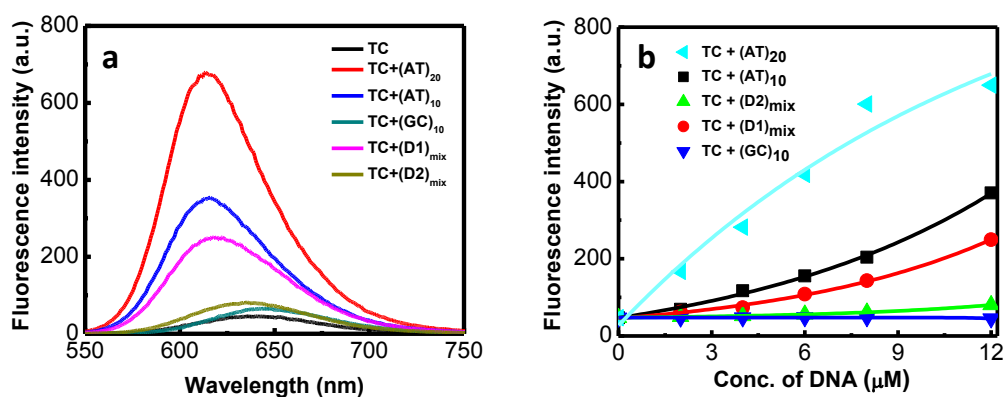


**Figure 5.** Emission spectra of probe **TC** in presence dsDNA. (a) Fluorescence spectra of probe **TC** (10 μM) in presence of various dsDNAs. (b) Fluorescence response of probe **TC** (10 μM) with increasing concentration of  $(AT)_{20}$ ,  $(AT)_{10}$ ,  $(GC)_{10}$ ,  $(D1)_{mix}$  and  $(D2)_{mix}$  upon excitation at 521 nm.

#### 2.4 Concentration dependent study of probe **TC** in presence of dsDNAs

Subsequently, the concentration-dependent fluorescence response of **TC** against fixed concentration of dsDNA (12 μM) containing AT-base pairs was investigated (Figure 6). In the absence of dsDNA, increasing concentrations of **TC** (0 to 20 μM) showed very weak fluorescence emission. In the presence of  $(AT)_{20}$ , increasing concentration of **TC** from 0 to 18 μM showed regular enhancement in fluorescence intensity. Saturation was achieved beyond 18 μM (18 to 22 μM). Interestingly, for concentrations of  $TC > 24$  μM a decrease in fluorescence intensity accompanied by bathochromic shift in the emission maxima was observed. Similar changes in the fluorescence emission were observed with increasing concentration of **TC** in the presence of  $(D1)_{mix}$  and  $(D2)_{mix}$  (Figure 7).



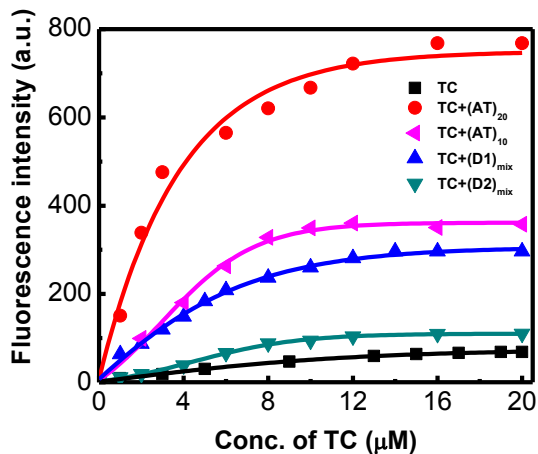


**Figure 6.** Plot of fluorescence intensity of increased concentration of TC (0 - 20  $\mu\text{M}$ ) in presence of fixed concentrations (12  $\mu\text{M}$ ) of (AT)<sub>20</sub>, (AT)<sub>10</sub>, (D1)<sub>mix</sub>, (D2)<sub>mix</sub>.

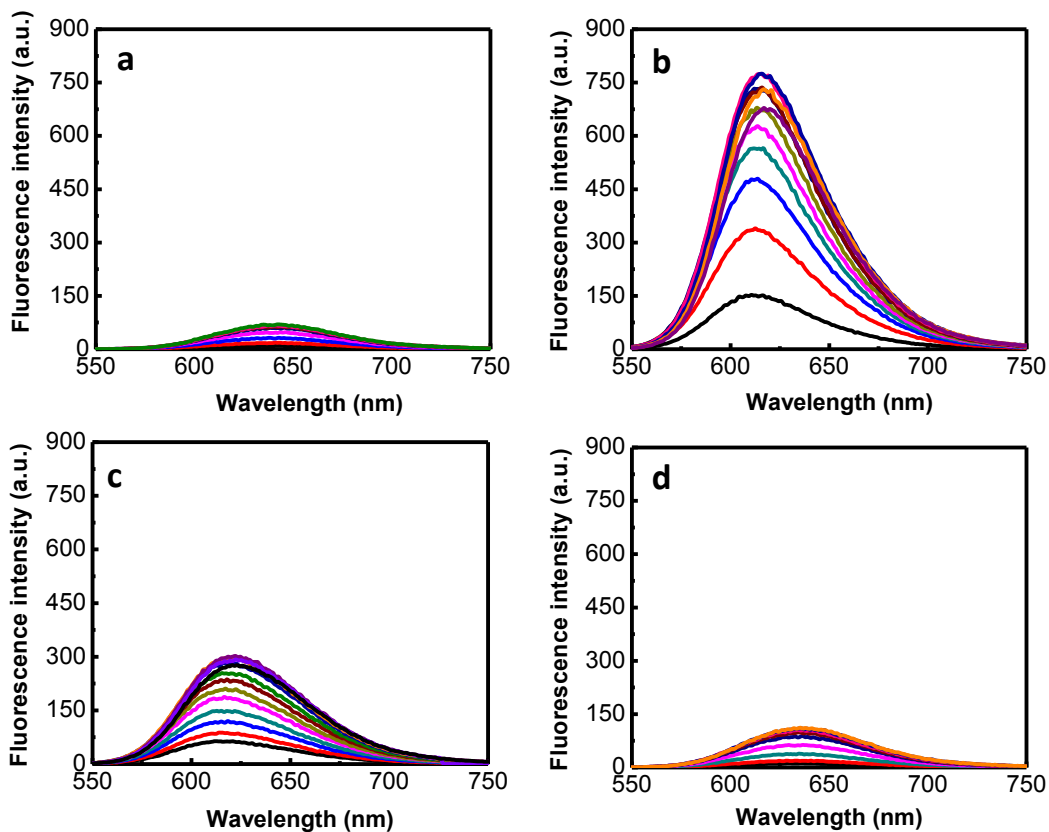


**Figure 7.** Fluorescence spectra of duplexes with increasing concentration of probe TC. (a-d) TC alone, (AT)<sub>20</sub>, (D1)<sub>mix</sub> and (D2)<sub>mix</sub> respectively upon excitation at 521 nm.

The observed fluorescence emission behavior of **TC** suggests that, at lower concentrations, **TC** can readily occupy the available binding sites (AT-region) of dsDNA, resulting in strong fluorescence enhancement. However, at higher concentrations of **TC** (18 - 22  $\mu\text{M}$ ) the fluorescence emission reaches a peak due to saturation of binding sites. After the saturation of binding sites (for  $> 24 \mu\text{M}$  of **TC**) in dsDNA (12  $\mu\text{M}$ ), competitive binding interactions occur between the unbound and bound **TC** molecules leading to displacement of some of the bound molecules from dsDNA.<sup>41</sup> This explains the linear increase in fluorescence at lower concentrations  $<18 \mu\text{M}$ , saturation at 18 - 22  $\mu\text{M}$  and a dramatic decrease in the fluorescence intensity at  $>24 \mu\text{M}$  of **TC**.

### 2.5 Gel-electrophoresis study of probe **TC** in presence of dsDNAs

The turn-on red fluorescence behavior of probe **TC** in the presence of AT-rich DNA inspired us to explore the use of **TC** as a staining agent for dsDNA in gel electrophoresis. The dsDNA samples (0.6  $\mu\text{g}$ ) of  $(\text{AT})_{20}$ ,  $(\text{D1})_{\text{mix}}$ ,  $(\text{D2})_{\text{mix}}$  and  $(\text{GC})_{10}$  were subjected to agarose gel electrophoresis and the gel was visualized under UV-illumination after staining with **TC**. UV-illuminated gel image showed strong fluorescence intensity for  $(\text{AT})_{20}$ ,  $(\text{D1})_{\text{mix}}$  and  $(\text{D2})_{\text{mix}}$ , respectively while the band for  $(\text{GC})_{10}$  was not stained by **TC** at all (Figure 8a).

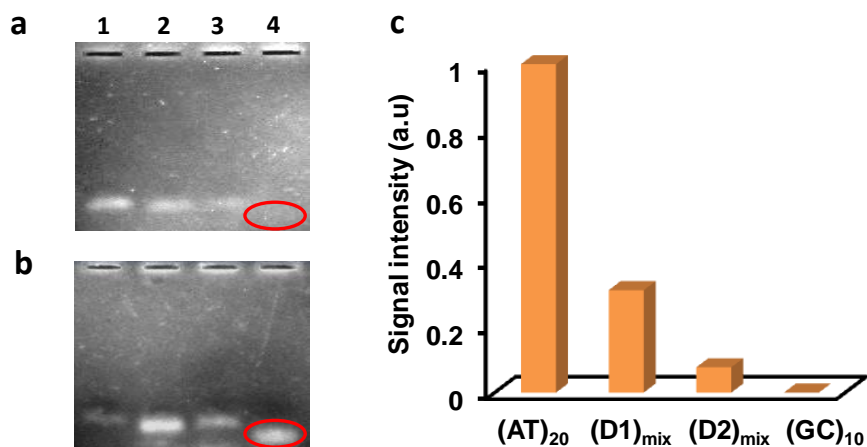


**Figure 8.** Gel-electrophoresis of probe **TC**. (a) & (b) are agarose gel-electrophoresis images of dsDNAs followed by staining the bands with probe **TC** and EtBr respectively. Lane 1-4:  $(\text{AT})_{20}$ ,  $(\text{D1})_{\text{mix}}$ ,  $(\text{D2})_{\text{mix}}$  and  $(\text{GC})_{10}$  respectively. Inset ring (red) in (a) shows non staining of  $(\text{GC})_{10}$  band by **TC**. Inset ring (red) in (b) shows staining of  $(\text{GC})_{10}$  band by EtBr. (c) Normalized densitometric signal intensity data of **TC** stained agarose-gel.

Besides, densitometric signal intensity data of **TC**-stained agarose gel exhibited relative fluorescence intensities in the following order:  $(AT)_{20} > (D1)_{mix} > (D2)_{mix}$  (Figure 8c). Next, the agarose gel was stained with the well-known gel staining agent ethidium bromide (EtBr). EtBr stained bands of  $(D1)_{mix}$ ,  $(D2)_{mix}$  and  $(GC)_{10}$  on the gel. While the staining was very weak for  $(AT)_{20}$ , it was strongest in the case of  $(GC)_{10}$  as expected from its weaker affinity towards AT-region as compared to GC-region of dsDNA (Figure 8b). From the gel-electrophoresis staining studies, it is clear that **TC** probe selectively discriminates dsDNA containing AT-base pairs from DNA containing only GC-base pairs. In addition, the comparative fluorescence response studies among **TC**, EtBr (Figure 9a) and propidium iodide (PI) (Figure 9b) in the presence of  $(AT)_{20}$  revealed **TC** as an excellent fluorescence marker for AT-rich DNAs while EtBr and PI did not display appreciable fluorescence changes.

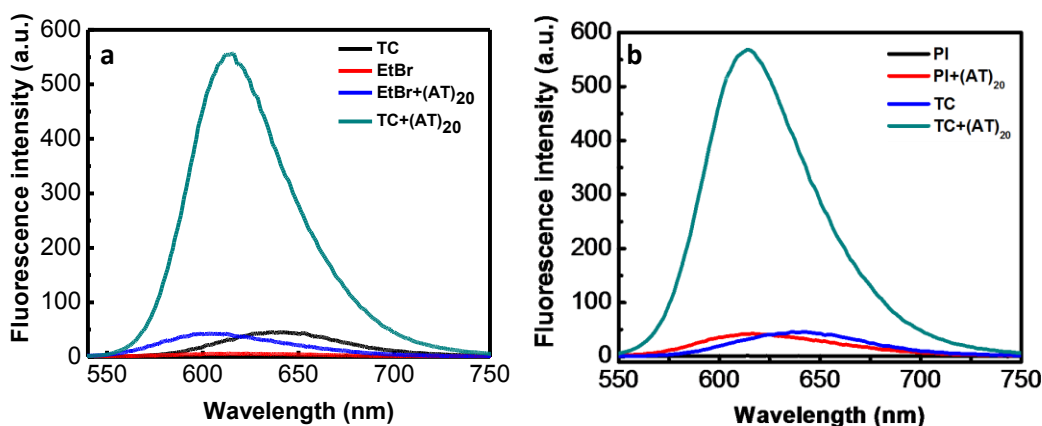


**Figure 9.** Photophysical properties of  $(AT)_{20}$  in **TC** and commercially available DNA-staining dyes. (a) Fluorescence spectra of  $(AT)_{20}$  in the presence of probe **TC** (10  $\mu$ M) and EtBr (10  $\mu$ M). (b) Fluorescence spectra of  $(AT)_{20}$  in the presence of probe **TC** (10  $\mu$ M) and PI (10  $\mu$ M) in Tris-HCl buffer (100 mM, pH = 7.4).

## 2.6 FRET study between probe **TC** and Hoechst 33258 in presence of $(AT)_{20}$

To gain insights into preferential binding of **TC** to AT-base pair regions in dsDNA, competitive binding studies with Hoechst were conducted. Hoechst dyes are known to interact with the minor groove of dsDNA. First, we recorded the emission spectrum of preformed  $(AT)_{20}$ -Hoechst 33258 complex upon excitation at 350 nm (corresponding to

Hoechst), which showed fluorescence enhancement at 450 nm. Next, we recorded the emission spectra of preformed (AT)<sub>20</sub>-Hoechst 33258 complex with increasing concentration of TC (0 to 40 μM) upon excitation at 350 nm (Figure 10a). A marked decrease in emission intensity of Hoechst at 450 nm was observed with increasing concentration of TC. Simultaneously, there was a gradual increase in emission at 610 nm of TC from 0 to 20 μM, above which emission intensity reached saturation (Figure 10c).

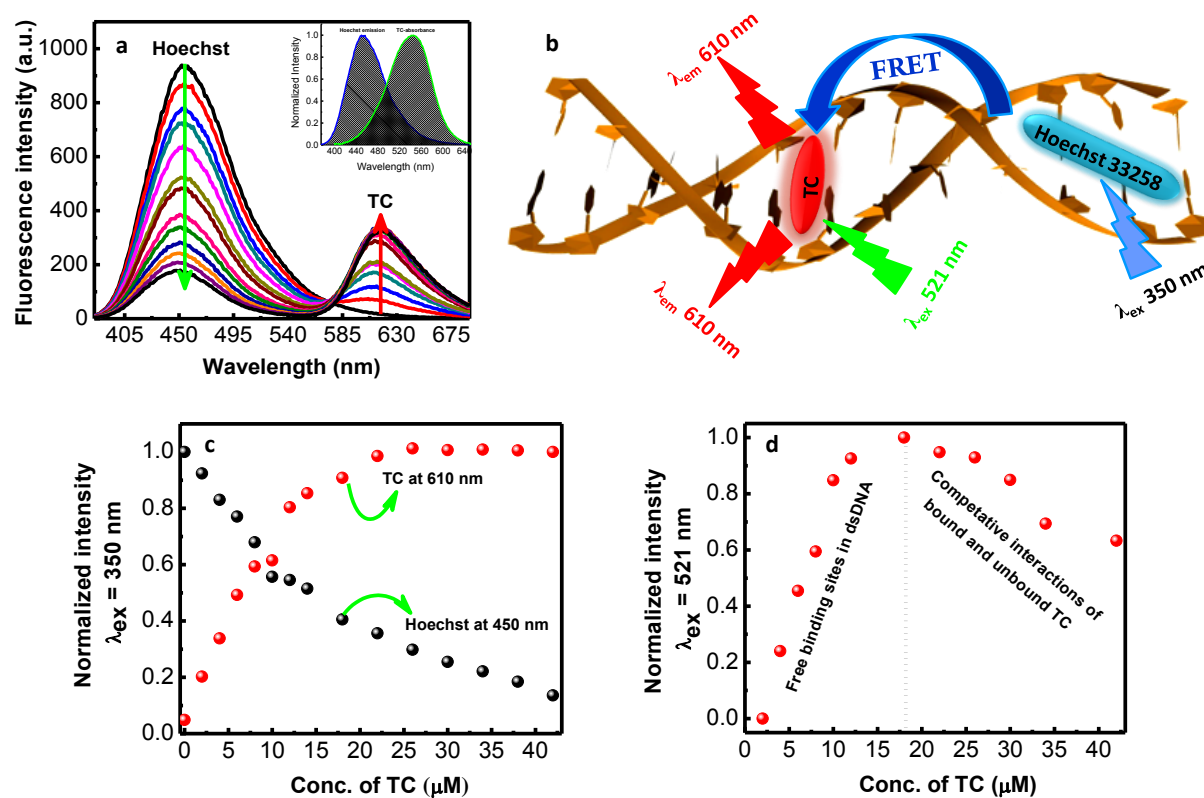


**Figure 10.** FRET between TC and Hoechst in presence of (AT)<sub>20</sub>. (a) Fluorescence spectra of preformed Hoechst (4 μM)+(AT)<sub>20</sub> complex with increasing concentration of TC from 0 μM to 40 μM. *Inset:* Overlap spectra of emission of preformed Hoechst (4 μM) + (AT)<sub>20</sub> complex and absorption spectra of TC (10 μM)+(AT)<sub>20</sub> complex. (b) Schematic representation of FRET between Hoechst 33258 (donor) and probe TC (acceptor) in presence of dsDNA upon excitation at 350 nm. (c) & (d) are fluorescence intensity plots of Hoechst at 450 nm and TC at 610 nm upon excitation at 350 nm and probe TC at 610 nm upon excitation at 521 nm of Hoechst (4 μM) + (AT)<sub>20</sub> with increasing concentration of TC respectively.

Interestingly, excitation at **TC** absorption (521 nm) showed strong fluorescence enhancement at 610 nm with increasing concentration of the probe from 0 to 20  $\mu\text{M}$ , which is specific of **TC** upon binding to dsDNA. This phenomenon of decrease in fluorescence intensity at 450 nm (Hoechst) and the corresponding increase in emission at 610 nm (**TC**) upon excitation at 350 nm (Hoechst) is due to efficient FRET from Hoechst to **TC** (Figure 10b). Further increase in concentration of **TC** (20 to 40  $\mu\text{M}$ ) led to a decrease in fluorescence, a characteristic phenomenon where unbound excess probe molecules (**TC**) assist the displacement of bound ones resulting in partial quenching of fluorescence (Figure 10d).<sup>41</sup>To understand this unprecedented fluorescence behavior observed in competitive study, circular dichroism (CD) studies of the (AT)<sub>20</sub>-Hoechst complex were conducted in the presence of **TC**. CD-spectrum of (AT)<sub>20</sub> displayed an intense positive and a negative Cotton signal in the 200-300 nm region. Hoechst alone has no characteristic CD signal but in the presence of (AT)<sub>20</sub> showed an induced positive Cotton signal in the 300-400 nm region (Figure 11).

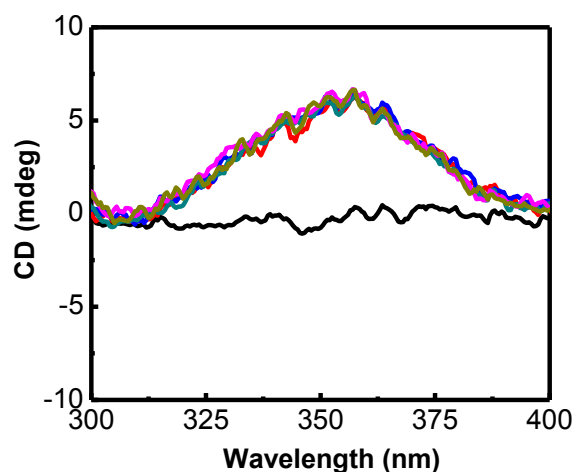


**Figure 11.** CD spectra of (AT)<sub>20</sub> + Hoechst (4  $\mu\text{M}$ ) with increasing concentration of **TC** from 0 to 40  $\mu\text{M}$  in Tris-HCl (100 mM, pH = 7.4) solution.

It is known that the minor groove of dsDNA comprises of chiral environment and upon binding induces its chirality to the achiral Hoechst dye molecules. However, increasing concentration of **TC** (0 to 40  $\mu\text{M}$ ) did not depict any detectable change in the CD signal of (AT)<sub>20</sub>-Hoechst complex. These data revealed that **TC** is not competing with Hoechst for

binding site in the minor groove of dsDNA. Rather, it bound to the adjacent region containing AT-base pairs. This is evident by the effective FRET from the Hoechst (donor) to the **TC** (acceptor). Normally, the efficient energy transfer in FRET mechanism depends on the distance between donor-acceptor pair and proper overlap of emission band of donor and absorption band of acceptor.<sup>42</sup> The effective spectral overlap of emission of Hoechst and excitation of **TC** indicated a perfectly matched donor-acceptor pair for the FRET process in AT-rich DNAs (Figure 10a *inset*). Thus, the observed FRET between the two probes clearly suggests that the binding site for **TC** must be in close proximity to that of Hoechst in the AT-rich minor groove of dsDNA. Similarly, FRET was also observed between DAPI (donor) and **TC** (acceptor) in the presence of dsDNA containing AT-base pairs.

## 2.7 Thermal studies of probe **TC** in presence of dsDNAs

To understand the thermal stability of dsDNA-**TC** complexes, we carried out temperature-dependent UV-vis absorption studies. The UV-melting data of **TC** bound (AT)<sub>20</sub>, (AT)<sub>10</sub>, (D1)<sub>mix</sub> and (D2)<sub>mix</sub> showed increasing melting temperatures ( $T_m$ ) with  $\Delta T_m = 3.8, 2.6, 1.9$  and  $1.6$  °C, respectively as compared to their unbound forms (Table 2). This moderate thermal stabilization of **TC**-bound AT-containing dsDNA is indicative of favorable interaction without any structural deformation in the duplex DNA structure. In contrast, melting study of (GC)<sub>10</sub> with the addition of **TC** showed an appreciable decrease in  $T_m$  ( $\Delta T_m = -1.7$  °C), which depicts the destabilization of duplex DNA structure in the presence of probe **TC**. Overall, a significant increase in  $T_m$  of **TC**-bound dsDNA containing AT-base pairs provided substantial evidence for preferential binding of **TC** to AT-base pairs region of DNA.

**Table 2.** Summary of melting temperatures ( $T_m$ ) of all the duplexes in absence and presence of probe **TC**.

DNA	$T_m$ (DNA) (°C)	$T_m$ (DNA + TC) (°C)	$\Delta T_m$ (°C)
(AT) <sub>20</sub>	45.98	49.74	+3.76
(AT) <sub>10</sub>	23.03	25.61	+2.58
(GC) <sub>10</sub>	62.00	60.37	-1.63
(D1) <sub>mix</sub>	59.73	61.60	+1.87
(D2) <sub>mix</sub>	71.92	73.53	+1.61

## 2.8 Simulation studies of probe TC binding to dsDNAs

To gain further insights into the binding mode and preferential fluorescence enhancement in AT-rich over GC-rich regions of dsDNA we carried out *ab initio* density functional theory (DFT) calculations of probe TC in the absence and presence of dsDNA. Each molecule was optimized with the help of DFT, and their photophysical properties were calculated using time-dependent DFT (TD-DFT) as implemented in Gaussian 09 package. For the optimization,  $\omega$ b97XD exchange correlation functional was used to include empirical dispersion while for TD-DFT calculations B3LYP exchange and correlation functional was employed. We used 6-31g(d) basis set for all the atoms. The DNA phosphate backbone was neutralized by protonating one of the oxygen atoms of the phosphate groups, which does not alter any property of the DNA duplex structure.<sup>43-45</sup> The DFT and TD-DFT calculations were performed with surrounding water, using a Polarized Continuum Model (PCM) to include the solvent (water) effect.

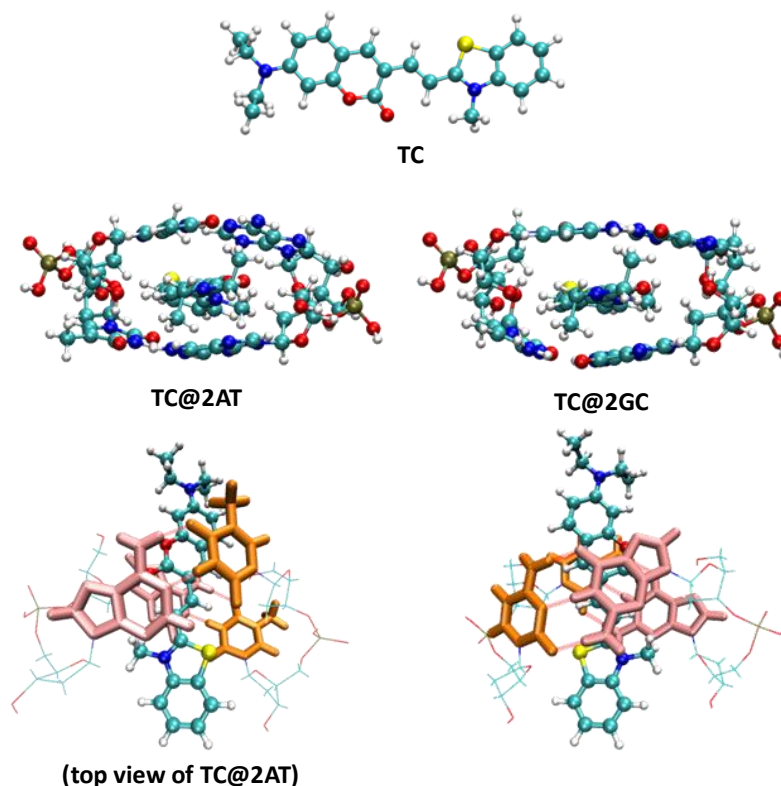


**Figure 12.** The side and top view of intercalation mode of probe TC in presence of 2AT- and 2GC-base pairs.

To predict the interaction mode and relative binding affinity of probe **TC**, we estimated the stabilization energies of **TC** in presence of AT- and GC-base pairs in all possible modes. The optimized structures showed that intercalation was the most preferred binding mode for **TC** (Figure 12). Studies also revealed that **TC** was stabilized more strongly by AT-base pairs ( $37.65 \text{ kcal mol}^{-1}$ ) than by GC-base pairs ( $34.98 \text{ kcal mol}^{-1}$ ). These energy values support the observed moderately-increased melting temperatures of AT-rich DNAs over GC-rich DNAs in the presence of probe **TC**. To predict the preferential fluorescence enhancement of probe **TC** in AT-base pair regions over the GC-base pairs, we calculated the absorbance and emission spectra using optimized ground state ( $S_0$ ) geometry and optimized first excited state ( $S_1$ ) geometry, respectively. The TD-DFT calculation provided excitation energies and oscillator strengths to the lowest singlet states (Table 3).

**Table 3.** Calculated absorption/emission transition with corresponding oscillator strength of **TC**, **TC@2AT** and **TC@2GC**.

Compound	Transition	Excitation energy (nm)	Oscillator Strength
<b>TC</b>	<b>Absorption</b>	<b>507.13</b>	<b>1.67</b>
	<b>Emission</b>	<b>599.02</b>	<b>2.07</b>
<b>TC@2AT</b>	<b>Absorption</b>	<b>514.11</b>	<b>0.89</b>
	<b>Emission</b>	<b>598.75</b>	<b>1.84</b>
<b>TC@2GC</b>	<b>Absorption</b>	<b>564.91</b>	<b>0.19</b>
	<b>Emission</b>	<b>-</b>	<b>-</b>

It was found that for all the possible modes, the lowest energy transitions occur from Highest Occupied Molecular Orbital (HOMO) to Lowest Unoccupied Molecular Orbital (LUMO). For both **TC** and **TC@2AT** complexes, the HOMOs and LUMOs were localized on the **TC** moiety for both absorption and emission. It is interesting to note that, in case of the **TC@2GC** complex for absorption, the corresponding MOs (HOMO and LUMO) were localized on the **TC** moiety but for emission, the transition occurred from the **TC** moiety to the guanine moiety of **TC@2GC** (Figure 13) which quenched the fluorescence emission. In fact, in the latter case the fluorescence quenched because of charge transfer.



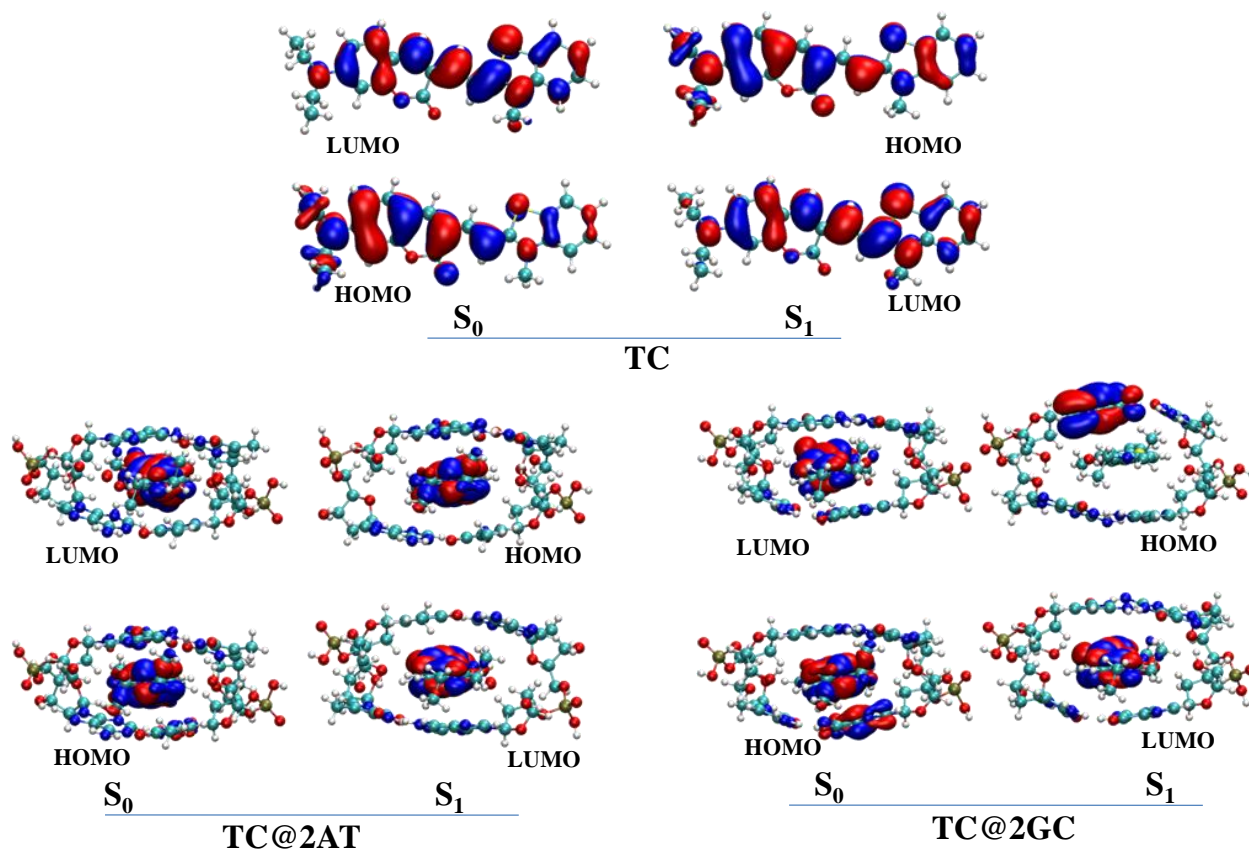


**Figure 13.** Frontier molecular orbital (FMO) diagrams of TC, TC@2AT and TC@2GC.

## 2.9 Cellular uptake and selective DNA-imaging properties of probe TC

The selective fluorescence enhancement of TC in the presence of AT-rich dsDNA further encouraged us to study its cellular uptake and application in nuclear DNA staining.

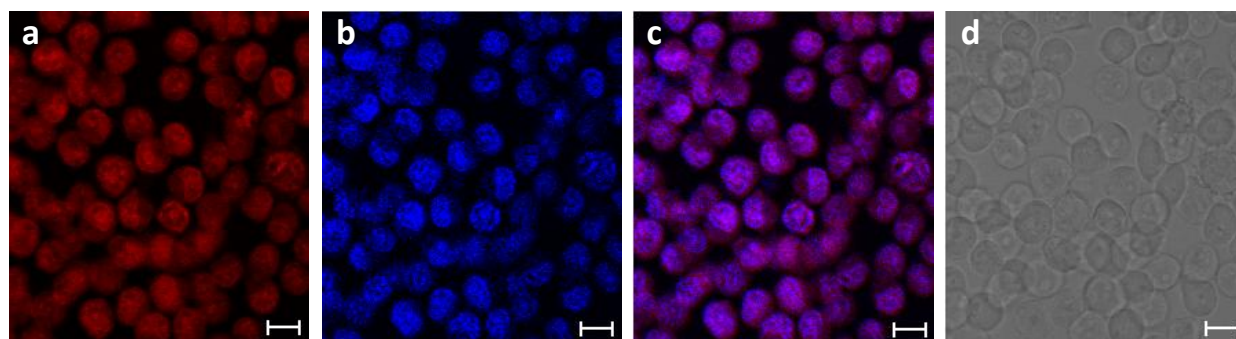


**Figure 14.** Immuno fluorescence images of TC in HeLa S3 cell lines. (a) Immuno fluorescence staining of TC (red). (b) Nuclear staining Hoechst (blue). (c) Overlay image of **a** and **b**. (d) Bright field image of the cell (grey) in HeLa S3 cell lines respectively. Scale bar 10 μm

The HeLa S3 cells were incubated with probe **TC** and then imaged using confocal fluorescence microscopy. HeLa S3 cells were excited at 521 nm, and the emission was measured at 540-750 nm, corresponding to the excitation of the probe **TC** for selective binding of nuclear DNA. Fluorescence imaging of HeLa S3 cell lines with probe **TC** (5 $\mu$ M) and co-staining with commercially available Hoechst 33258 nuclear stain showed selective targeting of cell nucleus by the probe **TC** (Figure 14).

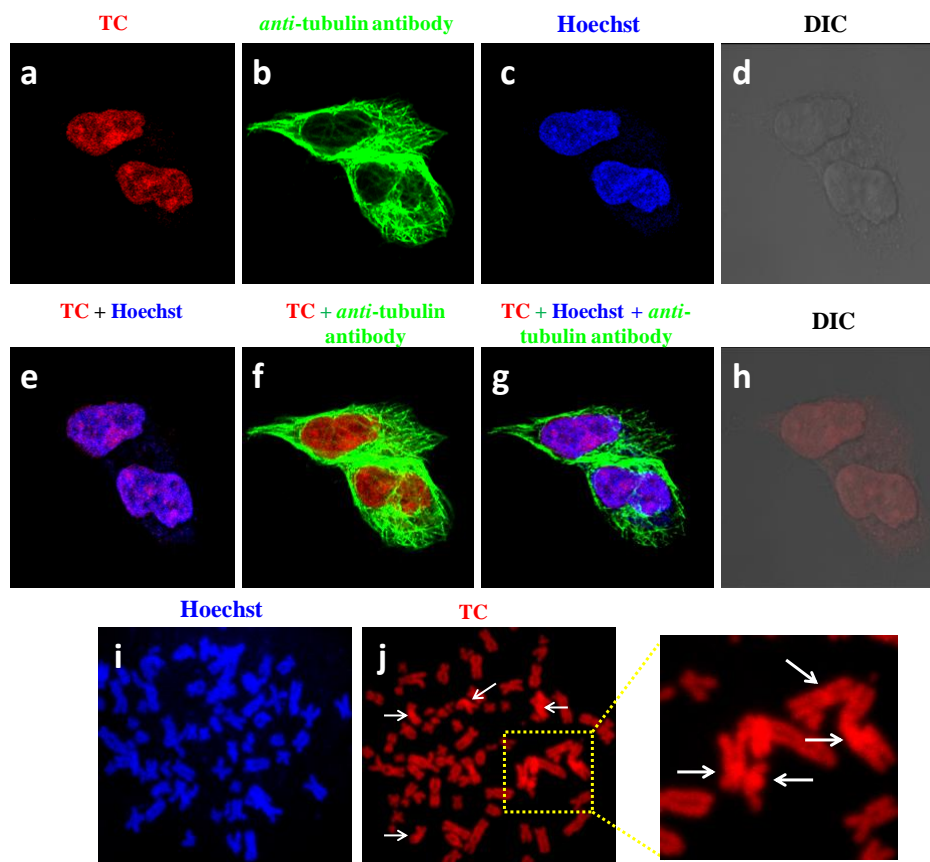


**Figure 15.** Cellular uptake properties of probe **TC**. (a-h) Confocal fluorescence microscope images of HEK 293T cells incubated (at 37 °C for 30 min) with (a) **TC** (5  $\mu$ M), (b) *anti-tubulin antibody*, (c) Hoechst 33258, (d) differential interference contrast (DIC, bright field image) of HEK 293T cells respectively. Overlay fluorescence images: (e) a and c, (f) a and b, (g) a, b and c, (h) a and d. Scale bar 5  $\mu$ m. (i-j) Metaphase chromosomal staining with Hoechst and probe **TC**. (i) Metaphase chromosomal plate was prepared using U87 glioblastoma cell line and stained with Hoechst (10  $\mu$ g/mL). (j) Probe **TC** (5  $\mu$ M). *Inset*: Arrow shows the maximum centromere localization of probe **TC**.

Further, we carried out nuclear staining studies in HEK293 cells with cytoplasmic  $\alpha$ -tubulin marker to demonstrate the specificity of **TC** to nuclei and did not stain the cytoplasm. It was revealed that the probe **TC** did not colocalize with the cytoplasmic  $\alpha$ -tubulin marker but did so with the properly placed nucleus (Figure 15a-h). Collectively, these results suggest that the probe **TC** is cell membrane-permeable and highly selective towards the nucleus. To further validate the nuclear DNA binding of **TC**, we performed staining of the metaphase chromosome of HEK 293 cell line. The results clearly illustrated that the probe **TC** (at 2 and 5  $\mu$ M concentration) stained the chromosomes efficiently (Figure 15i-j). The careful observation of these images revealed that some areas of chromosomes (for example, the AT-rich centromeric region) were more densely stained (shown with arrows in Figure 15i, *inset*). However, at higher concentration we observed uniform chromosomal staining compared to the lower concentration of probe **TC** which showed remarkably greater staining of centromere region (Figure 16).

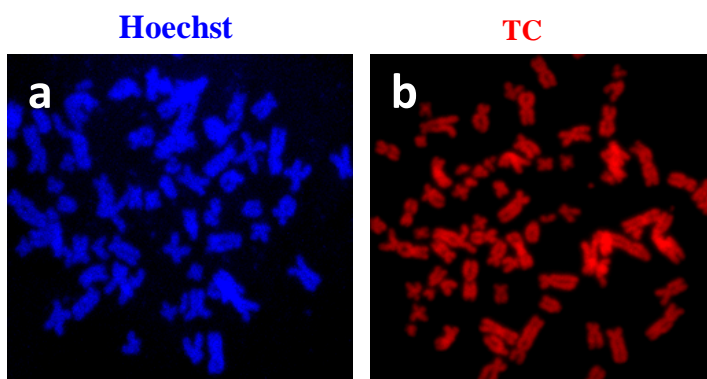


**Figure 16.** Metaphase chromosomal staining with Hoechst and probe **TC**. (a) Metaphase chromosomal plate was prepared using HEK 293 cell line and stained with Hoechst (10  $\mu$ g/mL). (b) probe **TC** (5  $\mu$ M).

### 2.10 Fidelity of probe **TC** to dsDNA

One of the foremost problems with most DNA staining dyes is non-specific binding with cellular ribonucleic acids (RNA), proteins and other biomacromolecules.<sup>46,47</sup> To explore the possibilities of such non-specific interactions, we recorded the emission spectrum of **TC** in the presence of fetal bovine serum albumin (FBA) which did not show any detectable change in basal fluorescence of the probe (Figure 17a). Further, we recorded the fluorescence spectra

of preformed  $[\text{TC} + \text{d}(\text{AATT})_5]$  with the addition of excess FBA and vice versa. Interestingly, we did not observe any detectable change in the strong fluorescence intensity of probe **TC**. While, upon addition of  $\text{d}(\text{AATT})_5$  to **TC** + FBA mixture,  $\sim 70\%$  fluorescence of probe **TC** was achieved compared to  $[\text{TC} + \text{d}(\text{AATT})_5]$  complex (Figure 17b). In order to check the effect of other parameters like salt and pH we have measured the fluorescence of  $[\text{TC} + \text{d}(\text{AATT})_5]$  complex in presence of NaCl (100 mM) and with the variation pH from 5 to 8 (Figure 17c-d). In presence of 100 mM NaCl,  $[\text{TC} + \text{d}(\text{AATT})_5]$  did not show appreciable change in the strong fluorescence intensity.

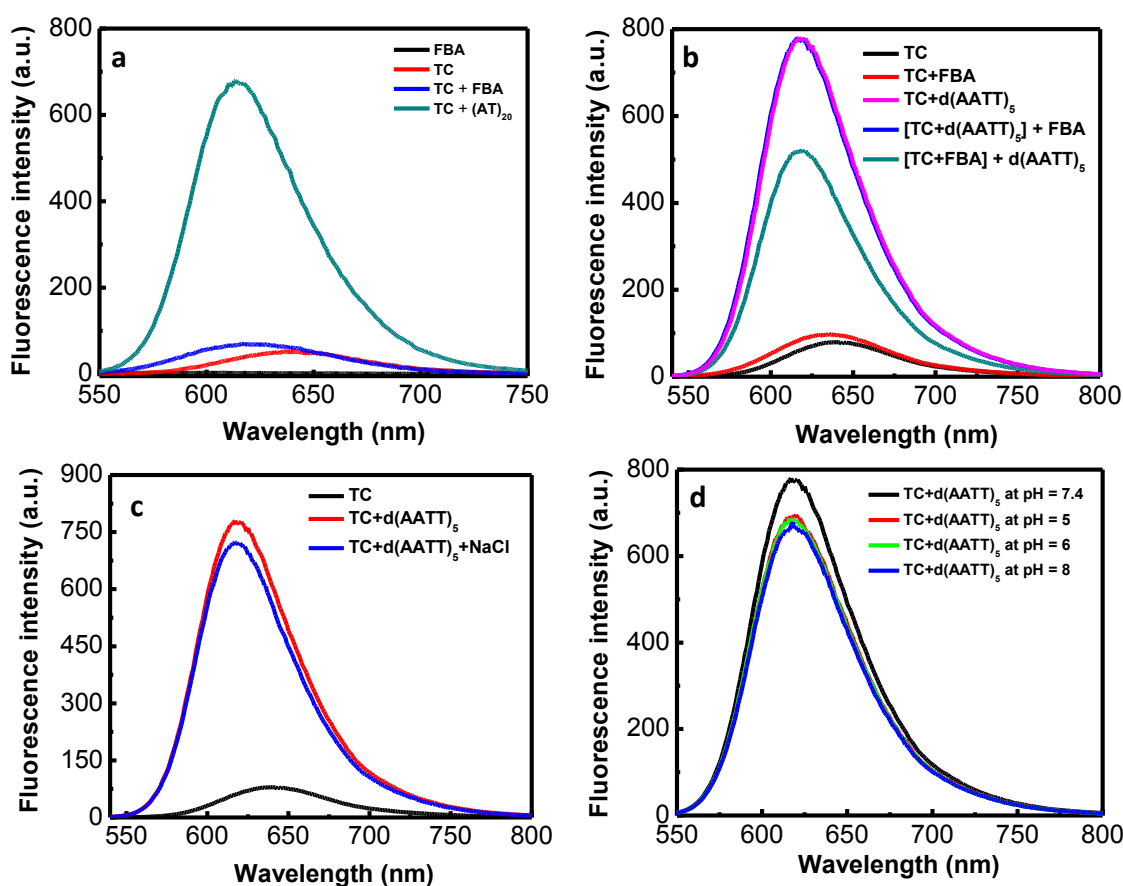


**Figure 17.** Emission spectra of **TC** in presence of DNA, proteins, salt and pH. (a) Fluorescence spectra of probe **TC** in the presence of  $(\text{AT})_{20}$  and fetal bovine serum albumin (FBA). (b)  $\text{TC}+\text{d}(\text{AATT})_5$  with addition of excess FBA solution and vice versa in Tris-HCl buffer (100 mM, pH = 7.4) upon excitation at 521 nm. (c) Fluorescence spectra of  $\text{TC}+\text{d}(\text{AATT})_5$  in presence of NaCl (100 mM). (d) Fluorescence spectra of  $\text{TC}+\text{d}(\text{AATT})_5$  by varying solution pH from 5 to 8 in Tris-HCl buffer solution.

Similarly, variation of pH from 5 to 8 had no effect on the fluorescence of [TC + d(AATT)<sub>5</sub>] complex. Overall, these results suggest probe TC is selective towards dsDNA and retains its fluorescence even in complex samples containing proteins and in presence of variable salt and pH conditions. To demonstrate the selectivity of TC for dsDNA over RNA, we performed deoxyribonuclease I (DNase I) and ribonuclease (RNase) digestion studies in HEK293 cell lines. DNase I is known to degrade nuclear DNA while RNase degrades RNA by catalyzing phosphodiester bond cleavage. After DNase I digestion of cells the fluorescence of probe TC (red) and control Hoechst 33258 (blue) almost completely diminished from the nuclear region compared to untreated cells. However, as predicted, the RNase treatment of HEK293 cells did not affect the fluorescence staining of TC and Hoechst 33258 in the nuclear region (Figure 18).

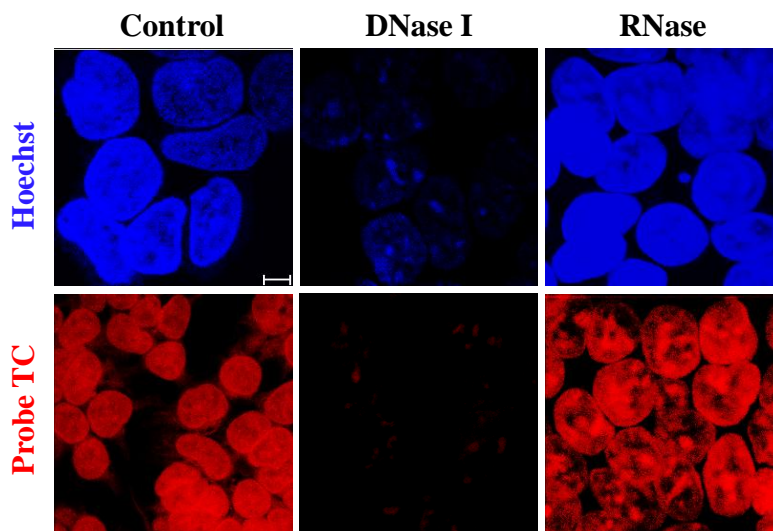


**Figure 18.** The DNase and RNase studies in HEK 293 cell lines. Immunofluorescence staining of control and cells treated with DNase I (100  $\mu\text{g}/\text{mL}$ ) and RNase (40  $\mu\text{g}/\text{mL}$ ) with TC (red). DNA was counterstained with Hoechst (blue). Scale bar, 5  $\mu\text{m}$

### 2.11 Application of probe TC in cell cycle analysis

The FACS analysis using flow cytometry is a versatile tool for cell cycle analysis with the aid of DNA-specific binders. To quantitate the DNA content in the cells, we employed probe TC for the cell cycle analysis of HEK293 cells using flow cytometry. For FACS analysis, HEK293 cells were separately stained with PI (10  $\mu\text{g}/\text{mL}$ ) and probe TC (5  $\mu\text{M}$ ) in the

presence and absence of RNase. FACS data showed a similar pattern of each cell cycle phase with almost similar percentage of populations of G1, S and G2-M (Figure 19). These results suggest that the probe **TC** binds to DNA only and may be applied in FACS analysis to quantify DNA and cell cycle estimation without employing RNase. It was also observed that the intensity of probe **TC** was more as compared to the same concentration of PI used in the cell cycle analysis at FL2-A scale.

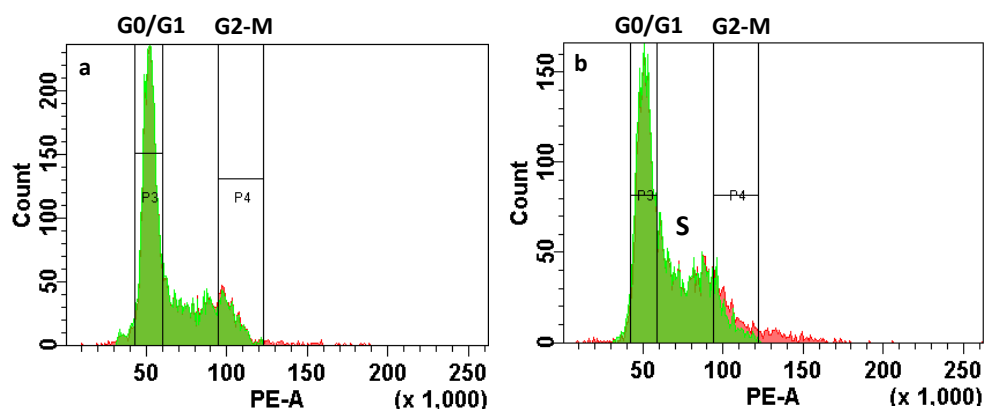


**Figure 19.** FACS-analysis of probe **TC**. (a-b) Cell cycle analysis of HEK 293 cells by staining with PI and probe **TC** respectively. HEK 293 cells stained with  $6\mu\text{g}$  of PI and probe **TC** for 30 min. FACS analysis was done by FACS aria instrument.

## 2.12 Cytotoxicity studies of probe **TC**

Another significant aspect is that of cytotoxicity which is a major constraint with several DNA-binding probes including PI. To understand whether probe **TC** displayed any cytotoxicity towards HEK293 cells, MTT assay was performed. In a dose-dependent experiment, three different concentrations of probe **TC** were taken. It was observed that **TC** was non-toxic to HEK293 cells for treatment time intervals (30 min) used in the present experiments (Figure 20a). Time-dependent experiments were also performed for 6, 12, 18 and 24 h by taking  $5\mu\text{M}$  of **TC**. These experiments revealed a gradual decrease in cell viability, but the percentage of dead cells was infinitesimal. As many as 64% of cells were viable after 24 h of treatment (Figure 20b).

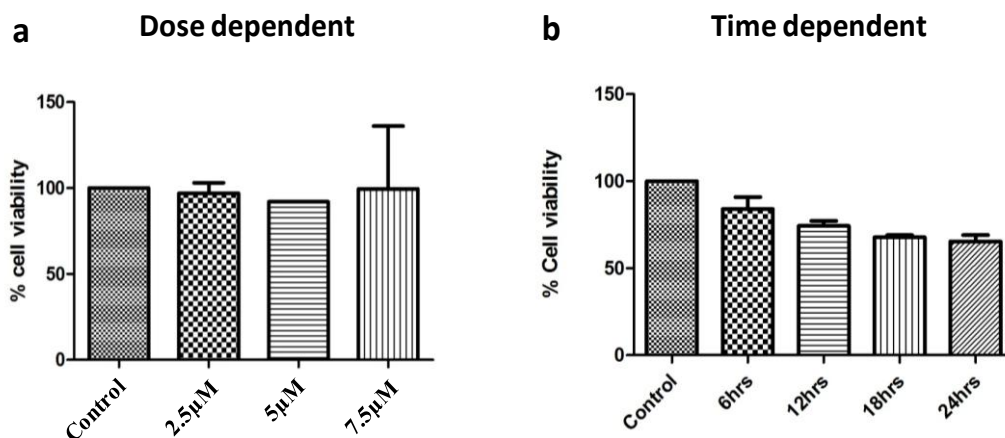


**Figure 20.** Cell cytotoxicity of probe **TC** by MTT-assay (HEK293 cells). (a) Dose dependent cell viability by taking 2.5  $\mu\text{M}$ , 5  $\mu\text{M}$  and 7.5  $\mu\text{M}$  of probe **TC** and water as control. (b) Time dependent MTT- assay for up to 24 h using 5  $\mu\text{m}$  of probe **TC** mean $\pm$ SEM.

### 2.13 Preferential fluorescence staining of malaria parasites

The strong and specific binding of probe **TC** towards the AT-rich DNA raises the possibility using this probe for purposes other than mammalian nuclear staining and cell sorting. To test this possibility we selected *Plasmodium falciparum* as a model system which has AT rich genome (~80%). The parasites were incubated with low concentrations of probe **TC** (1 and 2  $\mu\text{M}$ ) with trophozoite stage parasites growing in erythrocytes. Live fluorescence imaging of trophozoite stage parasites depicted that probe **TC** could specifically bind to the parasite cells within the red blood cells at 1 and 2  $\mu\text{M}$  concentrations. Vehicle control (water) did not show any detectable fluorescence under similar experimental conditions (Figure 21a). Incubation of the HepG2 cells (human liver cancer cells) with 2  $\mu\text{M}$  of probe **TC** did not show any detectable fluorescence (Figure 20b). These results clearly indicate that probe **TC** preferentially bound to the AT-rich genome of the parasite at very low concentrations. Collectively, these results suggest the selectivity of probe **TC** for AT-base pairs in dsDNA, fidelity to DNA over RNA and protein, non-toxicity, and preferential staining of malarial parasites in human erythrocytes, indicating that probe **TC** is a useful diagnostic and possibly therapeutic, red-fluorescence biomarker for AT-rich genomes.<sup>48-51</sup>

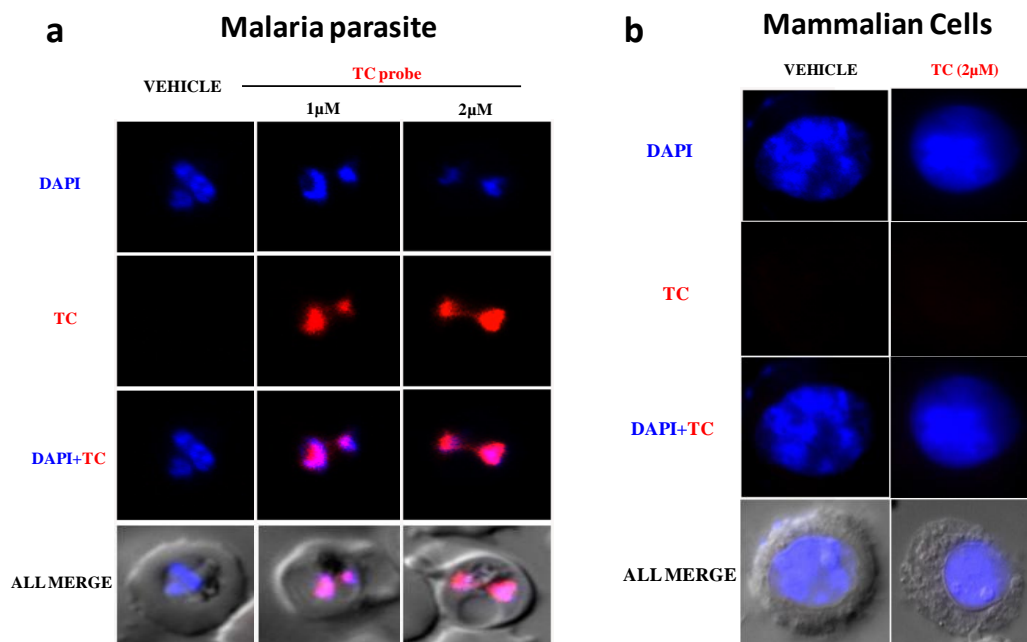


**Figure 21.** Binding of probe **TC** to the AT rich genome of *Plasmodium falciparum* and mammalian cells. (a) Live cell fluorescence imaging showed probe **TC** is accumulated specifically in the nucleus of the parasitized red blood cell at 1 and 2  $\mu\text{M}$ . Vehicle control (water) did not show any detectable fluorescence under the same experimental conditions. DAPI stains the nuclei and all merged panel shows phase images of the parasites along with DAPI and **TC** fluorescence signal. Scale bar: 2  $\mu\text{m}$ . (b) IFA analysis of mammalian HepG2 stained with very low concentration of probe **TC** (2  $\mu\text{M}$ ) and DAPI. No detectable uptake of probe **TC** was observed in HepG2 as seen in *P. falciparum* at same concentration.

## 2.14 Conclusion

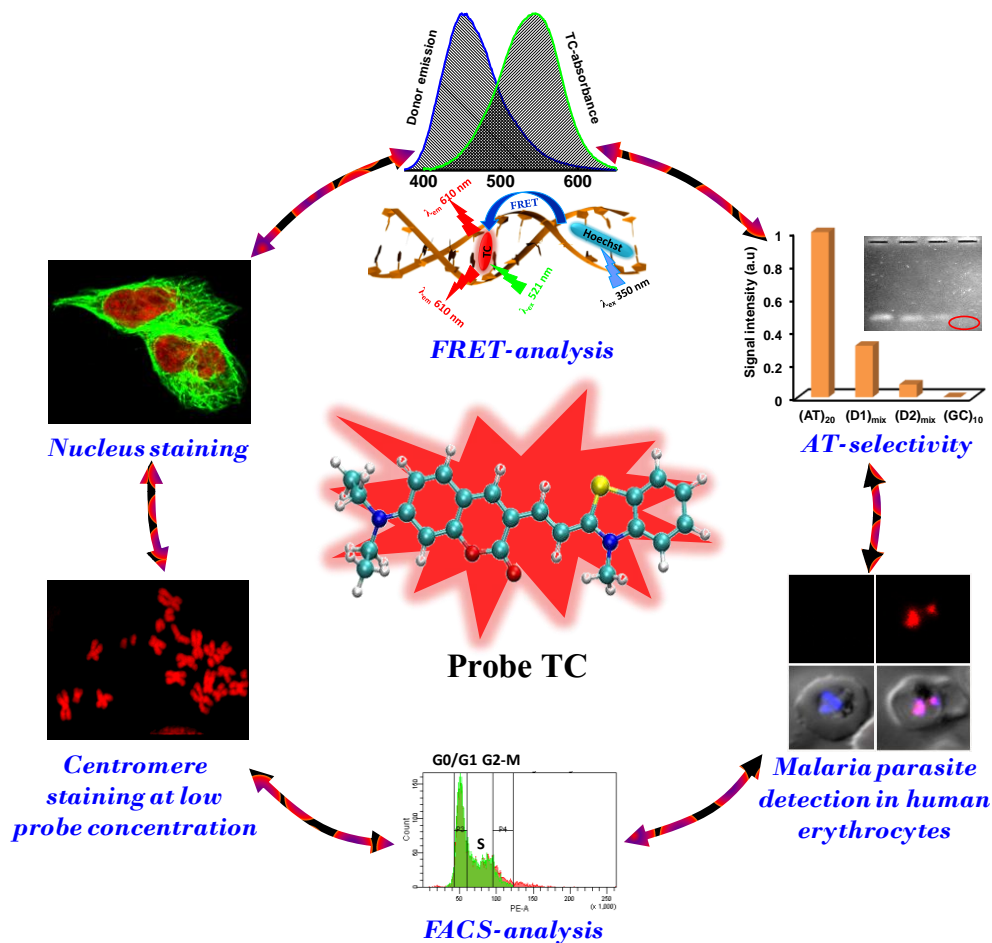
In summary, we have developed red fluorescence hemicyanine-based thiazole-coumarin (**TC**) probe for base pair-specific recognition of dsDNA. Fluorescence spectroscopy and gel-electrophoresis studies of **TC** showed strong fluorescence enhancement in the presence of DNA containing AT-base pairs but non-fluorescence with DNA containing only GC-base pairs, single-stranded DNA, RNA and proteins. The increase in fluorescence of **TC** as a function of consecutive AT-base pairs in dsDNA also suggests AT-rich regions are the preferable binding sites. The FRET studies demonstrated that minor groove binding Hoechst and probe **TC** act as an efficient donor-acceptor pair.



**Table 4.** Advantages of probe TC over other commercial available probes.

Dyes	Selectivity	Fluorescence maxima free/DNA bound dye (nm)	Fluorescence quantum yield ( $\Phi_F$ ) DNA bound dye	Cell permeability	Toxicity
DAPI	AT-rich	496/450	0.42 <sup>a</sup>	Semi-Permeable	Non-toxic
Hoechst33258	AT-rich	490/450	0.34 <sup>a</sup>	Permeable	Non-Toxic
Ethidium bromide	----	624/602	0.35 <sup>a</sup>	Impermeable	Toxic
Propidium iodide	----	646/617	0.13 <sup>a</sup>	Impermeable	Toxic
<b>Probe TC</b>	<b>AT-rich</b>	<b>641/610</b>	<b>0.36</b>	<b>Permeable</b>	<b>Non-Toxic</b>

<sup>a</sup> Cosa, G.; Focsaneanu, K.-S.; McLean, J. R. N.; McNamee, J. P.; Scaiano, J. C. *Photochem. Photobiol.* **2001**, 73, 585–599.

**Figure 22.** Multipurpose applications of probe TC.

The fluorescence spectroscopy studies, fluorescence-imaging of HeLaS3, HEK293, digestion by nuclease enzymes and flow cytometry studies of **TC** revealed AT-base pair-specific fluorescence enhancement, effective cell-permeability, non-toxicity, selective nuclear DNA staining over cytoplasmic region, cell cycle analysis and DNA quantitation. The tendency of **TC** to localize in a particular region of chromosomes and preferential affinity (at low concentrations) towards the malarial parasite DNA in human erythrocyte authenticate the diagnostic and therapeutic potential of probe **TC**. We anticipate that the AT-selective red fluorescence DNA probe **TC** could be a promising and useful reagent in molecular biology, cell biology and possibly other DNA-based techniques such as fluorescence spectroscopy, flow cytometry, DNA quantitation and also for the development of genome-specific binders of theranostic interest in conjugation with designed oligonucleotides (Figure 22 and Table 4).

## 2.15 Experimental Section

### General Information

All the chemicals, reagents, oligos (dA<sub>20</sub>, dT<sub>20</sub>, dA<sub>10</sub>, dT<sub>10</sub>, dG<sub>10</sub>, dC<sub>10</sub> and d(AATT)<sub>5</sub>), control probes (Hoechst 33258, ethidium bromide and propidium iodide), primary antibody, Alexa A488-coupled secondary antibody, DNase I and RNase were purchased from Sigma-Aldrich. <sup>1</sup>H and <sup>13</sup>C-NMR spectra were recorded on a Bruker AV-400 MHz spectrometer with chemical shifts reported as parts per million (*ppm*) (in CDCl<sub>3</sub>/DMSO-*d*<sub>6</sub>, tetramethylsilane as an internal standard) at 20 °C. UV-vis absorption and emission spectra were measured in quartz cuvettes of 1 cm path length. The absolute fluorescence quantum yields were determined using an integrating sphere for the samples on FLSP920 spectrometer (Edinburgh Instruments). High resolution Mass spectra (HRMS) were obtained on Agilent Technologies 6538 UHD Accurate-Mass Q-TOF LC/MS spectrometer.

### Synthetic procedure for probes **TC**, **CL** and **TP**

**Synthesis of compound 1.** To a stirred solution of 2-methyl benzothiazole (7.0 mmol) in dichloromethane (10 mL), methyl iodide (14.0 mmol) was added drop wise and allowed to

reflux for overnight. Completion of the reaction was monitored with TLC. After completion of the reaction white color precipitate was formed. The precipitate was filtered and washed with copious amount of diethyl ether for removing unreacted benzothiazole. The obtained product was dried under vacuum and then used without further purification.

**Synthesis of compound 2.** To a stirred solution of lepidine (5.0 mmol) in dichloromethane (10 mL), Methyl iodide (10.0 mmol) was added drop wise and allowed to reflux for overnight. After completion of the reaction yellow color precipitate was formed. The precipitate was filtered and washed with more amount of dichloromethane for removing unreacted lepidine. The obtained product was dried under vacuum and then used without further purification.

To a stirred solution of *N*-methylated benzothiazole (**1**) or lepidine (**2**) (1.2 eq.) in ethanol, piperidine (0.2 eq.) was added, and the reaction mixture was allowed to stir for 10 min. 7-(diethylamino)-2-oxo-2H-chromene-3-carbaldehyde<sup>51</sup> (1 eq.) in ethanol solution was added dropwise to the above reaction mixture, leading to immediate yellow to purple color change in the solution after which the reaction mixture was allowed to stir for 4 h. The completion of the reaction was monitored with thin layer chromatography (TLC). After completion of the reaction, the solvent was evaporated under vacuum. The crude product was purified using column chromatography on silica gel using CHCl<sub>3</sub>/MeOH as an eluent to afford **TC** or **CL** in good yields.

To a stirred solution of *N*-methylated benzothiazole (**1**) (164 mg, 5.65 mmol) in ethanol piperidine (60  $\mu$ L, 5.65 mmol) was added and allowed to stir for 10 min. Pyrene-1-carbaldehyde (100 mg, 4.347 mmol) in ethanol solution was added drop wise to the reaction mixture with pressure equalizer and stirred under reflux conditions for 7 h. The completion of the reaction was monitored with TLC. The crude product was purified using column chromatography on silica gel using DCM/MeOH (98/2) as eluent to afford probe **TP** in good yield.

**Characterization data for TC.** Brown color powder,

yield 50%<sup>51</sup>. <sup>1</sup>H-NMR (*DMSO-d*<sub>6</sub>, 400 MHz)  $\delta_{ppm}$  8.59

(s, 1H), 8.37 (dd,  $J = 0.8$  Hz,  $J = 8$  Hz, 1H), 8.21 (d,  $J =$

8.4 Hz, 1H), 8.02 (dd,  $J = 8$  Hz,  $J = 15.6$  Hz, 2H), 7.83

(m, 1H), 7.74 (td,  $J = 1.2$  Hz,  $J = 7.6$  Hz, 1H), 7.57 (d,  $J$

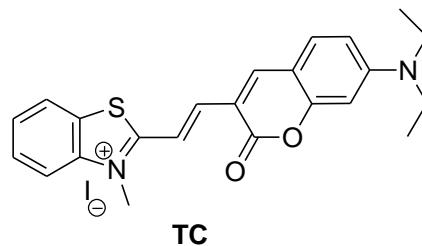
$= 9.2$  Hz, 1H), 6.87 (dd,  $J = 2.4$  Hz,  $J = 9.2$  Hz, 1H), 6.67 (d,  $J = 2.4$  Hz, 1H), 4.22 (s, 3H),

3.53 (q,  $J = 7.2$  Hz, 4H), 1.17 (t,  $J = 7.2$  Hz, 6H). <sup>13</sup>C-NMR (*DMSO-d*<sub>6</sub>, 100 MHz)  $\delta_{ppm}$

171.6, 159.5, 157.1, 153.3, 148.3, 144.3, 142.0, 131.8, 129.2, 128.0, 127.4, 124.1, 116.5,

112.0, 111.3, 110.9, 108.9, 96.4, 44.6, 35.8, 12.4. HRMS (ESI-MS): found 391.1456, calcd

$m/z = 391.1475$  for C<sub>23</sub>H<sub>23</sub>N<sub>2</sub>O<sub>2</sub>SI [M-I]<sup>+</sup>.



**Characterization data for CL.** Violet color powder, yield

60%. <sup>1</sup>H-NMR (*DMSO-d*<sub>6</sub>, 400 MHz)  $\delta_{ppm}$  9.25 (d,  $J = 6.4$

Hz, 1H), 8.72 (d,  $J = 8$  Hz, 1H), 8.43 (m, 4H), 8.24 (m, 1H),

8.02 (m, 2H), 7.54 (d,  $J = 9.2$  Hz, 1H), 6.82 (dd,  $J = 2.4$  Hz,

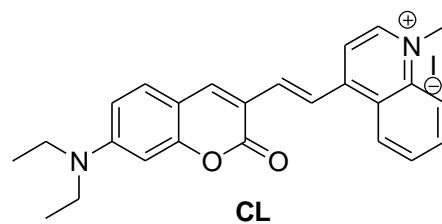
$J = 9.2$  Hz, 1H), 6.61 (d,  $J = 2.4$  Hz, 1H), 4.46 (s, 3H). <sup>13</sup>C-

NMR (*DMSO-d*<sub>6</sub>, 100 MHz)  $\delta_{ppm}$  160.0, 158.2, 157.8, 152.4, 152.1, 147.7, 145.1, 138.7,

138.2, 134.8, 130.9, 129.3, 126.0, 125.6, 119.4, 118.4, 115.3, 114.8, 113.9, 110.2, 108.6,

96.3, 44.4, 12.4. HRMS (ESI-MS): found 385.1902, calcd  $m/z = 385.1911$  for C<sub>25</sub>H<sub>25</sub>IN<sub>2</sub>O<sub>2</sub>

[M-I]<sup>+</sup>.



**Characterization data for TP.** Brown color powder, yield

78%. <sup>1</sup>H-NMR (*DMSO-d*<sub>6</sub>, 400 MHz)  $\delta_{ppm}$  9.19 (d,  $J = 15.6$

Hz, 1H), 8.97 (d,  $J = 8.4$  Hz, 1H), 8.88 (d,  $J = 9.6$  Hz, 1H),

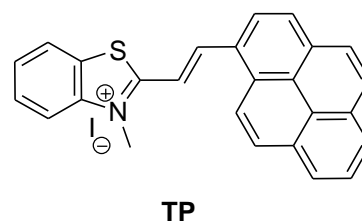
8.39 (m, 9H), 8.18 (t,  $J = 7.6$  Hz, 1H), 7.92 (m, 1H), 7.84 (td,  $J$

$= 0.8$  Hz,  $J = 7.6$  Hz, 1H), 4.46 (s, 3H). <sup>13</sup>C-NMR (*DMSO-d*<sub>6</sub>,

100 MHz)  $\delta_{ppm}$  171.5, 144.1, 142.0, 133.7, 130.8, 130.3, 130.1, 129.9, 129.5, 128.5, 128.1,

127.4, 127.3, 127.0, 126.7, 125.7, 125.5, 124.2, 124.0, 123.5, 122.6, 116.9, 115.4, 36.5.

HRMS (ESI-MS): found 376.1156, calcd  $m/z = 376.1154$  for C<sub>26</sub>H<sub>18</sub>INS [M-I]<sup>+</sup>.



**Sample preparation for UV-vis and fluorescence measurements.** Stock solutions of **TC**

and **CL** were prepared in double distilled water in the order of 10<sup>-3</sup> M. Stock solution of **TP**

was prepared by dissolving in HPLC-grade dimethyl sulfoxide (DMSO) in the order of 10<sup>-3</sup>

M. These stock solutions were completely covered with aluminum foil to avoid photo-bleaching and stored at -10 °C. DNA-stock solutions were prepared by dissolving oligo samples in double distilled water in the order of  $10^{-4}$  M. Double stranded (ds) DNA samples were prepared by mixing equimolar concentrations of complementary strands in Tris-HCl (100 mM, pH = 7.4) buffer solution and subjected to annealing by heating the sample to 85 °C for 15 min and cooled to room temperature for 7 h and stored in the refrigerator for 4 h.

**Absorption and emission spectra.** The UV–vis absorption spectra were recorded on a Perkin Elmer Model Lambda 900 spectrophotometer. Emission spectra were recorded on Perkin Elmer Model LS 55 spectrophotometer. Temperature-dependent absorption measurements (UV-Vis melting studies) were carried out on Cary 5000 UV-vis-NIR spectrophotometer equipped with Cary temperature controller in the range of 10 °C to 90 °C with ramp rate of 1 °C/min.

**Circular dichroism (CD) spectroscopy.** CD measurements were carried out on a Jasco J-815 spectrometer equipped with Peltier-type temperature controller (CDF-4265/15) under nitrogen atmosphere to avoid water condensation. Scans were performed over the range of 200-700 nm with a speed of 100 nm/min and the spectra represent an average of three scans. A blank sample containing buffer solution (Tris-HCl, 100 mM, pH = 7.4) was treated in the same manner and subtracted from the collected data.

**Thermal denaturation studies.** Thermal denaturation studies of double stranded DNA samples in the absence and presence of probe **TC** were recorded in the temperature range 10– 90°C with heating rate 1 °C/min. The variable temperature/wavelength mode was used. Absorption was monitored at 260 nm of 5 °C interval. Melting temperatures ( $T_m$ ) of DNA samples were calculated from the first derivatives of the absorption vs. temperature curves (thermal denaturation or melting curves) obtained by monitoring at 260 nm.

**Gel electrophoresis.** Agarose gel electrophoresis experiments were performed on custom-made horizontal gel system using 3% agarose gel at 100 V for 1 h at 25 °C. Then the dsDNA bands were visualized on the agarose gels by soaking in aqueous solution of **TC** or EtBr for 30 min.

**Computational methods.** Each molecule was optimized with the help of *ab initio* Density Functional Theory (DFT) combined with time-dependent DFT (TD-DFT) as implemented in Gaussian 09 package.<sup>53</sup> For the DFT calculation, we use ωb97XD<sup>54</sup> exchange correlation functional to includes empirical dispersion and for TD-DFT calculations we use B3LYP<sup>55-57</sup> exchange and correlation functional with 6-31g(d) basis set for all atoms. The DFT and TD-DFT calculations are performed with surrounding water, using a Polarized Continuum Model (PCM)<sup>58</sup> to include the solvent (water) effect.

**Immunofluorescence studies of HeLa S3 and HEK293 cell lines.** HeLa S3 and HEK293 cells were grown on the cover slip for 24 h in DMEM medium supplemented with 10% fetal bovine serum at 37 °C in a humidified atmosphere containing 5% CO<sub>2</sub>. Cells were fixed with 4% paraformaldehyde and permeabilized with 0.1% Triton X-100 in PBS for 2×5 min. After rinsing twice with PBS, HEK293 cells and HeLa S3 cells were treated separately with probe **TC** (5 μM) for 15 min at room temperature. After two washes in PBS, non-specific binding of antibodies was blocked with blocking buffer containing 10% FBS, 3% BSA, 0.1% Triton X-100. Subsequently, cover slips for HEK293 cells were incubated in primary antibody (α-tubulin) at 37 °C for 30 min. After two washes in PBS with 0.1% Triton X-100, cover slips were incubated with secondary antibodies coupled with Alexa dyes A488 at 37 °C for 30 min. Subsequently, cover slips were incubated with Hoechst 33258 at 10 μg/mL for nuclear staining. After two more washes in PBS with 0.1% Triton X-100, the cover slips were washed in PBS, rinsed in ddH<sub>2</sub>O and briefly dipped in 100% ethanol. After a quick dry, cover slips were mounted with 70% glycerol. Images were captured using a Carl Zeiss Laser Scanning Microscope (LSM510 META).

**DNase and RNase digestion studies.** HEK293 cells were fixed with chilled methanol for 1 min at room temperature and permeabilized with 0.1% Triton X-100 in PBS for 2×5 min. After rinsing with PBS twice, one set of experiment cells were treated with probe **TC** (5 μM) for 15 min at room temperature in three adjacent wells. A total of 200 μL PBS (as a control experiment), 100 μg/mL DNase I (Sigma), or 30 μg/mL DNase-Free RNase (GE) was added into the three adjacent wells and incubated at 37 °C for 2 h. For another set of experiment, instead of treating with probe **TC**, cells were only treated with 200 μL PBS (as a control

experiment) and 100 µg/mL DNase I (Sigma), or 30 µg/mL DNase-Free RNase (GE) was added into the three adjacent wells and incubated at 37 °C for 2 h. Subsequently, cover slips for both the experiments were incubated with Hoechst 33258 at 10 µg/mL for nuclear staining. After two more washes in PBS with 0.1% Triton X-100, the cover slips were washed in PBS, rinsed in ddH<sub>2</sub>O and briefly dipped in 100% ethanol. After a quick dry, cover slips were mounted with 70% glycerol. Images were captured using a Carl Zeiss Laser Scanning Microscope (LSM510 META) using an equal exposure time for control, DNase I, and RNase experiments. Experiments have been done in duplicate.

**FACS analysis for cell cycle stained with PI and probe TC.** HEK293 Cells were harvested by trypsinization with 0.25% EDTA-Trypsin and collected by centrifugation at 2000 rpm for 3 min at 4 °C. Cells were washed with 1×PBS twice. Then pellet was re-suspended in 200µL of PBS, after which the cells were fixed in 70% ethanol for 12 h at -80 °C. A second PBS wash was given following which the cells were again suspended in 1 mL of PBS. 6 µg of PI (6 µg of RNase for PI treated cells) and 6 µg of probe **TC** were added for staining (for 30 min) at 37 °C. 10,000 cells were analyzed by flow cytometry (FACS aria instrument).

**MTT assay.** 10,000 HEK293 cells were seeded in 96-well plate and cultured for 12 h. For dose-dependent experiment, cells were treated for 30 min with 2.5, 5 and 7.5 µM of probe **TC** and for time dependent set, 5 µM of **TC** was used for 6, 12, 18 and 24 h treatment were done. Water was used as a control. 20 µL of MTT (5 mg/mL) was added in each well, incubated for 3 h at 37 °C and 100 µL of DMSO was added. Readings were taken at 570 nm in ELISA reader (VERSA Max microplate reader, Molecular devices). The data was normalized with control and plotted with mean and standard error.

**Metaphase chromosome preparation and Probe TC staining.** HEK293 cells were cultured in a 60 mm dish, harvested with 0.25% EDTA-Trypsin and collected by centrifugation at 2000 rpm for 3 min. Supernatant was discarded and washed twice with 1XPBS. Cell pellet was resuspended in 10 mL hypotonic solution (0.56% KCl) and incubated for 30 min at 37 °C. Recentrifugation was conducted, and the pellet was again suspended in 8 mL fixative (glacial acetic acid: ethanol, 1:3). Then 2-3 drops of cell suspension were dropped at some distance on slide. Slides were either air dried or flame

dried. Hoechst (1µg/mL) and probe **TC** (5 µM) were poured on the slide and kept for 10 min for DNA staining and mounted with 70% glycerol. Images were taken at 100× by Carl Zeiss Laser Scanning Microscope (LSM510 META).

***Plasmodium falciparum* culture and probe TC treatment.** The growth and maintenance of parasite culture have been described elsewhere.<sup>59</sup> In brief, *P. falciparum* 3D7 strain was grown at 4-10% parasitemia in RPMI 1640 medium supplemented with 0.5% albumax (Invitrogen), 5% NaHCO<sub>3</sub>, 50 µg/mL gentamicin and 50 µg/mL ampicillin at 37 °C. The culture was synchronized by incubating ring-staged parasites for 5 minutes with 5% sorbitol. Probe **TC** (resuspended in Mili-Q water) was added to parasites (30±5 hpi) at a final concentration of 1 and 2µM, and the parasites were incubated for 30 minutes at 37 °C. Milli-Q water was used as a vehicle control. Fluorescence images were captured using Carl Zeiss AXIO Imager Z1 and the software used for image capturing was AxioVision Rel. 4.8.

## 2.16 References

1. Armitage, B. A. Cyanine Dye–DNA Interactions: Intercalation, Groove Binding, and Aggregation. *Top. Curr. Chem.* **2005**, 253, 55–76.
2. Ranasinghe, R. T.; Brown, T. Fluorescence based strategies for genetic analysis. *Chem. Commun.* **2005**, 5487–5502.
3. Waring, M. J. DNA Modification and Cancer. *Annu. Rev. Biochem.* **1981**, 50, 159-192.
4. Neidle, S. DNA minor-groove recognition by small molecules. *Nat. Prod. Rep.* **2001**, 18, 291-309.
5. Hurley, L. H. DNA and its associated processes as targets for cancer therapy. *Nat. Rev. Cancer.* **2002**, 2, 188-200.
6. Blackburn, G. M.; Gait, M. J.; Loakes, D.; Williams, D. M. *Nucleic Acids in Chemistry and Biology*. RSC Publishing, Cambridge, UK, **2006**.
7. Lerman, L. S. Structural considerations in the interactions of deoxyribonucleic acid and acridines. *J. Mol. Biol.* **1961**, 3, 18-30.
8. Waring, M. J. Drugs which affect the Structure and Function of DNA. *Nature* **1968**, 219, 1320-1325.



9. Zimmer, C.; Wahnert, U. Nonintercalating DNA-binding ligands: specificity of the interaction and their use as tools in biophysical, biochemical and biological investigations of the genetic material. *Prog. Biophys. Mol. Biol.* **1986**, *47*, 31-112.
10. Neidle, S.; Abraham, Z. Structural and sequence-dependent aspects of drug intercalation into nucleic acids. *CRC Crit. Rev. Biochem.* **1984**, *17*, 73-121.
11. White, S.; Szewczyk, J. W.; Turner, J. M.; Baird, E. E.; Dervan, P. B. Recognition of the four Watson-Crick base pairs in the DNA minor groove by synthetic ligands. *Nature* **1998**, *391*, 468–471.
12. Dervan, P. B. Molecular recognition of DNA by small molecules. *Bioorg. Med. Chem.* **2001**, *9*, 2215-2235.
13. Reddy, B. S. P.; Sondhi, S. M.; Lown, J. W. Synthetic DNA minor groove-binding drugs. *Pharmacol. Ther.* **1999**, *84*, 1–111.
14. Kubista, M.; Akerman, B.; Norden, B. Characterization of interaction between DNA and 4',6-diamidino-2-phenylindole by optical spectroscopy. *Biochemistry* **1987**, *26*, 4545–4553.
15. Crissman, H. A.; Hirons, G. T. Staining of DNA in live and fixed cells. *Methods Cell Biol.* **1994**, *41*, 195–209.
16. Pfeifer, G. P.; You, Y.-H.; Besaratinia, A. Mutations induced by ultraviolet light. *Mutat. Res.* **2005**, *571*, 19–31.
17. Loontjens, F. G.; Regenfuss, P.; Zechel, A.; Dumortier, L.; Clegg, R. M. Binding characteristics of Hoechst 33258 with calf thymus DNA, poly[d(A-T)], and d(CCGGAATTCCGG): multiple stoichiometries and determination of tight binding with a wide spectrum of site affinities. *Biochemistry* **1990**, *29*, 9029–9039.
18. Singer, V. L.; Jones, L. J.; Yue, S. T.; Haugland, R. P. Characterization of PicoGreen reagent and development of a fluorescence-based solution assay for double-stranded DNA quantitation. *Anal. Biochem.* **1997**, *249*, 228–238.
19. Tanious, F. A.; Veal, J. M.; Buczak, H.; Ratmeyer, L. S.; Wilson, W. D. DAPI (4',6-diamidino-2-phenylindole) binds differently to DNA and RNA: minor-groove binding at AT sites and intercalation at AU sites. *Biochemistry* **1992**, *31*, 3103-3112.
20. Zink, D.; Sadoni, N.; Stelzer, E. Visualizing chromatin and chromosomes in living cells. *Methods* **2003**, *29*, 42-50.
21. Erve, A.; Saoudi, Y.; Thiot, S.; Guetta-Landras, C.; Florent, J. C.; Nguyen, C. H.; Grierson, D. S.; Popov, A. V. BENA435, a new cell-permeant photoactivated green fluorescent DNA probe. *Nucleic Acids Res.* **2006**, *34*, e43.

22. Feng, S.; Kim, Y. K.; Yang, S.; Chang, Y. T. Discovery of a green DNA probe for live-cell imaging. *Chem. Commun.* **2010**, *46*, 436 – 438.
23. Gill, M. R.; Garcia-Lara, J.; Foster, S. J.; Smythe, C.; Battaglia, G.; Thomas, J. A. Ruthenium(II) polypyridyl complex for direct imaging of DNA structure in living cells. *Nat. Chem.* **2009**, *1*, 662 – 667.
24. Haugland, R. P. Handbook of Fluorescent Probes and Research Products; Molecular Probes. Inc.: Eugene, OR, **2002**.
25. Joo, C.; Balci, H.; Ishitsuka, Y.; Buranachai, C.; Ha, T. Advances in single-molecule fluorescence methods for molecular biology. *Annu. Rev. Biochem.* **2008**, *77*, 51– 76.
26. van Mameren, J.; Peterman, E. J. G.; Wuite, G. J. L. See me, feel me: methods to concurrently visualize and manipulate single DNA molecules and associated proteins. *Nucleic Acids Res.* **2008**, *36*, 4381– 4389.
27. Peng, X.; Wu, T.; Fan, J.; Wang, J.; Zhang, S.; Song, F.; Sun, S. An effective minor groove binder as a red fluorescent marker for live-cell DNA imaging and quantification. *Angew. Chem. Int. Ed.* **2011**, *50*, 4180-4183.
28. Selvin, P. Science innovation '92: the San Francisco sequel. *Science* **1992**, *257*, 885-886.
29. Glazer, A. N.; Rye, H. S. Stable dye-DNA intercalation complexes as reagents for high-sensitivity fluorescence detection. *Nature* **1992**, *359*, 859-861.
30. Rye, H. S.; Yue, S.; Wemmer, D. E.; Quesada, M. A.; Haugland, R. P.; Mathies, R. A.; Glazer, A. N. Stable fluorescent complexes of double-stranded DNA with bis-intercalating asymmetric cyanine dyes: properties and applications. *Nucleic Acids Res.* **1992**, *20*, 2803-2812.
31. Rye, H. S.; Yue, S.; Quesada, M. A.; Haugland, R. P.; Mathies, R. A.; Glazer, A. N. Picogram detection of stable dye-DNA intercalation complexes with two-color laser-excited confocal fluorescence gel scanner. *Methods Enzymol.* **1993**, *217*, 414-431.
32. Ogura, M.; Mitsuhashi, M. Fluorometric method for the measurement of nuclease activity on plastic plates. *BioTechniques.* **1995**, *18*, 231–233.
33. Ogura, M.; Mitsuhashi, M. Use of the fluorescent dye YOYO-1 to quantify oligonucleotides immobilized on plastic plates. *BioTechniques.* **1994**, *16*, 1032–1034.
34. Rye, H. S.; Glazer, A. N. Interaction of dimeric intercalating dyes with single-stranded DNA. *Nucleic Acids Res.* **1995**, *23*, 1215-1222.
35. Zipper, H.; Brunner, H.; Bernhagen, J.; Vitzthum, F. Investigations on DNA intercalation and surface binding by SYBR Green I, its structure determination and methodological implications. *Nucleic Acids Res.* **2004**, *32*, e103.

36. Narayanaswamy, N.; Kumar, M.; Das, S.; Sharma, R.; Samanta, P. K.; Pati, S. K.; Dhar, S. K.; Kundu, T. K.; Govindaraju, T. A thiazole coumarin (TC) turn-on fluorescence probe for AT-base pair detection and multipurpose applications in different biological systems. *Sci. Rep.* **2014**, *4*, 6476.
37. Yuan, L.; Lin, W.; Zheng, K.; Zhu, S. FRET-based small-molecule fluorescent probes: rational design and bioimaging applications. *Acc. Chem. Res.* **2013**, *46*, 1462-1473.
38. Furstenberg, A.; Julliard, M. D.; Deligeorgiev, T. G.; Gadjev, N. I.; Vasilev, A. A.; Vauthey, E. Ultrafast excited-state dynamics of DNA fluorescent intercalators: new insight into the fluorescence enhancement mechanism. *J. Am. Chem. Soc.* **2006**, *128*, 7661 – 7669.
39. Silva, G. L.; Ediz, V.; Yaron, D.; Armitage, B. A. Experimental and computational investigation of unsymmetrical cyanine dyes: understanding torsionally responsive fluorogenic dyes. *J. Am. Chem. Soc.* **2007**, *129*, 5710 – 5718.
40. Cosa, G.; Focsaneanu, K.-S.; McLean, J. R. N.; McNamee, J. P.; Scaiano, J. C. Photophysical properties of fluorescent DNA-dyes bound to single- and double-stranded DNA in aqueous buffered solution. *Photochem. Photobiol.* **2001**, *73*, 585–599.
41. Nguyen, B.; Neidle, S.; Wilson, W. D. A role for water molecules in DNA-ligand minor groove recognition. *Acc. Chem. Res.* **2009**, *42*, 11-21.
42. Dragan, A. I.; Casas-Finet, J. R.; Bishop, E. S.; Strouse, R. J.; Schenerman, M. A.; Geddes, C. D. Characterization of PicoGreen interaction with dsDNA and the origin of its fluorescence enhancement upon binding. *Biophys. J.* **2010**, *99*, 3010-3019.
43. Stender, A. S.; Marchuk, K.; Liu, C.; Sander, S.; Meyer, M. W.; Smith, E. A.; Neupane, B.; Wang, G.; Li, J.; Cheng, J. X.; Huang, B.; Fang, N. Single cell optical imaging and spectroscopy. *Chem. Rev.* **2013**, *113*, 2469-2527.
44. Samanta, P. K.; Manna, A. K.; Pati, S. K. Structural, electronic, and optical properties of metallo base pairs in duplex DNA: a theoretical insight. *Chem. Asian. J.* **2012**, *7*, 2718-2728.
45. Samanta, P. K.; Pati, S. K. Structural and magnetic properties of a variety of transition metal incorporated DNA double helices. *Chem. Eur. J.* **2014**, *20*, 1760-1764.
46. Churchill, C. D. M.; Wetmore, S. D. Developing a computational model that accurately reproduces the structural features of a dinucleoside monophosphate unit within B-DNA. *Phys. Chem. Chem. Phys.* **2011**, *13*, 16373-16383.
47. Martin, R. M.; Leonhardt, H.; Cardoso, M. C. DNA labeling in living cells. *Cytometry A.* **2005**, *67*, 45-52.
48. van Zandvoort, M. A.; de Grauw, C. J.; Gerritsen, H. C.; Broers, J. L.; oude Egbrink, M. G.; Ramaekers, F. C.; Slaaf, D. W. Discrimination of DNA and RNA in cells by a vital

- fluorescent probe: lifetime imaging of SYTO13 in healthy and apoptotic cells. *Cytometry* **2002**, *47*, 226-235.
49. Roset, R.; Subirana, J. A.; Messeguer, X. MREPATT: detection and analysis of exact consecutive repeats in genomic sequences. *Bioinformatics* **2003**, *19*, 2475-2476.
50. Smale, S. T.; Kadonaga, J. T. The RNA polymerase II core promoter. *Annu. Rev. Biochem.* **2003**, *72*, 449-479.
51. Maity, D.; Govindaraju, T. Highly selective colorimetric chemosensor for  $\text{Co}^{2+}$ . *Inorg. Chem.* **2011**, *50*, 11282-11284.
52. Sun, Y-Q.; Liu, J.; Zhang, J.; Yang, T.; Guo, W. Fluorescent probe for biological gas  $\text{SO}_2$  derivatives bisulfite and sulfite. *Chem. Commun.* **2013**, *49*, 2637-2639.
53. Frisch, M. J., Trucks, G. W., Schlegel, H. B., Scuseria, G. E., Robb, M. A., Cheeseman, J. R., Scalmani, G., Barone, V., Mennucci, B., Petersson, G. A., Nakatsuji, H., Caricato, M., Li, X., Hratchian, H. P., Izmaylov, A. F., Bloino, J., Zheng, G., Sonnenberg, J. L., Hada, M., Ehara, M., Toyota, K., Fukuda, R., Hasegawa, J., Ishida, M., Nakajima, T., Honda, Y., Kitao, O., Nakai, H., Vreven, T., Montgomery, Jr., J. A., Peralta, J. E., Ogliaro, F., Bearpark, M., Heyd, J. J., Brothers, E., Kudin, K. N., Staroverov, V. N., Keith, T., Kobayashi, R., Normand, J., Raghavachari, K., Rendell, A., Burant, J. C., Iyengar, S. S., Tomasi, J., Cossi, M., Rega, N., Millam, J. M., Klene, M., Knox, J. E., Cross, J. B., Bakken, V., Adamo, C., Jaramillo, J., Gomperts, R., Stratmann, R. E., Yazyev, O., Austin, A. J., Cammi, R., Pomelli, C., Ochterski, J. W., Martin, R. L., Morokuma, K., Zakrzewski, V. G., Voth, G. A., Salvador, P., Dannenberg, J. J., Dapprich, S., Daniels, A. D., Farkas, O., Foresman, J. B., Ortiz, J. V., Cioslowski, J. & Fox, D. J. *Gaussian 09, Revision C.01*, Gaussian, Inc., Wallingford CT, **2009**.
54. Chai, J. D.; Head-Gordon, M. Long-range corrected hybrid density functionals with damped atom-atom dispersion corrections. *Phys. Chem. Chem. Phys.* **2008**, *10*, 6615-6620.
55. Becke, A. D. Density-functional thermochemistry. III. The role of exact exchange. *J. Chem. Phys.* **1993**, *98*, 5648-5652.
56. Lee, C. T.; Yang, W. T.; Parr, R. G. Development of the Colle-Salvetti correlation-energy formula into a functional of the electron density. *Phys. Rev. B.* **1988**, *37*, 785-789.
57. Miehlich, B.; Savin, A.; Stoll, H.; Preuss, H. Results obtained with the correlation energy density functionals of Becke and Lee, Yang and Parr. *Chem. Phys. Lett.* **1989**, *157*, 200-206.
58. Scalmani, G.; Frisch, M. J. Continuous surface charge polarizable continuum models of solvation. I. General formalism. *J. Chem. Phys.* **2010**, *132*, 114110-114115.

59. Deshmukh, A. S.; Srivastava, S.; Herrmann, S.; Gupta, A.; Mitra, P.; Gilberger, T. W.; Dhar, S. K. The role of N-terminus of *Plasmodium falciparum* ORC1 in telomeric localization and var gene silencing. *Nucleic Acids Res.* **2012**, *40*, 5313-5331.

---

# Chapter 3

**Sequence-Specific Recognition of DNA Minor Groove by an  
NIR Fluorescence Switch-On Probe and its Potential  
Applications**

Sequence-specific recognition is an essential criterion to target and control DNA functions for gene-expression, bioimaging, diagnostics, therapeutics and biotechnological applications.<sup>1,2</sup> Over the years, many probes have been developed to target DNA, but there is still a pressing need for developing efficient new probes and therapeutic agents against gene-related diseases as DNA remains a promising biological receptor.<sup>3-5</sup> It is a daunting task indeed to design site-specific DNA binding molecules with high affinity and selectivity. To achieve this goal, base-pair and sequence-selective DNA binding probes ranging from small molecules to large peptides of natural and synthetic origin have been developed.<sup>6-10</sup> These probes interact with DNA mainly through two binding modes, intercalation and groove binding. Typically, small molecules binding to DNA through intercalation possess the site-specificity of three base-pairs that can differentiate only one out of 32 random sequences.<sup>11</sup> Factually, the human genome contains three billion base pairs and the small molecular probe is posed with the astonishingly large number of one billion unique binding sites.<sup>12</sup> To improve the binding specificity of small molecular probes over longer DNA sequences, researchers shifted their attention towards groove-binding agents. DNA grooves are sites with inherent hydrogen bond donors and acceptors at the edges of nucleobases, which makes them adaptable to recognition through hydrogen bonding interactions in a sequence-selective manner.<sup>9,10,13-17</sup> In comparison with DNA major groove, the minor groove is narrow in size, which makes it suitable for small molecular probes. In particular, sequence-specific targeting of DNA using minor groove-binding molecules is considered a promising molecular recognition strategy in chemistry and biology.<sup>9,10,13-17</sup>

Dervan and co-workers developed sequence-specific N-methylpyrrole and N-methylimidazole-containing crescent-shaped polyamides that can selectively recognize and bind DNA minor grooves through hydrogen bonding interactions.<sup>8,10,12-17</sup> These polyamides are one of the most elegantly designed molecules to recognize the minor groove of DNA with superior discrimination of all four Watson-Crick base pairs.<sup>12</sup> However, their difficult synthesis processes and non-fluorescent nature eventually limited their potential applications in biological systems. Recently, polyamide/fluorophore conjugates have been developed, and their cellular uptake properties studied in various cell lines.<sup>15-17</sup> Later, Wilson and coworkers

reported phenyl-furan-benzimidazole diamidine-based cell permeable and sequence-selective minor groove-binding molecules.<sup>5,18-24</sup> One of the common structural features of all these minor groove-binding ligands is the molecular curvature to complement the DNA minor groove concavity, referred to as “*iso-helicity*,” which enhances the binding affinity and selectivity of interaction.<sup>9,10,18-23</sup> Recent studies show that a majority of the minor groove-binding molecules actually target AT-rich mitochondrial kinetoplast DNA of eukaryotic cells and that of the protozoan parasite *Plasmodium falciparum*.<sup>5,23,25,26</sup> Such interactions induce topological changes in AT-rich DNA, which can generate biological response against certain diseases and also serve as model systems to gain insights into the structural organization of DNA.<sup>27</sup> Minor groove binding ligands such as distamycin A, netropsin, 4'-6-diamidino-2-phenylindole (DAPI) and bis-benzimide (Hoechst 33258) have been used as antibiotics as they bind to the minor groove of B-DNA with a preference for AT-rich sequences and are considerably more toxic to parasites than to mammalian cells.<sup>5</sup> Further, availability of myriad genome data warrants the need for developing efficient and highly predictive molecular tools to probe its organization and functional aspects. Overall, it is clear that sequence-specific targeting of DNA is crucial for studying sequence variation, structural organization and function in the cell nucleus.

Fluorescence probes have become powerful tools in cell biology and play a vital role in the modern era of biological research.<sup>28-31</sup> Apart from simple detection they offer the additional advantage of real-time monitoring of conformational changes and structural reorganization of biological macromolecules in living cells and organisms.<sup>28-31</sup> In this context, structural, functional and therapeutic study of DNA in the cell nucleus requires sequence-specific, minor groove-binding fluorescence probes.<sup>32,33</sup> Fluorescence imaging of DNA has been widely used to stain the nuclei of live or fixed cells and study structural reorganization of chromosome in the cell nucleus.<sup>32-34</sup> DAPI, bisbenzimidides (Hoechst dyes), and propidium iodide are well-known nuclear staining agents.<sup>35</sup> However, the blue fluorescence DNA staining probes (DAPI and Hoechst) require excitation in the ultraviolet (UV) region and the prolonged UV illumination is certain to damage cellular DNA. Additionally, propidium iodide and related dyes are intercalators suffering from poor cell-



permeability and high toxicity, apart from inducing structural alterations in the target DNA structure, which prohibits their use in biological applications.<sup>35</sup> The limitations of existing probes and the quest to develop novel probes with superior properties motivated us to design a new, sequence-specific NIR fluorescence probe for DNA. Such fluorescence DNA probe must satisfy the following properties i) excitation and emission in the longer wavelength region, ii) switch-on fluorescence response, iii) high sequence-specificity, iv) good quantum yield, v) non-toxicity, and vi) live-cell permeability. In recent years, NIR fluorescence probes have been gaining considerable attention due to their broad range of *in vivo* imaging applications that avoid interference from the absorbance and auto-fluorescence of cellular components.<sup>36-39</sup> The deep tissue penetration ability of NIR radiation makes these probes a versatile and inexpensive alternative to classical radioisotope-detection methods.<sup>36-39</sup> Our research group is particularly interested in developing novel red and NIR fluorescence probes for biomolecules and toxic protein aggregates.<sup>34,40,41</sup> Recently, we reported an AT-base pair selective, cell permeable, red emitting thiazole-coumarin (**TC**) hemicyanine probe for cell-cycle analysis, selective nuclear staining and other applications (Chapter 2).<sup>34</sup> Probe **TC** showed preferential AT-base pair selectivity with ~10-20 folds fluorescence enhancement, as a function of number of AT-base pairs with a moderate association constant ( $K_a = 1 \times 10^5 \text{ M}^{-1}$ ). The intercalation mode of binding and moderate binding affinity of probe **TC** to DNA encouraged us to design a new high affinity, sequence-specific NIR fluorescence switch-on probe for DNA minor groove recognition.

DNA probes such as thiazole orange (TO) and oxazole yellow (YO) belong to the cyanine family, but surprisingly, no NIR fluorescence probe with cyanine platform has been reported. Cyanine dyes are composed of polymethine bridges between the N-alkylated heterocyclic aromatic groups such as pyridine, quinoline, benzoxazole, and benzothiazole.<sup>42</sup> The fluorescence property of cyanine dyes depends on complete delocalization of  $\pi$ -electrons between the donor-acceptor nitrogen atoms connected by polymethine bridges. Non-fluorescence in the unbound-state and strong fluorescence in the bound-state nature of most of the cyanine probes inspired us to design a cyanine-based NIR probe for DNA. In this work, we present a one-donor-two-acceptor (D2A) quinone cyanine (QCy7)-based probe

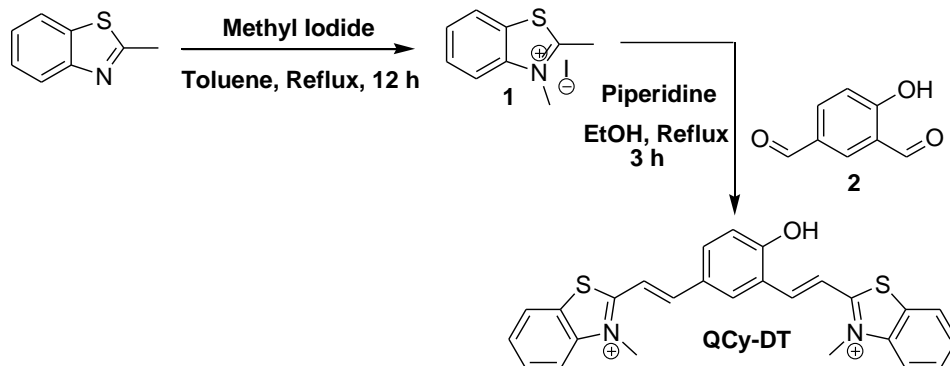
**QCy-DT** designed to recognize DNA minor groove by switch-on NIR fluorescence. Quinone cyanine (**QCy7**) fluorophore is a new class of NIR fluorescence cyanine probes reported by Shabat and coworkers.<sup>43-47</sup> Typically, these probes are composed of a donor phenol moiety conjugated with two heterocyclic electron acceptors such as alkylated quinolines, indolines or pyridines.

In the present work, we demonstrated a bent-shaped molecular probe quinone cyanine-dithiazole (**QCy-DT**), a D2A (one-donor-two-acceptor)  $\pi$ -electron system that is designed to undergo internal charge transfer to convert itself into a switch-on NIR-fluorophore upon binding to DNA. The bent shaped **QCy-DT** was expected to obey *isohelicity* and recognize the minor groove of duplex DNA with switch-on NIR fluorescence response. Remarkably, fluorescence and circular dichroism (CD) studies reveal that **QCy-DT** binding to AT-rich DNA minor groove, in fact, result in switch-on NIR-emission in a sequence-specific manner, especially with a 5'-AAATTT-3' sequence. Most of the desirable properties such as large Stokes shift, switch-on fluorescence (non-aggregated and non-fluorescent in unbound-state but emit NIR fluorescence in DNA bound-state), and sequence-specific binding of **QCy-DT** in buffer solution demonstrate its superiority as a DNA probe. The live cell imaging studies confirm non-toxicity, cell permeability, effective nuclear DNA staining and photostability by **QCy-DT** at low concentration ( $\leq 1 \mu\text{M}$ ) without the need of RNase treatment. Uptake of **QCy-DT** by *Plasmodium* nucleus at a very low concentration of 500 nM and a low ( $< 4 \mu\text{M}$ ) inhibitory concentration ( $\text{IC}_{50}$ ) against malarial parasites indicates that **QCy-DT** may have potential use against parasitic infections. **QCy-DT** displays high sequence-specificity (5'-AAATTT-3') for DNA minor groove and is a potential probe for nuclear DNA staining of live and fixed mammalian cells, among other molecular and cell biology applications.

### 3.1 Synthesis and NIR-activation of probe QCy-DT

**QCy-DT** was synthesized through Knoevenagel condensation of 4-hydroxyisophthalaldehyde with N-methylated benzothiazole in the presence of piperidine as a base (Scheme 1). We treated 2-methyl benzothiazole in presence of methyl iodide in dichloromethane under reflux conditions to get N-methylated benzothiazole (**1**) in good

yields. The obtained *N*-methylated benzothiazole (**1**) was reacted with 4-hydroxyisophthalaldehyde in presence of piperidine base in ethanol solvent under reflux conditions to offer probe **QCy-DT** (Scheme 1).



**Scheme 1.** Synthesis of probe **QCy-DT**.

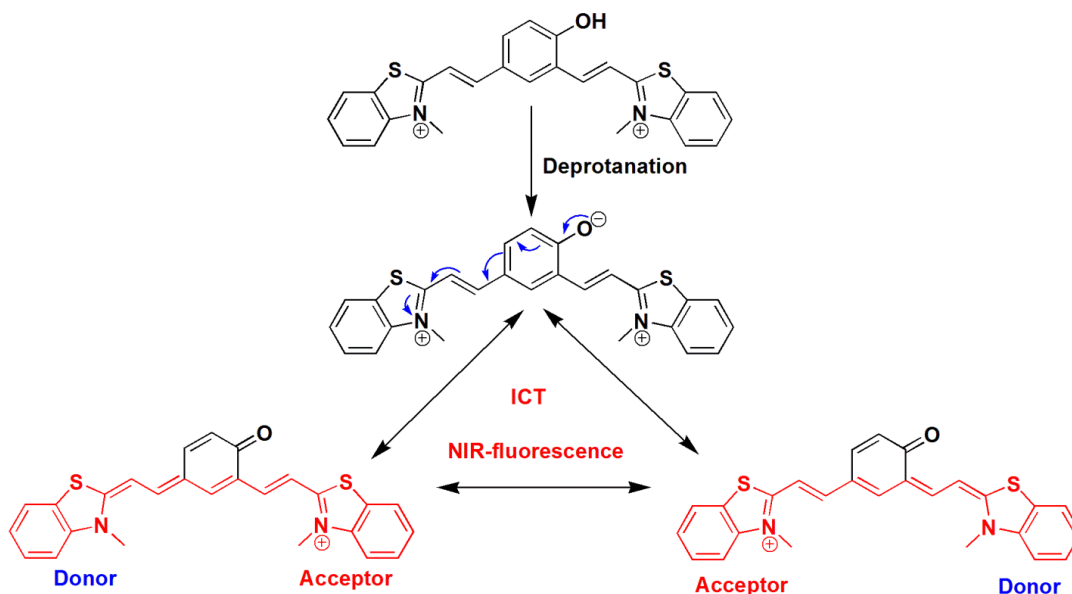


**Figure 1.** Activation of **QCy-DT** to form ‘NIR-ready’ fluorescence probe (Cy7 system).

This simple and straightforward synthesis route makes **QCy-DT** highly economical and, hence, a practically viable probe. As illustrated in Figure 1, deprotonation of phenol generates phenolate which donates electrons to one of the conjugated acceptors (*N*-alkylated

benzothiazole) and triggers internal charge transfer (ICT) to the quaternary nitrogen atom on another benzothiazole group. This ICT process results in the generation of a highly delocalized  $\pi$ -electron system, resembling the Cy7 fluorophore (Figure 1).

However, the protonated form of **QCy-DT** (*i.e.*, phenol form) is non-fluorescent or weakly fluorescent due to the lack of the ICT process. In order to assess the conditions for deprotonation of **QCy-DT** to generate phenolate, we performed pH-dependent fluorescence measurements in Tris-HCl solution (100 mM, pH = 7.4). Under acidic conditions (pH = 2-5), **QCy-DT** did not fluoresce owing to a stable phenol form. Interestingly, the probe showed weak but basal NIR fluorescence ( $\lambda_{\text{max}} = 680$  nm) in the pH range of 6-8 (Figure 2). Thus, pH-dependent fluorescence study revealed that under physiological conditions, **QCy-DT** exists mostly in the phenolate form with basal NIR fluorescence (NIR-ready). The weak but basal fluorescent nature of **QCy-DT** (NIR-ready fluorescence probe) under physiological conditions meets our prime criterion that the probe is relatively non-fluorescent in the unbound-state but fluoresces strongly in DNA bound-state.

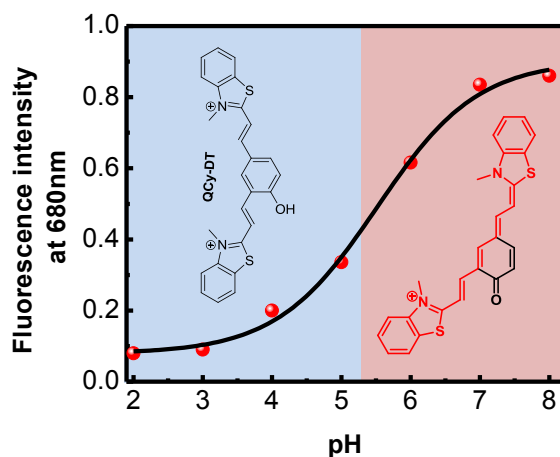


**Figure 2.** Plot of fluorescence intensity of **QCy-DT** at 680 nm as function of solution pH upon excitation at 530 nm.

### 3.2 Photophysical properties of probe **QCy-DT**

We studied the molecular interactions of **QCy-DT** by evaluating the absorption and emission properties in Tris-buffer (100 mM, pH = 7.4) under ambient conditions. The UV-vis

absorption spectra of **QCy-DT** (2  $\mu\text{M}$ ) exhibit two absorption maxima at 463 and 530 nm ( $\epsilon = 14,950 \text{ M}^{-1} \text{ cm}^{-1}$ ) (Figure 3). The absorption band at 530 nm originates from the delocalization of  $\pi$ -electrons between phenolic oxygen and *p*-substituted benzothiazolium vinyl moiety in **QCy-DT** while the band at 463 nm is from the similar conjugation of *o*-substituted benzothiazolium vinyl moiety in **QCy-DT**.<sup>43</sup> The absorption spectra of **QCy-DT** showed a linear increase in absorbance with increasing concentration from 0 to 8  $\mu\text{M}$  (Figure 4). This linear increase in absorbance in the range of 0 to 8  $\mu\text{M}$  of **QCy-DT** suggests molecularly dissolved and non-aggregated state in buffer solution, under ambient conditions. Upon excitation at 530 nm, **QCy-DT** showed a weak but basal emission peak in the NIR region at 680 nm with a large Stokes shift ( $\Delta\lambda_{\text{max}} = \sim 150 \text{ nm}$ ) (Figure 3). This is a very useful property as it helps avoiding self-absorption in the higher energy part of emission.

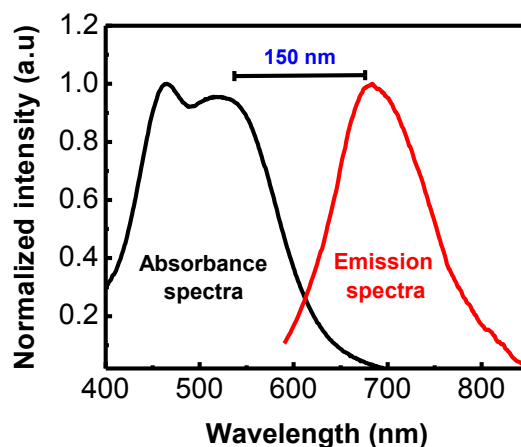


**Figure 3.** The absorbance and emission spectra of **QCy-DT** in Tris-HCl buffer solution (100 mM, pH = 7.4).

Furthermore, the large Stokes shift of **QCy-DT** makes it superior to many of the DNA-binding cyanine probes such as TO, YO, Picogreen, SYBR-Green I, cyanine dimers TOTO-1 and YOYO-1 (Table 1).<sup>48,49</sup> The NIR fluorescence of **QCy-DT** arises due to extended  $\pi$ -conjugation through the Cy7 backbone and ICT process. The weak or non-fluorescent behavior of dye molecules in buffer solution is mainly attributed to the intramolecular twisting processes which cause quenching of the fluorescence of cyanine dyes; solvation with water molecules also aids the fluorescence quenching by means of deactivation of radiative

pathways.<sup>50</sup> We believe both these processes contribute to the weak or non-fluorescent nature of QCy-DT in buffer solution.

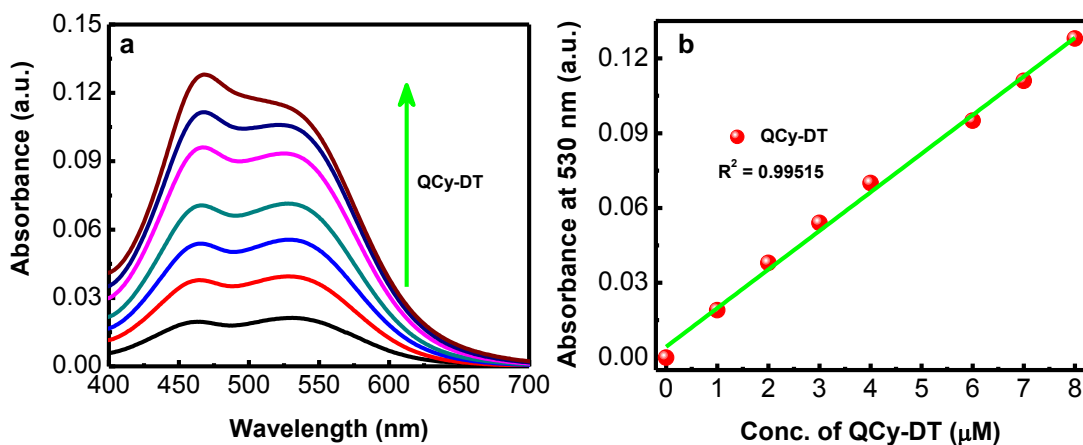


**Figure 4.** Absorption spectra of QCy-DT. (a) Absorption spectra of QCy-DT with increasing concentration from 0 to 8  $\mu\text{M}$  in Tris-HCl buffer solution (100 mM, pH = 7.4). (b) Plot of absorption intensity at 530 nm against the concentration of QCy-DT.

**Table 1.** Stokes shift values of cyanine dyes in presence and absence of DNA.

Cyanine Dye	In absence of DNA (nm)	In presence of DNA (nm)
Thiazole orange (TO) <sup>a</sup>	139	18
Oxazole yellow (YO) <sup>a</sup>	100	19
TOTO-1 <sup>a</sup>	149	19
YOYO-1 <sup>a</sup>	106	20
Picogreen <sup>b</sup>	30	21
SYBR Green I <sup>b</sup>	36	26
QCy-DT <sup>c</sup>	150	86

<sup>a</sup> Rye, H. S.; Yue, S.; Wemmer, D. E.; Quesada, M. A.; Haugland, R. P.; Mathies, R. A.; Glazer, A. N. *Nucleic Acids Res.*, **1992**, *20*, 2803–2812. <sup>b</sup> Cosa, G.; Focsaneanu, K.-S.; McLean, J. R. N.; McNamee, J. P.; Scaiano, J. C. *Photochem. Photobiol.*, **2001**, *73*, 585–599. <sup>c</sup> Present work.

Next, we performed the ground-state and excited-state calculations using density functional theory (DFT) with the PBE0<sup>51,52</sup> functional and 6-311++G(d,p) basis set for all atoms to support our assignments of the absorption and emission bands of **QCy-DT** in water. DFT calculations show that the two  $\pi$ - $\pi^*$  transitions located near 2.32 eV (S1) and 2.88 eV are in good agreement with two experimentally observed absorption bands of **QCy-DT** in buffer solution, as shown in Figure 3. The first  $\pi$ - $\pi^*$  state is the lowest transition dominated by the HOMO to LUMO (97%) configuration while the second  $\pi$ - $\pi^*$  state is dominated by the configuration HOMO to LUMO+1 (97%). Relevant molecular orbitals for these transitions are shown in Figure 5.

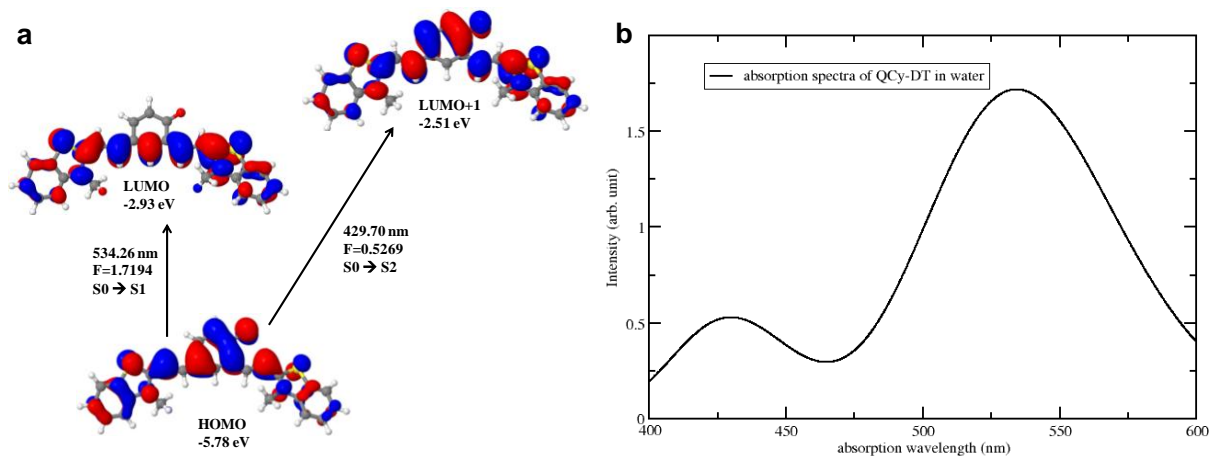


**Figure 5.** Optical transitions of **QCy-DT**. (a) Molecular orbitals involved in the S1 and S2 electronic transitions for **QCy-DT** in water. (b) Computed absorption spectra for **QCy-DT** in water.

### 3.3 Switch-on NIR fluorescence of probe **QCy-DT** in the presence of DNA

The large Stokes shift, molecularly dissolved-state and non-fluorescent behavior of **QCy-DT** in buffer solution prompted us to assess its recognition ability of DNA. For this, we chose poly AT-duplexes such as (A-T)<sub>20</sub>, self-complementary d(ATAT)<sub>5</sub>, Drew-AT (14 base pair self-complementary sequence with 6AT-base pairs in central core),<sup>53,54</sup> poly GC-duplex (G-C)<sub>20</sub>, (D1)<sub>mix</sub>, which is a 16 base pair long self-complementary duplex and CT-DNA as mixed AT/GC duplexes (Table 2). In the presence of Drew-AT, **QCy-DT** (2  $\mu$ M) showed

prominent red-shifted ( $\Delta\lambda_{\text{max}} = \sim 34$  nm) absorption spectrum with good hyperchromicity in the absorption intensity.

**Table 2.** DNAs used in this study (with sequence information).

Code	DNA duplex	Sequence
Drew AT	mixed DNA	5'- GCGCAAATTTGCGC-3' 3'-CGCGTTTAAACGCG-5'
(A-T) <sub>20</sub>	dA <sub>20</sub> -dT <sub>20</sub>	5'-AAAAAAAAAAAAAAAAAAAAA-3' 3'-TTTTTTTTTTTTTTTTTTTT-5'
d(ATAT) <sub>5</sub>	d(ATAT) <sub>5</sub>	5'-ATATATATATATATATAT-3' 3'-TATATATATATATATATA-5'
(G-C) <sub>20</sub>	dG <sub>20</sub> -dC <sub>20</sub>	5'-GGGGGGGGGGGGGGGGGG-3' 3'-CCCCCCCCCCCCCCCCCCC-5'
(D1) <sub>mix</sub>	mixed DNA	5'- CGATAAGCGCTTATCG-3' 3'-GCTATTCGCGAATAGC-5'
CT-DNA	mixed DNA	-----

Upon sequential addition of Drew-AT (0, 1, 2, 3 and 4  $\mu\text{M}$ ), the absorption spectra of **QCy-DT** showed a gradual red shift in the absorption maxima (463 to 479 nm and 530 to 564 nm) with hyperchromicity (Figure 6a). Remarkably, **QCy-DT** showed a  $\sim 200$ -fold enhancement in the fluorescence emission at  $\lambda_{\text{em}} = 650$  nm in the presence of Drew-AT with blue shift ( $\Delta\lambda_{\text{max}} = \sim 27$  nm) compared to basal fluorescence of the probe alone (Figure 6b). Further, we studied the absorption and emission properties of **QCy-DT** in the presence of poly AT- and GC-duplexes. In the presence of (A-T)<sub>20</sub>, **QCy-DT** showed red shift in the absorption maxima with hyperchromicity similar to that of Drew-AT (Figure 7a). **QCy-DT** exhibited only a slight red shift in the absorption maxima at 463 and 530 nm in the presence of (G-C)<sub>20</sub> (Figure 7b).



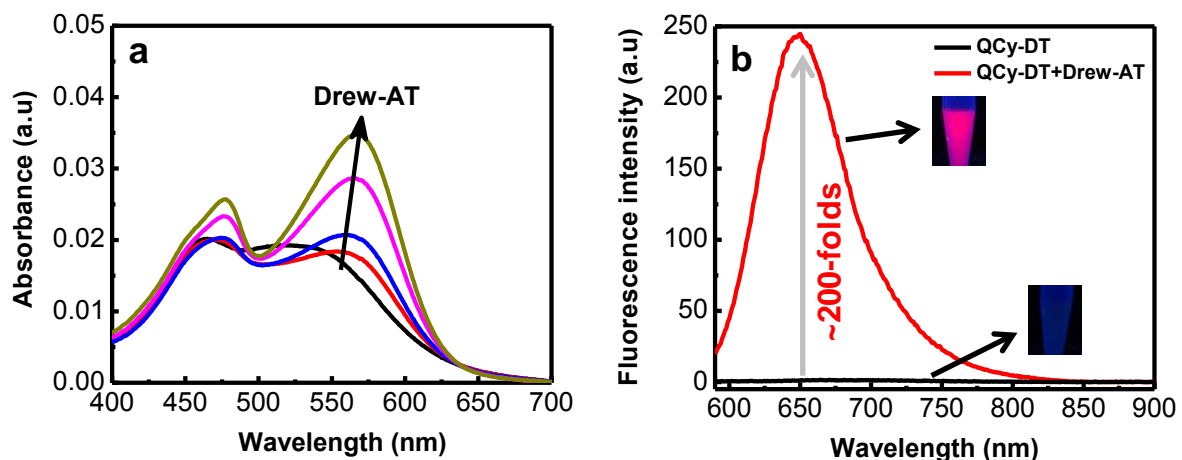


**Figure 6.** Photophysical properties of **QCy-DT**. (a) Absorption spectra of **QCy-DT** (2  $\mu\text{M}$ ) with increasing concentration of **Drew-AT** (0, 1, 2, 3 and 4  $\mu\text{M}$ ). (b) Fluorescence spectrum of **QCy-DT** (2  $\mu\text{M}$ ) in the presence of **Drew-AT** (4  $\mu\text{M}$ ).

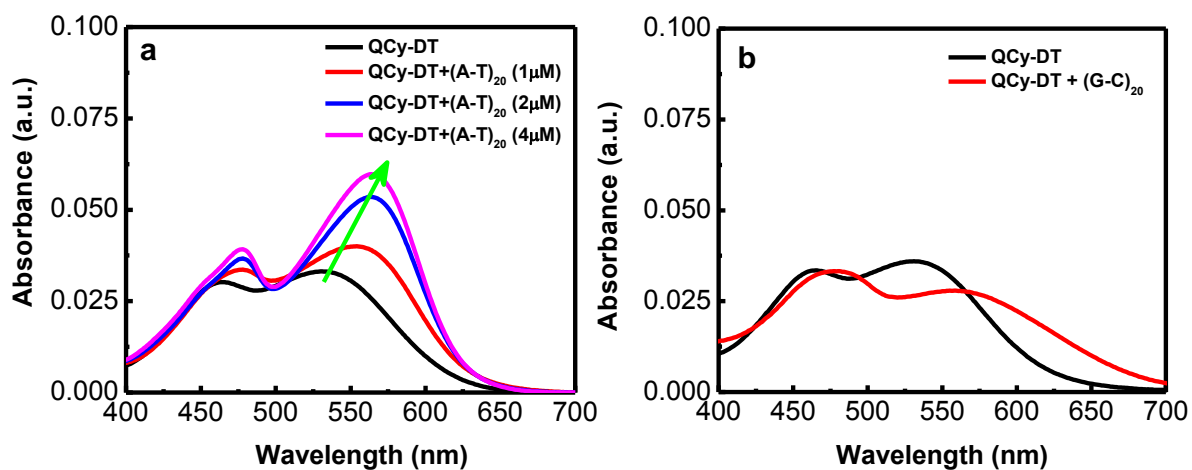


**Figure 7.** Absorption spectra of **QCy-DT** in presence of DNA duplex. (a) Absorption spectra of **QCy-DT** (2  $\mu\text{M}$ ) with increasing concentration of  $(\text{A-T})_{20}$  from 0 to 4  $\mu\text{M}$ . (b) Absorption spectra **QCy-DT** (2  $\mu\text{M}$ ) in presence of  $(\text{G-C})_{20}$  (4  $\mu\text{M}$ ), in Tris-HCl buffer solution.

Interestingly, **QCy-DT** showed almost  $\sim 250$ -fold fluorescence enhancement for  $(\text{A-T})_{20}$ , compared to the only 8-fold increase observed for  $(\text{G-C})_{20}$  duplex (Figure 8a). Further, we also studied the emission behavior of **QCy-DT** in the presence of CT-DNA,  $(\text{D1})_{\text{mix}}$  and

single-stranded (ss) DNAs. CT-DNA, (D1)<sub>mix</sub> and ssDNAs exhibited ~40, ~55 and ~2-fold enhancements, respectively. To ascertain the switch-on behavior of **QCy-DT** in the presence of AT-rich DNA duplex, we performed viscosity measurements by increasing the glycerol content in buffer solution.<sup>34</sup> With increasing glycerol content, fluorescence spectra of **QCy-DT** exhibited a gradual enhancement in the emission intensity at 680 nm (Figure 8b). This tendency of the probe to have increased emission intensity with an increase in the glycerol content clearly suggests that the restriction of intramolecular rotation is responsible for the fluorescence enhancement of **QCy-DT**.

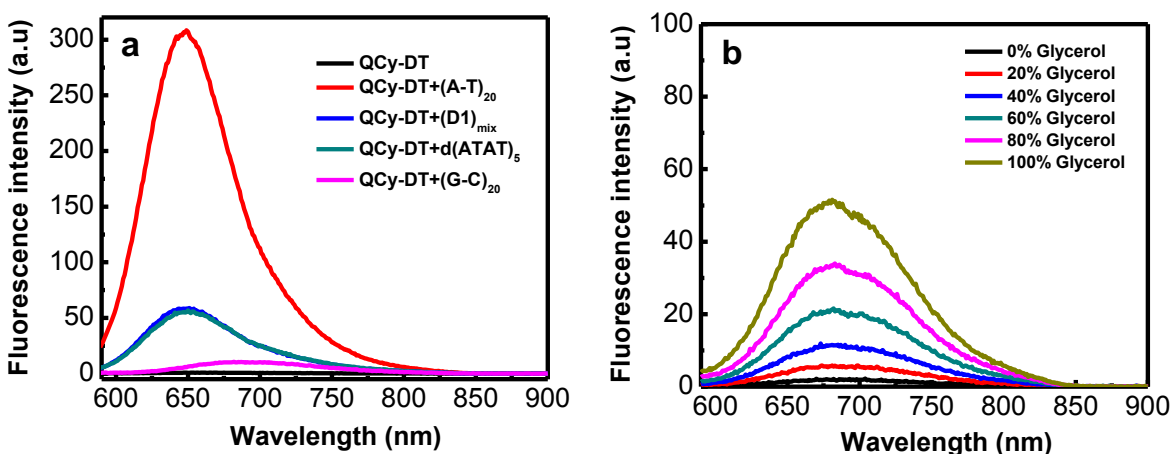


**Figure 8.** Fluorescence spectra of **QCy-DT**. (a) Fluorescence spectra of **QCy-DT** (2 μM) in presence of DNA duplex (4 μM) in Tris-HCl buffer solution. (b) Fluorescence spectra of **QCy-DT** (2 μM) with increasing glycerol content from 0 to 100 % in Tris-HCl buffer solution.

Consequently, the observed strong fluorescence enhancement in the presence of AT-rich DNA duplexes is the result of restriction of intramolecular rotation of probe **QCy-DT** in the constrained environments of DNA, which also facilitates the desolvation (water molecules) around **QCy-DT** in the hydrophobic environment of DNA duplex.<sup>9,55,56</sup> These preliminary results, thus, confirmed switch-on NIR fluorescence behavior of **QCy-DT** in the presence of AT-rich DNA duplexes compared to that of GC-rich DNA duplex and ssDNAs.

### 3.4 Base pair-specific recognition and switch-on fluorescence in the presence of DNA

To gain deeper insights into base pair selectivity of the probe, we performed comparative and base pair-dependent fluorescence measurement in the presence of (A-T)<sub>20</sub>, d(ATAT)<sub>5</sub>, Drew-AT, (D1)<sub>mix</sub> and (G-C)<sub>20</sub> duplexes with 20, 6, 4 and 0 sets of AT-base pairs, respectively. We observed ~8, ~55, ~54, ~200 and ~250-folds fluorescence enhancement in the presence of (G-C)<sub>20</sub>, (D1)<sub>mix</sub>, d(ATAT)<sub>5</sub>, Drew-AT and (A-T)<sub>20</sub> with increasing number of AT-base pairs, respectively (Figure 9).

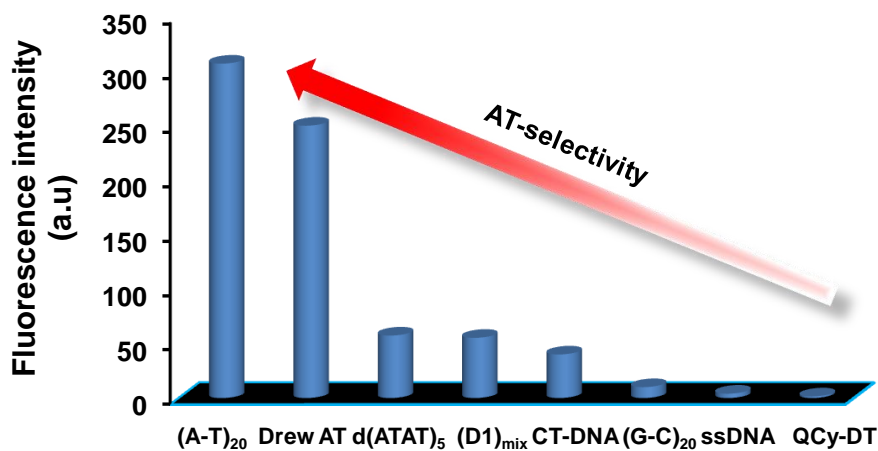


**Figure 9.** Base pair-dependent recognition of AT-rich DNA by **QCy-DT**.

Further, we carried out concentration-dependent studies with (A-T)<sub>20</sub> and Drew-AT duplexes by adding increasing concentrations of **QCy-DT**. With increasing concentration of **QCy-DT** (0 - 8  $\mu$ M) to (A-T)<sub>20</sub> duplex, the fluorescence intensity gradually increased at 650 nm and attained saturation at  $\geq 6$   $\mu$ M (Figure 10a). Similar spectral changes were observed for **QCy-DT** in the presence of Drew-AT (Figure 10b). We also recorded the fluorescence spectra of **QCy-DT** with increasing concentrations of (A-T)<sub>20</sub>, Drew-AT, d(ATAT)<sub>5</sub> and (D1)<sub>mix</sub> duplexes. Figure 11a shows a gradual increase in fluorescence with increasing concentration of Drew-AT from 0 to 2  $\mu$ M and saturation  $\geq 2$   $\mu$ M. Upon increasing concentration of other duplexes (A-T)<sub>20</sub>, d(ATAT)<sub>5</sub> and (D1)<sub>mix</sub> **QCy-DT** showed similar fluorescence enhancement (Figure 11b). Overall, the strong fluorescence enhancements

suggest **QCy-DT** is a selective and NIR fluorescence-ready probe for DNA containing AT-base pairs.

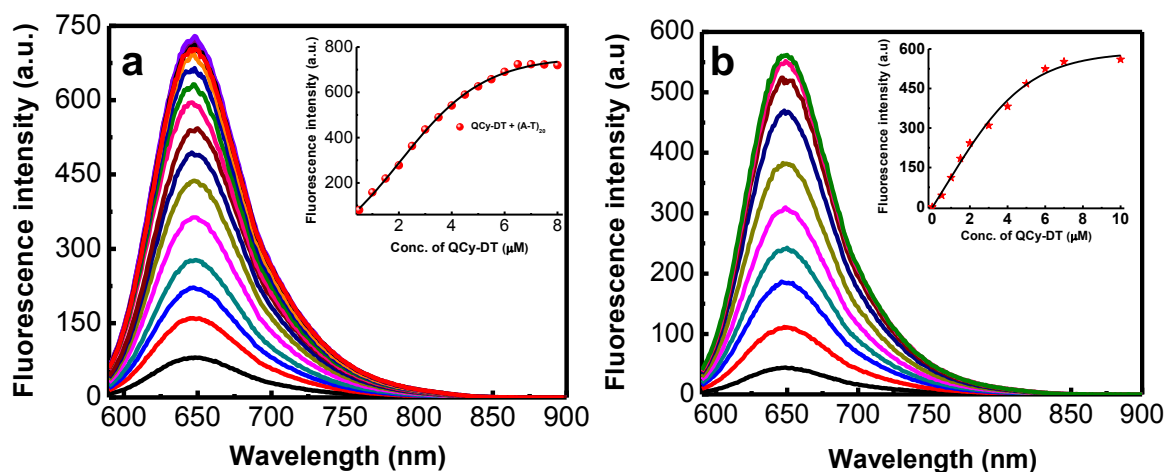


**Figure 10.** Fluorescence spectra of DNA duplexes with increasing concentration of **QCy-DT** from 0 to 8  $\mu\text{M}$ . (a) (A-T)<sub>20</sub> and (b) Drew-AT. *Insets:* Plot of fluorescence intensity at 650 nm as function of **QCy-DT** concentration.

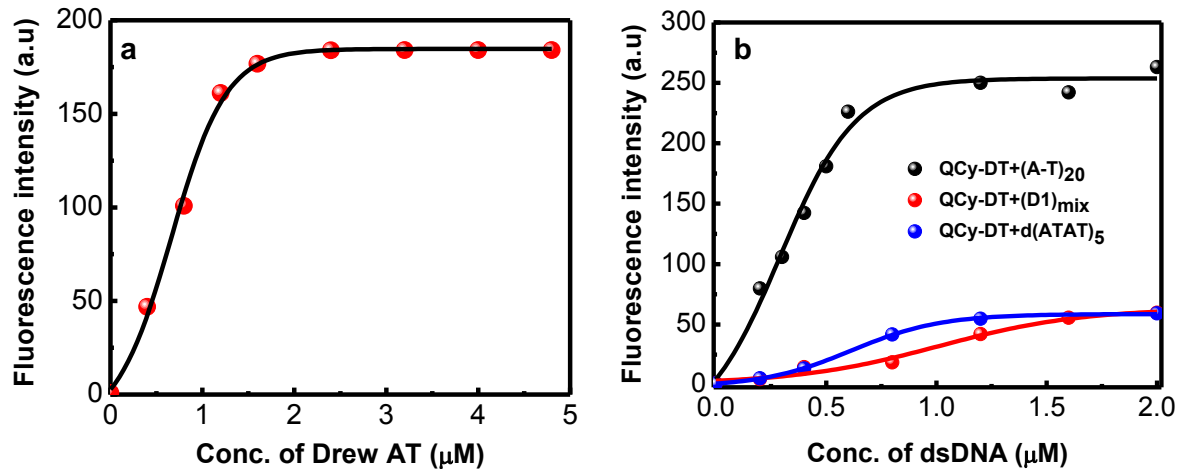


**Figure 11.** Fluorescence response of **QCy-DT**. (a) Fluorescence titration curve of **QCy-DT** (2  $\mu\text{M}$ ) with increasing concentration of Drew-AT (0 to 5  $\mu\text{M}$ ). (b) Fluorescence titration curve of **QCy-DT** with increasing concentration of DNA duplexes (A-T)<sub>20</sub>, (D1)<sub>mix</sub> and d(ATAT)<sub>5</sub> from 0 to 2  $\mu\text{M}$  in buffer solution.

### 3.5 Binding stoichiometry, affinity and quantum yield of probe QCy-DT for DNA

To determine the binding stoichiometry of **QCy-DT** with Drew-AT, we employed the continuous variation method, varying the ligand concentrations to generate the Job plot by fixing the total concentration of [**QCy-DT**+ Drew-AT] at 2  $\mu\text{M}$ .<sup>57</sup> The Job plot analysis showed maximum fluorescence at 0.5, indicating 1:1 binding stoichiometry for the [**QCy-DT**: Drew-AT] complex (Figure 12).

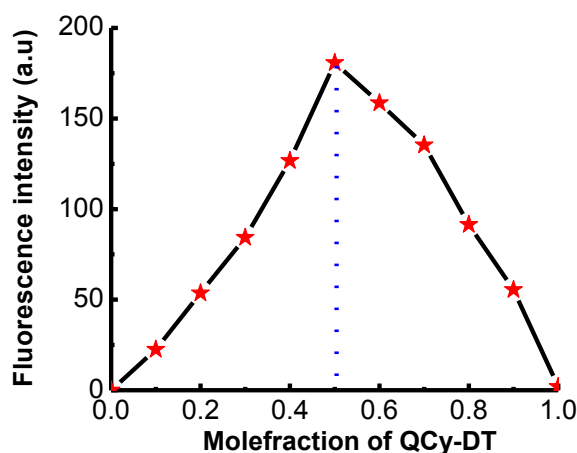


**Figure 12.** Job plot of **QCy-DT** with Drew-AT, which show 1:1 binding stoichiometry.

We calculated the binding constants of [**QCy-DT**+DNA] complexes from the fluorescence titration experiments using non-linear (single-binding mode) curve fitting analysis.<sup>58</sup> **QCy-DT** showed the maximum binding affinity ( $K_a = 2.9 \times 10^6 \text{ M}^{-1}$ ) for (A-T)<sub>20</sub>, which is 2-folds higher than that for Drew-AT ( $K_a = 1.5 \times 10^6 \text{ M}^{-1}$ ). The mixed sequence (D1)<sub>mix</sub> showed relatively weaker binding affinity ( $K_a = 4.3 \times 10^5 \text{ M}^{-1}$ ) compared to AT-rich DNA duplexes (Figure 13). Next, we estimated the fluorescence quantum yield of **QCy-DT** in the presence of AT- and GC-rich DNA duplexes (Table 3). **QCy-DT** alone showed very low fluorescence quantum yield ( $\Phi_F = \sim 0.004$ ) and increased significantly in the presence of glycerol ( $\Phi_F = \sim 0.07$ ). Remarkably, **QCy-DT** showed maximum fluorescence quantum yield in the presence of (A-T)<sub>20</sub> ( $\Phi_F = \sim 0.32$ ) and Drew-AT ( $\Phi_F = \sim 0.25$ ) compared to other duplexes used in our study. The quantum yield values of **QCy-DT** in the presence of AT-rich DNA duplex are comparable to commonly employed fluorescence probes.<sup>34</sup>

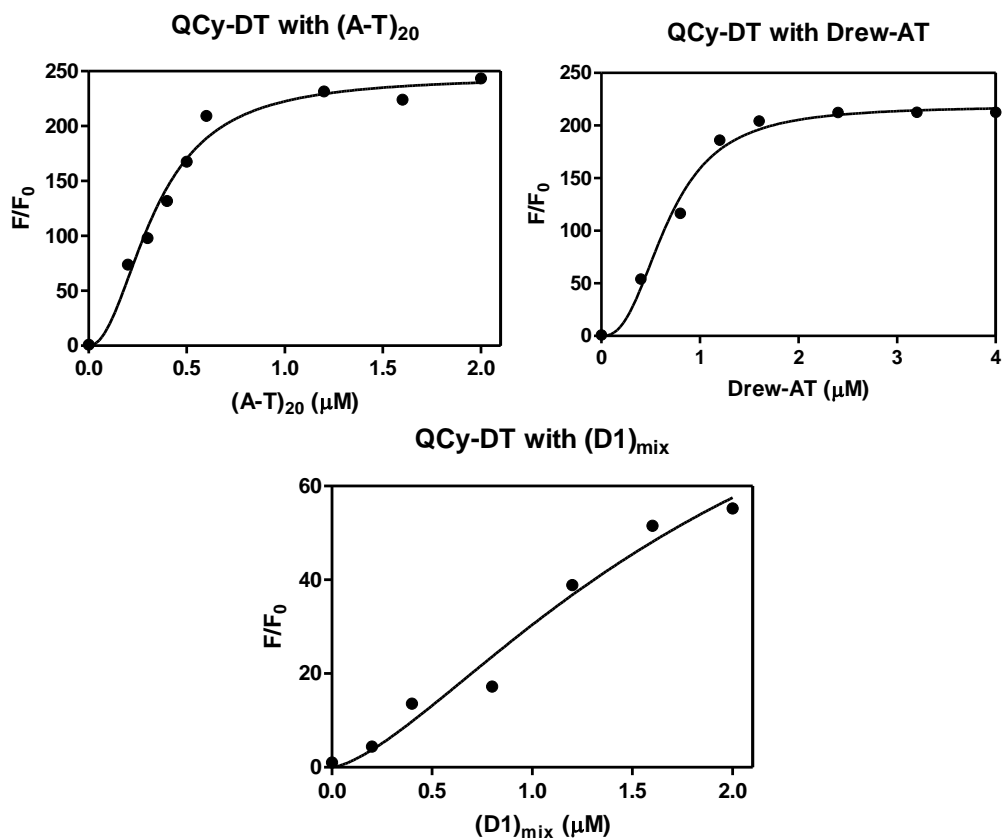


**Figure 13.** Fluorescence titration curves of QCy-DT (2 μM) in presence of DNA duplexes (A-T)<sub>20</sub>, Drew-AT and (D1)<sub>mix</sub> in buffer solution.

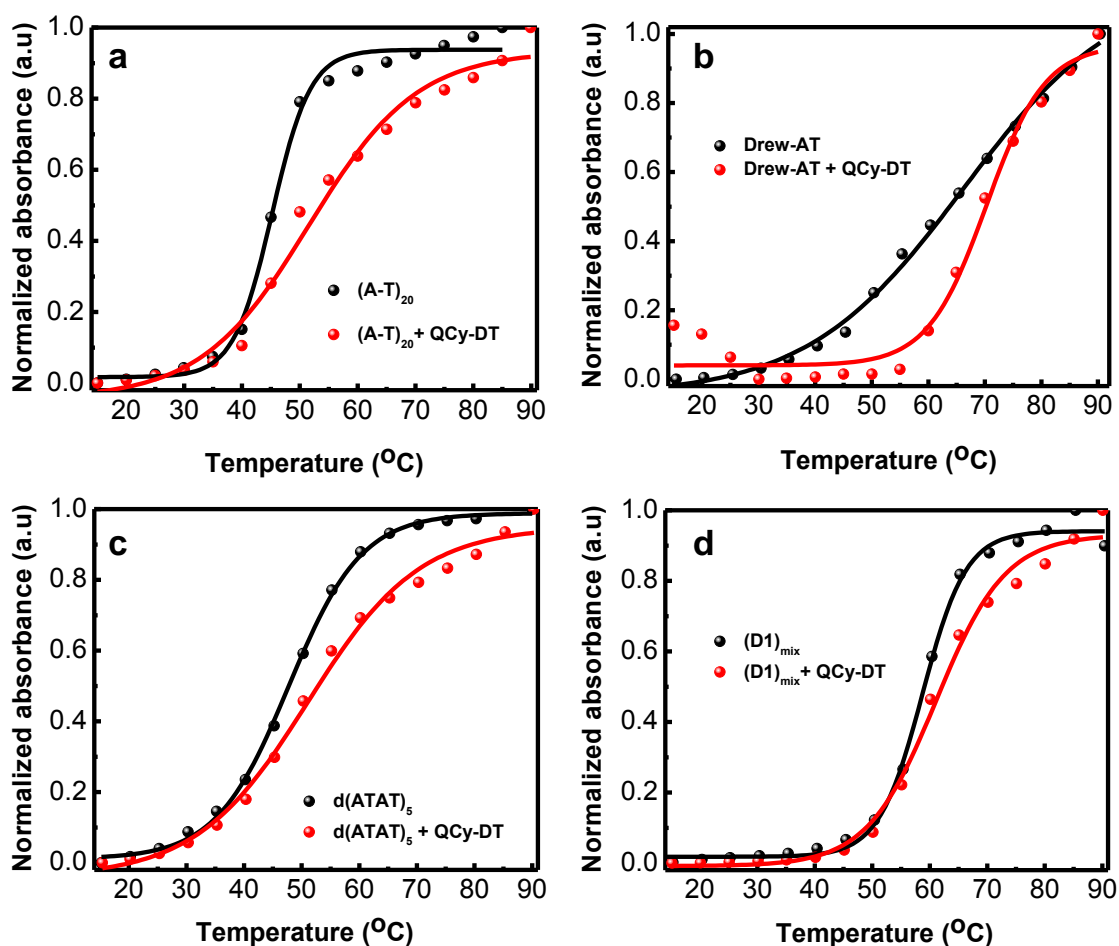
**Table 3.** The fluorescence quantum yields of QCy-DT in the absence and presence of DNA.

QCy-DT	Quantum Yield ( $\Phi_F$ )
Tris-HCl	0.0039
Glycerol	0.07
(A-T) <sub>20</sub>	0.32
Drew-AT	0.25
d(ATAT) <sub>5</sub>	0.08
(D1) <sub>mix</sub>	0.08

$\Phi_F$ : Fluorescence quantum yields were measured using Cresol Violet in ethanol as reference. Experimental conditions: Tris-HCl buffer (100 mM, pH = 7.4). Molar absorption coefficient for QCy-DT: 14,950 M<sup>-1</sup> cm<sup>-1</sup>

**Table 4.** Melting temperatures of dsDNAs in presence of **QCy-DT**.

DNA-Duplex	$\Delta T_m$ (°C)
(A-T) <sub>20</sub>	6.2
Drew AT	4.2
d(ATAT) <sub>5</sub>	3.5
(D1) <sub>mix</sub>	2.5

**Figure 14.** Temperature dependent UV-vis spectra of dsDNA monitored at 260 nm. (a-d) are melting curves of (A-T)<sub>20</sub>, Drew-AT, d(ATAT)<sub>5</sub> and (D1)<sub>mix</sub> duplexes in the absence and presence of **QCy-DT**, respectively.

To understand the effect of **QCy-DT** binding to DNA on the thermal stability of DNA, we performed temperature-dependent UV-melting studies (UV- $T_m$ ) on different [**QCy-DT**: DNA] complexes. The UV- $T_m$  studies of **QCy-DT**-bound (A-T)<sub>20</sub>, Drew-AT, d(ATAT)<sub>5</sub> and (D1)<sub>mix</sub> showed increase in melting temperatures ( $T_m$ ) with  $\Delta T_m = 6.2, 4.2, 3.5$  and  $2.5$  °C, respectively (Table 4 and Figure 14). The  $T_m$  data showed moderate stabilization of DNA duplexes in the presence of **QCy-DT**. Therefore, the binding affinity, fluorescence quantum yield, and UV- $T_m$  data validated the preferential recognition of AT-rich DNA by **QCy-DT** probe compared to GC-rich DNA.

### 3.6 Mode of AT-rich DNA recognition by probe **QCy-DT**

To determine the binding mode of **QCy-DT** to AT-rich (A-T)<sub>20</sub> and Drew-AT DNA duplexes, circular dichroism (CD) studies were carried out under ambient conditions. CD spectrum of (A-T)<sub>20</sub> alone showed a positive and a negative signal at 280 and 248 nm, respectively. Similarly, Drew-AT showed a positive and a negative signal at 280 and 250 nm, respectively. These characteristic positive and negative CD signals confirm the typical B-form DNA duplex structure.<sup>59,60</sup> At this point, two binding modes -intercalation and minor groove binding are expected for **QCy-DT** binding to DNA. From the CD data, we can distinguish between these modes by means of induced CD signal for the guest (probe) to confirm groove binding over intercalation. Keeping this in mind, interactions between **QCy-DT** and DNA could be monitored by induced CD signals in the >300 nm region that gives information about the chiral environment around the probe on DNA. The concentration-dependent CD spectra recorded by the addition of increased concentrations of **QCy-DT** (2-16  $\mu$ M) to fixed concentration of (A-T)<sub>20</sub> (4  $\mu$ M) showed strong induced positive CD signals at 564 and 366 nm and a negative signal at 476 nm in the absorption regions of **QCy-DT** (Figure 15a). Similarly, we observed induced CD signals for **QCy-DT** in the presence of Drew-AT, though with relatively low intensity (Figure 15b). Thus, characteristic induced CD signal in the **QCy-DT** absorption region revealed that the probe bound to the minor groove of AT-rich DNA duplexes.<sup>60</sup>



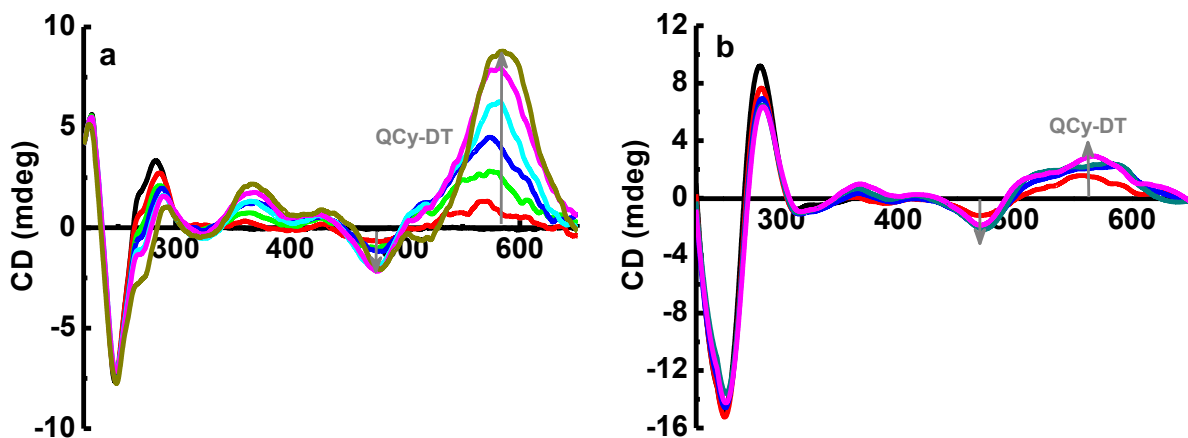


**Figure 15.** CD spectra of **QCy-DT** in the presence of AT-rich DNA duplexes and view of minor groove binding mode of **QCy-DT**. (a) & (b) CD spectra of (A-T)<sub>20</sub> (4 μM) and Drew-AT (4 μM) with increasing concentration of **QCy-DT** from 0 to 16 μM respectively.

Furthermore, we performed *ab initio* theoretical calculations to unravel various features of **QCy-DT**/DNA interaction using density functional theory (DFT) methods. Two possible modes (intercalation and groove binding) were considered for the binding of the bent **QCy-DT** to duplex DNA. The DNA phosphate backbone was neutralized by adding hydrogen to one of the oxygen atoms of the phosphate groups, which does not alter any property of the DNA duplex structure.<sup>61-63</sup> To calculate the binding energies of **QCy-DT** with DNA, we chose AT- and GC-rich duplexes (A/T and G/C) for each of these modes (Table 5). Our computed binding energy values confirm that **QCy-DT** prefers to bind in the minor groove of duplex DNA irrespective of the sequences. An inspection of the binding energy table reveals that the probe binds more strongly to AT-base pair (-105 to -110 kcal/mol) compared to GC-base pair (-85 to -90 kcal/mol) containing duplexes. It is known that minor groove of AT-rich duplexes is narrower than minor groove of GC-rich duplexes.<sup>9</sup> Thus, **QCy-DT** is found to be better accommodating in the minor groove of AT-rich DNA than GC-rich ones, which is apparent from the binding energy values (Figure 16). Generally, the floor of minor groove with AT-base pairs has the highest negative electrostatic potentials while GC-base pairs possess the highest positive potentials. Naturally, the positively charged

**QCy-DT** prefers to bind in the AT-rich minor grooves of DNA compared to minor groove consisting of GC-base pairs.

**Table 5.** Binding mode and binding energies of **QCy-DT** in presence of AT-rich and GC-rich DNA duplexes.

DNA-Duplex	Binding mode	Binding energy (kcal/mol)
5'-AAATTT-3' 3'-TTTAAA-5'	Minor	-105.51
	major	-45.08
	intercalation	-65.38
5'-AAAAAA-3' 3'-TTTTTT-5'	Minor	-108.48
	major	-62.26
	intercalation	-60.29
5'-GCGCGC-3' 3'-CGCGCG-5'	Minor	-85.34
	major	-54.01
	intercalation	-60.50
5'-GGGGGG-3' 3'-CCCCCC-5'	Minor	-91.01
	major	-86.56
	intercalation	-61.39

In our calculations, we considered two possible orientations of **QCy-DT** in the minor groove of AT-base pair-containing DNA, and the cationic quaternary nitrogen centres of the molecule can be located either (i) inside or (ii) outside of the groove. In this respect, binding energy values suggest that the former orientation where the cationic centres are arranged inside the minor groove of DNA are stabilized by -35 kcal/mol more than the latter. These results support the early reported literature that the positively charged surface of the molecule always projects towards the minor groove of DNA.<sup>9</sup> Snapshots of the optimization process of 5'-AAATTT-3'/**QCy-DT** complex are shown in Figure 17. Overall, computational results are well-corroborated with the experimental data that **QCy-DT** prefers to bind in the minor groove, with a preference for AT-base pairs over GC-base pair containing DNA.

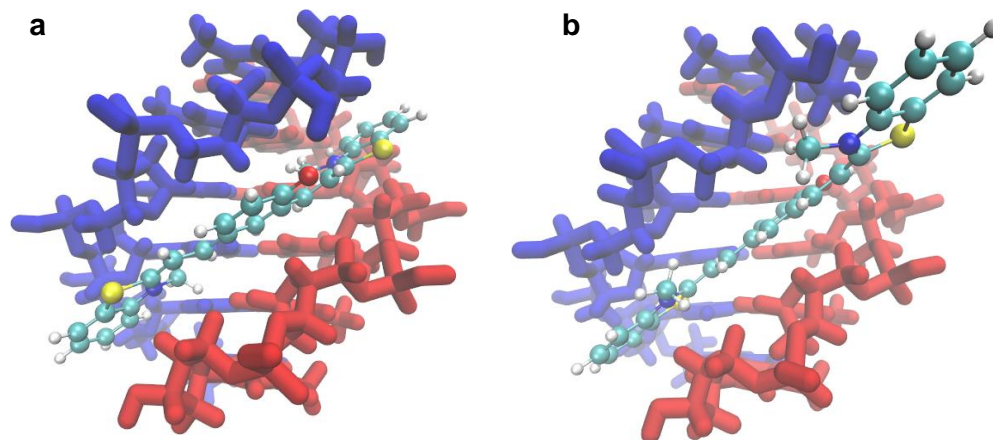


**Figure 16.** Geometry optimized structure of the AT-rich DNA complexed with **QCy-DT** in the minor groove. (a) Molecule with its cationic centers inside the minor groove. (b) Molecule with its cationic centers outside the minor groove.

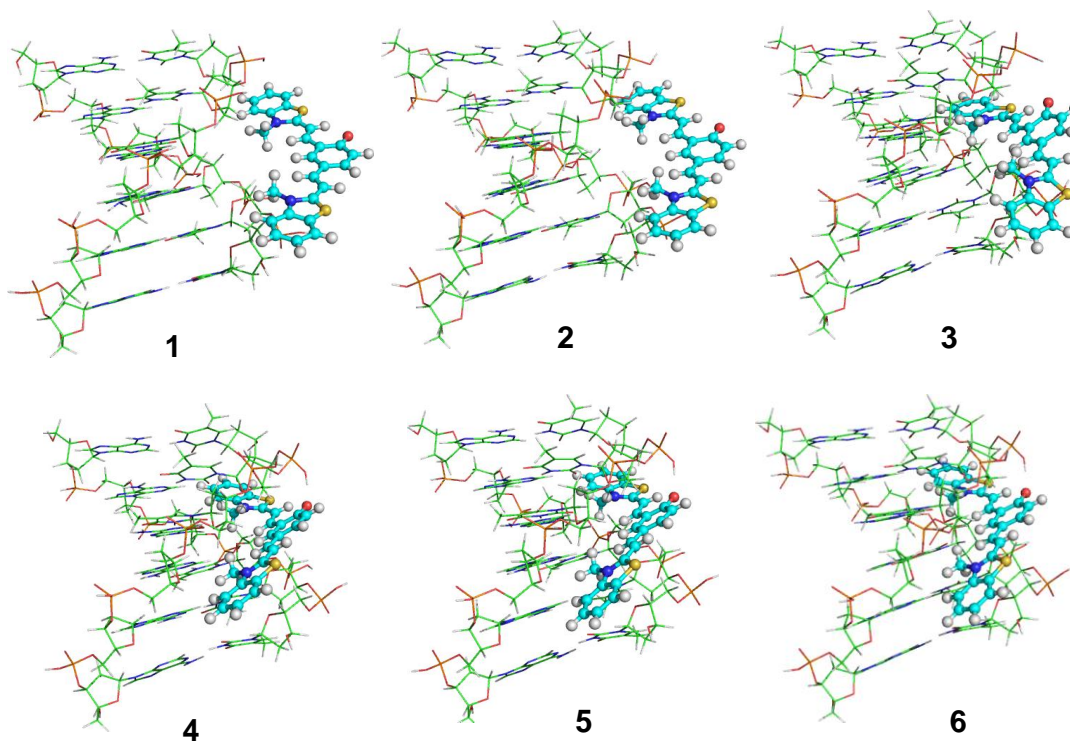


**Figure 17.** Snapshots of optimization process of 5'-AAATTT-3'/**QCy-DT** complex.

### 3.7 Sequence-specific recognition of DNA by probe QCy-DT

Surprisingly, we noticed almost ~4-folds difference in fluorescence enhancement of **QCy-DT** in the presence of (A-T)<sub>20</sub> compared to self-complementary, alternative AT-base pair containing d(ATAT)<sub>5</sub> duplex, although both contain total 20 AT-base pairs (Figure 9). This finding hinted at the highly sequence-specific recognition ability of **QCy-DT** for a specific combination of AT-base pairs in DNA duplex. As per our knowledge, there is no red or NIR fluorescence probe that sequence-specifically recognizes the minor groove of AT-rich DNA. The possible sequence-selectivity among AT-base pairs and the typical length of the bent shaped **QCy-DT** encouraged us to investigate its ability to bind with a specific combination of AT-sequence with a sequence length of four base pairs. For this purpose, we designed four DNA duplexes with variable (A/T)<sub>4</sub> base pairs such as 5'-ATAT-3' (DM1), 5'-ATTA-3' (DM2), 5'-AAAA-3' (DM3) and 5'-AATT-3' (DM4) at the central core (Table 6).<sup>64</sup>

**Table 6.** DNA sequences used in used in this study and DNA-sequence represents the following sequence of 5'-GCGC-B<sub>n</sub>-GCGC-3', where B is nucleobase with n = 4, 6 is AT-rich central core.

Code	Central DNA core (B4)	Code	Central DNA core (B6)
DM1	5'-ATAT-3'	Drew-AT	5'-AAATT7-3'
DM2	5'-ATTA-3'	DM5	5'-TAATTA-3'
DM3	5'-AAAA-3'	DM6	5'-CAATTG-3'
DM4	5'-AATT-3'	DM7	5'-GAATTC-3'

**QCy-DT** showed ~8, ~15, ~40 and ~72-folds fluorescence enhancement in the presence of DM1, DM2, DM3 and DM4 with 5'-ATAT-3', 5'-ATTA-3', 5'-AAAA-3' and 5'-AATT-3' core sequences, respectively, with promising blue shift ( $\Delta\lambda_{\max} = \sim 32$  nm) in fluorescence maxima (Figure 18a). Interestingly, **QCy-DT** showed the highest and lowest fluorescence enhancement in the presence of DM4 (5'-AATT-3') and DM1 (5'-ATAT-3'), respectively. It is well known that most of the minor groove binders like netropsin, distamycin, Hoechst (bisimidazole dyes) and phenyl-furan-benzimidazole diamidine

derivatives have the ability to recognize variable (A/T)<sub>4</sub> base pairs. Here, “minor groove width” is one of the key parameters that dictate the sequence-selective binding ability of small molecules in the presence of variable (A/T)-rich sequences, depending on their base pair roll (degree of departure of the mean plane of base pairs from the perpendicular helix axis on short axis of base pairs).<sup>65,66</sup>

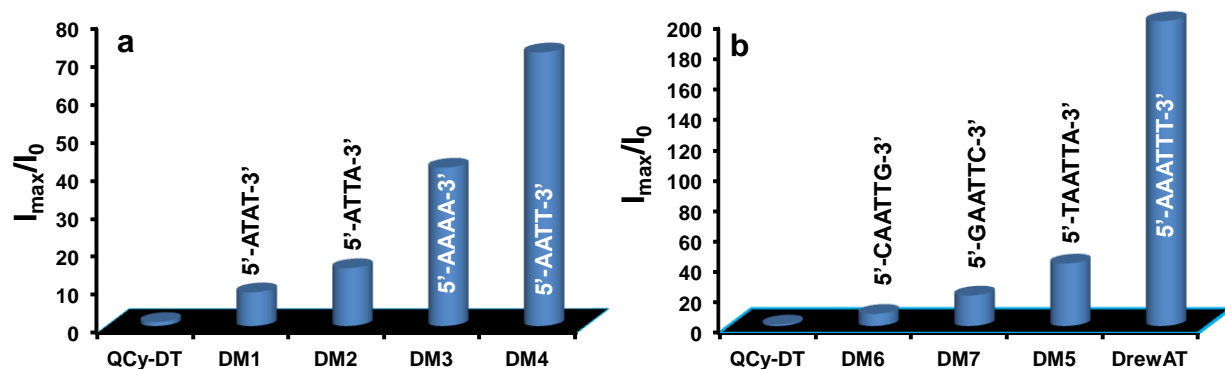


**Figure 18.** Sequence-specific recognition of AT-rich DNA minor groove by QCy-DT. (a) Plot of fluorescence intensity of QCy-DT ratio against the variable (A/T)<sub>4</sub> sequence. (b) Plot of fluorescence intensity ratio of QCy-DT against local variations around 5'-X(AATT)Y-3' sequences.

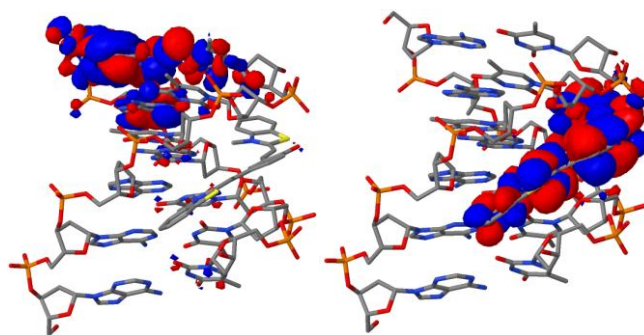


**Figure 19.** Relevant molecular orbitals involved in optical transitions of 5'-AAATTT-3'/QCy-DT complex.

Among all the variable (A/T)<sub>4</sub>-sequences, 5'-AATT-3' and 5'-ATAT-3' are the two sequences that exhibit narrower and wider minor groove width with zero and large base pair

roll, respectively.<sup>67,68</sup> Therefore, we correlate that our probe **QCy-DT** recognizes the narrow minor groove width of 5'-AATT-3' sequence in a DNA duplex, which favors fluorescence enhancement through the restriction of intramolecular rotation of **QCy-DT** compared to the relatively wider groove of 5'-ATAT-3' sequence. These results clearly establish the high sequence sensitivity of the probe **QCy-DT** to the variation of (A/T)<sub>4</sub> base pairs as the width and interactions vary in the minor groove. This study established the sequence-specificity of **QCy-DT** in recognizing AT-rich DNA duplex minor groove containing 5'-AATT-3' sequence.

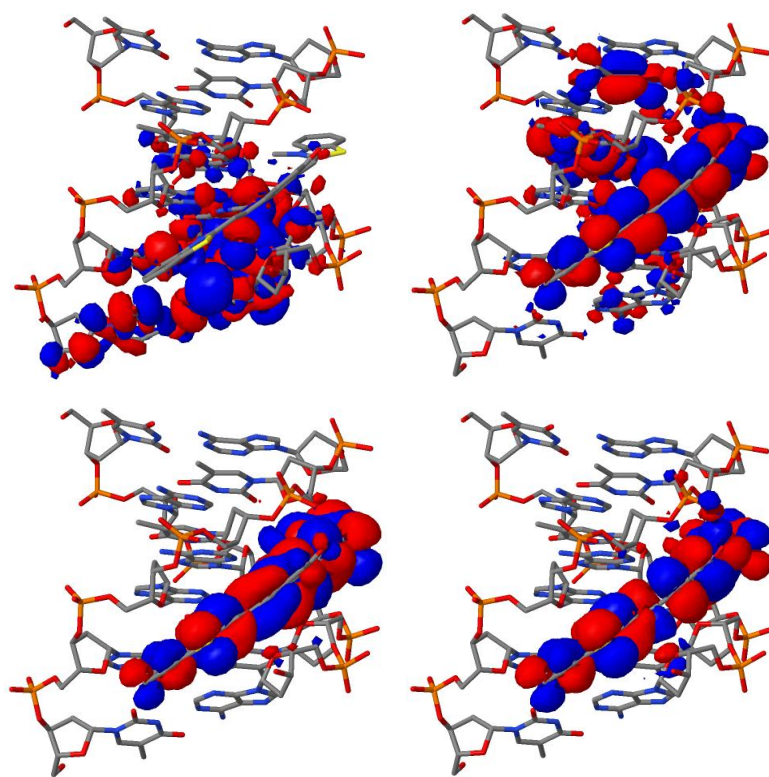


**Figure 20.** Relevant molecular orbitals involved in optical transitions of 5'-TAATTA-3'/**QCy-DT** complex.

To understand finer details of the interactions of **QCy-DT** with local variations around 5'-AATT-3' sequence in the minor groove of DNA duplex, we performed fluorescence studies in the presence of DNA containing core hexanucleotide sequences such as 5'-X(AATT)Y-3' (where X = A/T/G/C and Y is complementary base of X) (Table 6). **QCy-DT**, in

the presence of DNAs containing 5'-GAATTC-3' and 5'-CAATTG-3' cores, showed very weak fluorescence enhancement. Remarkably, enormous fluorescence enhancement was observed in the presence of DNA with 5'-AAATTT-3' core, which was ~4-folds higher than the DNA with 5'-AATT-3' core sequence alone. Surprisingly, replacing A with T at X in 5'-X(AATT)Y-3' sequence reduced the fluorescence enhancement of **QCy-DT**, which was ~1.5-folds lesser than 5'-AATT-3' sequence (Figure 18b).

### 3.8 Fluorescence imaging, cytotoxicity studies and photostability of probe **QCy-DT**

Sequence-specific recognition of AT-rich DNA minor groove by switch-on NIR fluorescence of **QCy-DT** encouraged us to further study its cellular uptake and applications in nuclear DNA staining.

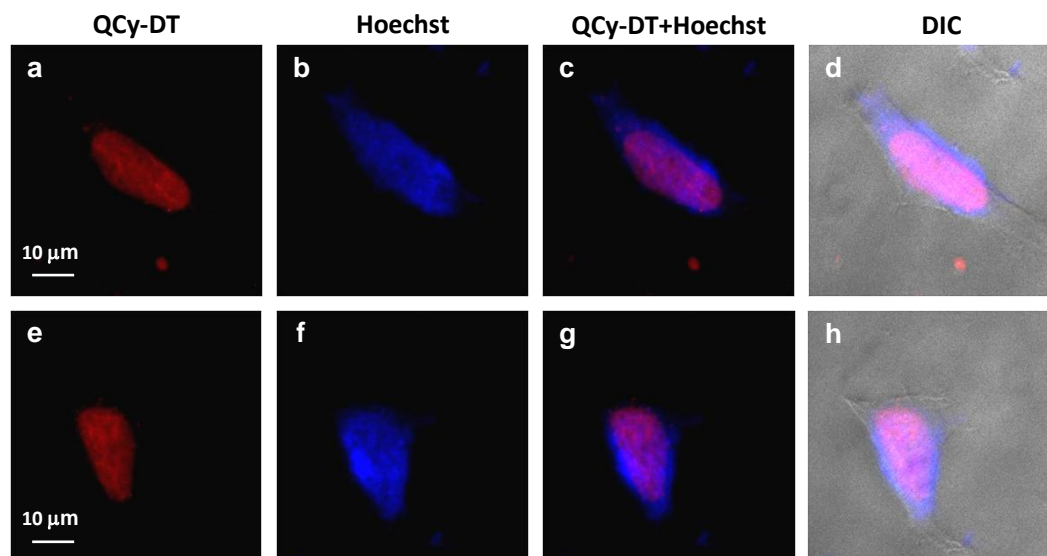


**Figure 21.** Cellular uptake properties of **QCy-DT** in live MCF-7 cells. (a-d) Fluorescence microscope images of live MCF-7 cells incubated with **QCy-DT**. a: **QCy-DT** (0.5  $\mu$ M); b: Hoechst (0.5  $\mu$ M); c: overlay image of a and b; d: differential interference contrast (DIC, bright field image) with overlay of a and b. (e-h) Confocal microscope images of live MCF-7 cells incubated with **QCy-DT**. e: **QCy-DT** (1.0  $\mu$ M); f: Hoechst (1.0  $\mu$ M); g: overlay image of e and f; h: differential interference contrast (DIC, bright field image) with overlay of e and f. Images were collected from 600-800 nm upon excitation at 520 nm.

In order to check its permeability, we carried out cellular uptake studies in live and fixed conditions of MCF-7 and HeLa cells, respectively. First, MCF-7 cells were incubated with probe **QCy-DT** (0.5, and 1  $\mu\text{M}$ ) without fixing, and live cell imaging was conducted using Carl Zeiss fluorescence microscope. Fluorescence imaging of MCF-7 cells with **QCy-DT** showed selective targeting of the cell nucleus by the probe, suggesting that **QCy-DT** is cell membrane-permeable and highly selective towards the nucleus (Figure 21). Next, we fixed HeLa cells and incubated with **QCy-DT** (0.5 and 1  $\mu\text{M}$ ) along with Hoechst as the control nuclear staining dye. Fluorescence images showed selective targeting of the cell nucleus, and remarkable co-localization with Hoechst dye (Figure 22). Further, cells showed the pattern of black nucleoli, which is a characteristic feature of specific DNA minor groove binders over single-strand DNA and RNAs.<sup>69</sup>

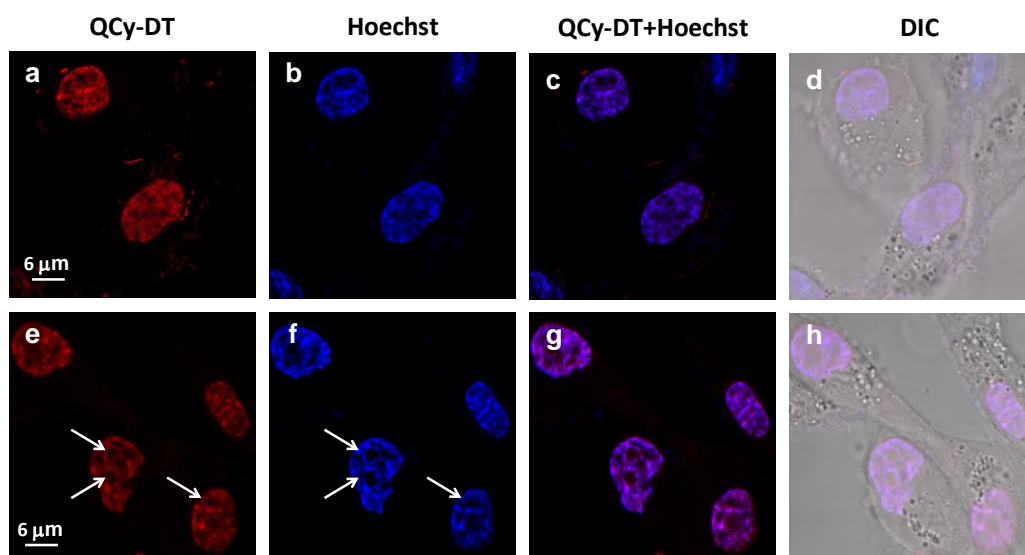


**Figure 22.** Cellular uptake properties of **QCy-DT** in fixed HeLa cells. (a-d) Fluorescence microscope images of fixed HeLa cells incubated with **QCy-DT**. a: **QCy-DT** (0.5  $\mu\text{M}$ ); b: Hoechst (0.5  $\mu\text{M}$ ); c: overlay image of a and b; d: differential interference contrast (DIC, bright field image) with overlay of a and b. (e-h) Confocal microscope images of fixed HeLa cells incubated with **QCy-DT**. e: **QCy-DT** (1  $\mu\text{M}$ ); f: Hoechst (1  $\mu\text{M}$ ); g: overlay image of e and f; h: differential interference contrast (DIC, bright field image) with overlay of e and f. Arrows indicates the black nucleoli, which is characteristic feature of specific DNA minor groove binders. Images were collected from 600-720 nm upon excitation at 520 nm.



Therefore, staining results obtained with live and fixed cells confirmed high cell permeability, efficiency (low staining concentration of 1  $\mu\text{M}$ ), and preferential targeting of cell nuclear DNA. Cytotoxicity is a major constraint with several DNA binding probes. To investigate the cytotoxicity of **QCy-DT**, we performed cell viability assay (MTT assay) in MCF-7 cells after incubation of 72 h. It was observed that **QCy-DT** was non-toxic to MCF-7 cells for up to 8  $\mu\text{M}$  of **QCy-DT**, as  $> 76\%$  viability was observed over a treatment period of more than 72 h (Figure 23a). Another important criterion for a fluorescent molecule to be used as a probe for cell imaging applications is its stability upon excitation.<sup>70</sup> To evaluate whether the cells could sustain the excitation of an argon ion laser and still provide a fluorescent signal bright enough for cell imaging, photostability assay was performed for **QCy-DT** in MCF-7 cells. After continuous 120-second argon ion laser excitation at 568 nm, **QCy-DT** exhibited a remainder fluorescence intensity of  $\sim 80\%$ . Also,  $\sim 50\%$  fluorescent signal intensity could be detected even after 300 sec excitation (Figure 23b). Overall, cell staining and viability assays confirmed the non-toxicity, cell permeability, photostability and selective nuclear targeting ability of **QCy-DT**.

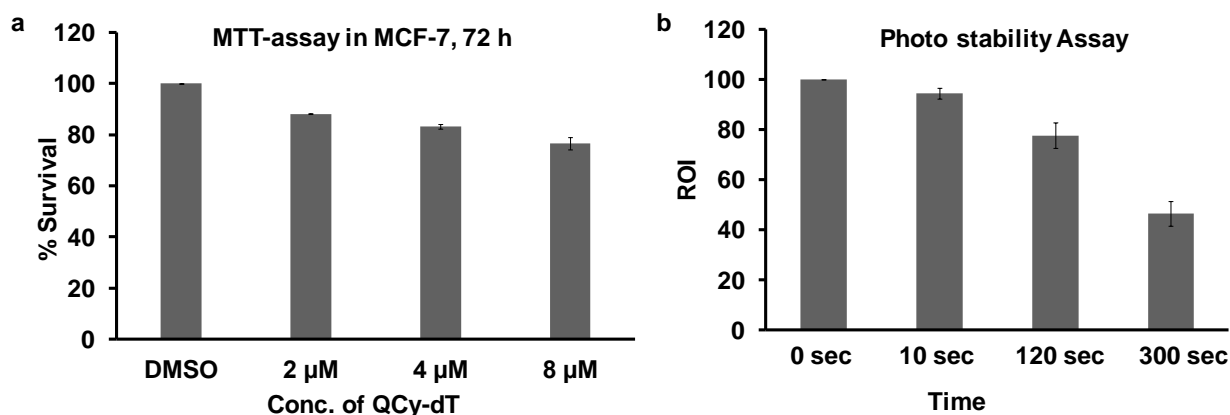


**Figure 23.** Cell viability and photostability of MCF-7 cells in presence of **QCy-DT**. (a) Cell viability of MCF-7 cells in presence of **QCy-DT** in dose dependent manner by taking 2  $\mu\text{M}$ , 4  $\mu\text{M}$  and 8  $\mu\text{M}$  of probe **QCy-DT**. Mean $\pm$ SEM. (b) Photostability of **QCy-DT** (2  $\mu\text{M}$ ) in MCF-7 cells by continuous scanning using OLYMPUS FV1000 confocal microscope, under 568 nm line of an argon ion laser for different time durations; 10 sec, 120 sec and 300 sec respectively. Representative images are shown with graph for mean intensity at different time points with standard error.

### 3.9 Selective staining of *Plasmodium falciparum* nucleus and toxicity to malaria parasites by minor groove binding probe QCy-DT

We selected *Plasmodium falciparum* as a model system to confirm the selectivity of probe QCy-DT towards AT-rich dsDNA in a cellular environment as the malarial parasite possesses a genome exceptionally rich in A-T base pairs (~80%). The parasites were incubated with 0.5  $\mu\text{M}$  concentration of probe QCy-DT at early trophozoite stage. Live fluorescence imaging of these parasites showed that probe QCy-DT could specifically stain the parasite nuclei within the red blood cells (Figure 24). These results clearly indicate that probe QCy-DT binds to the AT-rich genome of the parasite at low concentrations. Also, uptake by malaria parasites and specific enrichment of the probe QCy-DT within the nucleus of the parasites indicate the possibility of the molecule's potential to interfere with the DNA metabolism of *P. falciparum*.

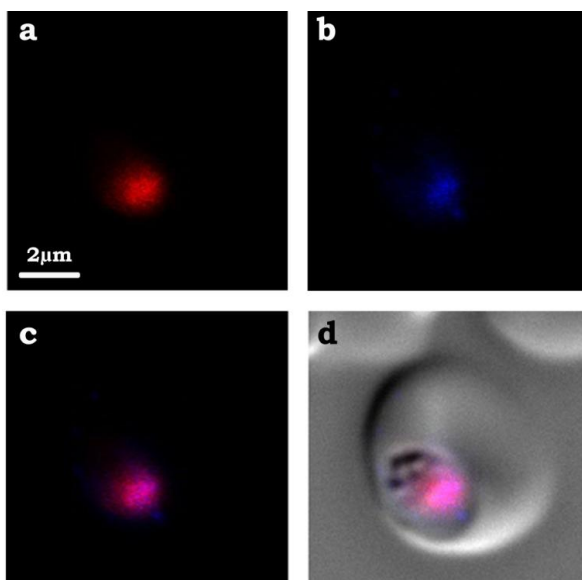


**Figure 24.** Uptake of QCy-DT in live *Plasmodium falciparum* parasites. (a-d) Fluorescence microscope images of blood stages of *Plasmodium falciparum* incubated with QCy-DT. a: QCy-DT (0.5  $\mu\text{M}$ ); b: DAPI; c: Overlay of images of a and b; d: differential interference contrast (DIC, bright field image) with overlay of a and b. Fluorescence images were collected from 600-720 nm upon excitation at 520 nm.

Minor groove binding ligands like distamycin A, netropsin, 4'-6-diamidino-2-phenylindole (DAPI) and bis-benzimide (Hoechst 33258) have been known to inhibit the growth and propagation of *Plasmodium falciparum* in culture.<sup>71</sup> Therefore, we were interested in assessing the inhibitory action of **QCy-DT** in malarial parasites. To assess this,  $IC_{50}$  of the probe **QCy-DT** was determined by treating early trophozoite stage *P. falciparum* (when DNA replication initiates) and the parasites were followed for the next cycle when new rings are formed.  $IC_{50}$  for **QCy-DT** against *P. falciparum* parasites was found to be  $< 4 \mu\text{M}$  (Figure 25), similar to netropsin. It was observed that parasites were arrested in the trophozoite stage and could not form rings in the following cycle at a higher concentration of  $8 \mu\text{M}$  (data not shown). The arrest of the cells during trophozoite stage suggests that the uptake of **QCy-DT** in the parasite nucleus may abrogate the process of DNA replication.

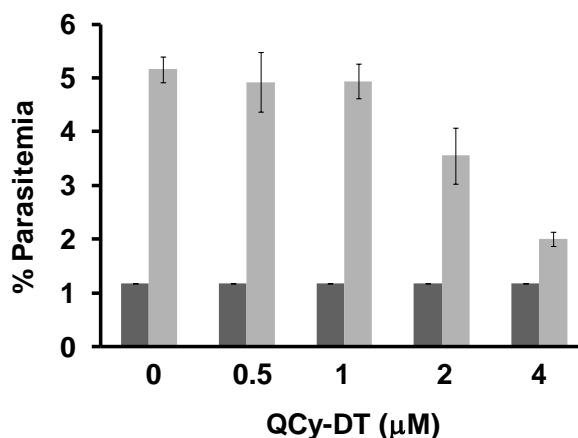


**Figure 25.**  $IC_{50}$  determination of **QCy-DT** in malaria parasites. A concentration range of 0, 0.5, 1, 2 and  $4 \mu\text{M}$  of **QCy-DT** was used. The graphs were plotted for the percentage of parasitemia against **QCy-DT** concentration, with mean and standard error.

### 3.10 Conclusion

In conclusion, we demonstrated the unique sequence-specific and minor groove recognition properties of a newly designed NIR fluorescence probe **QCy-DT** for AT-rich DNA. Probe **QCy-DT** belongs to a new class of D2A (one-donor-two-acceptor) fluorophore (**QCy7**) with a distinctive ICT process responsible for the NIR fluorescence. The inherent non-fluorescent behavior of **QCy-DT** in unbound-state and switch-on fluorescence in the bound-state makes

it a versatile DNA probe. Fluorescence studies of **QCy-DT** demonstrated its selective fluorescence enhancement in the presence of AT-rich duplexes over GC-rich DNA and single-stranded DNA. CD studies confirmed the selective minor groove recognition of AT-rich DNA, which induces the characteristic CD signal to **QCy-DT**. Computational studies further supported the minor groove recognition of AT-rich DNA in which the positively charged edge of **QCy-DT** was located inside the minor groove of DNA. Fluorescence studies of variable (A/T)<sub>4</sub> base pairs containing DNA duplexes revealed sequence-specific fluorescence enhancement in the presence of 5'-AATT-3'. Furthermore, investigations on the local variations around 5'-X(AATT)Y-3' confirmed that  $X = A$  and  $Y = T$  (i.e., 5'-AAATTT-3') is the most preferred sequence for depicting maximum fluorescence enhancement of **QCy-DT**. To the best of our knowledge, **QCy-DT** is the first switch-on NIR fluorescence probe to recognize minor groove of AT-rich DNA in a sequence-specific manner (Figure 26). Confocal fluorescence imaging and cell viability studies of MCF-7 and HeLa cells showed effective cell permeability, non-toxicity and selective staining of nuclear DNA both in live and fixed cell lines. Selective nuclear staining of *P. falciparum* and inhibition of its growth and propagation by **QCy-DT**, possibly through targeting cellular DNA, indicates **QCy-DT** as a potential therapeutic agent against particular parasitic infections similar to other minor groove binders.

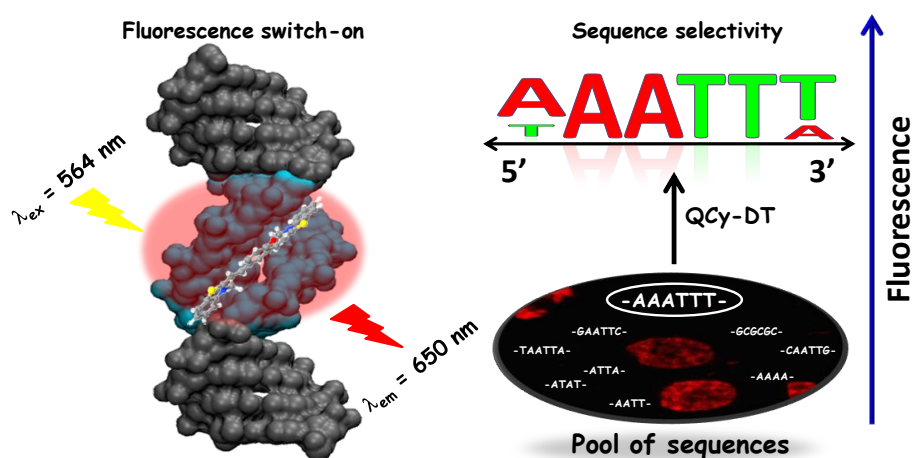


**Figure 26.** ‘NIR-ready’ fluorescence probe **QCy-DT** in presence of AT-rich DNA-duplex in sequence selectivity.

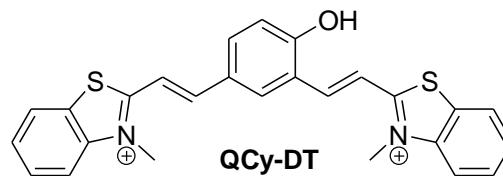
Remarkably, the IC<sub>50</sub> value for *Plasmodium* parasites (< 4 μM) is considerably low when a majority of the mammalian cells (~75%) are still viable at a concentration of 8 μM. We envision that ease of synthesis, switch-on NIR fluorescence, large Stokes shift, cell permeability, non-toxicity and cell imaging of both live and fixed cells makes our new probe **QCy-DT** practically viable, inexpensive and a superior DNA probe compared to commercially available dyes routinely used. The chemical diversity of our probe also offers means to design new enzymatic or chemically-triggered self-immolative theranostic prodrugs for abnormal cells.

### 3.11 Experimental Section

**General information.** All the chemicals, reagents, single-stranded oligos (dA<sub>20</sub>, dT<sub>20</sub>, dG<sub>20</sub>, dC<sub>20</sub>), self-complementary oligos {d(ATAT)<sub>5</sub>, (D1)<sub>mix</sub>, Drew-AT, Calf-Thymus DNA (CT-DNA), (DM1, DM2, DM3, DM4, DM5, DM6 and DM7)}, Hoechst 33258 and Cresol Violet were purchased from Sigma-Aldrich. <sup>1</sup>H and <sup>13</sup>C NMR spectra were recorded on a Bruker AV-400 MHz spectrometer with chemical shifts reported as parts per million (*ppm*) (in DMSO-*d*<sub>6</sub>, tetramethylsilane as an internal standard) at 20 °C. UV-vis absorption and emission spectra were measured in quartz cuvettes of 1 cm path length. High resolution mass spectra (HRMS) were obtained on Agilent Technologies 6538 UHD Accurate-Mass Q-TOF LC/MS spectrometer.

**Synthetic procedure for probe QCy-DT.** To a stirred solution of 2-methyl benzothiazole (7.0 mmol) in dichloromethane (10 mL), methyl iodide (14.0 mmol) was added dropwise and allowed to reflux overnight. Completion of the reaction was monitored by thin layer chromatography (TLC). After completion of the reaction, a white colored precipitate was formed. The precipitate was filtered and washed with copious amount of diethyl ether for removing the unreacted benzothiazole. The obtained product (N-methyl-2-methylbenzothiazole) was dried under vacuum and used for the next reaction without further purification.

Piperidine (8  $\mu\text{L}$ ) was added to a stirred solution of N-methyl-2-methylbenzothiazole (0.1 g, 0.34 mmol) in ethanol (8 mL). After 10 min, 4-hydroxyisophthalaldehyde (**2**) (20 mg, 0.14 mmol)



in ethanol (2 mL) was added and the reaction mixture was stirred at 80  $^{\circ}\text{C}$  for 3 h under nitrogen atmosphere. After completion of reaction, solvent was evaporated and the crude product was purified by preparative RP-HPLC (grad. 50–65% acetonitrile in water, 12 min) to obtain the probe **QCy-DT** as a yellow powder. Yield 45%. IR (neat): 3390, 3065, 3015, 1682, 1667, 1582, 1505, 1121  $\text{cm}^{-1}$ ;  $^1\text{H}$  NMR (400 MHz,  $\text{DMSO-}d_6$ )  $\delta_{\text{ppm}}$  8.59 (d,  $J = 2$  Hz, 1H), 8.42 (d,  $J = 8.1$  Hz, 2H), 8.30 (d,  $J = 8.2$  Hz, 1H), 8.26 (d,  $J = 3.3$  Hz, 1H), 8.23 (d,  $J = 10.7$  Hz, 1H), 8.19 (dd,  $J = 2$  Hz,  $J = 8.7$  Hz, 1H), 8.13 (dd,  $J = 8.1$  Hz,  $J = 16$  Hz, 2H), 7.98–7.89 (m, 3H), 7.86 (dd,  $J = 1.1$  Hz,  $J = 9.5$  Hz, 1H), 7.83–7.78 (m, 2H), 7.22 (d,  $J = 8.7$  Hz, 1H), 4.36 (s, 6H).  $^{13}\text{C}$  NMR (100 MHz,  $\text{DMSO-}d_6$ )  $\delta_{\text{ppm}}$  172.1, 171.8, 161.8, 147.7, 142.2, 142.1, 142.0, 134.8, 132.6, 129.5, 128.5, 127.8, 127.6, 125.9, 124.1, 121.5, 117.7, 116.9, 116.8, 114.3, 111.8, 36.3, 36.2. HRMS (ESI-MS): found 441.1070, calcd  $m/z = 441.1095$  for  $\text{C}_{26}\text{H}_{22}\text{N}_2\text{OS}_2$   $[\text{M}-2\text{H}]^{1+}$ .

**Sample preparation for UV-vis and fluorescence measurements.** Stock solutions of **QCy-DT** were prepared in double-distilled (dd) water in the order of  $10^{-3}$  M and stored at  $-10$   $^{\circ}\text{C}$ . DNA stock solutions were prepared by dissolving oligo samples in double-distilled (dd) water in the order of  $10^{-4}$  M. Solutions of DNA duplexes were prepared in Tris-HCl (100 mM, pH = 7.4) buffer solution by mixing complementary DNA strands in equimolar concentration; this solution was then subjected to annealing by heating up to 85  $^{\circ}\text{C}$  for 15 min., subsequently cooled to room temperature for 7 h and stored in the refrigerator (4  $^{\circ}\text{C}$ ) for 4 h.<sup>34</sup>

**Absorption and emission spectra.** The UV-vis absorption and emission spectra were recorded on Agilent Technologies Cary series UV-vis-NIR absorbance and Cary eclipse fluorescence spectrophotometers, respectively. Thermal denaturation (UV-melting) studies were carried out on Cary 5000 UV-vis-NIR spectrophotometer equipped with Cary

temperature controller in the range of 10 °C to 90 °C with a ramp rate of 1 °C/min. The variable temperature/wavelength mode was used. Absorption was monitored at 260 nm with regular 5 °C intervals. Melting temperatures ( $T_m$ ) of DNA samples were calculated from the first derivatives of the absorption vs. temperature curves (thermal denaturation or melting curves) obtained by monitoring at 260 nm.

**Circular dichroism (CD) spectroscopy.** CD measurements were carried out on Jasco J-815 spectrometer equipped with a Peltier-type temperature controller (CDF-4265/15) under a nitrogen atmosphere to avoid water condensation. Scans were performed over the range of 200-700 nm with a speed of 100 nm/min, and the spectra represent an average of three scans. A blank sample containing Tris-HCl buffer solution (100 mM, pH = 7.4) was treated in the same manner and subtracted from the collected data.

**Non-linear curve analysis for the binding constant measurements.** DNA duplex was titrated to a fixed concentration of **QCy-DT** (2  $\mu$ M). Then, we plotted the fluorescence intensity  $F/F_0$  as a function of DNA duplex concentration. Where  $F$  = Fluorescence intensity of **QCy-DT**:DNA complex at 650 nm and  $F_0$  is initial fluorescence intensity of free **QCy-DT** probe. The binding constant values of [**QCy-DT** + DNA] complexes were obtained by non-linear (single-binding mode) curve fitting analysis using Graph Pad Prism 5.0 (GraphPad Software, Inc., La Jolla, CA, USA).

**Quantum yield calculation.** Cresyl violet perchlorate in ethanol ( $\phi = 0.54$ ) was used as the standard for the fluorescence quantum yield calculation using the absorption of the test sample. The emission spectral area is obtained in the 550-800 nm regions. Dilute solutions ( $10^{-6}$  M) were used to minimize reabsorption effects of the dyes. Quantum yields were determined using the following equation,

$$\phi_s = \phi_r (F_s/F_r) \times (A_r/A_s) \times (n_s^2/n_r^2)$$

Where,  $\phi_r$  and  $\phi_s$  are the quantum yield of reference and sample respectively,  $F_r$  and  $F_s$  are the integrated intensities (areas) of standard and sample spectra,  $n_r$  and  $n_s$  are the refractive

indices of the reference and sample solution,  $A_r$  and  $A_s$  are the absorbance intensities of reference and sample respectively.

**Computational details.** We performed the ground-state and excited-state calculations using density functional theory (DFT) with the PBE0 functional and 6-311++G(d,p) basis set for all atoms to further support our assignments of the absorption and emission bands of the molecule. All excited state calculations were performed using Gaussian 09 suite of programs.<sup>72</sup> Implicit solvent (water) effects have been taken into account by polarizable continuum model (PCM).<sup>73</sup> Vertical excitation energies are predicted using time dependent DFT (TDDFT) as implemented in Gaussian 09 Package. Emission spectra were calculated on optimized lowest excited state geometry ( $S_1$ ) of the molecule using TDDFT methods.

All geometry optimizations (for DNA/**QCy-DT** complexes) were performed using GPW formalism, paired with Perdew-Burke-Ernzerhof (PBE) functional,<sup>74</sup> as implemented in the QUICKSTEP module of CP2K package.<sup>75-77</sup> Since we are interested in the noncovalent interactions between DNA and molecule, Grimme's empirical dispersion corrections were employed.<sup>78</sup> CP2K uses a mixed gaussian and an auxiliary plane wave basis for electronic structure calculation which is a unique feature of the package. Norm-conserving Goedecker-Teter-Hutter (GTH)<sup>79-81</sup> pseudopotentials were used along with the double-zeta valence polarized basis sets to expand the Kohn-sham valence orbitals. We used a 320 Ry mesh cutoff to represent the charge density for the auxiliary basis set of plane waves. A supercell of 35\*40\*35 angstrom size is used for all calculations to ensure no interaction with the periodic images. Broyden-Fletcher-Goldfarb-Shanno (BFGS) minimization algorithm<sup>82-86</sup> was employed for all geometry optimization calculation with the convergence threshold for force optimization set to 0.0001 hartree/bohr. All DFT calculations using SIESTA package<sup>87</sup> were performed using PBE<sup>3</sup> exchange correlational function and double- zeta polarized basis set along with norm-conserving pseudo-potentials<sup>88</sup> for all the atoms. We have used a mesh cut-off of 400 Ry for the grid integration to represent the charge density.

**Fluorescence study in live cells.** MCF-7 cells were propagated on 20 mm cover slips in a 6-well plate in DMEM medium supplemented with 10% fetal bovine serum at 37 °C in a humidified atmosphere containing 5% CO<sub>2</sub> till 80% confluency was achieved. Cells were

---



incubated for 60 min with probe **QCy-DT** (resuspended in Mili-Q water) at various concentrations (0.5  $\mu\text{M}$  and 1  $\mu\text{M}$ ) in a humidified  $\text{CO}_2$  incubator at 37 °C. Milli-Q water was used as a vehicle control. Following the treatment, fluorescence microscopy was performed using Carl Zeiss AXIO Imager Z1 and the software used for image capturing was AxioVision Rel. 4.8.

**Fluorescence study in fixed cells.** HeLa S3 cells were grown on the cover slip for 24 h in DMEM medium supplemented with 10% fetal bovine serum at 37 °C in a humidified atmosphere containing 5%  $\text{CO}_2$  till 80% confluency was achieved. Then cells were fixed with 4% paraformaldehyde in PBS for 2 $\times$ 5 min. After rinsing twice with PBS, HeLa S3 cells were treated separately with probe **QCy-DT** at various concentrations (0.5  $\mu\text{M}$  and 1  $\mu\text{M}$ ) for 10 min at room temperature. Subsequently, cover slips were incubated with Hoechst 33258 at 10  $\mu\text{g}/\text{mL}$  for nuclear staining. Fluorescence images were taken by Carl Zeiss Laser Scanning Microscope (LSM510 META).

***Plasmodium falciparum* culture, synchronization and treatment of malaria parasites with probe QCy-DT.** *P. falciparum* strain 3D7 was cultured as described previously.<sup>89</sup> Briefly, malaria parasites were cultured in human erythrocytes in T75 flasks with RPMI 1640 (Gibco) supplemented with 10  $\mu\text{g}/\text{mL}$  gentamicin (Sigma), 50  $\mu\text{g}/\text{mL}$  ampicillin, 0.2%  $\text{NaHCO}_3$  (Sigma), 0.5% albumax (Invitrogen) and Hypoxanthine (27 mg/L). The culture was maintained under standard conditions (37 °C in 90% nitrogen, 5%  $\text{CO}_2$ , and 5%  $\text{O}_2$ ). For synchronization of the parasites, ring-staged parasites were treated with 5% sorbitol at 37 °C for 5-10 min, followed by washing with pre-warmed incomplete medium twice, and placed back in complete medium. **QCy-DT** probe (resuspended in Mili-Q water) was added to parasites (25 $\pm$ 2 hpi) at a final concentration of 0.5  $\mu\text{M}$  and the parasites were incubated for 30 min at 37 °C. Following treatment fluorescence imaging of the parasites was performed using Carl Zeiss AXIO Imager Z1 and the software used for image capturing was AxioVision Rel. 4.8.

**IC<sub>50</sub> determination in malaria parasites.** To determine the IC<sub>50</sub> value of **QCy-DT** against *P. falciparum*, parasites were synchronized in ring stages and parasitaemia was

maintained at 1-2%, followed by treatment with 0, 0.5, 1, 2 and 4  $\mu\text{M}$  range of **QCy-DT**. After 40 h of the **QCy-DT** treatment, Geimsa stained slides were prepared, and parasitaemia was counted. At least six homogenous microscopic fields were counted for each treatment, and each experiment was done in triplicates. The graphs were plotted for the percentage of parasitemia against **QCy-DT** concentration, with mean and standard error.

**Cell viability assay.** MCF-7 cells ( $4 \times 10^3$  cells/well) were seeded in 96-well plate (flat bottom) and cultured for 12 h. Following this, cells were treated with 2, 4 and 8  $\mu\text{M}$  of probe **QCy-DT** respectively for 72 h and further incubated in a humidified  $\text{CO}_2$  incubator at 37 °C. 20  $\mu\text{L}$  of MTT (5 mg/mL in PBS) solution was added to each well and incubated for 4 h at 37 °C in the  $\text{CO}_2$  incubator. DMSO (200  $\mu\text{L}$ ) was then added to each well. After 1 h, absorbance was taken in ELISA microplate reader at 570 nm wavelength. Following formula was applied for the calculation of percentage of cell viability (CV):

$$\text{CV} = (\text{absorbance of the experimental samples} / \text{absorbance of the control sample}) \times 100$$

The data was normalized with control and plotted with mean and standard error.

**Photostability assay in MCF-7 by confocal fluorescence microscopy imaging.** MCF-7 Cells were propagated on 20mm coverslips in a 6-well plate in DMEM medium supplemented with 10% fetal bovine serum at 37 °C in a humidified atmosphere containing 5%  $\text{CO}_2$  till 80% confluency was achieved. Cells were incubated for duration of 60 min with probe **QCy-DT** (resuspended in Milli-Q water) at 2  $\mu\text{M}$  concentration in a humidified  $\text{CO}_2$  incubator at 37 °C for. Following treatment, the photostability of **QCy-DT** was measured by continuous scanning using OLYMPUS FV1000 confocal fluorescence microscope, under 568 nm line of an Argon ion laser for different time durations 10 sec, 120 sec and 300 sec. Olympus Fluoview software was used to quantitatively investigate the intensity of signals of **QCy-DT** at zero time points and after photo bleaching. The data was plotted with mean and standard error.

### 3.12 References

1. Rohs, R.; Jin, X.; West, S. M.; Joshi, R.; Honig, B.; Mann, R. S. Origins of specificity in protein-DNA recognition. *Annu. Rev. Biochem.* **2010**, *79*, 233–269.
2. Rohs, R.; West, S. M.; Sosinsky, A.; Liu, P.; Mann, R. S.; Honig, B. The role of DNA shape in protein-DNA recognition. *Nature* **2009**, *461*, 1248–1253.
3. Waring, M. J. DNA modification and cancer. *Annu. Rev. Biochem.* **1981**, *50*, 159–192.
4. Balasubramanian, S.; Hurley, L. H.; Neidle, S. Targeting G-quadruplexes in gene promoters: a novel anticancer strategy?. *Nat. Rev. Drug Discov.* **2011**, *10*, 261–275.
5. Wilson, W. D.; Tanius, F. A.; Mathis, A.; Tevis, D.; Hall, J. E.; Boykin, D. W. Antiparasitic compounds that target DNA. *Biochimie* **2008**, *90*, 999–1014.
6. Lerman, L. S. Structural considerations in the interaction of DNA and acridines. *J. Mol. Biol.* **1961**, *3*, 18–30.
7. Waring, M. J. Drugs which affect the structure and function of DNA. *Nature* **1968**, *219*, 1320–1325.
8. White, S.; Szewczyk, J. W.; Turner, J. M.; Baird, E. E.; Dervan, P. B. Recognition of the four Watson-Crick base pairs in the DNA minor groove by synthetic ligands. *Nature* **1998**, *391*, 468–471.
9. Neidle, S. DNA minor-groove recognition by small molecules. *Nat. Prod. Rep.* **2001**, *18*, 291–309.
10. Dervan, P. B. Molecular recognition of DNA by small molecules. *Bioorg. Med. Chem.* **2001**, *9*, 2215–2235.
11. Moore, M. H.; Hunter, W. N.; Destaintot, B. L.; Kennard, O. DNA-drug interactions. The crystal structure of d(CGATCG) complexed with daunomycin. *J. Mol. Biol.* **1989**, *206*, 693–705.
12. Dervan, P. B. Design of sequence-specific DNA-binding molecules. *Science* **1986**, *232*, 464–471.
13. Wemmer, D. E.; Dervan, P. B. Targeting the minor groove of DNA. *Curr. Opin. Struct. Biol.* **1997**, *7*, 355–361.
14. Wemmer, D. E. Ligands recognizing the minor groove of DNA: development and applications. *Biopolymers* **2001**, *52*, 197–211.
15. Belitsky, J. M.; Leslie, S. J.; Arora, P. S.; Beerman, T. A.; Dervan, P. B. Cellular uptake of N-methylpyrrole/N-methylimidazole polyamide-dye conjugates. *Bioorg. Med. Chem.* **2002**, *10*, 3313–3318.

16. Best, T. P.; Edelson, B. S.; Nickols, N. G.; Dervan, P. B. Nuclear localization of pyrrole-imidazole polyamide-fluorescein conjugates in cell culture. *Proc. Natl. Acad. Sci. U.S.A.* **2003**, *100*, 12063–12068.
17. Edelson, B.; Best, T.; Olenyuk, B.; Nickols, N.; Doss, R.; Foister, S.; Heckel, A.; Dervan, P. B. Influence of structural variation on nuclear localization of DNA-binding polyamide-fluorophore conjugates. *Nucleic Acids Res.*, **2004**, *32*, 2802-2818.
18. Tanious, F. A.; Hamelberg, D.; Bailly, C.; Czarny, A.; Boykin, D. W.; Wilson, W. D. DNA sequence dependent monomer-dimer binding modulation of asymmetric benzimidazole derivatives. *J. Am. Chem. Soc.* **2004**, *126*, 143–153.
19. Athri, P.; Wilson, W. D. Molecular dynamics of water-mediated interactions of a linear benzimidazole-biphenyl diamidine with the DNA minor groove. *J. Am. Chem. Soc.* **2009**, *131*, 7618–7625.
20. Liu, Y.; Kumar, A.; Depauw, S.; Nhili, R.; David-Cordonnier, M.-H.; Lee, M. P.; Ismail, M. A.; Farahat, A. A.; Say, M.; Chackal-Catoen, S.; Batista-Parra, A.; Neidle, S.; Boykin, D. W.; Wilson, W. D. Water-mediated binding of agents that target the DNA minor groove. *J. Am. Chem. Soc.* **2011**, *133*, 10171–10183.
21. Liu, Y.; Chai, Y.; Kumar, A.; Tidwell, R. R.; Boykin, D. W.; Wilson, W. D. Designed compounds for recognition of 10 base pairs of DNA with two at binding sites. *J. Am. Chem. Soc.* **2012**, *134*, 5290-5299.
22. Wilson, W. D.; Nguyen, B.; Tanious, F. A.; Mathis, A.; Hall, J. E.; Stephens, C. E.; Boykin, D. W. Dications that target the DNA minor groove: compound design and preparation, DNA interactions, cellular distribution and biological activity. *Curr. Med. Chem. Anticancer Agents.* **2005**, *5*, 389–408.
23. Mathis, A. M.; Bridges, A. S.; Ismail, M. A.; Kumar, A.; Francesconi, I.; Anbazhagan, M.; Hu, Q.; Tanious, F. A.; Wenzler, T.; Saulter, J.; Wilson, W. D.; Brun, R.; Boukin, D. W.; Tidwell, R. R.; Hall, J. E. Diphenyl furans and aza analogs: effects of structural modification on in vitro activity, DNA binding, and accumulation and distribution in trypanosomes. *Antimicrob. Agents Chemother.* **2007**, *51*, 2801–2810.
24. Tang, C.; Paul, A.; Alam, M. P.; Roy, B.; Wilson, W. D.; Hecht, S. M. A Short DNA Sequence Confers Strong Bleomycin Binding to Hairpin DNAs. *J. Am. Chem. Soc.* **2014**, *136*, 13715–13726.

25. Paine, M. F.; Wang, M. Z.; Generaux, C. N.; Boykin, D. W.; Wilson, W. D.; De Koning, H. P.; Olson, C. A.; Pohlig, G.; Burri, C.; Brun, R.; Murilla, G. A.; Thuita, J. K.; Barrett, M. P.; Tidwell, R. R. Diamidines for human African trypanosomiasis. *Curr. Opin. Investig. Drugs.* **2010**, *11*, 876–883.
26. Soeiro, M. N.; de Castro, S. L.; de Souza, E. M.; Batista, D. G.; Silva, C. F.; Boykin, D. W. Diamidine activity against trypanosomes: the state of the art. *Curr. Mol. Pharmacol.* **2008**, *2*, 151–161.
27. Hunt, R. A.; Munde, M.; Kumar, A.; Ismail, M. A.; Farahat, A. A.; Arafa, R. K.; Say, M.; Batista-Parra, A.; Tevis, D.; Boykin, D. W.; Wilson, W. D. Induced topological changes in DNA complexes: influence of DNA sequences and small molecule structures. *Nucleic Acids Res.* **2011**, *39*, 4265–4274.
28. Haugland, R. P.; Spence, M. T. Z.; Johnson, I. D.; Basey, A. *The Handbook: A Guide to Fluorescent Probes and Labeling Technologies*, 10th ed., Molecular Probes, Eugene, OR, **2005**.
29. Lavis, L. D.; Raines, R. T. Bright ideas for chemical biology. *ACS Chem Biol.* **2008**, *3*, 142–155.
30. Sinkeldam, R. W.; Greco, N. J.; Tor, Y. Fluorescent analogs of biomolecular building blocks: design, properties, and applications. *Chem. Rev.* **2010**, *110*, 2579–619.
31. Wysocki, L. M.; Lavis, L. D. Advances in the chemistry of small molecule fluorescent probes. *Curr. Opin. Chem. Biol.* **2011**, *15*, 752–759.
32. Crissman, H. A.; Hirons, G. T. Staining of DNA in live and fixed cells. *Methods Cell Biol.* **1994**, *41*, 195–209.
33. Gill, M. R.; Garcia-Lara, J.; Foster, S. J.; Smythe, C.; Battaglia, G.; Thomas, J. A. A ruthenium(II) polypyridyl complex for direct imaging of DNA structure in living cells. *Nat. Chem.* **2009**, *1*, 662–667.
34. Narayanaswamy, N.; Kumar, M.; Das, S.; Sharma, R.; Samanta, P. K.; Pati, S. K.; Dhar, S. K.; Kundu, T. K.; Govindaraju, T. A thiazole coumarin (TC) turn-on fluorescence probe for AT-base pair detection and multipurpose applications in different biological systems. *Sci. Rep.* **2014**, *4*, 6476.
35. Pfeifer, G. P.; You, Y.-H.; Besaratinia, A. Mutations induced by ultraviolet light. *Mutat. Res.* **2005**, *571*, 19–31.
36. Pham, W.; Choi, Y.; Weissleder, R.; Tung, C. H. Developing a peptide-based near-infrared molecular probe for protease sensing. *Bioconjugate Chem.* **2004**, *15*, 1403–1407.

37. Blum, G.; von Degenfeld, G.; Merchant, M. J.; Blau, H. M.; Bogoy, M. Noninvasive optical imaging of cysteine protease activity using fluorescently quenched activity-based probes. *Nat. Chem. Biol.* **2007**, *3*, 668–677.
38. Lee, H.; Akers, W.; Bhushan, K.; Bloch, S.; Sudlow, G.; Tang, R.; Achilefu, S. Near-infrared pH-activatable fluorescent probes for imaging primary and metastatic breast tumors. *Bioconjugate Chem.* **2011**, *22*, 777–784.
39. Yuan, L.; Lin, W.; Yang, Y.; Chen, H. A unique class of near-infrared functional fluorescent dyes with carboxylic-acid-modulated fluorescence ON/OFF switching: rational design, synthesis, optical properties, theoretical calculations, and applications for fluorescence imaging in living animals. *J. Am. Chem. Soc.* **2012**, *134*, 1200–1211.
40. Maity, D.; Govindaraju, T. A turn-on NIR fluorescence and colourimetric cyanine probe for monitoring the thiol content in serum and the glutathione reductase assisted glutathione redox process. *Org. Biomol. Chem.* **2013**, *11*, 2098–2104.
41. Maity, D.; Raj, A.; Samanta, P. K.; Karthigeyan, D.; Kundu, T. K.; Pati, S. K.; Govindaraju, T. A probe for ratiometric near-infrared fluorescence and colorimetric hydrogen sulfide detection and imaging in live cells. *RSC Adv.* **2014**, *4*, 11147–11151.
42. Armitage, B. A. Cyanine dye-DNA interactions: intercalation, groove binding, and aggregation. *Top. Curr. Chem.* **2005**, *253*, 55–76.
43. Karton-Lifshin, N.; Segal, E.; Omer, L.; Portnoy, M.; Satchi-Fainaro, R.; Shabat, D. A unique paradigm for a Turn-ON near-infrared cyanine-based probe: noninvasive intravital optical imaging of hydrogen peroxide. *J. Am. Chem. Soc.* **2011**, *133*, 10960–10965.
44. Karton-Lifshin, N.; Albertazzi, L.; Bendikov, M.; Baran, P.S.; Shabat, D. Donor-two-acceptor dye design: a distinct gateway to NIR fluorescence. *J. Am. Chem. Soc.* **2012**, *134*, 20412–20420.
45. Kisin-Finfer, E.; Shabat, D. New repertoire of 'donor-two-acceptor' NIR fluorogenic dyes. *Bioorg. Med. Chem.* **2013**, *21*, 3602–3608.
46. Redy-Keisar, O.; Kisin-Finfer, E.; Ferber, S.; Satchi-Fainaro, R.; Shabat, D. Synthesis and use of QCy7-derived modular probes for the detection and imaging of biologically relevant analytes. *Nat. Protoc.* **2014**, *9*, 27–36.
47. Gnaim, S.; Shabat, D. Quinone-methide species, a gateway to functional molecular systems: from self-immolative dendrimers to long-wavelength fluorescent dyes. *Acc. Chem. Res.* **2014**, *47*, 2970–2984.

48. Rye, H. S.; Yue, S.; Wemmer, D. E.; Quesada, M. A.; Haugland, R. P.; Mathies, R. A.; Glazer, A. N. Stable fluorescent complexes of double-stranded DNA with bis-intercalating asymmetric cyanine dyes: properties and applications. *Nucleic Acids Res.* **1992**, *20*, 2803–2812.
49. Cosa, G.; Focsaneanu, K.-S.; McLean, J. R. N.; McNamee, J. P.; Scaiano, J. C. Photophysical properties of fluorescent DNA-dyes bound to single- and double-stranded DNA in aqueous buffered solution. *Photochem. Photobiol.* **2001**, *73*, 585–599.
50. Silva, G. L.; Ediz, V.; Yaron, D.; Armitage, B. A. Experimental and computational investigation of unsymmetrical cyanine dyes: understanding torsionally responsive fluorogenic dyes. *J. Am. Chem. Soc.* **2007**, *129*, 5710–5718.
51. Adamo, C.; Barone, V. Toward reliable density functional methods without adjustable parameters: The PBE0 model. *J. Chem. Phys.* **1999**, *110*, 6158–6170.
52. Adamo, C.; Scuseria, G. E.; Barone, V. Accurate excitation energies from time-dependent Density functional theory: assessing the PBE0 model. *J. Chem. Phys.* **1999**, *111*, 2889–2899.
53. Spink, N.; Brown, D. G.; Skelly, J. V.; Neidle, S. Sequence-dependent effects in drug-DNA interaction: the crystal structure of Hoechst 33258 bound to the d(CGCAAATTTGCG)<sub>2</sub> duplex. *Nucleic Acids Res.* **1994**, *22*, 1607-1612.
54. Vega, M. C.; Saez, I. G.; Aymami, J.; Eritja, R.; van der Marel, G. A.; van Boom, J. H.; Rich, A.; Coll, M. Three-dimensional crystal structure of the A-tract DNA dodecamer d(CGCAAATTTGCG) complexed with the minor-groove-binding drug Hoechst 33258. *Eur. J. Biochem.* **1994**, *222*, 721–726.
55. Nguyen, B.; Neidle, S.; Wilson, W. D. A role for water molecules in DNA-ligand minor groove recognition. *Acc. Chem. Res.* **2009**, *42*, 11-21.
56. Zhu, X.; Schatz, G. C. Molecular dynamics study of the role of the spine of hydration in DNA A-tracts in determining nucleosome occupancy. *J. Phys. Chem. B* **2012**, *116*, 13672–13681.
57. Job, P. *Ann. Chim. (Paris)*, **1928**, *9*, 113–203.
58. McGhee, J. D.; von Hippel, P. H. Theoretical aspects of DNA-protein interactions: co-operative and non-co-operative binding of large ligands to a one-dimensional homogeneous lattice. *J. Mol. Biol.* **1974**, *86*, 469–489.
59. Ardhammar, M.; Norde´n, B.; Kurucsev, T. DNA–drug interactions. in *Circular Dichroism: Principles and Applications*, eds. Berova, N., Nakanishi, K. & Woody, R.W., John Wiley & Sons Inc., New York, **2000**, 741–768.

60. Garbett, N. C.; Ragazzon, P. A.; Chaires, J. B. Circular dichroism to determine binding mode and affinity of ligand-DNA interactions. *Nat. Protoc.* **2007**, *2*, 3166–3172.
61. Churchill, C. D. M.; Wetmore, S. D. Developing a computational model that accurately reproduces the structural features of a dinucleoside monophosphate unit within B-DNA. *Phys. Chem. Chem. Phys.* **2011**, *13*, 16373–16383.
62. Samanta, P. K.; Manna, A. K.; Pati, S. K. Structural, electronic, and optical properties of metallo base pairs in duplex DNA: a theoretical insight. *Chem. Asian. J.* **2012**, *7*, 2718–2728.
63. Samanta, P. K.; Pati, S. K. Structural and magnetic properties of a variety of transition metal incorporated DNA double helices. *Chem. Eur. J.* **2014**, *20*, 1760–1764.
64. Breusegem, S. Y.; Clegg, R. M.; Loontjens, F. G. Base-sequence-specificity of Hoechst 33258 and DAPI binding to five (A/T)<sub>4</sub> DNA sites with kinetic evidence for more than one high-affinity Hoechst 33258-AATT complex. *J. Mol. Biol.* **2002**, *315*, 1049–1061.
65. Packer, M. J.; Hunter, C. A. Sequence-dependent DNA structure: the role of the sugar-phosphate backbone. *J. Mol. Biol.* **1998**, *280*, 407–420.
66. Laughton, C.; Luisi, B. The mechanics of minor groove width variation in DNA, and its implications for the accommodation of ligands. *J. Mol. Biol.* **1999**, *288*, 953–963.
67. Soler-LoÂpez, M.; Malinina, L.; Subirana, J. A. Solvent organization in an oligonucleotide crystal. The structure of d(GCGAATTTCG)<sub>2</sub> at atomic resolution. *J. Biol. Chem.* **2000**, *275*, 23034–23044.
68. Cheng, J.-W.; Chou, S.-H.; Salazar, M.; Reid, B. R. Solution structure of [d(GCGTATACGC)]<sub>2</sub>. *J. Mol. Biol.* **1992**, *228*, 118–137.
69. Spitzer, G. M.; Fuchs, J. E.; Markt, P.; Kirchmair, J.; Wellenzohn, B.; Langer, T.; Liedl, K. R. Sequence-specific positions of water molecules at the interface between DNA and minor groove binders. *Chemphyschem* **2008**, *9*, 2766–2771.
70. Song, G.; Sun, Y.; Liu, Y.; Wang, X.; Chen, M.; Miao, F.; Zhanga, W.; Yua, X.; Jin, J. Low molecular weight fluorescent probes with good photostability for imaging RNA-rich nucleolus and RNA in cytoplasm in living cells. *Biomaterials* **2014**, *35*, 2103–2112.
71. Turner, P. R.; Denny, W. A. The genome as a drug target: sequence-specific minor groove binding ligands. *Current Drug Targets* **2000**, *1*, 1–14.
72. Frisch, M. J.; Trucks, G. W.; Schlegel, H. B.; Scuseria, G. E.; Robb, M. A.; Cheeseman, J. R.; Scalmani, G.; Barone, V.; Mennucci, B.; Petersson, G. A.; Nakatsuji, H.; Caricato, M.; Li, X.; Hratchian, H. P.; Izmaylov, A. F.; Bloino, J.; Zheng, G.; Sonnenberg, J. L.; Hada, M.; Ehara, M.;



- Toyota, K.; Fukuda, R.; Hasegawa, J.; Ishida, M.; Nakajima, T.; Honda, Y.; Kitao, O.; Nakai, H.; Vreven, T.; Montgomery, Jr.; J. A.; Peralta, J. E.; Ogliaro, F.; Bearpark, M.; Heyd, J. J.; Brothers, E.; Kudin, K. N.; Staroverov, V. N.; Keith, T.; Kobayashi, R.; Normand, J.; Raghavachari, K.; Rendell, A.; Burant, J. C.; Iyengar, S. S.; Tomasi, J.; Cossi, M.; Rega, N.; Millam, J. M.; Klene, M.; Knox, J. E.; Cross, J. B.; Bakken, V.; Adamo, C.; Jaramillo, J.; Gomperts, R.; Stratmann, R. E.; Yazyev, O.; Austin, A. J.; Cammi, R.; Pomelli, C.; Ochterski, J. W.; Martin, R. L.; Morokuma, K.; Zakrzewski, V. G.; Voth, G. A.; Salvador, P.; Dannenberg, J. J.; Dapprich, S.; Daniels, A. D.; Farkas, O.; Foresman, J. B.; Ortiz, J. V.; Cioslowski, J. Fox, D. J. Gaussian 09, Revision C.01, Gaussian, Inc., Wallingford CT, **2009**.
73. Scalmani, G.; Frisch, M. J. *J. Chem. Phys.* **2010**, *132*, 114110.
74. Perdew, J. P.; Burke, K.; Ernzerhof, M. Generalized Gradient Approximation Made Simple. *Phys. Rev. Lett.* **1996**, *77*, 3865-3868.
75. VandeVondele, J.; Krack, M.; Mohamed, F.; Parrinello, M.; Chassaing, T.; Hutter, J. Quickstep: Fast and accurate density functional calculations using a mixed Gaussian and plane waves approach. *Comput. Phys. Commun.* **2005**, *167*, 103-128.
76. Santarossa, G.; Iannuzzi, M.; Vargas, A.; Baiker, A. Adsorption of naphthalene and quinoline on Pt, Pd and Rh: a DFT study. *ChemPhysChem* **2008**, *9*, 401-413.
77. Vargas, A.; Santarossa, G.; Iannuzzi, M.; Baiker, A. Chiral Recognition on Catalytic Surfaces: Theoretical Insight in a Biomimetic Heterogeneous Catalytic System. *J. Phys. Chem. C* **2008**, *112*, 10200-10208.
78. Grimme, S. Semiempirical GGA-type density functional constructed with a long-range dispersion correction. *J. Comput. Chem.* **2006**, *27*, 1787-1799.
79. Goedecker, S.; Teter, M. Hutter, J. Separable dual-space Gaussian pseudopotentials. *Phys. Rev. B: Condens. Matter Mater. Phys.* **1996**, *54*, 1703-1710.
80. Hartwigsen, C.; Goedecker, S.; Hutter, J. Relativistic separable dual-space Gaussian pseudopotentials from H to Rn. *Phys. Rev. B: Condens. Matter Mater. Phys.* **1998**, *58*, 3641-3662.
81. Krack, M. Pseudopotentials for H to Kr optimized for gradient-corrected exchange-correlation functional. *Theor. Chem. Acc.* **2005**, *114*, 145-152.
82. Broyden, C. G. The convergence of single-rank quasi-Newton methods. *Math. Comp.* **1970**, *24*, 365-382.

83. Shanno, D. F.; Ketter, P. C. "Optimal conditioning of quasi-Newton methods". *Math. Comp.* **1970**, *24*, 657-664.
84. Goldfarb, D. A family of variable-metric methods derived by variational means. *Math. Comp.* **1970**, *24*, 23-26.
85. Nocedal, J. Updating quasi-Newton matrices with limited storage. *Math. Comp.* **1980**, *35*, 773-782.
86. Liu, D.; Nocedal, J. Algorithms with conic termination for nonlinear optimization. *SIAM J. Sci. Stat. Comput.* **1989**, *10*, 1-17.
87. Soler, J. M.; Artacho, E.; Gale, J. D.; García, A.; Junquera, J.; Ordejo'n, P.; Sa'nchez-Portal, D. The SIESTA method for *ab initio* order-*N* materials simulation. *J. Phys.: Condens. Matter* **2002**, *14*, 2745-2779.
88. Troullier, N. Martins, J. L. Efficient pseudopotentials for plane-wave calculations. *Phys. Rev. B: Condens. Matter Mater. Phys.* **1991**, *43*, 1993-2006.
89. Trager, W.; Jensen, J. B. Human malaria parasites in continuous culture. *Science* **1976**, *193*, 673-675.

---

# Chapter 4

**Spatiotemporal Cellular ROS Targeting by Stimuli Responsive  
NIR Fluorescence Combination Probe**

The regulation of redox homeostasis is essential for maintaining normal cellular functions such as signaling, growth, survival and death.<sup>1,2</sup> Anomalous behavior of redox homeostasis adversely affects the normal physiological functions and in turn responsible for numerous pathological conditions.<sup>1,2</sup> Normally, cells in the disease state exhibits high levels of aerobic glycolysis (Warburg effect) which results in oxidative stress.<sup>3,4</sup> For example, the oxidative stress in cancer cells results in accumulation of high levels of reactive oxygen species (ROS).<sup>4-8</sup> ROS are important class of chemically reactive species that are essential for normal cellular functions including cell proliferation and differentiation.<sup>9-11</sup> The optimum levels of ROS are controlled by various cellular redox homeostasis mechanisms and abrupt increase in their concentration levels directly linked to oxidative stress related disorders. Abnormally high levels of ROS are generated in response to adverse environmental and physiological stress, exposure to ultraviolet (UV) light, and ionizing and heat radiations.<sup>7</sup> It is crucial to monitor the levels of intracellular ROS for maintaining effective cellular homeostasis. Notably, different levels ROS are responsible for different biological responses.<sup>12,13</sup> Cell maintains different levels of ROS by activating the ROS-scavenging systems such as superoxide dismutases, glutathione peroxidase, redox enzymes (peroxiredoxins, glutaredoxin and thioredoxin) and catalase. Misregulation in any of these ROS-scavenging processes leads to generation of excess amounts of ROS. Accumulation of high levels of ROS causes oxidative damage of cellular components such as proteins, lipids and nucleic acids which is responsible for aging and many pathological conditions including cancer and cardiovascular, inflammatory and neurodegenerative diseases.<sup>14-19</sup> Therefore, it is necessary to develop molecular tools which are highly sensitive and can be activated by high levels of ROS to distinguish disease and normal cells.

ROS mainly comprises free radicals such as hydroxyl radical ( $\text{OH}\cdot$ ) and superoxide ( $\text{O}_2^{\cdot-}$ ) and reactive molecular species such as hydrogen peroxide ( $\text{H}_2\text{O}_2$ ).  $\text{H}_2\text{O}_2$  is one of the most prominent and essential ROS in biological systems and significantly high levels are generated in cancer cells than normal cells.<sup>20,21</sup> In fact,  $\text{H}_2\text{O}_2$  is a small molecular metabolite and plays a vital role in the regulation of various physiological processes in living organisms.<sup>22</sup> Most importantly,  $\text{H}_2\text{O}_2$  serves as a messenger in normal cellular signal transduction and is also a known marker for oxidative damage in many disease associated cells.<sup>22</sup> In cells,  $\text{H}_2\text{O}_2$  is generated through the receptor mediated NADPH oxidase (Nox)

activation which effect the functioning of signaling proteins that control cell signaling, proliferation, senescence and death.<sup>23-32</sup> The biological significance of H<sub>2</sub>O<sub>2</sub> in human physiology and pathology has generated great interest in understanding the mechanistic details of H<sub>2</sub>O<sub>2</sub> generation, partition and its role in cellular function and signaling pathways. In comparison to other ROS, relatively high stability and diffusion across the plasma membrane makes it a versatile candidate to study its signaling pathways in living cells.<sup>23-32</sup> The role of H<sub>2</sub>O<sub>2</sub> as an essential messenger for cellular signal transduction and its chemical reactivity and chemical instability limits its spatiotemporal tracking in real-time, especially in living cells. Molecular imaging of H<sub>2</sub>O<sub>2</sub> using fluorescence probes is a highly attractive tool for studying the generation, accumulation,<sup>33-38</sup> trafficking and its role in biological processes in a spatiotemporal manner, in living cells.<sup>39-41</sup>

In recent years, stimuli responsive fluorescence probes gaining momentum due to their flexibility to introduce diversity through chemical modification and liberation of biological active probe at the site of target cellular organelles in response to biological analytes of interest.<sup>42-45</sup> Moreover, targeting specific subcellular organelles (mitochondria) and biomolecules such as DNA and proteins using stimuli responsive fluorescence probes is an emerging powerful imaging technique for biomedical applications related to diagnostics and therapeutics.<sup>46-51</sup> In this context, we envisaged functionalization of DNA binding fluorescence dye with a stimuli responsive (H<sub>2</sub>O<sub>2</sub>) appendage as a promising and unconventional but efficient method to generate the biologically active probe in a spatiotemporal manner. Such a probe with signal capturing and amplification assisted by an additional recognition event for instance DNA binding, is a highly beneficial for probing specific biological activity in a cellular environment and has the potential to be used in diagnostic and therapeutic applications.<sup>46-51</sup> Our group has been actively involved in the development of novel red fluorescence probes for biologically relevant thiols, metal ions and nucleic acids.<sup>52-55</sup> Recently, we have developed a first NIR-fluorescence and sequence-specific DNA minor groove probe **QCy-DT** which show switch-on NIR fluorescence specifically in presence AT-rich DNA (Chapter 3).<sup>56</sup> Structurally, **QCy-DT** has a free hydroxyl group readily available for functionalization with enumerable number of chemically or enzymatically cleavable appendages to make it a versatile and promising stimuli responsive probe. In response to specific stimulus (chemical or enzyme) the appendage

functionality is cleaved to release NIR-fluorescence ready **QCy-DT** probe which upon binding DNA minor groove fluoresce strongly aiding the imaging and quantification of stimulus itself. We anticipated that functionalizing the DNA binding fluorescence probe **QCy-DT** with aryl boronates is an attractive strategy for the development of stimuli responsive fluorescence probes for H<sub>2</sub>O<sub>2</sub>. Therefore, **QCy-DT** hydroxyl group was functionalized to obtain phenyl boronic acid (**QCy-BOH**) which is expected to react selectively with H<sub>2</sub>O<sub>2</sub> to release the parent DNA binding dye. We selected phenyl boronate as the preferred appendage owing to the fact that the reaction between H<sub>2</sub>O<sub>2</sub> and boronic acids or ester is highly chemospecific, bioorthogonal and biocompatible while the byproducts are non-toxic to living cells.<sup>37,57,58</sup>

Here, we developed a phenyl boronic acid conjugated one-donor-two-acceptor (D2A)  $\pi$ -electron based quinone-cyanine (**QCy-BOH**) as stimuli responsive probe for H<sub>2</sub>O<sub>2</sub> in combination with AT-rich DNA. In presence of H<sub>2</sub>O<sub>2</sub>, **QCy-BOH** releases non-fluorescent **QCy-DT** which upon binding AT-rich DNA show enhanced fluorescence in the NIR region. Nuclear magnetic resonance (NMR) and UV-vis absorption studies revealed the efficient conversion of **QCy-BOH** to **QCy-DT** and quinone methide through selective 1,6-elimination rearrangement in presence of H<sub>2</sub>O<sub>2</sub> over other ROS.<sup>59</sup> Fluorescence studies of **QCy-BOH** showed strong NIR fluorescence enhancement in presence of H<sub>2</sub>O<sub>2</sub> and AT-rich DNA (Drew-AT) which clearly endorse the use of **QCy-BOH**∩Drew-AT (combination probe) for the fluorometric detection of H<sub>2</sub>O<sub>2</sub>. Glucose oxidase assay confirms combination probe **QCy-BOH**∩Drew-AT is capable of monitoring *in situ* generated H<sub>2</sub>O<sub>2</sub> by the oxidation of glucose using glucose oxidase (GOx). Further, live cell imaging studies show the spatiotemporal targeting of cell nucleus by the *in situ* generated NIR fluorescence-ready probe in presence of H<sub>2</sub>O<sub>2</sub>. Fluorescence activated cell sorting (FACS)-analysis showed that probe **QCy-BOH** is equally efficient in detecting the normal and *in situ* generated H<sub>2</sub>O<sub>2</sub> levels by Nox-mediated growth factor signaling pathways. Therefore, probe **QCy-BOH** in combination with exogenous or cellular DNA is a promising stimuli responsive fluorescence probe for investigating H<sub>2</sub>O<sub>2</sub> production and concentration levels in living cells which further facilitate the imaging and diagnosis of disease related cells.

#### 4.1 H<sub>2</sub>O<sub>2</sub> triggered activation of DNA minor groove binder

Aryl boronates are unique chemical moieties with selective reactivity towards the ambiphilic H<sub>2</sub>O<sub>2</sub>, a desirable property to achieve specificity and selectivity over other biologically relevant ROS.<sup>33-38</sup> Initially, boronate functionality acts as electrophilic center and reacts with nucleophile to generate tetrahedral-boronate complex.<sup>37</sup> Subsequently, carbon-boron (C-B) bond becomes labile and acts as a nucleophile to electrophilic oxygen center of H<sub>2</sub>O<sub>2</sub>. In particular, aryl boronate functionality become a specific reorganization center for H<sub>2</sub>O<sub>2</sub> among all other biological oxygen metabolites and ROS which operate through one electron transfer or electrophilic oxidation pathways.<sup>33-38</sup>

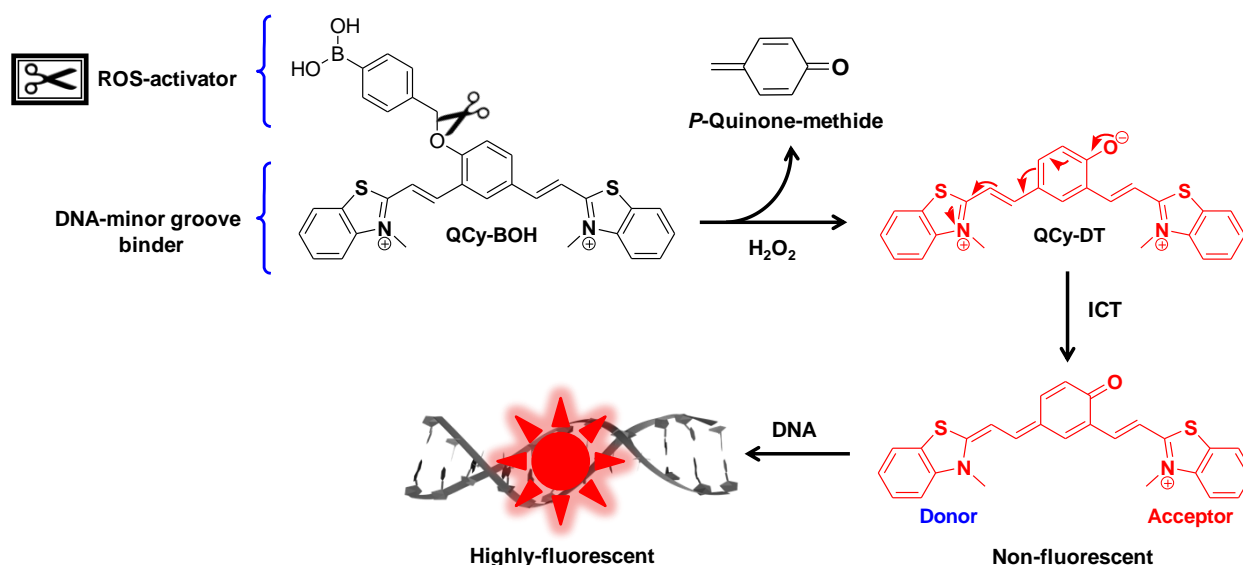


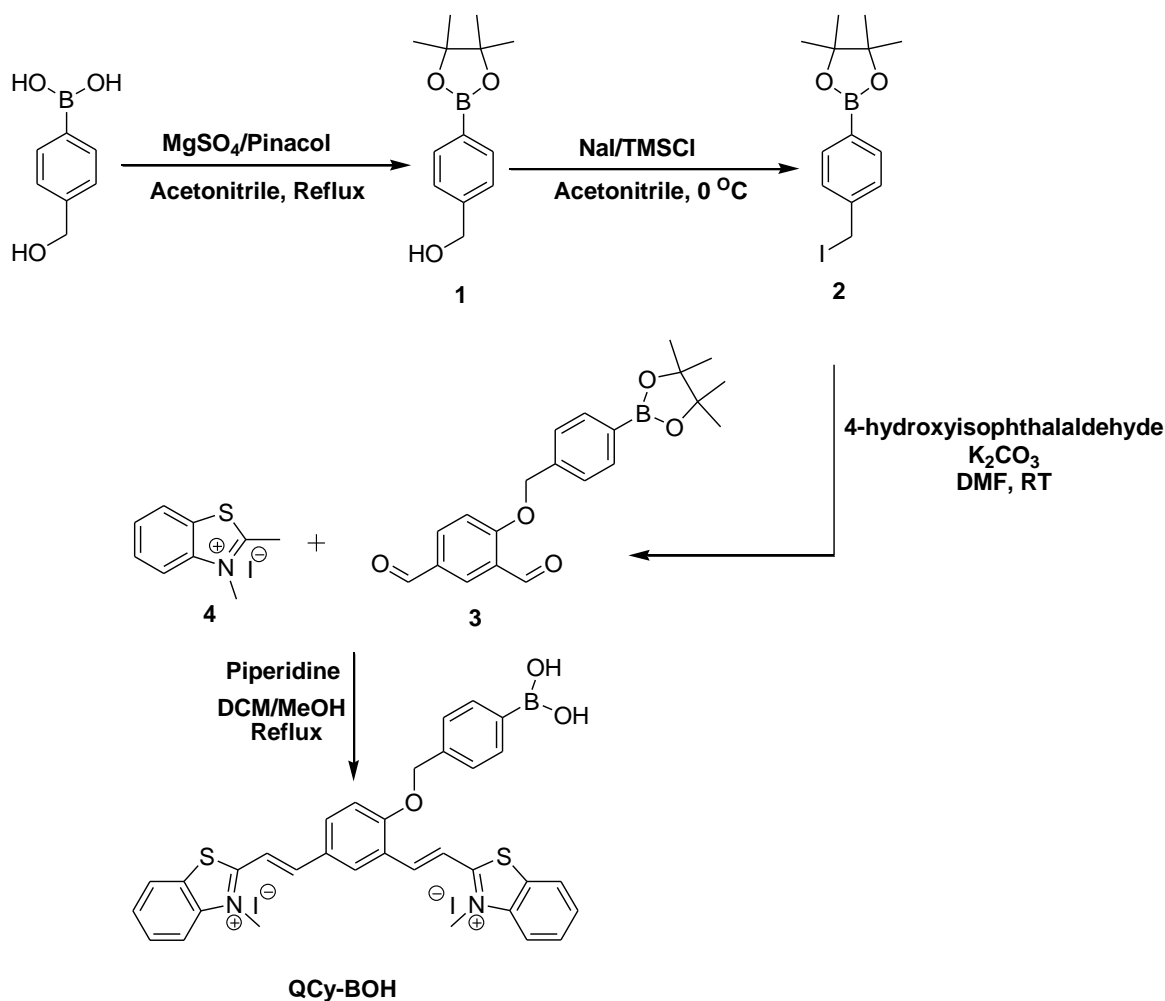
**Figure 1.** Schematic representation of conversion of QCy-BOH to *p*-quinone-methide and QCy-DT a DNA minor groove binder, in presence of H<sub>2</sub>O<sub>2</sub>.

Herein, we present stimuli responsive probe QCy-BOH, a DNA minor groove binder (QCy-DT) functionalized with phenyl boronic acid. Although, QCy-BOH shares the backbone of Cy7 dyes, the major structural difference comes from two positively charged nitrogen atom containing benzothiazoles with distinct conjugation patterns around central phenolic moiety derivatized with phenyl boronic acid functionality.<sup>60-64</sup> Furthermore, the electron delocalization in QCy-BOH is disrupted as a consequence of masking the central

phenolic hydroxyl with phenyl boronic acid functionality. Upon slicing of the phenyl boronic acid functionality in response to  $\text{H}_2\text{O}_2$  stimulus **QCy-BOH** transform to negatively charged phenolate of **QCy-DT**. The generation of phenolate restores the electron transfer towards one of the positively charged nitrogen atom of benzothiazole acceptor. This restores internal charge transfer (ICT) to generate a highly electron delocalized  $\pi$ -system similar to Cy-7 dye with NIR-fluorescence in presence of DNA as shown in Figure 1.<sup>56</sup>

## 4.2 Synthesis of QCy-BOH

Synthesis of **QCy-BOH** was achieved by treating 4-(hydroxymethyl)phenyl boronic acid with a pinacol in presence of magnesium sulfate in acetonitrile to obtain 4-(hydroxymethyl)phenyl boronic ester (**1**) (Scheme 1).



**Scheme 1.** Synthesis of **QCy-BOH**.



The phenyl boronic ester **1** was treated with NaI and trimethyl silyl chloride in acetonitrile at ice temperature to give 4-(iodomethyl)phenyl boronic ester (**2**).<sup>60</sup> The 4-(iodomethyl)phenyl boronic ester (**2**) was coupled to 4-hydroxy isophthalaldehyde using potassium carbonate as a base in dimethylformamide (DMF) at room temperature to obtain phenyl boronic ester dialdehyde (**3**) in good yield. Finally, the dialdehyde **3** was coupled with *N*-methylated benzothiazole in presence of piperidine to yield probe **QCy-BOH**. All the intermediates and probe **QCy-BOH** were characterized by NMR and high-resolution mass spectroscopy (HRMS).

### 4.3 NMR analysis of H<sub>2</sub>O<sub>2</sub> triggered release of DNA minor groove binder

In a preliminary study, we carried out time-dependent NMR spectroscopy analysis of **QCy-BOH** in presence of H<sub>2</sub>O<sub>2</sub> to assess the stimuli responsive slicing of phenyl boronic acid functionality (Figure 2a). The <sup>1</sup>H NMR spectrum of **QCy-BOH** (2 mM) alone in D<sub>2</sub>O (0.5 mL) showed a singlet peak at 5.05 ppm corresponding to the O-CH<sub>2</sub> (C-H<sub>a</sub>) bearing phenyl boronic acid group and peaks at 8.2-7.2 ppm corresponding to aromatic protons of parent **QCy-DT**. The chemical shifts of O-CH<sub>2</sub>, aromatic region of **QCy-BOH** and appearance possible new peaks for *p*-quinone methide (sliced byproduct corresponding to phenyl boronic acid functionality) upon sequential addition of H<sub>2</sub>O<sub>2</sub> was monitored. After 1 h of addition of H<sub>2</sub>O<sub>2</sub> (10 mM, 5 μL from the stock H<sub>2</sub>O<sub>2</sub> of 1M), the peak intensity at 5.05 ppm *i.e.*, C-H<sub>a</sub> (O-CH<sub>2</sub>) gradually decreases and new peaks appeared at 5.20 ppm and 6.5-7.0 ppm region suggest the coexistence of both phenyl boronic acid protected and deprotected forms of **QCy-BOH**. The peaks at 5.20 ppm and aromatic region 6.5-7.0 ppm correspond to newly formed exocyclic C-H<sub>b</sub> protons of *p*-quinone-methide and **QCy-DT** moieties respectively. After 2 h, we observed a singlet peak at 5.20 ppm and prominent new peaks at 6.5-7.0 ppm indicating the complete conversion of **QCy-BOH** to **QCy-DT** and *p*-quinone methide (Figure 2b). This study confirmed the H<sub>2</sub>O<sub>2</sub> stimulus triggered slicing of phenyl boronic acid functionality of **QCy-BOH** to release **QCy-DT**, a DNA minor groove binding probe. Interestingly, color of the solution changed from yellow to brown after addition of H<sub>2</sub>O<sub>2</sub>, a naked eye detection for the formation of *p*-quinone-methide and **QCy-DT** (Figure 2c).

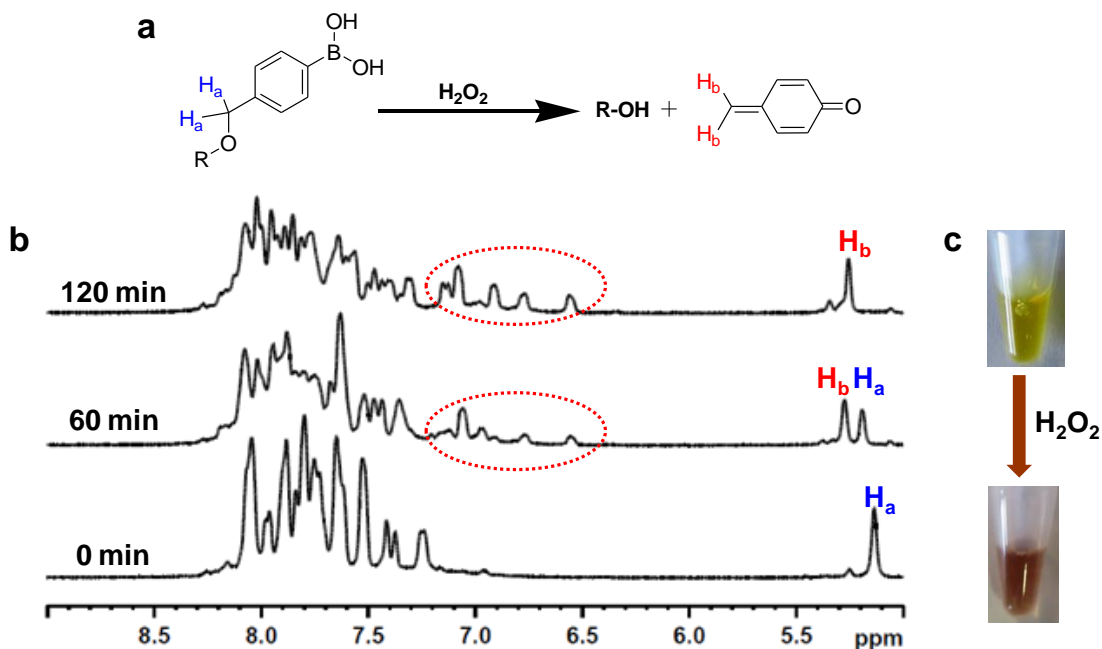


**Figure 2.** NMR-analysis of **QCy-BOH** in presence of  $\text{H}_2\text{O}_2$ . (a) 1,6-Elimination and rearrangement of phenyl boronic acid functionality of **QCy-BOH** in presence of  $\text{H}_2\text{O}_2$ . (b) Time-dependent  $^1\text{H}$  NMR spectral monitoring of slicing of phenyl boronic acid of **QCy-BOH** in presence of  $\text{H}_2\text{O}_2$ . Red circle highlight the appearance of new signals for newly formed quinone system and **QCy-DT**.  $\text{H}_a$  and  $\text{H}_b$  represents the  $\text{O}-\text{CH}_2$  ( $\text{C}-\text{H}_a$ ) bearing phenyl boronic acid group and newly formed exocyclic ( $\text{C}-\text{H}_b$ ) protons of *p*-quinone-methide respectively. (c) The change in solution color upon addition of  $\text{H}_2\text{O}_2$  to **QCy-BOH**, as visualized after 2 h.

#### 4.4 Photophysical properties of **QCy-BOH** in presence of $\text{H}_2\text{O}_2$

Next, we studied the photophysical properties of **QCy-BOH** in absence and presence of  $\text{H}_2\text{O}_2$  using UV-vis absorption and emission studies in PBS-buffer solution (10 mM, pH = 7.4) under ambient conditions. UV-vis absorption spectrum of **QCy-BOH** (5  $\mu\text{M}$ ) showed broad absorbance in the 300-500 region with absorption maximum ( $\lambda_{\text{max}}$ ) at 400 nm (Figure 3a). Upon excitation at 400 nm emission spectrum of **QCy-BOH** (5  $\mu\text{M}$ ) showed weak fluorescence with emission maximum ( $E_{\text{max}}$ ) at 565 nm (Figure 3b). As expected, **QCy-BOH** did not emit in the NIR region due to phenyl boronic acid protection of backbone-phenolic hydroxyl moiety. Interestingly, absorption spectrum of **QCy-BOH** (5  $\mu\text{M}$ ) in presence of  $\text{H}_2\text{O}_2$  (1 mM) showed gradual decrease in absorption maxima at 400 nm accompanied by the appearance of a new absorption band at 465 nm with a shoulder at 530 nm (Figure 3a). The

new absorption bands at 465 nm and 530 nm revealed the transformation of **QCy-BOH** to phenolate form of **QCy-DT**. In agreement with NMR study (Figure 2b), UV-vis absorption data confirmed the generation of **QCy-DT** through  $\text{H}_2\text{O}_2$  assisted oxidation of boronic acid in **QCy-BOH** followed by the hydrolysis and 1,6-elimination of *p*-quinone-methide group.<sup>60</sup> Evidently, UV-vis absorption spectral characteristics clearly support the observed change in solution color from yellow to brown, as a result of newly formed **QCy-DT** ( $\lambda_{\text{max}}$  at 465 and 530 nm) from **QCy-BOH** ( $\lambda_{\text{max}} = 400$  nm) (Figure 2c). The emission spectra of **QCy-BOH** (5  $\mu\text{M}$ ) in presence of  $\text{H}_2\text{O}_2$  (1 mM) displayed gradual decrease in fluorescence intensity at 565 nm and a weak basal level fluorescence band at 680 nm with a large Stokes shift ( $\Delta\lambda_{\text{max}} = \sim 280$  nm) upon excitation at 400 nm (Figure 3b). Therefore,  $\text{H}_2\text{O}_2$  triggered slicing of phenyl boronic acid functionality of **QCy-BOH** is a highly useful transformation for the generation of stimuli responsive switch-on DNA binding fluorescence probe **QCy-DT** owing to its large Stokes shift and non-fluorescence in unbound state.

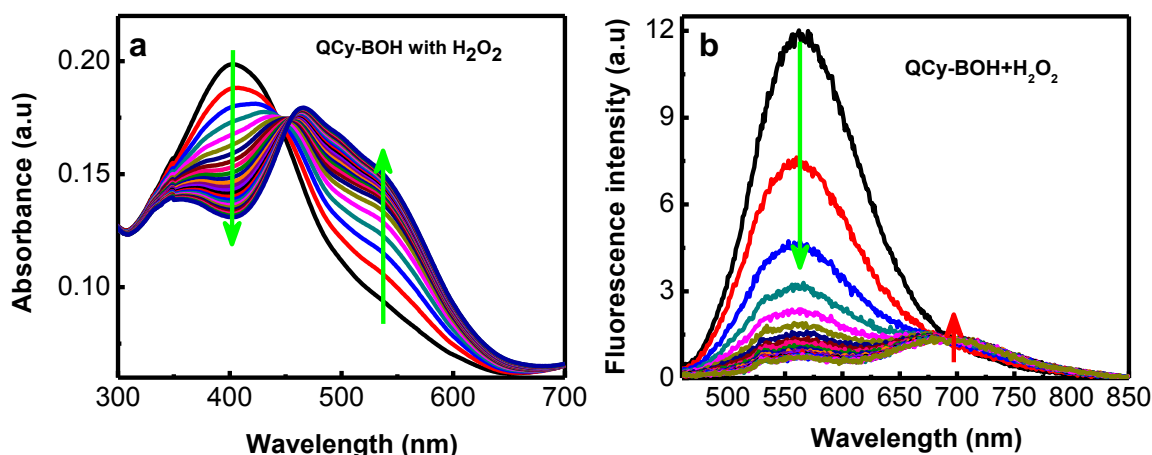


**Figure 3.** Absorption and emission spectra of **QCy-BOH**. (a) Absorption spectra of **QCy-BOH** (5  $\mu\text{M}$ ) in presence of  $\text{H}_2\text{O}_2$  (1 mM). (b) Emission spectra of **QCy-BOH** (5  $\mu\text{M}$ ) in presence of  $\text{H}_2\text{O}_2$  (1 mM) in PBS-buffer solution with increasing time.

Further, we performed concentration-dependent fluorescence study of slicing of phenyl boronic acid functionality of **QCy-BOH** (5  $\mu\text{M}$ ) in response to sequential addition of  $\text{H}_2\text{O}_2$  (5 to 100  $\mu\text{M}$ ) stimulus. The fluorescence intensity of **QCy-BOH** at 565 nm was decreased in response to added  $\text{H}_2\text{O}_2$  in concentration range of 5 to 50  $\mu\text{M}$  and subsequently reached saturation at 100  $\mu\text{M}$ . A linear relationship ( $R^2 = 0.9877$ ) was observed with increasing

concentration of  $\text{H}_2\text{O}_2$  in the concentration range of 5-50  $\mu\text{M}$ , based on  $3\sigma/\text{slope}$  the limit of detection (LOD) of  $\text{H}_2\text{O}_2$  using the decrease in fluorescence of **QCy-BOH** at 565 nm was found to be 5.3  $\mu\text{M}$  (Figure 4).<sup>65</sup>

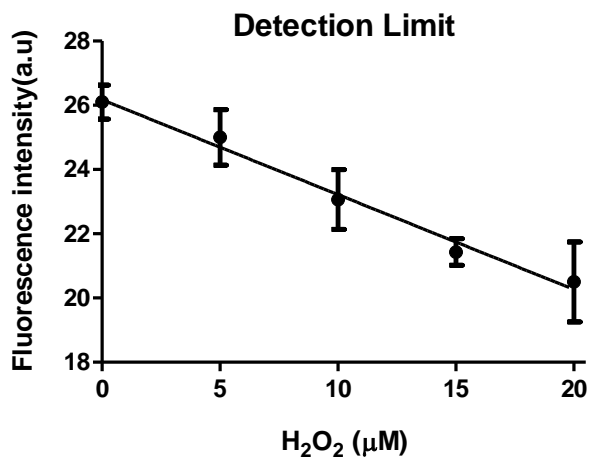


**Figure 4.** Plot of the fluorescence intensity of **QCy-BOH** at 550 nm against the concentration of  $[\text{H}_2\text{O}_2]$  PBS-buffer solution. Each data point was acquired 1 h after  $\text{H}_2\text{O}_2$  addition at 25 °C. The detection limit (5.3  $\mu\text{M}$ ) was calculated with  $3\sigma/k$ ; where  $\sigma$  is the standard deviation of blank measurement,  $k$  is the slope (-0.30).

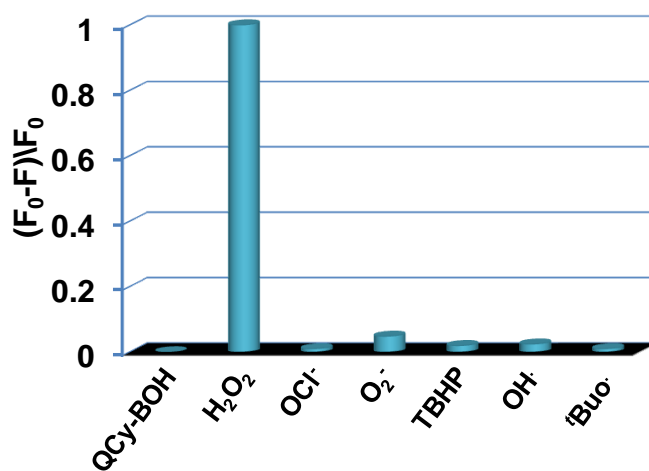


**Figure 5.** Fluorescence response of **QCy-BOH** (5  $\mu\text{M}$ ) to various reactive oxygen species (ROS) at individual concentration of 100  $\mu\text{M}$ .

$\text{H}_2\text{O}_2$  is one of the many ROS present in biological system and it is necessary to test the probe **QCy-BOH** against all of them to assess the selectivity and specificity. Therefore, we investigated the response of **QCy-BOH** towards  $\text{H}_2\text{O}_2$  (100  $\mu\text{M}$ ) in presence of other ROS (100  $\mu\text{M}$ ), include tertbutylhydroperoxide (TBHP), superoxide ( $\text{O}_2^-$ ), hydroxyl radical ( $\text{HO}\cdot$ ), tert-butoxy radical ( $^t\text{BuO}\cdot$ ) and hypochlorite ( $\text{OCl}^-$ ). Remarkably, only  $\text{H}_2\text{O}_2$  efficiently decreased the fluorescence emission at 565 nm owing to slicing of phenyl boronic acid functionality of the **QCy-BOH** (5  $\mu\text{M}$ ). On the other hand, we observed very minimal or no effect on the probe response in presence superoxide ( $\text{O}_2^-$ ), hydroxyl radical ( $\text{HO}\cdot$ ), tert-butoxy radical ( $^t\text{BuO}\cdot$ ) and hypochlorite ( $\text{OCl}^-$ ) (Figure 5). These results are in agreement with selective 1,6-elimination of phenyl boronic acid functionality of **QCy-BOH** as *p*-quinone-methide moiety to liberate **QCy-DT**, only in presence of  $\text{H}_2\text{O}_2$  over other ROS.<sup>59-64</sup>

#### 4.5 Photophysical properties of **QCy-BOH** in presence of **Drew-AT** and $\text{H}_2\text{O}_2$

To further validate the conversion of **QCy-BOH** to **QCy-DT** a DNA minor groove binder in response to  $\text{H}_2\text{O}_2$  stimulus, the transformation was monitored using UV-vis absorption and emission studies in presence of an AT-rich DNA (**Drew-AT**: 5'-GCGCAAATTTGCGC-3'). **QCy-DT** binds AT-rich DNA minor groove with high sequence-specificity (5'-AAATTT-3') which reflect in the strong NIR-fluorescence.<sup>56</sup> Thus, we chose **Drew-AT** a self-complementary 14-base pair (bp) sequence containing central 5'-AAATTT-3' sequence for fluorescence reporting of  $\text{H}_2\text{O}_2$  stimulus released **QCy-DT** by means of strong emission in the NIR region.<sup>66-68</sup> The absorption spectrum of **QCy-BOH** (2  $\mu\text{M}$ ) in the presence of **Drew-AT** (2  $\mu\text{M}$ ) duplex showed an increase in absorption maxima at 416 nm with bathochromic shift ( $\Delta\lambda_{\text{max}} = 16$  nm) (Figure 6a). While the fluorescence spectrum of **QCy-BOH** (2  $\mu\text{M}$ ) in presence of **Drew-AT** showed emission maxima at 500 nm with hypsochromic shift ( $\Delta\lambda_{\text{max}} = \sim 50$  nm) (Figure 6b). These changes in absorption and emission spectra are attributed to weak interactions between **QCy-BOH** and **Drew-AT** duplex through electrostatic and hydrophobic interactions. Next, absorption and emission spectra of **QCy-BOH** were recorded in presence of **Drew-AT** duplex and  $\text{H}_2\text{O}_2$  (100  $\mu\text{M}$ ). The absorption spectrum showed gradual decrease in absorption at 416 nm with corresponding increase in the absorption at 564 nm which is in agreement with the absorption characteristics observed for **QCy-DT/Drew-AT** complex (Figure 7).<sup>56</sup>

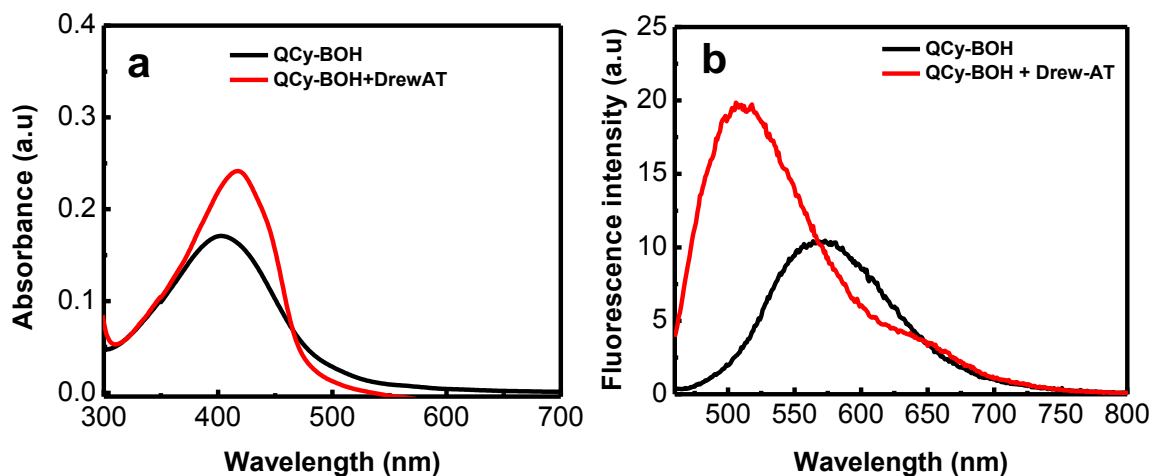


**Figure 6.** Absorption and emission spectra of **QCy-BOH** in presence of Drew-AT. (a) Absorption spectra of **QCy-BOH** (2  $\mu\text{M}$ ) in presence of Drew-AT (2  $\mu\text{M}$ ). (b) Emission spectra of **QCy-BOH** (2  $\mu\text{M}$ ) in presence of Drew-AT (2  $\mu\text{M}$ ) in PBS-buffer solution.

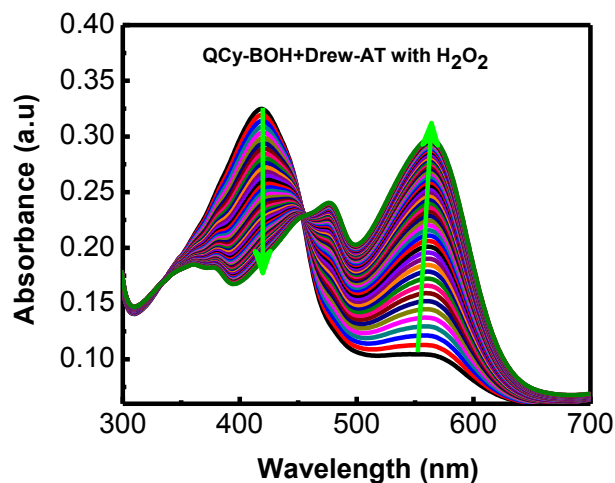


**Figure 7.** Absorption spectra of **QCy-BOH** in presence of Drew-AT (2  $\mu\text{M}$ ) and hydrogen peroxide (100  $\mu\text{M}$ ) with increasing time.

Similarly, the emission spectrum of **QCy-BOH** (excitation at  $\lambda_{\text{max}} = 400 \text{ nm}$ ) in presence of Drew-AT duplex and  $\text{H}_2\text{O}_2$  showed fluorescence decrease at 500 nm and corresponding increase at 650 nm (Figure 8a). Further, upon excitation at 564 nm ( $\lambda_{\text{max}}$  of **QCy-DT** bound to Drew-AT duplex) strong fluorescence enhancement at 650 nm was

observed (Figure 8b). These results reiterated the  $\text{H}_2\text{O}_2$  triggered conversion of **QCy-BOH** to a DNA (Drew-AT) minor groove binder **QCy-DT**.

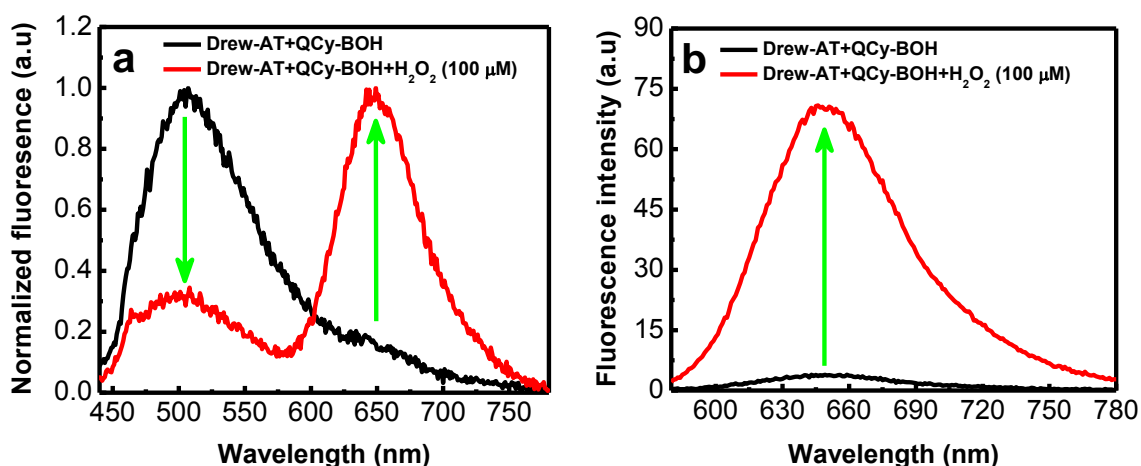


**Figure 8.** Fluorescence response of combination probe **QCy-BOH** in presence of **Drew-AT**. (a) Normalized fluorescence spectra of **QCy-BOH** (2  $\mu\text{M}$ ) in presence of **Drew-AT** (2  $\mu\text{M}$ ) upon excitation at 400 nm. (b) Fluorescence spectra of **QCy-BOH** (2  $\mu\text{M}$ ) in presence of **Drew-AT** (2  $\mu\text{M}$ ) upon excitation at 564 nm. All the spectra are acquired in presence of  $\text{H}_2\text{O}_2$  (100  $\mu\text{M}$ ).

The time-dependent fluorescence study was carried out to evaluate the release kinetics of **QCy-BOH** (2  $\mu\text{M}$ ) to **QCy-DT** in response to  $\text{H}_2\text{O}_2$  (100  $\mu\text{M}$ ) stimulus, in presence of **Drew-AT** duplex. The change in fluorescence intensities at 500 nm and 650 nm corresponding to emission maxima ( $E_{\text{max}}$ ) of **QCy-BOH** and **QCy-DT** in the presence of **Drew-AT** was monitored. Upon excitation at 400 nm, fluorescence intensity of **QCy-BOH** gradually decreases at 500 nm while that of **QCy-DT** increased at 650 nm (Figure 9a). Similarly, the fluorescence spectra recorded upon excitation at 564 nm showed an exponential increase in emission intensity at 650 nm as a function of time and reached saturation  $\geq 4\text{h}$  (Figure 9b). The calculation of kinetics parameter using pseudo-first-order conditions for conversion of **QCy-BOH** (2  $\mu\text{M}$ ) to **QCy-DT** in presence of  $\text{H}_2\text{O}_2$  (1 mM) and **Drew-AT** (2  $\mu\text{M}$ ) gave the rate constant of  $k_{\text{obs}} = 1.0 \times 10^{-3} \text{ s}^{-1}$  (Figure 10). Overall, photophysical (absorption and emission) studies demonstrated that  $\text{H}_2\text{O}_2$  trigger the slicing of phenyl boronic acid functionality of **QCy-BOH** to generate **QCy-DT** a DNA minor binding probe which show switch-on NIR-fluorescence in presence of **Drew-AT** duplex.

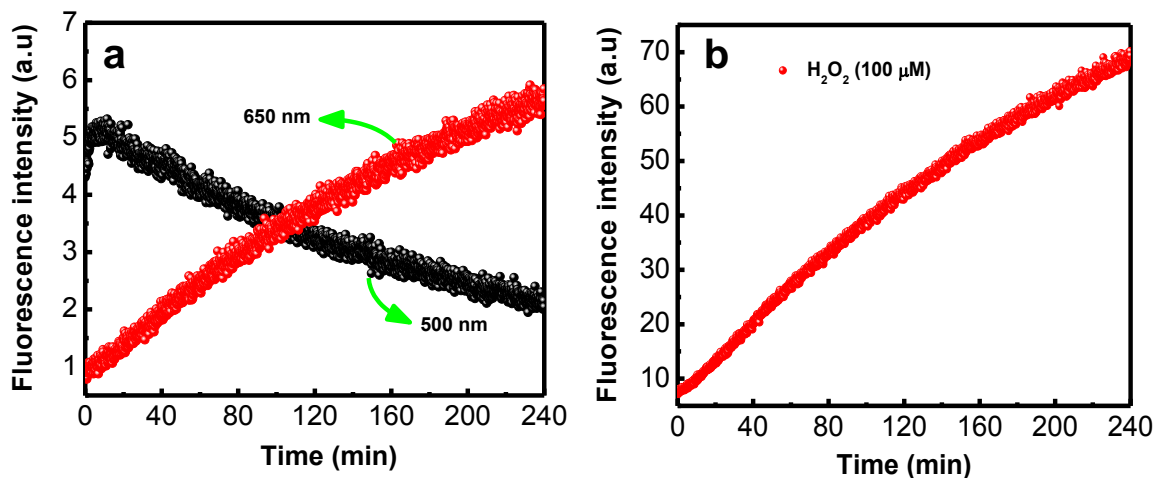


**Figure 9.** Time dependent fluorescence response of combination probe **QCy-BOH@Drew-AT**. (a-b) Time-dependent fluorescence spectra of **QCy-BOH** (2  $\mu\text{M}$ ) in presence of **Drew-AT** (2  $\mu\text{M}$ ) after the addition of  $\text{H}_2\text{O}_2$  (100  $\mu\text{M}$ ). (a) Upon excitation at 400 nm. (b) Upon excitation at 564 nm.

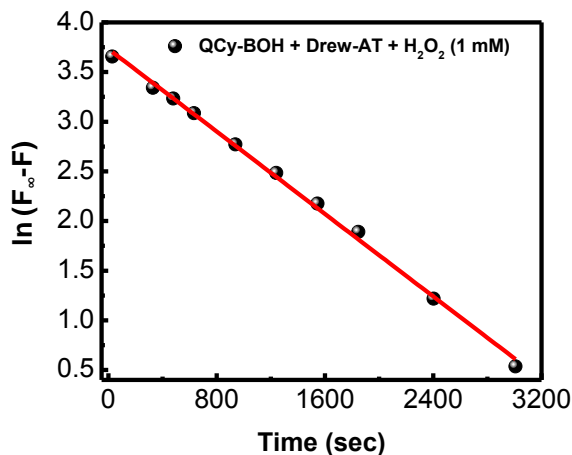


**Figure 10.** Plot of  $\ln(F_\infty - F)$  of combination probe **QCy-BOH@Drew-AT** (2  $\mu\text{M}$ ) as a function of time at 650 nm upon addition of  $\text{H}_2\text{O}_2$  (1 mM), where  $F_\infty$  and  $F$  are the fluorescence intensities at 650 nm at  $t_\infty$  (= 60 min) and  $t$ , respectively. The  $k_{\text{obs}}$  calculated from the slope of this plot is  $1.04 \times 10^{-3} \text{ s}^{-1}$ .

#### 4.6 Probing of *in situ* generated $\text{H}_2\text{O}_2$ using combination probe **QCy-BOH@Drew-AT**

In biological systems, class of enzymes such as oxidases generates  $\text{H}_2\text{O}_2$  by the oxidation of numerous biochemicals. Glucose oxidase (GOx) is one of the most important enzymes known to selectively catalyze the oxidation of glucose to gluconic acid in presence of oxygen to generate  $\text{H}_2\text{O}_2$ .



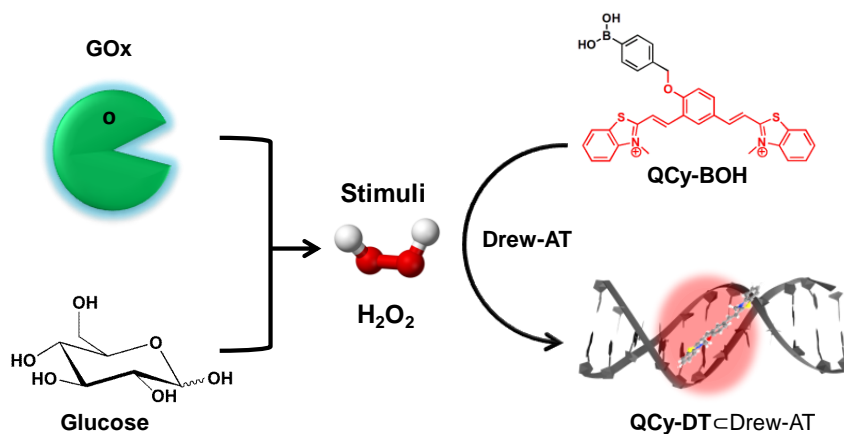


**Figure 11.** Schematic diagram show the GOx-assay where Gox oxidize glucose to gluconic acid generating H<sub>2</sub>O<sub>2</sub> and fluorescence reporting by the combination probe **QCy-BOH** ⊂ Drew-AT.

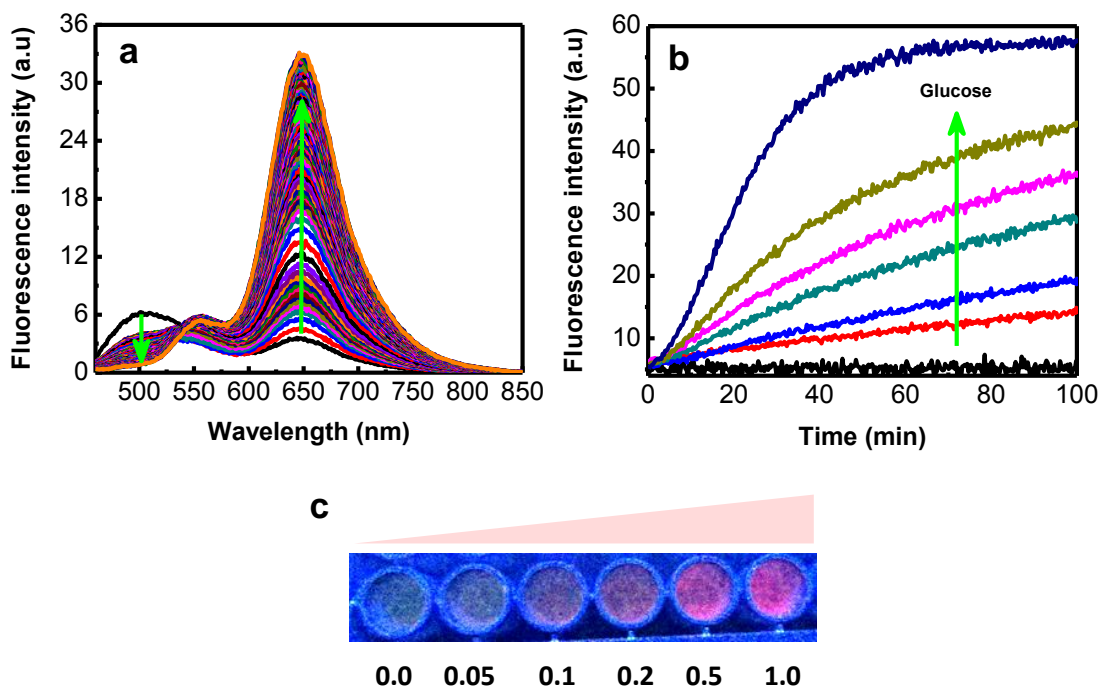


**Figure 12.** Glucose oxidase (Gox) assay. (a) Fluorescence spectra of combination probe **QCy-BOH** ⊂ Drew-AT in presence of Gox (4 U/mL) and glucose (1 mM) with time, upon excitation at 400 nm. (b) Plot of fluorescence intensity of combination probe **QCy-BOH** ⊂ Drew-AT at 650 nm as a function of time, in presence of Gox (4 U/mL) with increasing concentration of glucose from 0 to 1 mM upon excitation at 564 nm. (c) Photographs of combination probe **QCy-BOH** ⊂ Drew-AT complex under UV-light in presence of Gox (4 U/mL) with increasing glucose concentration 0.0 to 1.0 mM.

In this context, we set out to probe the *in situ* generation of  $H_2O_2$  by the oxidation of glucose in presence of GOx using our combination probe **QCy-BOH** $\subset$ Drew-AT (Figure 11). To monitor the *in situ* generation of  $H_2O_2$ , glucose was added to a PBS buffer (10 mM, pH = 7.4) containing GOx (4 U/mL) and **QCy-BOH** $\subset$ Drew-AT (2  $\mu$ M). The reaction mixture showed gradual decrease in fluorescence at 500 nm ( $\lambda_{max} = 400$  nm) and corresponding increase in fluorescence intensity at 650 nm (Figure 12a). Similarly, upon excitation at 564 nm the fluorescence spectra showed strong enhancement in fluorescence emission at 650 nm attributed to release and binding of **QCy-DT** to Drew-AT (Figure 13a).

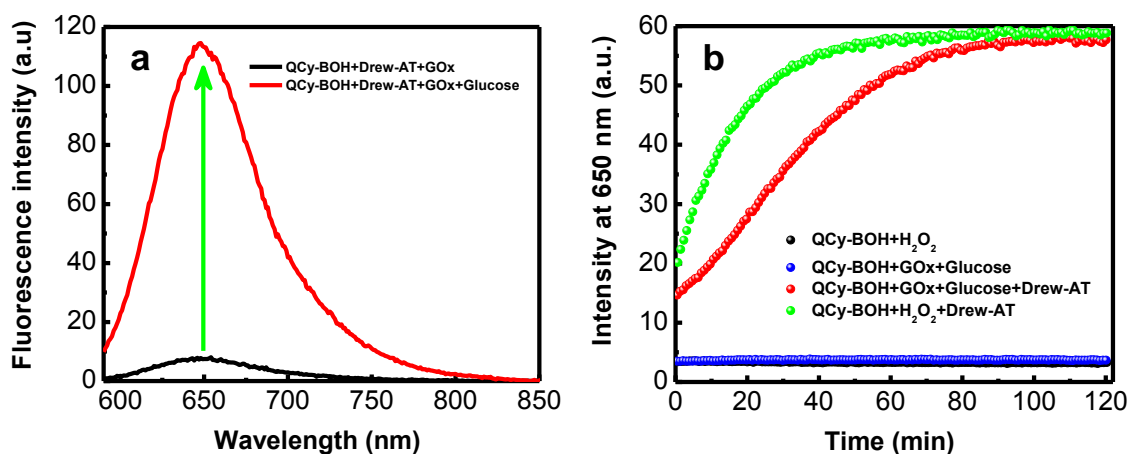


**Figure 13.** Fluorescence response of **QCy-BOH** $\subset$ Drew-AT in presence of Gox and glucose. (a) Fluorescence spectra of combination probe **QCy-BOH** $\subset$ Drew-AT in presence of Gox (4 U/mL) and upon addition of glucose (1 mM). (b) Time-dependent fluorescence of combination probe **QCy-BOH** $\subset$ Drew-AT in presence and absence of Gox (4 U/mL) upon addition of glucose (1 mM).

Next, the reaction kinetics of *in situ* generation of  $H_2O_2$  through the oxidation of glucose by GOx was investigated using **QCy-BOH** $\subset$ Drew-AT, upon excitation at 564 nm. The plot of fluorescence intensity at 650 nm as a function of time after addition of glucose is shown in Figure 13b. Upon addition of glucose (1 mM) in presence of GOx, **QCy-BOH** $\subset$ Drew-AT showed gradual increase in fluorescence intensity at 650 nm and reached saturation at 1 h. However, in the absence of glucose, GOx and **QCy-BOH** $\subset$ Drew-AT did not show such increase in fluorescence intensity. Further, the fluorescence was monitored by adding increasing concentration of glucose (0 to 1 mM) to the mixture of GOx and **QCy-**

**BOH**⌊Drew-AT. The fluorescence emission at 650 nm increases and showed a linear relationship in the concentration range of 0 to 0.2 mM (Figure 12b and 12c).

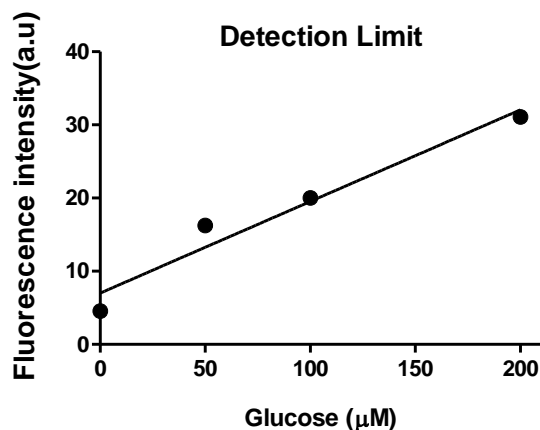


**Figure 14.** The plot of the fluorescence intensity of combination probe **QCy-BOH**⌊Drew-AT in the presence of GOx (4 U/mL) against the concentration of glucose at 650 nm. Each data point was acquired 1 h after addition of glucose and GOx at 25 °C. The detection limit (6.11 μM) was calculated with  $3\sigma/k$ ; where  $\sigma$  is the standard deviation of blank measurement,  $k$  is the slope (0.12).

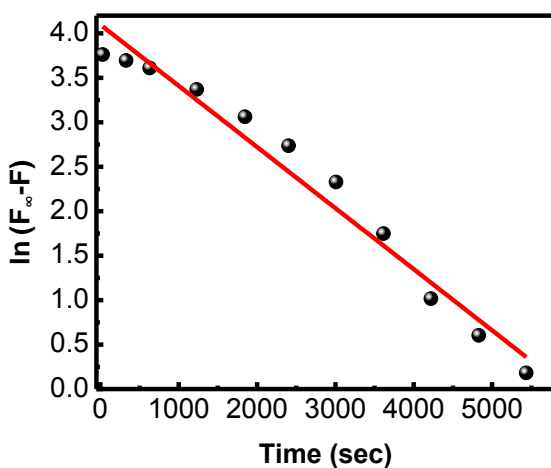


**Figure 15.** Plot of  $\ln(F_{\infty}-F)$  of combination probe **QCy-BOH**⌊Drew-AT in presence of Gox (4 U/mL) as a functions of time at 650 nm upon addition of glucose (1 mM), where  $F_{\infty}$  and  $F$  are the fluorescence intensities at 650 nm at  $t_{\infty}$  (= 60 min) and  $t$ , respectively. The  $k_{\text{obs}}$  calculated from the slope of this plot is  $6.87 \times 10^{-4} \text{ s}^{-1}$ .

Based on  $3\sigma$ /slope, the LOD of  $\text{H}_2\text{O}_2$  was found to be  $6.11\ \mu\text{M}$  (from the concentration of glucose) and is in good agreement with LOD of  $\text{H}_2\text{O}_2$  ( $5.33\ \mu\text{M}$ ) using **QCy-BOH** (Figure 14). From the pseudo-first-order calculations, combination probe **QCy-BOH**-Drew-AT ( $2\ \mu\text{M}$ ) showed the rate constant of  $k_{\text{obs}} = 6.87 \times 10^{-4}\ \text{s}^{-1}$  in presence of Gox ( $4\ \text{U/mL}$ ) and glucose ( $1\ \text{mM}$ ) (Figure 15).<sup>65</sup> Overall, Gox assay demonstrated the *in situ* monitoring of  $\text{H}_2\text{O}_2$  generated from the oxidation of glucose. Next, we studied the effect of enzymes which spontaneously decompose  $\text{H}_2\text{O}_2$ , on the conversion of **QCy-BOH** to **QCy-DT** by the action  $\text{H}_2\text{O}_2$ .

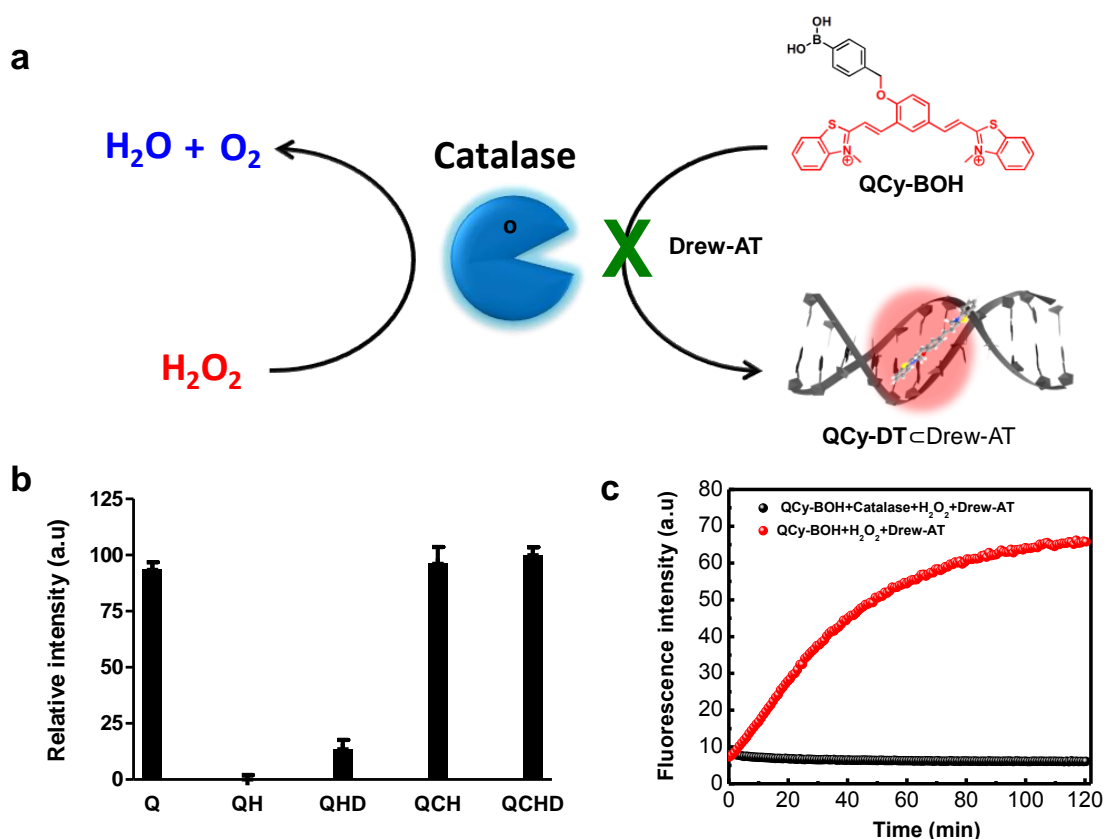


**Figure 16.** Catalase activity. (a) Schematic diagram represents the catalase activity in presence of  $\text{H}_2\text{O}_2$  and combination probe **QCy-BOH**-Drew-AT. (b) Fluorescence intensity of **QCy-BOH** at 565 nm. Where **Q**: **QCy-BOH**, **QH**: **QCy-BOH**+ $\text{H}_2\text{O}_2$ , **QHD**: **QCy-BOH**+ $\text{H}_2\text{O}_2$ +Drew-AT, **QCH**: **QCy-BOH**+Catalase+ $\text{H}_2\text{O}_2$ , **QCHD**: **QCy-BOH**+Catalase+ $\text{H}_2\text{O}_2$ +Drew-AT. (c) Time dependent fluorescence of combination probe **QCy-BOH**-Drew-AT in presence and absence of catalase upon addition of  $\text{H}_2\text{O}_2$  ( $1\ \text{mM}$ ) upon excitation at 564 nm.

Catalase is one of the most efficient enzymes that convert  $\text{H}_2\text{O}_2$  to water and oxygen to protect cells from oxidative damage and ROS. Catalase exhibits highest turnover number for  $\text{H}_2\text{O}_2$  and capable of decomposing almost  $10^6$  molecules per second to water and oxygen. The fluorescence emission was not observed at 650 nm upon addition of  $\text{H}_2\text{O}_2$  (1 mM) to a solution of **QCy-BOH**-Drew-AT (2  $\mu\text{M}$ ) containing catalase (4 U/mL). The seized fluorescence emission at 650 nm is owing to prevention of **QCy-BOH** to **QCy-DT** conversion, as the added  $\text{H}_2\text{O}_2$  is used as a substrate by the catalase (Figure 16). These results validate that our combination probe **QCy-BOH**-Drew-AT is a promising molecular tool for monitoring the *in situ* turnover of  $\text{H}_2\text{O}_2$  involving oxidase and catalases.

#### 4.7 Fluorescence imaging and cytotoxicity studies of **QCy-BOH** in presence of $\text{H}_2\text{O}_2$

Remarkable selectivity of **QCy-BOH** towards  $\text{H}_2\text{O}_2$  and its detection through switch-on NIR fluorescence assisted by DNA inspired us to evaluate the cellular uptake and spatiotemporal imaging of cell nucleus. For this purpose, confocal fluorescence imaging of HeLa cells treating with  $\text{H}_2\text{O}_2$  (exogenous) was carried out. First, the HeLa cells were incubated with **QCy-BOH** (5  $\mu\text{M}$ ) for 30 min and imaged under confocal microscope. Fluorescence images of HeLa cells showed weak fluorescence under blue channel and no emission in red channel (Figure 17a-c). **QCy-BOH** treated HeLa cells were then treating with  $\text{H}_2\text{O}_2$  (100  $\mu\text{M}$ ) for 15 min, confocal images of these cells showed strong fluorescence in the red channel with maximum localization in the cell nucleus (Figure 17d-e).

Interestingly, cells also showed the pattern of black nucleoli, a characteristic feature of specific DNA minor groove binders over single strand DNA and RNAs.<sup>69</sup> In a control study, experiments were performed in presence of dihydrodichloro-fluoresceindiacetate (DCFDA-H2) probe a known ROS maker in cells, under similar conditions. Upon addition of  $\text{H}_2\text{O}_2$  (100  $\mu\text{M}$ ), fluorescence images of cells showed green fluorescence throughout the cell without any specificity towards cell nucleus. This comparative study infers that probe **QCy-BOH** is a highly selective molecular tool specifically lights-up the nucleus in response to  $\text{H}_2\text{O}_2$  stimulus. In order to check the cytotoxicity of probe **QCy-BOH** cell viability assay was performed in HeLa cells.

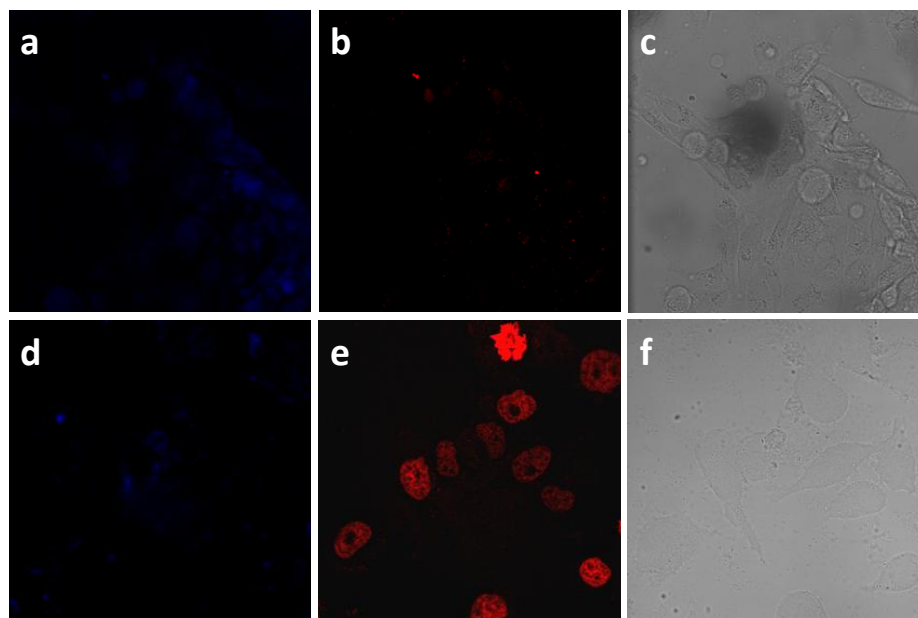


**Figure 17.** Cellular uptake of **QCy-BOH** and fluorescence reporting of  $\text{H}_2\text{O}_2$  in HeLa cells. (a-c) Fluorescence microscope images of HeLa cells incubated with **QCy-BOH** ( $5 \mu\text{M}$ ) in absence of  $\text{H}_2\text{O}_2$ . a: blue channel, b: red channel, c: differential interference contrast (DIC, bright field image). (d-f) Fluorescence microscope images of HeLa cells incubated with **QCy-BOH** ( $5 \mu\text{M}$ ) in presence of  $\text{H}_2\text{O}_2$  ( $100 \mu\text{M}$ ). d: blue channel, e: red channel, f: differential interference contrast (DIC, bright field image).

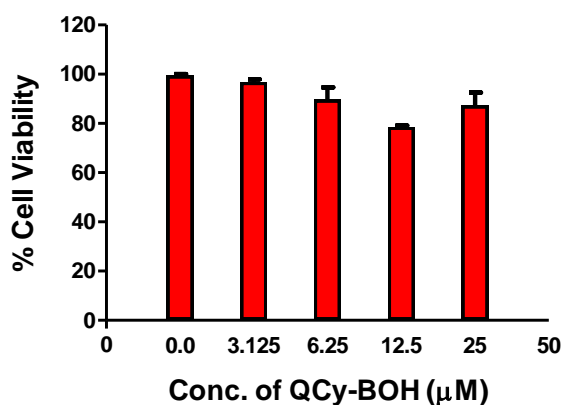


**Figure 18.** Dose dependent cell viability of HeLa cells by taking 0.0-25  $\mu\text{M}$  of probe **QCy-BOH** for 24 h. Error bars represent  $\pm$ standard deviation.

Upon incubation with **QCy-BOH**, more than 80 % of cells were viable even at 25  $\mu\text{M}$  concentration after 24 h (Figure 18). In general, above results confirm the permeability

and non-toxicity of **QCy-BOH**, and detection of exogenously added  $\text{H}_2\text{O}_2$  in HeLa cells through selective fluorescence staining of the cell nucleus.

#### 4.8 Probing of *in situ* generated $\text{H}_2\text{O}_2$ in live cells using **QCy-BOH**

NMR, photophysical study, GOx-assay and confocal fluorescence imaging of HeLa cells showed the detection of exogenously added  $\text{H}_2\text{O}_2$  using **QCy-BOH**. Next, we employed **QCy-BOH** for probing cellular (physiologically generated)  $\text{H}_2\text{O}_2$  levels, in live cells. HeLa cells were incubated with **QCy-BOH** ( $5\ \mu\text{M}$ ) for 30 min in absence and presence of N-acetyl-L-cysteine (NAC), a well-known  $\text{H}_2\text{O}_2$  scavenger.<sup>70</sup> In absence of NAC, flow cytometry analysis of cells treated with **QCy-BOH** ( $5\ \mu\text{M}$ ) showed an increase in mean fluorescence intensity of PerCP compare to control cells (Figure 19).

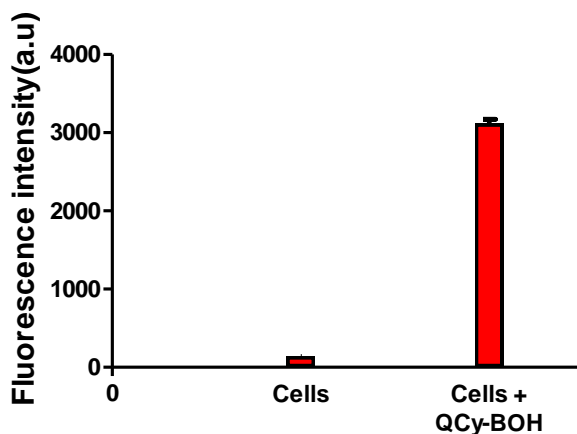


**Figure 19.** FACS/flow cytometry analysis show the PerCP mean fluorescence intensity in HeLa cells in presence of **QCy-BOH** ( $5\ \mu\text{M}$ ).

Upon addition of NAC ( $8\ \text{mM}$ ), fluorescence intensity of PerCP decreased significantly. In a control experiment, flow cytometry analysis of live HeLa cells treated with **QCy-BOH** and  $\text{H}_2\text{O}_2$  ( $100\ \mu\text{M}$ ) for 15 min at  $37\ ^\circ\text{C}$  showed increase in mean fluorescence intensity of PerCP (Figure 20a). Thus, probe **QCy-BOH** is capable of detecting the cellular  $\text{H}_2\text{O}_2$  levels in live cells. Further, our study was extended to visualize the *in situ*  $\text{H}_2\text{O}_2$  generation by a known signaling pathway, in live cells. We selected well-known epidermal growth factor (EGF) binding to epidermal growth factor receptors (EGFR) signaling pathway which stimulates the production of  $\text{H}_2\text{O}_2$  in cells by activating the Nox/PI3K pathways.<sup>27</sup> In

this experiment, live HeLa cells were incubated with epidermal growth factor (EGF) (500 ng/mL) for 1 h under physiological conditions (37 °C, pH = 7.4). EGF treated live HeLa cells were incubated with **QCy-BOH** (5  $\mu$ M) for 30 min and flow cytometry analysis of these cells showed strong fluorescence intensity in the PerCP region (Figure 20b). On the other hand, the control experiment performed on live HeLa cells without EGF showed modest fluorescence due to the presence of cellular H<sub>2</sub>O<sub>2</sub> level. In contrast, NAC treated cells showed decrease in the fluorescence in presence of EGF (Figure 20b). These results provided concrete evidence that **QCy-BOH** is a versatile and practically viable molecular probe for monitoring concentration levels of H<sub>2</sub>O<sub>2</sub> in live cells under normal diseased conditions.

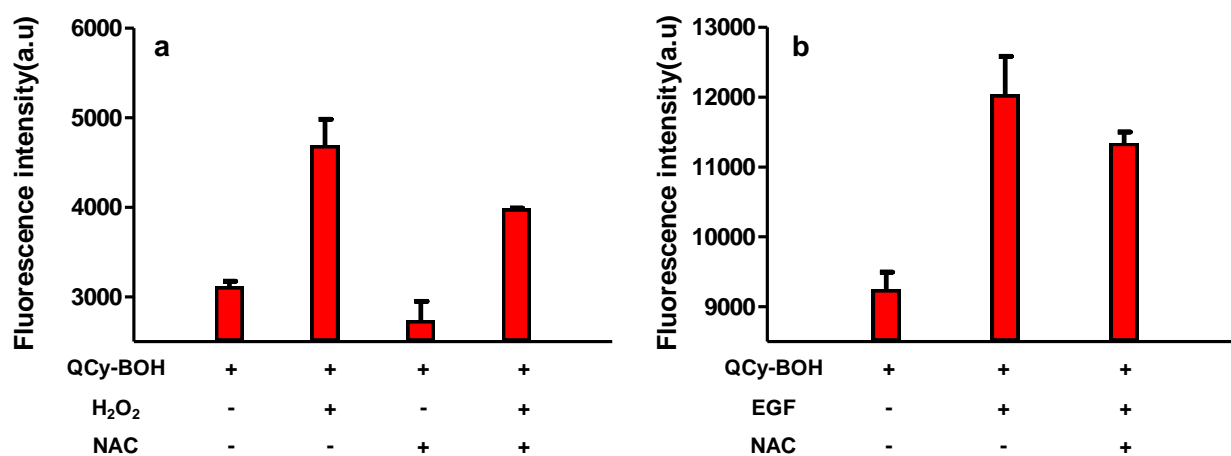


**Figure 20.** FACS/flow cytometry analysis show the PerCP mean fluorescence intensity in HeLa cells. (a) Fluorescence intensity of **QCy-BOH** in HeLa cells upon addition of H<sub>2</sub>O<sub>2</sub> and N-acetyl-L-cysteine (NAC). (b) Fluorescence intensity of **QCy-BOH** in HeLa cells upon addition of epithelial growth factor (EGF) and N-acetyl-L-cysteine (NAC). Error bars represent  $\pm$  standard deviation.

#### 4.9 Conclusion

In conclusion, we developed a stimuli responsive, switch-on NIR-fluorescence probe (**QCy-BOH** in combination with AT-rich DNA (Drew-AT)) for H<sub>2</sub>O<sub>2</sub>. In **QCy-BOH**, the phenyl boronic acid functionality effectively mask the NIR fluorescence of **QCy-DT** a DNA minor groove binder and restored selectively in presence of H<sub>2</sub>O<sub>2</sub>. NMR and UV-vis absorption study showed selective conversion of **QCy-BOH** to **QCy-DT** and quinine methide in



response to  $\text{H}_2\text{O}_2$  while the solution color changes from yellow to brown for naked eye detection of  $\text{H}_2\text{O}_2$  over other ROS. Fluorescence study demonstrated selective conversion of **QCy-BOH** to **QCy-DT** in response to  $\text{H}_2\text{O}_2$  stimulus which showed NIR fluorescence in presence of AT-rich DNA duplex (Drew-AT). Further, glucose oxidase assay confirmed the use of combination probe **QCy-BOH**⊂Drew-AT for probing *in situ* generated  $\text{H}_2\text{O}_2$  by the oxidation of glucose to gluconic acid. Cell viability and confocal fluorescence imaging of HeLa cells showed the cell permeability, non-toxicity and preferential nuclear staining selectively in presence of  $\text{H}_2\text{O}_2$  (Figure 21). Furthermore, **QCy-BOH** is sensitive probe to detect normal and *in situ* generated level  $\text{H}_2\text{O}_2$  by EGF/Nox pathways in live cells. We anticipated that our approach of conjugating DNA fluorescence probes with stimuli responsive appendages open up a new approach in the development of DNA targeting theranostic prodrugs for spatiotemporal targeting of disease related cells. This approach can be further expanded to create new stimuli responsive probes for various biochemical processes including enzymatic activities.

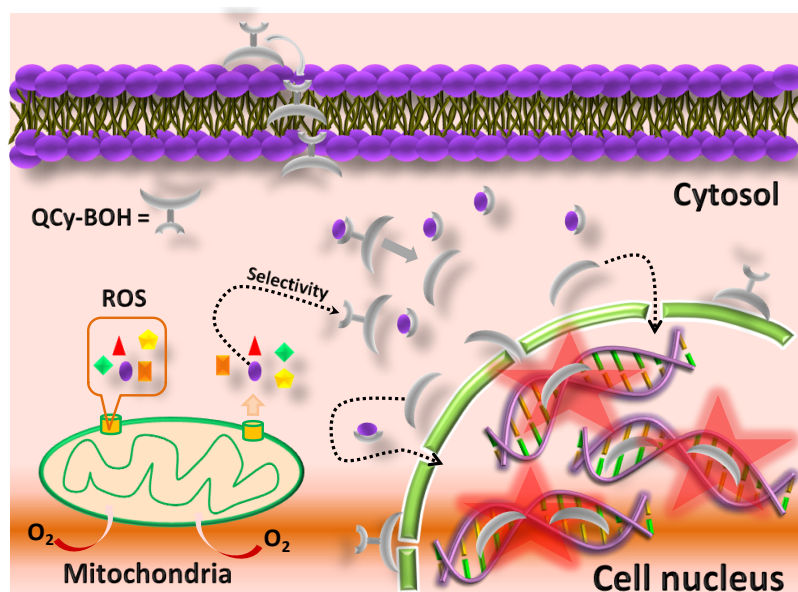


**Figure 21.** Schematic representation of hydrogen peroxide triggered NIR-fluorescent DNA-minor groove binder **QCy-BOH**.

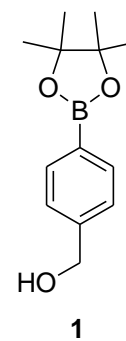
#### 4.10 Experimental Section

**General information.** All the chemicals, reagents, self complementary Drew-AT, Hoechst 33258, Phosphate buffer saline (PBS) and N-acetyl-L-Cysteine (NAC) were purchased from Sigma-Aldrich. All compounds were purified column chromatography using Rankem silica gel (60-120 mesh).  $^1\text{H}$  and  $^{13}\text{C}$ -NMR spectra were recorded on a Bruker AV-400 MHz spectrometer with chemical shifts reported as parts per million (*ppm*) (in  $\text{CDCl}_3$ ,  $\text{DMSO-d}_6$ , tetramethylsilane as an internal standard) at 20 °C. High resolution Mass spectra (HRMS) were obtained on Agilent Technologies 6538 UHD Accurate-Mass Q-TOF LC/MS spectrometer. The UV-vis absorption and emission spectra were recorded on Agilent Technologies Cary series UV-vis-NIR absorbance and Cary eclipse fluorescence spectrophotometers respectively. UV-vis absorption and emission spectra were measured in quartz cuvettes of 1 cm path length.

#### Synthetic procedures for QCy-BOH

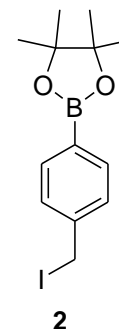
##### Preparation of (4-(4,4,5,5-tetramethyl-1,3,2-dioxaborolan-2-yl)phenyl)methanol (1)

(1). To a stirred solution of 4-(hydroxymethyl)phenylboronic acid (0.4 g, 2.63 mmol) in acetonitrile (15 mL),  $\text{MgSO}_4$  (3 g) and pinacol (0.37 g, 3.156 mmol) were added. The reaction mixture was heated up to 80 °C and allowed to reflux for 24 h. After the completion of reaction, solvent was evaporated under vacuum. The crude mixture was dissolved in dichloromethane and filtered. The obtained product (4-(4,4,5,5-tetramethyl-1,3,2-dioxaborolan-2-yl)phenyl)methanol (1) was used without further purification.



##### Preparation of 2-(4-(iodomethyl)phenyl)-4,4,5,5-tetramethyl-1,3,2-dioxaborolane (2)

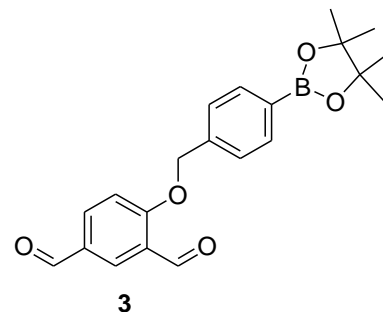
(2). To a stirred solution of (4-(4,4,5,5-tetramethyl-1,3,2-dioxaborolan-2-yl)phenyl)methanol (1) (0.55 g, 2.35 mmol) in acetonitrile (20mL), sodium iodide (1.056 g, 7.047 mmol) and Trimethylsilyl chloride (0.65 mL, 7.047 mmol) were added at 0 °C. The reaction mixture was allowed to stir at room temperature for 1 h. After the completion of reaction solvent was evaporated under vacuum. The crude product was dissolved in saturated solution of  $\text{Na}_2\text{S}_2\text{O}_3$  to quench the unreacted iodide and the product was extracted with dichloromethane. The crude product was purified by



column chromatography on silica gel using ethyl acetate\hexane (5:95) as an eluent to give product 2-(4-(iodomethyl)phenyl)-4,4,5,5-tetramethyl-1,3,2-dioxaborolane (**2**) in good yield, 90%.  $^1\text{H-NMR}$  (400 MHz,  $\text{CDCl}_3$ )  $\delta_{ppm}$  7.73 (d,  $J = 8$  Hz, 2H), 7.37 (d,  $J = 8$  Hz, 2H), 4.45 (s, 2H), 1.34 (s, 12H).  $^{13}\text{C-NMR}$  (100 MHz,  $\text{CDCl}_3$ )  $\delta_{ppm}$  142.3, 135.3, 128.0, 24.9, 5.4

**Preparation of 4-(4-(4,4,5,5-tetramethyl-1,3,2-dioxaborolan-2-yl)benzyloxy)isophthalaldehyde (**3**).**

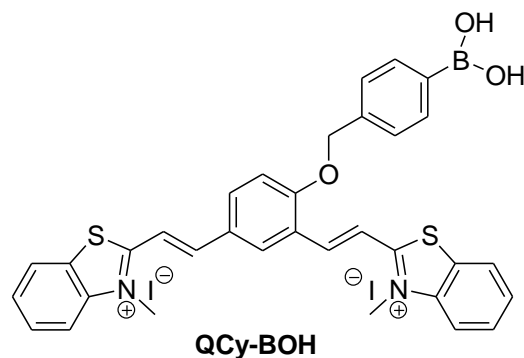
To a stirred solution of 4-hydroxyisipthalaldehyde (0.11 g, 0.73 mmol) in DMF (5 mL),  $\text{K}_2\text{CO}_3$  (0.3 g, 2.17 mmol) was added and allowed to stir for 20 minutes. After 20 minutes, 2-(4-(iodomethyl)phenyl)-4,4,5,5-tetramethyl-1,3,2-dioxaborolane



(**2**) (0.3 g, 0.87 mmol) was added and stir for overnight at room temperature. The completion of reaction was monitored by TLC. After completion of reaction, solvent was evaporated and product was extracted with diethylether ( $3 \times 100$  mL). The crude product was purified by column chromatography on silica gel using ethyl acetate\hexane (20:80) as an eluent to obtained compound **3** in good yield 60%.  $^1\text{H-NMR}$  (400 MHz,  $\text{CDCl}_3$ )  $\delta_{ppm}$  10.56 (s, 1H), 9.95 (s, 1H), 8.35 (d,  $J = 2.4$  Hz, 1H), 8.08 (dd,  $J = 2$  Hz, 8.8 Hz, 1H), 7.86 (d,  $J = 8$  Hz, 2H), 7.44 (d,  $J = 8$  Hz, 2H), 7.17 (d,  $J = 8$  Hz, 1H), 5.32 (s, 2H), 1.35 (s, 12H).  $^{13}\text{C-NMR}$  (100 MHz,  $\text{CDCl}_3$ )  $\delta_{ppm}$  190.1, 188.5, 164.9, 137.9, 135.5, 135.3, 131.9, 129.9, 126.5, 125.2, 113.7, 84.0, 71.0, 24.9

**Preparation of QCy-BOH.**

To a stirred solution of 2-methyl benzothiazole (7.0 mmol) in dichloromethane (10 mL), methyl iodide (14.0 mmol) was added dropwise and allowed to reflux overnight. Completion of the reaction was monitored by thin layer chromatography (TLC). After completion of the reaction, a white colored precipitate was formed. The precipitate was



filtered and washed with copious amount of diethyl ether for removing the unreacted benzothiazole. The obtained product (N-methyl-2-methylbenzothiazole) (**4**)<sup>55</sup> was dried under vacuum and used for the next reaction without further purification.

To a stirred solution of compound (**4**)<sup>1</sup> (80 mg, 0.27 mmol) in methanol (10 mL) and dichloromethane (5 mL), piperidine (8  $\mu$ L) was added and allowed to stir for 10 minutes. After 10 min, 4-(4-(4,4,5,5-tetramethyl-1,3,2-dioxaborolan-2-yl)benzyloxy)isophthalaldehyde (**3**) (45 mg, 0.12 mmol) in DCM (2 mL) was added and heated up to 50 °C for 3 h. After the completion of reaction solvent was evaporated. The crude brown color solid was washed with diethylether (50 mL) to remove the unreacted starting materials. The brown solid was dissolved in acetonitrile/water mixture and purified by reverse phase HPLC using 0.1% trifluoroacetic acid (TFA) in water/acetonitrile (50-100%) as a mobile phase. However, boronic ester was converted to boronic acid conjugate (**QCy-BOH**) while doing HPLC in moderate yield 30%. <sup>1</sup>H-NMR (400 MHz, *DMSO-d*<sub>6</sub>)  $\delta_{ppm}$  8.69 (d, *J* = 2Hz, 1H), 8.44 (ddd, *J* = 2.8 Hz, *J* = 4.0 Hz, *J* = 7.6 Hz, 2H), 8.34-8.25 (m, 4H), 8.21 (d, *J* = 4.2 Hz, 1H), 8.16 (d, *J* = 12.4 Hz, 1H), 8.10 (d, *J* = 8.2 Hz, 1H), 7.92-7.88 (m, 4H), 7.81 (td, *J* = 0.8 Hz, *J* = 7.6 Hz, 2H), 7.56 (dd, *J* = 4 Hz, *J* = 8.4 Hz, 3H), 5.48 (s, 2H), 4.39 (s, 3H), 4.25 (s, 3H). <sup>13</sup>C-NMR (100 MHz, *DMSO-d*<sub>6</sub>)  $\delta_{ppm}$  171.9, 171.8, 160.6, 158.3, 158.0, 147.0, 142.1, 142.0, 141.6, 137.5, 135.0, 134.5, 132.3, 129.5, 129.4, 128.6, 128.4, 127.9, 127.8, 127.3, 127.0, 124.3, 124.2, 123.1, 118.1, 117.0, 116.9, 115.6, 115.1, 114.4, 113.0, 71.0, 36.4, 36.2. HRMS (ESI-MS): found 288.0875, calcd *m/z* = 288.0851 for C<sub>33</sub>H<sub>29</sub>BN<sub>2</sub>O<sub>3</sub>S<sub>2</sub> [M-2I]<sup>2+</sup>.

**Sample preparation for UV-vis and fluorescence measurements.** Stock solution of probe **QCy-BOH** was prepared in milli molar concentration in milli Q-water (MQ-water) and stored at -10 °C. DNA-stock solutions were prepared by dissolving oligo samples in double distilled water in the order of 10<sup>-4</sup> M. Double stranded DNA samples were prepared in PBS (10 mM, pH = 7.4) buffer solution and subjected annealing by heating up to 85 °C for 15 min and subsequently cooled to room temperature for 7h and stored in refrigerator for 4h.

**HeLa cells maintenance.** Human cervix carcinoma cell line (HeLa) was cultured in DMEM (Dulbecco's Modified Eagle's Medium) with 10 % FBS (Fetal Bovine Serum). The antibiotics Pencilin and Streptomycin (1 %) was mixed with 10 % FBS medium. The cells were incubated at 37 °C temperature and 5 % CO<sub>2</sub> humidified chamber. All cell culture work was carried out under laminar flow hood and auspicious conditions.

**Cytotoxicity studies on HeLa cells (MTT Assay).** MTT [(3-(4,5-dimethylthiazol-2-yl)-2,5-diphenyltetrazolium bromide] assay was carried out with probe **QCy-BOH** on HeLa cells to determine the cytotoxicity effect. In a tissue cultured 96-well plate, 10,000 cells per well were plated and incubated for 24 h cells to attach. After completion of 24 h incubation, the attached and healthy cells were treated with various concentrations (25  $\mu\text{M}$ , 12.5  $\mu\text{M}$ , 6.25  $\mu\text{M}$ , 3.125  $\mu\text{M}$  and 0  $\mu\text{M}$ ) of probe **QCy-BOH** and further incubated for 24 h. All the treatments were carried out in triplicates. The required concentrations of **QCy-BOH** were made from stock solution in 0.2% DMEM. Stock solution of probe **QCy-BOH** (1 mg/mL) was made in water. Four hours before stipulated time of experiment, MTT-solution (5 mg/mL of 20  $\mu\text{L}$ ) was added in each well and incubated to form formazan crystals. The culture medium was completely removed by 1 mL pipette and 200  $\mu\text{L}$  of DMSO was added to dissolve formazan crystals. The purple colored formazan was estimated by determining absorbance at 590 nm with the help of spectrophotometer (Bio-RAD model 1680, Microplate reader). The results were shown in bar graphs (concentration of **QCy-BOH** vs % cell viability).

**Exogenous and endogenous detection of  $\text{H}_2\text{O}_2$  in HeLa cells by QCy-BOH.** In each well,  $3 \times 10^6$  cells were plated in 12-well tissue culture plates and incubated for 24 h. These cells were serum deprived for 1 h. In addition, the serum deprived cells of 6-well were treated with N-acetyl-L-cysteine (NAC) (8 mM) solution and incubated for 1 h and probe **QCy-BOH** (5  $\mu\text{M}$ ) was treated to cells and incubated for 30 min. After 30 min incubation of cells with probe **QCy-BOH**, the cells were washed with DPBS (Dulbecco's Phosphate buffer saline) to remove the excesses of **QCy-BOH**. These cells were harvested after trypsinization. Exogenously,  $\text{H}_2\text{O}_2$  (100  $\mu\text{M}$ ) was added to **QCy-BOH** and NAC + **QCy-BOH** treated cells and incubated for 15 min. These samples were subjected to FACS.

**Epidermal Growth Factor (EGF) produced  $\text{H}_2\text{O}_2$  detection by QCy-BOH in HeLa cells.**<sup>27</sup> To determine the EGF produced ROS in cells by **QCy-BOH**. In a 12-well plate,  $3 \times 10^6$  HeLa cells were plated in each well and incubated for 24 h. These cells were serum deprived for 1h. Cells were incubated with epidermal growth factor (EGF) (500 ng/mL) for 40 min and further treated with NAC (8 mM) for 1 h. Then cells were treated with **QCy-BOH** (5  $\mu\text{M}$ ) for 30 min. After 30 min incubation of cells with **QCy-BOH**, cells were

washed with DPBS (Dulbecco's Phosphate Buffer Saline) to remove the excesses of **QCy-BOH**. These cells were harvested after trypsinization. The samples were subjected to FACS.

**Immuno fluorescence studies with QCy-BOH for detection of exogenous and endogenous H<sub>2</sub>O<sub>2</sub> in HeLa cells.** An Immuno fluorescence studies were carried out on HeLa cells to validate exogenous and endogenous detection of H<sub>2</sub>O<sub>2</sub> by **QCy-BOH**. The HeLa cells (10,000 cells) were grown on cover slips. These cells were treated with 5 μM concentration of **QCy-BOH** for 30 min. The cells were washed with DPBS for several times to remove the excesses of **QCy-BOH**. The cells were treated with H<sub>2</sub>O<sub>2</sub> (100 μM) for 30 min. These samples were subjected to confocal microscopy for immune fluorescence images.

#### 4.11 References

1. Winterbourn, C. C. Reconciling the chemistry and biology of reactive oxygen species. *Nat. Chem. Biol.* **2008**, *4*, 278 – 286.
2. Ray, P. D.; Huang, B.-W.; Tsuji, Y. Reactive oxygen species (ROS) homeostasis and redox regulation in cellular signaling. *Cell Signal.* **2012**, *24*, 981 – 990.
3. Cairns, R. A.; Harris, I. S.; Mak, T. W. Regulation of cancer cell metabolism. *Nature Rev. Cancer* **2011**, *11*, 85–95.
4. Gorrini, C.; Harris, I. S.; Mak, T. W. Modulation of oxidative stress as an anticancer strategy. *Nat. Rev. Drug Discovery* **2013**, *12*, 931– 947.
5. Sztatowski, T. P.; Nathan, C. F. Production of large amounts of hydrogen peroxide by human tumor cells. *Cancer Res.* **1991**, *51*, 794-798.
6. Toyokuni, S.; Okamoto, K.; Yodoi, J.; Hiai, H. Persistent oxidative stress in cancer. *FEBS Lett.* **1995**, *358*, 1-3.
7. Mishra, K. P. Cell membrane oxidative damage induced by gamma-radiation and apoptotic sensitivity. *J. Environ. Pathol. Toxicol. Oncol.* **2004**, *23*, 61-66.
8. Kawanishi, S.; Hiraku, Y.; Pinlaor, S.; Ma, N. Oxidative and nitrative DNA damage in animals and patients with inflammatory diseases in relation to inflammation-related carcinogenesis. *Biol. Chem.* **2006**, *387*, 365-372.
9. Schafer, F. Q.; Buettner, G. R. Redox environment of the cell as viewed through the redox state of the glutathione disulfide/glutathione couple. *Free Radic Biol. Med.* **2001**, *30*, 1191–1212.

10. Boonstra, J.; Post, J. A. Molecular events associated with reactive oxygen species and cell cycle progression in mammalian cells. *Gene* **2004**, *337*, 1–13.
11. Murphy, M. P.; Holmgren, A.; Larsson, N.-G.; Halliwell, B.; Chang, C. J.; Kalyanaraman, B.; Rhee, S. G.; Thornalley, P. J.; Gems, D.; Nyström, T.; Belousov, V.; Schumacker, P. T.; Winterbourn, C. C. Unraveling the biological roles of reactive oxygen species. *Cell Metab.* **2011**, *13*, 361–366.
12. Perry, G.; Raine, K. A.; Nunomura, A.; Watayc, T.; Sayre, L. M.; Smith, M. A. How important is oxidative damage? Lessons from Alzheimer's disease. *Free Radic Biol. Med.* **2001**, *28*, 831–834.
13. Halliwell, B.; Gutteridge, J. M. C. *Free Radicals in Biology and Medicine*, Oxford University Press, Oxford, **2007**, 1–677.
14. Lin, M. T.; Beal, M. F. Mitochondrial dysfunction and oxidative stress in neurodegenerative diseases. *Nature* **2006**, *443*, 787–795.
15. Houstis, N.; Rosen, E. D.; Lander, E. S. Reactive oxygen species have a causal role in multiple forms of insulin resistance. *Nature* **2006**, *440*, 944–948.
16. Jay, D.; Hitomi, H.; Griendling, K. K. Oxidative stress and diabetic cardiovascular complications. *Free Radical Biol. Med.* **2006**, *40*, 183–192.
17. Fruehauf, J. P.; Meysken, F. L. Jr. Reactive oxygen species: a breath of life or death?. *Clin. Cancer Res.* **2007**, *448*, 789–794.
18. Finkel, T.; Serrano, M.; Blasco, M. A. The common biology of cancer and ageing. *Nature* **2007**, *448*, 767–774.
19. Trachootham, D.; Alexandre, J.; Huang, P. Targeting cancer cells by ROS-mediated mechanisms: a radical therapeutic approach?. *Nat. Rev. Drug Discov.* **2009**, *8*, 579–591.
20. Chance, B.; Sies, H.; Boveris, A. Hydroperoxide metabolism in mammalian organs. *Physiol. Rev.* **1979**, *59*, 527–605.
21. Lopez-Lazaro, M. Dual role of hydrogen peroxide in cancer: possible relevance to cancer chemoprevention and therapy. *Cancer Lett.* **2007**, *252*, 1–8.
22. Rhee, S.G. Cell signaling. H<sub>2</sub>O<sub>2</sub>, a necessary evil for cell signaling. *Science* **2006**, *312*, 1882–1883.
23. Schmidt, K. N.; Amstad, P.; Cerutti, P.; Baeuerle, P.A. The roles of hydrogen peroxide and superoxide as messengers in the activation of transcription factor NF-kappa B. *Chem. Biol.* **1995**, *2*, 13–22.
24. Kimura, T.; Okajima, F.; Sho, K.; Kobayashi, I.; Kondo, Y. Thyrotropin-induced hydrogen peroxide production in FRTL-5 thyroid cells is mediated not by adenosine 3',5'-monophosphate,

- but by Ca<sup>2+</sup> signaling followed by phospholipase-A2 activation and potentiated by an adenosine derivative. *Endocrinology* **1995**, *136*, 116–123.
25. Sundaresan, M.; Yu, Z. X.; Ferrans, V. J.; Irani, K.; Finkel, T. Requirement for generation of H<sub>2</sub>O<sub>2</sub> for platelet-derived growth factor signal transduction. *Science* **1995**, *270*, 296–299.
26. Guyton, K. Z.; Liu, Y.; Gorospe, M.; Xu, Q.; Holbrook, N. J. Activation of mitogen-activated protein kinase by H<sub>2</sub>O<sub>2</sub>. Role in cell survival following oxidant injury. *J. Biol. Chem.* **1996**, *271*, 4138–4142.
27. Bae, Y. S.; Kang, S. W.; Seo, M. S.; Baines, I. C.; Tekle, E.; Chock, P. B.; Rhee, S. G. Epidermal growth factor (EGF)-induced generation of hydrogen peroxide. Role in EGF receptor-mediated tyrosine phosphorylation. *J. Biol. Chem.* **1997**, *272*, 217–221.
28. Lee, S. R.; Kwon, K. S.; Kim, S. R.; Rhee, S. G. Reversible inactivation of protein-tyrosine phosphatase 1B in A431 cells stimulated with epidermal growth factor. *J. Biol. Chem.* **1998**, *273*, 15366–15372.
29. Mukhin, Y. V.; Garnovskaya, M. N.; Collinsworth, G.; Grewal, J. S.; Pendergrass, D.; Nagai, T.; Pinckney, S.; Greene, E. L.; Raymond, J. R. 5-Hydroxytryptamine<sub>1A</sub> receptor/Gibetagamma stimulates mitogen-activated protein kinase via NAD(P)H oxidase and reactive oxygen species upstream of src in chinese hamster ovary fibroblasts. *Biochem. J.* **2000**, *347*, 61–67.
30. Avshalumov, M. V.; Rice, M. E. Activation of ATP-sensitive K<sup>+</sup> (K(ATP)) channels by H<sub>2</sub>O<sub>2</sub> underlies glutamate-dependent inhibition of striatal dopamine release. *Proc.Natl. Acad. Sci. USA* **2003**, *100*, 11729–11734.
31. Wood, Z. A.; Poole, L. B.; Karplus, P. A. Peroxiredoxin evolution and the regulation of hydrogen peroxide signaling. *Science* **2003**, *300*, 650–653.
32. Lee, J.W.; Helmann, J. D. The PerR transcription factor senses H<sub>2</sub>O<sub>2</sub> by metal-catalysed histidine oxidation. *Nature* **2006**, *440*, 363–367.
33. Miller, E. W.; Albers, A. E.; Pralle, A.; Isacoff, E. Y.; Chang, C. J. Boronate-based fluorescent probes for imaging cellular hydrogen peroxide. *J. Am. Chem. Soc.* **2005**, *127*, 16652–16659.
34. Dickinson, B. C.; Chang, C. J. A targetable fluorescent probe for imaging hydrogen peroxide in the mitochondria of living cells. *J. Am. Chem. Soc.* **2008**, *130*, 9638-9639.
35. Dickinson, B. C.; Huynh, C.; Chang, C. J. A palette of fluorescent probes with varying emission colors for imaging hydrogen peroxide signaling in living cells. *J. Am. Chem. Soc.* **2010**, *132*, 5906-5915.
36. Dickinson, B. C.; Tang, Y.; Chang, Z.; Chang, C. J. A nuclear-localized fluorescent hydrogen peroxide probe for monitoring sirtuin-mediated oxidative stress responses in vivo. *Chem. Biol.* **2011**, *18*, 943–948.



37. Lippert, A. R.; Van de Bittner, G. C.; Chang, C. J. Boronate oxidation as a bioorthogonal reaction approach for studying the chemistry of hydrogen peroxide in living systems. *Acc. Chem. Res.* **2011**, *44*, 793–804.
38. Chan, J.; Dodani, S. C.; Chang, C. J. Reaction-based small-molecule fluorescent probes for chemoselective bioimaging. *Nat. Chem.* **2012**, *4*, 973–984.
39. Miller, E. W.; Tulyathan, O.; Isacoff, E. Y.; Chang, C. J. Molecular imaging of hydrogen peroxide produced for cell signaling. *Nat. Chem. Biol.* **2007**, *3*, 263–267.
40. Van de Bittner, G. C.; Bertozzi, C. R.; Chang, C. J. Strategy for dual-analyte luciferin imaging: in vivo bioluminescence detection of hydrogen peroxide and caspase activity in a murine model of acute inflammation. *J. Am. Chem. Soc.* **2013**, *135*, 1783–1795.
41. Weinstein, R.; Savariar, E. N.; Felsen, C. N.; Tsien, R. Y. In vivo targeting of hydrogen peroxide by activatable cell-penetrating peptides. *J. Am. Chem. Soc.* **2014**, *136*, 874–877.
42. Caamaño, A. M.; Vázquez, M. E.; Martínez-Costas, J.; Castedo, L.; Mascareñas, J. L. A light-modulated sequence-specific DNA-binding peptide. *Angew. Chem. Int. Ed.* **2000**, *39*, 3104–3107.
43. Rautio, J.; Kumpulainen, H.; Heimbach, T.; Oliyai, R.; Oh, D.; Järvinen, T.; Savolainen, J. Prodrugs: design and clinical applications. *Nat. Rev. Drug Discovery*, **2008**, *7*, 255–270.
44. Lee, H. M.; Larson, D. R.; Lawrence, D. S. Illuminating the chemistry of life: design, synthesis, and applications of "caged" and related photoresponsive compounds. *ACS Chem. Biol.* **2009**, *4*, 409–427.
45. Deiters, A. Principles and applications of the photochemical control of cellular processes. *ChemBioChem* **2010**, *11*, 47–53.
46. Sanchez, M. I.; Costas, J. M.; Gonzalez, F.; Bermudez, M. A.; Vazquez, M. E.; Mascareñas, J. L. In vivo light-driven DNA binding and cellular uptake of nucleic acid stains. *ACS Chem. Biol.* **2012**, *7*, 1276–1280.
47. Murat, P.; Gormally, M. V.; Sanders, D.; Antonio, M. D.; Balasubramanian, S. Light-mediated in cell downregulation of G-quadruplex-containing genes using a photo-caged ligand. *Chem. Commun.* **2013**, *49*, 8453–8455.
48. Sanchez, M. I.; Penas, C.; Vazquez, M. E.; Mascareñas, J. L. Metal-catalyzed uncaging of DNA-binding agents in living cells. *Chem. Sci.* **2014**, *5*, 1901–1907.
49. Hu, Q.; Gao, M.; Feng, G.; Liu, B. Mitochondria-targeted cancer therapy using a light-up probe with aggregation-induced-emission characteristics. *Angew. Chem., Int. Ed.* **2014**, *53*, 14225–14229.

50. Kumar, R.; Han, J.; Lim, H. J.; Ren, W. X.; Lim, J. Y.; Kim, J. H.; Kim, J. S. Mitochondrial induced and self-monitored intrinsic apoptosis by antitumor theranostic prodrug: in vivo imaging and precise cancer treatment. *J. Am. Chem. Soc.* **2014**, *136*, 17836-17843.
51. Kim, E.-J.; Bhuniya, S.; Lee, H.; Kim, H. M.; Cheong, C.; Maiti, S.; Hong, K. S.; Kim, J. S. An activatable prodrug for the treatment of metastatic tumors. *J. Am. Chem. Soc.* **2014**, *136*, 13888–13894.
52. Maity, D.; Raj, A.; Karthigeyan, D.; Kundu, T. K.; Govindaraju, T. Reaction-based probes for Co(II) and Cu(I) with dual output modes: fluorescence live cell imaging. *RSC Adv.* **2013**, *3*, 16788 – 16794.
53. Maity, D.; Govindaraju, T. A turn-on NIR fluorescence and colourimetric cyanine probe for monitoring the thiol content in serum and the glutathione reductase assisted glutathione redox process. *Org. Biomol. Chem.* **2013**, *11*, 2098-2104.
54. Maity, D.; Raj, A.; Samanta, P. K.; Karthigeyan, D.; Kundu, T. K.; Pati, S. K.; Govindaraju, T. A probe for ratiometric near-infrared fluorescence and colorimetric hydrogen sulfide detection and imaging in live cells. *RSC Adv.* **2014**, *4*, 11147-11151.
55. Narayanaswamy, N.; Kumar, M.; Das, S.; Sharma, R.; Samanta, P. K.; Pati, S. K.; Dhar, S. K.; Kundu, T. K.; Govindaraju, T. A thiazole coumarin (TC) turn-on fluorescence probe for AT-base pair detection and multipurpose applications in different biological systems. *Sci. Rep.* **2014**, *4*, 6476.
56. Narayanaswamy, N *et al.*, manuscript communicated.
57. Kuivila, H. G.; Armour, A. G. Electrophilic displacement reactions. IX. effects of substituents on rates of reactions between hydrogen peroxide and benzenboronic acid<sup>1-3</sup>. *J. Am. Chem. Soc.* **1957**, *79*, 5659-5662.
58. Yang, W. Q.; Gao, X.; Wang, B. H. In *Boronic Acids*; Hall, D. G., Ed.; Wiley-VCH: Weinheim, **2005**, 481-512.
59. Greenwald, R. B.; Pendri, A.; Conover, C. D.; Zhao, H.; Choe, Y. H.; Martinez, A.; Shum, K.; Guan, S. Drug delivery systems employing 1,4- or 1,6-elimination: poly(ethylene glycol) prodrugs of amine-containing compounds. *J. Med. Chem.* **1999**, *42*, 3657–3667.
60. Karton-Lifshin, N.; Segal, E.; Omer, L.; Portnoy, M.; Satchi-Fainaro, R.; Shabat, D. A unique paradigm for a Turn-ON near-infrared cyanine-based probe: noninvasive intravital optical imaging of hydrogen peroxide. *J. Am. Chem. Soc.* **2011**, *133*, 10960-10965.
61. Karton-Lifshin, N.; Albertazzi, L.; Bendikov, M.; Baran, P.S.; Shabat, D. "Donor-two-acceptor" dye design: a distinct gateway to NIR fluorescence. *J. Am. Chem. Soc.* **2012**, *134*, 20412–20420.

62. Kisin-Finfer, E.; Shabat, D. New repertoire of 'donor-two-acceptor' NIR fluorogenic dyes. *Bioorg. Med. Chem.* **2013**, *21*, 3602–3608.
63. Redy-Keisar, O.; Kisin-Finfer, E.; Ferber, S.; Satchi-Fainaro, R.; Shabat, D. Synthesis and use of QCy7-derived modular probes for the detection and imaging of biologically relevant analytes. *Nat. Protoc.* **2014**, *9*, 27-36.
64. Gnaim, S.; Shabat, D. Quinone-methide species, a gateway to functional molecular systems: from self-immolative dendrimers to long-wavelength fluorescent dyes. *Acc. Chem. Res.* **2014**, *47*, 2970–2984.
65. Chang, C.; Srikun, D.; Lim, C. S.; Chang, C. J.; Cho, B. R. A two-photon fluorescent probe for ratiometric imaging of hydrogen peroxide in live tissue. *Chem. Commun.* **2011**, *47*, 9618-9620.
66. Coll, M.; Frederick, C. A.; Wang, A. H. J.; Rich, A. A bifurcated hydrogen-bonded conformation in the d(A.T) base pairs of the DNA dodecamer d(CGCAAATTTGCG) and its complex with distamycin. *Proc. Natl. Acad. Sci. U.S.A* **1987**, *84*, 8385-8389.
67. Spink, N.; Brown, D. G.; Skelly, J. V.; Neidle, S. Sequence-dependent effects in drug-DNA interaction: the crystal structure of Hoechst 33258 bound to the d(CGCAAATTTGCG)<sub>2</sub> duplex. *Nucleic Acids Res.* **1994**, *22*, 1607-1612.
68. Vega, M. C.; Saez, I. G.; Aymami, J.; Eritja, R.; van der Marel, G. A.; van Boom, J. H.; Rich, A.; Coll, M. Three-dimensional crystal structure of the A-tract DNA dodecamer d(CGCAAATTTGCG) complexed with the minor-groove-binding drug Hoechst 33258. *Eur. J. Biochem.* **1994**, *222*, 721–726.
69. Spitzer, G. M.; Fuchs, J. E.; Markt, P.; Kirchmair, J.; Wellenzohn, B.; Langer, T.; Liedl, K. R. Sequence-specific positions of water molecules at the interface between DNA and minor groove binders. *Chemphyschem* **2008**, *9*, 2766–2771.
70. Winterbourn, C. C.; Metodiewa, D. Reactivity of biologically important thiol compounds with superoxide and hydrogen peroxide. *Free Radical Biol. Med.* **1999**, *27*, 322-328.

---

# Chapter 5

## Small Molecule and Proton Induced Non-Canonical DNA- Structures and their Significance

## Chapter 5a: Molecular Beacon based DNA-Switch for Accurate and Reversible pH Sensing

Intracellular pH is one of the most essential physiological factors that regulate many biological functions ranging from enzymatic catalysis, protein folding and degradation, membrane function as well as cell proliferation and apoptosis.<sup>1</sup> In a typical mammalian cell, lysosomes are important class of acidic organelles, they receive and degrade the biological macromolecules through the phagocytic, endocytic and autophagic pathways.<sup>2,3</sup> However, a small discrepancy of lysosomal pH results in dysfunction of cellular organelles. Furthermore, abnormal change in the intracellular pH leads to cellular dysfunction which is a typical hall mark of many disorders like cancer and Alzheimer's disease.<sup>4,5</sup> Therefore, it is crucial to monitor the intracellular pH in physiological and pathological processes.<sup>1,6-9</sup> There have been variety of techniques developed to measure the intracellular pH including H<sup>+</sup>-permeable microelectrodes, <sup>31</sup>P-NMR spectroscopy and optical (colorimetric and fluorometric) techniques.<sup>6-17</sup> Among all, fluorescence-based techniques have an advantage of monitoring the intracellular pH in spatiotemporal manner and in real-time.<sup>10,11</sup> Over the past few years, several fluorescence sensors have been reported for pH monitoring which includes small organic molecules, proteins and nanoparticles.<sup>12-17</sup> However, major drawbacks such as aqueous solubility, stability, broad range of pH and biocompatibility limits their usage in intracellular pH measurements. These drawbacks necessitated the need for the design and development of highly efficient and sensitive molecular scaffolds for the detection of intracellular pH. In this regard, DNA is an attractive molecular scaffold for sensing and diagnosis applications due to their unique molecular recognition, quick response time, efficiency over several cycles, biocompatibility and high sensitive to conformational changes induced by pH.<sup>18-23</sup> The high sensitivity and programmable nature of DNA inspired scientific community to design DNA based probes and nanodevices for sensing and diagnosis applications.<sup>24-28</sup> Notably, DNA nanotechnology is one such field which uses the simple but robust base-pairing code information to create complex molecular architectures in nanoscale dimension with high accuracy and precision.<sup>29-31</sup> These complex molecular architectures have been shown to be useful in numerous applications including *in vivo* imaging, diagnosis and drug delivery.<sup>32,33</sup>

As most of the aforementioned DNA architectures display conformational changes depending on specific protonation of nucleobases which results in the formation of non-canonical DNA structures including *i*-motifs,<sup>34</sup> inter and intramolecular triplexes,<sup>35</sup> DNA-tweezers<sup>36,37</sup> and A-motifs.<sup>38</sup> Inspired from the pH-dependent conformational switching behavior of DNA secondary structures several pH responsive molecular probes have been reported.<sup>39-42</sup> Interestingly, the majority of DNA based pH sensors utilized the conformation transition in the form of *i*-motif which works in the pH regime of 5.5-7.6.<sup>43-48</sup> Typically, *i*-motif sequence is a complementary sequence of quadruplex forming guanine (G)-rich human telomere.<sup>34</sup> Under acidic conditions hemi-protonation of cytosine (C) nucleobase drives the formation of non-canonical C-C<sup>+</sup> base pair which leads to the conformational change from a random coil to non-canonical tetraplex structure with promising stability.<sup>34</sup> Recently, Yamuna and coworkers have designed *i*-motif based molecular DNA-switch for the real time monitoring of intracellular pH.<sup>49-51</sup> This DNA-switch required four strands of cytosine rich tracts for *i*-motif transformation and reports pH in the range of 5.0 to 7.0.<sup>49-51</sup> However, it should be noted that most of the biological processes occurs under acidic conditions in living organisms are regulated through small pH variations (*i.e.*, 0.2-0.4 pH units).<sup>52</sup> Hence, it is a daunting task to design a molecular DNA devices or probes which are highly sensitive to slightest variations in pH viz., 0.2-0.4 units.

Similar to cytosine-rich sequence which undergo random coil to *i*-motif transformation, adenine (A)-rich polydeoxyadenylic acid (poly-dA<sub>n</sub>) or polyadenylic acid (poly-rA<sub>n</sub>) have attracted considerable attention due to their single-stranded to right-handed parallel duplex (A-motif) transformation at acidic conditions in very short time scale (milliseconds).<sup>38</sup> Under acidic conditions, the protonation of N<sup>1</sup>-position of adenine of poly adenine rich sequences triggers the formation of a non-canonical right handed parallel homoduplex of poly(dA)<sub>n</sub> strands (A-motif) held together by AH<sup>+</sup>-H<sup>+</sup>A reverse Hoogsteen hydrogen bonded base pairs and the positively charged N<sup>1</sup> further stabilized by electrostatic interactions with phosphate backbone.<sup>38</sup> Recently, random coil single-stranded poly(dA)<sub>n</sub> to A-motif transformation on gold nanoparticle has been reported as a colorimetric pH sensor with a sensitivity of 0.3 pH units.<sup>53,54</sup> To the best of our knowledge, there is no A-motif based pH sensor. The high sensitivity, quick response and easy accessibility of A-rich oligonucleotide motivated us to design a DNA-based device as a fluorescence sensor to

effectively report very small variations in the low pH regime. In the present study, we report a thoughtfully designed DNA device wherein A-rich molecular beacon (MB) transforms itself to A-motif under narrow acidic pH window. MB is a predesigned hairpin DNA structure functionalized with chromophores (e.g., donor and acceptor fluorophores for FRET-based measurements) on the 5'- and 3'-ends.<sup>55</sup> The loop contains probe sequence which is complementary to the target sequence or responsive to external stimuli (present work), stem contains the complementary Watson-Crick (WC) base pairs sequence at 5'- and 3'-end of hairpin structure. Depending on the target sequence or external stimuli, it switches between closed- and open-states and such structural transition leads to alterations in the proximity of donor and acceptor fluorophores. Over the past few years, MBs have been employed for various biological applications including miRNA detection and PCR-analysis.<sup>56-58</sup> Herein, our DNA-switch undergo reversible transformation between closed- (MB) and open (A-motif)-states in response to pH which clearly reflect in the fluorescence intensity ratios ( $I_D/I_A$ ) of donor (Cy3) and acceptor (Cy5) of **LMB**. Fluorescence and circular dichroism (CD) studies reveal that our DNA-switch (**LMB**) efficiently works in the pH regime of 3 to 5 with good sensitivity.

### 5.1 Design principle

Our **MB** consists of 24-nucleobases and adopt hairpin like structure (MB). In hairpin-like MB consists 12-consecutive A-bases are in the loop and five complementary base pairs each at b 5'- and 3'-ends forms the duplex stem structure (Table 1). The 5'- and 3'-ends of MB are labeled with Cy3 and Cy5 dyes as fluorescence reporting units respectively.

**Table 1.** Sequence information used in this study.

Code	Sequence
<b>LMB</b>	Cy3-5'-GACGCCAAAAAAAAAAAAACGCGTC-3'-Cy5
<b>UMB</b>	5'-GACGCCAAAAAAAAAAAAACGCGTC-3'
<b>CMB</b>	3'-CTGCGGTTTTTTTTTTTTCGCGAG-5'
<b>dA<sub>20</sub></b>	5'-AAAAAAAAAAAAAAAAAAAAA-3'

We opted for Cy3 (donor) and Cy5 (acceptor) combination because of their high fluorescence quantum yield, an efficient fluorescence resonance energy transfer (FRET) between them and more importantly their individual fluorescence is insensitive to acidic conditions (up to pH =3).<sup>59</sup> This pH (<5) insensitive nature of fluorophores (Cy3 and Cy5) circumvent one of the major drawback with most of the commonly reported fluorescence pH sensors which adversely affect the fluorescence and pH sensing applications. Under normal physiological conditions (pH = 7.2), our DNA-switch (**LMB**) exists in the hairpin-like structure *i.e.*, closed-state (MB). In closed-state, the predisposed close proximity of Cy3 (donor,  $\lambda_{em} = 570$  nm) and Cy5 (acceptor,  $\lambda_{ex} = 650$  nm) dyes in MB is appropriately placed for efficient FRET. In acidic conditions, adenine nucleobases undergo protonation at  $N^7$  ( $AH^+$ ) position which drive the transformation of closed MB-state to an open A-motif state [ $AH^+ \cdot H^+ A$ ]. Accordingly, closely positioned FRET pairs (Cy3 and Cy7) in MB-state move apart in the open A-motif state leading to decrease or suppression of FRET process (Figure 1). This pH dependent structural transformation and DNA-switching behavior of MB under acidic conditions is thoroughly characterized and investigated through the UV-vis absorption, fluorescence resonance energy transfer (FRET) between donor (Cy3) and acceptor (Cy5) and CD studies. Subsequently, we demonstrate the utility of our DNA-switch for accurate and reversible sensing of pH in the vesicles to mimic the artificial cell like environments and in live cells.

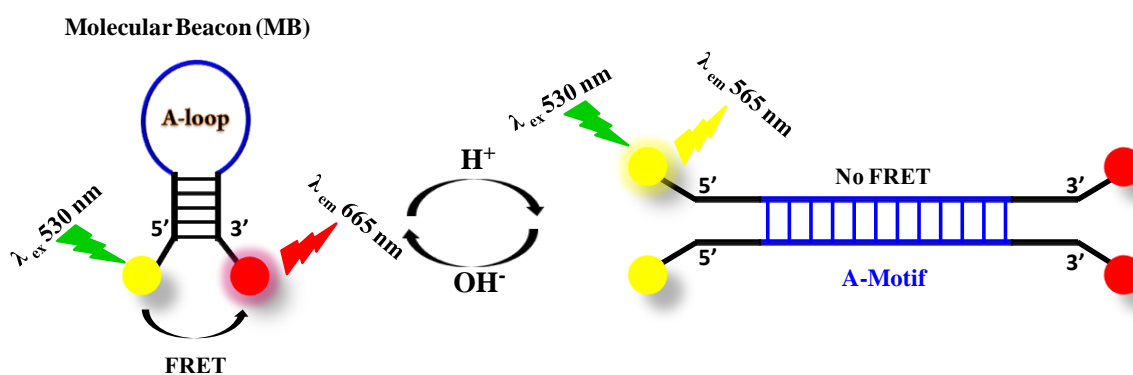


**Figure 1.** Schematic representation of pH triggered transformation from molecular beacon (MB) to non-canonical parallel right handed duplex (A-motif) structure.



## 5.2 Photophysical properties of Cy3 and Cy5 labeled DNA-switch

The pH dependent structural transformation of DNA-switch (**UMB** and **LMB**) from closed-state (MB) to open-state (A-motif) was studied by UV-vis absorption and fluorescence measurements in phosphate buffer solution (Na-PBS, 10 mM, pH = 7) under ambient conditions. The solution pH was varied by adding small aliquots of aq. HCl (1N) and aq. NaOH (1N). First, we measured the absorption spectra of **UMB** (Unlabeled MB) by decreasing solution pH from 7 to 3. **UMB** showed decrease in absorption intensity at 256 nm (nucleobase absorption) while a new shoulder band emerged at 285 nm, as the pH decreased from 7 to 3. This change in absorption behavior of **UMB** is well-corroborated with spectral features reported for A-motif forming poly(dA)<sub>n</sub> sequence (Figure 2a).<sup>38</sup> This clearly suggest the transformation of our DNA-switch (**UMB**) from closed-state (MB) to an open-state (A-motif). In order to study the reversibility of DNA-switch transformation from MB to A-motif, we recorded the absorption spectra of **UMB** in buffer (pH = 3) upon addition of small aliquots of aq. NaOH. Absorption spectra showed increase in intensity at 256 nm and disappearance of shoulder band at 285 nm indicating the reversibility of the molecular transformations between MB and A-motif (Figure 2b). Therefore, DNA-switch (**UMB**) can operate reversibly by switching between closed-state (MB) and open-state (A-motif) in the pH regime of 7 to 3.

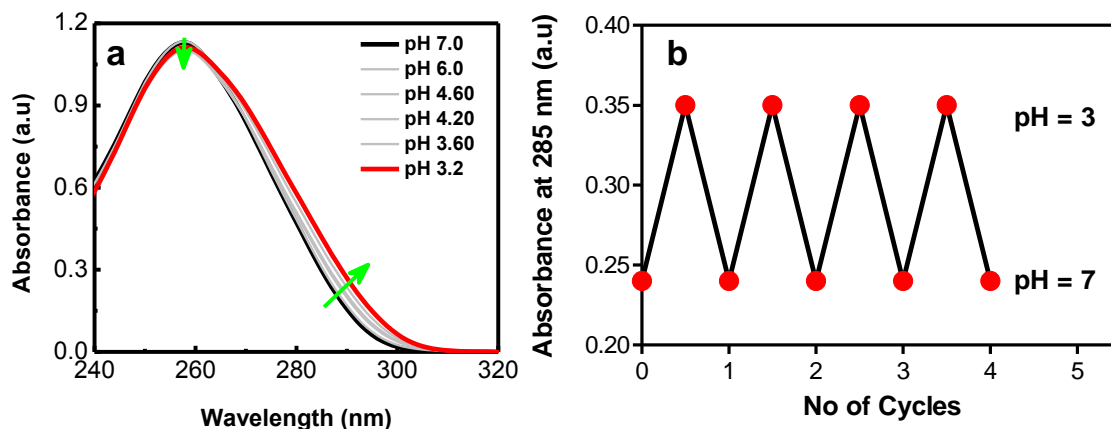


**Figure 2.** Absorption spectra of un-labeled DNA-switch (**UMB**). (a) Absorption spectra of **UMB** (4 μM) with decreasing pH from 7 to 3. (b) Graph represents the structural transformation of **UMB** (4 μM) from the closed state to open state by alternative addition of acid and base for several cycles in phosphate buffer solution.

Next, we recorded the absorption spectrum of Cy3 and Cy5 labeled DNA-switch (**LMB**) under neutral conditions at pH = 7. The spectrum showed absorption maxima at 260, 536 and 650 nm corresponding to nucleobase, Cy3 and Cy5 absorptions respectively (Figure 3). Upon excitation at 530 nm under neutral pH conditions fluorescence spectrum of **LMB** showed emission maxima at 565 and 665 nm corresponds to Cy3 and Cy5 respectively. As expected, maximum fluorescence intensity was observed for Cy5 compared to Cy3 which is attributed to FRET from Cy3 to Cy5. Therefore, it is evident from the emission study that DNA-switch (**LMB**) under neutral pH condition exists mostly in closed-state enabling the close proximity of donor and acceptor dyes facilitating efficient FRET between Cy3 and Cy5 (Figure 4a). We have calculated the FRET efficiency between Cy3 and Cy5 in a closed-state (MB) using the un-labeled complementary strands of UMB (CMB) in 10-fold excess to make sure that DNA switch mostly exists in open-state through the formation of duplex conformation. At neutral conditions (pH = 7) **LMB** showed FERT efficiency of 70-80 % between Cy3 and Cy5 (Figure 4b). Further, we recorded the fluorescence spectra of **LMB** with decreasing pH from 7 to 3. Upon decreasing solution pH from 7 to 3, fluorescence spectra of **LMB** showed the decrease in emission at 665 nm and corresponding increase at 565 nm (Figure 4a). These fluorescence spectral changes suggest that Cy3 and Cy5 dyes fall apart from their close proximity as a function of pH leading to decrease in the FRET efficiency between Cy3 and Cy5 dyes. As the solution pH decreases from 7 to 3, **LMB** transform from a closed-state (MB) to open-state (A-motif).

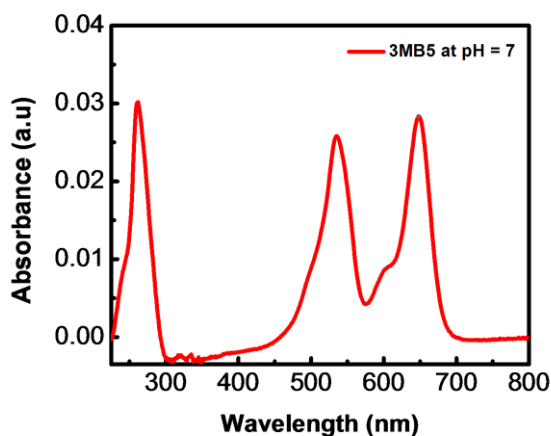


**Figure 3.** Absorption spectra of Cy3 and Cy5 labeled DNA-switch (**LMB**) (160 nM) in PBS-buffer solution (10 mM, pH = 7).

To estimate the relative ratios of closed- and open-states of DNA-switch (**LMB**) at various pH intervals, we plotted the fluorescence intensity ratios of donor (Cy3) and acceptor (Cy5) as a function of solution pH. Detectable change in the fluorescence intensity ratio of donor and acceptors in pH regime 7 to 5 was not observed. Interestingly, plot of fluorescence intensity ratios of Cy3 to Cy5 showed slight change in the pH from 5 to 4 while significantly increased in pH regime of 4 to 3 (Figure 5). These results suggest that **LMB** DNA-Switch efficiently works in the pH regime of 3 to 5. Overall, fluorescence studies revealed that the **LMB** transform from MB to A-motif by changing solution pH from neutral and acidic conditions.

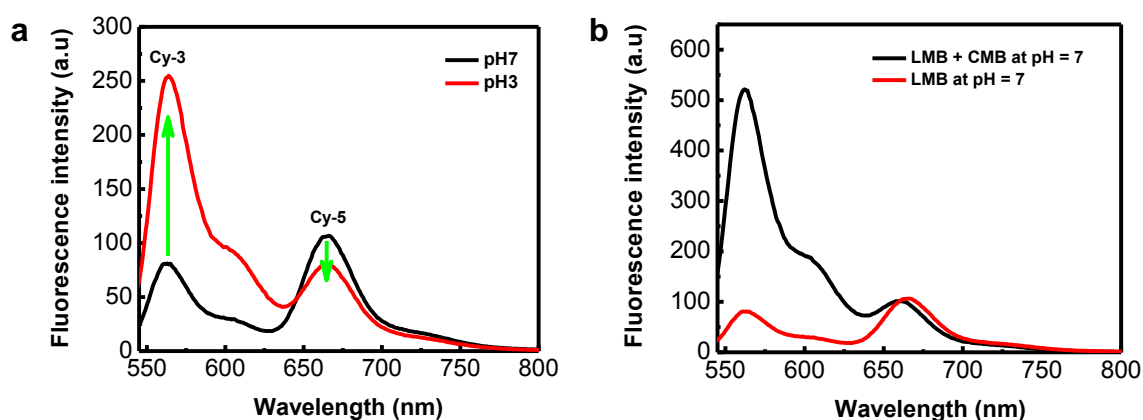


**Figure 4.** pH dependent fluorescence studies of Cy3 and Cy5 labeled DNA-switch (**LMB**). (a) Fluorescence emission spectra of **LMB** (160 nM) in PBS-buffer solution (10 mM) at pH = 3 and 7 under ambient conditions. (b) Fluorescence spectra of DNA-switch (**LMB**) (160 nM) in absence and presence of 10 eq. of unlabeled complementary DNA-switch (**CMB**) in phosphate buffer solution.

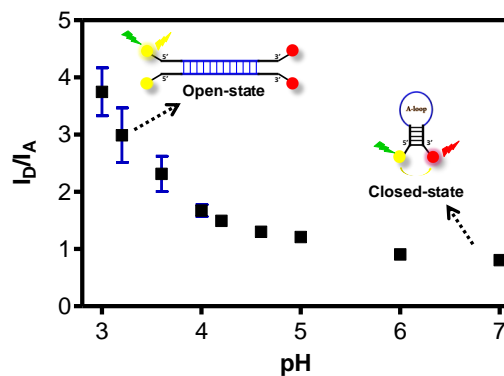


**Figure 5.** Fluorescence intensity ratio's of donor vs. acceptors ( $I_D/I_A$ ) of **LMB** by varying the solution pH from 7 to 3.

### 5.3 Circular dichroism (CD) studies of DNA-switch

To gain more insights into the structural integrity of DNA-switch, we performed CD studies of DNA-switch (**UMB**) in phosphate buffer solution under ambient conditions. CD spectroscopy is one of most versatile tool for the characterization conformational changes of nucleic acid secondary structures.<sup>60</sup> In order to assess the transformation of DNA-switch from MB to A-motif, first we chose to dA<sub>20</sub> as model A-motif forming sequence. At pH = 7, CD spectrum of dA<sub>20</sub> showed a strong positive band at 217 nm with shoulder at 232 nm, a weak positive band at 275 nm and a negative band at 250 nm. These observed spectral features are characteristic of single stranded poly dA<sub>n</sub>. Under acidic conditions (*i.e.*, pH = 2), the positive band at 217 nm decreases and a strong positive band was observed at 265 nm (Figure 6).<sup>38</sup> These characteristic spectral features well-corroborated with non-canonical right-handed parallel dA<sub>20</sub> duplex *known as* A-motif.<sup>38</sup>

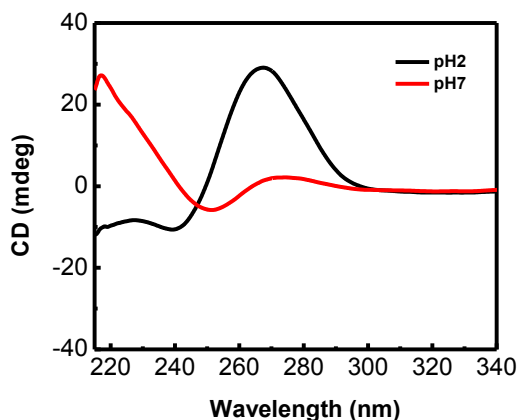


**Figure 6.** CD spectra of dA<sub>20</sub> (4 μM) at neutral pH = 7 and acidic pH = 2 in PBS-buffer solution.

Next, we performed the CD studies of **UMB** under neutral and acidic conditions. CD spectra of **UMB** at pH = 7 showed a strong positive bands at 217 nm, a positive band at 281 nm and a negative band at 250 nm (Figure 7a). These positive and negative CD bands at 281 nm and 250 nm of **UMB** were more promising when compared with CD spectra of dA<sub>20</sub>. These spectral features suggest that **UMB** DNA-switch exists in MB form rather than single stranded random coil form. At pH = 2 CD spectrum of **UMB** showed CD features similar to that of dA<sub>20</sub> revealing the formation A-motif structure under acidic conditions (Figure 7a). To probe the reversible switching of **UMB** between closed- and open-states, we recorded the CD

spectra by alternative addition of aq.HCl and aq.NaOH. As shown Figure 7b, the switching between the closed- and open-states of **UMB** is highly reversible and efficiently works over more than ten cycles. Therefore, CD studies confirmed that **UMB** DNA-switch undergo reversible transformation between closed-state to open-state in response to solution pH from neutral to acidic conditions respectively. The formation of A-motif, right handed parallel duplex structure supported by the  $AH^+-H^+A$  reverse Hoogsteen base pairing and electrostatic interactions is the main driving force behind the switching action of our DNA-switch (Figure 7c).

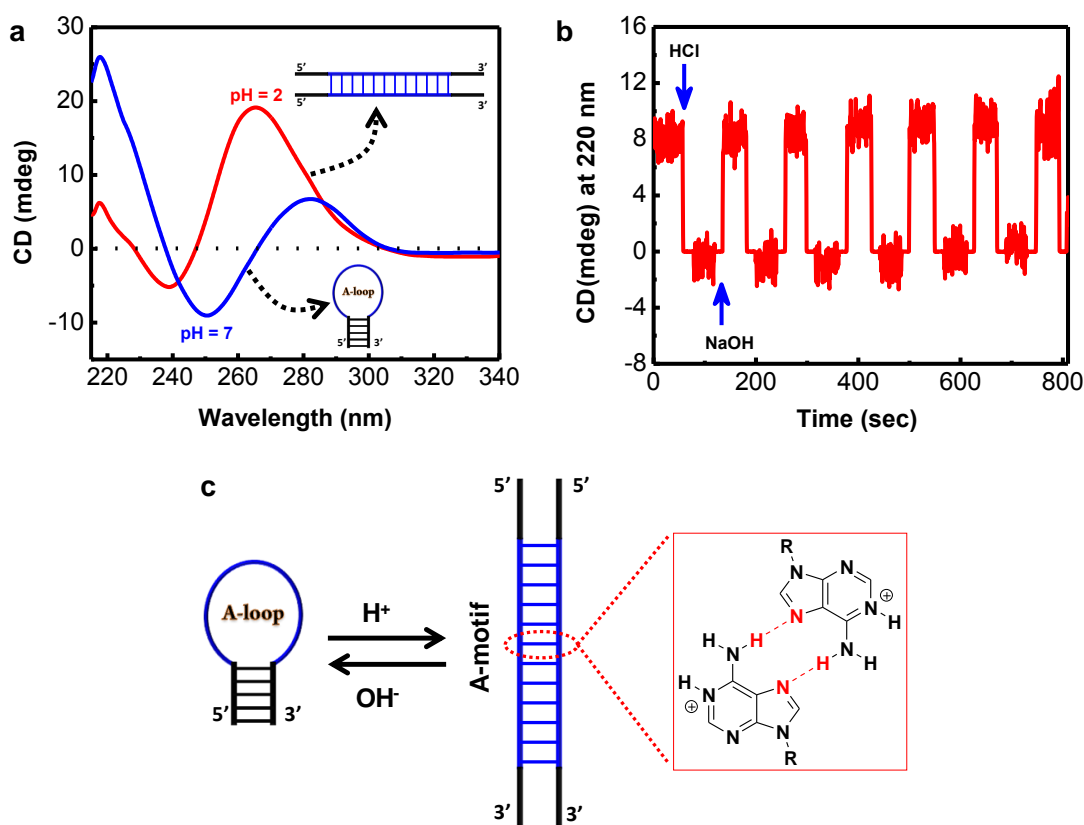


**Figure 7.** pH dependent circular dichroism (CD) spectra of **UMB**. (a) CD spectra of **UMB** at pH = 7 and 2. (b) CD spectra represent the structural transformation of **UMB** from the closed state to open state by alternative addition of acid and base for several cycles. (c) Schematic view of closed state to open state. *Inset:* shows the Hoogsteen  $[AH^+-H^+A]$  base pairing interactions of non-canonical right handed parallel duplex structure (*i.e.*, A-motif).

#### 5.4 Structural transformation of DNA-switch in vesicles (cell-like environment)

Fluorescence and CD studies revealed the effective transformation of **LMB** between closed-state (MB) and noncanonical A-motif (open-state) in the solution pH regime of 7 to 3. Such transformation leads to significant change in the relative fluorescence intensities of Cy3 and Cy5. The rapid and highly reversible responses of **LMB** DNA-switch motivated us to assess the feasibility of switching action in cell-like environments. To create the cell-like environment, we prepared vesicles by using inverted emulsion technique following the reported procedures.<sup>61,62</sup> One of major advantages using vesicle based systems is that different environments can be maintained inside and outside of vesicles similar to intra and extra-cellular environments.<sup>63</sup> These synthetic vesicles can incorporated with fluorescence dyes, proteins and drugs molecules to study various environmental/physiological effects on fluorescence of dyes, conformational changes of proteins and release kinetics of drug molecules respectively.<sup>64</sup> Synthetic vesicles were prepared by using positively charged lipid L- $\alpha$ -phosphatidylcholine and the detailed procedure of vesicle preparation in buffer solution is provided in experimental section (Figure 8).

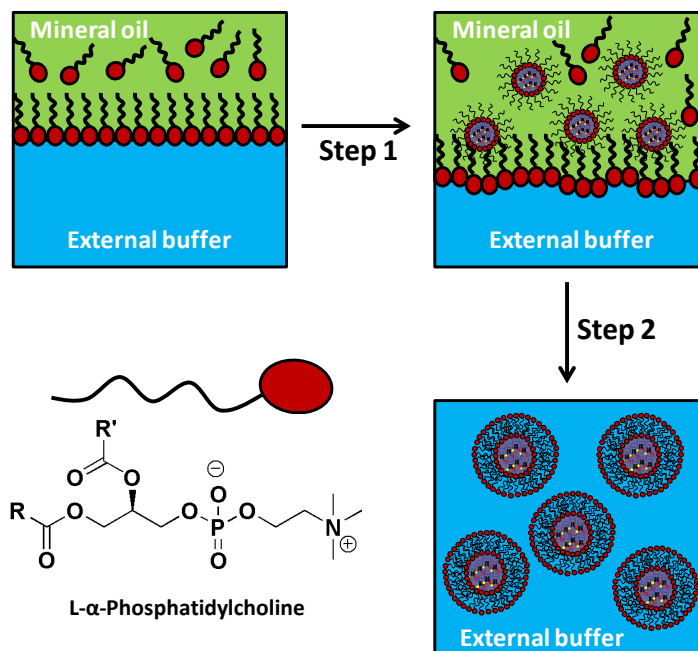


**Figure 8.** Schematic view of preparation of vesicles from an inverted emulsion method.

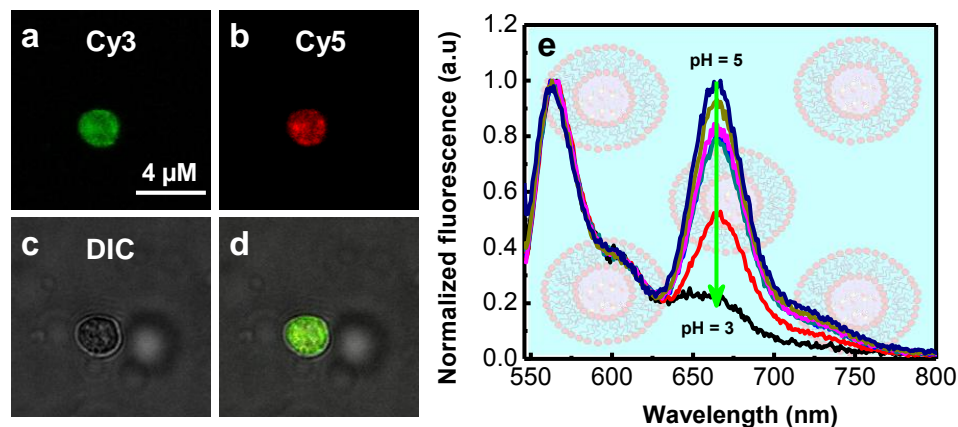


**Figure 9.** pH dependent fluorescence imaging of **LMB** encapsulated vesicles. (a-d) Confocal fluorescence microscope images of **LMB** encapsulated vesicles in buffer solution, (a) Cy3; (b) Cy5; (c) bright field image (DIC) and (d) overlay image of a, b and c. (e) Fluorescence spectra of vesicle by varying solution pH from 3-5.

We encapsulated the vesicle with Cy3 and Cy5 labeled **LMB** DNA-switch at neutral pH. To prove the successful encapsulation of **LMB** in vesicles, vesicles were visualized under confocal scanning fluorescence microscopy (CLSM). At neutral pH = 7, vesicle showed fluorescence in both green and red-channels which corresponds to the Cy3 and Cy5 dyes of **LMB** respectively (Figure 9 a-d). The section profile analysis revealed that fluorescence in the inner core of vesicles not on the walls or outside of the vesicles and this excluded the unwanted background fluorescence from the outside solution of the vesicles (Figure 10). From the fluorescence studies, we did not observed any detectable change in relative fluorescence intensity ratios of donor (Cy3) and acceptor (Cy5) as function of solution pH from 7-5 (Figure 5). Next, we recorded the fluorescence spectra of **LMB** encapsulated vesicle in the pH range of 5 to 3 (Figure 9e). We observed marginal change in fluorescence intensity ratio  $I_D/I_A$  of vesicle by changing the pH from 5 to 4. However, significant and regular change in ratio of  $I_D/I_A$  was observed from pH = 4 to 3.4 (Figure 11). These fluorescence microscopy data in vesicles is well-corroborated with fluorescence and circular dichroism spectroscopy studies of DNA-switch (**LMB**) under acidic and neutral conditions. Overall, this study confirms the successful switching between the open to closed state of **LMB** in vesicle by changing their relative ratios  $I_D/I_A$  of Cy3 and Cy5 dyes.

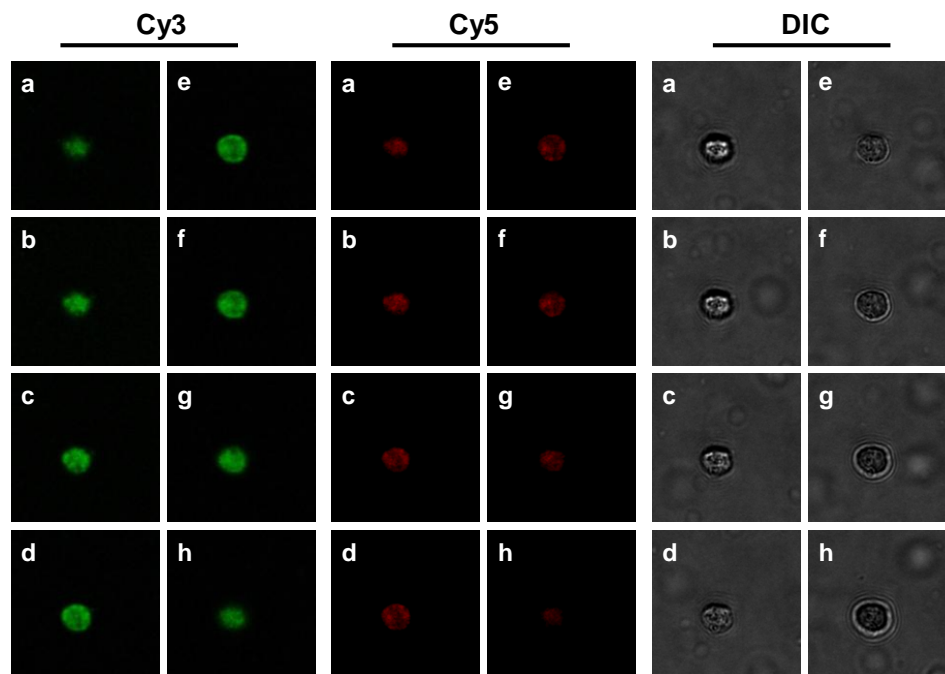


**Figure 10.** Fluorescent confocal micrographs with a cross sectional analysis showing the encapsulation of labeled DNA-switch (**LMB**) inside the vesicles not on the walls.

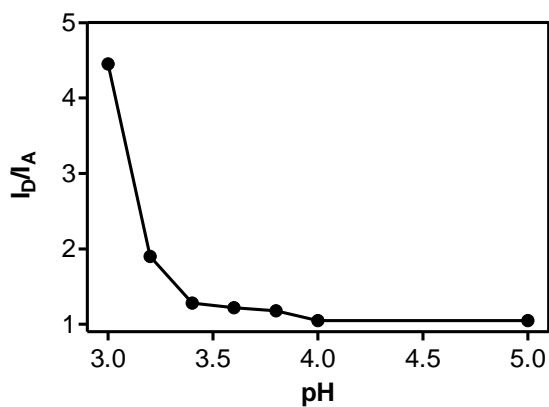


**Figure 11.** Fluorescence intensity ratio's of donor vs. acceptors ( $I_D/I_A$ ) of **LMB** encapsulated in vesicles by varying the solution pH from 7 to 3.

## 5.5 Conclusion

In conclusion, we demonstrated pH induced structural transitions of simple and highly efficient molecular beacon-based DNA-switch (**UMB** and **LMB**) in the range of pH 3 to 5. Design principle is structural transition between Cy3 and Cy5 labeled molecular beacon (MB) to A-motif depending on solution pH. At neutral pH conditions, DNA-switch exists in



the molecular beacon (closed-state) and results in FRET between Cy3 and Cy5 dyes. Under acidic conditions, DNA-switch transforms from molecular beacon to A-motif (open-state) and results in decreasing FRET. UV-vis and fluorescence studies revealed that our DNA-switch (**UMB** and **LMB**) undergo reversible structural transformation between closed-state and an open-state efficiently in the pH regime from 3 to 4. Circular dichroism studies supported the switching between molecular beacon and non-canonical A-motif structure in a highly reversible manner and can be switched between the states over more than 10 cycles. Further, we demonstrated the pH induced structural transitions of DNA-switch (**LMB**) by encapsulating in synthetic vesicles to mimic the cell-like environments. We anticipated that the simple, rapid response and highly reversible nature of our DNA-switch is an efficient DNA-based device for the real-time monitoring of intracellular pH in cells. Further, we also predict that molecular beacon to A-motif transformation-based DNA-switch for designing various pH induced DNA probes or nanodevices and may find applications in drug delivery systems.

## 5.6 Experimental section

**General information.** HPLC purified oligonucleotides (**LMB**, **UMB** and **CMB**), L- $\alpha$ -phosphatidylcholine, and phosphate buffered saline (Na-PBS) were purchased from Sigma–Aldrich. All other reagents were used as received unless otherwise mentioned. UV-vis, fluorescence and circular dichroism (CD) spectra of samples were analyzed in quartz cuvette of 10 mm path length.

**Sample preparation for UV-vis, emission and CD measurements.** DNA stock solutions were prepared by dissolving oligo samples in double-distilled (dd) water in the order of  $10^{-4}$  M. Solutions of DNA duplexes were prepared in phosphate buffer solution (10 mM, pH = 7) buffer solution by mixing complementary DNA strands in equimolar concentration; this solution was then subjected to annealing by heating up to 85 °C for 15 min., subsequently cooled to room temperature for 7h and stored in the refrigerator (4 °C) for 4 h.

**UV-vis absorption and emission spectroscopy.** The UV–vis absorption and emission spectra were recorded on Agilent Technologies Cary series UV-vis-NIR absorbance and Cary eclipse fluorescence spectrophotometers, respectively. Thermal denaturation (UV-melting) studies were carried out on Cary 5000 UV-vis-NIR spectrophotometer equipped

with Cary temperature controller in the range of 10 °C to 90 °C with a ramp rate of 1 °C/min. The variable temperature/wavelength mode was used. Absorption was monitored at 260 nm with regular 5 °C intervals. Melting temperatures ( $T_m$ ) of DNA samples were calculated from the first derivatives of the absorption vs. temperature curves (thermal denaturation or melting curves) obtained by monitoring at 260 nm. A blank sample containing PBS buffer solution (10 mM, pH = 7) was recorded and subtracted from the collected data.

**Circular Dichroism (CD) spectroscopy.** CD measurements were carried out on Jasco J-815 spectrometer equipped with a Peltier-type temperature controller (CDF-4265/15) under a nitrogen atmosphere to avoid water condensation. Scans were performed over the range of 200-400 nm with a speed of 100 nm/min, and the spectra represent an average of three scans. A blank sample containing phosphate buffer solution (10 mM, pH = 7) was treated in the same manner and subtracted from the collected data.

**FRET efficiency between Cy3 and Cy5 dyes.**<sup>49</sup> Stock solutions of Cy3 and Cy5 labeled DNA-switch (**LMB**) of 30  $\mu$ M and unlabeled complementary DNA-switch (**CMB**) of 300  $\mu$ M were prepared by dissolving in MQ-water solution. Stock solution of DNA-switch (**LMB**) was diluted to 160 nM with buffer solution in all the fluorescence measurements. Fluorescence spectra of DNA-switch (**LMB**) were measured upon excitation at 530 nm and emission was collected from 545-800 nm in absence and presence of complementary DNA-switch (**CMB**) (10 eq.). FRET efficiencies were calculated from the following formula,

$$E = 1 - I_{DA}/I_D = 1/[1+(R/R_0)^6]$$

Where,  $I_D$  is intensity of Cy3 in presence of 10 eq. of complementary DNA-switch (**CMB**) to make sure that DNA-switch exists in open state,  $I_{DA}$  is intensity of Cy3 in presence of Cy5,  $R_0$  is Förster's distance and  $R$  is the intrafluorophore distance.

**Preparation of vesicles.** Vesicles were prepared according to early reported procedures from an inverted emulsion method.<sup>61,62</sup> In brief we have described below.

**Lipid-dodecane mixture.** L- $\alpha$ -phosphatidylcholine (PC) (2 mg) was taken in a sample vial (8 mL) and dichloromethane (1 mL) was added. A thin film of lipid was made by flushing with nitrogen and kept in high vacuum for 40 min and vacuum was released under nitrogen atmosphere. Then, 5 mL of dodecane was added to thin film and sonicated for 30 min. After

sonication, lipid-dodecane mixture was heated up to 50 °C for 3h and cooled to room temperature, stored at 4 °C.

**Mixture A.** A 100 µL of lipid-dodecane mixture was slowly placed on the top of external buffer (200 µL) for the formation of lipid mono layer under ice cooled temperature for 2h.

**Mixture B.** 5 µL of **LMB** containing buffer solution [Internal buffer (**IB**)] was added to lipid-dodecane solution (600 µL) and sonicated for 30 min to form the emulsion. The obtained emulsion was stored at 4 °C for 15 min.

Next, DNA-switch (**LMB**) containing mixture B (200 µL) was added slowly on the top of mixture A and incubated at 4 °C for 15 min. Then, above mixture was centrifugated at 4 °C for 12 min with 2000 rpm, followed by 5 min with 4000 rpm and 4 min with 6000 rpm. After centrifugation, upper dodecane layer was removed carefully with pipette. The remaining solution contains the vesicles in external buffer solution.

## Chapter 5b: Small Molecule Induced Non-Canonical Secondary DNA Structure of Alternative Guanine-Adenine Rich Sequences

In living cells, DNA predominantly exists in antiparallel, right handed duplex helix conformation two strands held together canonical Watson-Crick (WC) base pairing interactions.<sup>65</sup> Apart from biological significance, attributed to its simple, robust and high predictable base pair coding interactions of B-DNA has been extensively used as material building block for designing novel 1D-, 2D- and 3D-architectures in the celebrated area of DNA nanotechnology.<sup>18-23</sup> Interestingly, canonical B-DNA under some specific conditions transform into non-canonical B-DNA conformations namely hairpin, triplex (H-DNA), G-quadruplex, I-motif, A-motif and poly  $d(GA)_n$  duplex with non WC base pairing interactions.<sup>66</sup> These non-canonical B-DNA structures may have beneficial-biological effects, influence the gene metabolism processes and cause human diseases.<sup>67-70</sup> Therefore, it is crucial to understand the role and biological significance of non B-DNA structures that may offer novel approaches to develop new therapeutic agents targeting DNA.<sup>67-70</sup> Furthermore, analogous to the use of canonical B-DNA in DNA nanotechnology applications, these non-canonical B-DNA forming sequence can be harvested to create fascinating nanosystems and materials for various diagnosis and biomaterials applications. In this context, inducing non-canonical DNA conformations is one of the major challenges. There are have been few reports which describe the formation of non-canonical B-DNA structures in presence of metals ions and small molecules.<sup>69-72</sup>

In recent studies, molecular beacon (MB) systems with thymine and cytosine rich sequences at the stem structure have been reported to undergo canonical to non-cononical structural transformation in response to metal ions. For instance metal ions such as  $Hg^{2+}$  and  $Ag^+$  induce non-canonical DNA structures in these systems through  $dT-Hg^{2+}-dT$  and  $dC-Ag^+-dC$  interactions.<sup>73-79</sup> Further, the  $[dT-Hg^{2+}-dT]_n$  non-canonical DNA system was used for the sensing of thiol-containing compounds.<sup>80,81</sup> In contrast, it is a daunting task to design small molecules to induce and stabilize the non-canonical DNA structures from single stranded or double stranded DNA. Recently, Nicholas Hud and coworkers have shown that coralyne triggers the formation of non-canonical homoduplex of polyadenine  $[poly(dA)_n]$  sequences at neutral pH.<sup>71</sup> Small molecule coralyne is a crescent shaped polyaromatic

molecule specifically binds adenine-rich sequences with high binding affinity through the intercalation mode to induce and stabilize the non-canonical right handed antiparallel homoduplex of  $[\text{poly}(dA)_n]$ . Coralyne binds with  $\text{poly}(dA)_n$  sequences in the stoichiometric ratio of one coralyne molecule per four adenine bases and stabilizes adenine homoduplex in a cooperative manner.<sup>71</sup> These  $\text{poly}(dA:dA)_n$ :coralyne complexes have been used to design turn-on-off fluorescence probe for various biological analytes including nucleic acids, heparin and monitoring of enzymatic activities.<sup>82-84</sup>

In the growing list of DNA sequences which are known to adapt various conformational structures to relieve the super helical stress in genome is  $\text{poly}(\text{homopurine}.\text{homopyrimidine})$   $[\text{d}(GA).\text{d}(TC)]_n$  structures.<sup>85,86</sup> The  $[\text{d}(GA).\text{d}(TC)]_n$  sequences are abundant in eukaryotic DNA (0.4% of total mammalian genome) and play vital role in various biological processes in eukaryotic cells.<sup>87</sup> The polypurine.polypyrimidine stretches present in both chromatin and super helical plasmids are hypersensitive to single strand specific nucleases, a clear indication that these DNA stretches might exist in non B-DNA conformations.<sup>88-90</sup> This is one of the possible reasons to study the conformational changes of alternative guanine-adenine sequences  $d(GA)_n$ . Depending on the ionic, pH and temperature conditions this sequence is known to form a broad range of non-canonical DNA structures including parallel, antiparallel, hairpin duplexes and two hairpin tetraplex.<sup>91-95</sup> Interestingly, this sequence also adapts ordered single stranded (intramolecular helix) form under  $\text{pH} < 6$  in presence of  $\text{Na}^+$  ions (10 mM).<sup>96,97</sup> To the best of our knowledge, there is no report on small molecule induced structural transitions of  $d(GA)_n$  sequences.

Biological significance and highly polymorphic nature of  $d(GA)_n$  inspired us to study their conformational changes in presence of small molecular probes. In this context, we selected three polyaromatic molecules berberine, coralyne and palmatine and studied their interactions with  $d(GA)_n$  sequences. One of the common structural features in all three molecules is their crescent molecular shape. In addition, coralyne and palmatine have two adjacent methoxy groups on each of the terminal aromatic rings while berberine has methylenedioxy group at one the terminal aromatic ring and two adjacent methoxy groups on other terminal aromatic ring (Figure 12). These small molecules have wide range of biological properties like antimicrobial, antiviral, anti-inflammatory, anticancer and anticholesterol effects.<sup>98-102</sup> Furthermore, various studies have been performed to study their

interaction and mode of binding to DNA and RNA.<sup>103-111</sup> All these studies revealed that they mostly interact with DNA in an intercalation mode. These interesting studies further encouraged us to investigate the structural transitions of d(GA)<sub>n</sub> sequence in presence of coralyne, berberine and palmatine. We presumed that the characteristic crescent shaped molecular structure attained by the polyaromatic systems facilitate and stabilize non-canonical secondary structures of d(GA)<sub>n</sub> sequences. UV-vis absorption and circular dichroism (CD) studies revealed that among three polyaromatics coralyne specifically induces ordered non-canonical parallel homoduplex of d(GA)<sub>n</sub>.

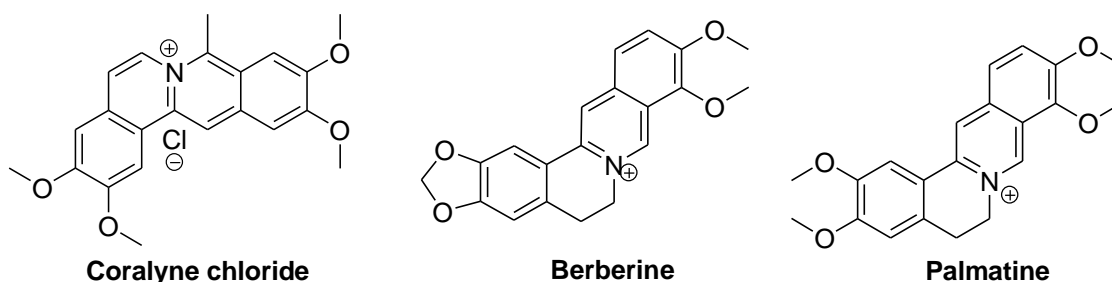


**Figure 12.** Molecular structures of coralyne, berberine and palmatine.

### 5.7 Photophysical properties small molecules in presence of deoxyoligonucleotides

Herein, we studied the structural integrity of alternative guanine-adenine containing d(GA)<sub>n</sub> sequences in presence of small polyaromatics coralyne, berberine and palmatine. First, we investigated the photophysical properties of small polyaromatic molecules in presence of d(GA)<sub>n</sub> (n = 4, 6 and 8) in Tris-HCl (100 mM, pH = 7.4) buffer under ambient conditions. UV-vis spectra of individual coralyne, berberine and palmatine molecules showed absorption maxima at 415, 420 and 382 nm respectively, at 12 μM concentration (Figure 13 and 14). The absorption bands are very broad this indicates in buffer solution molecules are mostly in aggregated form. Next, we recorded the absorption spectra of these molecules in presence of deoxyoligonucleotides dC<sub>10</sub>, dG<sub>10</sub>, dT<sub>20</sub>, (D1)<sub>mix</sub>, (D2)<sub>mix</sub> and d(GA)<sub>6</sub> (Table 2). Upon addition of d(GA)<sub>6</sub>, absorption spectrum of berberine showed slight blue shift in bands at 415 and 345 nm. The absorption spectrum of palmatine showed hyperchromic shift in presence of d(GA)<sub>6</sub>. From the absorption spectra, it is clear that berberine and palmatine have very minimal or negligible effect on binding interaction to d(GA)<sub>6</sub> (Figure 13).

**Table 2.** Sequence information of deoxyoligonucleotides used in this study.

Code	Sequence	Structure
$d(GA)_4$	5'- GAGAGAGA-3'	random coil
$d(GA)_6$	5'- GAGAGAGAGAGA-3'	random coil
$d(GA)_8$	5'- GAGAGAGAGAGAGAGA-3'	random coil
$dC_{10}$	5'- CCCCCCCCCC-3'	random coil
$dG_{10}$	5'- GGGGGGGGGG-3'	random coil
$dA_{20}$	5'- AAAAAAAAAAAAAAAAAAAA-3'	random coil
$dT_{20}$	5'- TTTTTTTTTTTTTTTTTTTT-3'	random coil
$(D1)_{mix}$	5'- CGATAAGCGCTTATCG-3' 3'-GCTATTCGCGAATAGC-5'	duplex
$(D2)_{mix}$	5'- CGGTACCGCGGTACCG -3' 3'-GCCATGGCGCCATGGC-5'	duplex

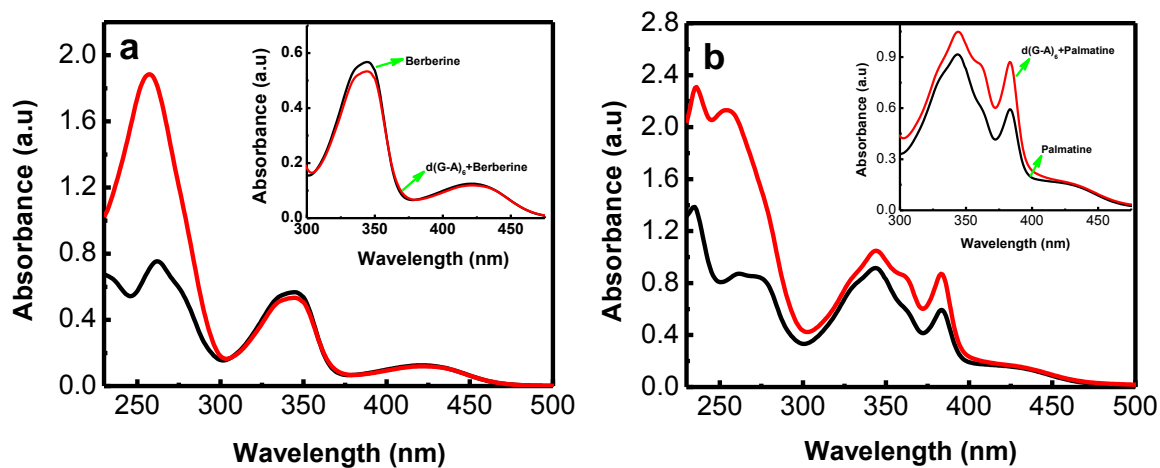


**Figure 13.** Absorption spectra. (a) Absorption spectra of berberine (12  $\mu$ M) in absence and presence of  $d(GA)_6$  (8  $\mu$ M). *Inset:* Absorption spectra in 300-480 nm region. (b) Absorption spectra of palmatine (12  $\mu$ M) in absence and presence of  $d(GA)_6$  (8  $\mu$ M) in Tris-HCl buffer solution (100 mM, pH = 7.4). *Inset:* Absorption spectra in 300-480 nm region.

Interestingly, absorption spectrum of coralyne showed the red shift in absorption maxima ( $\Delta\lambda_{\text{max}} = \sim 21$ ) with hyperchromic shift (Figure 14). Unlike berberine and palmatine, the absorption spectrum of coralyne showed well-resolved absorption bands at 412 and 436 nm this is an indicative of coralyne binding interaction of the molecules to d(GA)<sub>6</sub>, mostly likely in the intercalation mode.<sup>103</sup> To compare its binding mode, we measured the absorption spectra of coralyne in presence of ssDNA (dA<sub>20</sub>, dC<sub>10</sub>, dG<sub>10</sub>, dT<sub>20</sub>), dsDNA {(D1)<sub>mix</sub>, (D2)<sub>mix</sub>} sequences. It is known that coralyne bind to dsDNA in intercalation mode and specifically in presence of poly-adenine (dA<sub>n</sub>) sequences it induces the antiparallel homoduplex in a cooperative manner.<sup>71,103</sup>

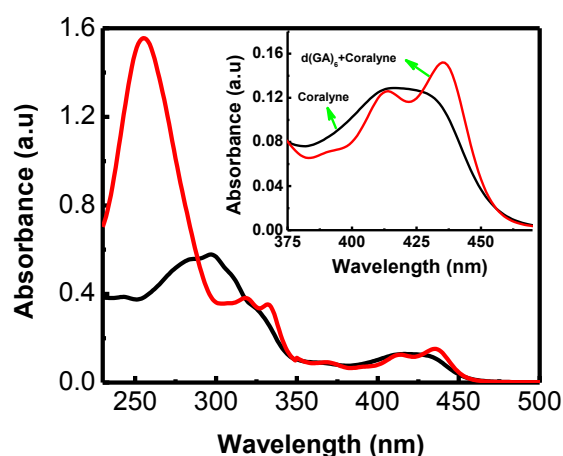


**Figure 14.** Absorption spectra of coralyne (12  $\mu\text{M}$ ) in absence and presence of d(GA)<sub>6</sub> (8  $\mu\text{M}$ ). *Inset:* Absorption spectra in 300-480 nm region.

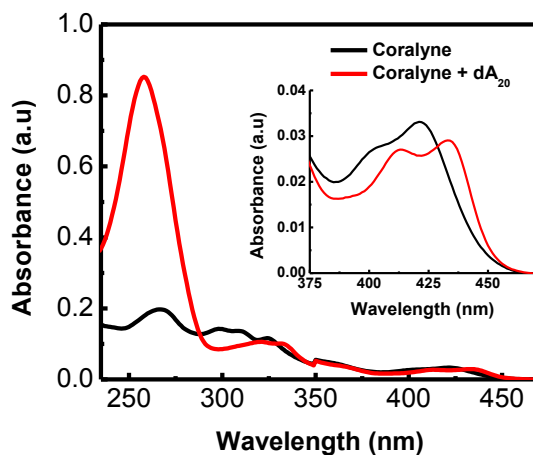


**Figure 15.** Absorption spectra of coralyne (6  $\mu\text{M}$ ) in presence of dA<sub>20</sub> (4  $\mu\text{M}$ ) in Tris.HCl buffer solution. *Inset:* Absorption spectra in 300-480 nm region.



Remarkably, the spectral features of coralyne in presence of  $dA_{20}$  were similar that in case of coralyne/ $d(GA)_6$  (Figure 15). In other words, the absorption spectra of coralyne did not show any appreciable change in presence of pyrimidine rich  $dT_{20}$  and  $dC_{10}$  (Figure 16a and 16b). However, absorption spectra showed red shift in the absorption maxima in presence of purine-rich  $dG_{10}$  and double stranded DNA such as  $(D1)_{\text{mix}}$  and  $(D2)_{\text{mix}}$  (Figure 16c and 16b). These results confirm that coralyne is more prone to bind single stranded polypurine  $d(GA)_6$ ,  $dG_{10}$  and  $dA_{20}$  sequences compare to single stranded polypyrimidine strands  $dC_{10}$  and  $dT_{20}$ .

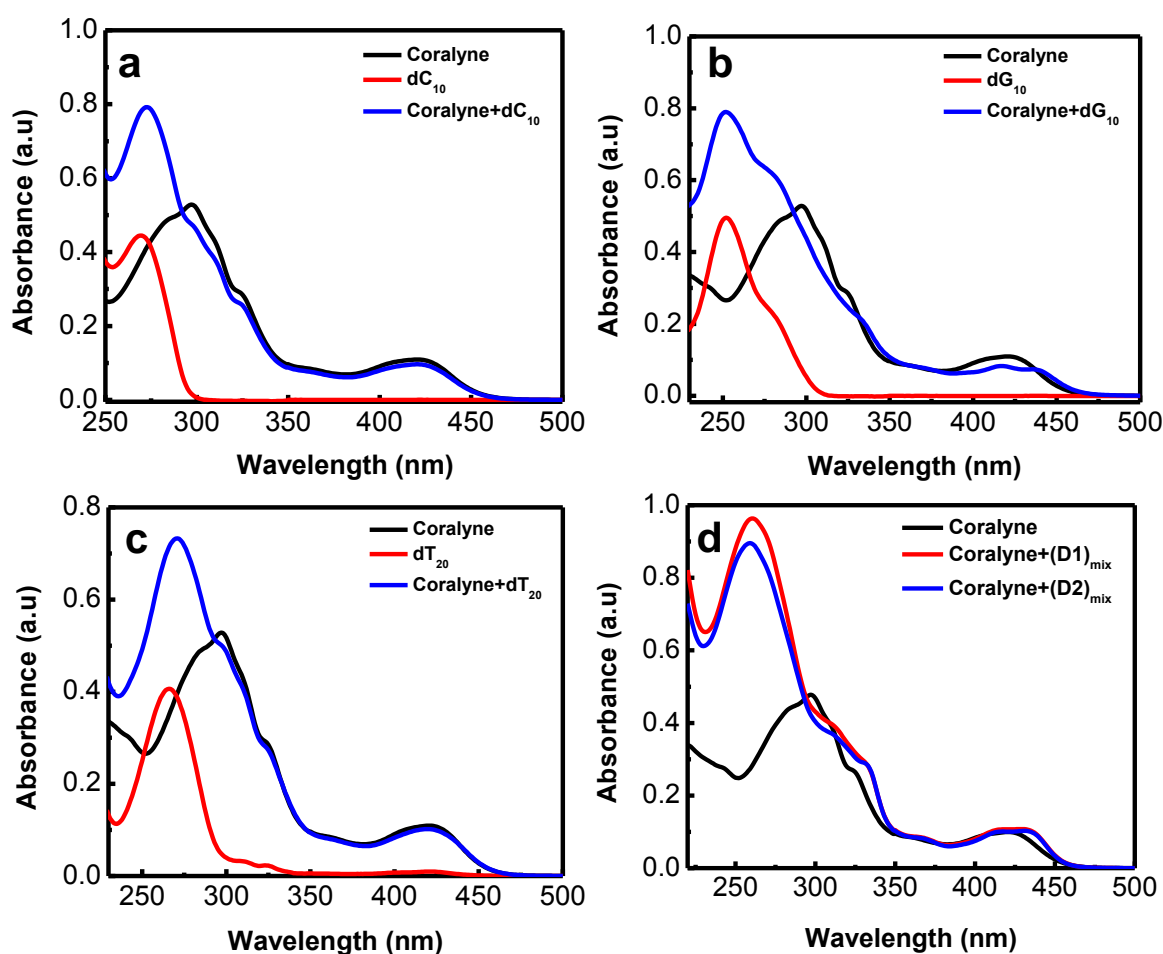


**Figure 16.** Absorption of coralyne (12  $\mu\text{M}$ ) in presence of deoxyoligonucleotides. (a)  $dC_{10}$ , (b)  $dG_{10}$ , (c)  $dT_{20}$  and (d)  $(D1)_{\text{mix}}$  and  $(D2)_{\text{mix}}$  respectively, in Tris.HCl buffer solution.

### 5.8 Binding stoichiometry of coralyne with d(GA)<sub>6</sub>

To determine binding stoichiometry of coralyne with d(GA)<sub>6</sub>, we performed the concentration-dependent UV-vis absorption studies. In this study, we added increased concentration of d(GA)<sub>6</sub> from 0 to 8  $\mu\text{M}$  (nucleobase concentration 0 to 96  $\mu\text{M}$ ) to a fixed concentration of coralyne (12  $\mu\text{M}$ ). The absorption spectra of coralyne showed drastic changes in absorption bands at 412 and 436 nm (Figure 17). Initially, at low ratio of coralyne:nucleotide in d(GA)<sub>6</sub> (1:0.83), absorption spectra showed slight hypochromic shift with red shifted in absorption maxima of coralyne absorption region at 400-450 nm. With increasing ratio of coralyne:nucleobase in d(GA)<sub>6</sub> from 1:0.83 to 1:4 absorption spectra showed red shift with hyperchromic shift and subsequently reaches saturation at  $\geq 1:4$  ratio (Figure 17 *inset*). These data revealed that coralyne binds to d(GA)<sub>6</sub> in stoichiometric ratio of one coralyne molecule per four nucleobases of d(GA)<sub>6</sub>. Overall, above studies confirms coralyne specifically induces the structural transition of d(GA)<sub>6</sub> from random coil to ordered secondary structure.

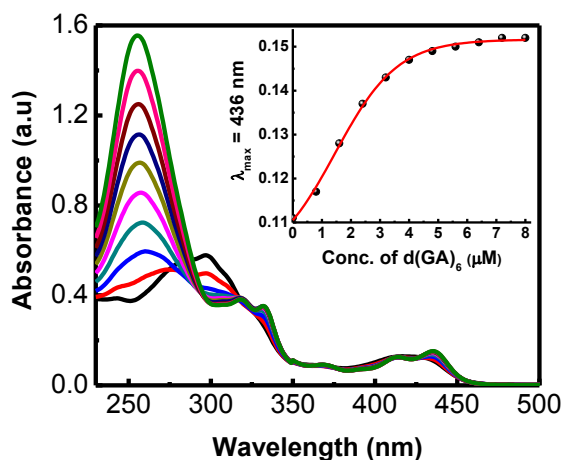


**Figure 17.** Absorption spectra of coralyne (12  $\mu\text{M}$ ) with increasing concentration of d(GA)<sub>6</sub> from 0 to 8  $\mu\text{M}$  in Tris-HCl buffer solution. *Inset:* Plot of absorption intensity at 436 nm as a function of concentration of d(GA)<sub>6</sub>.

### 5.9 Temperature dependent stability and binding kinetics of coralyne with d(GA)<sub>6</sub>

In order to assess the thermal stability and binding kinetics of coralyne and d(GA)<sub>6</sub>, we performed the temperature- and time-dependent absorption studies. Temperature-dependent

UV-vis absorption spectra of d(GA)<sub>6</sub> with coralyne were performed by heating the samples from 5 °C to 75 °C. At lower temperatures the absorption bands of coralyne were more prominent which indicates coralyne binds to d(GA)<sub>6</sub> in intercalation mode. With increasing temperature from 5 °C to 75 °C, the absorbance of prominent absorption bands at 412 and 436 nm decreases and the absorption bands were blue shifted (*i.e.*,  $\lambda_{\text{max}}$  at 436 nm to 421 nm and  $\lambda_{\text{max}}$  at 412 nm to 400 nm). At higher temperatures, the observed spectral features were resemble to free coralyne in buffer solution which indicates transformation of ordered secondary structure coralyne bind d(GA)<sub>6</sub> to random coil conformation (Figure 18a). The plot absorption maxima at 436 nm as a function of temperature to obtain melting curves as shown in Figure 3a *insert*. Melting curve analysis showed that increase in melting temperature from 10 °C to 33 °C ( $\Delta T_m = 23$  °C) compared to d(GA)<sub>6</sub> (Figure 18a *inset*). Similarly, we performed temperature-dependent absorption spectra of coralyne in presence of double stranded duplex (D2)<sub>mix</sub> containing WC base pairs (Figure 19a). Melting curve analysis showed slight decrease in melting temperature from 73.8 °C to 69.8 °C ( $\Delta T_m = -4.0$  °C) and indicates coralyne is more prone to stabilizes the d(GA)<sub>6</sub> sequence than dsDNA.

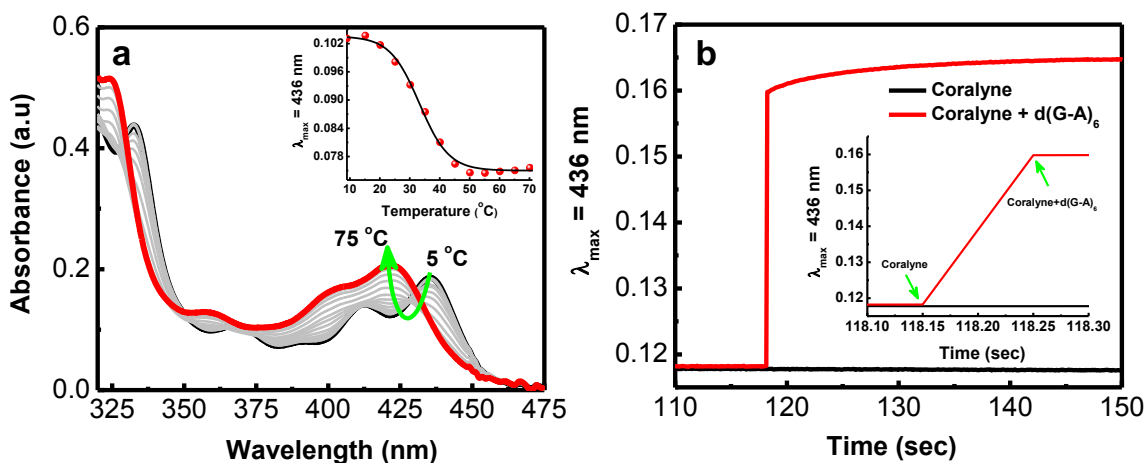


**Figure 18.** Temperature-dependent stability and binding kinetics of coralyne with d(GA)<sub>6</sub>. (a) Temperature dependent absorption spectra of coralyne in presence of d(GA)<sub>6</sub> in Tris. HCl buffer solution. *Inset*: Plot of absorption intensity of coralyne (12 μM) at 436 nm as function of time in presence of d(GA)<sub>6</sub> (8 μM). (b) Plot of absorption intensity of coralyne (12 μM) at 436 nm as function of time in presence of d(GA)<sub>6</sub> (8 μM) in Tris. HCl buffer solution. *Inset*: Kinetic response of binding of coralyne with d(GA)<sub>6</sub> and found to be  $\tau = 100$  ms.

To determine the response time for the structural transition of d(GA)<sub>6</sub> in presence of coralyne kinetic experiments using absorption studies were carried out. To a solution of coralyne (12 μM) in Tris-HCl buffer solution, d(GA)<sub>6</sub> was added which caused a rapid increase in the absorption maxima at 436 nm (Figure 18b). The time scale of structural transition of d(GA)<sub>6</sub> in presence of coralyne was quick and found to be  $\tau = 100$  ms (Figure 18b inset). Further, we compared the kinetic response of binding interaction of coralyne with duplex DNA (D2)<sub>mix</sub> using time dependent absorption studies. Coralyne is known to intercalates duplex DNA and our study showed that intercalation processes of coralyne with (D2)<sub>mix</sub> also showed quick response time i.e.,  $\tau = 100$  ms (Figure 19b). From the above data it is clear that coralyne induce and stabilize the ordered secondary structure of d(GA)<sub>6</sub> and possess quick response time for the transformation involving random coil to order secondary structure (*i.e.* < 100 ms).

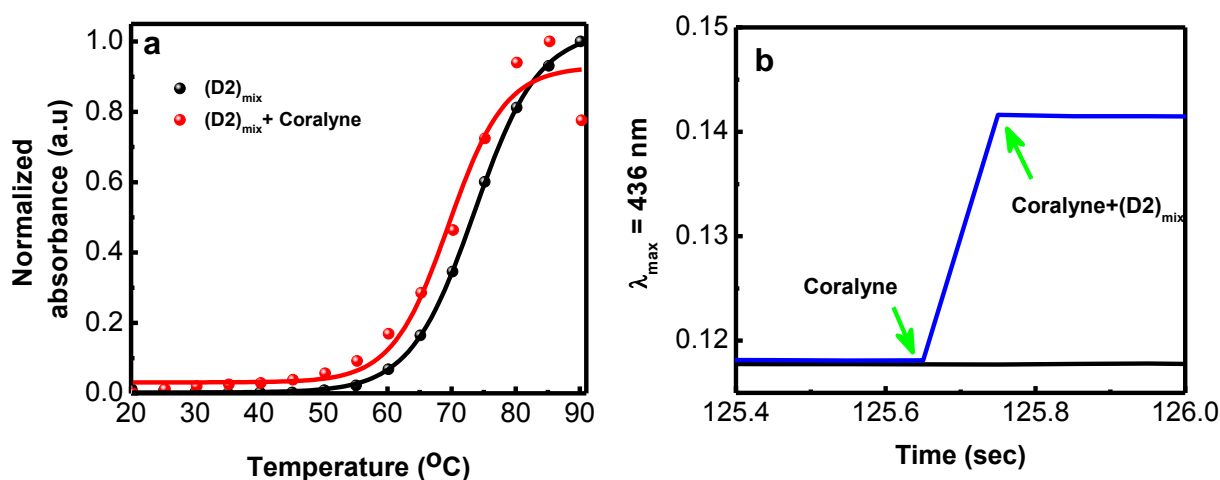


**Figure 19.** Temperature-dependent stability and binding kinetics of coralyne with (D2)<sub>mix</sub>. (a) Melting curve of (D2)<sub>mix</sub> (8 μM) in presence of coralyne (12 μM) monitored at 260 nm as a function of temperature. (b) Plot of absorption intensity of coralyne (12 μM) at 436 nm as function of time in presence of (D2)<sub>mix</sub> (8 μM) in Tris-HCl buffer solution.

### 5.10 CD studies of coralyne in presence of d(GA)<sub>6</sub>

To gain more insight on the structural integrity of coralyne induced secondary structure of d(GA)<sub>6</sub>, we performed CD studies in Tris-HCl buffer solution under ambient conditions. CD is one of the best spectroscopic tool to characterize the conformational changes of nucleic

acids as well as small molecule DNA interactions.<sup>112</sup> CD spectrum of  $d(GA)_6$  showed a negative signal at 285 nm and a positive signals at 220 and 245 nm (Figure 20a). These CD features are well-corroborated with that of single stranded random coil structure of  $d(GA)_6$  sequence at room temperature and neutral pH.<sup>91</sup> CD spectrum of  $d(GA)_6$  did not show any detectable changes in the CD signals of  $d(GA)_6$  in presence of berberine and palmatine (Figure 21). Interestingly, addition of coralyne (12  $\mu\text{M}$ ) to  $d(GA)_6$  (8  $\mu\text{M}$ ) showed completely different CD features in the nucleobase absorption region, a positive signal at 272 nm and negative signal at 252 nm. The observed positive CD signal at 260-280 nm and negative CD-signal near 245 nm indicates  $d(GA)_6$  transforms from random coil conformation to typical B-form of DNA.<sup>113</sup> An induced positive CD signals were observed in coralyne absorption region 310-360 nm and 400-460 nm with maximum CD intensity at 337 and 436 nm respectively (Figure 20a).

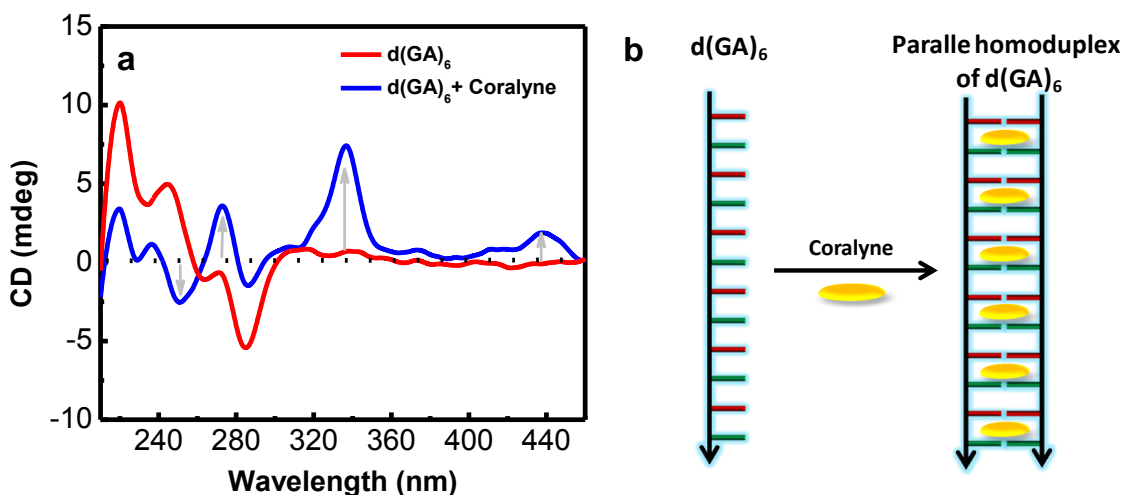


**Figure 20.** CD spectra and mode of binding of coralyne in presence of  $d(GA)_6$ . (a) CD spectra of  $d(GA)_6$  (8  $\mu\text{M}$ ) in presence of coralyne (12  $\mu\text{M}$ ) in Tris-HCl buffer solution. (b) Schematic view of coralyne induced parallel homoduplex of  $d(GA)_6$  in intercalation binding mode.

As a control, coralyne alone did not show any CD signal in 310-360 nm and 400-460 nm which confirms that an induced CD signal in coralyne absorption region arised from the binding of coralyne to ordered secondary structure of  $d(GA)_6$  sequence. In CD studies, induced signal by the small molecule is greatly affected by binding affinity and relative orientation within the chiral environment of duplex DNA structure.<sup>112</sup> An induced positive

CD signal in coralyne absorption region is assumed to be originated from the orientation of transitions moments of coralyne parallel to long axis of duplex conformation of  $d(GA)_6$  (Figure 20b). In addition, the strong induced positive band also suggests coralyne located exactly at center of the interaction site in double conformation of  $d(GA)_6$ .<sup>112</sup> Therefore, above results suggest that coralyne induces ordered duplex conformation of  $d(GA)_6$  with an intercalation binding mode.

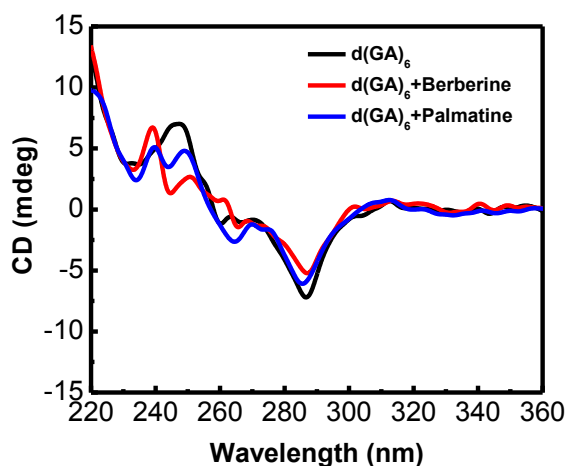


**Figure 21.** CD spectra of  $d(GA)_6$  ( $8 \mu\text{M}$ ) in presence of berberine ( $12 \mu\text{M}$ ) and palmitine ( $12 \mu\text{M}$ ) in Tris-HCl solution.

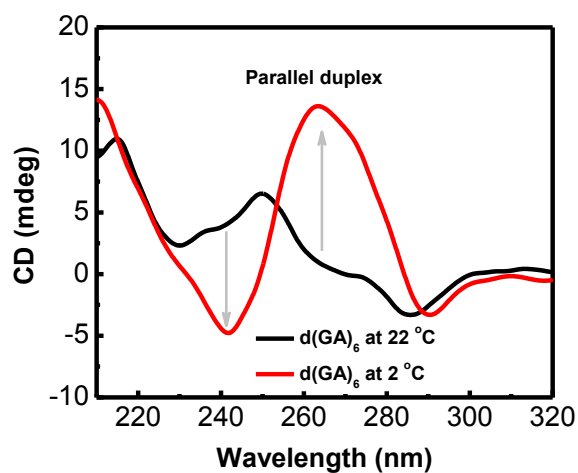


**Figure 22.** CD spectra of parallel homoduplex of  $d(GA)_6$  ( $8 \mu\text{M}$ ) at lower temperature in Tris-HCl buffer solution.

It is known that  $d(GA)_n$  triggers the formation of parallel homoduplex with decreasing temperature in Tris-HCl buffer solution under neutral pH conditions.<sup>91</sup> We recorded the CD spectra of  $d(GA)_6$  alone with decreasing temperature from 22 °C to 2 °C. At lower temperature 2 °C, CD spectra showed strong positive signal at 264 nm and a negative signal at 242 nm suggests the formation of parallel homoduplex of  $d(GA)_6$  (Figure 22).<sup>91</sup> Interestingly, CD features of coralyne/ $d(GA)_6$  complex are well-corroborated with a low temperature (2 °C) structure of  $d(GA)_6$ . Overall, CD studies proved beyond doubt that coralyne induce the formation of parallel homoduplex of  $d(GA)_6$  and the induced positive CD signal also suggest that coralyne binds  $d(GA)_6$  in an intercalation mode.

### 5.11 Effect of sequence length and salt concentration on the stability of coralyne/ $d(GA)_n$

We studied the effect of sequence length, salt and temperature on the stability of coralyne induced parallel homoduplex of  $d(GA)_n$  ( $n = 4, 6$  and  $8$ ). The CD spectra of  $d(GA)_4$  showed a negative and positive signals at 283 and 245 nm respectively. In presence of coralyne, a weak positive induced signal in presence of  $d(GA)_4$  was observed at 340 nm suggests  $d(GA)_4$  is not sufficient to form the duplex conformation (Figure 23a).

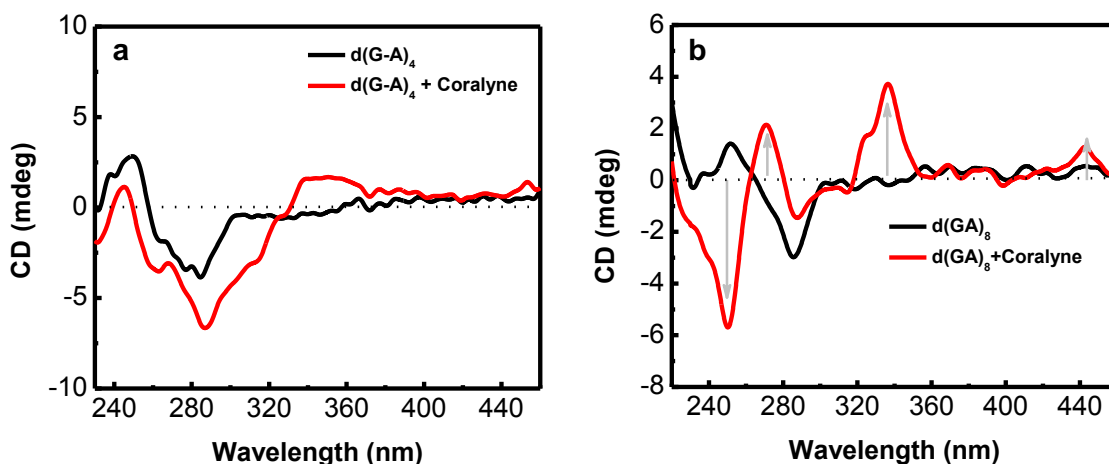


**Figure 23.** CD spectra of  $d(GA)_n$  ( $n = 4$  and  $8$ ) in presence of coralyne. (a) CD spectra of  $d(GA)_4$  ( $8 \mu\text{M}$ ) in presence of coralyne ( $12 \mu\text{M}$ ). (b) CD spectra of  $d(GA)_8$  ( $4 \mu\text{M}$ ) in presence of coralyne ( $8 \mu\text{M}$ ) in Tris.HCl buffer solution.

Further, the CD spectra of  $d(GA)_8$  in presence of coralyne showed strong positive and negative CD signals at 272 and 252 nm in nucleobase absorption region and an induced positive CD signal in coralyne absorption region at 337 and 436 nm respectively (Figure 23b). The observed CD features of coralyne/ $d(GA)_8$  are more prominent in both nucleobase and coralyne absorption region confirms that the formation of duplex of  $d(GA)_n$  is highly depends on the length of sequence and reveals that minimum it requires 12 base pairs (*i.e.*,  $n = 6$ ) to induce the duplex conformation. Thus,  $d(GA)_n$   $n \geq 6$  is suitable for the formation of parallel duplex in presence of coralyne. To investigate the effect of salt on the stability of coralyne induced parallel duplex of  $d(GA)_6$ , we recorded CD spectra of coralyne (12  $\mu\text{M}$ ) bound  $d(GA)_6$  (8  $\mu\text{M}$ ) in presence of NaCl (100 mM). CD spectra of coralyne induced duplex of  $d(GA)_6$  retains its CD features in the presence of NaCl (100 mM) and indicates formation duplex of  $d(GA)_6$  in presence of coralyne is independent of salt concentration (Figure 24a).

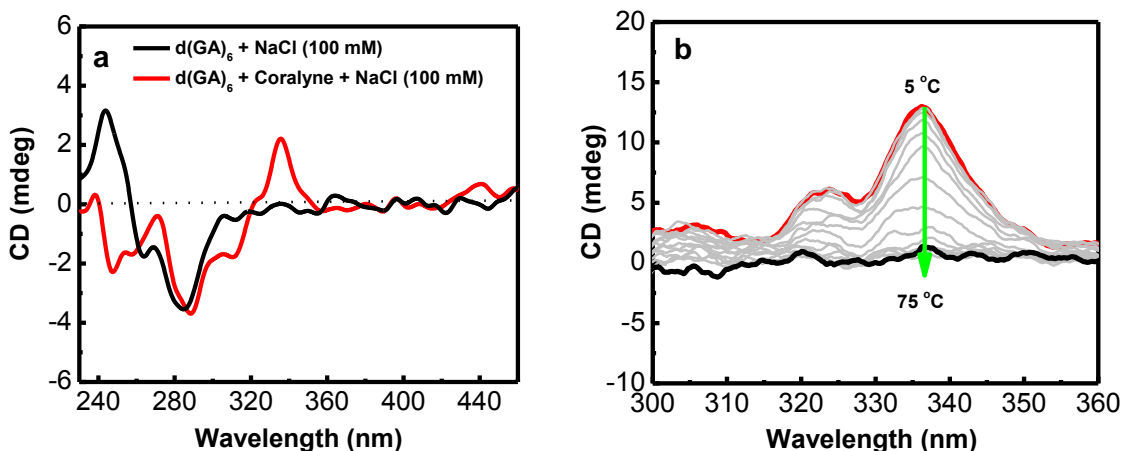


**Figure 24.** CD spectra of coralyne/ $d(GA)_6$ . (a) CD spectra of coralyne/ $d(GA)_6$  in presence of NaCl (100 mM) in Tris-HCl buffer solution. (b) Temperature-dependent CD spectra of coralyne/ $d(GA)_6$  with increasing temperature from 5 °C to 75 °C.

Next, we performed variable temperature dependent CD studies for coralyne/ $d(GA)_6$ . CD spectra showed a gradual decrease in positive signal 272 and a negative CD signal at 252 nm and positive CD signal at 337 nm with increasing temperature from 5 °C to 75 °C (Figure 24b). The plot of CD-intensity at 337 nm as function of temperature gave the melting temperature of  $\sim 35$  °C and it is well corroborated with observed melting temperature of



coralyne/d(GA)<sub>6</sub> from the temperature dependent UV-absorption studies shown in Figure 18a. Therefore, above results suggests the formation of parallel homoduplex of d(GA)<sub>n</sub> (n ≥ 6) in presence of coralyne is highly stable and its stability is independent of salt concentration.

## 5.12 Discussion

As we have discussed in the previous section, canonical B-DNA exists in antiparallel right handed duplex conformation where two strands held together by canonical WC base pairing interactions of nucleobases. Under specific conditions, nucleobases in B-DNA are capable of forming non WC base pairing (non-canonical) interactions which results in the formation of various non-canonical DNA structures including A-motif, parallel and antiparallel triplexes, G-quadruplex and I-motifs.<sup>66</sup> Notably, in A-motif and G-quadruplex DNA structures purine nucleobases (adenine and guanine) plays a vital role due to their inherent self-complementary canonical and non-canonical hydrogen bonding and strong  $\pi$ - $\pi$  stacking interactions. Therefore, adenine-adenine and guanine-guanine base pairing interactions triggers the formation A-motif and G-quadruplex structures in adenine or and guanine-rich sequences respectively.<sup>38,66,114</sup> Another important purine-rich sequence is alternative guanine-adenine d(GA)<sub>n</sub> topic of this work which is also abundant in human genome. From the previous reports, it is known that d(GA)<sub>n</sub> sequences depending on the pH, salt and metal ions forms highly ordered secondary structures including single stranded helix, hairpins, parallel and antiparallel homoduplexes, triplexes and tetraplexes through the non WC base pairing (non-canonical) interactions.<sup>91-97</sup> In this context, our efforts in using small molecules (coralyne, berberine and palmatine) to study the conformational changes of alternative guanine-adenine d(GA)<sub>n</sub> (n = 4, 6 and 8) sequence is valuable to understand their structure and function with significant impact in the biological and materials science. From our study discussed so far, coralyne found to induce and stabilize the parallel homoduplex of d(GA)<sub>n</sub> (n ≥ 6) sequence. Concentration- and temperature-dependent studies supported the formation of stable duplex of d(GA)<sub>6</sub> with the binding stoichiometry of one coralyne per four nucleotide bases. The observed induced positive CD signal in coralyne absorption region suggest binding of the probe in the chiral environments of duplex d(GA)<sub>6</sub>. We presume that coralyne induces the parallel homoduplex of d(GA)<sub>6</sub> through the non WC guanine-guanine and adenine-adenine

base pairing (non-canonical) interactions (Figure 20b). From early studies, it is well documented that parallel homoduplex of d(GA)<sub>6</sub>, adenine and guanine base are in *anti* and *syn* conformations respectively.<sup>91</sup> The *syn*-conformation of guanine residues results in formation of guanine-guanine (G-G) homo base pairs via symmetrical *N*<sup>1</sup>-H...*O*<sup>6</sup> hydrogen bonds and *anti*-conformation of adenine residues forms the adenine-adenine (A-A) base pairs *N*<sup>3</sup>-H...*N*<sup>7</sup> hydrogen bonds.<sup>91</sup> In our study, we are expecting that coralyne also induces the similar non-canonical hydrogen bonding (G-G and A-A) patterns to form parallel homoduplex of d(GA)<sub>6</sub>. Overall, non WC guanine-guanine and adenine-adenine hydrogen bonding plays a vital role in the formation of non-canonical duplex of d(GA)<sub>6</sub> sequence with coralyne.

### 5.13 Conclusion

We have demonstrated coralyne induced non-canonical parallel homoduplex of alternative guanine-adenine d(GA)<sub>n</sub> sequence through non WC guanine-guanine and adenine-adenine base pairing interactions. We have chosen three crescent shaped molecules coralyne, berberine and palmatine and studied their interactions with d(GA)<sub>n</sub> sequence. UV-vis absorption studies showed that among three small molecules coralyne selectively induces the structural transitions of d(GA)<sub>n</sub> sequence with stoichiometry of one coralyne molecule per four nucleotide bases. Further, temperature and time dependent studies revealed that coralyne stabilizes d(GA)<sub>6</sub> sequence in cooperative manner and induces the structural transitions in very short time (<100 ms). Circular dichroism (CD) studies confirm that coralyne binds the d(GA)<sub>n</sub> sequence in intercalation mode and length dependent studies confirms that n≥6 is more suitable for the formation of parallel duplex in presence of coralyne. We anticipated that small molecule induced non-canonical DNA structures opens a new avenue for targeting DNA based therapeutic agents. Further, the fast responsive structural transitions of d(GA)<sub>n</sub> sequence with coralyne has a potential to create a new non B-DNA structure architectures in structural DNA nanotechnology.

### 5.14 Experimental section

**General information.** Small molecules coralyne chloride hydrate, palmatine, berberine, oligonucleotides {d(GA)<sub>4</sub>, d(GA)<sub>6</sub>, d(GA)<sub>8</sub>, dC<sub>10</sub>, dG<sub>10</sub>, dT<sub>20</sub> and (D1)<sub>mix</sub> and (D2)<sub>mix</sub>} and

Tris.HCl were purchased from Sigma–Aldrich. All other reagents were used as received unless otherwise mentioned. UV-vis, fluorescence and circular dichroism (CD) spectra of samples were analyzed in quartz cuvette of 10 mm path length.

**Sample preparation for UV-vis and CD measurements.** Stock solutions of Coralyne chloride, palmatine and berberine were prepared by dissolving small molecules in double-distilled (dd) water in the order of  $10^{-3}$  M. DNA stock solutions were prepared by dissolving oligo samples in dd-water in the order of  $10^{-4}$  M. Solutions of DNA duplexes were prepared in Tris.HCl buffer solution (100 mM, pH = 7.4) buffer solution by mixing complementary DNA strands in equimolar concentration; this solution was then subjected to annealing by heating up to 85 °C for 15 min., subsequently cooled to room temperature for 7 h and stored in the refrigerator (4 °C) for 4 h.

**UV-vis absorption and emission spectroscopy.** The UV–vis absorption and emission spectra were recorded on Agilent Technologies Cary series UV-vis-NIR absorbance and Cary eclipse fluorescence spectrophotometers, respectively. Thermal denaturation (UV-melting) studies were carried out on Cary 5000 UV-vis-NIR spectrophotometer equipped with Cary temperature controller in the range of 10 °C to 90 °C with a ramp rate of 1 °C/min. The variable temperature/wavelength mode was used. Absorption was monitored at 260 nm with regular 5 °C intervals. Melting temperatures ( $T_m$ ) of DNA samples were calculated from the first derivatives of the absorption vs. temperature curves (thermal denaturation or melting curves) obtained by monitoring at 260 nm. A blank sample containing Tris.HCl buffer solution (100 mM, pH = 7.4) was recorded and subtracted from the collected data.

**CD spectroscopy.** CD measurements were carried out on Jasco J-815 spectrometer equipped with a Peltier-type temperature controller (CDF-4265/15) under a nitrogen atmosphere to avoid water condensation. Scans were performed over the range of 200-400 nm with a speed of 100 nm/min, and the spectra represent an average of three scans. A blank sample containing Tris.HCl buffer solution (100 mM, pH = 7.4) was treated in the same manner and subtracted from the collected data.

## Chapter 5c: Fluorescence Reporting of G-Quadruplex Structures and Modulating their DNAzyme Activity Using Polyethylenimine-Pyrene Conjugate

Four-stranded G-quadruplex is a classic example of non-canonical secondary DNA structure that exists at the 3'-end of the chromosomes (telomeres) and gene promoter regions.<sup>70,114</sup> Normally, G-quadruplex structures are formed by the stacking of square tetrads of guanine bases through Hoogsteen hydrogen bonding that are further stabilized by the electrostatic interactions of mono- and divalent cations with  $O^6$  lone pairs of guanine bases.<sup>70,114</sup> These non-canonical secondary structures of DNA are presumed to be associated with many important genome functions such as telomere maintenance, transcription and replication.<sup>115-120</sup> Besides, recent studies have shown that the stabilization of these non-canonical G-quadruplex structures with small molecules has the ability to activate DNA damage response machinery in cancer cells.<sup>121,122</sup> This indicates that research in the area of G-quadruplex is highly promising and significantly impact cancer diagnostics and therapeutics.

Apart from their biological importance, the structural diversity and stability of G-quadruplex structures play vital role in a wide range of applications from DNA nanotechnology to supramolecular chemistry and materials science.<sup>123</sup> For instance, G-quadruplex/hemin complex is one of the most popular DNAzymes known to exhibit horseradish peroxidase-like activity and is widely used for the colorimetric detection of various target analytes, including biological molecules and metal ions.<sup>124-126</sup> DNAzymes are known to catalyze the oxidation of many substrates like Amplex Red (AR) to the fluorescent resorufin, and 2,2'-azino-bis-(3-ethylbenzthiazoline-6-sulphonic acid) (ABTS<sup>2-</sup>) to the colored radical anion ABTS<sup>1-</sup> in the presence of H<sub>2</sub>O<sub>2</sub>.<sup>127,128</sup> With this background, it is apparent that accurate and quantitative detection of G-quadruplex structures is of supreme importance. Evidently, the most important and challenging task in the development of G-quadruplex binding ligands as cancer therapeutic agents is the accurate and quantitative detection of G-quadruplex structures in the cellular context. To address this task, several fluorescence molecules have been designed based on two emission mechanisms i) the restriction of intramolecular rotation (cyanine family, benzimidazole and carbazole dyes) and ii) aggregation-induced emission (AIE).<sup>129,130</sup> Although many fluorescence probes have been reported for G-quadruplex structures, still there is a need for designing fluorescence probes

with better selectivity over duplex DNA.<sup>131-136</sup> An effective fluorescence-based approach to probe the G-quadruplex structure of G-rich DNA sequences and subsequent modulation of their DNzyme activity, with equally high fidelity and efficiency, is the need of the moment.

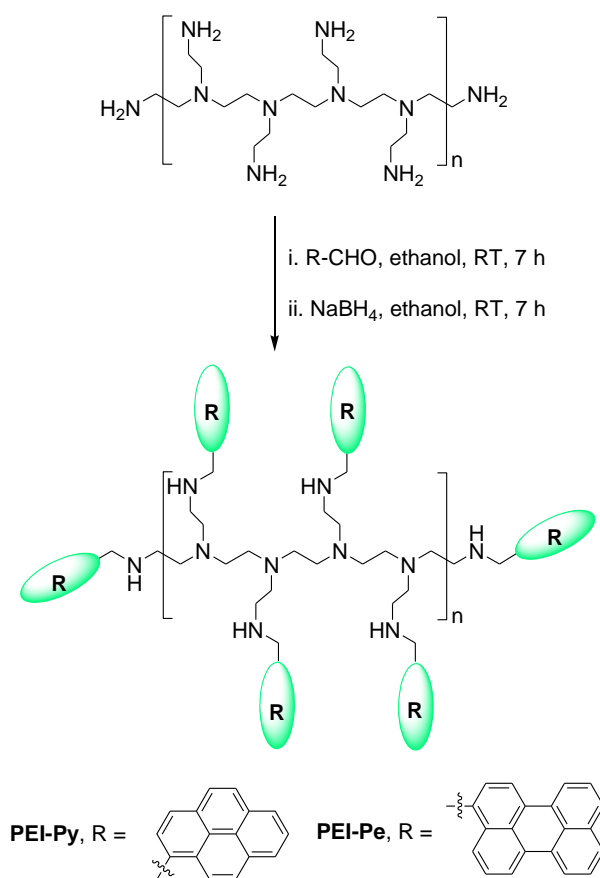
We envisioned to devise a new approach using fluorophore/chromophore-tagged polyamine conjugates for reporting the G-quadruplex structures and their subsequent DNzyme activity.<sup>137</sup> Pyrene was the fluorophore/chromophore of choice due to its ratiometric fluorescence nature (*i.e.*, relative ratios of monomeric to excimeric emission) which makes it a versatile probe for the detection of biological components like nucleotides, DNA and RNA.<sup>138-142</sup> Our choice of polyamine was inspired by the natural polyamines such as spermine (SPM), spermidine (SPMD) and putrescine (PTS). Millimolar concentrations of these polyamines are known to be present in cells and at physiological pH they are prone to bind nucleic acids and stabilizing their compact structures through electrostatic interactions between the negatively charged DNA backbone and the positively charged amino groups of spermine and spermidine.<sup>143-145</sup> The polyamine interaction with nucleic acids is known to stabilize and protect both double and triple-stranded DNA from oxidative stress, mutagens and endonuclease digestion.<sup>143-145</sup> Polyethylenimines (PEIs) are a class of synthetic polyamines with a high degree of branching, molar mass and cationic charge density. PEIs are known to complex with DNA and condense them into small insoluble aggregates (polyplexes), thus facilitating its delivery into cells.<sup>146,147</sup> Besides their applications in gene delivery, PEIs are suitable for a wide variety of applications. PEIs complex with metal ions and anionic species, thus, finding application in waste water treatment for removing heavy metal ions and in the recovery of noble metals during hydrometallurgy.<sup>148</sup>

In the present work, we demonstrated pyrene (Py) and perylene (Pe)-conjugated PEIs for reporting G-quadruplex structures of G-rich deoxyoligonucleotides, and telomeric and gene promoter DNA regions. We further describe the modulation of their DNzyme activity. Fluorescence studies of pyrene-conjugated PEI (**PEI-Py**) showed enhancement in the excimeric emission of pyrene chromophore in the presence of G-rich deoxyoligonucleotides, and telomere and gene promoter sequences but less so with various other oligonucleotides and DNAs. Our study also revealed that **PEI-Py** is capable of modulating the DNzyme activity of various G-quadruplex structures in the presence of hemin and hydrogen peroxide

by lowering the reaction rates. Therefore, **PEI-Py** serves as a common platform to report G-quadruplex structures and modulate their DNAzyme activity.

### 5.15 Synthesis of polyethylenimine (PEI)-chromophore conjugates

Polyamine conjugates **PEI-Py** and **PEI-Pe** were prepared by the condensation of pyrene and perylene carbaldehydes with PEI in ethanol, followed by the reduction of the resultant Schiff bases ( $-C=N-$ ) using sodium borohydride ( $\text{NaBH}_4$ ) at room temperature (Scheme 1).



**Scheme 1.** Synthesis of polyethylenimine (PEI) conjugates **PEI-Py** and **PEI-Pe**.

### 5.16 Photophysical properties of PEI-chromophore conjugates

We investigated the photophysical properties of PEI-conjugates **PEI-Py** and **PEI-Pe** in the absence and presence of single-stranded, double-stranded and G-quadruplex DNAs. The absorption spectra of **PEI-Py** and **PEI-Pe** showed absorption bands in the 300-400 nm and 350-500 nm regions, respectively in sodium phosphate buffer solution (Na-PBS, 10 mM, pH

= 7.3) (Figure 25a). The fluorescence spectrum of **PEI-Py** showed both monomeric ( $\lambda_{\max}$ = 375 nm) and excimeric ( $\lambda_{\max}$ = 490 nm) emissions in the 350-600 nm region whereas **PEI-Pe** showed only monomeric ( $\lambda_{\max}$ = 455 nm) emission in the 450-600 nm region (Figure 25b). Notably, it was clear from the **PEI-Py** fluorescence spectrum that the intensity of excimeric emission band was weaker compared to the monomeric emission band.

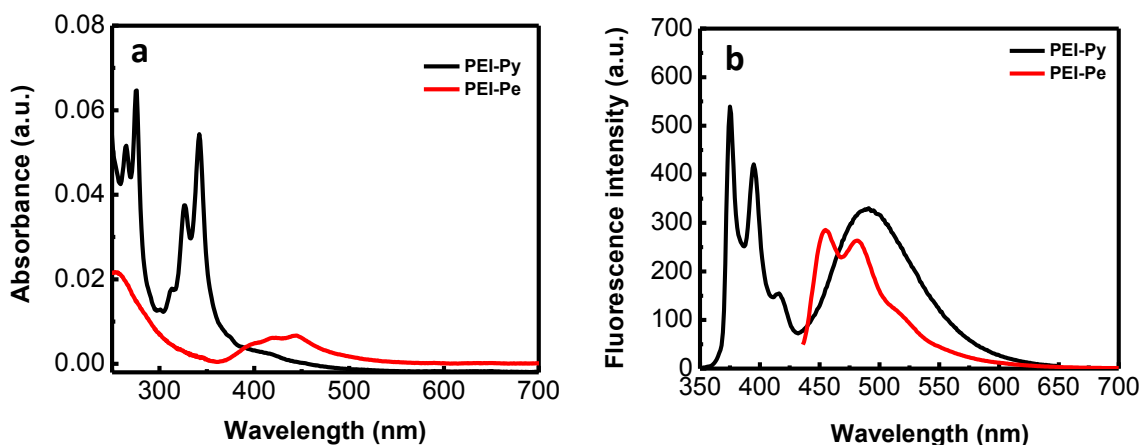


**Figure 25.** (a) & (b) are absorption spectra and emission spectra of **PEI-Py** and **PEI-Pe** in PBS-buffer solution respectively. Concentrations: **PEI-Py** (10  $\mu\text{g/mL}$ ) and **PEI-Pe** (10  $\mu\text{g/mL}$ ).

Next, we measured the fluorescence of **PEI-Py** in the presence of deoxyoligonucleotides ( $\text{dB}_{10}$ ;  $\text{B} = \text{A/T/G/C}$ ), double-stranded DNA ( $(\text{AT})_{10}$ ,  $(\text{GC})_{10}$ , and  $(\text{D2})_{\text{mix}}$ ), double-stranded calf thymus DNA (CT-DNA), and G-quadruplex forming sequences (Te-22, BCL-2, c-MYC, c-KIT2 and TBA) (Table 3).<sup>149</sup> The fluorescence behavior of **PEI-Py** was unaffected in the presence of  $\text{dB}_{10}$  ( $\text{B} = \text{A/T/C}$ ), CT-DNA,  $(\text{AT})_{10}$ ,  $(\text{GC})_{10}$  and  $(\text{D2})_{\text{mix}}$  (Figure 26). Interestingly, **PEI-Py** exhibited an enhancement in pyrene-excimer emission ( $\lambda_{\max}$ = 490 nm) in the presence of  $\text{dG}_{10}$  (Figure 27a). This enhancement in excimeric emission of pyrene chromophore, specifically in the presence of G-rich sequence suggested mutual interaction between **PEI-Py** and  $\text{dG}_{10}$ . To further validate this result, we performed concentration-dependent study on **PEI-Py** with increasing concentration of  $\text{dG}_{10}$ . Upon sequential addition of increasing concentrations of  $\text{dG}_{10}$  to a fixed concentration of **PEI-Py**, linear increase in the pyrene-excimeric emission at 490 nm was observed (Figure 27b). The enhancement in pyrene-excimeric emission of **PEI-Py** in the presence of G-rich deoxyoligonucleotide is a useful property because most of the commonly employed staining dyes display very weak fluorescence in the presence of G-rich sequences as a consequence of

photoinduced electron transfer (PET) between the guanine moiety and dyes.<sup>136</sup> Although, G-quadruplex formation and stabilization by spermine, spermidine and PEI is reported,<sup>150-154</sup> it was not possible to confirm the identity of the secondary structure as G-quadruplex using simple optical techniques such as fluorescence spectroscopy.

**Table 3.** Single and double stranded DNA used to study the effect of PEI-conjugates.

Code	Sequence	Structure
dA <sub>10</sub>	5'-AAAAAAAAAA-3'	Random coil
dT <sub>10</sub>	5'-TTTTTTTTTT-3'	Random coil
dC <sub>10</sub>	5'-CCCCCCCCCC-3'	Random coil
<sup>1</sup> dG <sub>10</sub>	5'-GGGGGGGGGG-3'	Random coil
(AT) <sub>10</sub>	5'-AAAAAAAAAA-3' 3'-TTTTTTTTTT-5'	Duplex
(GC) <sub>10</sub>	5'-GGGGGGGGGG-3' 3'-CCCCCCCCCC-5'	Duplex
(D2) <sub>mix</sub>	5'-CGGTACCGCGGTACCG-3' 3'-GCCATGGCGCCATGGC-5'	Duplex
CT-DNA	---	Duplex
Te-22	5'-AGGGTTAGGGTTAGGGTTAGGG-3'	Quadruplex
BCL-2	5'-GGGCGCGGGAGGAAGGGGGCGGG-3'	Quadruplex
c-KIT2	5'-CGGGCGGGCGCGAGGGAGGGG-3'	Quadruplex
TBA	5'-GGGTTGGTGTGGTTGGA-3'	Quadruplex
c-MYC	5'-TGGGGAGGGTGGGGAGGGTGGGGAAGG-3'	Quadruplex

<sup>1</sup>In presence of salt conditions forms parallel quadruplex structure.

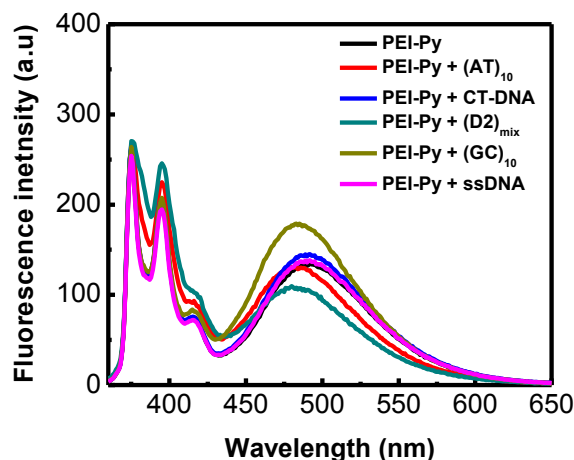


**Figure 26.** Fluorescence spectra of **PEI-Py** in presence of CT-DNA, (AT)<sub>10</sub>, (GC)<sub>10</sub>, ssDNA and (D2)<sub>mix</sub> in PBS-buffer solution. Concentrations: **PEI-Py** (10 µg/mL), ssDNA and dsDNA (2 µM).



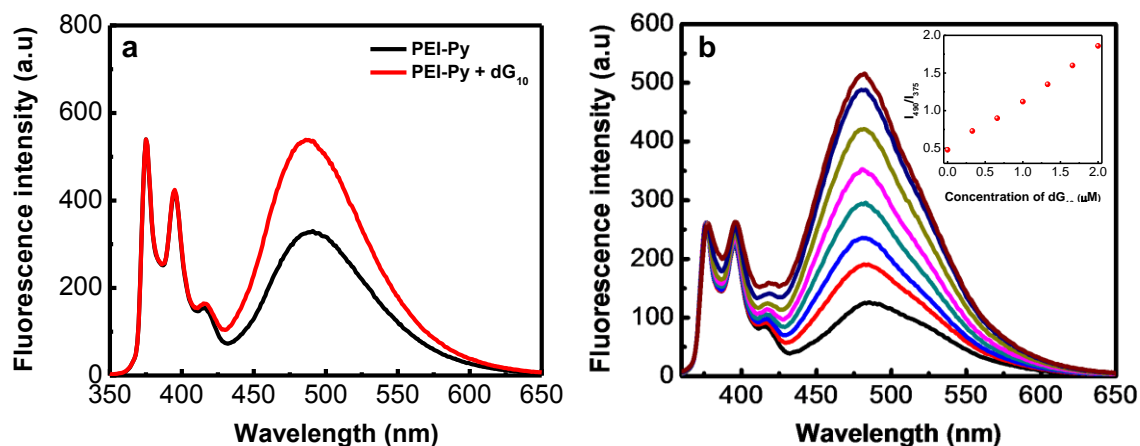


**Figure 27.** (a) Fluorescence spectra of **PEI-Py** in presence of  $dG_{10}$  in PBS-buffer solution. Concentrations:  $dG_{10}$  (2  $\mu\text{M}$ ) and **PEI-Py** (10  $\mu\text{g}/\text{mL}$ ). (b) Fluorescence spectra of **PEI-Py** with increasing concentration of  $dG_{10}$  in PBS-buffer solution. *Inset:* Shows the ratio of excimer and monomeric fluorescence of pyrene against the concentration of  $dG_{10}$ . Concentrations: **PEI-Py** (10  $\mu\text{g}/\text{mL}$ ) and  $dG_{10}$  (from 0 to 2  $\mu\text{M}$ ).

### 5.17 Preferential fluorescence in presence of G-quadruplex forming sequences

Selective fluorescence reporting of G-quadruplex structures of G-rich deoxyoligonucleotides, human telomere sequence and G-rich oncogenes is an important analytical tool for cancer diagnostics and therapeutics. We measured the fluorescence spectra of **PEI-Py** in the presence of biologically relevant G-rich human telomere sequence (Te-22), promoter regions of human oncogenes (BCL-2, c-MYC, c-KIT2), and thrombin-binding aptamer (TBA) in PBS buffer solution. Remarkably, fluorescence spectra of **PEI-Py** showed enhanced pyrene-excimeric emission in the presence of the G-rich human telomere and oncogene sequences (Figure 28 and 29a). Further, we performed the fluorescence studies of **PEI-Py** with Te-22 in presence of  $\text{Na}^+$  and  $\text{K}^+$ . It is well-known in the literature that,  $\text{Na}^+$  and  $\text{K}^+$  stabilize anti-parallel and mixed hybrid conformations of Te-22, respectively.<sup>70,114</sup> From the fluorescence studies, we observed minimal changes in relative ratio of monomeric and excimeric emission of pyrene (Figure 29b). These results show that **PEI-Py** cannot distinguish the parallel, anti-parallel and mixed hybrid conformations G-quadruplex structures. From the above results, we presume that the compact size and highly negatively charged surface or high charge density of G-quadruplex structure might be one of the main reasons for its selective

interaction with **PEI-Py**. Overall, **PEI-Py** showed prominent enhancement in the excimer emission of pyrene in presence of G-quadruplex structures over other DNA forms (Figure 30).

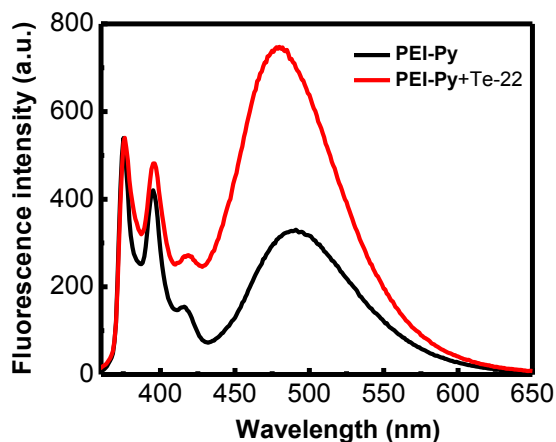


**Figure 28.** Fluorescence spectra of **PEI-Py** in presence of Te-22. Concentrations: Te-22 (2  $\mu\text{M}$ ) and **PEI-Py** (10  $\mu\text{g/mL}$ ).

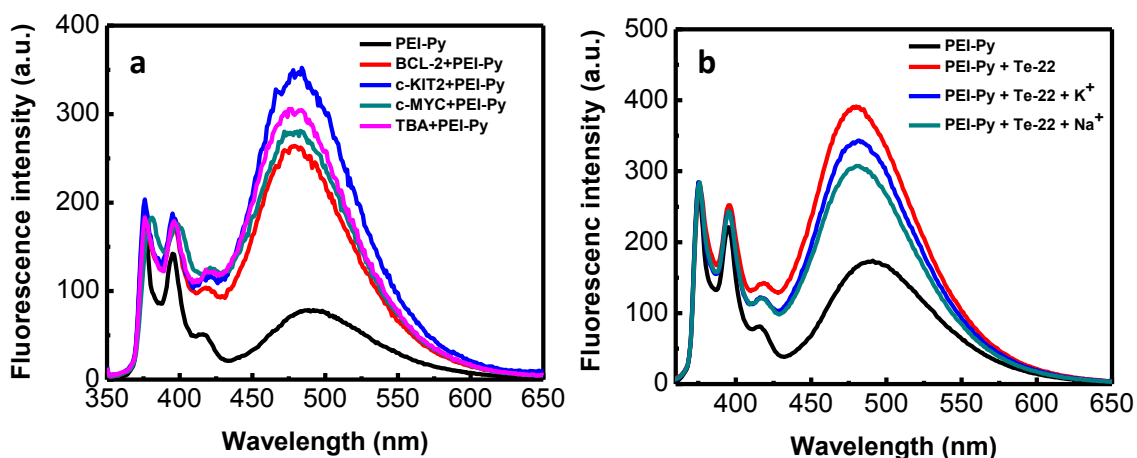


**Figure 29.** (a) Fluorescence spectra of **PEI-Py** in presence of other G-quadruplex sequences in PBS-solution. Concentrations: **PEI-Py** (10  $\mu\text{g/mL}$ ) and G-quadruplex forming sequences (2  $\mu\text{M}$ ). (b) Fluorescence spectra of **PEI-Py** with Te-22 in presence of  $\text{K}^+$  and  $\text{Na}^+$  ions in PBS-buffer solution. Concentrations: **PEI-Py** (10  $\mu\text{g/mL}$ ), Te-22 (2  $\mu\text{M}$ ), NaCl (100 mM) and KCl (100 mM).

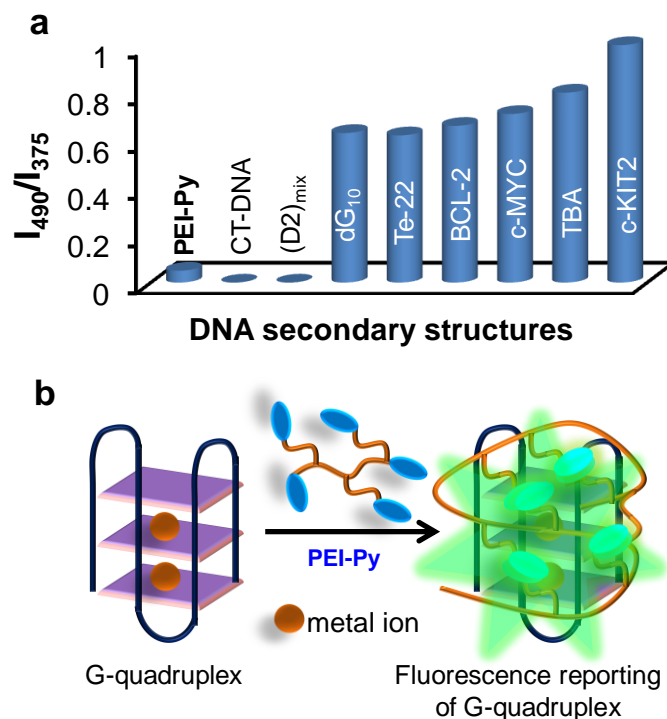


**Figure 30.** Fluorescence spectra of **PEI-Py**. (a) Relative ratios of excimeric and monomeric emission intensity of pyrene in presence of dG<sub>10</sub>, Te-22, Calf thymus DNA (CT-DNA), (D2)<sub>mix</sub>, BCL-2, c-MYC, c-KIT2 and TBA in Na-PBS buffer solution. (b) Schematic representation of **PEI-Py** interaction with G-rich sequences. Concentrations: ssDNA, dsDNA and G-quadruplex forming DNA (2  $\mu$ M) and **PEI-Py** (10  $\mu$ g/mL).

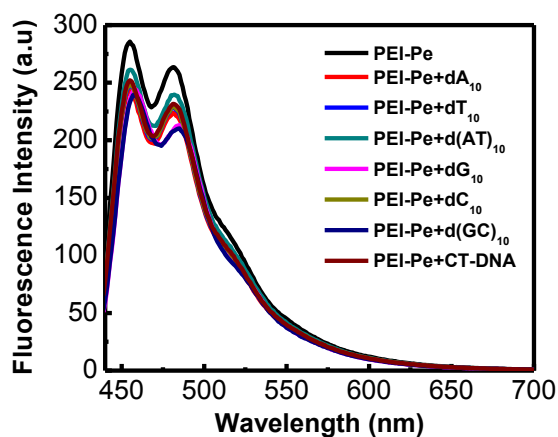


**Figure 31.** Fluorescence spectra of **PEI-Pe** in presence of deoxyoligonucleotides in PBS-buffer solution. Concentrations: **PEI-Pe** (10  $\mu$ g/mL), ssDNA and dsDNA (2  $\mu$ M).

However, fluorescence measurements revealed that the **PEI-Pe** was ineffective in reporting the presence of various deoxyoligonucleotides, double-stranded DNA and G-quadruplexes (Figure 31). Thus, we employed **PEI-Py** for detailed investigations towards selective and efficient reporting of various G-quadruplex structures of G-rich deoxyoligonucleotides and biologically important human telomere and oncogene sequences.

### 5.18 Isothermal titration calorimetry (ITC)-measurements of PEI-Py in presence of deoxyoligonucleotides

To ascertain the selectivity of our probe towards G-quadruplexes, we carried out isothermal titration calorimetry (ITC) measurements of **PEI-Py** in presence of single stranded dC<sub>10</sub>, double stranded-(D2)<sub>mix</sub> and G-quadruplex of Te-22.

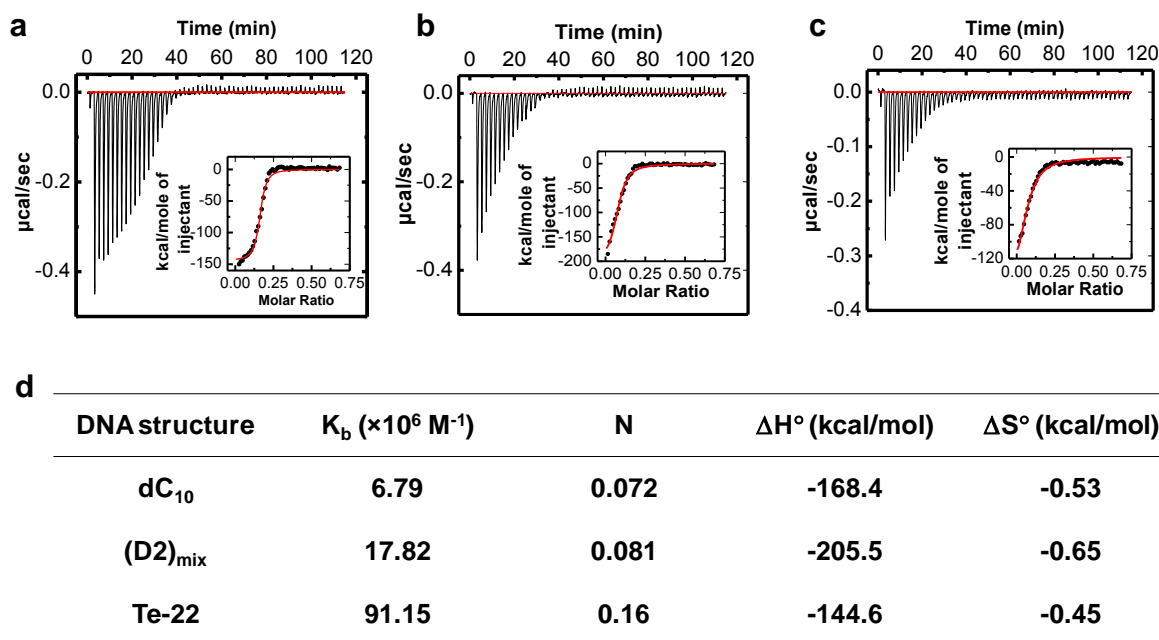


**Figure 32.** ITC data obtained for the interaction of **PEI-Py** with various forms of DNA. Curves (a-c) are the ITC profiles of **PEI-Py** upon interaction with G-Quadruplex of Te-22, duplex DNA (D2)<sub>mix</sub> and single stranded DNA dC<sub>10</sub> respectively. *Inset:* The obtained data points as results of heat burst for every injection and were fitted to single binding model. (d) Table show thermodynamic parameters obtained from the ITC profiles (a-c). Where, N: denotes the binding site size,  $K_b$ : binding constant,  $\Delta H^\circ$ : change in enthalpy and  $\Delta S^\circ$ : change in entropy.

ITC is the most sensitive and preferred tool for examining the thermodynamic properties of biological systems such as protein-protein, DNA-DNA, DNA-protein and small molecule-protein/DNA interactions.<sup>155,156</sup> Our ITC measurements showed that interaction between **PEI-Py** and various DNA structures (single stranded, double stranded and G-quadruplex) are highly exothermic in nature (Figure 32a-c). The obtained raw ITC data was fitted to single site binding model for the interaction of **PEI-Py** with single strand, double strand and G-quadruplex structures (*Insets* in Figure 32a-c). The binding constant, enthalpy and entropy values of **PEI-Py** in presence of different DNA structures are shown in Figure 32d. The thermodynamic parameters obtained from ITC profiles showed maximum binding affinity of **PEI-Py** towards G-quadruplex of Te-22 which is ~5- and ~13-folds higher than the double and single stranded DNAs, respectively. Thus, the high binding affinity of **PEI-Py** towards G-quadruplex compared to single and double stranded DNAs is in perfect agreement with selectivity and fluorescence enhancement of **PEI-Py** (pyrene excimer) in presence of G-quadruplex structures.

### 5.19 CD studies of PEI-Py in presence of G-quadruplex structures

To gain further insights into the recognition of G-quadruplex structures by **PEI-Py**, CD studies of dG<sub>10</sub> and human telomere sequence (Te-22) in buffer solution under ambient conditions were performed. CD-spectroscopy is a versatile tool to study secondary structures of nucleic acids, particularly DNA, as this technique selectively distinguishes distinct conformational states depending on the salt and metal ion concentrations.<sup>157</sup> CD spectrum of dG<sub>10</sub> alone in PBS buffer (10 mM, pH = 7.3) solution showed positive and negative CD signals at 260 and 240 nm respectively, suggesting the formation of a well-ordered parallel G-quadruplex structure.<sup>158,159</sup> The CD spectrum of dG<sub>10</sub>, in the presence of **PEI-Py** retained positive and negative CD signals at 260 and 240 nm, respectively, with a slight decrease in CD intensity of the positive signal (Figure 33a).<sup>159</sup> Further, we recorded CD spectra of the human telomere sequence (Te-22) in the presence of **PEI-Py** in PBS buffer solution. In the absence of **PEI-Py**, CD spectrum of Te-22 showed positive signals at 240 nm and 295 nm, and a negative signal at 260 nm. These CD signals revealed the formation of a typical antiparallel G-quadruplex structure.<sup>158,159</sup> Interestingly, all the CD signals of Te-22 were retained in the presence of **PEI-Py** as the polyamine conjugate stabilized the antiparallel G-quadruplex conformation (Figure 33b).

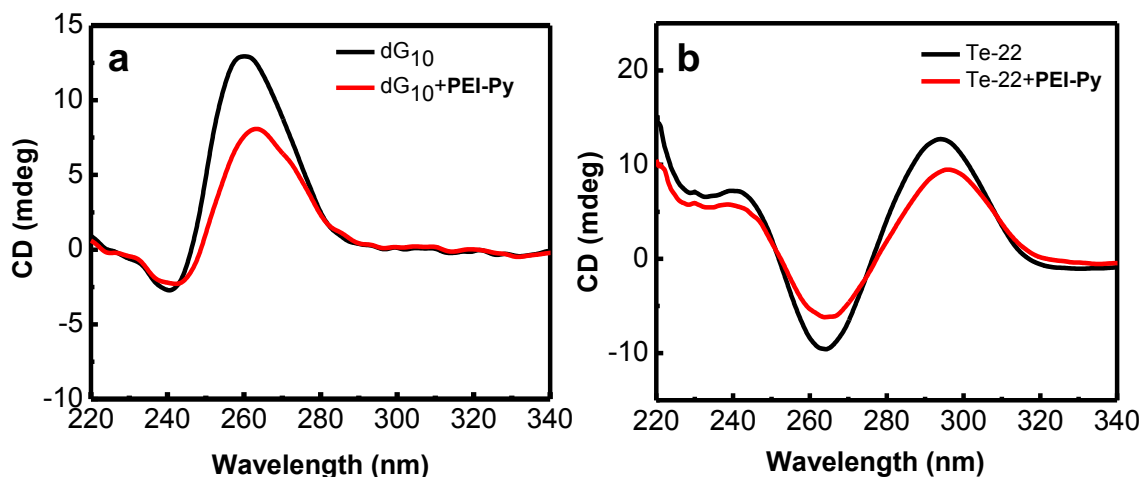


**Figure 33.** CD spectra of dG<sub>10</sub> and Te-22. (a) & (b) CD spectra of dG<sub>10</sub> and Te-22 in presence of **PEI-Py** in Na-PBS buffer solution respectively. Concentrations: DNA (4  $\mu$ M) and **PEI-Py** (20  $\mu$ g/mL).

To exclude the role of sodium cations that are present in PBS buffer solution, we recorded the CD spectra in Tris-HCl buffer (100 mM, pH = 7.4) solution in the absence and presence of **PEI-Py**. In Tris-HCl, dG<sub>10</sub> showed two negative CD signals at 279 and 233 nm and a positive CD signal at 257 nm. These CD features corresponds to random coil conformation of dG<sub>10</sub> in Tris-HCl buffer.<sup>158,159</sup> However, dG<sub>10</sub> showed distinct spectral features with a prominent positive and a negative CD signal at 265 and 240 nm, respectively, in the presence of **PEI-Py** (Figure 34a). The striking difference in the CD features of dG<sub>10</sub>, in the absence and presence of **PEI-Py**, suggests the conformational change from random coil to ordered secondary structure. However, CD spectra of Te-22 in Tris-HCl buffer solution showed the existence of random coil conformation both in the presence and absence of **PEI-Py** (Figure 34b). CD data confirmed the existence of ordered secondary (G-quadruplex) structures of dG<sub>10</sub> and Te-22 in the absence and presence of **PEI-Py** in Na-PBS. On the other hand, the random coil conformation of dG<sub>10</sub> in Tris-HCl buffer solution transformed to ordered secondary structure due to preferential stabilizing effect of **PEI-Py**. In general, CD studies confirmed that **PEI-Py** recognized G-quadruplex structures without altering their conformational features and, therefore, **PEI-Py** is a potential fluorescence reporting probe for G-quadruplex structures of G-rich deoxyoligonucleotides and biologically important gene sequences, by means of enhancement in the pyrene-excimeric emission.

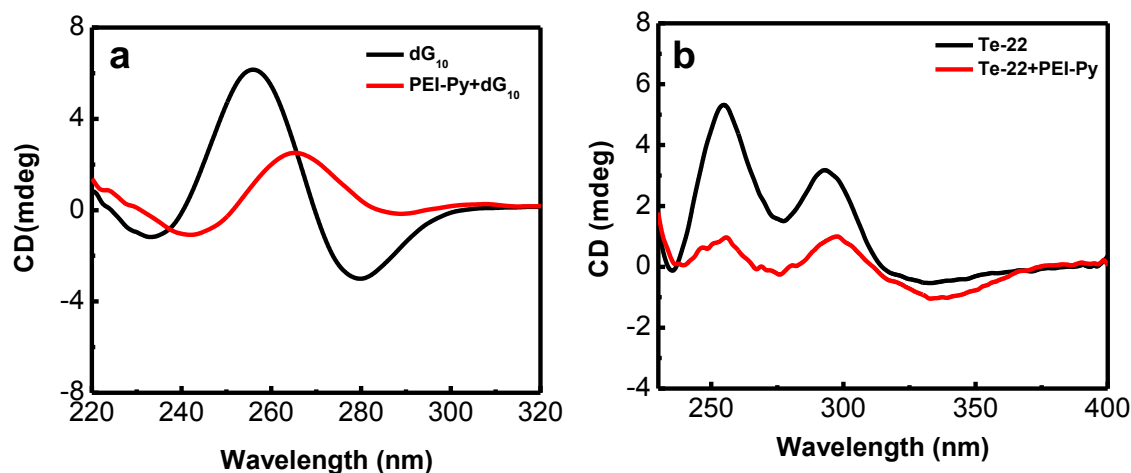


**Figure 34.** Circular dichroism spectra of dG<sub>10</sub> and Te-22 (a) & (b) CD spectra of dG<sub>10</sub> and Te-22 in presence of **PEI-Py** in Tri-HCl buffer solution. Concentrations: DNA (4  $\mu$ M) and **PEI-Py** (20  $\mu$ g/mL).

### 5.20 DNAzyme activity of PEI-Py in presence G-quadruplex/hemin complex

We anticipated that the **PEI-Py** could modulate the peroxidase (DNAzyme) activity of G-quadruplex structures upon complexation with hemin. In order to study the effect of **PEI-Py** on the DNAzyme activity of G-quadruplex structures, we prepared preformed complexes of Te-22 and dG<sub>10</sub> with hemin in the absence and presence of PEI and **PEI-Py** in PBS buffer (10 mM, pH = 7.3) solutions. Non-fluorescent Amplex red (AR) was used as a DNAzyme reporter which is known to release red fluorescent resorufin during the reaction.<sup>128</sup> Recently, DNAzyme activity of G-quadruplex/hemin complex in presence of natural polyamine spermine has been studied.<sup>160</sup> In the absence of PEI and **PEI-Py**, the preformed Te-22-hemin complex showed maximum fluorescence intensity at 587 nm suggesting the conversion of non-fluorescent AR to red fluorescent resorufin in the presence of hydrogen peroxide (H<sub>2</sub>O<sub>2</sub>) after one minute. In the presence of PEI, we observed a slight decrease in the fluorescence intensity at 587 nm. However, almost ~4-fold decrease in fluorescence was observed with preformed Te-22-hemin complex in the presence of **PEI-Py** (Figure 35a). Further, we did not observe any detectable change in the pyrene-excimer emission of **PEI-Py**.

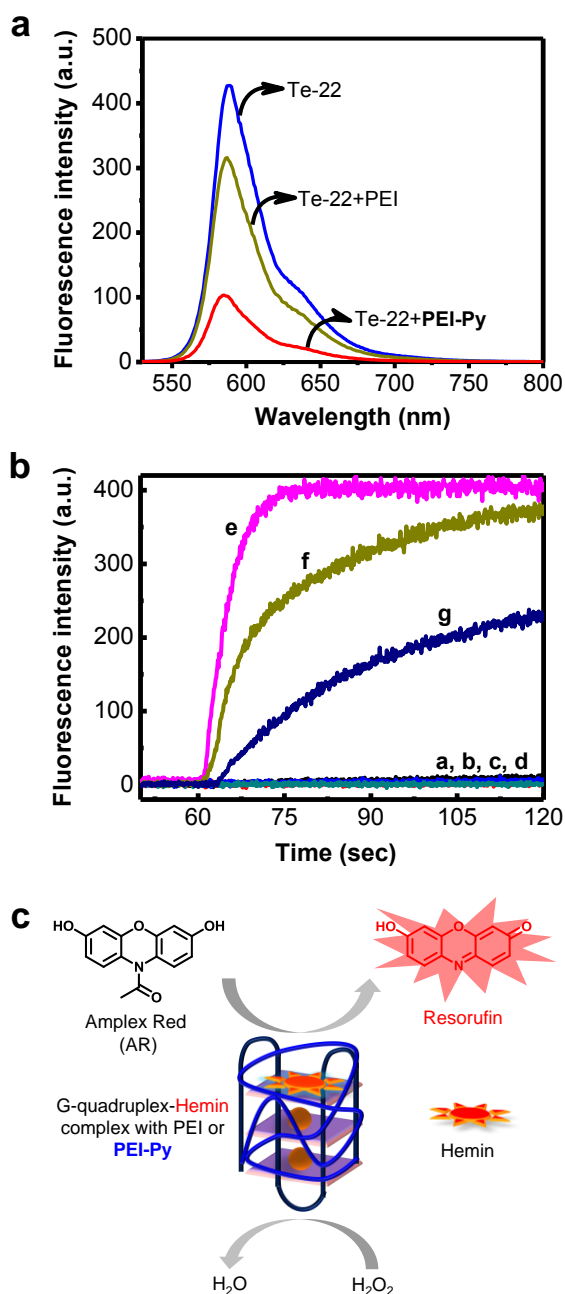


**Figure 35.** DNAzyme activity of Te-22. (a) Fluorescence spectra of Te-22 in presence of PEI and **PEI-Py** in Na-PBS buffer solution. (b) Time-dependent fluorescence response as result of oxidation of Amplex red (AR) to resorufin in presence of Te-22-Hemin with PEI and **PEI-Py**. a: H<sub>2</sub>O<sub>2</sub>+AR, b: Hemin+AR, c: PEI+AR, d: **PEI-Py**+AR, e: Te-22+Hemin+H<sub>2</sub>O<sub>2</sub>+AR, f: Te-22+PEI+Hemin+H<sub>2</sub>O<sub>2</sub>+AR and g: Te-22+**PEI-Py**+Hemin+H<sub>2</sub>O<sub>2</sub>+AR. (c) Schematic representation of DNAzyme activity of G-quadruplex/hemin complex in presence of PEI and **PEI-Py**. Concentrations: Te-22 (2  $\mu$ M), Hemin (2  $\mu$ M), AR (5  $\mu$ M), **PEI-Py** (10  $\mu$ g/mL) and PEI (10  $\mu$ g/mL) and Hydrogen peroxide (10 mM) at ambient conditions.



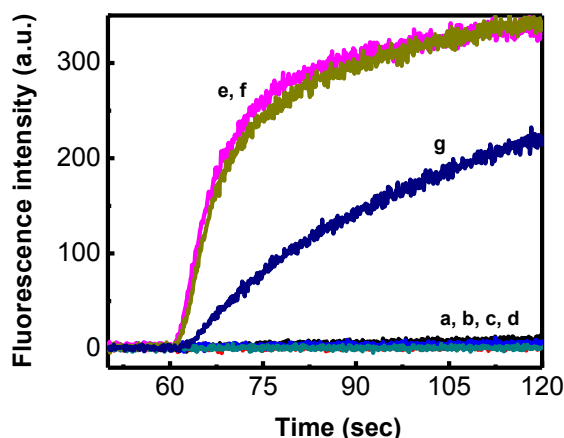


**Figure 36.** Time-dependent fluorescence response as results of oxidation of AR to resorufin in presence of dG<sub>10</sub>-Hemin with PEI and **PEI-Py**. a: H<sub>2</sub>O<sub>2</sub>+AR, b: Hemin+AR, c: PEI+AR, d: **PEI-Py**+AR, e: dG<sub>10</sub>+Hemin+H<sub>2</sub>O<sub>2</sub>+AR, f: dG<sub>10</sub>+PEI+Hemin+H<sub>2</sub>O<sub>2</sub>+AR and g: dG<sub>10</sub>+**PEI-Py**+Hemin+H<sub>2</sub>O<sub>2</sub>+AR. Concentrations: dG<sub>10</sub> (2  $\mu$ M), Hemin (2  $\mu$ M), AR (5  $\mu$ M), **PEI-Py** (10  $\mu$ g/mL) and PEI (10  $\mu$ g/mL) and Hydrogen peroxide (10 mM) at ambient conditions.

Next, we assessed DNAzyme activity of dG<sub>10</sub>-hemin complex in PBS buffer (10 mM, pH = 7.3) solution with the addition of H<sub>2</sub>O<sub>2</sub> (10 mM). In the absence of PEI and **PEI-Py**, addition of H<sub>2</sub>O<sub>2</sub> (10 mM) to preformed dG<sub>10</sub>-hemin complex showed maximum fluorescence of resorufin comparing to hemin or hydrogen peroxide alone. The presence of PEI slightly decreased the fluorescence intensity of resorufin, whereas the presence of **PEI-Py** exhibited almost ~4-fold decrease in the fluorescence intensity of resorufin. These studies clearly highlight the ability of **PEI-Py** to decrease the DNAzyme activity of G-quadruplexes. To corroborate the effect of **PEI-Py** in decreasing the DNAzyme activity, we performed the time-dependent fluorescence measurements of Te-22-hemin and dG<sub>10</sub>-hemin complexes in the presence of PEI and **PEI-Py**. In time-dependent fluorescence studies, we monitored the fluorescence intensity of resorufin at 587 nm as a function of time, after the addition of H<sub>2</sub>O<sub>2</sub> (10 mM). The time-dependent fluorescence measurements showed almost basal fluorescence of resorufin in the presence of only hemin or PEI or **PEI-Py**. However, Te-22 G-quadruplex/hemin complex showed a rapid increase in fluorescence intensity of resorufin with time and reached saturation within 15 secs. In the presence of PEI and Te-22 G-quadruplex/hemin complex, the fluorescence intensity of resorufin gradually increased and

reached a plateau after 60 secs. Interestingly, in the presence of **PEI-Py** and Te-22-hemin complex, only ~50 % resorufin fluorescence was recovered even after 60 secs (Figure 35b). Similar fluorescence recovery of resorufin was observed with dG<sub>10</sub>-hemin complex, in the presence of PEI and **PEI-Py** (Figure 36). Overall, the time-dependent fluorescence studies revealed that the DNAzyme activity of Te-22-hemin and dG<sub>10</sub>-hemin complexes was delayed as well as reduced in the presence of **PEI-Py**. From the above results, we presume that the interaction of PEI and **PEI-Py** with G-quadruplex structures of Te-22 and dG<sub>10</sub> can affect their complexation with hemin which results in the delay as well as decrease in the DNAzyme activity (Figure 35c).

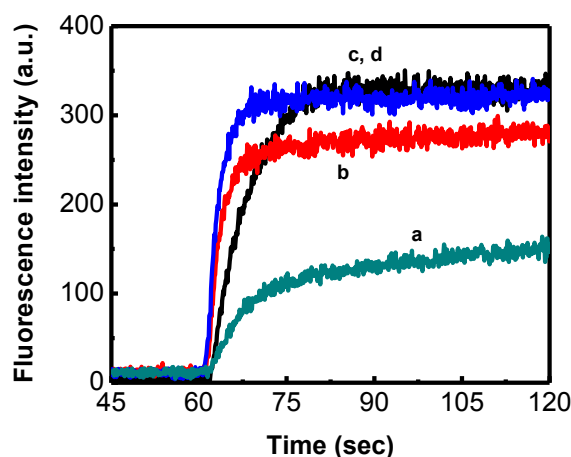


**Figure 37.** Time-dependent fluorescence response as result of oxidation of AR to resorufin in presence of Te-22-Hemin with poly-L-Lysine, Chitosan and PAMAM3.0 in PBS-buffer solution. a: Te-22+PAMAM3.0+Hemin+H<sub>2</sub>O<sub>2</sub>+AR, b: Te-22+poly-L-Lysine+Hemin+H<sub>2</sub>O<sub>2</sub>+AR, c: Te-22+Chitosan+Hemin+H<sub>2</sub>O<sub>2</sub>+AR d: Te-22+Hemin+H<sub>2</sub>O<sub>2</sub>+AR. Concentrations: Te-22 (2  $\mu$ M), Hemin (2  $\mu$ M), AR (5  $\mu$ M), polycationic polymers (10  $\mu$ g/mL) and H<sub>2</sub>O<sub>2</sub> (10 mM) at ambient conditions.

Further, we performed the DNAzyme activity of Te-22 G-quadruplex in presence of linear (poly L-lysine and chitosan) and dendritic (PAMAM3.0) polyamines. Time-dependent fluorescence study showed slight or negligible effect of DNAzyme activity of Te-22 G-quadruplex/hemin complexes in presence of linear polyamines while prominent effect (decrease in fluorescence) in presence of PAMAM3.0 dendrimer (Figure 37). This study revealed that branched (PEI) or dendritic (PAMAM3.0) polyamines form strong polyionic complexes with G-quadruplex structures compare to linear polyamine. The strong

complexation of branched or dendritic polyamines with G-quadruplex structure hinders the accessibility of substrate like AR and ABTS to DNAzyme reactive sites. Therefore, oxidation of AR to resorufin in presence DNAzyme is inhibited which subsequently reflected in the decrease in fluorescence intensity. Hence, our study showed that DNAzyme activity of G-quadruplex/hemin complexes can be modulated using PEI and **PEI-Py**.

### 5.21 Conclusion

In conclusion, we successfully demonstrated the potential of pyrene-conjugated polyethylenimine (**PEI-Py**) as a fluorescence probe to report G-quadruplex structures of G-rich deoxyoligonucleotide and biologically important human telomere and oncogene promoter sequences. **PEI-Py** selectively reports the G-quadruplex structures by means of enhancement in the pyrene-excimeric emission. The integrity of the G-quadruplex structures in the presence of **PEI-Py** was confirmed by circular dichroism studies. The parallel G-quadruplex structures of dG<sub>10</sub> and antiparallel G-quadruplex structure of Te-22 were intact in the presence of **PEI-Py**. Our study on the DNAzyme activity of G-quadruplex/hemin complexes revealed that **PEI-Py** could be used to effectively modulate their activity. The selective fluorescence reporting of G-quadruplex structures of G-rich human telomere and oncogene sequences using **PEI-Py** may assist the development of diagnostics and therapeutics against these sequences in various cancers. Further, we anticipate that polyamine conjugates such as **PEI-Py** are useful probes for reporting the biologically important nucleic acid secondary structures and their functions.

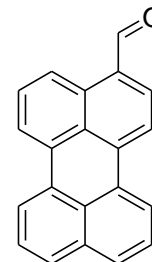
### 5.22 Experimental Section

**General information.** All the reagents, deoxyoligonucleotides (dA<sub>10</sub>, dT<sub>10</sub>, dG<sub>10</sub>, dC<sub>10</sub>), telomeric sequences (Te-22), gene promoter sequences (BCL-2, c-MYC and c-KIT2), thrombin-binding aptamer (TBA), Calf-thymus DNA, Amplex Red (AR), Tris-HCl, pyrene-1-carbaldehyde, hydrogen peroxide and phosphate buffered saline were purchased from Sigma-Aldrich. PEI-600 and perylene were purchased from Alfa-Aesar. <sup>1</sup>H and <sup>13</sup>C NMR spectra were recorded on a Bruker AV-400 MHz spectrometer with chemical shifts reported as parts per million (*ppm*) (in CDCl<sub>3</sub>/D<sub>2</sub>O tetramethylsilane as an internal standard) at 20 °C.

UV-vis absorption and emission spectra were measured in quartz cuvettes of 1 cm path length.

### Detailed synthesis of PEI-conjugates

**Synthesis of perylene-3-carbaldehyde.** To a stirred solution of DMF (0.6 mL), phosphoryl chloride (0.4 mL) was added and allowed to stir for 10 min at 0 °C. After 10 min, solution of perylene (0.5 g, 1.8 mmol) in 1, 2-dichlorobenzene (8 mL) was added to above reaction mixture at 0 °C. The resulting mixture was stirred under cold conditions for 30 min and then shifted to an oil-bath where reaction



**Perylene-3-carbaldehyde**

mixture was allowed to stir at 75 °C under inert conditions for overnight. After the reaction, the mixture was poured into ice-cold water and the solution pH was adjusted to neutral. The product was extracted with chloroform and solvent was evaporated under vacuum. The crude product was purified using column chromatography on silica gel using ethyl acetate/petroleum ether (20:80) as an eluent to afford perylene-3-carbaldehyde in good yield (60%). <sup>1</sup>H-NMR (*CDCl*<sub>3</sub>, 400 MHz,  $\delta_H$  ppm): 10.32 (s, 1H, CHO), 9.18-9.15 (d, *J* = 8.5 Hz, 1H, Ar-H), 8.31-8.26 (m, 4H, Ar-H), 7.94-7.93 (d, *J* = 7.8 Hz, 1H, Ar-H), 7.82-7.80 (d, *J* = 8 Hz, 1H, Ar-H), 7.76-7.67 (m, 2H, Ar-H), 7.57-7.52 (m, 2H, Ar-H). <sup>13</sup>C NMR (*CDCl*<sub>3</sub>, 100 MHz,  $\delta_C$  ppm): 192.7, 137.6, 137.1, 134.3, 132.3, 131.2, 130.6, 130.0, 129.9, 129.8, 129.3, 128.9, 128.5, 128.1, 126.9, 126.6, 124.6, 122.8, 121.5, 121.1, 119.1.

**Synthesis procedure for PEI-Py and PEI-Pe.** To a stirred solution of PEI-600 (1 equiv.) in an ethanol: dichloromethane (5:5 mL) mixture, perylene-3-carbaldehyde or pyrene-1-carbaldehyde (4 equiv.) was added, and the resulting reaction mixture was allowed to stir for 7 h at room temperature. After completion of the reaction, sodium borohydride (4 equiv.) was added followed by few drops of aq. NaOH (1N) solution. The reaction mixture was stirred for another 7 h at room temperature. After completion of the reaction, solvent was evaporated under vacuum. The crude mixture was dissolved in water, and 50  $\mu$ L of HCl (1N) was added to neutralize the pH. Unreacted starting compounds were extracted using dichloromethane and water. The water layer was evaporated, and the product was dried in a vacuum oven at 45 °C. **PEI-Py:** <sup>1</sup>H-NMR (*D*<sub>2</sub>*O*, 400 MHz) (pyrene region)  $\delta$  8.0-6.5 (Ar-H), 3.2-1.5 (C-H). **PEI-Pe:** <sup>1</sup>H-NMR (*D*<sub>2</sub>*O*, 400 MHz) (peryene region)  $\delta$  8.5-8.0 (Ar-H), 3.5-2 (C-H).

**Sample preparation for UV-vis and fluorescence measurements.** Stock solutions of PEI, PEI-Py and PEI-Pe were prepared in double distilled water in the order of 1 mg/mL. These stock solutions were completely covered with aluminum foil and stored at -10 °C. DNA stock solutions were prepared by dissolving deoxyoligonucleotide samples in double distilled water in the order of  $10^{-4}$  M. Double-stranded (ds) DNA samples were prepared by mixing equimolar concentrations of complementary strands in PBS (10 mM, pH = 7.3) buffer solution. The samples were annealed by heating them to 85 °C for 15 min and cooling to room temperature for 7 h, followed by storage in the refrigerator for 4 h. Similarly, G-quadruplex samples were prepared by dissolving G-quadruplex forming deoxyoligonucleotides in PBS buffer and subjecting to the annealing process described above.

**UV-vis Absorption and fluorescence emission spectra.** The UV-vis absorption spectra were recorded on Cary 500 UV-vis-NIR spectrophotometer equipped with Cary temperature controller. Fluorescence emission spectra were recorded on Cary eclipse fluorescence spectrophotometer with temperature controller.

**Circular dichroism (CD) spectroscopy.** CD measurements were carried out on a JASCO J-815 spectrometer equipped with Peltier-type temperature controller (CDF-4265/15) under nitrogen atmosphere to avoid water condensation. Scans were performed over the range of 200-500 nm with a speed of 100 nm/min, and the spectra represented an average of three scans. A blank sample containing buffer solution was treated in the same manner and subtracted from the collected data.

**ITC-measurements.** ITC experiments were performed using Micro-Cal VP-ITC instrument at 21 °C, wherein 250  $\mu$ L of PEI-Py (0.5 mg/mL) in PBS buffer solution at pH 7 were injected in equal steps of 5  $\mu$ L into 1.47 mL of DNA (2  $\mu$ M) in PBS buffer solution.

### 5.23 References

1. Casey, J. R.; Grinstein, S.; Orlowski, J. Sensors and regulators of intracellular pH. *Nat. Rev. Mol. Cell Biol.* **2010**, *11*, 50-61.
2. Luzio, J. P.; Pryor, P. R.; Bright, N. A. Lysosomes: fusion and function. *Nat. Rev. Mol. Cell Biol.* **2007**, *8*, 622-632.

3. Saftig, P.; Klumperman, J. Lysosome biogenesis and lysosomal membrane proteins: trafficking meets function. *Nat. Rev. Mol. Cell Biol.* **2009**, *10*, 623-635.
4. Schindler, M.; Grabski, S.; Hoff, E.; Simon, S. M. Defective pH regulation of acidic compartments in human breast cancer cells (MCF-7) is normalized in adriamycin-resistant cells (MCF-7adr). *Biochemistry* **1996**, *35*, 2811-2817.
5. Wolfe, D. M.; Lee, J. H.; Kumar, A.; Lee, S.; Orenstein, S. J.; Nixon, R. A. Autophagy failure in Alzheimer's disease and the role of defective lysosomal acidification. *Eur. J. Neurosci.* **2013**, *37*, 1949-1961.
6. Roos, A.; Boron, W. F. Intracellular pH. *Physiol. Rev.* **1981**, *61*, 296-434.
7. Srivastava, J.; Barber, D. L.; Jacobson, M. P. Intracellular pH sensors: design principles and functional significance. *Physiology* **2007**, *22*, 30-39.
8. Madsen, J.; Canton, I.; Warren, N. J.; Themistou, E.; Blanz, A.; Ustbas, B.; Tian, X.; Pearson, R.; Battaglia, G.; Lewis, A. L.; Armes, S. P. Nile Blue-based nanosized pH sensors for simultaneous far-red and near-infrared live bioimaging. *J. Am. Chem. Soc.* **2013**, *135*, 14863-14870.
9. Berbasova, T.; Nosrati, M.; Vasileiou, C.; Wang, W.; Lee, K. S.; Yapici, I.; Geiger, J. H.; Borhan, B. Rational design of a colorimetric pH sensor from a soluble retinoic acid chaperone. *J. Am. Chem. Soc.* **2013**, *135*, 16111-16119.
10. Chen, S.; Hong, Y.; Liu, Y.; Liu, J.; Leung, C. W. T.; Li, M.; Kwok, R. T. K.; Zhao, E.; Lam, J. W. Y.; Yu, Y.; Tang, B. Z. Full-range intracellular pH sensing by an aggregation-induced emission-active two-channel ratiometric fluorogen. *J. Am. Chem. Soc.* **2013**, *135*, 4926-4929.
11. Kim, H. J.; Heo, C. H.; Kim, H. M. Benzimidazole-based ratiometric two-photon fluorescent probes for acidic pH in live cells and tissues. *J. Am. Chem. Soc.* **2013**, *135*, 17969-17977.
12. Hauglang, P. R. *The Handbook: A Guide to Fluorescent Probes and Labeling Technologies*, 10th ed.; Molecular Probes: Eugene, OR, **2005**.
13. Llopis, J.; McCaffery, J. M.; Miyawaki, A.; Farquhar, M. G.; Tsien, R. Y. Measurement of cytosolic, mitochondrial, and Golgi pH in single living cells with green fluorescent proteins. *Proc. Natl. Acad. Sci. U.S.A* **1998**, *95*, 6803-6808.
14. Tantama, M.; Hung, Y. P.; Yellen, G. Imaging intracellular pH in live cells with a genetically encoded red fluorescent protein sensor. *J. Am. Chem. Soc.* **2011**, *133*, 10034-10037.
15. Shi, W.; Li, X.; Ma, H. A tunable ratiometric pH sensor based on carbon nanodots for the quantitative measurement of the intracellular pH of whole cells. *Angew. Chem., Int. Ed.* **2012**, *51*, 6432-6435.

16. Zhou, K.; Liu, H.; Zhang, S.; Huang, X.; Wang, Y.; Huang, G.; Sumer, B. D.; Gao, J. Multicolored pH-tunable and activatable fluorescence nanoplatfrom responsive to physiologic pH stimuli. *J. Am. Chem. Soc.* **2012**, *134*, 7803-7811.
17. Marín, M. J.; Galindo, F.; Thomas, P.; Russell, D. A. Localized intracellular pH measurement using a ratiometric photoinduced electron-transfer-based nanosensor. *Angew. Chem., Int. Ed.* **2012**, *51*, 9657-9661.
18. Bath, J.; Tuberfield, A. J. DNA nanomachines. *Nat. Nanotechnol.* **2007**, *2*, 275-284.
19. Seeman, N. C. Nanomaterials based on DNA. *Annu. Rev. Biochem.* **2010**, *79*, 65-87.
20. Teller, C.; Willner, I. Functional nucleic acid nanostructures and DNA machines. *Curr. Opin. Biotechnol.* **2010**, *21*, 376-391.
21. Bhatia, D.; Sharma, S.; Krishnan, Y. Synthetic, biofunctional nucleic acid-based molecular devices. *Curr. Opin. Biotechnol.* **2011**, *22*, 475-484.
22. Krishnan, Y.; Simmel, F. C. Nucleic acid based molecular devices. *Angew. Chem., Int. Ed.* **2011**, *50*, 3124-3156.
23. McLaughlin, C. K.; Hamblin, G. D.; Sleiman, H. F. Supramolecular DNA assembly. *Chem. Soc. Rev.* **2011**, *40*, 5647-5656.
24. Wetmur, J. G. DNA probes: applications of the principles of nucleic acid hybridization. *Crit. Rev. Biochem. Mol. Biol.* **1991**, *26*, 227-259.
25. Didenko, V. V. DNA probes using fluorescence resonance energy transfer (FRET): designs and applications. *Biotechniques.* **2001**, *31*, 1106-1121.
26. Drummund, T. G.; Hill, M. G.; Barton, J. K. Electrochemical DNA sensors. *Nat. Biotechnol.* **2003**, *21*, 1192-1199.
27. Rosi, N. L.; Mirkin, C. A. Nanostructures in biodiagnostics. *Chem. Rev.* **2005**, *105*, 1547-1562.
28. Sassolas, A.; Leca-Bouvier, B. D.; Blum, L. J. DNA biosensors and microarrays. *Chem. Rev.* **2008**, *108*, 109-139.
29. Winfree, E.; Liu, F.; Wenzler, L. A.; Seeman, N. C. Design and self-assembly of two-dimensional DNA crystals. *Nature* **1998**, *394*, 539-544.
30. Rothemund, P. W. K. Folding DNA to create nanoscale shapes and patterns. *Nature* **2006**, *440*, 297-302.
31. Douglas, S. M.; Bachelet, I.; Church, G. M. A logic-gated nanorobot for targeted transport of molecular payloads. *Science* **2012**, *335*, 831-834.
32. Krishnan, Y.; Bathe, M. Designer nucleic acids to probe and program the cell. *Synth. Cell Biol.* **2012**, *22*, 624-633.

33. Lu, C. H.; Willner, B.; Willner, I. DNA nanotechnology: from sensing and DNA machines to drug-delivery systems. *ACS Nano* **2013**, *7*, 8320-8332.
34. Gehring, K.; Leroy, J. L.; Gueron, M. A tetrameric DNA structure with protonated cytosine-cytosine base pairs. *Nature* **1993**, *363*, 561–565.
35. Chen, Y.; Lee, S-H; Mao, C. A DNA nanomachine based on a duplex-triplex transition. *Angew. Chem., Int. Ed.* **2004**, *43*, 5335-5338.
36. Elbaz, J.; Want, Z. G.; Orbach, R.; Willner, I. pH-stimulated concurrent mechanical activation of two DNA "tweezers". A "SET-RESET" logic gate system. *Nano Lett.* **2009**, *9*, 4510-4514.
37. Shimron, S.; Magen, N.; Elbaz, J.; Willner, I. pH-programmable DNAzyme nanostructures. *Chem. Commun.* **2011**, *47*, 8787-8789.
38. Chakraborty, K.; Sharma, S.; Maiti, P. K.; Krishnan, Y. The poly dA helix: a new structural motif for high performance DNA-based molecular switches. *Nucleic Acids Res.* **2009**, *97*, 2810-2817.
39. Ohmichi, T.; Kawamoto, Y.; Wu, P.; Miyoshi, D.; Karimata, H.; Sugimoto, N. DNA-based biosensor for monitoring pH in vitro and in living cells. *Biochemistry* **2005**, *44*, 7125-7130.
40. Brucale, M.; Zuccheri, G.; Samorì, B. The dynamic properties of an intramolecular transition from DNA duplex to cytosine-thymine motif triplex. *Org. Biomol. Chem.* **2005**, *3*, 575-577.
41. Liu, D.; Bruckbauer, A.; Abell, C.; Balasubramanian, S.; Kang, D.; Klenerman, D.; Zhou, D. A reversible pH-driven DNA nanoswitch array. *J. Am. Chem. Soc.* **2006**, *128*, 2067-2071.
42. Li, T.; Famulok, M. I-motif-programmed functionalization of DNA nanocircles. *J. Am. Chem. Soc.* **2013**, *135*, 1593-1599.
43. Liu, D.; Balasubramanian, S. A proton-fuelled DNA nanomachine. *Angew. Chem., Int. Ed.* **2003**, *42*, 5734-5736.
44. Liedl, T.; Simmel, F. C. Switching the conformation of a DNA molecule with a chemical oscillator. *Nano Lett.* **2005**, *5*, 1894-1898.
45. Chen, Y.; Mao, C. pH-induced reversible expansion/contraction of gold nanoparticle aggregates. *Small* **2008**, *4*, 2191-2194.
46. Chen, C.; Song, G.; Ren, J.; Qu, X. A simple and sensitive colorimetric pH meter based on DNA conformational switch and gold nanoparticle aggregation. *Chem. Commun.* **2008**, 6149-6151.
47. Li, T.; Ackermann, D.; Hall, A. M.; Famulok, M. Input-dependent induction of oligonucleotide structural motifs for performing molecular logic. *J. Am. Chem. Soc.* **2012**, *134*, 3508-3516.
48. Li, T.; Famulok, M. I-motif-programmed functionalization of DNA nanocircles. *J. Am. Chem. Soc.* **2013**, *135*, 1593-1599.



49. Modi, S.; Swetha, M. G.; Goswami, D.; Gupta, G. D.; Mayor, S.; Krishnan, Y. A DNA nanomachine that maps spatial and temporal pH changes inside living cells. *Nat. Nanotechnol.* **2009**, *4*, 325-330.
50. Surana, S.; Bhat, J. M.; Koushika, S. P.; Krishnan, Y. An autonomous DNA nanomachine maps spatiotemporal pH changes in a multicellular living organism. *Nat. Commun.* **2011**, *2*, 340.
51. Modi, S.; Nizak, C.; Surana, S.; Halder, S.; Krishnan, Y. Two DNA nanomachines map pH changes along intersecting endocytic pathways inside the same cell. *Nat. Nanotechnol.* **2013**, *8*, 459-467.
52. Cardone, R. A.; Casavola, V.; Reshkin, S. J. The role of disturbed pH dynamics and the Na<sup>+</sup>/H<sup>+</sup> exchanger in metastasis. *Nat. Rev. Cancer* **2005**, *5*, 786-795.
53. Saha, S.; Chakraborty, K.; Krishnan, Y. Tunable, colorimetric DNA-based pH sensors mediated by A-motif formation. *Chem. Commun.* **2012**, *48*, 2513-2515.
54. Zheng, B.; Cheng, S.; Liu, W.; Lam, M. H.; Liang, H. A simple colorimetric pH alarm constructed from DNA-gold nanoparticles. *Analytica Chimica Acta.* **2012**, *741*, 106-113.
55. Tyagi, S.; Kramer, F. R. Molecular beacons: probes that fluoresce upon hybridization. *Nat. Biotechnol.* **1996**, *14*, 303-308.
56. Kong, D.; Jin, Y.; Yin, Y.; Mi, H.; Shen, H. Real-time PCR detection of telomerase activity using specific molecular beacon probes. *Anal. Bioanal. Chem.* **2007**, *388*, 699-709.
57. Wang, K.; Tang, Z.; Yang, C. J.; Kim, Y.; Fang, X.; Li, W.; Wu, Y.; Medley, C. D.; Cao, Z.; Li, J.; Colon, P.; Lin, H.; Tan, W. Molecular engineering of DNA: molecular beacons. *Angew. Chem., Int. Ed.* **2009**, *48*, 856-870.
58. Bose, D.; Jayaraj, G. G.; Kumar, S; Maiti, S. A molecular-beacon-based screen for small molecule inhibitors of miRNA maturation. *ACS Chem. Biol.* **2013**, *8*, 930-938.
59. Kim, S.; Choi, J.; Majima, T. Self-assembly of polydeoxyadenylic acid studied at the single-molecule level. *J. Phys. Chem. B* **2011**, *115*, 15399-15405.
60. Kypr, J.; Kejnovska, I.; Renciuik, D., Vorlickova, M. Circular dichroism and conformational polymorphism of DNA. *Nucleic Acids Res.* **2009**, *37*, 1713-1725.
61. Pautot, S.; Frisken, B. J.; Weitz, D. A. Production of unilamellar vesicles using an inverted emulsion. *Langmuir* **2003**, *19*, 2870-2879.
62. Saha, A.; Mondal, G.; Biswas, A.; Chakraborty, I.; Jana, B.; Ghosh, S. *In vitro* reconstitution of a cell-like environment using liposomes for amyloid beta peptide aggregation and its propagation. *Chem. Commun.* **2013**, *49*, 6119-6122.
63. Menger, F. M.; Angelova, M. I. Giant vesicles: imitating the cytological processes of cell membranes. *Acc. Chem. Res.* **1998**, *31*, 789-797.

64. Tanner, P.; Baumann, P.; Enea, R.; Onaca, O.; Palivan, C.; Meier, W. Polymeric vesicles: from drug carriers to nanoreactors and artificial organelles. *Acc. Chem. Res.* **2011**, *44*, 1039–1049.
65. Blackburn, G. M.; Gait, M. J.; Loakes, D.; Williams, D. M. *Nucleic Acids in Chemistry and Biology*, RSC Publishing, Cambridge, UK, **2006**.
66. Choi, J.; Majima, T. Conformational changes of non-B DNA. *Chem. Soc. Rev.* **2011**, *40*, 5893–5909.
67. Zhao, J.; Bacolla, A.; Wang, G.; Vasquez, K. M. Non-B DNA structure-induced genetic instability and evolution. *Cell. Mol. Life Sci.* **2010**, *67*, 43–62.
68. Wang, G.; Vasquez, K. M. Non-B DNA structure-induced genetic instability. *Mutat. Res.* **2006**, *598*, 103–119.
69. Ou, T.; Lu, Y.; Tan, Y.; Huang, Z.; Wong, K. Y.; Gu, L. G-quadruplexes: targets in anticancer drug design. *ChemMedChem* **2008**, *3*, 690-713.
70. Balasubramanian, S.; Hurley, L. H.; Neidle, S. Targeting G-quadruplexes in gene promoters: a novel anticancer strategy?. *Nat. Rev. Drug Discov.* **2011**, *10*, 261-275.
71. Persil, O.; Santai, C. T.; Jain, S. S.; Hud, N. V. Assembly of an antiparallel homo-adenine DNA duplex by small-molecule binding. *J. Am. Chem. Soc.* **2004**, *126*, 8644–8645.
72. Franceschin, M. G-Quadruplex DNA structures and organic chemistry: more than one connection. *Eur. J. Org. Chem.* **2009**, 2225-2238.
73. Liu, J.; Lu, Y. Rational design of “turn-on” allosteric DNAzyme catalytic beacons for aqueous mercury ions with ultrahigh sensitivity and selectivity. *Angew. Chem.* **2007**, *119*, 7731–7734.
74. Liu, X. F.; Tang, Y. L.; Wang, L. H.; Zhang, J.; Song, S. P.; Fan, C.; Wang, S. Optical detection of mercury(II) in aqueous solutions by using conjugated polymers and label-free oligonucleotides. *Adv. Mater.* **2007**, *19*, 1471–1474.
75. Ono, A.; Cao, S.; Togashi, H.; Tashiro, M.; Fujimoto, T.; Machinami, T.; Oda, S.; Miyake, Y.; Okamoto, I.; Tanaka, Y. Specific interactions between silver(I) ions and cytosine-cytosine pairs in DNA duplexes. *Chem. Commun.* **2008**, 4825–4827.
76. Chiang, C. K.; Huang, C. C.; Liu, C. W.; Chang, H. T. Oligonucleotide-based fluorescence probe for sensitive and selective detection of mercury(II) in aqueous solution. *Anal. Chem.* **2008**, *80*, 3716–3721.
77. Li, D.; Wieckowska, A.; Willner, I. Optical analysis of Hg<sup>2+</sup> ions by oligonucleotide–gold-nanoparticle hybrids and DNA-based machines. *Angew. Chem.* **2008**, *120*, 3991–3995.
78. Liu, C. W.; Hsieh, Y. T.; Huang, C. C.; Lin, Z. H.; Chang, H. T. Detection of mercury(II) based on Hg<sup>2+</sup>-DNA complexes inducing the aggregation of gold nanoparticles. *Chem. Commun.* **2008**, 2242–2244.

79. Wang, Z.; Lee, J. H.; Lu, Y. Highly sensitive "turn-on" fluorescent sensor for Hg<sup>2+</sup> in aqueous solution based on structure-switching DNA. *Chem. Commun.* **2008**, 6005–6007.
80. Xu, H.; Hepel, M. "Molecular beacon"-based fluorescent assay for selective detection of glutathione and cysteine. *Anal. Chem.* **2011**, 83, 813–819.
81. Li, J.; Yang, S.; Zhou, W.; Liu, C.; Jia, Y.; Zheng, J.; Li, Y.; Li, J.; Yang, R. A gold nanocarrier and DNA-metal ligation-based sensing ensemble for fluorescent assay of thiol-containing amino acids and peptides. *Chem. Commun.* **2013**, 49, 7932-7934.
82. Lin, Y. H.; Tseng, W. L. Fluorescence detection of coralyne and polyadenylation reaction using an oligonucleotide-based fluorogenic probe. *Chem. Commun.* **2011**, 47, 11134–11136.
83. Lin, Y. H.; Tseng, W. L. A room-temperature adenosine-based molecular beacon for highly sensitive detection of nucleic acids. *Chem. Commun.* **2012**, 48, 6262–6264.
84. Kuo, C. Y.; Tseng, W. L. Adenosine-based molecular beacons as light-up probes for sensing heparin in plasma. *Chem. Commun.* **2013**, 49, 4607–4609.
85. Hoffman, E. K.; Trusko, S. P.; Murphy, M.; George, D. L. An S1 nuclease-sensitive homopurine/homopyrimidine domain in the c-Ki-ras promoter interacts with a nuclear factor. *Proc. Natl. Acad. Sci. USA* **1990**, 87, 2705–2709.
86. Reaban, M. E.; Griffin, J. A. Induction of RNA-stabilized DNA conformers by transcription of an immunoglobulin switch region. *Nature* **1990**, 348, 342–344.
87. Manor, H.; Rao, B. S.; Martin, R.G. Abundance and degree of dispersion of genomic d(GA)<sub>n</sub>d(TC)<sub>n</sub> sequences. *J. Mol. Evol.* **1988**, 27, 96-101.
88. Wells, R. D.; Collier, D. A.; Hanvey, J. C.; Shimizu, M.; Wohlrab, F. The chemistry and biology of unusual DNA structures adopted by oligopurine.oligopyrimidine sequences. *FASEB J.* **1988**, 2, 2939 -2949.
89. Yagil, G. Paranemic structures of DNA and their role in DNA unwinding. *CRC Crit. Rev. Biochem. Mol. Biol.* **1991**, 26, 475-559.
90. Tripathi, J.; Brahmachari, S. K. Distribution of simple repetitive (TG/CA)<sub>n</sub> and (CT/AG)<sub>n</sub> sequences in human and rodent genomes. *J. Biomol. Struct. Dynam.* **1991**, 9, 387-397.
91. Rippe, K.; Fritsch, V.; Westhof, E.; Jovin, T. M. Alternating d(G-A) sequences form a parallel-stranded DNA homoduplex. *EMBO J.* **1992**, 11, 3777-3786.
92. Casanovas, J. M.; Huertas, D.; Ortiz-Lombardia, M.; Kypr, J.; Azorin, F. Structural polymorphism of d(GA.TC)<sub>n</sub> DNA sequences. Intramolecular and intermolecular associations of the individual strands. *J. Mol. Biol.* **1993**, 233, 671-681.

93. Huertas, D.; Bellolell, L.; Casasnovas, J. M.; Coll, M.; Azorin, F. Alternating d(GA)<sub>n</sub> DNA sequences form antiparallel stranded homoduplexes stabilized by the formation of G.A base pairs. *EMBO J.* **1993**, *12*, 4029-4038.
94. Evertsz, E. M.; Rippe, K.; Jovin, T. M. Parallel-stranded duplex DNA containing blocks of trans purine-purine and purine-pyrimidine base pairs. *Nucleic Acids Res.* **1994**, *22*, 3293-3303.
95. Ortiz-Lombardia M.; Eritja, R.; Azorin, F.; Kypr, J. Tejralova, I.; Vorlickova, M. Divalent zinc cations induce the formation of two distinct homoduplexes of a d(GA)<sub>20</sub> DNA sequence. *Biochemistry* **1995**, *34*, 14408- 14415.
96. Dolinnaya, N. G.; Fresco, J. R. Single-stranded nucleic acid helical secondary structure stabilized by ionic bonds: d(A<sup>+</sup>-G)<sub>10</sub>. *Proc. Natl. Acad. Sci. U.S.A.* **1992**, *89*, 9242-9246.
97. Dolinnaya, N. G.; Braswell, E. H.; Fossella, J. A.; Klump, H.; Fresco, J. R. Molecular and thermodynamic properties of d(A<sup>+</sup>-G)<sub>10</sub>, a single-stranded nucleic acid helix without paired or stacked bases. *Biochemistry* **1993**, *32*, 10263-10270.
98. Iwasa, K.; Moriyasu, M.; Yamori, T.; Turuo, T.; Lee, D-U.; Wiegerebe, W. In vitro cytotoxicity of the protoberberine-type alkaloids. *J. Natl. Prod.* **2001**, *64*, 896–898.
99. Kong, W.; Wei, J.; Abidi, P.; Lin, M.; Inaba, S.; Li, C.; Wang, Y.; Wang, Z.; Si, S.; Pan, H.; Wang, S.; Wu, J.; Wang, Y.; Li, Z.; Liu, J.; Jiang, J.-D. Berberine is a novel cholesterol-lowering drug working through a unique mechanism distinct from statins. *Nat. Med.* **2004**, *10*, 1344–1351.
100. Kuo, C. L.; Chi, C. W.; Liu, T. Y. Modulation of apoptosis by berberine through inhibition of cyclooxygenase-2 and Mcl-1 expression in oral cancer cells. *In Vivo* **2005**, *1*, 247–252.
101. Letasiova, S.; Jantova, S.; Cipak, L.; Muckova, M. Berberine-antiproliferative activity in vitro and induction of apoptosis/necrosis of the U937 and B16 cells. *Cancer Lett.* **2006**, *239*, 254–262.
102. Letašiová, S.; Jantová, S.; Miko, M.; Ovadekova, R.; Horvathova, M. Effect of berberine on proliferation, biosynthesis of macromolecules, cell cycle and induction of intercalation with DNA, dsDNA damage and apoptosis in Ehrlich ascites carcinoma cells. *J. Pharm. Pharmacol.* **2006**, *58*, 263–270.
103. Wilson, W. D.; Gough, A. N.; Doyle, J. J. Coralyne. Intercalation with DNA as a possible mechanism of antileukemic action. *J. Med. Chem.* **1976**, *19*, 1261-1263.
104. Polak, M.; Hud, N. V. Complete disproportionation of duplex poly(dT)\*poly(dA) into triplex poly(dT)\*poly(dA)\*poly(dT) and poly(dA) by coralyne. *Nucleic Acids Res.* **2002**, *30*, 983-992.

105. Jain, S. S.; Polak, M.; Hud, N. V. Controlling nucleic acid secondary structure by intercalation: effects of DNA strand length on coralyne-driven duplex disproportionation. *Nucleic Acids Res.* **2003**, *31*, 4608-4615.
106. Giri, P.; Hossain, M.; Kumar, G. S. RNA specific molecules: cytotoxic plant alkaloid palmatine binds strongly to poly(A). *Bioorg. Med. Chem. Lett.* **2006**, *16*, 2364-2368.
107. Bhadra, K.; Maiti, M.; Kumar, G. S. Molecular recognition of DNA by small molecules: AT base pair specific intercalative binding of cytotoxic plant alkaloid palmatine. *Biochim. Biophys. Acta.* **2007**, *1770*, 1071-1080.
108. Maiti, M.; Kumar, G. S. Molecular aspects on the interaction of protoberberine, benzophenanthridine, and aristolochia group of alkaloids with nucleic acid structures and biological perspectives. *Med. Res. Rev.* **2007**, *27*, 649-695.
109. Bhadra, K.; Maiti, M.; Kumar, G. S. Berberine-DNA complexation: new insights into the cooperative binding and energetic aspects. *Biochim. Biophys. Acta, Gen. Subj.* **2008**, *1780*, 1054-1061.
110. Bhadra, K.; Maiti, M.; Kumar, G. S. Interaction of isoquinoline alkaloids with polymorphic DNA structures. *Chem. Biodivers.* **2009**, *6*, 1323-1342.
111. Islam, M. M.; Chowdhury, S. R.; Kumar, G. S. Spectroscopic and calorimetric studies on the binding of alkaloids berberine, palmatine and coralyne to double stranded RNA polynucleotides. *J. Phys. Chem. B* **2009**, *113*, 1210-1224.
112. Garbett, N. C.; Ragazzon, P. A.; Chaires, J. B. Circular dichroism to determine binding mode and affinity of ligand-DNA interactions. *Nat. Protoc.* **2007**, *2*, 3166-3172.
113. Kypr, J.; Kejnovska, I.; Renciuik, D.; Vorlickova, M. Circular dichroism and conformational polymorphism of DNA. *Nucleic Acids Res.* **2009**, *37*, 1713-1725.
114. Sen, D.; Gilbert, W. Formation of parallel four-stranded complexes by guanine-rich motifs in DNA and its implications for meiosis. *Nature* **1988**, *334*, 364-366.
115. Folini, M.; Venturini, L.; Cimino-Reale, G.; Zaffaroni, N. Telomeres as targets for anticancer therapies. *Expert Opin. Ther. Targets* **2011**, *15*, 579-593.
116. Neidle, S. Human telomeric G-quadruplex: the current status of telomeric G-quadruplexes as therapeutic targets in human cancer. *FEBS J.* **2010**, *277*, 1118-1125.
117. Cheung, I.; Schertzer, M.; Rose, A.; Lansdorp, P. M. Disruption of dog-1 in *Caenorhabditis elegans* triggers deletions upstream of guanine-rich DNA. *Nature Genet.* **2002**, *31*, 405-409.
118. Wang, X. D.; Ou, T. M.; Lu, Y. J.; Li, Z.; Xu, Z.; Xi, C.; Tan, J. H.; Huang, S. L.; An, L. K.; Li, D.; Gu, L. Q.; Huang, Z. S. Turning off transcription of the bcl-2 gene by stabilizing the bcl-2 promoter quadruplex with quindoline derivatives. *J. Med. Chem.* **2010**, *53*, 4390-4398.

119. Johnson, J. E.; Cao, K.; Ryvkin, P.; Wang, L. S.; Johnson, F. B. Altered gene expression in the Werner and Bloom syndromes is associated with sequences having G-quadruplex forming potential. *Nucleic Acids Res.* **2010**, *38*, 1114-1122.
120. Siddiqui-Jain, A.; Grand, C. L.; Bearss, D. J.; Hurley, L. H. Direct evidence for a G-quadruplex in a promoter region and its targeting with a small molecule to repress c-MYC transcription. *Proc. Natl. Acad. Sci. USA.* **2002**, *99*, 11593-11598.
121. Rodriguez, R.; Miller, K. M.; Forment, J. V.; Bradshaw, C. R.; Nikan, M.; Britton, S.; Oelschlaegel, T.; Xhemalce, B.; Balasubramanian, S.; Jackson, S. P. Small-molecule-induced DNA damage identifies alternative DNA structures in human genes. *Nat. Chem. Biol.* **2012**, *8*, 301-310.
122. Paul, A.; Bhattacharya, S. Chemistry and biology of DNA-binding small molecules. *Curr. Sci.* **2012**, *102*, 212-231.
123. Davis, J. T. G-quartets 40 years later: from 5'-GMP to molecular biology and supramolecular chemistry. *Angew. Chem. Int. Ed.* **2004**, *43*, 668-698.
124. Du, F.; Tang, Z. Colorimetric detection of PCR product with DNazymes induced by 5'-nuclease activity of DNA polymerases. *ChemBioChem.* **2011**, *12*, 43-46.
125. Willner, I.; Shlyahovsky, B.; Zayats, M.; Willner, B. DNazymes for sensing, nanobiotechnology and logic gate applications. *Chem. Soc. Rev.* **2008**, *37*, 1153-1165.
126. Li, T.; Wang, E.; Dong, S. Potassium-lead-switched G-quadruplexes: a new class of DNA logic gates. *J. Am. Chem. Soc.* **2009**, *131*, 15082-15083.
127. Zhu, L.; Li, C.; Zhu, Z.; Liu, D.; Zou, Y.; Wang, C.; Fu, H.; Yang, C. J. In vitro selection of highly efficient G-quadruplex-based DNazymes. *Anal. Chem.* **2012**, *84*, 8383-8390.
128. Golub, E.; Freeman, R.; Niazov, A.; Willner, I. Hemin/G-quadruplexes as DNazymes for the fluorescent detection of DNA, aptamer-thrombin complexes, and probing the activity of glucose oxidase. *Analyst* **2011**, *136*, 4397-4401.
129. Vummidi, B. R.; Alzeer, J.; Luedtke, N. W. Fluorescent probes for G-quadruplex structures. *ChemBioChem.* **2013**, *14*, 540-558.
130. Mohanty, J.; Barooah, N.; Dhamodharan, V.; Harikrishna, S.; Pradeepkumar, P. I.; Bhasikuttan, A. C. Thioflavin T as an efficient inducer and selective fluorescent sensor for the human telomeric G-quadruplex DNA. *J. Am. Chem. Soc.* **2013**, *135*, 367-376.
131. Koepfel, F.; Riou, J.-F.; Laoui, A.; Mailliet, P.; Arimondo, P. B.; Labit, D.; Petitgenet, O.; Hélène, C.; Mergny, J.-L. Ethidium derivatives bind to G-quartets, inhibit telomerase and act as fluorescent probes for quadruplexes. *Nucleic Acids Res.* **2001**, *29*, 1087-1096.

132. Chang, C. C.; Kuo, I. C.; Ling, I. F.; Chen, C. T.; Chen, H. C.; Lou, P. J.; Lin, J. J.; Chang, T. C. Detection of quadruplex DNA structures in human telomeres by a fluorescent carbazole derivative. *Anal. Chem.* **2004**, *76*, 4490-4494.
133. Allain, C.; Monchaud, D.; Teulade-Fichou, M. P. FRET templated by G-quadruplex DNA: a specific ternary interaction using an original pair of donor/acceptor partners. *J. Am. Chem. Soc.* **2006**, *128*, 11890-11893.
134. Ma, D. L.; Che, C. M.; Yan, S. C. Platinum(II) complexes with dipyridophenazine ligands as human telomerase inhibitors and luminescent probes for G-quadruplex DNA. *J. Am. Chem. Soc.* **2009**, *131*, 1835-1846.
135. Yang, P.; De Cian, A.; Teulade-Fichou, M. P.; Mergny, J. L.; Monchaud, D. Engineering bisquinolinium/thiazole orange conjugates for fluorescent sensing of G-quadruplex DNA. *Angew. Chem., Int. Ed.* **2009**, *48*, 2188-2191.
136. Heinlein, T.; Knemeyer, J. P.; Piestert, O.; Sauer, M. Photoinduced electron transfer between fluorescent dyes and Guanosine residues in DNA-hairpins. *J. Phys. Chem. B* **2003**, *107*, 7957-7964.
137. Narayanaswamy, N.; Unnikrishnan, M.; Gupta, M.; Govindaraju, T. Fluorescence reporting of G-quadruplex structures and modulating their DNAzyme activity using polyethylenimine-pyrene conjugate. *Bioorg. Med. Chem. Lett.* **2015**, *25*, 2395-2400.
138. Hernandez-Folgado, L.; Schmuck, C.; Tomić, S.; Piantanida, I. A novel pyrene-guanidiniocarbonyl-pyrrole cation efficiently differentiates between ds-DNA and ds-RNA by two independent, sensitive spectroscopic methods. *Bioorg. Med. Chem. Lett.* **2008**, *18*, 2977-2981.
139. Wu, J.; Zou, Y.; Li, C.; Sicking, W.; Piantanida, I.; Yi, T.; Schmuck, C. A molecular peptide beacon for the ratiometric sensing of nucleic acids. *J. Am. Chem. Soc.* **2012**, *134*, 1958-1961.
140. Kim, H. N.; Lee, E. -H.; Xu, Z.; Kim, H. -E.; Lee, H. -S.; Lee, J. -H.; Yoon, J. A pyrene-imidazolium derivative that selectively recognizes G-quadruplex DNA. *Biomaterials* **2012**, *33*, 2282-2288.
141. Hariharan, M.; Ramaiah, D. Novel bifunctional viologen-linked pyrene conjugates: Synthesis and study of their interactions with nucleosides and DNA. *J. Phys. Chem. B* **2006**, *110*, 24678-24686.
142. Rajagopal, S. K.; Hariharan, M. Non-natural G-quadruplex in a non-natural environment. *Photochem. Photobiol. Sci.* **2014**, *13*, 157-161.
143. Gosule, L. C.; Schellman, J. A. Compact form of DNA induced by spermidine. *Nature* **1976**, *259*, 333-335.

144. Gosule, L. C.; Schellman, J. A. DNA condensation with polyamines I. Spectroscopic studies. *J. Mol. Biol.* **1978**, *121*, 311-326.
145. Wilson, R. W.; Bloomfield, V. A. Counterion-induced condensation of deoxyribonucleic acid. A light-scattering study. *Biochemistry* **1979**, *18*, 2192-2196.
146. Boussif, O.; Lezoualc'h, F.; Zanta, M. A.; Mergny, M. D.; Scherman, D.; Demeneix, B.; Behr, J. P. A versatile vector for gene and oligonucleotide transfer into cells in culture and in vivo: polyethylenimine. *Proc. Natl. Acad. Sci. U.S.A.* **1995**, *92*, 7297-7301.
147. Godbey, W. T.; Wu, K. K.; Mikos, A. G. Poly(ethylenimine) and its role in gene delivery. *J. Controlled Release* **1999**, *5*, 149-160.
148. Rossier, M.; Koehler, F. M.; Athanassiou, E. K.; Grass, R. N.; Waelle, M.; Birbaum, K.; Günther, D.; Stark, W. J. Energy-efficient noble metal recovery by the use of acid-stable nanomagnets. *Ind. Eng. Chem. Res.* **2010**, *49*, 9355-9362.
149. Yang, D.; Okamoto, K. Structural insights into G-quadruplexes: towards new anticancer drugs. *Future Med. Chem.* **2010**, *2*, 619-646.
150. Sun, H.; Xiang, J.; Liu, Y.; Li, L.; Li, Q.; Xu, G.; Tang Y. A stabilizing and denaturing dual-effect for natural polyamines interacting with G-quadruplexes depending on concentration. *Biochimie* **2011**, *93*, 1351-1356.
151. Sun, H.; Zhou, Q.; Xiang, J.; Tang, Y. Polyethylenimine effectively induces, stabilizes, and regulates intramolecular G-quadruplexes. *Bioorg. Med. Chem. Lett.* **2009**, *19*, 4669-4672.
152. Keniry, M.A. A comparison of the association of spermine with duplex and quadruplex DNA by NMR. *FEBS Letters* **2003**, *542*, 153-158.
153. Kumar, N.; Basundra, R.; Maiti, S. Elevated polyamines induce c-MYC overexpression by perturbing quadruplex-WC duplex equilibrium. *Nucleic Acids Res.* **2009**, *37*, 3321-3331.
154. Fu, Y.; Wang, X.; Zhang, J.; Xiao, Y.; Li, W.; Wang, J. Orderly microaggregates of G-/C-rich oligonucleotides associated with spermine. *Biomacromolecules* **2011**, *12*, 747-756.
155. O'Brien, R.; Haq, I. Applications of biocalorimetry: binding, stability and enzyme kinetics, in: J.E. Ladbury, M. Doyle (Eds.), *Biocalorimetry*, John Wiley and Sons Ltd, West Sussex, England, **2004**.
156. Buurma, N. J.; Haq, I. Advances in the analysis of isothermal titration calorimetry data for ligand-DNA interactions. *Methods* **2007**, *42*, 162-172.
157. Chang, Y. M.; Chen, C. M.; Hou, M. H. Conformational changes in DNA upon ligand binding monitored by circular dichroism. *Int. J. Mol. Sci.* **2012**, *13*, 3394-3413.
158. Vorlickova, M.; Kejnovska, I.; Sagi, J.; Renciuik, D.; Bednarova, K.; Motlova, J.; Kypr, J. Circular dichroism and guanine quadruplexes. *Methods* **2012**, *57*, 64-75.



159. Saminathan, M.; Thomas, T.; Shirahata, A., Pillai, C. K. S.; Thomas, T. J. Polyamine structural effects on the induction and stabilization of liquid crystalline DNA: potential applications to DNA packaging, gene therapy and polyamine therapeutics. *Nucleic Acids Res.* 2002, *30*, 3722-3731.
160. Qi, C.; Zhang, N.; Yan, J.; Liu, X.; Bing, T.; Mei, H.; Shangguan, D. Activity enhancement of G-quadruplex/hemin DNzyme by spermine. *RSC Adv.* **2014**, *4*, 1441-1448.

---

# Chapter 6

Exploring Canonical and Non-Canonical Hydrogen Bonding

Potential of Adenine for Construction of Hybrid DNA

Structures

## Chapter 6a: Exploring Hydrogen Bonding and Weak Aromatic Interactions Induced Assembly of Adenine and Thymine Functionalised Naphthalenediimides

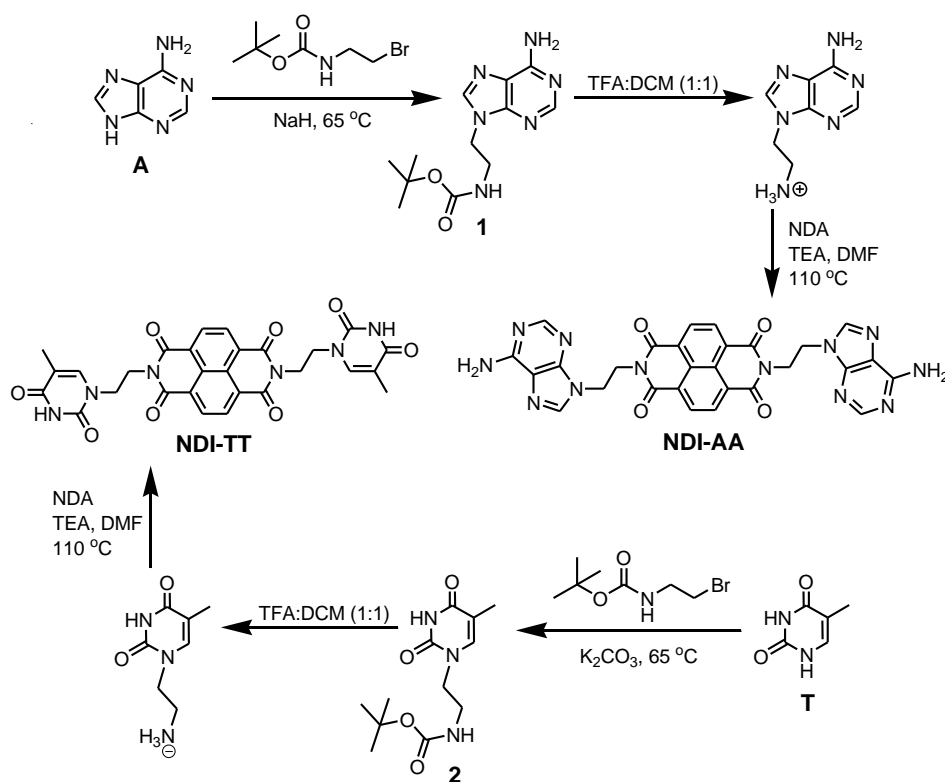
One of the most fascinating aspects of biological systems is their selectivity and specificity, emphasizing their grandeur in structure-property correlations.<sup>1-5</sup> This unparalleled characteristic of natural systems could be exemplified by the elegant molecular design and functioning of nucleic acids.<sup>4-7</sup> These polynucleotides with their specific sequence of nucleobases facilitate coding and encoding of genetic information and are also known to form a variety of complex molecular assemblies.<sup>6,7</sup> It is this intriguing property of nucleobases to form hydrogen bonded molecular structures inspired us to explore their efficacy to achieve controllable molecular assemblies. Such a concept in the name of DNA nanotechnology was evoked by Nadrian C. Seeman and it has been an area of active research for the past two decades.<sup>8</sup> However, when aiming for a solution processable controlled molecular assembly of  $\pi$ -conjugated organic molecules, DNA nanotechnology in its original form would be impractical. Therefore, in a minimalistic approach, one could envision  $\pi$ -conjugated molecules appended with nucleobases as an attractive alternative. Herein, we demonstrate the synthesis and molecular assembly of adenine and thymine functionalised naphthalene diimides (NDIs).<sup>9</sup>

NDI is one of the most promising n-type organic semiconductor with wide range of applications in the fields of electronics, materials and biomedicine.<sup>10-16</sup> This work complements the bio-inspired molecular engineering approach reported from our group and also the pioneering works on DNA templated assembly.<sup>17-31</sup> In addition, complementary peptide nucleic acid (PNA) dimers were employed as template for the molecular assembly of nucleobase modified NDIs. PNAs are the DNA mimics with nucleobases attached to pseudopeptide backbone.<sup>32-36</sup> PNAs form complexes with complementary nucleobase sequences with greater affinity and strength than natural oligonucleotides.<sup>32-36</sup> Furthermore, this work represents a unique example of constructing supramolecular polymers by exploiting Watson-Crick and Hoogsteen type hydrogen bonding of adenine base. As a consequence of unusual hydrogen bonding of adenine and thymine besides weak aromatic interactions (NDI-core), adenine-NDI-adenine (**NDA-AA**) organized into well-defined nanoribbons by solution processing whereas complementary **TT** molecular clamp resulted in

2D microstructures. While thymine-NDI-thymine (**NDA-TT**) conjugates assemble into porous spheres, tapes and petal-like 2D sheets with complementary **AA** molecular clamp. The obtained nano- and micro-structures find importance from fundamental science perspective as well as for technological implications.

### 6.1 Synthesis of naphthalenediimide-nucleobase conjugates

We incorporated ethylene linker spacer between nucleobase and NDI-core to reduce the dominating role of aromatic  $\pi$ - $\pi$  interaction by taking advantage of its flexibility via C-C bond rotation and hence the terminal nucleobases will facilitate the assembly of NDI conjugate through dominating hydrogen bonding interactions.



**Scheme 1.** Synthesis of Adenine and Thymine conjugated NDIs, **NDI-AA** and **NDI-TT**.

Boc-protected adeninyl-9-ethyl amine (**1**) was prepared in good yield by *N*-alkylation of adenine (*N*<sup>9</sup>-H) using 1-(butyloxycarbonyl)-2-bromo ethylamine and sodium hydride as base in DMF at 65 °C. Similarly Boc-protected thyminyl-1-ethyl amine (**2**) was synthesized by the *N*-alkylation of thymine (*N*<sup>1</sup>-H) with 1-(butyloxycarbonyl)-2-bromo ethylamine and potassium carbonate as base in DMF at 65 °C. Boc-protected **1** and **2** were condensed with

1,4,5,8-naphthalenetetracarboxylic dianhydride (NDA) in presence of triethylamine (TEA) in DMF to obtain the corresponding nucleobase appended **NDI-AA** and **NDI-TT** conjugates in good yield (Scheme 1). Molecular clamps **TT** and **AA** were shown in Figure 1.<sup>35</sup>

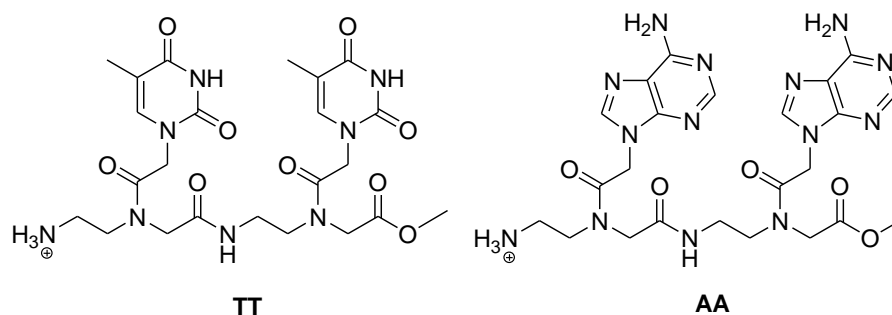


**Figure 1.** Chemical structures of molecular clamps **TT** and **AA**.

## 6.2 Photophysical properties of **NDI-AA** and **NDI-TT**

We investigated the molecular interactions of **NDI-AA** and **NDI-TT** in solution using UV-vis absorption spectroscopy. It should be noted that **NDI-AA** is sparingly soluble in most of the organic solvents due to strong aromatic and hydrogen bonding interactions; however trace amount of trifluoroacetic acid (TFA) rendered increased solubility in DMSO. The UV-vis absorption spectra of **NDI-AA** (100  $\mu$ M) and **NDI-TT** (100  $\mu$ M) in DMSO exhibited absorption bands in 300-400 nm region due to characteristic  $\pi$ - $\pi^*$  transitions of NDI chromophore polarized along the  $z$ -axis. The absorption spectra of **NDI-AA** in water/DMSO (Figure 2a) did not show any significant spectral changes. Interestingly, the intensity of absorption band (300-400 nm region) of **NDI-TT** in DMSO gradually decreases with addition of water and a new absorption band appeared at 404.5 nm with an appreciable bathochromic shift of 25 nm (Figure 2b). This spectral change is attributed to J-type aggregation of aromatic core and the molecules arranged in an edge to edge fashion to attain the minimum free energy for stability. In DMSO/acetonitrile (CH<sub>3</sub>CN) solvent system **NDI-AA** exhibited blue shift in the absorption band with enhanced absorption intensity (Figure 2c). This enhancement in the intensity of absorption band is attributed to weakening of  $\pi$ -stacking interactions as a consequence of probable strengthening of intermolecular (adenine-adenine) hydrogen bonding interactions. Increasing the CH<sub>3</sub>CN percentage from 0 to 70% in DMSO solution of **NDI-TT** also lead to blue shift in the absorption band (300-400 nm

region). However on further increasing the CH<sub>3</sub>CN percentage to 90% a new band was observed at 403.5 nm (Figure 2d). This clearly suggests the improved aromatic  $\pi$ -stacking interactions among **NDI-TT** molecules in 90% CH<sub>3</sub>CN /DMSO solvent system.

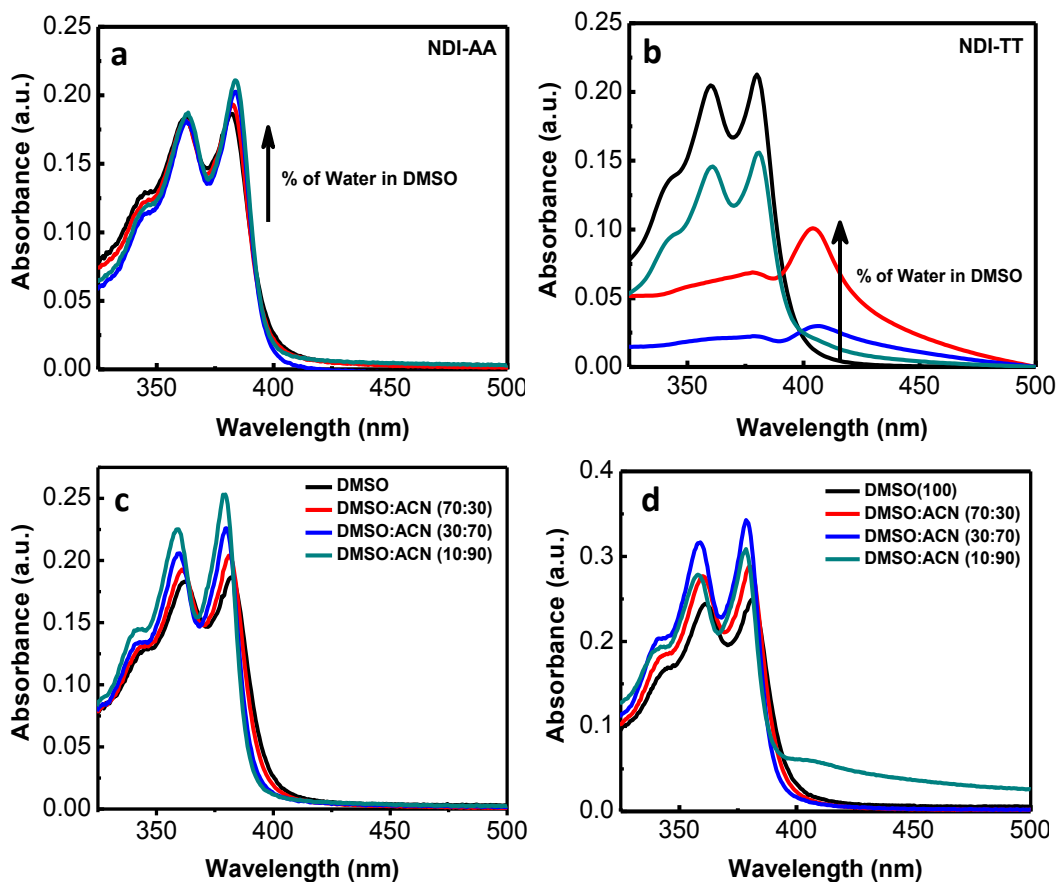


**Figure 2.** UV-vis absorption spectra of NDI-nucleobase conjugates. (a) & (b) are absorption spectra of **NDI-AA** and **NDI-TT** in DMSO/water solution respectively. (c) & (d) are absorption spectra of **NDI-AA** and **NDI-TT** in DMSO/acetonitrile solution respectively.

### 6.3 Photophysical properties of NDI-nucleobase conjugates in presence of molecular clamps

Next we studied the effect of molecular clamps (PNA-dimers) *viz.* **TT** (100  $\mu$ M) and **AA** (100  $\mu$ M) on the molecular aggregation of **NDI-AA** and **NDI-TT** respectively. Room temperature UV-vis absorption studies did not show any detectable spectral changes for both **NDI-AA** and **NDI-TT** with the addition of respective complementary molecular clamps. Interestingly, temperature dependent absorption study provided more insights on the

interaction among individual **NDI-AA** or **NDI-TT** and with their respective complementary PNA dimers. Surprisingly in case of **NDI-AA** absorption in the 300-400 nm region gradually decreases with increase in temperature from 20 °C to 80 °C (Figure 3a). This can be ascribed to disruption of hydrogen bonding among the adenine bases at higher temperature and subsequent strengthening of aromatic  $\pi$ -stacking interactions between NDI chromophores.

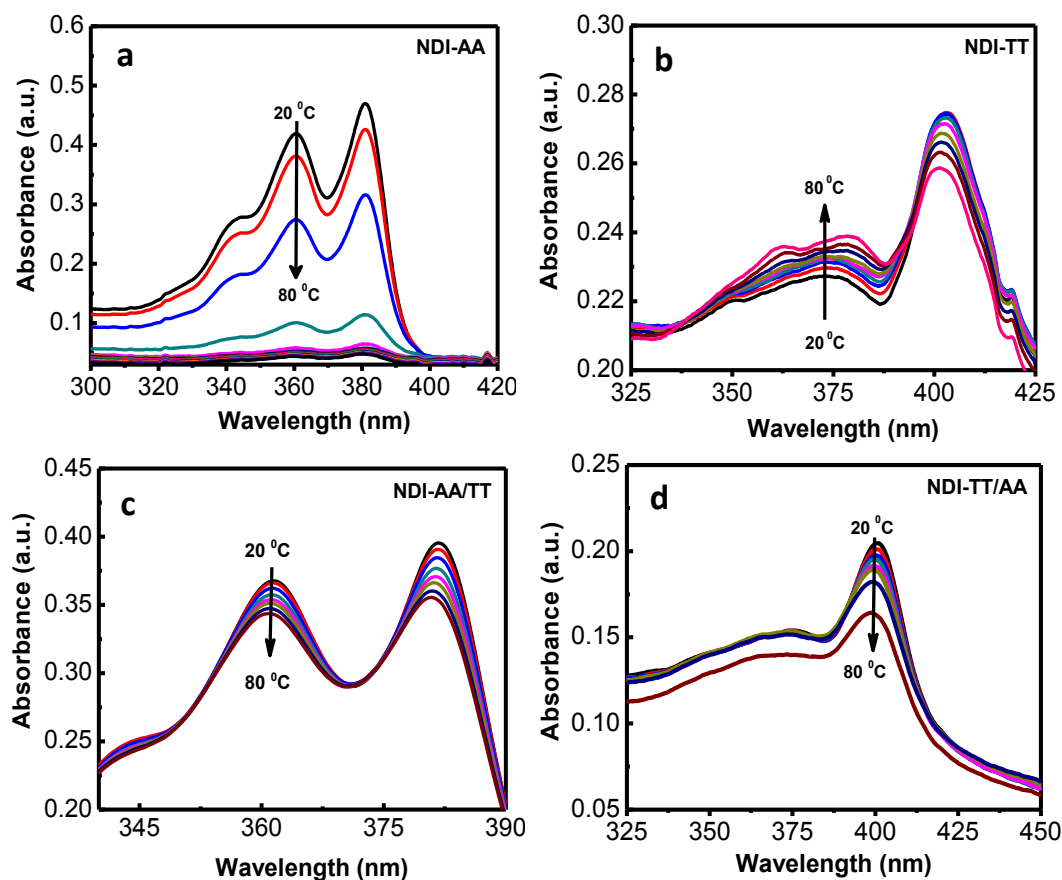


**Figure 3.** Temperature dependent UV-vis absorption spectra NDI-nucleobase conjugates with molecular clamps. (a) & (b) are absorption spectra of **NDI-AA** and **NDI-TT** in DMSO/Water solution respectively. (c) & (d) are absorption spectra of **NDI-AA/TT** and **NDI-TT/AA** in DMSO/Water solution respectively.

Interestingly distinct spectral features were observed for **NDI-TT**. The J-type aggregation band at ~ 405 nm gradually decreased while experiencing hyperchromic effect with respect to absorption band at 300-400 nm as the temperature increased from 20 °C to 80 °C (Figure 3b). The gradual decrease in the intensity of J-type aggregation band at higher

temperature indicates the transformation of aggregated system to molecularly dissolved state due to disruption of hydrogen bonding and aromatic interactions in **NDI-TT**. There was no significant change in the absorption band at 300-400 nm for **NDI-AA/TT** (Figure 3c). However, in case of **NDI-TT/AA** the absorption band at 405 nm decreases gradually with blue shift of 2 nm as function of increasing temperature from 20 °C to 80 °C and there was no change in 300-400 nm spectral region (Figure 3d). Overall the observed changes in absorption spectra of **NDI-AA** and **NDI-TT** in presence and absence of respective complementary molecular clamps (PNA-dimers) suggest the crucial role of hydrogen bonding from nucleobases and relatively weaker  $\pi$ - $\pi$  interactions of NDI-core in their molecular aggregation.

#### 6.4 Morphological studies of NDI-nucleobase conjugates

We investigated the morphology of supramolecular structures of **NDI-AA** and **NDI-TT** by using microscopy techniques by drop casting their respective solution on to silicon (111) substrates. FESEM (field emission scanning electron microscopy) micrographs revealed the formation of fibrous network by **NDI-AA** in pure DMSO (Figure 4a). While **NDI-AA** in 90% acetonitrile/DMSO assembled into ribbons with relatively uniform length (>10  $\mu\text{m}$ ) and width (1-1.5  $\mu\text{m}$ ) throughout the sample (Figure 4b). AFM (atomic force microscopy) and Transmission electron microscopy (TEM) measurements revealed that these ribbons have a topographical thickness in the range of 50-60 nm (Figure 5).

Interestingly solution of **NDI-TT** in pure DMSO formed porous sphere like structures (Figure 4d). In contrast, solution of **NDI-TT** in 90% acetonitrile/DMSO resulted in belt-like structures with high aspect ratios (5-10  $\mu\text{m}$  length and 500 nm width) (Figure 4e). Next, we studied the effect of molecular clamp **TT** on the morphology of **NDI-AA**. The annealed solution **NDI-AA/TT** (1:1) was drop casted on to a silicon (111) substrate. The FESEM image showed the formation of rectangular 2D microstructures (Figure 4c). Whereas petal-like 2D sheets were observed for **NDI-TT/AA** (1:1) (Figure 4f). Thus, molecular clamps **AA** and **TT** reengineer the morphological structures of **NDI-AA** and **NDI-TT** from 1D to extended 2D structures.<sup>37</sup>



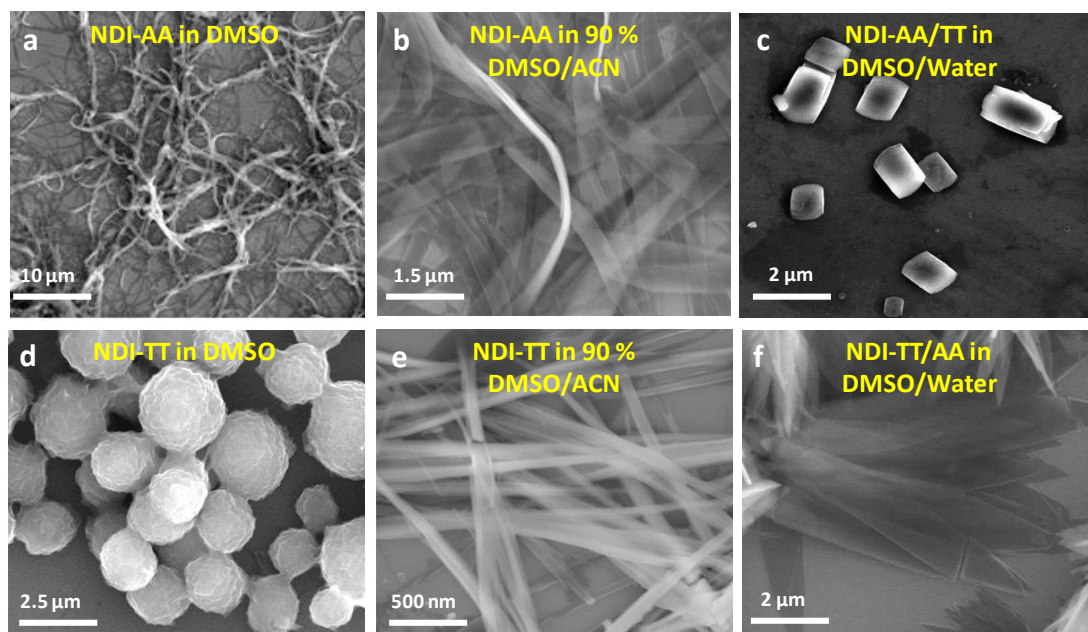


**Figure 4.** FESEM micrographs of NDI-nucleobase conjugates in presence of molecular clamps. (a) Fibers obtained from **NDI-AA** in 100% DMSO solution. (b) Nanoribbons obtained from **NDI-AA** in 90% acetonitrile/DMSO solution. (c) FESEM micrograph of **NDI-AA/TT** (1:1) rectangular 2D microstructures obtained from DMSO/Water solution. (d) Porous spheres obtained from **NDI-TT** in 100% DMSO solution. (e) Bundle of belts obtained from **NDI-TT** in 90% acetonitrile/DMSO solution. (f) FESEM micrograph of **NDI-TT/AA** (1:1) petal-like 2D sheets obtained from DMSO/Water solution.

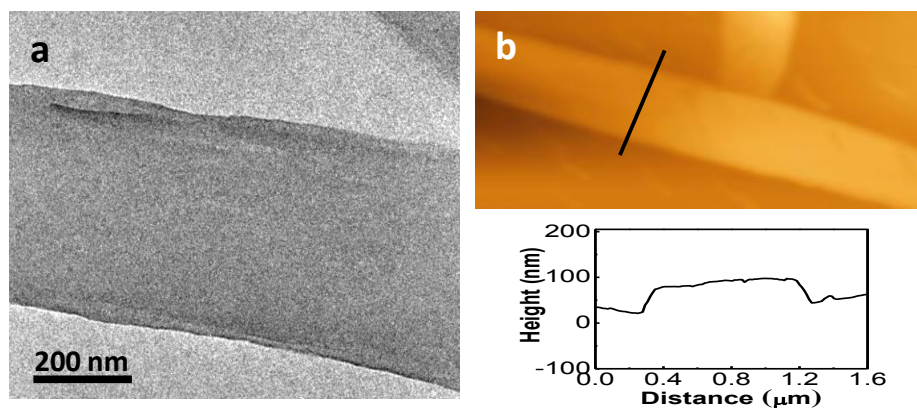


**Figure 5.** (a) TEM micrograph of the **NDI-AA** nanoribbon. (b) AFM image of **NDI-AA** nanoribbon and the corresponding height profile (along the black trace).

### 6.5 NMR-analysis of NDI-nucleobase conjugates in presence of molecular clamps

To understand the aggregation of **NDI-AA** and **NDI-TT** and role of nucleobases, we have performed temperature dependent  $^1\text{H-NMR}$  and 2D-NOESY spectra. At ambient temperature (25 °C), two separate broad signals were observed for  $\text{NH}_2$  protons ( $\text{H}_a$  and  $\text{H}_b$ ) of adenine (**NDI-AA**) in the downfield region of 8.5 to 10 ppm. This clearly suggests that two N-H protons ( $\text{H}_a$  and  $\text{H}_b$ ) of adenine possess different hydrogen bonding environments.<sup>38,39</sup> Upon increasing the temperature from 25 °C to 60 °C, these two N-H signals merge to a single broad peak as a consequence of disruption of hydrogen bonds and hence two N-H protons become equivalent at higher temperature (Figure 6a). Two C-H protons ( $\text{C}^8\text{-H}_c$  and  $\text{C}^2\text{-H}_d$ ) at 8.535 and 8.185 ppm undergo upfield shift (0.03 and 0.05 ppm respectively) with increase in temperature from 25 °C to 60 °C. Therefore temperature dependent  $^1\text{H-NMR}$  spectra confirmed the involvement of two distinct hydrogen bonds of  $\text{N}^1$  and  $\text{N}^7$  of adenine base. Further, the imide proton ( $\text{N-H}_e$ ) of thymine in **NDI-AA/TT** also appeared in downfield region (11.3 ppm) due to its participation in hydrogen bonding. This was further confirmed by the upfield shift (0.2 ppm) of imide  $\text{N-H}_e$  proton of thymine at higher temperature (Figure 6b).

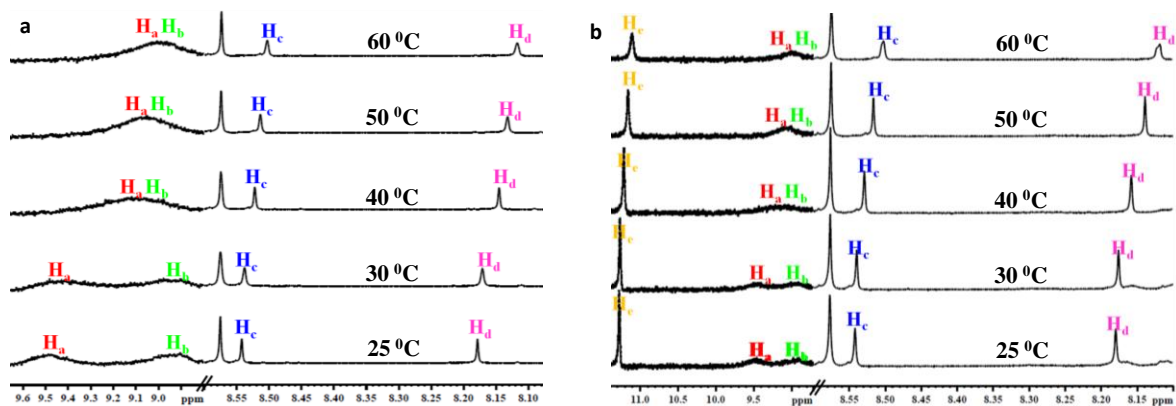


**Figure 6.** Temperature dependent  $^1\text{H-NMR}$ -spectra of **NDI-AA** and **NDI-AA/TT**. (a) Temperature dependent  $^1\text{H-NMR}$  spectra of **NDI-AA** in  $\text{DMSO-}d_6$ . (b) Temperature dependent  $^1\text{H-NMR}$  spectra of **NDI-AA/TT** (1:1) in  $\text{DMSO-}d_6$ .

The 2D-NOESY studies further revealed the interaction between the adenine bases of **NDI-AA** (Figure 7a). Further, 2D-NOESY spectra of **NDI-AA/TT** showed the absence of

spatial coupling between N-H<sub>a</sub> and N-H<sub>b</sub> of adenine (Figure 7b). While the appearance of new set of spatial interactions for N-H<sub>a</sub> and N-H<sub>b</sub> (**NDA-AA**) with N-H<sub>e</sub> of thymine (**TT**) proved the cross hydrogen bonding between the two nucleobases. Normally, involvement of *N*<sup>1</sup> and *N*<sup>10</sup>-H of adenine indicate Watson-Crick type hydrogen bonding, while that of *N*<sup>7</sup> and *N*<sup>10</sup>-H suggests Hoogsteen type hydrogen bonding. In conventional Watson-Crick hydrogen bonding between adenine and thymine, *N*<sup>1</sup>- and *N*<sup>10</sup>-H of adenine yield hydrogen bonded eight member ring.

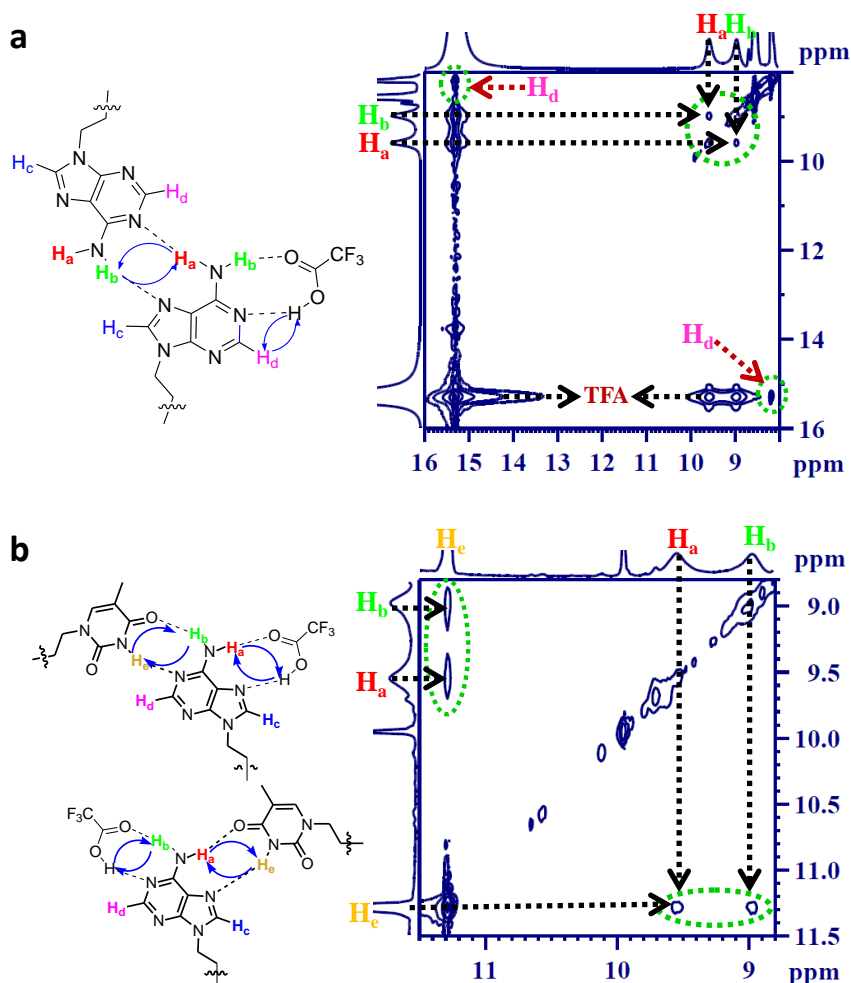


**Figure 7.** 2D-NOESY and mode of hydrogen bonding interactions in nucleobases. (a) left: Intermolecular adenine-adenine hydrogen bonding among **NDI-AA** molecule, right: 2D-NOESY spectra of **NDI-AA** (with trace amount of TFA) in *DMSO-d*<sub>6</sub>. (b) left: Intermolecular adenine-thymine hydrogen bonding interactions in **NDI-AA/TT** complex, right: 2D-NOESY spectra of **NDI-AA/TT** (1:1) in *DMSO-d*<sub>6</sub>.

However, for Hoogsteen type hydrogen bonding,  $N^7$  and  $N^{10}$ -H of adenine are involved in the formation of hydrogen bonded nine member ring. Surprisingly, in case of **NDI-AA**  $N^1$ ,  $N^7$  and  $N^{10}$ -H ( $H_a$  and  $H_b$ ) are all involved in hydrogen bonding as discussed earlier. This unusual hydrogen bonding among **NDI-AA** molecules through adenine and relatively weak aromatic interaction of NDI-core as indicated by the UV-vis absorption studies believed to be the major driving force for the formation of 1D fibers and nanoribbons. Moreover, the participation of  $N^1$ ,  $N^7$  and  $N^{10}$ -H of adenine in hydrogen bonding interactions indicates that the adenine nucleobase bind to thymine in **PNA-TT** by either Watson-Crick or Hoogsteen type complementary hydrogen bonding. However, the flexibility of ethylene linker and the relative orientation of thymine functionalities in PNA dimer are also believed to be the major determinants for the assembly of **NDI-AA/PNA-TT** to rectangular 2D microstructures. Similarly, the hydrogen bonding of thymine base and weak aromatic interaction of NDI-core plays crucial role in the formation of porous spheres, belts by **NDI-TT** and petal-like 2D sheets from **NDI-TT/PNA-AA**. Nevertheless, the marked difference in the molecular assembly from 1D fibres, 1D nanoribbon, belts to 2D microstructures and petal-like 2D sheets clearly emphasize the role of complementary **PNA** dimers as effective templates.

## 6.6 Conclusion

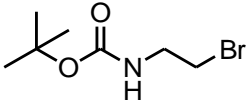
We developed a new strategy for controlling the morphology of NDI-chromophore by conjugating with nucleobases. These NDI-nucleobase conjugates self-assembled into well-defined fibres, nanoribbons, porous spheres, belts, 2D microstructures, and petal-like 2D sheets based on hydrogen bonding between the nucleobases (adenine and thymine) and weak aromatic interactions of NDI-core. This work further emphasizes the unusual existence of Watson-Crick and Hoogsteen hydrogen bonding interactions among the nucleobases. Bio-inspired strategy comprising molecular recognition of nucleobases are believed to pave way for the design and development of various functional supramolecular polymers with interesting optical and biological properties.

## 6.7 Experimental Section

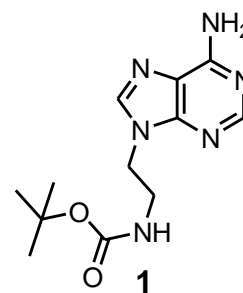
**General information.** 1, 4, 5, 8-Naphthalenetetracarboxylic dianhydride (NDA), thymine, 1-acetic acid, 2-bromo-ethylamine hydrogen bromide were obtained from Sigma–Aldrich.

Di-*tert*-butyl dicarbonate, bromo-methyl acetate, adenine, ethylenediamine were obtained from Spectrochem Pvt. Ltd. Mumbai (India). All reagents were used as received unless otherwise mentioned.

### Synthetic procedure for NDI-AA and NDI-TT

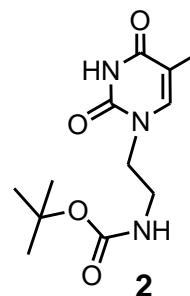
**Synthesis of *tert*-butyl 2-bromoethylcarbamate.** To a stirred solution of 2-bromo-ethylamine hydrogen bromide (2 g, 9.85 mmol) in  in chloroform, triethyl amine (1.75 mL, 9.85 mmol) was added at 0 °C. After 10 min. Di-*tert*-butyl dicarbonate in chloroform solution was added drop wise to the above solution and the reaction was allowed to stir for 6 h. After completion of the reaction, solvent was evaporated under vacuo. The compound was extracted with DCM (100 mL); organic layer was washed with water (200 mL). Organic layer was dried on anhydrous sodium sulfate. The crude product was purified using column chromatography on silica gel using EtOAc/petroleum ether (15/85) as an eluent to afford colorless liquid in good yield (93 %). <sup>1</sup>H-NMR (400 MHz, CDCl<sub>3</sub>) δ<sub>ppm</sub> 4.87 (br, 1H), 3.46 (t, *J* = 5.5 Hz, 2H), 3.39 (t, *J* = 5.3 Hz, 2H), 1.38 (s, 9H),. <sup>13</sup>C-NMR (100 MHz, CDCl<sub>3</sub>) δ<sub>ppm</sub> 155.2, 79.0, 41.3, 31.8, 27.3. MALDI-TOF-MS: found 223.40, calcd *m/z* = 223.02 for C<sub>7</sub>H<sub>14</sub>BrNO<sub>2</sub> [M]<sup>+</sup>.

**Synthesis of boc-protected adeninyl-9-ethylamine (1).** Adenine (1 g, 7.40 mmol) and sodium hydride (0.59 g, 14.8 mmol) were dissolved in DMF solution at 0 °C and stirred for 30 min. To this mixture, *tert*-butyl-2-bromoethylcarbamate (1.65 g, 7.40 mmol) was added. The reaction mixture was heated to 65 °C and allowed to stir for 24 h. The completion of the reaction was monitored with TLC. After completion of reaction, the



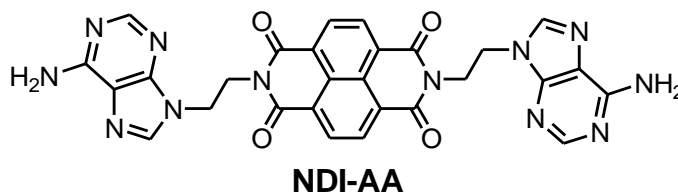
solution was dissolved in 0.5 N HCl solution at 0 °C, solvent was evaporated under vacuo. The crude product was purified using column chromatography on silica gel using MeOH/CHCl<sub>3</sub> (2/98) as an eluent to afford white solid of **1** in moderate yield (30%). <sup>1</sup>H-NMR (400 MHz, CDCl<sub>3</sub>) δ<sub>ppm</sub> 8.34 (s, 1H), 7.76 (s, 1H), 5.61 (br, 2H), 5.03 (s, 1H), 4.35 (d, *J* = 5.2 Hz, 2H), 3.57 (q, *J* = 6 Hz, 2H), 1.40 (s, 9H). <sup>13</sup>C-NMR (100 MHz, CDCl<sub>3</sub>) δ<sub>ppm</sub> 155.0, 152.9, 150.1, 140.9, 119.7, 79.9, 43.7, 40.4, 28.2. MALDI-TOF-MS: found 278.54, calcd *m/z* = 278.14 for C<sub>12</sub>H<sub>18</sub>N<sub>6</sub>O<sub>2</sub> [M]<sup>+</sup>.

**Preparation of boc-protected thymine-1-ethyl amine (2).** To a stirred solution of thymine (0.1 g, 0.79 mmol) and potassium carbonate (0.13 g, 0.95 mmol) in DMF. After 10 min, *tert*-butyl -2-bromoethylcarbamate (0.18 g, 0.79 mmol) was added to the above reaction mixture. The reaction mixture was heated up to 65 °C and allowed to stir for 24 hours. After completion of the reaction the solvent was evaporated, the crude product



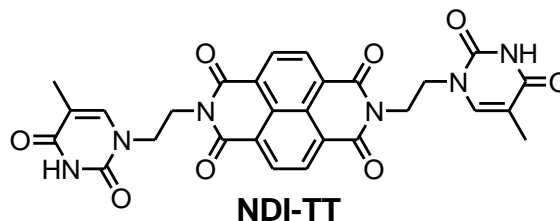
was purified using column chromatography on silica gel using MeOH/CHCl<sub>3</sub> (3:97) as an eluent afford white color solid compound **2** in good yield (45 %). <sup>1</sup>H-NMR (400 MHz, CDCl<sub>3</sub>) δ<sub>ppm</sub> 8.42 (s, 1H), 6.99 (s, 1H), 4.85 (s, 1H), 3.84 (t, *J* = 6 Hz, 2H), 3.39 (q, *J* = 6.0 Hz, 2H), 1.90 (d, *J* = 1.2 Hz, 3H), 1.43 (s, 9H). <sup>13</sup>C-NMR (100 MHz, CDCl<sub>3</sub>) δ<sub>ppm</sub> 164.1, 156.1, 150.9, 141.0, 110.4, 79.9, 48.0, 40.2, 28.3, 12.2. MALDI-TOF-MS: found 269.23, calcd *m/z* = 269.13 for C<sub>12</sub>H<sub>19</sub>N<sub>3</sub>O<sub>4</sub> [M]<sup>+</sup>.

**Synthesis of NDI-AA.** Boc-protected adenine-9-ethylamine **1** (2.2 equiv.) was dissolved in a mixture of DCM/TFA (1:1) (10 mL). The reaction was allowed to stir for 4 h. After completion of the reaction, solvent was evaporated. The trace amount of TFA was removed by formation of azeotropic mixture with toluene. The crude product was dissolved in DMF (10 mL)



containing triethyl amine (1mL), to this solution 1,4,5,8-naphthalenetetracarboxylic acid dianhydride (NDA) (1 equiv.) was added slowly. The resulting solution was heated up to 110 °C and allowed to stir for 6 h. The completion of the reaction was monitored by TLC. The reaction mixture was cooled to room temperature, solution was filtered, and the precipitate was washed with chloroform and methanol. The obtained product (**NDA-AA**) was dried on under vacuum at 40 °C for 12 h. Yellow color powder, Yield 75%. <sup>1</sup>H-NMR (400 MHz, DMSO-*d*<sub>6</sub>+TFA) δ<sub>ppm</sub> 9.55 (br, 2H), 8.97 (br, 2H), 8.56 (s, 4H), 8.54 (s, 2H), 8.19 (s, 2H), 4.64 (d, *J* = 5.2 Hz, 4H), 4.54 (d, *J* = 5.2 Hz, 4H). <sup>13</sup>C-NMR (100 MHz, DMSO-*d*<sub>6</sub>+TFA) δ<sub>ppm</sub> 162.9, 150.0, 149.13, 144.7, 130.6, 126.3, 118.2, 42.5, 40.2. LCMS (ESI): found 589.25, calcd *m/z* = 589.18 for C<sub>28</sub>H<sub>21</sub>N<sub>12</sub>O<sub>4</sub> [M+H]<sup>+</sup>.

**Synthesis of NDI-TT.** Boc-protected thyminy-1-ethyl amine **2** (2.2 equiv.) was dissolved in a mixture of DCM/TFA (1:1) (10 mL). The reaction was allowed to stir for 4 h. After completion of the reaction, solvent was evaporated. The trace



amount of TFA was removed by the formation of azeotropic mixture with toluene. The crude product was dissolved in DMF (10 mL) containing triethyl amine (1 mL), to this solution 1,4,5,8-naphthalenetetracarboxylic acid dianhydride (NDA) (1 equiv.) was added slowly. The resulting solution was heated up to 110 °C and allowed to stir for 6 h. The completion of the reaction was monitored by TLC. The reaction mixture was cooled to room temperature, solution was filtered, and the precipitate was washed with chloroform and methanol. The obtained product **NDA-TT** was dried under vacuum at 40 °C for 10 h. White colour powder, Yield 58 %. <sup>1</sup>H-NMR (400 MHz, *DMSO-d*<sub>6</sub>)  $\delta_{ppm}$  11.06 (s, 2H), 8.67 (s, 4H), 7.58 (d, *J* = 0.8 Hz, 2H), 4.36 (t, *J* = 5.2 Hz, 4H), 4.02 (t, *J* = 4.8 Hz, 4H), 1.64 (d, *J* = 0.8 Hz, 6H). <sup>13</sup>C-NMR (100 MHz, *DMSO-d*<sub>6</sub>)  $\delta_{ppm}$  164.2, 162.7, 151.4, 141.5, 130.5, 126.2, 108.6, 45.8, 40.2, 11.8 MALDI-TOF-MS: found 571.066, calcd *m/z* = 571.15 for C<sub>28</sub>H<sub>23</sub>N<sub>6</sub>O<sub>8</sub> [M+H]<sup>+</sup>.

**NMR spectroscopy, mass spectroscopy and elemental analysis.** <sup>1</sup>H, 2D-NOESY and <sup>13</sup>C NMR spectra were recorded on a Bruker AV-400 spectrometer with chemical shifts reported as ppm (in CDCl<sub>3</sub>/*DMSO-d*<sub>6</sub>, tetramethylsilane as internal standard) at 20 °C. The variable-temperature NMR spectra were recorded by monitoring the temperature with ± 1 °C variation. Mass spectra were obtained on Shimadzu GC-MS 2010 and Bruker Ultraflex II MALDI-TOF spectrometers. Elemental analysis was carried on Thermo Scientific FLASH 2000 Organic Element Analyzer.

**UV-vis spectroscopy.** The UV-vis absorption spectra were recorded on a Perkin Elmer Model Lambda 900 spectrophotometer. 100 μM solution of the sample was analyzed in quartz cuvette of 1 mm path length.

**Field emission scanning electron microscopy (FESEM).** FESEM imaging of the samples were carried out using FESEM, FEI Nova nanoSEM-600. Freshly prepared solutions were drop casted on a clean one side polished surface of silicon (111). These samples were thoroughly dried under vacuo and imaging was carried out by operating the field emission

gun at 5 KV.

**Transmission electron microscopy (TEM).** TEM micrographs were obtained by drop casting the sample solution on a 200 mesh holey carbon supported copper grids and dried at 40 °C. The images were recorded using JEOL, JEM 3010 instrument operating at 300 kV.

**Atomic force microscopy (AFM).** AFM measurements were performed on Innova (Veeco) AFM instrument in tapping mode. The samples were prepared by drop casting the sample solutions on Silicon (111) surface.



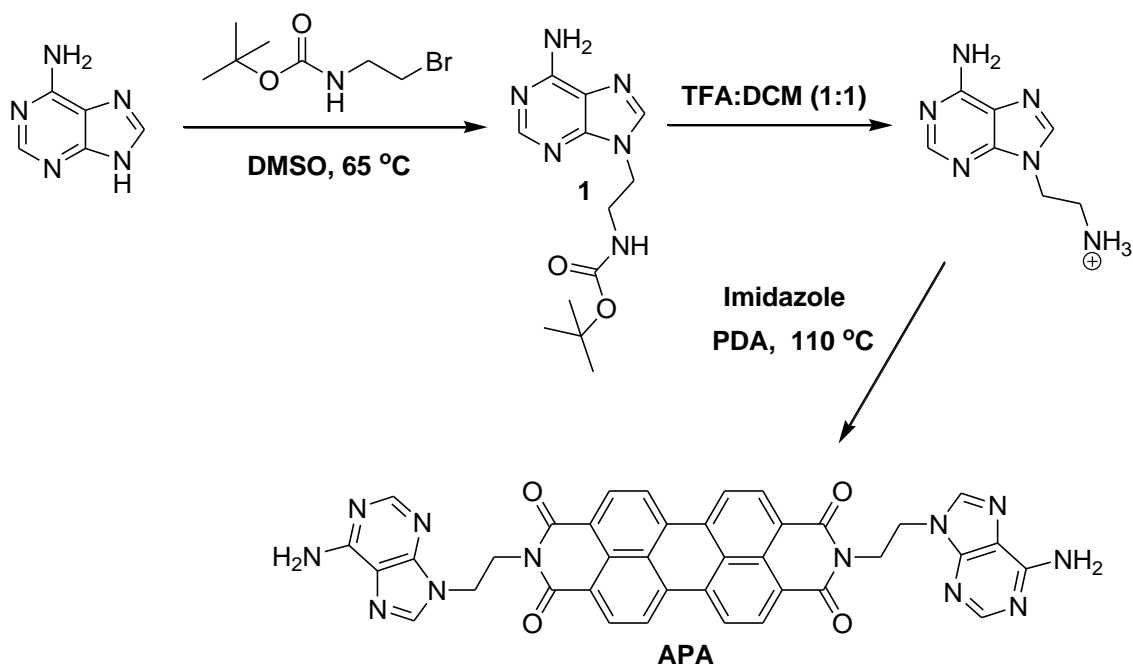
---

## Chapter 6b: Double Zipper Helical Assembly of Deoxyoligonucleotides: Mutual Templating and Chiral Imprinting to Form Hybrid DNA Ensembles

The magnificent structure-property correlations of biological systems is exemplified by the elegant molecular design and functioning of nucleic acids.<sup>1,3</sup> In particular, deoxyribonucleic acid (DNA) has structurally evolved over billions of years to effectively store and communicate the genetic information in majority of all living organisms.<sup>5,40,41</sup> In recent times, numerous efforts have been directed at utilizing DNA as a potential biomaterial, a biomolecular system capable of conducting electricity, single molecular wire and material building block in celebrated nanotechnological advances.<sup>20,24,42-46</sup> Here, we demonstrate an adenine functionalized perylene bisimide (PBI) conjugate (**APA**) as a promising molecular template to construct hybrid DNA ensembles through double zipper helical assembly.<sup>47</sup> The intriguing property of adenine to form hydrogen bond with complementary (thymine) and non-complementary (adenine and guanine) nucleobases inspired us to design **APA** as a double zipper template to construct new hybrid DNA structures.<sup>48-52</sup> PBI is one of the most promising aromatic  $\pi$ -conjugated systems with potential applications in organic electronics biology and supramolecular architecture.<sup>53-55</sup> Recently, supramolecular architecture resulting from covalent functionalization of PBI with single-stranded (ss) DNA has been reported.<sup>56,57</sup> In this work, **APA** operates through non-covalent interactions, thus avoiding synthetic difficulties prevalent in the covalent approaches. To the best of our knowledge, this is the first report on the construction of ordered hybrid DNA ensembles through double zipper helical assembly of deoxyoligonucleotides employing versatile hydrogen bonding and  $\pi$ -stacking potential of adenine in **APA**.

### 6.8 Synthesis of adenine appended perylenediimide (**APA**)

Boc-protected adeninyl-9-ethyl amine (**1**) was prepared in good yield by *N*-alkylation of adenine (*N*<sup>9</sup>-H) using 1-(butyloxycarbonyl)-2-bromo ethylamine and sodium hydride as base in DMSO at 65 °C. Boc-protected **1** was condensed with perylene-3,4,9,10-tetracarboxylic dianhydride (PDA) in imidazole to obtain the corresponding adenine appended perylenediimide (**APA**) conjugate in good yield (Scheme 2).



**Scheme 2.** Synthesis of Adenine conjugated PBI (APA).

### 6.9 Photophysical properties of hybrid DNA ensembles

Herein, we present a new strategy for the construction of hybrid DNA ensembles of deoxyoligonucleotides ( $\text{dB}_n$ ) employing APA. APA conjugate was prepared following our earlier reported procedure (Chapter 6, section 6.6)<sup>9,58</sup> and various  $\text{dB}_n$  ( $\text{dA}_n/\text{T}_n/\text{G}_n/\text{C}_n$ ) were employed to construct double helical assembly of APA and  $\text{dB}_n$  (Table 1). First, the molecular interactions of APA were studied by evaluating its photophysical properties. The UV-vis absorption spectrum of APA ( $50\text{ }\mu\text{M}$ ) in DMSO exhibited three strong characteristic bands at 530, 493 and 461 nm corresponding to characteristic 0-0, 0-1 and 0-2 electronic transitions of perylene chromophore, respectively.<sup>59</sup> The absorption spectrum of APA ( $50\text{ }\mu\text{M}$ ) in aqueous solution (Water/DMSO = 90:10, v/v%) exhibited hypsochromic shift in the 400-550 nm region and a new band at 561 nm, which is attributed to the hydrophobic force-induced aggregation of APA (Figure 8a). The fluorescence spectrum of APA in DMSO displayed mirror image emission bands and these bands were completely quenched in aqueous solution as a result of aggregation (Figure 8b). Interestingly, the absorption spectrum of APA ( $50\text{ }\mu\text{M}$ ) in PBS buffer (10 mM, pH = 7, 10% DMSO) showed bathochromic shift with an appreciable hypochromicity (Figure 8a).

**Table 1.** Sequence information of deoxyoligonucleotides (dB<sub>n</sub>; B = A/T/G/C) used in this study.

Code	DNA-Sequence
dA <sub>10</sub>	5'-AAAAAAAAAAA-3'
dT <sub>10</sub>	5'-TTTTTTTTTTT-3'
dC <sub>10</sub>	5'-CCCCCCCCCC-3'
dG <sub>10</sub>	5'-GGGGGGGGGG-3'
dA <sub>20</sub>	5'-AAAAAAAAAAAAAAAAAAAA-3'
dT <sub>20</sub>	5'-TTTTTTTTTTTTTTTTTTTT-3'
dC <sub>20</sub>	5'-CCCCCCCCCCCCCCCCCCCC-3'
dG <sub>20</sub>	5'-GGGGGGGGGGGGGGGGGGGG-3'

Next, we investigated photophysical properties of **APA** in the presence of complementary and non-complementary dB<sub>n</sub> in PBS buffer. **APA** (50 μM) showed hyperchromicity in the absorption with increasing concentration (1-10 μM) of dB<sub>n</sub> (Figure 9). These results revealed the existence of mutual interactions between **APA** and complementary as well as non-complementary dB<sub>n</sub> through non-covalent forces to form hybrid assembly structures.

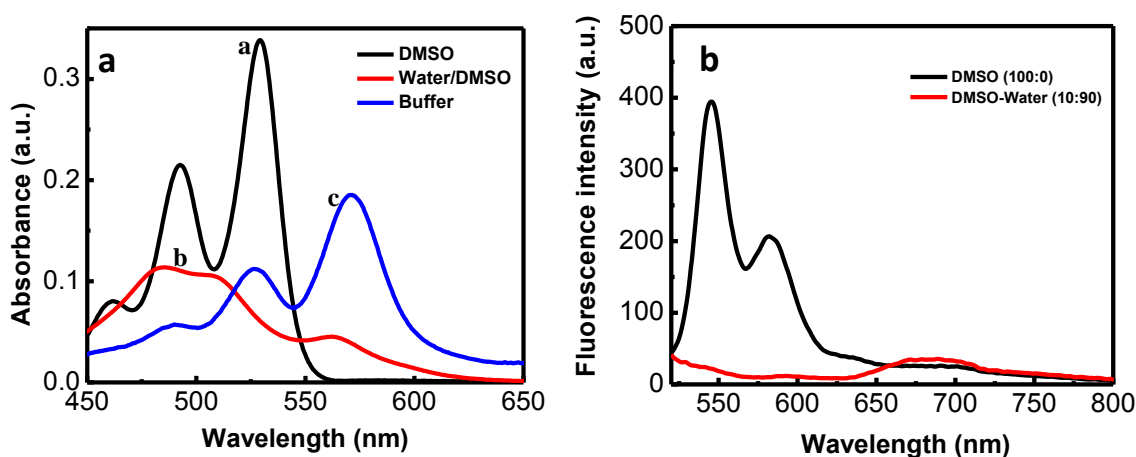


**Figure 8.** UV-vis absorption and emission spectra of **APA**. (a) **APA** in a: DMSO; b: Water/DMSO (90/10) and c: buffer/DMSO (90/10) solutions. (b) Fluorescence spectra of **APA** (50 μM) in DMSO and aq. DMSO solution.

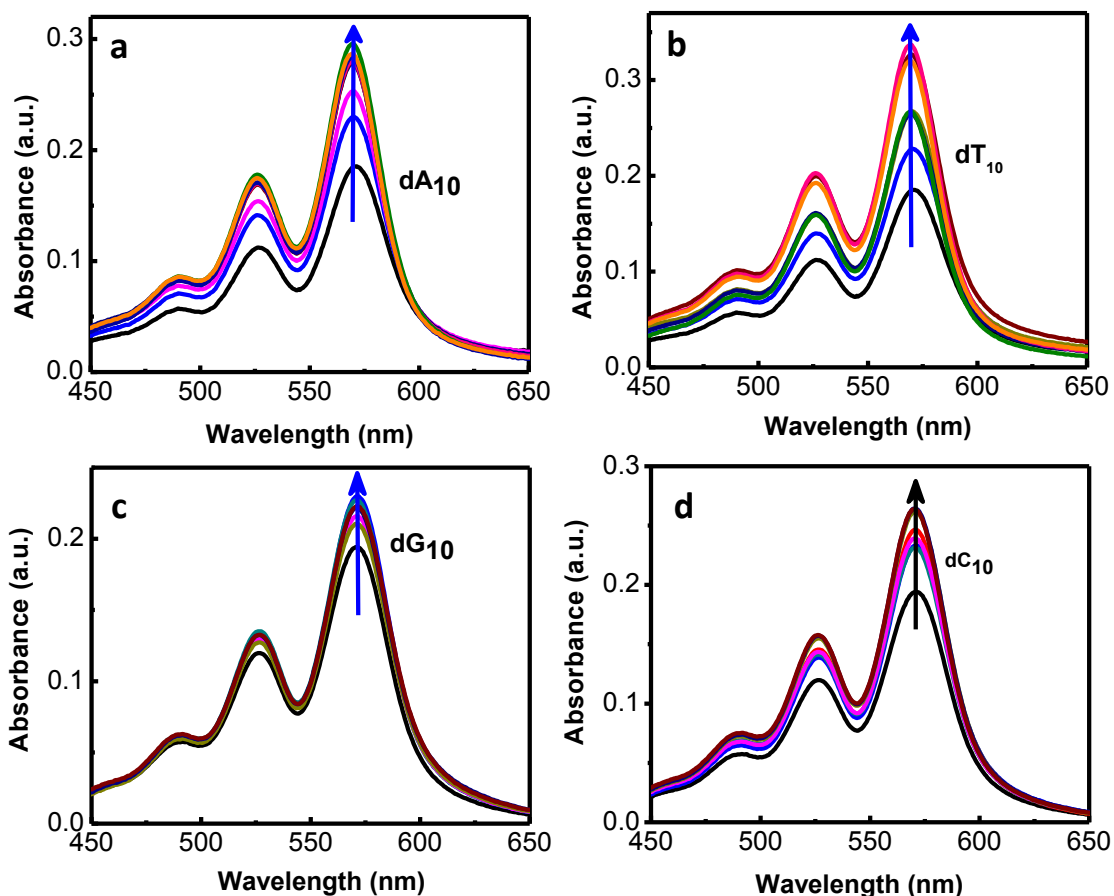


**Figure 9.** UV-vis absorption spectra of **APA** with deoxyoligonucleotides ( $\text{dB}_n$ ). (a) **APA** with increasing concentration of  $\text{dA}_{10}$  in buffer solution, (b) **APA** with increasing concentration of  $\text{dT}_{10}$  in buffer solution, (c) **APA** with increasing concentration of  $\text{dG}_{10}$  in buffer solution and (d) **APA** with increasing concentration of  $\text{dC}_{10}$  in buffer solution. Buffer: 10 mM, PBS containing 10% DMSO,  $\text{pH} = 7$ .

### 6.10 Circular dichroism studies of hybrid DNA ensembles

To understand the nature of molecular organizations of **APA** in the presence and absence of  $\text{dB}_n$ , we performed circular dichroism (CD) spectroscopy studies at ambient temperature (25 °C). **APA** (50  $\mu\text{M}$ ) gave a flat CD signal, which is ascribed to the existence of equal amounts of right- and left-handed helical aggregates. **APA**: $\text{dT}_{10}$  (10 : 2) exhibited a bisignated CD signal in the 400–600 nm region and a negative CD signal in the 250–300 nm region corresponding to the absorption of **APA** and  $\text{dT}_{10}$ , respectively (Figure 10a). The intense negative CD signal in the **APA** absorption region originated from the orientation of transition

moments of perylene chromophores in the counter-clockwise direction (M-helix). The negative CD signal in the 250–300 nm region revealed M-helical arrangement of dT<sub>10</sub> strands around the molecular template APA. Next, CD spectra of APA in the presence of non-complementary dA<sub>10</sub>, dG<sub>10</sub> and dC<sub>10</sub> were recorded. Notably, APA:dC<sub>10</sub> (10:2) combination did not display any characteristic CD signals indicating the absence of ordered assembly between APA and dC<sub>10</sub> (Figure 10a). Surprisingly, APA:dA<sub>10</sub> (10 : 2) and APA:dG<sub>10</sub> (10 : 2) showed unprecedented P-(right handed) and M-helical arrangements with respect to both perylene chromophore (400–600 nm) and dB<sub>n</sub> (B = A or G) (250–300 nm) (Figure 10a). This indicated mutual templating between APA and dA<sub>10</sub>/dG<sub>10</sub> through unconventional hydrogen bonding leading to P- and M-helical imprinting in the hybrid DNA ensembles.

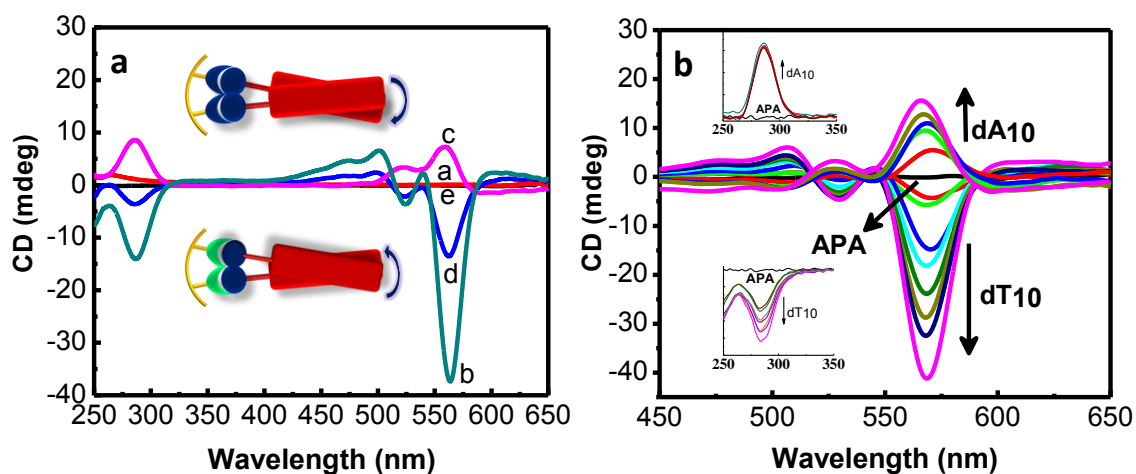


**Figure 10.** CD spectra of APA. (a) a: APA, and APA:dB<sub>n</sub> (10:2 ratio), b: dT<sub>10</sub>, c: dA<sub>10</sub>, d: dG<sub>10</sub> and e: dC<sub>10</sub> in PBS buffer (10 mM, pH = 7, 10% DMSO). *Inset:* Right and left-handed helical orientation of APA in the presence of dA<sub>10</sub> (top) and dT<sub>10</sub>/G<sub>10</sub> (bottom). (b) Spectra of APA with variable concentration of dA<sub>10</sub> and dT<sub>10</sub>. *Inset:* Spectral features of APA and dA<sub>10</sub> or dT<sub>10</sub> in the A/T absorption region.

In the control study, spectra of individual dA<sub>10</sub> showed positive and negative signals at 270 nm and 250 nm respectively (Figure 11). Similarly, dT<sub>10</sub> showed positive and negative signals at 280 nm and 250 nm respectively. These CD signals correspond to their respective random coil structures. Therefore, the characteristic features in the CD spectra of dT<sub>10</sub>, dA<sub>10</sub>

and dG<sub>10</sub> with **APA** in the nucleobase and perylene absorption regions, as discussed above, signify the formation of ordered chiral assemblies. The spectra of **APA** as a function of added dT<sub>10</sub>/dA<sub>10</sub> exhibited an increase in the intensity of CD signals in the perylene chromophoric region (Figure 10b). These data suggest that the dB<sub>n</sub> concentration drives the formation of ordered [dB<sub>n</sub>:(APA)<sub>n</sub>:dB<sub>n</sub>] ensembles. Furthermore, we observed similar CD changes of APA with dA<sub>20</sub>/dT<sub>20</sub>/dG<sub>20</sub> (Figure 12). Overall, CD studies confirmed the formation of ordered chiral ensembles of two-component systems (**APA** and dB<sub>n</sub>) by the way of mutual templating and chiral imprinting through double zipper assembly.

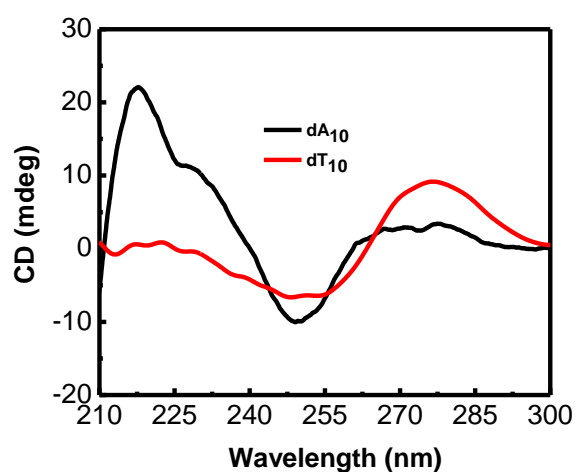


**Figure 11.** CD spectra of dA<sub>10</sub> and dT<sub>10</sub> (10 μM) in PBS-buffer solution (10 mM, pH = 7).

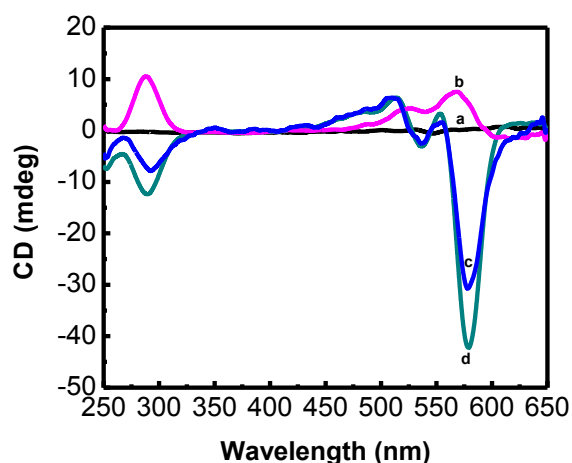


**Figure 12.** CD spectra of **APA**. a: **APA**, b: **APA**:dA<sub>20</sub> (20:2 ratio), c: **APA**:dG<sub>20</sub> (20:2 ratio), and d: **APA**:dT<sub>20</sub> (20:2 ratio) in PBS buffer containing 10% DMSO, pH = 7.

### 6.11 Stoichiometry binding of hybrid DNA ensembles

To validate our proposed stoichiometric ratio of **APA**:dT<sub>10</sub> (10:2), we performed concentration dependent CD measurements by titrating increasing concentrations of **APA** (0 to 70 μM) to a fixed concentration of dT<sub>10</sub> (10 μM). The stoichiometry of **APA**:dT<sub>10</sub> in hybrid DNA ensembles is given in terms of the base pair ratio i.e. A:T (A of **APA** :T of dT<sub>10</sub>). The plot of CD intensity at 561 nm (perylene) against the A/T ratio showed saturation at 1:1 suggesting a stoichiometry of 10:2 for the formation of the [dT<sub>10</sub>:(**APA**)<sub>10</sub>:dT<sub>10</sub>] type ensemble (Figure 13a). We also recorded the CD spectra of fixed concentration of **APA** (50 μM) by adding increasing concentration of dT<sub>10</sub> (0 to 12 μM). The plot of CD intensity monitored at 561 nm against concentration of dT<sub>10</sub> showed saturation at 10 μM (Figure 14). The stoichiometry study performed with **APA** and dB<sub>10</sub> (dA<sub>10</sub> and dG<sub>10</sub>) also suggested the formation of [dB<sub>10</sub>:(**APA**)<sub>10</sub>:dB<sub>10</sub>] in the ratio of 10:2 (**APA**:dB<sub>10</sub>) (Figure 13b and 13c). Thus, CD studies confirmed a stoichiometric ratio of 10:2 for the complexation of **APA** and dT<sub>10</sub> to form [dT<sub>10</sub>:(**APA**)<sub>10</sub>:dT<sub>10</sub>] ensembles.

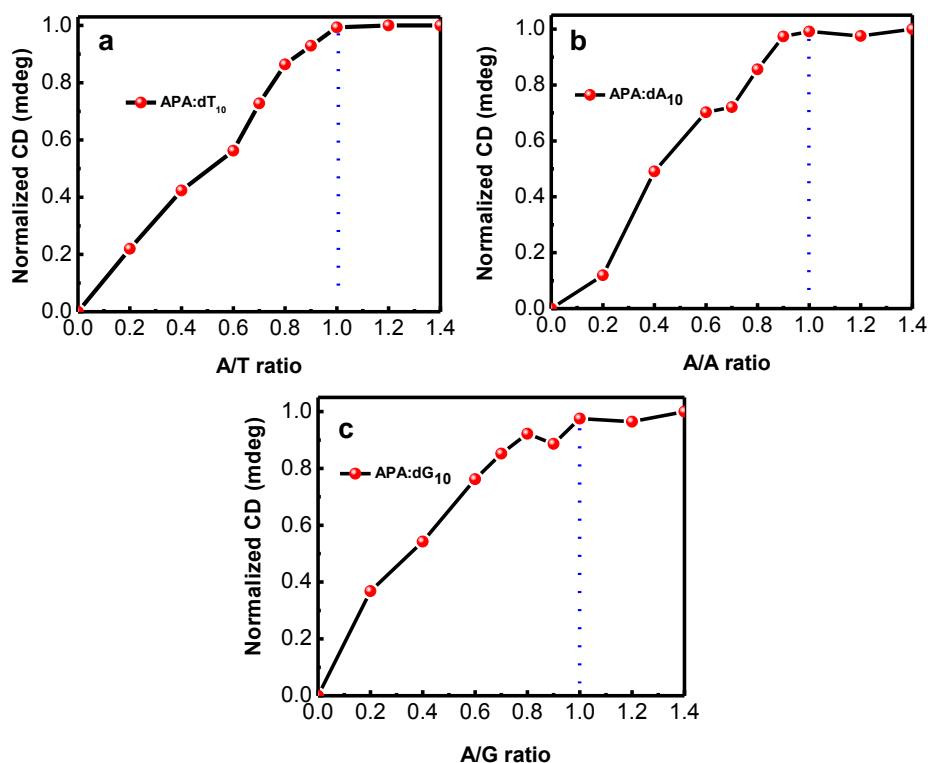


**Figure 13.** Stoichiometry binding of **APA**:dB<sub>n</sub>. (a-c) are the plots of CD intensity monitored at 561 nm for different combinations of **APA** against the A/T, A/A and A/G ratio at with fixed concentration of dT<sub>10</sub> (10 μM), dA<sub>10</sub> (10 μM) and dG<sub>10</sub> (10 μM) respectively.

In general, analysis of DNA-templated self-assembly revealed 100% binding efficiency of guest (**APA**) to host (DNA) can be achieved only if the relative number of guest ( $\phi_g$ ) are greater than the host binding sites ( $\phi_h$ ), i.e.  $\eta = \phi_g / \phi_h > 1$ .<sup>60</sup> Therefore, to validate our proposed stoichiometric ratio of **APA**:dB<sub>10</sub> (10:2), we performed the concentration dependent CD studies of fixed concentration of dB<sub>n</sub> with increasing concentration of **APA**. In this experiment, we recorded the CD spectra of preformed complexes of **APA**:dT<sub>10</sub> with increasing concentration of **APA** from 0 to 70  $\mu$ M. Upon increasing concentration of **APA** from 0 to 50  $\mu$ M, CD spectra showed an increase in CD signal intensity in the perylene absorption region(400-600 nm) with fixed concentration of dT<sub>10</sub> (10  $\mu$ M) (*i.e.*, A:T = 0:1 to 1:1). With further increase in concentration of **APA** from 50 to 70  $\mu$ M, CD signal in perylene absorption region reaches saturation for A:T  $\geq$  1:1. These results showed the saturation of CD signal at greater than 50  $\mu$ M which indicates  $\eta = \phi_g / \phi_h > 1$ .

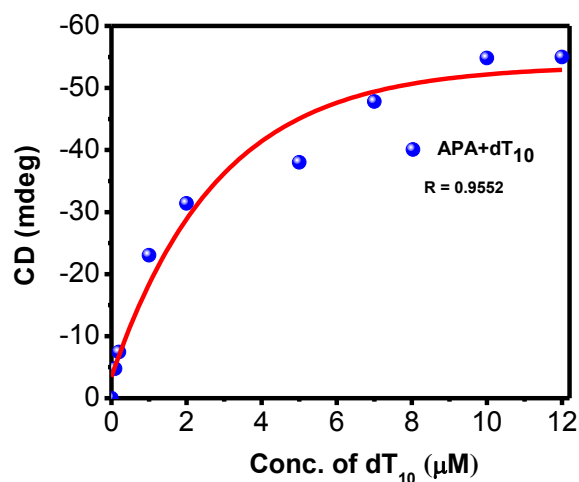


**Figure 14.** CD spectra of **APA** (50  $\mu$ M) with increasing concentration of dT<sub>10</sub> in buffer solution.

### 6.12 pH effect on the formation of hybrid DNA ensembles

CD-results prompted us to study the effect of pH, one of the key factors that influence hydrogen bonding (nucleobases) and electrostatic (sugar phosphate backbone) interactions of dB<sub>n</sub>.<sup>41</sup> In the pH range of 2-11, a flat CD signal was observed for **APA** in the absence of dB<sub>n</sub>. **APA**:dT<sub>10</sub> (10:2) and **APA**:dT<sub>20</sub> (20:2) showed very weak CD features corresponding to perylene chromophore (400-600 nm) and dT<sub>10</sub>/dT<sub>20</sub> (250-300 nm) absorption regions in the



acidic pH range of 2-4 (Figure 15a and 16a). However, strong CD signals were observed for perylene chromophore (400-600 nm) and  $dT_{10}/dT_{20}$  (250-300 nm) in the pH range of 7-11. CD spectra of  $APA:dA_{10}/dA_{20}$  displayed a flat signal in the 400-600 nm region under acidic conditions (pH = 2-4). Remarkably, at neutral pH  $APA:dA_{10}/dA_{20}$  exhibited strong positive CD signals in the 400-600 nm and 250-300 nm regions. The intensities of these signals were further enhanced by increasing the pH from 7 to 11 (Figure 15b and 16b).

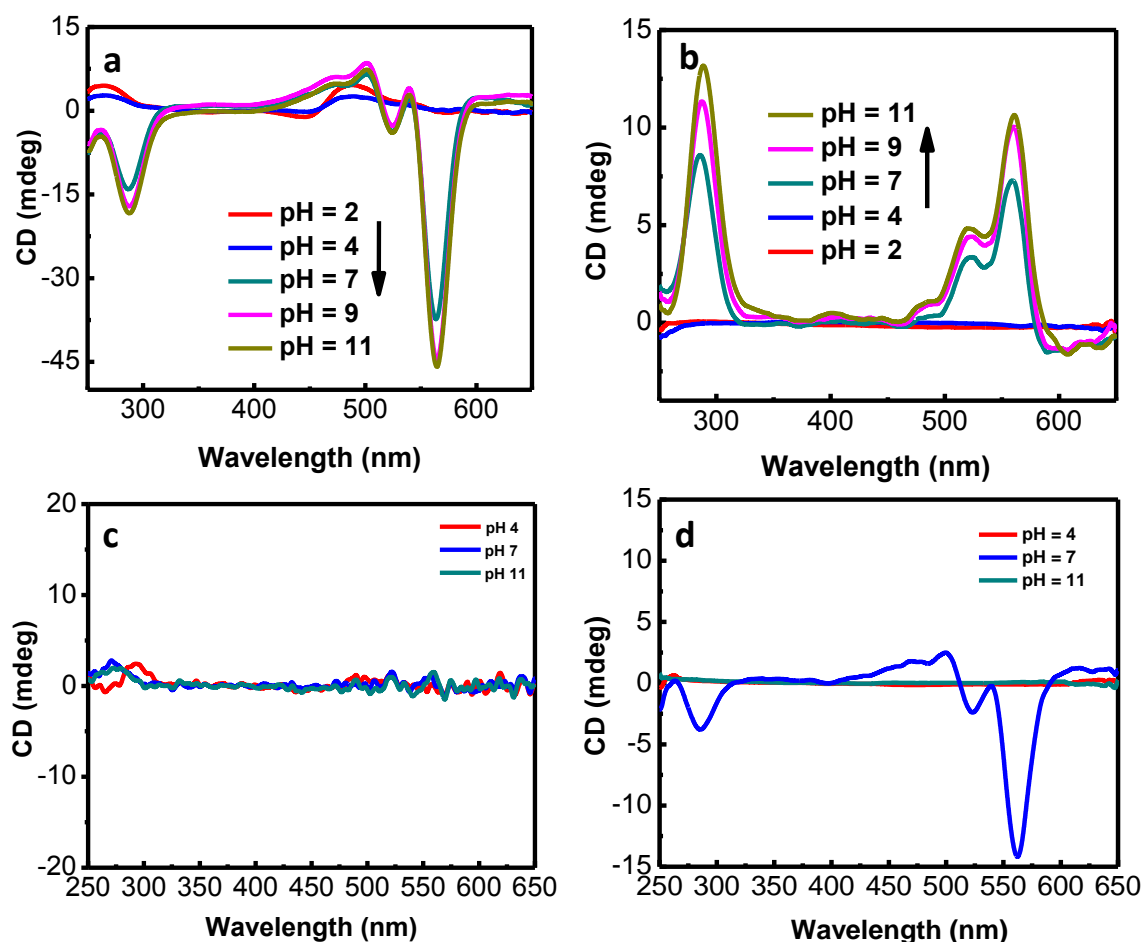


**Figure 15.** pH-dependent spectra of  $APA$  templated hybrid DNA ensembles of  $dT_{10}$  (a),  $dA_{10}$  (b),  $dC_{10}$  (c) and  $dG_{10}$  (d) respectively.

Interestingly,  $APA:dA_{20}$  showed a positive CD signal while  $APA:dA_{10}$  did not show any appreciable CD signal in the adenine absorption region (250-300 nm) under acidic conditions (pH = 2-4). These pH-dependent transformations in the CD signatures of  $APA:dA_{10}/dA_{20}$  are mainly attributed to protonation of adenine. In acidic media (pH = 2-4),

adenine ( $N^1$ ) underwent protonation with the protonated  $N^1$ -H, triggering self-complementary base pairing [ $d(AH^+):d(AH^+)$ ] through reverse Hoogsteen (H) hydrogen bonding.<sup>49</sup> This facilitates the formation of homoduplexes (A-motifs) of  $dA_{10}/dA_{20}$ , which are further stabilized by electrostatic interactions with the phosphate backbone.<sup>49</sup> It should be noted that well-defined and characteristic CD signature for self-complementary A-motif is observed with  $dA_n$  where  $n \geq 12$ . However, under neutral and basic conditions the unconventional A:A hydrogen bonding interaction driven by **APA** templating of  $dA_{10}/dA_{20}$  dominates to form hybrid DNA ensembles.

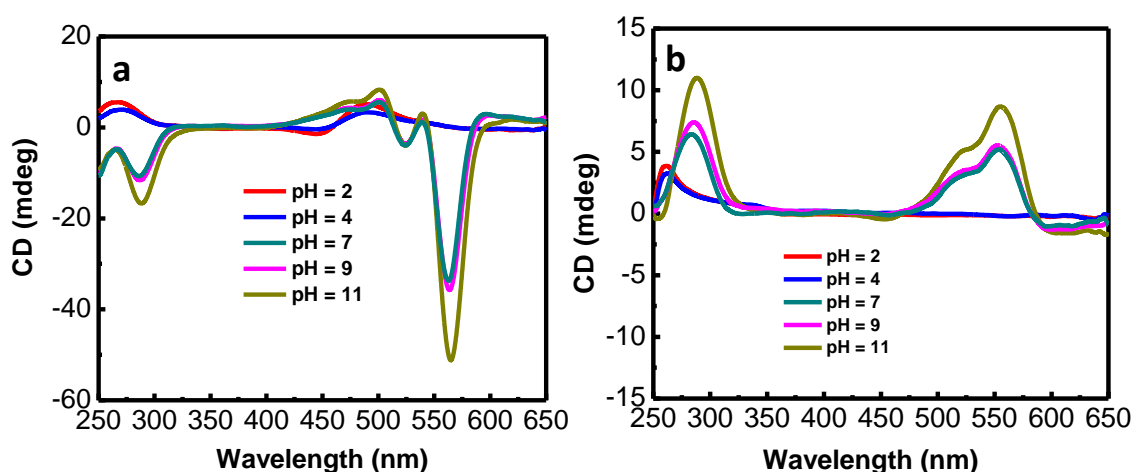


**Figure 16.** pH dependent CD spectra. (a) **APA**: $dT_{20}$  (20:2) and (b) **APA**: $dA_{20}$  (20:2) in the range of pH = 2-11.

Next, we recorded CD spectra of **APA** in the presence of  $dG_{10}$  and  $dC_{10}$  over a pH range of 2-11. Surprisingly, **APA**: $dG_{10}$  (10:2) showed CD features similar to **APA**: $dT_{10}$  (10:2), albeit only under neutral pH conditions (Figure 15c). Stable unconventional hydrogen bonding-driven G-A pairing between **APA** and  $dG_{10}$  at neutral conditions led to the formation of [ $dG_{10}:(\mathbf{APA})_{10}:dG_{10}$ ] ensemble.<sup>51,52</sup> The CD spectra of **APA** and  $dC_{10}$  mixture (10:2) displayed a flat signal in the pH range of 7-11, as these conditions do not favor the formation of A-C base pairing. However, under acidic conditions (pH = 4) an intense positive CD signal at 294 nm and a negative CD-signal at 265 nm were observed. These are the characteristic CD features well-documented in the literature for *i-motifs* of  $dC_{10}$  under acidic conditions (Figure 15d).<sup>61</sup> Overall, pH  $\geq 7$  favored the mutual templating and chiral

imprinting of **APA** and  $\text{dB}_n$  ( $B = \text{T/A/G}$ ) through conventional and unconventional hydrogen bonding to form hybrid DNA ensembles of the type  $[\text{dB}_n:(\text{APA})_n:\text{dB}_n]$ .

### 6.13 Thermal melting studies of hybrid DNA ensembles

In order to ascertain the thermal stability of helical ensembles of  $\text{dB}_n$  and **APA**, we carried out variable-temperature absorption and CD studies. Hybrid ensembles of purine-containing  $\text{dB}_n$  and **APA** exhibited high thermal stability as indicated by the melting temperatures ( $T_m$ ) (Table 2). The thermal denaturation data revealed that all helical DNA ensembles of **APA** and  $\text{dB}_n$  were highly stable under ambient conditions.

**Table 2.** Melting temperatures ( $T_m$ ) of hybrid DNA ensembles.

DNA complex	$T_m$ (at pH = 7)	$T_m$ (at pH = 9)
ds( $\text{A}_{10}+\text{T}_{10}$ )	21.1 °C	---
ds( $\text{G}_{10}+\text{C}_{10}$ )	62.0 °C	---
d $\text{T}_{10}+(\text{APA})_{10}+\text{dT}_{10}$	55.2 °C	60.1 °C
d $\text{T}_{20}+(\text{APA})_{20}+\text{dT}_{20}$	63.3 °C	64.1 °C
d $\text{A}_{10}+(\text{APA})_{10}+\text{dA}_{10}$	67.4 °C	65.7 °C
d $\text{A}_{20}+(\text{APA})_{20}+\text{dA}_{20}$	75.4 °C	65.7 °C
d $\text{G}_{10}+(\text{APA})_{10}+\text{dG}_{10}$	73.8 °C	---
d $\text{G}_{20}+(\text{APA})_{20}+\text{dG}_{20}$	78.3 °C	---

### 6.14 Morphological studies of hybrid DNA ensembles

To visualize the structural morphology of hybrid helical DNA ensemble, we carried out the atomic force microscopy (AFM) measurements on **APA**:d $\text{T}_{20}$  ( $\text{A/T} = 1:1$ ) assembly structures. AFM micrograph clearly showed formation of ordered left-handed helical co-assembly of **APA**:d $\text{T}_{20}$  (Figure 17a). The left-handed helical co-assembly of **APA**:d $\text{T}_{20}$  is well- corroborated with the observed negative cotton effect in the circular dichroism (CD) spectrum of  $[\text{dT}_{20}:(\text{APA})_{20}:\text{dT}_{20}]$  ensembles (Figure 12).

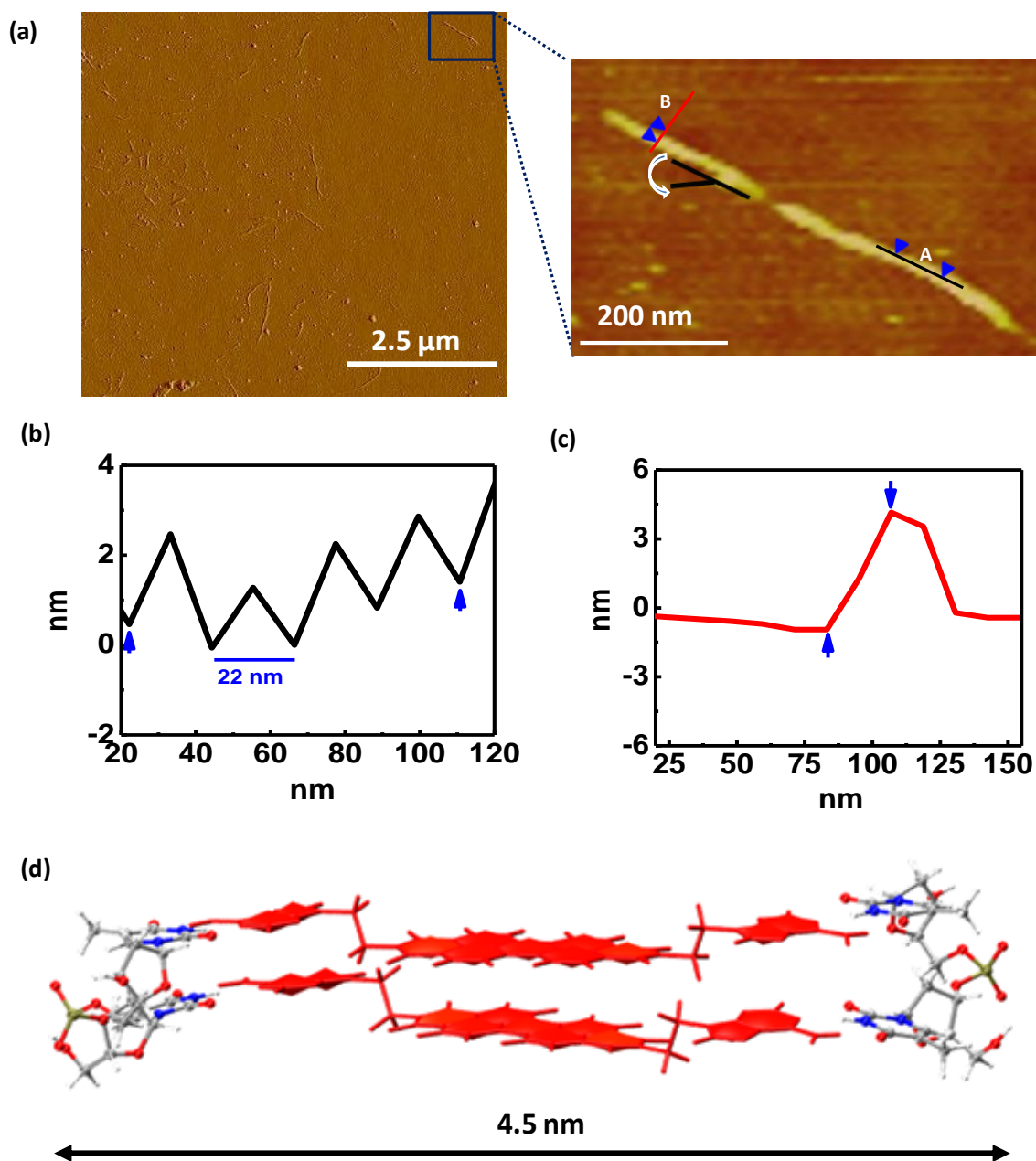


**Figure 17.** Atomic force microscopic images of hybrid DNA ensembles. (a) AFM image of left-handed helical DNA ensemble of  $[\text{dT}_{20}\text{-(APA)}_{20}\text{-dT}_{20}]$ . (b) & (c) are the section profiles of DNA ensemble in (a) along A- and B-axis.  $\sim 22 \text{ nm}$  along axis-A indicates the helical pitch (b) and  $5 \text{ nm}$  along B-axis corresponding to height of DNA-ensembles (c). For clarity, helical pitch and thickness measurements are shown on different structures of DNA ensembles. *Inset:* Arrow shows the CCW direction of DNA ensembles to the symmetry axis. (d) Typical thickness ( $4.5 \text{ nm}$ ) of  $[\text{dT}_2\text{-(APA)}_2\text{-dT}_2]$  calculated from theoretical model.

The AFM measurements of [dT<sub>20</sub>:(**APA**)<sub>20</sub>:dT<sub>20</sub>] ensembles revealed the typical helical pitch ~ 22 nm (Figure 17b) and section profile showed height (thickness) of 5 ± 0.5 nm along B-axis of the ensemble (Figure 17c) which is in agreement with the theoretically calculated thickness value of 4.5 nm across hydrogen bonded **APA** and dT<sub>20</sub> (Figure 17d). Further, the lengths of the left handed assembly structures showed are ranges 100-400 nm. Moreover, the observed longer helical stacks of **APA**:dT<sub>20</sub> which allows us to consider the fact that the hybrid helical DNA ensembles are extends through the interactions of DNA ensembles (**APA**:dT<sub>20</sub>). Overall, these studies proved the versatility of conventional and unconventional hydrogen bonding potential of adenine as the key factor for constructing stable helical hybrid DNA ensembles.

### 6.15 Theoretical studies of hybrid DNA ensembles

To understand the structure and energetics of the double zipper assembly, quantum mechanical (QM) calculations were performed on carefully chosen model systems. PBI dimer, optimized using the M06 and PM7 methods, yielded a non-planar structure (Figure 18a and 18b). Several model systems for **APA** have been built appropriately including several conformations. High level QM calculations at the RI-MP2 level of theory indicated that both A:A and A:G prefer W:W type base pairing over other possibilities. The relative energies of four model systems with two base pair steps for each of the *M*- and *P*-helical forms were calculated at the semi-empirical PM7 and the Boltzmann weighted differences are presented in Figure 18c. The energies suggest that dT<sub>n</sub> and dG<sub>n</sub> prefer *M*-helical forms, whereas dA<sub>n</sub> prefers to form the *P*-helix, which is in excellent agreement with the experimental observation discussed above. Based on these structures, three-dimensional model for the most stable helical ensemble in each of the three cases were built and are given in Figure 18d-f. A complex combination of several factors including unique conformational preferences of the backbone increased pitch, and solvent effects are proposed to yield such structures of the assemblies.

In detail, PBI dimer was modeled by placing the optimized structures of the two identical monomers such that the interplanar distance between the two was 3 Å and by twisting one of the PBI monomers with respect to the other by 20° along the helical axis. Visualization of the optimized geometries at the M06 and PM7 levels indicates that the PBI

molecules lost their planarity within the dimer structure. Though identical in terms of energy, both P- and M-forms of the helical dimers were optimized for further model building. The interaction energy between the two monomers was calculated to be -22.45 and -36.86 kcal/mol at the M06 and PM7 levels of theory respectively indicating strong non-bonded interactions.

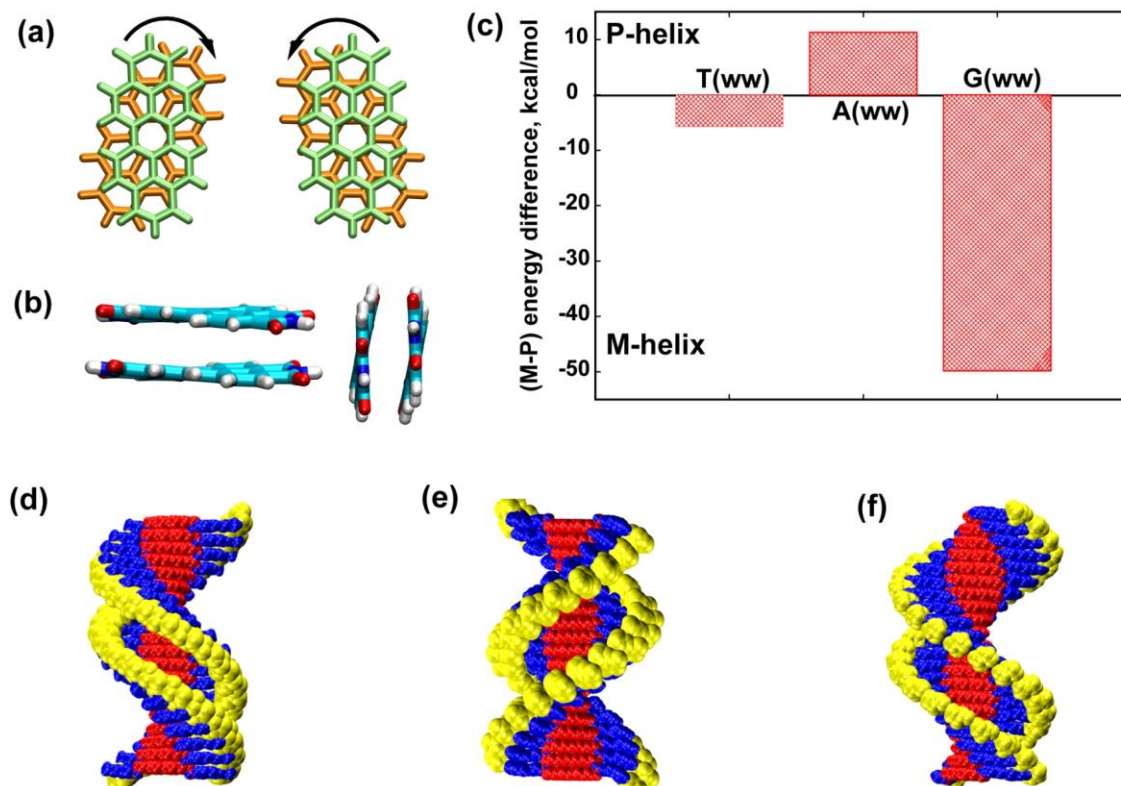


**Figure 18.** Modeling PBI core of **APA** in dimer geometries. (a) Top view of the clock and anti-clockwise twisting in PBI dimers. (b) Observed bent in optimized PBI dimer structure and (c) Difference between Boltzmann weighted averages of heat of formation values (in kcal/mol) of the left (*M*) and right (*P*) handed  $[dB_n-(\mathbf{APA})_n-dB_n]$  ( $B = A/T/G$ ) helices. (d-f) Models of hybrid DNA ensembles  $[dT_{20}-(\mathbf{APA})_{20}-dT_{20}]$ ,  $[dA_{20}-(\mathbf{APA})_{20}-dA_{20}]$ , and  $[dG_{20}-(\mathbf{APA})_{20}-dG_{20}]$ , in their stable form.

Similar to PBI dimer, models for the dimers of **APA** were built and were optimized at the PM7 level. Possible conformational isomers of **APA** based on the orientation of C-C single bond of alkyl chain and C-N (Adenine) has been considered to model the helices. However, only a few of these conformers can interact with the DNA strands via base pair

interactions (Figure 19). These dimers and respective monomers were subjected to geometry optimization at PM7 level and respective interaction energies were computed by taking the difference of energies between dimer and respective monomers (Table 3). As indicated by the interaction energies, the **APA** monomers in all the four conformations can potentially aggregate to form supramolecular structures via strong non-bonded interactions. Since the P- and M-helical structures are equally preferred and are expected to be present in equal amounts, the supramolecular structures formed by only **APA** is not expected to exhibit CD signal.

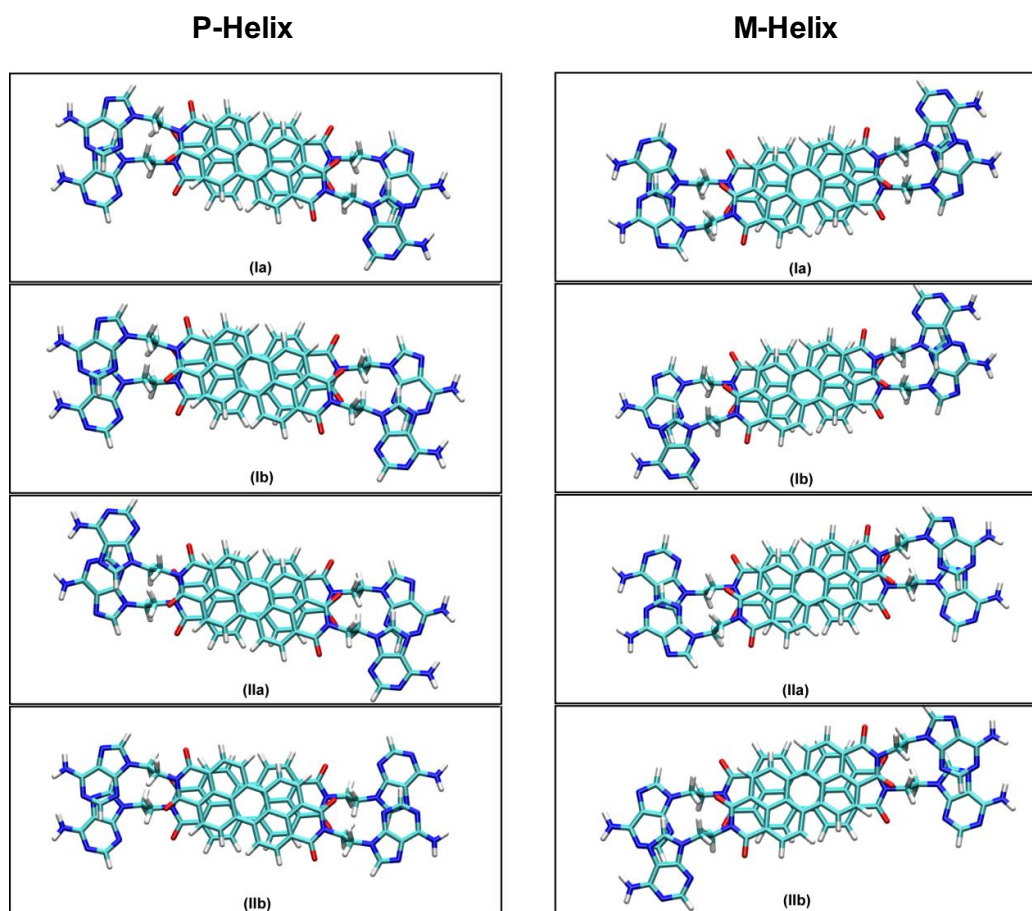


**Figure 19.** Various possible conformers for **APA** dimers in M- and P-helices which form antiparallel (Ia, Ib) and parallel (IIa, IIb) helices when interacted with deoxyoligonucleotides  $\text{dB}_n$  ( $B=A, T, G$ ).

The model systems corresponding to the **APA** and  $\text{dB}$  ( $B = A, T, G$ ) hybrid assemblies were modeled using Visual molecular dynamics (VMD). The left and right handed DNA strands were constructed using the nucleic acid builder developed by Case and coworkers.

These model systems were subjected to geometry optimization by employing molecular mechanics CHARMM36 all-atom force field. The geometry optimizations at the quantum mechanical level were done on the dimer steps corresponding to all the model systems using semi empirical method PM7 in MOPAC2012.

**Table 3.** Interaction energies (in kcal/mol) of PBI and **APA** dimers in various conformations calculated by using PM7 method in MOPAC2012. Interaction energy corresponding to PBI dimer at M06 level is also specified.

Structure	Interaction energy
<b>PBI dimer</b>	-36.86 (-22.45)
<b>A-PBI-A dimer</b>	
Ia	-62.25
Ib	-64.05
IIa	-59.59
IIb	-65.11

**Table 4.** Heat of formation values of M- and P- helices at dimeric steps level in several orientations comparing two antiparallel (Ia, Ib) and the two parallel (IIa, IIb) for both M- and P- type helices (Figure 19).

Helix type	Orientation	A:T (WW)	A:A (WW)	A:G (WW)
M-Helix	Ia	<b>-1280.3</b>	-645.0	-874.6
	Ib	-1270.1	-681.9	<b>-895.9</b>
	IIa	-1275.2	-675.0	-833.0
	IIb	-1279.5	-683.5	-851.3
P-Helix	Ia	-1268.1	-673.1	-842.2
	Ib	-1249.3	-688.8	-846.0
	IIa	-1274.5	<b>-694.7</b>	-846.1
	IIb	-1257.1	-634.2	-806.4



The respective heat of formation values were used to calculate the Boltzmann weighted relative energies (M-P helices), which are presented in the manuscript. The Boltzmann weighted average of relative energies of the heat of formation corresponding to all the model systems considered for a particular base pair combination are provided in Figure 18 which indicates that the most stable helix for AT and AG is M-type whereas the most stable helix for AA is P-type. This is consistent with the experimental findings. Further, the absolute heat of formation values suggest that the most stable DNA assemblies formed by AT and AG are arranged in antiparallel manner whereas parallel in case of AA (Table 4).

### **6.16 Conclusion**

We demonstrated the versatility of conventional and unconventional hydrogen bonding ability of adenine in **APA** as a robust double zipper molecular template to construct hybrid DNA ensembles of random coiled deoxyoligonucleotides. The formation of ordered M- and P-helical DNA ensembles was achieved by distinctive base pairing (A–T, A–A and A–G) in the processes of mutual templating and chiral imprinting of APA and deoxyoligonucleotides at  $\text{pH} \geq 7$  (Figure 20). These experimental results were further supported by AFM analysis and computational calculations. DNA-templated studies that have been reported so far probe the helical assembly of chromophores based on their characteristic CD signatures. In the present work, we showed mutual helical assembly of functional chromophores and oligonucleotides with corresponding characteristic CD signatures in their respective absorption regions for the formation of M- and P-helical DNA ensembles. The results reported here are likely to inspire the development of new hybrid DNA ensembles of functional molecules (organic chromophores with interesting optical, electronic and biological properties) and oligonucleotides for diverse applications. The properties and applications range from electronics to nanotechnology to biomedicine. The pH dependent hydrogen bonding ability of nucleobases in the DNA ensembles can be used as a tool for the development of stimuli responsive (pH-triggered) delivery systems for therapeutic small molecules and oligonucleotides.

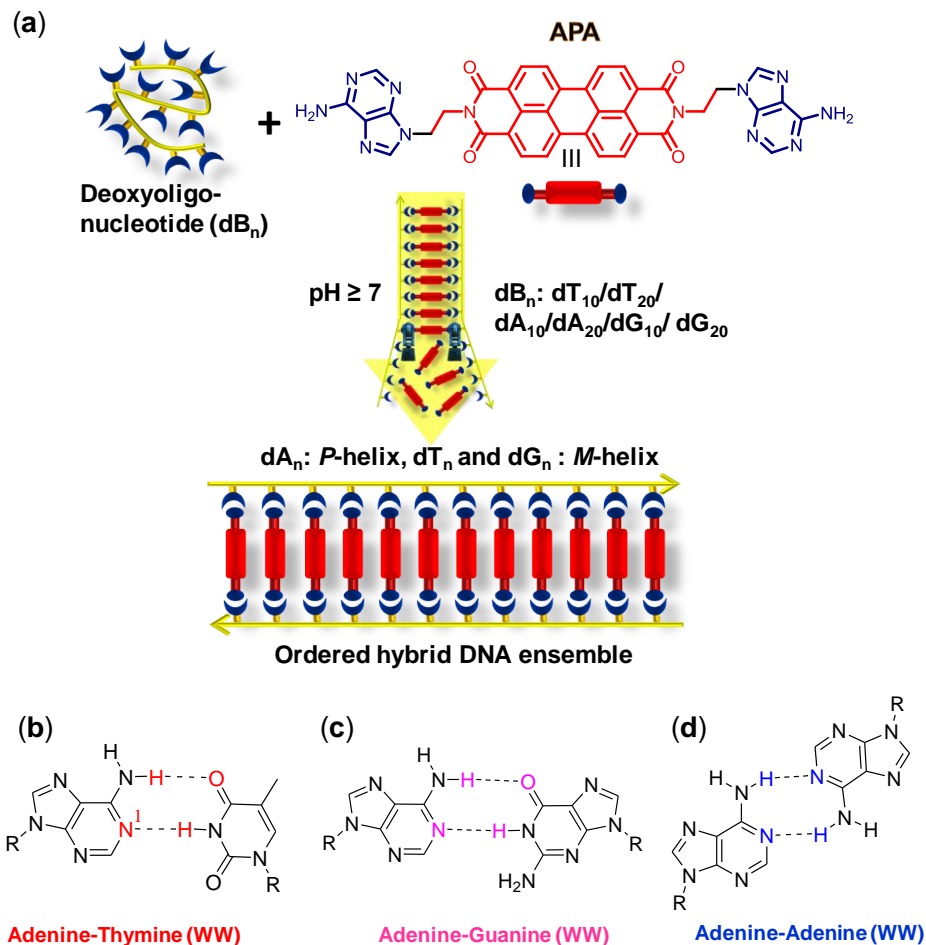


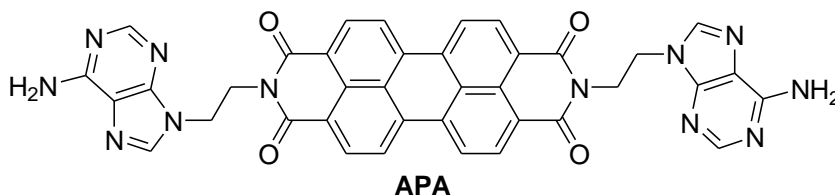
**Figure 20.** (a) Molecular structure of APA and deoxyoligonucleotides (dB<sub>n</sub>) used in the present study and schematic of hybrid DNA ensemble formation. (b-d) Hydrogen bonding in A-T, A-G and A-A base pairs. W = Watson-Crick hydrogen bonding site.

### 6.17 Experimental section

**General information.** Perylene-3,4,9,10-tetracarboxylicdianhydride (PDA), deoxyoligonucleotides (dB<sub>n</sub>/oligos: dA<sub>10</sub>, dT<sub>10</sub>, dA<sub>20</sub>, dT<sub>20</sub>, dG<sub>10</sub>, dG<sub>20</sub>, dC<sub>10</sub>, dC<sub>20</sub>), phosphate buffered saline (PBS) and 2-bromo-ethylamine hydrogen bromide were purchased from Sigma–Aldrich. Di-*tert*-butyl dicarbonate and adenine were obtained from Spectrochem Pvt. Ltd. Mumbai (India). All other reagents were used as received unless otherwise mentioned. <sup>1</sup>H and <sup>13</sup>C-NMR spectra were recorded on a Bruker AV-400 spectrometer with chemical shifts reported as ppm (in CDCl<sub>3</sub>/DMSO-*d*<sub>6</sub>, tetramethylsilane as internal standard) at 20 °C. UV-vis and CD spectra of samples were analyzed in quartz cuvette of 1 mm path length. High resolution mass spectra (HRMS) were obtained on Agilent Technologies 6538 UHD

Accurate-Mass Q-TOF LC/MS spectrometer.

**Synthesis of APA.** Adenine derivatives **1** was prepared following the synthetic procedure from our early reports.<sup>9</sup> Boc-protected adeninyl-9-ethylamine **2** (2.2 equiv.) was added to stirred a mixture of perylene-3,4,9,10-tetracarboxylic dianhydride (PDA) (141 mg, 3.59 mmol) and imidazole (5g) at 110 °C. The reaction mixture was allowed to stir for 3 h. After completion of the reaction, the reaction mixture



was cooled to room temperature. A mixture of ethanol (50 mL) and aq. HCl (1N, 50 mL) were added to the above reaction mixture and allowed to stir for 20 min. The reaction mixture was filtered and precipitate was washed with distilled water to achieve neutral pH. The obtained product (**APA**) was dried on under vacuum at 50 °C. Brown color solid, yield 72 %. <sup>1</sup>H-NMR (400 MHz, *DMSO-d*<sub>6</sub>+*TFA*)  $\delta_{ppm}$  9.53 (br, 2H), 8.93 (br, 2H), 8.73 (d, *J* = 8 Hz, 4H), 8.54 (s, 2H), 8.34 (d, *J* = 8 Hz, 4H), 8.21 (s, 2H), 4.65 (t, *J* = 5.2 Hz, 4H), 4.53 (t, *J* = 5.2 Hz, 4H). <sup>13</sup>C-NMR (100 MHz, *DMSO-d*<sub>6</sub>+*TFA*)  $\delta_{ppm}$  162.3, 149.9, 148.9, 144.5, 144.1, 133.0, 130.0, 127.4, 124.1, 123.6, 121.2, 118.0, 42.4, 41.2. HRMS (ESI) : found 713.2065, and calcd *m/z* = 713.2122 for C<sub>38</sub>H<sub>25</sub>N<sub>12</sub>O<sub>4</sub> [M+H]<sup>+</sup>.

**Sample preparation for UV-vis and CD measurements.** Samples for UV-vis and CD measurements were prepared by dissolving **APA** in DMSO with trace amount of trifluoroacetic acid in the order of 10<sup>-3</sup> M. Oligo-stock solutions were prepared by dissolving the oligos in double deionized water in the order of 10<sup>-4</sup> M. Double zipper assembly (hybrid DNA ensembles) of oligos were effected by adding the **APA** (in DMSO) in PBS-buffer solution (10 mM, pH = 7, 10% DMSO) and subjected to annealing by heating the sample to 85 °C for 15 min followed by cooling the sample solutions to room temperature for 7 h, stored in refrigerator for 4 h.

**UV-vis absorption spectroscopy.** The UV-vis absorption spectra were recorded on a Perkin Elmer Model Lambda 900 spectrophotometer at ambient conditions *i.e.*, 25 °C. Temperature dependent measurements were carried out on Cary 500 UV-vis-NIR spectrophotometer

equipped with Cary temperature controller in the range of 20 °C to 90 °C with ramp rate of 1 °C/min. A blank sample containing PBS buffer solution (10 mM, pH = 7, 10% DMSO) was recorded and subtracted from the collected data.

**Circular Dichroism (CD) spectroscopy.** CD experiments were carried out on a Jasco J-815 spectrometer under nitrogen atmosphere to avoid water condensation. Temperature dependent measurements were performed employing Peltier-type temperature controller (CDF-4265/15) in the range of 20 °C to 90 °C with a ramp rate of 1 °C/min. Scans were performed over the wavelength range of 250-700 nm with a speed of 200 nm/min and the spectra represent an average of three scans. A blank sample containing PBS buffer solution was recorded and subtracted from the collected data.

**Thermal denaturation studies.** Thermal denaturation curves of oligos in presence of **APA** (hybrid DNA ensembles) were recorded in the 10–90 °C range with heating rate 1 °C/min. The variable temperature/wavelength mode was used. CD signal was recorded at 560 nm and the complete CD spectra were recorded in the wavelength region of 250–700 nm with data collection for every 5 °C. Melting temperatures ( $T_m$ ) of hybrid DNA ensembles [**dB<sub>n</sub>**-(**APA**)<sub>n</sub>-**dB<sub>n</sub>**] were calculated from the first derivative curve of the molar ellipticity change vs. temperature.

**Atomic force microscopy (AFM).** AFM measurements were performed on Bruker AFM instrument under ambient conditions. Preformed complexes of **APA** and dT<sub>20</sub> were prepared by drop casting the sample solutions on the silicon (111) surface and air dried. AFM section analysis was done offline.

**Additional information for NMR spectra.** **APA** exhibit strong  $\pi$ - $\pi$  and hydrogen bonding interaction attributed to central perylene core and adenine moieties. Unlike our mutual templating studies of **APA** and **dB<sub>n</sub>** where we use relatively lower concentrations of **APA**, we need much higher concentration of **APA** for NMR study. At higher concentration (milligrams quantity) solubility of **APA** was poor. To enhance its solubility and to obtain good spectra we added trace amount of trifluoroacetic acid (TFA). It is known that TFA acts as hydrogen bond breaker (e.g., in case of many peptides). Thus, we were able to record good <sup>1</sup>H and <sup>13</sup>C NMR spectra. NMR peaks at 110.7, 113.6, 116.4, 119.3, 157.8, 158.3, 158.6, 159.0 ppm values corresponding TFA in <sup>13</sup>C are not reported in the <sup>13</sup>C NMR data of **APA**.

**Computational studies.** All the model systems were built using Gauss View 05<sup>62</sup> and Visual molecular dynamics (VMD)<sup>63</sup> softwares. Initially perylenebisimide (PBI) monomer was built, and optimized at the M06 level<sup>64</sup> along with the 6-31+G\* basis set using the Gaussian 09 suite of programs<sup>65</sup> and using semi empirical PM7 level of theory<sup>66</sup> using the MOPAC2012 program.<sup>67</sup> M06 and PM7 methods were chosen since they have been shown to account for dispersion type non-bonded interactions.<sup>58,68</sup> PBI and **APA** monomers, and respective dimers were built using the optimized PBI molecule in Gauss View 05.

## 6.18 References

1. Jeffrey, G. A.; Saenger, W. *Hydrogen Bonding in Biological Structures*, Springer, Berlin, **1991**.
2. Meyers, M. A.; Chen, P. Y.; Lin, A. Y. M.; Seki, Y. *Biological materials: Structure and mechanical properties*. *Prog. Mater. Sci.* **2008**, *53*, 1–206.
3. Whitesides, G. M.; Grzybowski, B. Self-assembly at all scales. *Science* **2002**, *295*, 2418–2421.
4. Watson, J. D.; Crick, F. H. Molecular structure of nucleic acids; a structure for deoxyribose nucleic acid. *Nature* **1953**, *171*, 737-738.
5. Clayton, J.; Dennis, C. *50 Years of DNA*, Nature Publishing Group, Palgrave Macmillan, New York, **2003**.
6. Sivakova, S.; Rowan, S. J. Nucleobases as supramolecular motifs. *Chem. Soc. Rev.* **2005**, *34*, 9–21.
7. Sessler, J. L.; Lawrence, C. M.; Jayawickramarajah, J. Molecular recognition via base-pairing. *Chem. Soc. Rev.* **2007**, *36*, 314–325.
8. Seeman, N. C. Nanomaterials based on DNA. *Ann. Rev. Biochem.* **2010**, *79*, 65-87.
9. Narayanaswamy, N.; Avinash, M. B.; Govindaraju, T. Exploring hydrogen bonding and weak aromatic interactions induced assembly of adenine and thymine functionalised naphthalenediimides. *New J. Chem.* **2013**, *37*, 1302-1306.
10. Bhosale, S. V.; Jani, C. H.; Langford, S. J. Chemistry of naphthalene diimides. *Chem. Soc. Rev.* **2008**, *37*, 331-342.
11. Shao, H.; Nguyen, T.; Romano, N. C.; Modarelli, D. A.; Parquette, J. R. Self-assembly of 1-D n-type nanostructures based on naphthalene diimide-appended dipeptides. *J. Am. Chem. Soc.* **2009**, *131*, 16374-16376.
12. Sakai, N.; Bhosale, R.; Emery, D.; Mareda, J.; Matile, S. Supramolecular n/p-heterojunction photosystems with antiparallel redox gradients in electron- and hole-transporting pathways. *J. Am. Chem. Soc.* **2010**, *132*, 6923-6925.

13. Bhosale, R.; Misek, J.; Sakai, N.; Matile, S. Supramolecular n/p-heterojunction photosystems with oriented multicolored antiparallel redox gradients (OMARG-SHJs). *Chem. Soc. Rev.* **2010**, *39*, 138-149.
14. Holman, G. G.; Zewail-Foote, M.; Rhoden-Smith, A.; Johnson, K. A.; Iverson, B. L. A sequence-specific threading tetra-intercalator with an extremely slow dissociation rate constant. *Nat. Chem.* **2011**, *3*, 875-881.
15. Tu, S.; Kim, S. H.; Modarelli, D. A.; Parquette, J. R. Self-assembly of a donor-acceptor nanotube. A strategy to create bicontinuous arrays. *J. Am. Chem. Soc.* **2011**, *133*, 19125-19130.
16. Molla, M. R.; Ghosh, S. Hydrogen-bonding-mediated J-aggregation and white-light emission from a remarkably simple, single-component, naphthalenediimide chromophore. *Chem. Eur. J.* **2012**, *18*, 1290-1294.
17. Shimizu, T.; Iwaura, R.; Masuda, M.; Hanada, T.; Yase, K. Internucleobase-interaction-directed self-assembly of nanofibers from homo- and heteroditopic 1, $\omega$ -nucleobase bolaamphiphiles. *J. Am. Chem. Soc.* **2001**, *123*, 5947-5955.
18. Iwaura, R.; Yoshida, K.; Masuda, M.; Kameyama, M. O.; Yoshida, M.; Shimizu, T. Oligonucleotide-templated self-assembly of nucleotide bolaamphiphiles: DNA-like nanofibers edged by a double-helical arrangement of A-T base pairs. *Angew. Chem. Int. Ed.* **2003**, *42*, 1009-1012.
19. Iwaura, R.; Shimizu, T. Reversible Photochemical Conversion of Helicity in Self-Assembled Nanofibers from a 1, $\omega$ -Thymidylic Acid Appended Bolaamphiphile. *Angew. Chem.* **2006**, *118*, 4717-4720.
20. Iwaura, R.; Hoeben, F. J. M.; Masuda, M.; Schenning, A. P. H. J.; Meijer, E. W.; Shimizu, T. Molecular-level helical stack of a nucleotide-appended oligo(p-phenylenevinylene) directed by supramolecular self-assembly with a complementary oligonucleotide as a template. *J. Am. Chem. Soc.* **2006**, *128*, 13298-13304.
21. Iwaura, R.; Kikkawa, Y.; Kameyama, M. O.; Shimizu, T. Effects of oligoDNA template length and sequence on binary self-assembly of a nucleotide bolaamphiphile. *Org. Biomol. Chem.* **2007**, *5*, 3450-3455.
22. Iwaura, R.; Kameyama, M. O.; Iizawa, T. Construction of helical J-aggregates self-assembled from a thymidylic acid appended anthracene dye and DNA as a template. *Chem. Eur. J.* **2009**, *15*, 3729-3735.
23. Wang, M.; Silva, G. L.; Armitage, B. A. DNA-Templated formation of a helical Cyanine dye J-aggregate. *J. Am. Chem. Soc.* **2000**, *122*, 9977-9986.

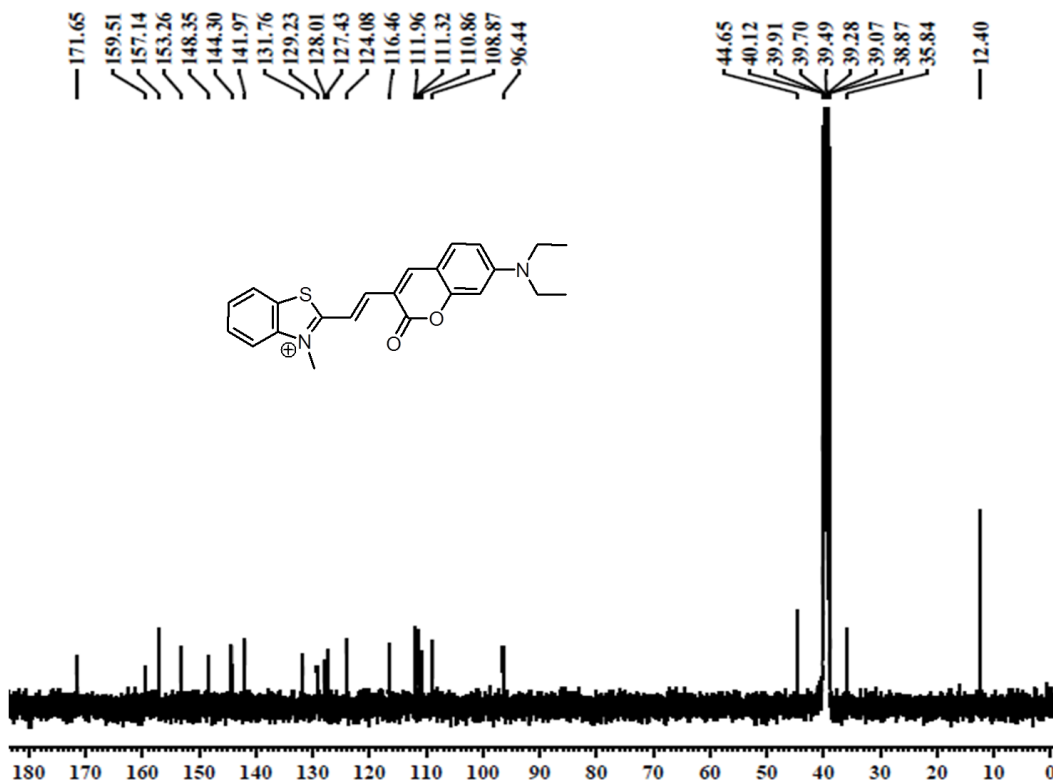
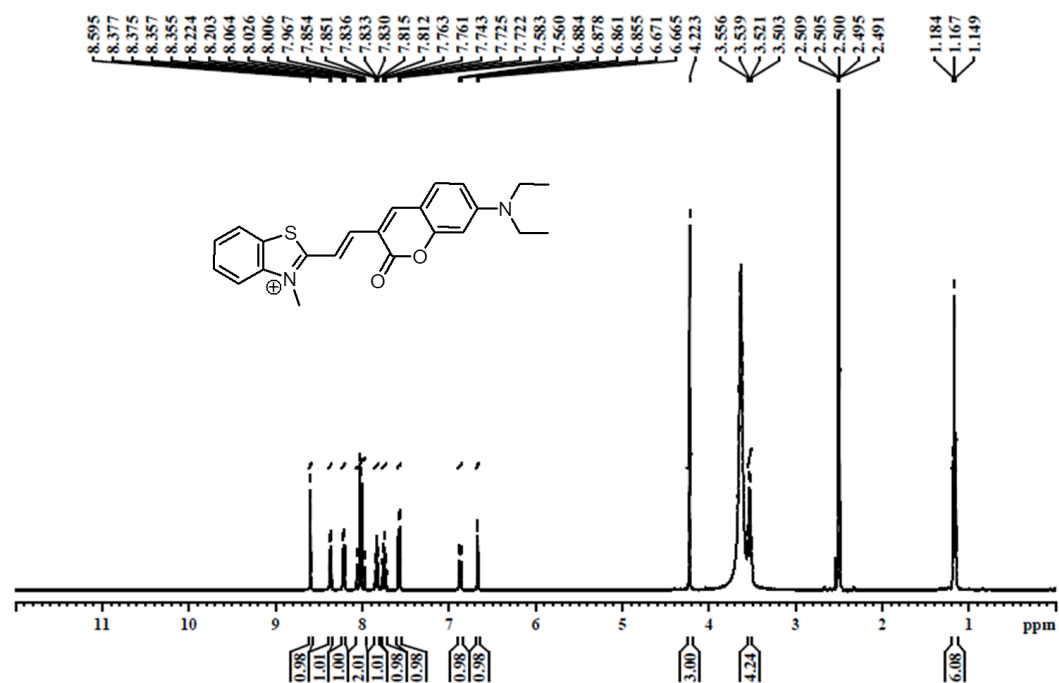
24. Hannah, K. C.; Armitage, B. A. DNA-templated assembly of helical cyanine dye aggregates: a supramolecular chain polymerization. *Acc. Chem. Res.* **2004**, *37*, 845-853.
25. Benveniste, A. L.; Creeger, Y.; Fisher, G. W.; Ballou, B.; Waggoner, A. S.; Armitage, B. A. Fluorescent DNA nanotags: supramolecular fluorescent labels based on intercalating dye arrays assembled on nanostructured DNA templates. *J. Am. Chem. Soc.* **2007**, *129*, 2025–2034.
26. Avinash, M. B.; Govindaraju, T. A bio-inspired design strategy: Organization of tryptophan-appended naphthalenediimide into well-defined architectures induced by molecular interactions. *Nanoscale*, **2011**, *3*, 2536-2543.
27. Avinash, M. B.; Govindaraju, T. Engineering molecular organization of Naphthalenediimides: large nanosheets with metallic conductivity and Attoliter containers. *Adv. Funct. Mater.* **2011**, *21*, 3875-3882.
28. Pandeeswar, M.; Avinash, M. B.; Govindaraju, T. Chiral transcription and retentive helical memory: probing peptide auxiliaries appended with naphthalenediimides for their one-dimensional molecular organization. *Chem. Eur. J.* **2012**, *18*, 4818–4822.
29. Avinash, M. B.; Govindaraju, T. Amino acid derivatized arylenediimides: a versatile modular approach for functional molecular materials. *Adv. Mater.* **2012**, *24*, 3905-3922.
30. Avinash, M. B.; Verheggen, E.; Schmuck, C.; Govindaraju, T. Self-cleaning functional molecular materials. *Angew. Chem.* **2012**, *124*, 10470-10474.
31. Avinash, M. B.; Govindaraju, T. Extremely slow dynamics of an Abiotic helical assembly: unusual relevance to the secondary structure of proteins. *J. Phys. Chem. Lett.* **2013**, *4*, 583-588.
32. Nielsen, P. E.; Egholm, M.; Berg, R. H.; Buchardt, O. Sequence-selective recognition of DNA by strand displacement with a thymine-substituted polyamide. *Science* **1991**, *254*, 1497–1500.
33. Dueholm, K. L.; Egholm, M.; Behrens, C.; Christensen, L.; Hansen, H. F.; Vulpius, T.; Petersen, K. H.; Berg, R. H.; Nielsen, P. E.; Buchardt, O. Synthesis of peptide nucleic acid monomers containing the four natural nucleobases: Thymine, Cytosine, Adenine, and Guanine and their oligomerization. *J. Org. Chem.* **1994**, *59*, 5767–5773.
34. Ganesh, K. N.; Nielsen, P. E. Peptide Nucleic Acids: analogs and derivatives. *Curr. Org. Chem.* **2000**, *4*, 1931–1943.
35. Govindaraju, T.; Gonnade, R. G.; Bhadbhade, M. M.; Kumar, V. A.; Ganesh, K. N. (1S,2R/1R,2S)-aminocyclohexyl glyceryl thymine PNA: synthesis, monomer crystal structures, and DNA/RNA hybridization studies. *Org. Lett.* **2003**, *5*, 3013–3016.
36. Govindaraju, T.; Kumar, V. A.; Ganesh, K. N. (SR/RS)-cyclohexanyl PNAs: conformationally preorganized PNA analogues with unprecedented preference for duplex formation with RNA. *J. Am. Chem. Soc.* **2005**, *127*, 4144–4145.

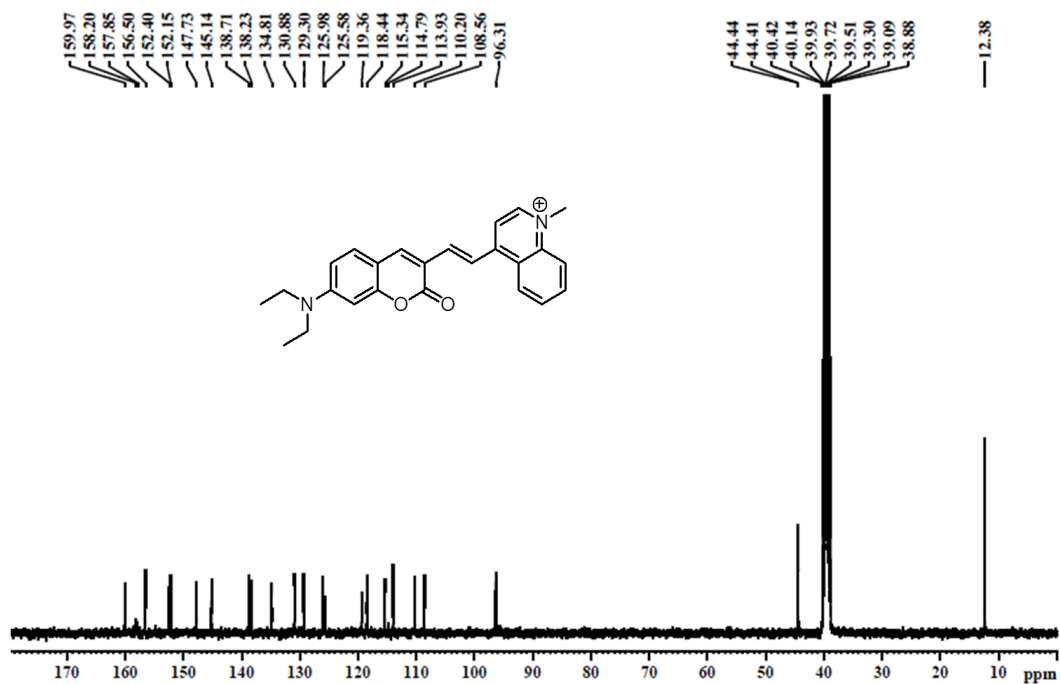
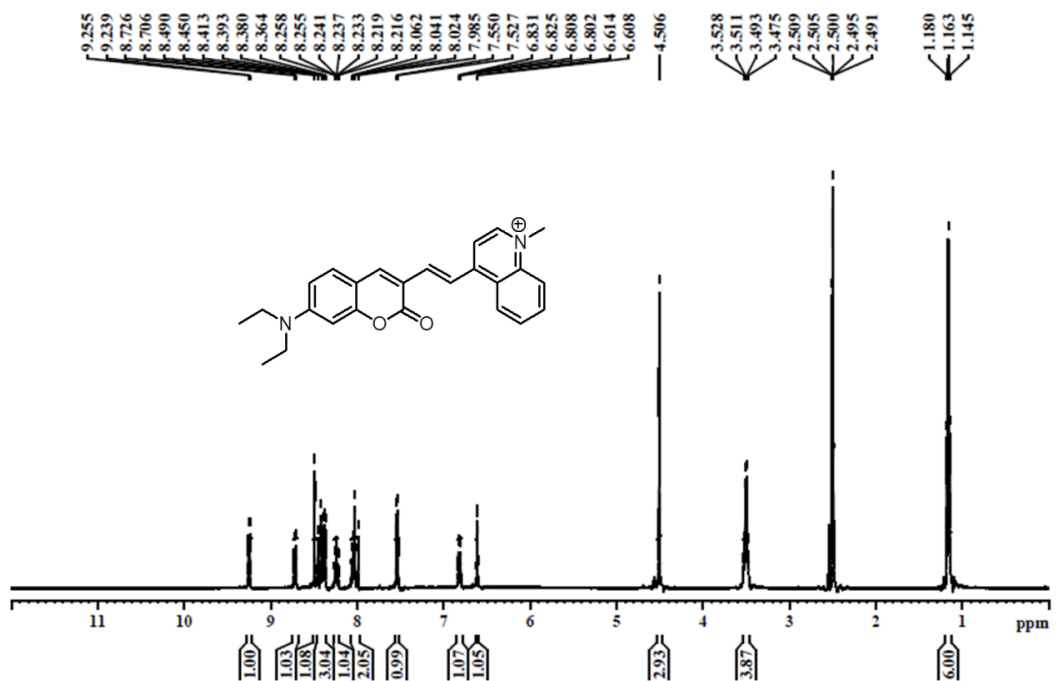
37. Govindaraju, T.; Avinash, M. B. Two-dimensional nanoarchitectonics: organic and hybrid materials. *Nanoscale* **2012**, *4*, 6102-6117.
38. Rao, P.; Ghosh, S.; Maitra, U. Binding of 9-*N*-Butyladenine by carboxylic acids: evidence that Hoogsteen binding can dominate in solution. *J. Phys. Chem. B.* **1999**, *103*, 4528-4533.
39. Basilio Janke, E. M.; Limbach, H. H.; Weisz, K. Binding of an acetic acid ligand to adenosine: a low-temperature NMR study. *J. Am. Chem. Soc.* **2004**, *126*, 2135-2141.
40. Hershey, A.; Chase, M. Independent functions of viral protein and nucleic acid in growth of bacteriophage. *J. Gen. Physiol.* **1952**, *36*, 39-56.
41. Blackburn, G. M.; Gait, M. J.; Loakes, D.; Williams, D. M. *Nucleic Acids in Chemistry and Biology*. RSC Publishing, Cambridge, UK, **2006**.
42. Genereux, J. G.; Barton, J. K. Mechanisms for DNA charge transport. *Chem. Rev.* **2010**, *110*, 1642-1662.
43. Ruiz-Carretero, A.; Janssen, P. G. A.; Kaeser, A.; Schenning, A. P. H. J. DNA-templated assembly of dyes and extended  $\pi$ -conjugated systems. *Chem. Commun.* **2011**, *47*, 4340-4347.
44. Nakamura, M.; Okaue, T.; Takada, T.; Yamana, K. DNA-templated assembly of naphthalenediimide arrays. *Chem. Eur. J.* **2012**, *18*, 196-201.
45. Singer, A.; Rapireddy, S.; Ly, D. H.; Mellar, A. Electronic barcoding of a viral gene at the single-molecule level. *Nano Lett.* **2012**, *12*, 1722-1728.
46. Teo, Y. N.; Kool, E. T. DNA-multichromophore systems. *Chem. Rev.* **2012**, *112*, 4221-4245.
47. Narayanaswamy, N.; Suresh, G.; Priyakumar, U. D.; Govindaraju, T. Double zipper helical assembly of deoxyoligonucleotides: mutual templating and chiral imprinting to form hybrid DNA ensembles. *Chem. Commun.* **2015**, *51*, 5493-5496.
48. Rich, A.; Davies, D. R.; Crick, F. H. C.; Watson, J. D. The molecular structure of polyadenylic acid. *J. Mol. Biol.* **1961**, *3*, 71-86.
49. Chakraborty, S.; Sharma, S.; Maiti, P. K.; Krishnan, Y. The poly dA helix: a new structural motif for high performance DNA-based molecular switches. *Nucleic Acids Res.* **2009**, *37*, 2810-2817.
50. Verma, S.; Mishra, A. K.; Kumar, J. The many facets of adenine: coordination, crystal patterns, and catalysis. *Acc. Chem. Res.* **2010**, *43*, 79-91.
51. Suda, T.; Mishima, Y.; Asakura, H.; Kominami, R. Formation of a parallel-stranded DNA homoduplex by d(GGA) repeat oligonucleotides. *Nucleic Acids Res.* **1995**, *23*, 3771-3777.
52. Shiber, M. C.; Braswell, E. H.; Klump, H.; Fresco, J. R. Duplex-tetraplex equilibrium between a hairpin and two interacting hairpins of d(A-G)<sub>10</sub> at neutral pH. *Nucleic Acids Res.* **1996**, *24*, 5004-5012.

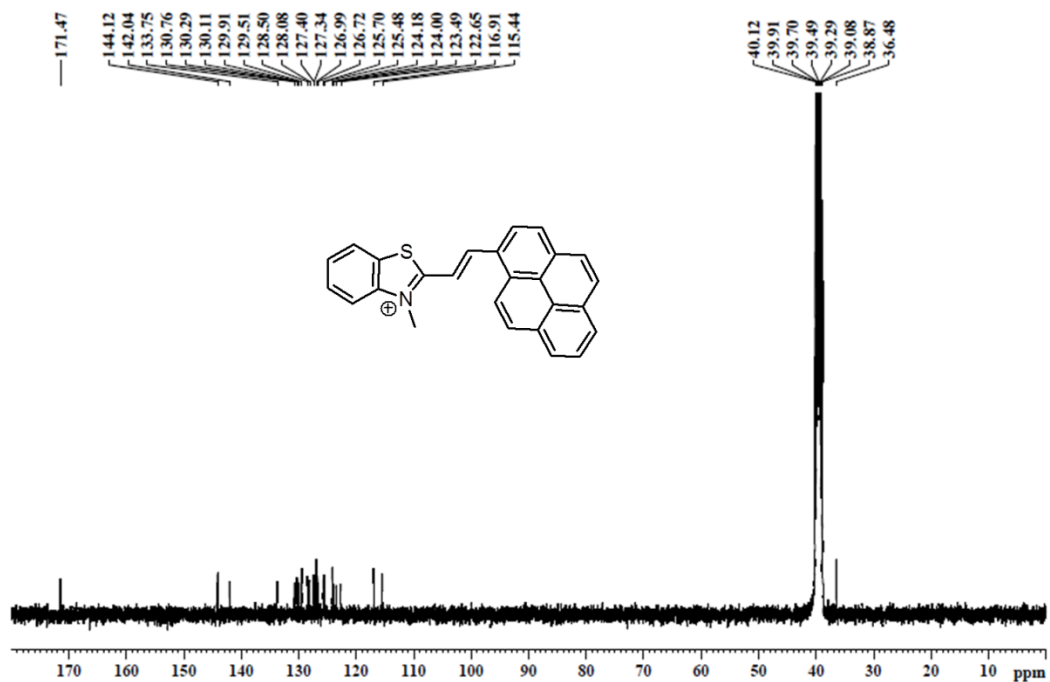
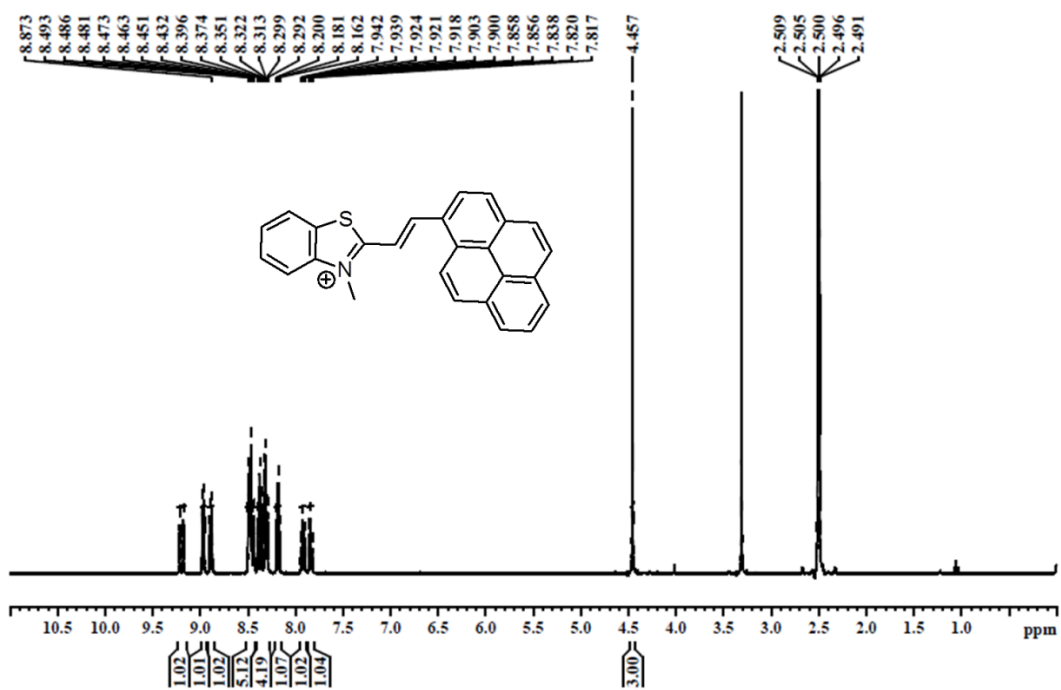


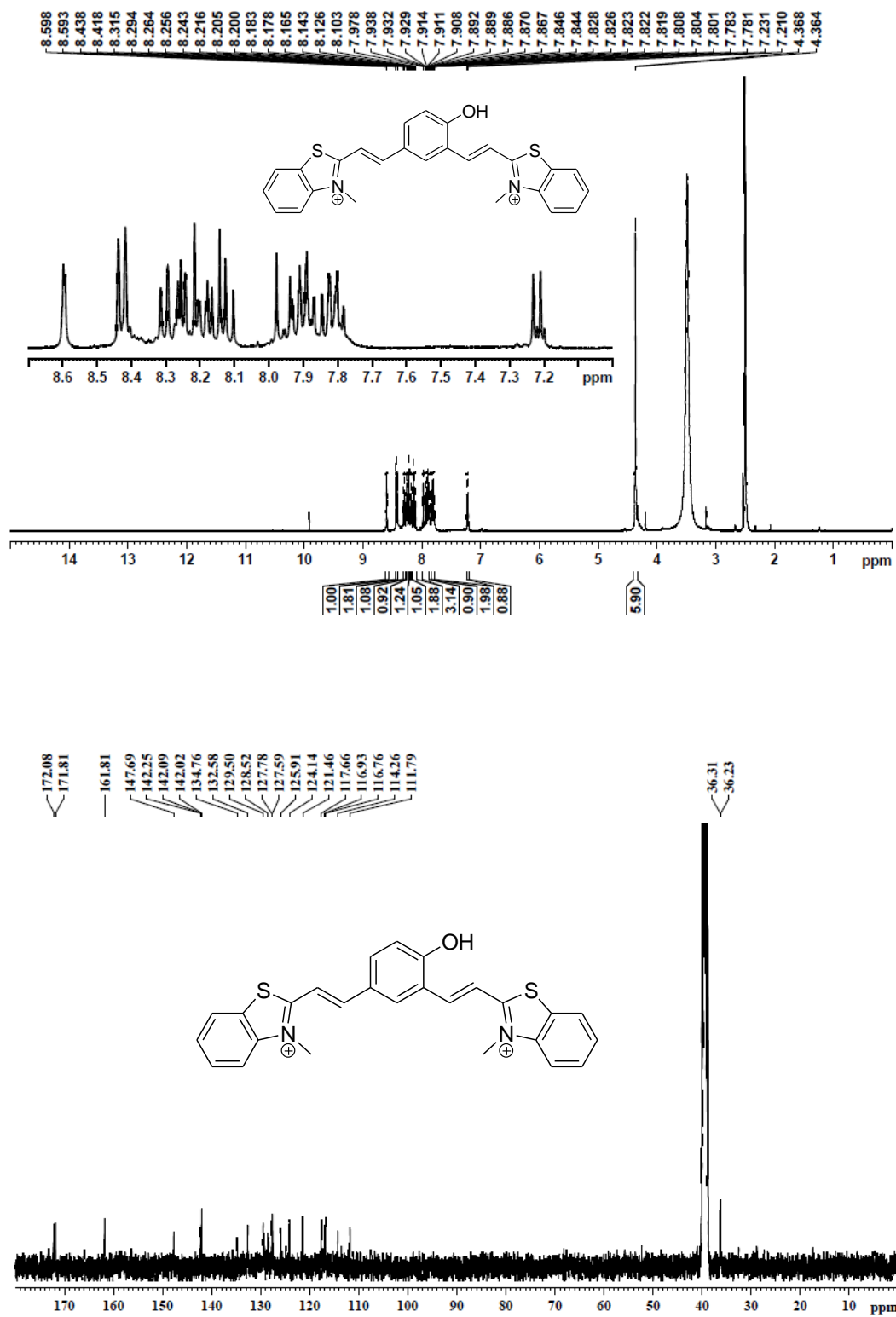
- 
53. Würthner, F. Perylene bisimide dyes as versatile building blocks for functional supramolecular architectures. *Chem. Commun.* **2004**, 1564-1579.
54. Avinash, M. B.; Govindaraju, T. Amino acid derivatized arylenediimides: a versatile modular approach for functional molecular materials. *Adv. Mater.* **2012**, *24*, 3905-3922.
55. Li, M.; Zhao, C.; Yang, X.; Ren, J.; Qu, X. In situ monitoring Alzheimer's disease  $\beta$ -amyloid aggregation and screening of A $\beta$  inhibitors using a perylene probe. *Small* **2013**, *9*, 52-55.
56. Wang, W.; Wan, W.; Zhou, H. H.; Niu, S.; Li, A. D. Q. Alternating DNA and pi-conjugated sequences. Thermophilic foldable polymers. *J. Am. Chem. Soc.* **2003**, *125*, 5248-5249.
57. Zheng, Y.; Long, H.; Schatz, G. C.; Lewis, F. D. A cooperative beads-on-a-string approach to exceptionally stable DNA triplexes. *Chem. Commun.* **2006**, 3830-3832.
58. Manchineella, S.; Prathyusha, V.; Priyakumar, U. D.; Govindaraju, T. Solvent-induced helical assembly and reversible chiroptical switching of chiral cyclic-dipeptide-functionalized naphthalenediimides. *Chem. Eur. J.* **2013**, *19*, 16615-16624.
59. Balakrishnan, K.; Datar, A.; Oitker, R.; Chen, H.; Zuo, J. M.; Zang, L. Nanobelt self-assembly from an organic n-type semiconductor: propoxyethyl-PTCDI. *J. Am. Chem. Soc.* **2005**, *127*, 10496-10497.
60. Janssen, P. G. A.; Jabbari-Farouji, S.; Surin, M.; Vila, X.; Gielen, J. C.; de Greef, J. T. F. A.; Vos, M. R. J.; Bomans, P. H. H.; Sommerdijk, N. A. J. M.; Christianen, P. C. M.; Leclère, P. H.; Lazzaroni, R.; van der Schoot, P.; Meijer, E. W.; Schenning, A. P. H. J. Insights into templated supramolecular polymerization: binding of naphthalene derivatives to ssDNA templates of different lengths. *J. Am. Chem. Soc.* **2009**, *131*, 1222-1231.
61. Gehring, K.; Leroy, J. L.; Guéron, M. A tetrameric DNA structure with protonated cytosine-cytosine base pairs. *Nature* **1993**, *363*, 561-565.
62. Dennington, R.; Keith, T.; Millam, J. *Semichem Inc.*, Shawnee Mission KS, *GaussView Version 5*, **2009**.
63. Humphrey, W.; Dalke, A.; Schulten, K. VMD: Visual molecular dynamics. *J. Molec. Graphics.* **1996**, *14*, 33-38.
64. Zhao, Y.; Truhlar, D. G. The M06 suite of density functionals for main group thermochemistry, thermochemical kinetics, non-covalent interactions, excited states, and transition elements: two new functionals and systematic testing of four M06-class functionals and 12 other functionals. *Theor. Chem. Acc.* **2008**, *120*, 215-241.
65. Frisch, M. J.; Trucks, G. W.; Schlegel, H. B.; Scuseria, G. E.; Robb, M. A.; Cheeseman, J. R.; Scalmani, G.; Barone, V.; Mennucci, B.; Petersson, G. A.; Nakatsuji, H.; Caricato, M.; Li, X.; Hratchian, H. P.; Izmaylov, A. F.; Bloino, J.; Zheng, G.; Sonnenberg, J. L.; Hada, M.; Ehara, M.;
-

- Toyota, K.; Fukuda, R.; Hasegawa, J.; Ishida, M.; Nakajima, T.; Honda, Y.; Kitao, O.; Nakai, H.; Vreven, T.; Montgomery, Jr.; J. A.; Peralta, J. E.; Ogliaro, F.; Bearpark, M.; Heyd, J. J.; Brothers, E.; Kudin, K. N.; Staroverov, V. N.; Keith, T.; Kobayashi, R.; Normand, J.; Raghavachari, K.; Rendell, A.; Burant, J. C.; Iyengar, S. S.; Tomasi, J.; Cossi, M.; Rega, N.; Millam, J. M.; Klene, M.; Knox, J. E.; Cross, J. B.; Bakken, V.; Adamo, C.; Jaramillo, J.; Gomperts, R.; Stratmann, R. E.; Yazyev, O.; Austin, A. J.; Cammi, R.; Pomelli, C.; Ochterski, J. W.; Martin, R. L.; Morokuma, K.; Zakrzewski, V. G.; Voth, G. A.; Salvador, P.; Dannenberg, J. J.; Dapprich, S.; Daniels, A. D.; Farkas, O.; Foresman, J. B.; Ortiz, J. V.; Cioslowski, J. Fox, D. J. Gaussian 09, Revision C.01, Gaussian, Inc., Wallingford CT, **2009**.
66. Stewart, J. J. Optimization of parameters for semiempirical methods VI: more modifications to the NDDO approximations and re-optimization of parameters. *J. Mol. Model.* **2013**, *19*, 1-32.
67. Stewart, J. J. P. Stewart Computational Chemistry. Colorado Springs, CO, USA, MOPAC2012, **2012**, 151.
68. Zhao, Y.; Truhlar, D. G. Computational characterization and modeling of buckyball tweezers: density functional study of concave-convex pi...pi interactions. *Phys Chem Chem Phys.* **2008**, *10*, 2813-2818.

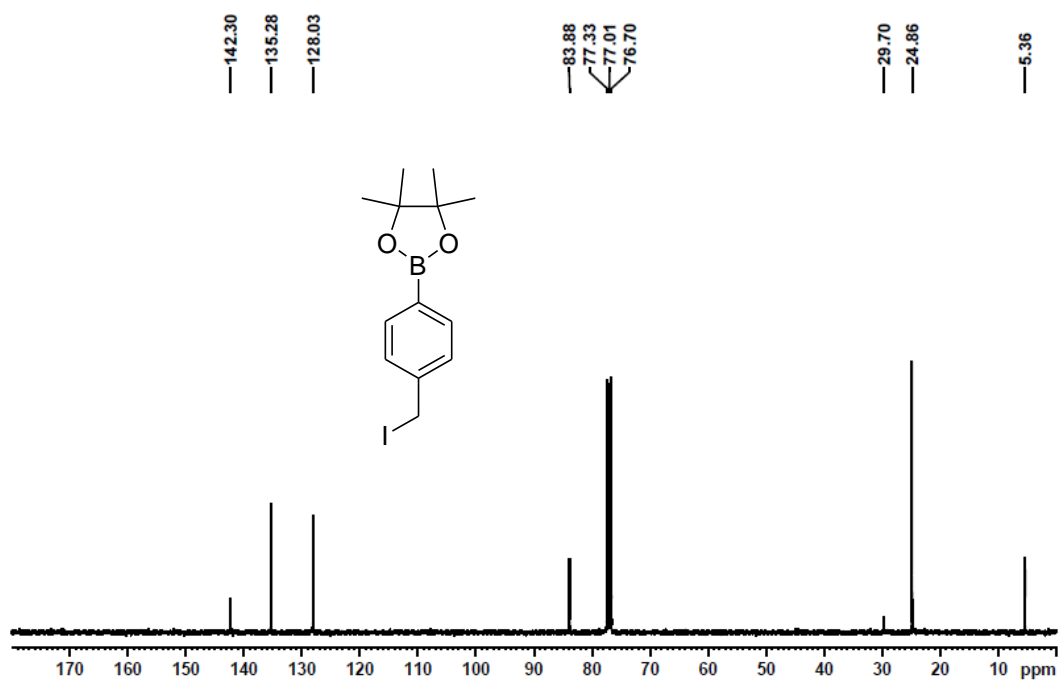
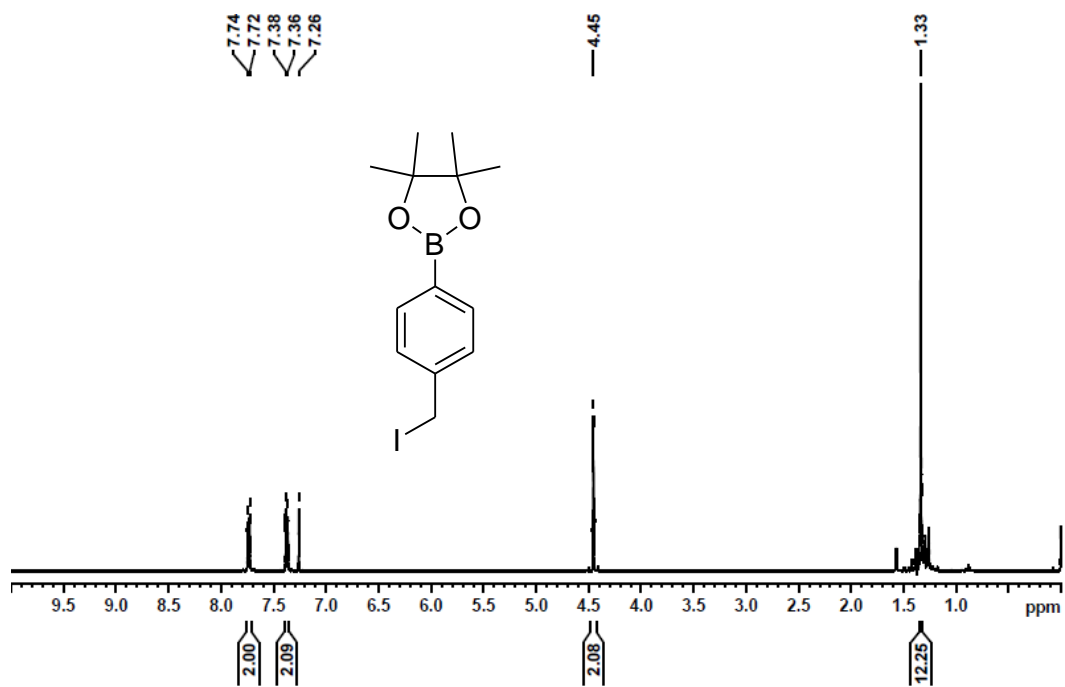
$^1\text{H}$  and  $^{13}\text{C}$  NMR spectra of probe TC

$^1\text{H}$  and  $^{13}\text{C}$  NMR spectra of probe CL

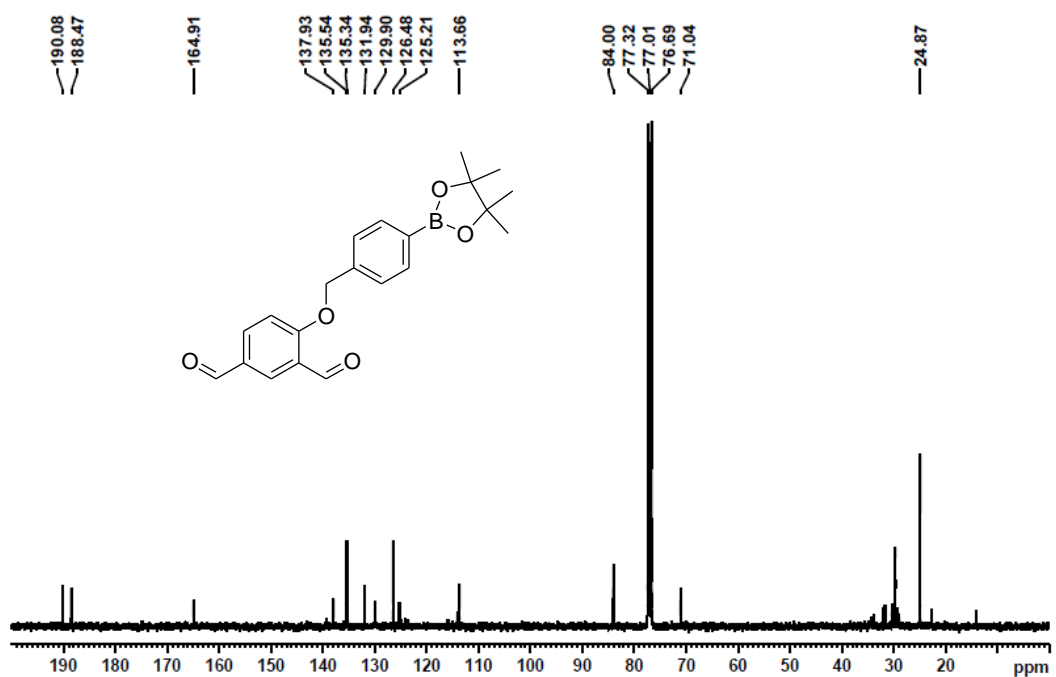
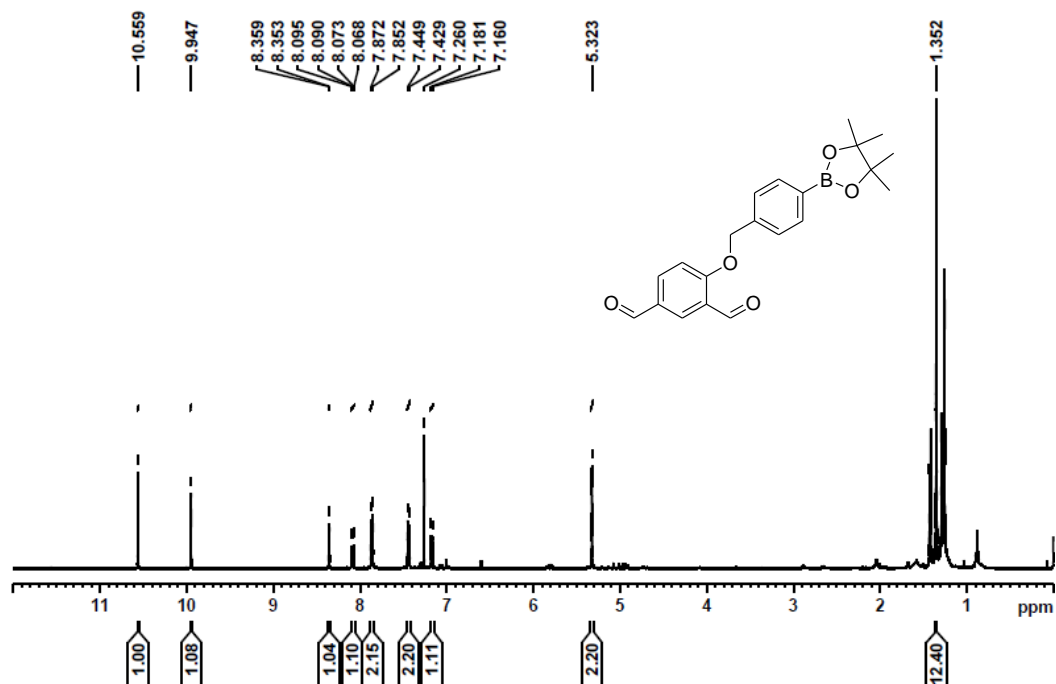
$^1\text{H}$  and  $^{13}\text{C}$  NMR spectra of probe TP

$^1\text{H}$  and  $^{13}\text{C}$  NMR spectra of QCy-DT

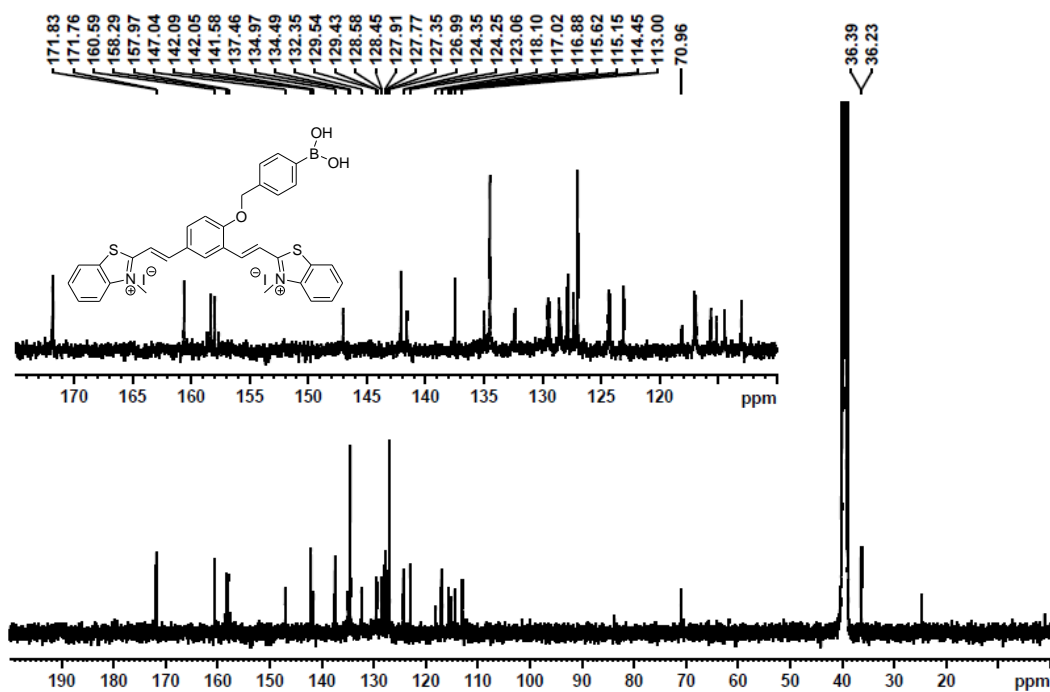
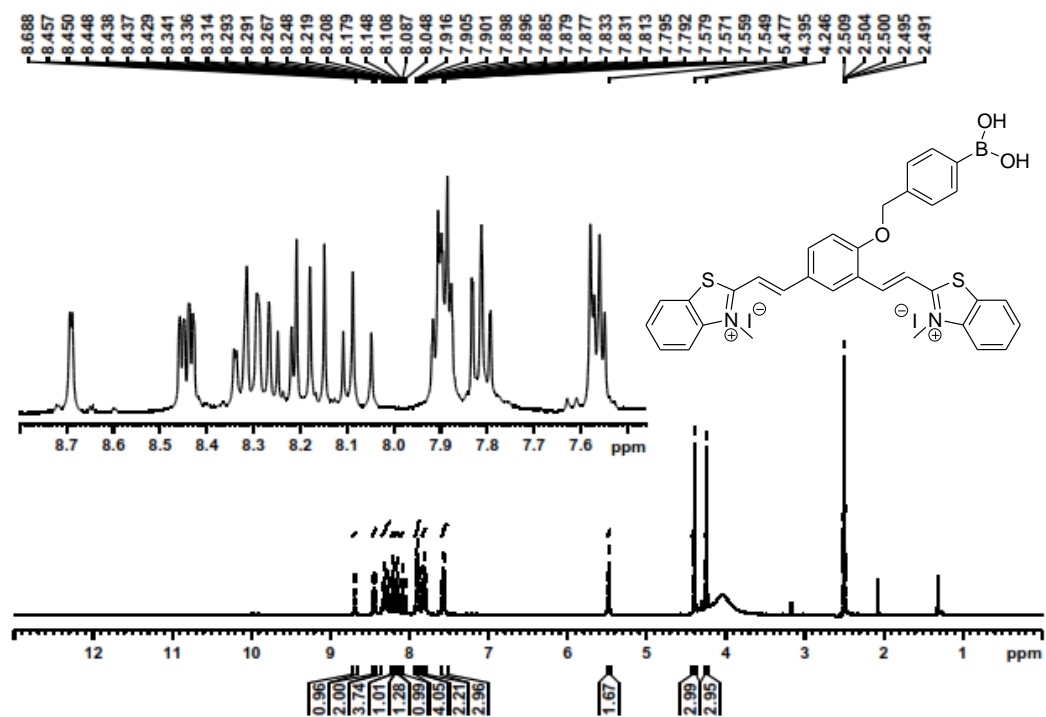
$^1\text{H}$  and  $^{13}\text{C}$  NMR spectra of 2-(4-(iodomethyl)phenyl)-4,4,5,5-tetramethyl-1,3,2-dioxaborolane (2)

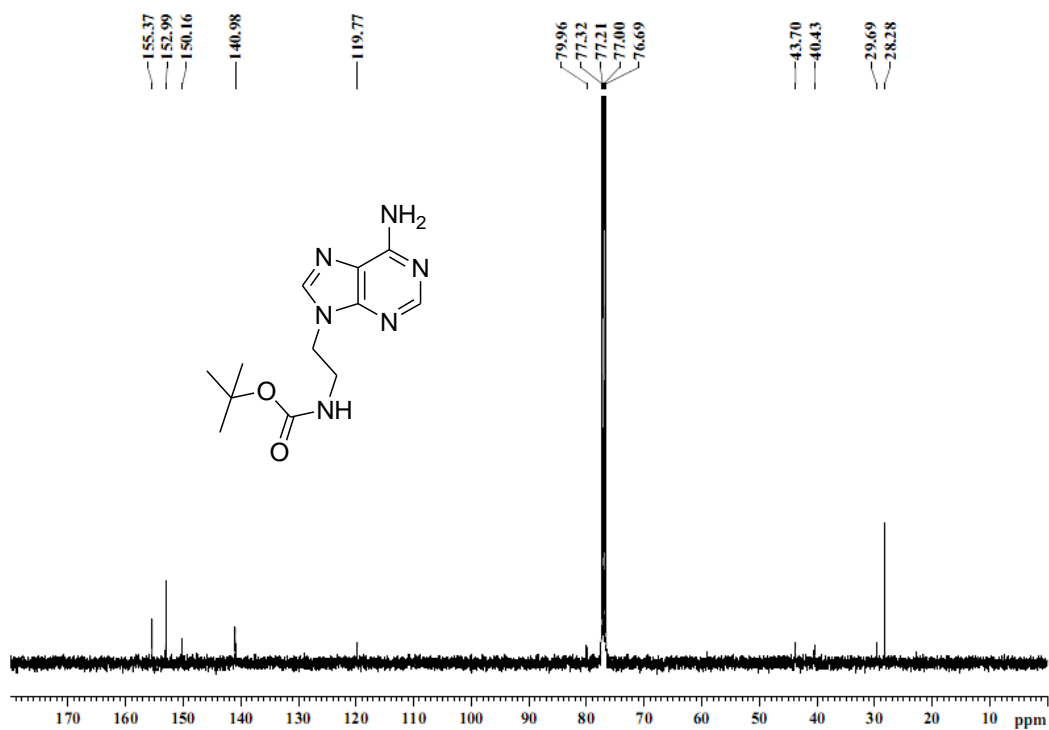
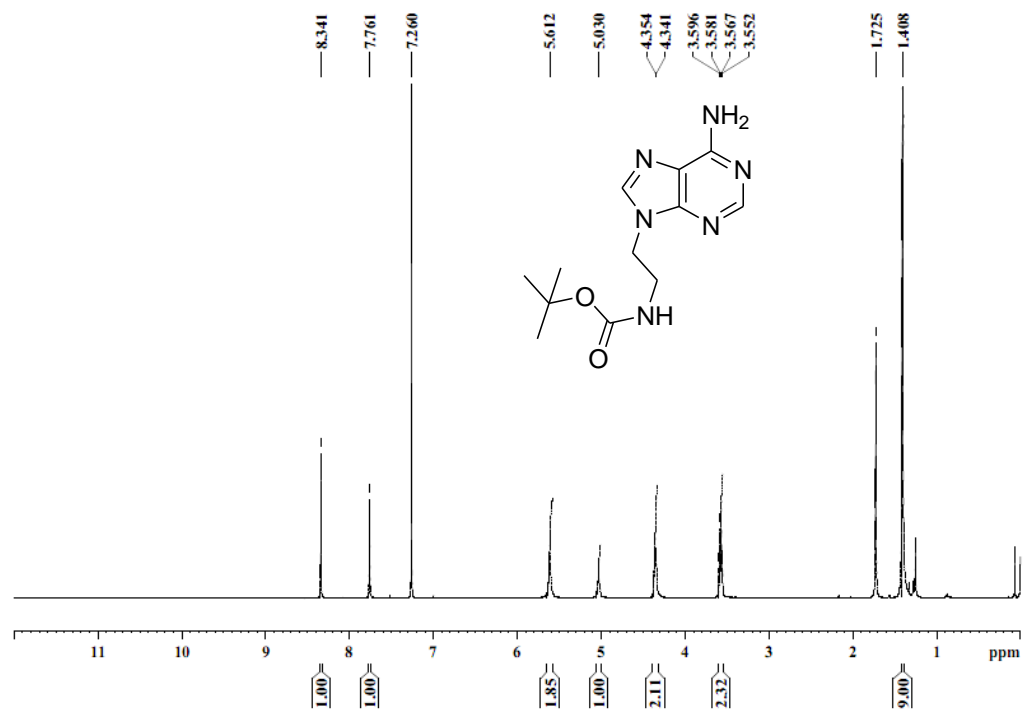


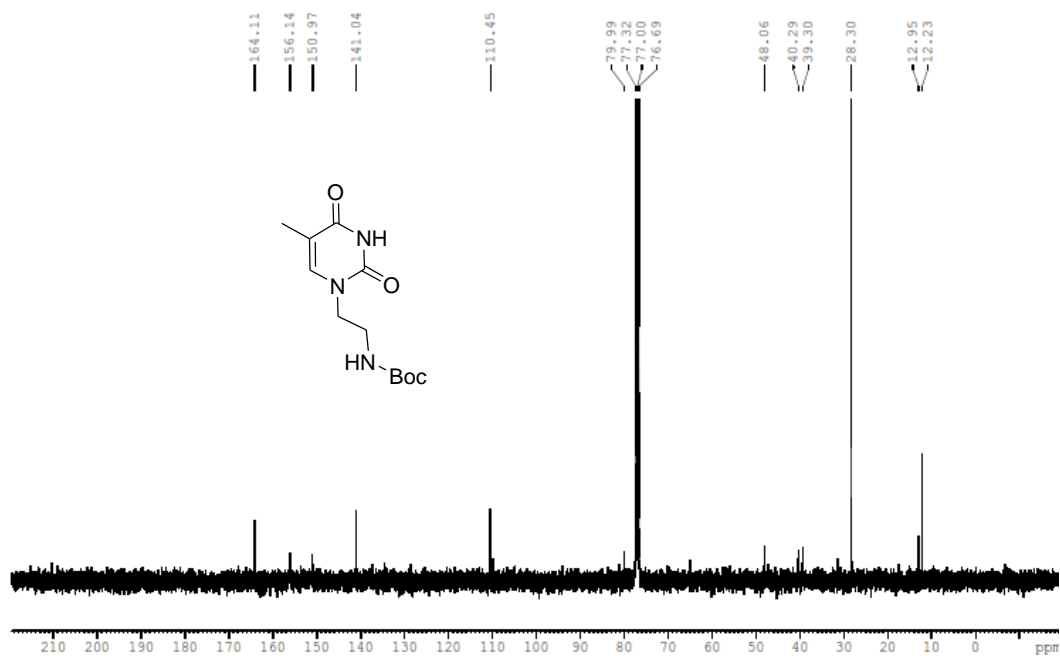
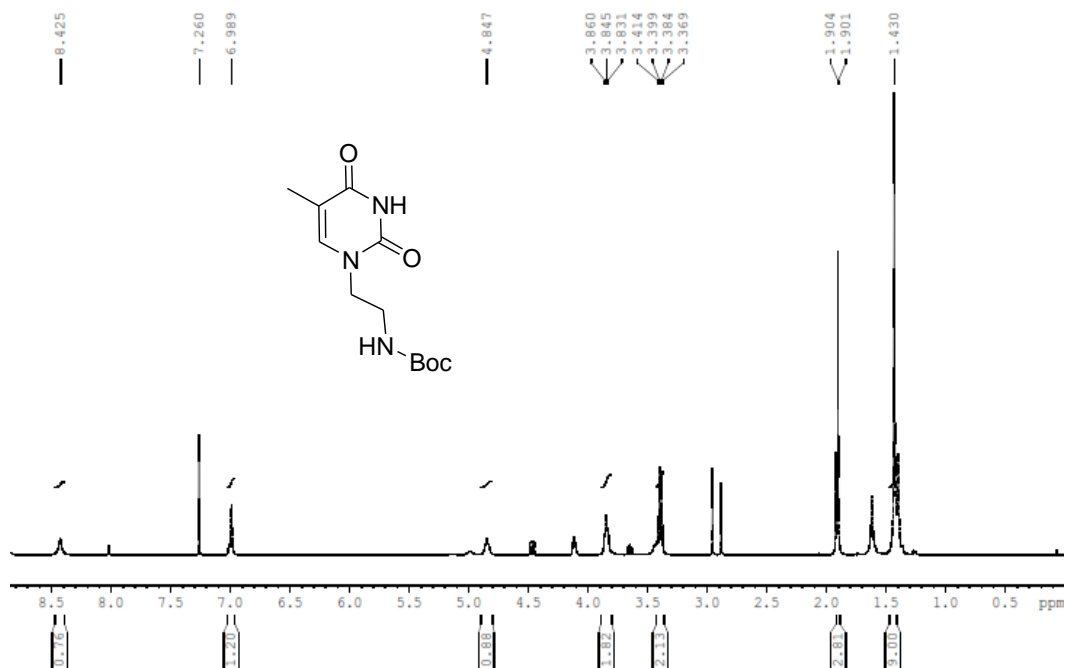
$^1\text{H}$  and  $^{13}\text{C}$  NMR spectra of 4-(4-(4,4,5,5-tetramethyl-1,3,2-dioxaborolan-2-yl)benzyloxy)isophthalaldehyde (3)

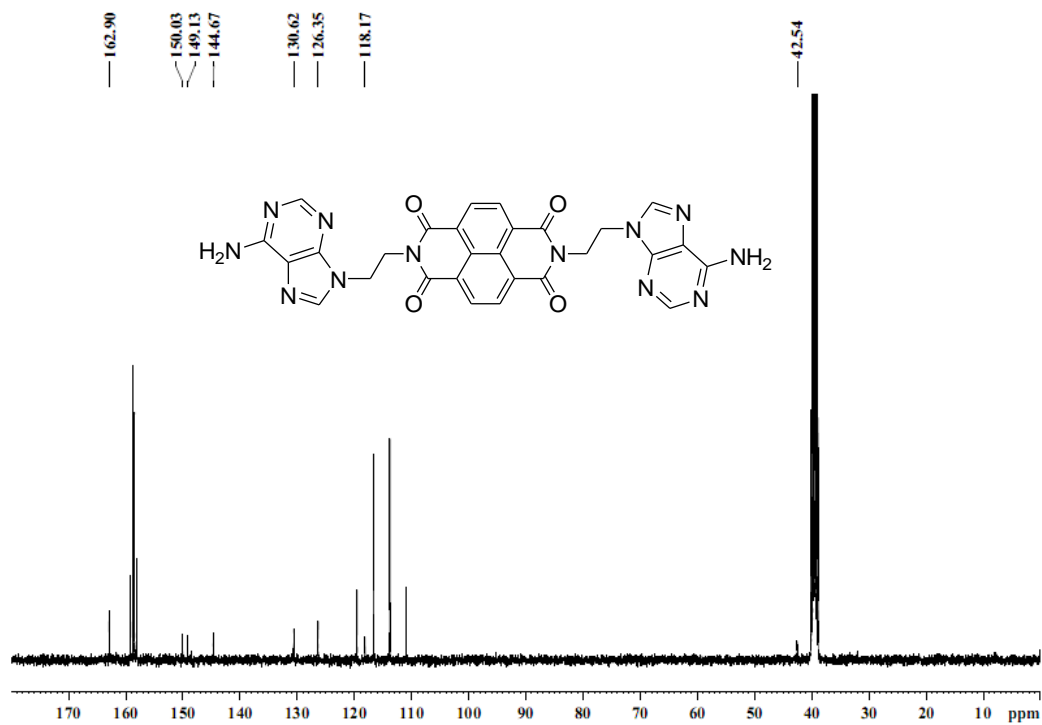
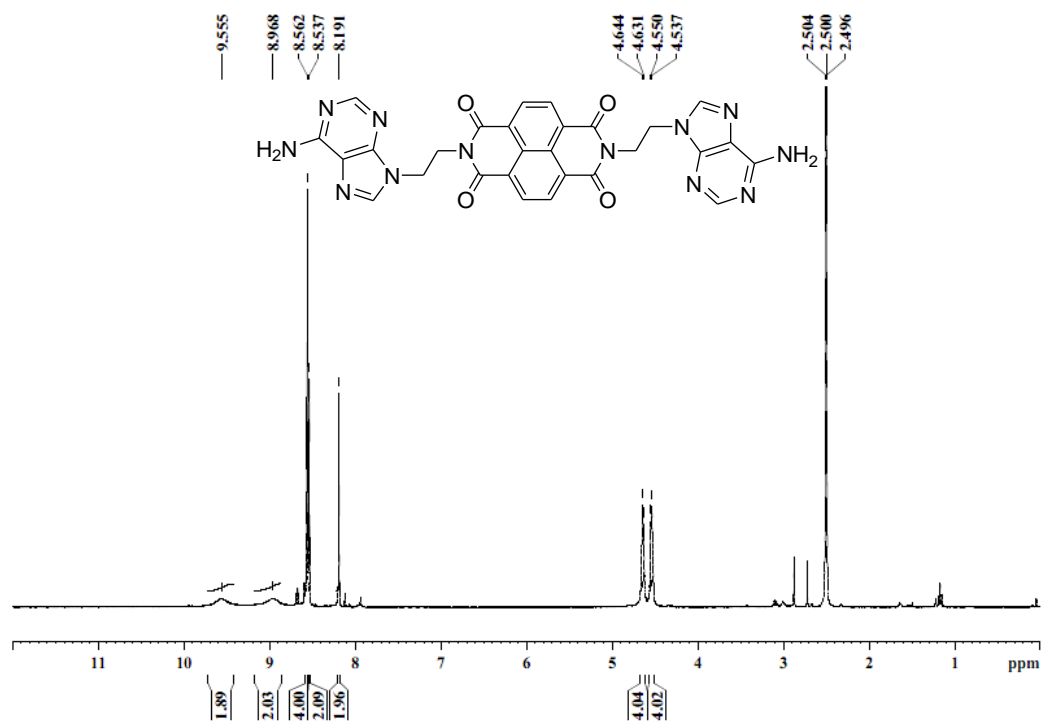


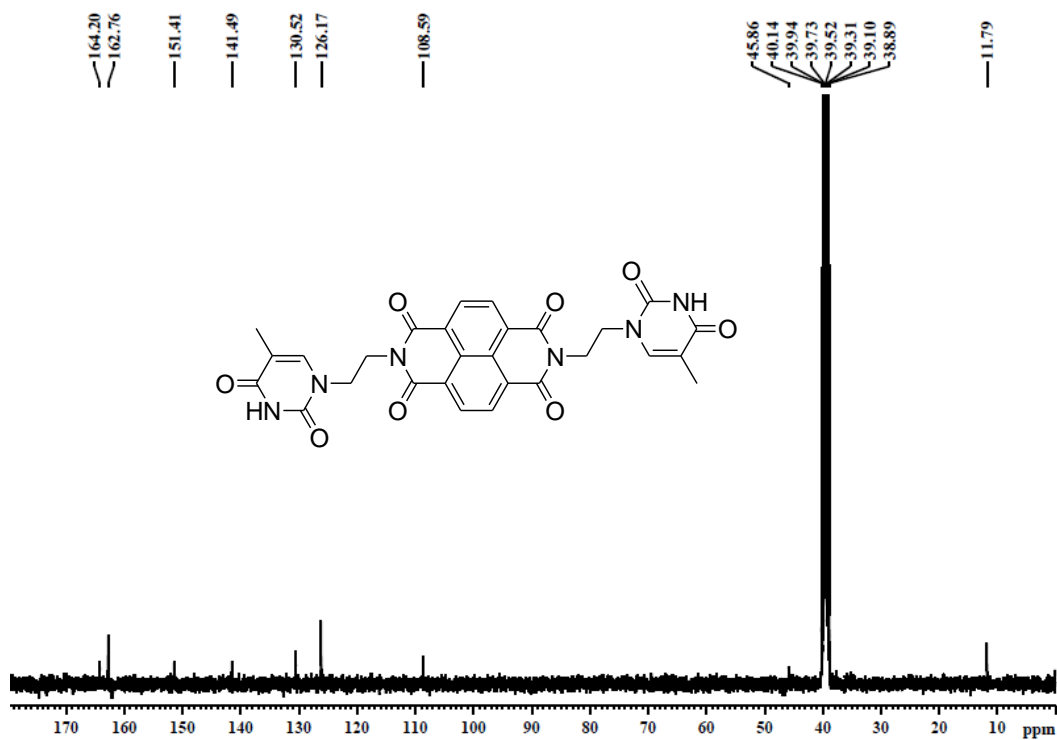
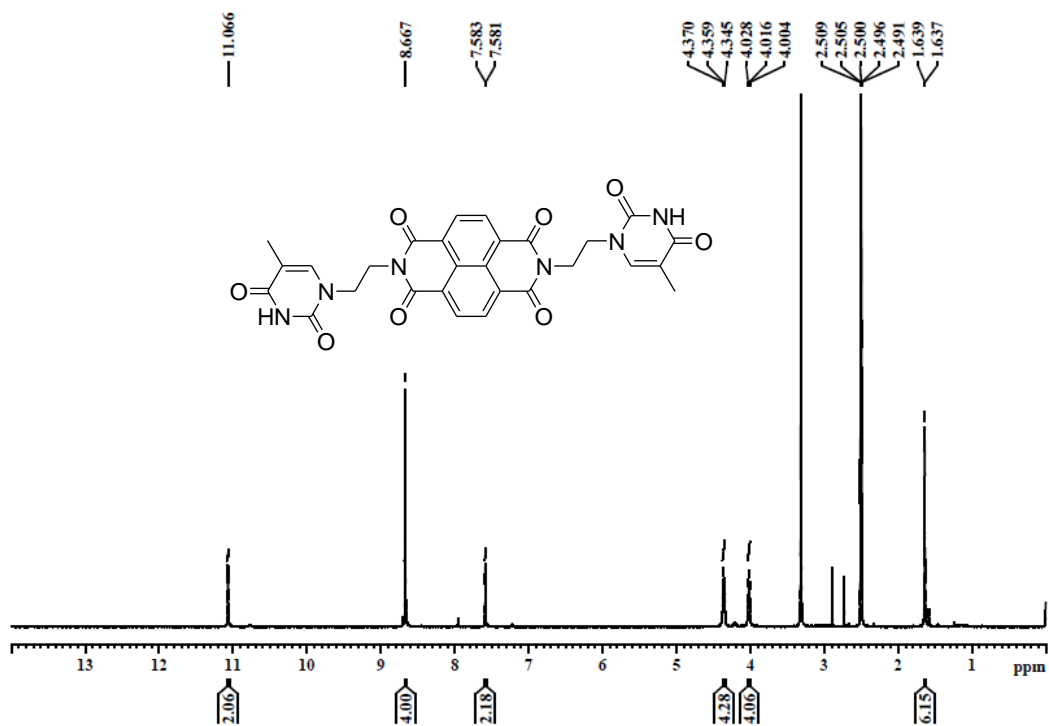


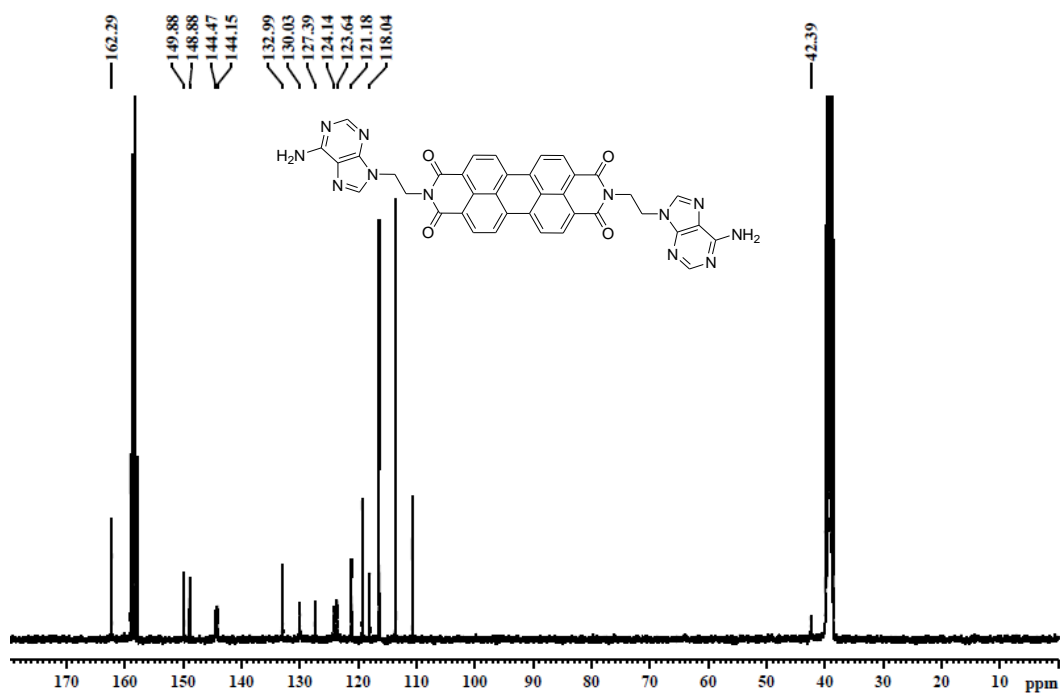
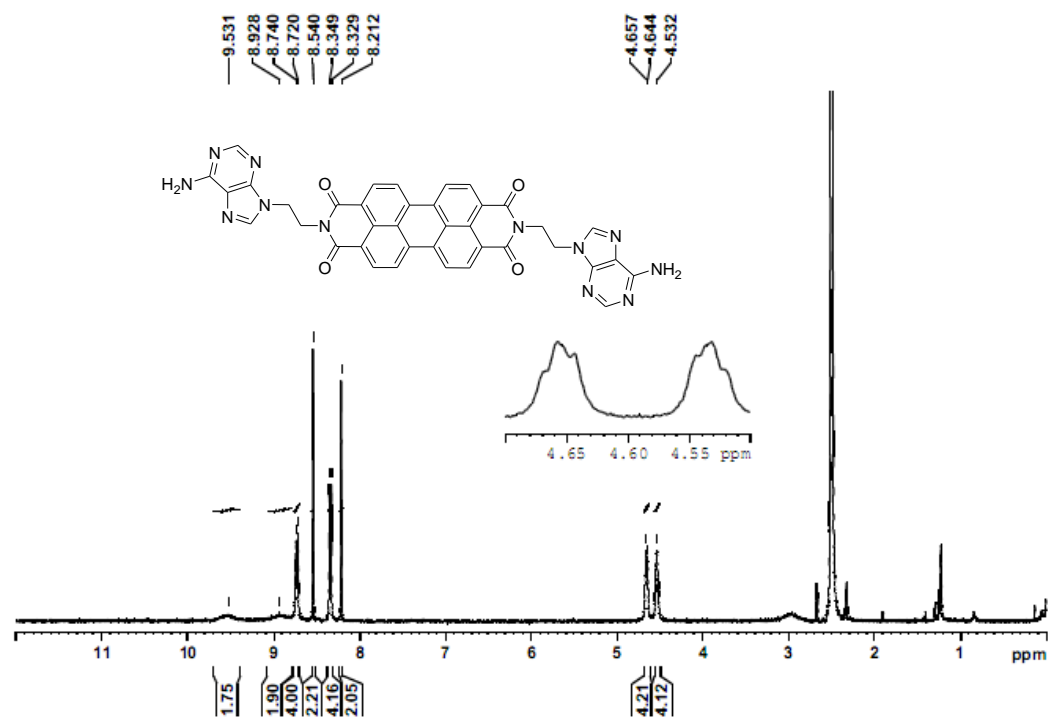
$^1\text{H}$  and  $^{13}\text{C}$  NMR spectra of QCy-BOH

$^1\text{H}$  and  $^{13}\text{C}$  NMR spectra of boc-protected adenine-9-ethyl amine (1)

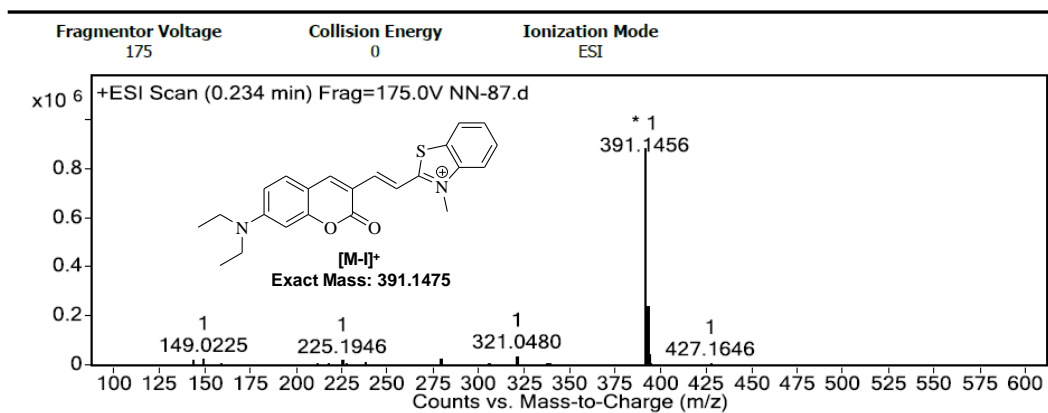
$^1\text{H}$  and  $^{13}\text{C}$  NMR spectra of boc-protected thyminy-1-ethyl amine (2)

$^1\text{H}$  and  $^{13}\text{C}$  NMR spectra of NDI-AA

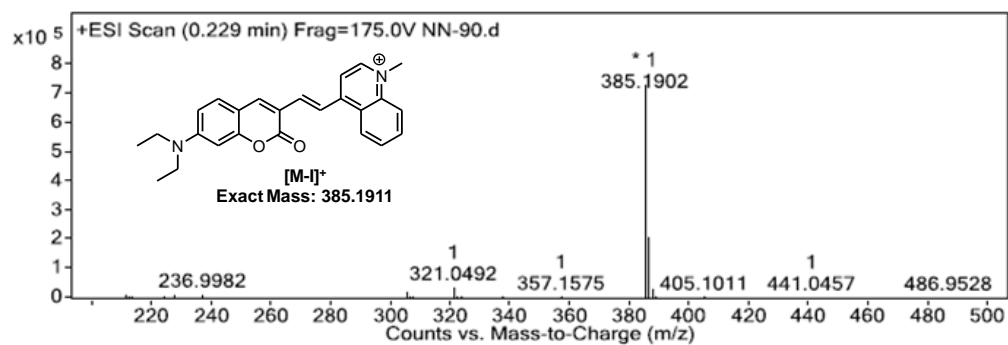
$^1\text{H}$  and  $^{13}\text{C}$  NMR spectra of NDI-TT

$^1\text{H}$  and  $^{13}\text{C}$  NMR spectra of APA

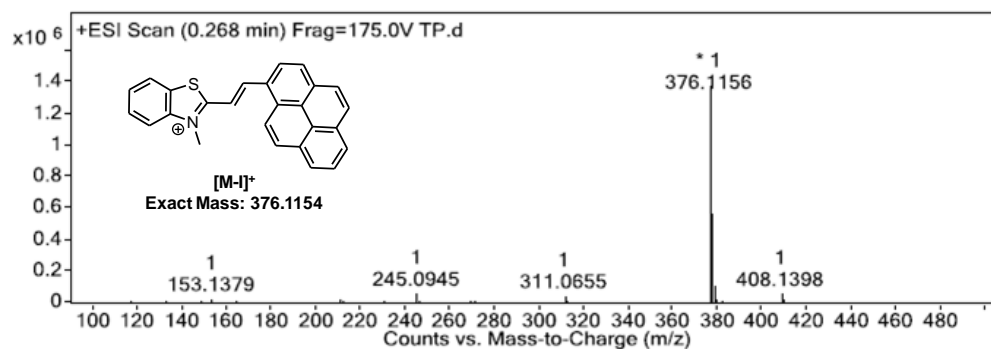
## HRMS spectrum of probe TC



## HRMS spectrum of probe CL

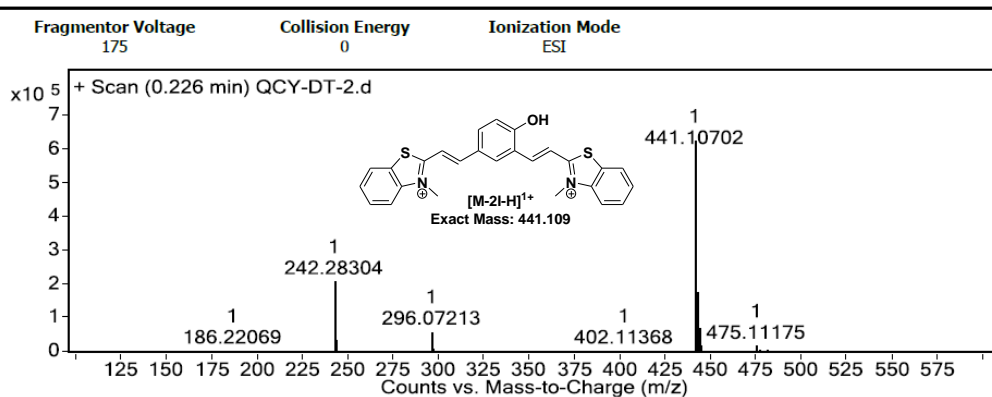


## HRMS spectrum of probe TP



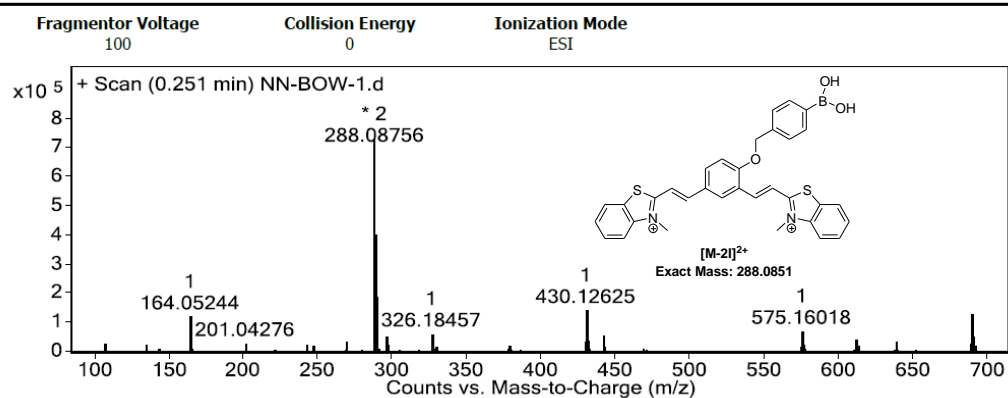
## HRMS spectrum of probe QCy-DT

## User Spectra

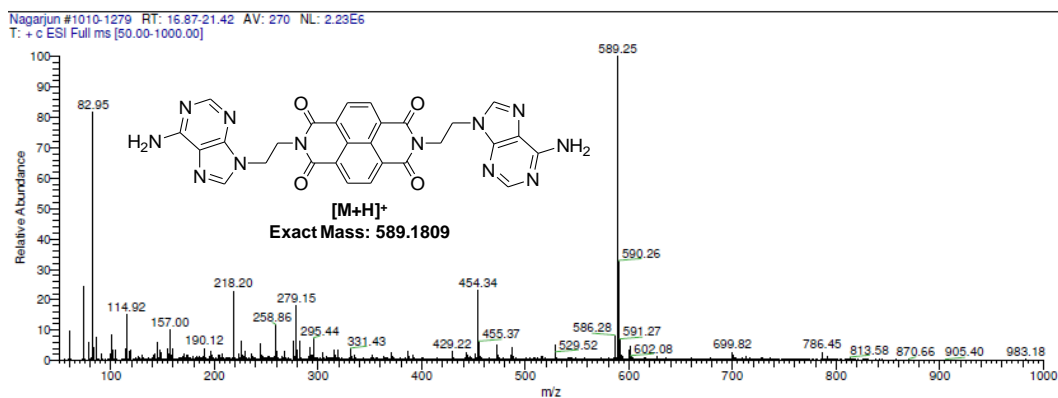


## HRMS spectrum of probe QCy-BOH

## User Spectra

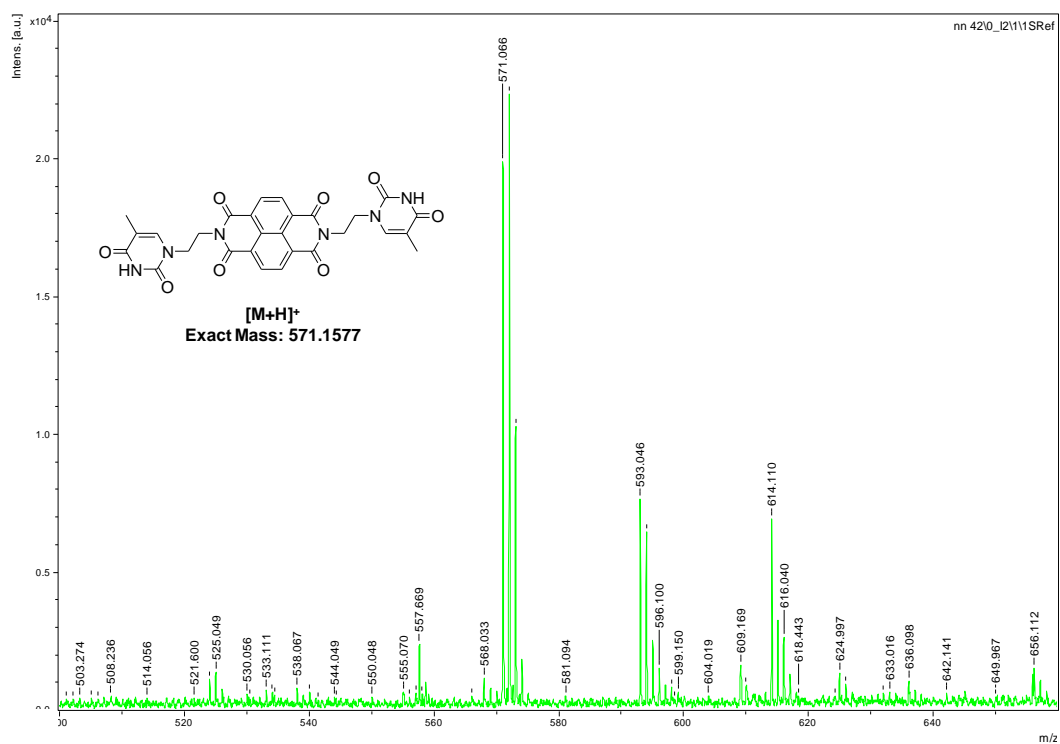


## LCMS spectrum of NDI-AA

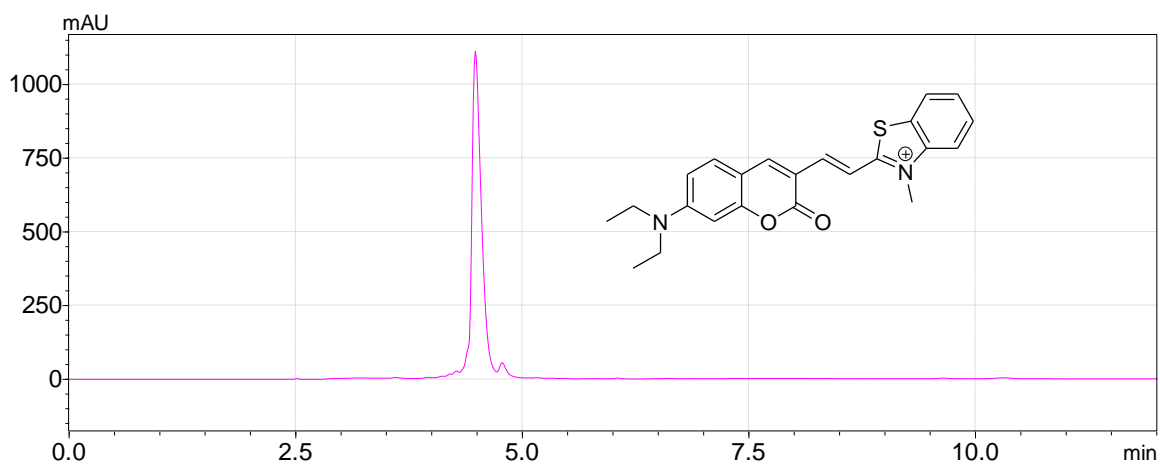


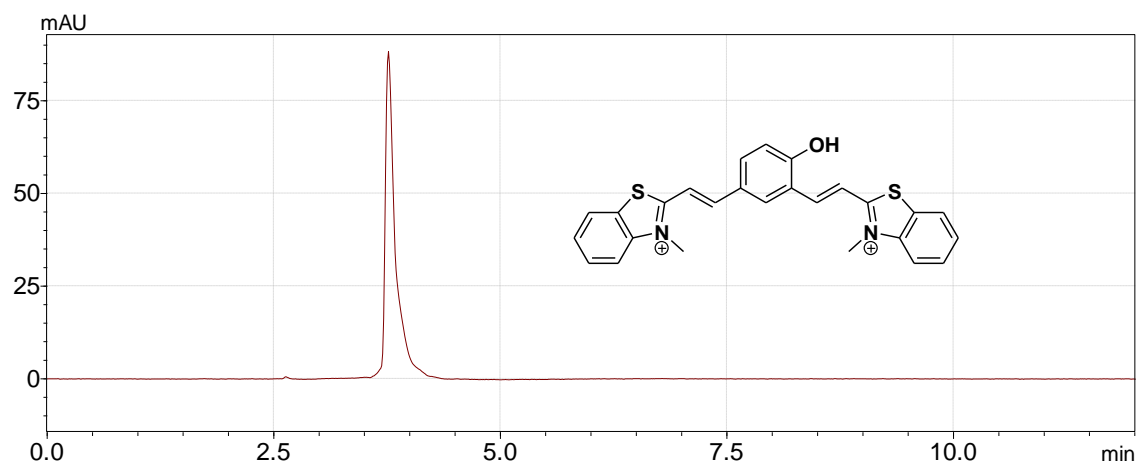
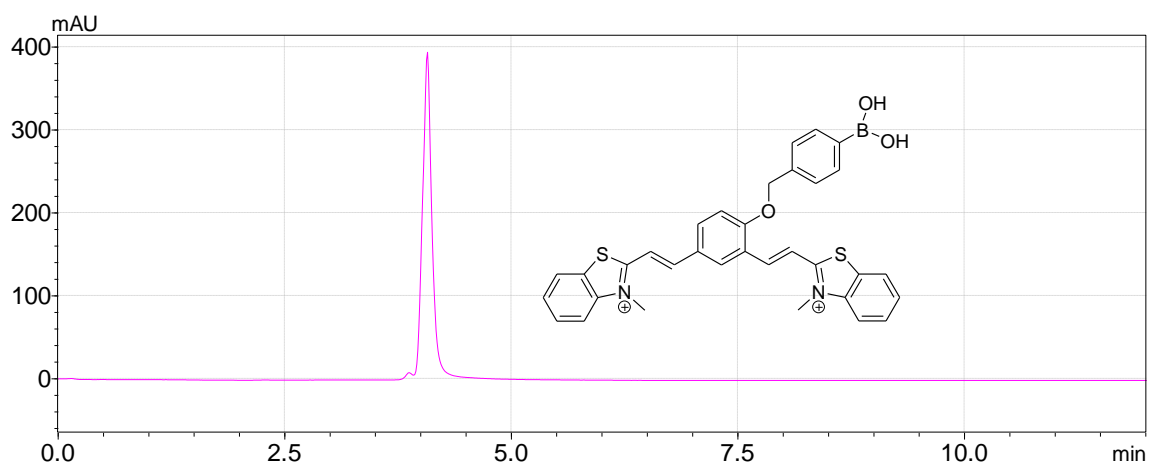


## MALDI spectrum of NDI-TT



## HPLC trace of probe TC



**HPLC trace of QCy-DT****HPLC trace of QCy-BOH**

---

---

## List of publications

- **Narayanaswamy, N.;** Avinash, M. B.; Govindaraju. T. Exploring hydrogen bonding and weak aromatic interactions induced assembly of adenine and thymine functionalised naphthalenediimides. *New J. Chem.* **2013**, *37*, 1302-1306.
- **Narayanaswamy, N.;** Kumar, M.; Das, S.; Sharma, R.; Samanta, P. K.; Pati, S. K.; Dhar, S. K.; Kundu, T. K.; Govindaraju. T. A thiazole coumarin (TC) turn-on fluorescence probe for AT-base pair detection and multipurpose applications in different biological systems. *Sci. Rep.* **2014**, *4*, 6476.
- **Narayanaswamy, N.;** Suresh, G.; Priyakumar, U. D.; Govindaraju. T. Double zipper helical assembly of deoxyoligonucleotides: mutual templating and chiral imprinting to form hybrid DNA ensembles. *Chem. Commun.* **2015**, *51*, 5493-5496.
- **Narayanaswamy, N.;** Unnikrishnan, M.; Gupta, M.; Govindaraju, T. Fluorescence reporting of G-quadruplex structures and modulating their DNAzyme activity using polyethylenimine-pyrene conjugate. *Bioorg. Med. Chem. Lett.* **2015**, *25*, 2395-2400.
- **Narayanaswamy, N.;** Das, S.; Samanta, P. K.; Banu, K.; Sharma, G. P.; Mondal, N.; Dhar, S. K.; Pati, S. K.; Govindaraju, T. Sequence-specific recognition of DNA minor groove by an NIR-fluorescence switch-on probe and its potential applications. (*Under revision*).
- **Narayanaswamy, N.;** Narra, S.; Nair, R. R.; Saini, D. K.; Kondaiah, P.; Govindaraju, T. Spatiotemporal cellular ROS targeting by stimuli responsive NIR fluorescence combination probe. (*To be communicated*).
- **Narayanaswamy, N.;** Govindaraju, T. Molecular beacon based DNA-switch for accurate and reversible pH sensing. (*To be communicated*).
- **Narayanaswamy, N.;** Govindaraju, T. Small molecule induced non-canonical secondary DNA structure of alternative guanine-adenine rich sequences. (*To be communicated*).

---

---

### Miscellaneous publications

- **Narayanaswamy, N.**; Maity, D.; Govindaraju, T. Reversible fluorescence sensing of  $Zn^{2+}$  based on pyridine-constrained bis(triazole-linked hydroxyquinoline) sensor. *Supramol. Chem.* **2011**, *23*, 703-709.
- **Narayanaswamy, N.**; Govindaraju, T. Aldazine-based colorimetric sensors for Cu(II) and Fe(III), *Sens. Actuators B: Chemical*, **2012**, *161*, 304 – 310.
- Rajasekhar, K.; **Narayanaswamy, N.**; Mishra, P.; Suresh, S. N.; Manjithaya, R.; Govindaraju, T. Synthesis of hybrid cyclic peptoids and identification of autophagy enhancer. *ChemPlusChem* **2014**, *79*, 25-30.
- Pandeewar, M.; Senanayak, S. P.; **Narayanaswamy, N.**; Narayan, K. S.; Govindaraju, T. Mutual templating of nucleobase conjugated naphthalenediimide (NDI) and Oligonucleotide ( $dT_n$ ) for ultrasensitive detection of  $Hg^{2+}$ . (*Under preparation*)
- Rajasekhar, K.; **Naryanaswamy, N.**; Murugan, N. A.; Kuang, G.; Ågren, H.; Govindaraju, T. An effective high affinity red fluorescent and colorimetric probe for Amyloid  $\beta$  aggregation. (*To be communicated*)

## Erratum

As per reviewer suggestions, we insert following text as erratum in the thesis preface “Subsequently in *fourth chapter*, we present phenyl boronic acid-functionalized quinone-cyanine (**QCy-BOH**) in combination with AT-rich DNA (exogenous or endogenous cellular DNA), *i.e.*, **QCy-BOH**⊂DNA as a stimuli-responsive NIR fluorescence probe for *in vitro* levels of H<sub>2</sub>O<sub>2</sub>. In response to cellular H<sub>2</sub>O<sub>2</sub> stimulus, **QCy-BOH** converts into **QCy-DT**, a one-donor-two-acceptor (D2A) system that exhibits switch-on NIR fluorescence upon binding to the DNA minor groove. Fluorescence studies and glucose oxidase (GOx) assay confirmed the high efficiency of the combination probe **QCy-BOH**⊂DNA for probing H<sub>2</sub>O<sub>2</sub> generated *in situ* through GOx-mediated glucose oxidation. Quantitative analysis through the fluorescence plate reader, flow cytometry and live imaging approaches showed that **QCy-BOH** is a promising probe to detect the normal as well as elevated levels of H<sub>2</sub>O<sub>2</sub> produced by EGF/Nox pathways in live cells.” (Page VIII, line 1)